

UNIVERSITÀ
DEGLI STUDI
DI PADOVA

Head Office: Università degli Studi di Padova

Department of Biology

Ph.D. COURSE IN BIOSCIENCES

CURRICULUM: Biochemistry & Biotechnology

SERIES: XXXIV

**Exploring the Pathogenesis of the
Neurodegenerative Disease Friedreich's Ataxia:
an Integrated Molecular, Biochemical and Cell
Biology Approach**

Coordinator: *Prof. Ildikò Szabò*

Supervisor: *Prof. Paola Costantini*

Co-Supervisor: *Prof. Donatella Carbonera*

Ph.D. student: *Davide Doni*

*“We shall not cease from exploration
And the end of all our exploring
Will be to arrive where we started
And know the place for the first time”*

T.S. ELIOT, *Four Quartets*, 1942

Contents

Summary	1
Part I - Introduction	5
Chapter 1. Insight into Mitochondrial Architecture and Functions	7
1.1 Structure-Function Relationship in Mitochondria	7
1.2 Oxidative Phosphorylation.....	11
1.2.1 Respiratory Chain Complexes.....	12
1.2.1.1 Complex I or NADH:Ubiquinone Oxidoreductase	13
1.2.1.2 Complex II or Succinate:Ubiquinone Oxidoreductase.....	15
1.2.1.3 Complex III or Ubiquinol:Cytochrome <i>c</i> Reductase.....	16
1.2.1.4 Complex IV or Cytochrome <i>c</i> Oxidase	17
1.2.2 Respiratory Chain Supercomplexes	18
Chapter 2. Mitochondrial Diseases	25
2.1 Pathophysiology of Human Mitochondrial Diseases.....	25
2.2 Occurrence, Clinical Features and Syndromes.....	28
Chapter 3. Friedreich's Ataxia	31
3.1 Phenotypic Traits	31
3.2 Genetics and Molecular Basis of the Disease	32
3.3 Mitochondrial Pathophysiology	35
3.3 Therapeutic Approaches.....	37
3.3.1 Antioxidants and Enhancer of Energy Metabolism	38
3.3.2 Iron Chelators	38
3.3.3 Frataxin Increase and Gene Therapy.....	39
Chapter 4. Frataxin	41
4.1 Frataxin Sequence Conservation	41
4.2 Cellular Localization and Mitochondrial Maturation	42

4.3 Folding and Structure.....	43
4.3.1 The Effect of Point Mutations on Protein Structure	45
4.3.2 Iron-Binding Properties.....	47
4.4 Frataxin, a Moonlighting Protein.....	49
4.4.1 The Involvement in Iron Metabolism as an Iron-Storage Protein.....	49
4.4.2 The Role in the Oxidative Stress	51
4.4.3 The Participation in the Biosynthesis of Iron Cofactors	53
4.4.3.1 Chemistry and Biochemistry of Heme and Iron-Sulfur Clusters	54
4.4.3.2 The Interaction with Ferrochelatase in Heme Biogenesis.....	57
4.4.3.3 The Role in Iron-Sulfur Cluster Biogenesis.....	60
4.4.4 Existence and Functions of Extramitochondrial Isoforms of Frataxin	65
Chapter 5. EPR Spectroscopy in the Study of Biological Systems	67
5.1 Basic Introduction to EPR Theory	67
5.2 Site-Directed Spin Labeling	75
5.2.1 Spin Label and Mobility	76
5.3 The Study of Mitochondrial Diseases by EPR Spectroscopy.....	80
 Aim of the Thesis	 85
 Part II – Experimental Section	 87
Chapter 1. Deciphering the Role of Frataxin in Mitochondrial Pathophysiology of Friedreich’s Ataxia	89
Introduction	91
Materials & Methods.....	95
Cell Lines and Culture Conditions	95
Genotyping and RT-PCR.....	96
SDS-PAGE and Protein Immunoblotting	98
Blue Native Gel Electrophoresis (BNGE).....	99
Biochemical Analysis of Respiratory Complexes	101

Oxygen Consumption Studies.....	101
Isolation of Mitochondria for EPR Samples	102
EPR Measurements	103
Immunogold Staining and Electron Microscopy.....	103
Morphometric Analysis of Mitochondria	104
Immunofluorescence.....	104
Proximity Ligation Assay (PLA)	105
Statistical Analysis	106
Results	107
Comparative Analysis of Frataxin in FRDA Patients' Cells	107
Comparative Analysis of Respiratory Complexes I-IV Subunits and Mitochondrial Aconitase in FRDA Patients' Cells	109
Biochemical and Functional Analyses of Mitochondrial Respiratory Complexes in FRDA and G130V-FRDA Patients' Cells	114
EPR Measurements on Isolated Mitochondria from FRDA Cells.....	118
Frataxin Co-localizes with the Fe-S Clusters Assembly Machinery in the Mitochondrial Cristae in Healthy Cells and Redistributes to the Matrix in FRDA Cells.....	122
Mitochondrial Cristae Morphology in FRDA Patient's Cells	125
Frataxin is in Close Proximity with Mitochondrial Respiratory Chain in Human Cells.....	128
Discussion & Conclusions	137
Chapter 2. Insight into the Iron-Binding Properties of Human Frataxin and its Interaction with Mitochondrial Superoxide Dismutase	145
Introduction	147
Materials & Methods.....	151
Materials	151
Heterologous Expression and Purification of Human Wild Type and Frataxin Mutants.....	152
SDS-PAGE Electrophoresis and Western Blot Analysis.....	154
Spin Labeling	156

EPR Spectroscopy.....	157
Simulation of EPR Spectra	157
Fluorescence Spectroscopy	158
Circular Dichroism (CD) Spectroscopy.....	158
Protein-Protein Docking.....	159
Results.....	161
Structural Remarks, Choice of Labelling Sites and Molecular Dynamics of Frataxin.....	161
Human Frataxin & Iron.....	164
<i>EPR Spectra of FXN Interacting with Fe³⁺</i>	164
<i>EPR Spectra of FXN Interacting with Fe²⁺</i>	170
<i>Fluorescence Spectra of FXN Interacting with Fe³⁺</i>	173
<i>Fluorescence Spectra of FXN Interacting with Fe²⁺</i>	175
<i>Circular Dichroism Spectra of FXN Interacting with Fe³⁺ and Fe²⁺</i>	177
Human Frataxin & SOD2.....	178
<i>EPR Spectra of FXN Interacting with SOD2</i>	178
<i>Fluorescence Spectra of FXN Interacting with SOD2</i>	182
<i>Protein-Protein Docking of FXN and SOD2</i>	184
Discussion & Conclusions	189
References.....	197
Part III – List of Publications	231

Summary

Friedreich's ataxia (FRDA) is a mitochondrial cardio-neurodegenerative disease, characterized by a progressive damage to the nervous system, muscle weakness and cardiomyopathy, which is the main cause of death [Harding A.E. & Hewer R.L., 1983]. FRDA is due to an abnormally expanded GAA triplet repeat in the first intron of the nuclear *FXN* gene, which leads to a transcriptional silencing of *FXN* and to a reduced expression of frataxin (FXN), a ubiquitous and highly conserved protein localized in mitochondria [Campuzano V. et al., 1996]. There are currently no options to prevent or specifically treat the disease and the main pharmacological strategies are aimed at mitigating the clinical symptoms and slowing the progression rate of the disorder. Several roles have been proposed for FXN, ranging from biogenesis of iron-sulfur clusters (ISCs) [Huynen M.A. et al., 2001] and heme [Yoon T. & Cowan J.A., 2004] (key redox cofactors of the mitochondrial respiratory chain), to iron-binding/storage [Cavadini P. et al., 2002] and iron chaperone [Yoon T. & Cowan J.A., 2003]. All these potential functions are in agreement with the main biochemical features that characterize FRDA patients' cells, i.e. a deficit of proteins containing Fe-S clusters as cofactors [Rötig A. et al., 1997], imbalance in iron homeostasis accompanied by mitochondrial iron overload [Puccio H. et al., 2001] and increased susceptibility to oxidative stress [Schulz J.B., 2000]. To date, however, a definite relationship between FXN levels, dysregulation in iron metabolism/Fe-S clusters assembly and bioenergetics failure has not been established yet and, although FRDA has been unequivocally associated to the depletion of frataxin, a clear cause-effect relationship is still elusive.

Based on these premises, the objective of my Ph.D. project has been to explore the role of FXN in the context of iron metabolism and ISCs biogenesis, as well as to rationalize the molecular mechanisms underlying the pathophysiological effects of FXN depletion in mitochondria. The present thesis has been structured into three parts: in Part I a general introduction is reported, in order to give an exhaustive overview of the background of my research; Part II includes the experimental section, in which the results of my scientific activity are reported; Part III consists of a collection of published papers in which I gave my contribution. The experimental section, which is summarized below, has been divided into two chapters, in which the two main working lines of my research

activity, conducted performing parallel studies *in vitro*, both with purified recombinant proteins and intact cells, are reported.

In the first part of my research activity, lymphoblastoid cell lines (LCLs) from three different FRDA patients, along with an LCL from a healthy age-matched control, were thoroughly analyzed in terms of mitochondrial phenotype. Defects in bioenergetics efficiency and in mitochondrial ultrastructure morphology were disclosed, along with a reduced capability to assemble the respiratory complexes in supercomplexes (SCs), supramolecular structures which in healthy cells improve the performance of the electron transport chain and the overall mitochondrial respiration. Interestingly, it was found that, in healthy cells, frataxin and the Fe-S cluster assembly machinery are enriched in the mitochondrial cristae, the functional subcompartment housing the respiratory (super)complexes. On the contrary, in FRDA cells, while proteins belonging to the Fe-S cluster assembly machinery retain their association with the mitochondrial cristae as in healthy cells, part of the residual frataxin moves towards the matrix. This evidence suggests that the mitochondrial morphological and ultrastructural changes observed in FRDA cells could be intimately connected to the partial loss of FXN from the cristae to the matrix and that this displacement could in turn affect its functional interaction with the ISCs assembly machinery, as well as with the mitochondrial respiratory chain. The hypothesis of a functional interaction between frataxin and the complexes of the respiratory chain was further investigated and, taken together, the obtained results suggest an involvement of frataxin in the assembly and/or stability of supercomplexes, especially those containing complex I. This could help to focus the study of possible therapeutic approaches for FRDA disease on a more specific target.

The second part of my research was dedicated to study the iron-binding properties of human FXN through different spectroscopic techniques. All the hypothetical functions proposed for frataxin are indeed essentially based on the capability of the protein to bind iron; however, literature on this topic is often controversial. By means of fluorescence spectroscopy and circular dichroism, the behavior of FXN in the presence of ferrous (Fe^{2+}) and ferric (Fe^{3+}) ions has been investigated. Moreover, to gain more information about the potential structural changes of frataxin promoted by iron-binding, it was taken advantage of an approach never used before in the study of FXN, *i.e.* Site Directed Spin Labeling (SDSL) coupled to Electron Paramagnetic Resonance (EPR) spectroscopy. This experimental technique is based on labeling cysteines in selected positions of the

protein with sensitive paramagnetic probes allowing to detect, at local level, possible conformational changes of the backbone dynamics induced by ligand binding or by a potential interacting partner. The results obtained by the combination of SDSL-EPR, fluorescence and circular dichroism spectroscopies have allowed to shed light on the iron-binding properties of frataxin, in relation to its possible physiological roles at cellular level. In this regard, contextually to the proposed roles for FXN, a recent *in vitro* study demonstrated a direct interaction between yeast frataxin and superoxide dismutases (SODs), key enzymes involved in the regulation of the reactive oxygen species in cellular environment [Han T.H.L. *et al.*, 2019]. On the basis of this evidence, it was addressed if also human FXN is potentially able to interact *in vitro* with human SOD2, the mitochondrial isoform of the enzyme. In order to fulfill this purpose, SDSL-EPR has been applied using the same labelled FXN proteins previously obtained to detect the effects of iron-binding. EPR experiments, combined with fluorescence experiments and with an *in silico* approach, demonstrated that human SOD2 interacts with human FXN *in vitro*, supporting the hypothesis that frataxin could also be involved in the protection against oxidative damage, a biochemical trait which commonly characterizes FRDA disease.

Part I

Introduction

Chapter 1

Insight into Mitochondrial Architecture and Functions

Known as the “powerhouses of the cell”, mitochondria are organelles responsible for the cellular energetic sustainability, using oxygen and nutrients to produce adenosine triphosphate (ATP), the molecule which provides the driving force for many biological processes. Beyond their direct involvement in cellular bioenergetics, mitochondria have been demonstrated to play a key role in several other cellular processes, such as signalling and differentiation, immune response and cell death. To exert their functions, mitochondria present a distinct ultrastructure which constantly reshapes and dynamically changes in response to the rearrangements of cellular metabolic pathways. In this chapter the intimate linkage between the structural features and the functional roles of mitochondria will be described, focusing particularly on the mitochondrial bioenergetic process and the molecular components which belong to it.

1.1 Structure-Function Relationship in Mitochondria

Mitochondria, whose structure has been firstly described by George Palade in 1953 [Palade G.E., 1953], are characterized by a singular and distinct morphology where each constituent has a precise functional role [for comprehensive reviews, see Pernas L. & Scorrano L, 2016 and Giacomello et al., 2020]. These organelles, which could present different shapes in terms of width, length or roundness, present a high degree of compartmentalization: they are characterized by two membranes, the outer mitochondrial membrane (OMM) and the inner mitochondrial membrane (IMM), which physically separate two other subcompartments, the intermembrane space (IMS) and the matrix, or lumen (Figure 1.1A). The IMM consists in two distinct spatial domains, the inner boundary membrane (IBM), close and parallel to the outer membrane, and the cristae membranes (CMs), which form pleomorphic invaginations towards mitochondrial matrix. Depending on the cell type or cellular energetic *status*

(Figures 1.1B,C), the mitochondrial cristae could adopt very different shapes, from curved tubular to more lamellar morphology; however, they are commonly characterized by two distinguishable regions, *i.e.* cristae rims (CRs) and cristae junctions (CJs), narrow tubular segments connecting the inner boundary membrane to the cristae domain (Figure 1.1D).

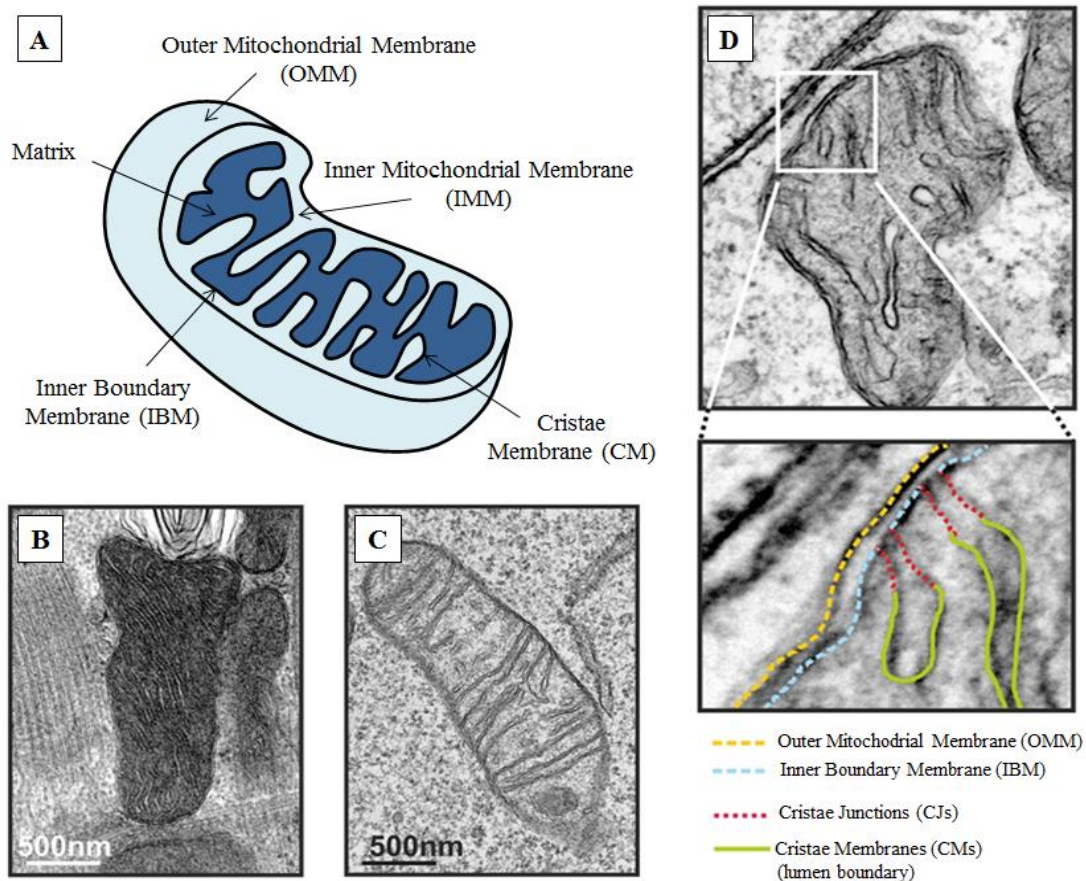


Figure 1.1. Morphological features of mitochondria and their ultrastructure organization. (A) Schematic representation of mitochondrial structure and compartments of mitochondrial membranes. (B,C) Micrograph of a mitochondrion from muscle fibers (B) and from murine fibroblasts (C). To note that mitochondria of tissues with high energetic demands, such as muscles, present a high number of cristae, well organized, which occupy most of the inner space of the organelle; a different display is shown in mitochondria from cells which do not have high energetic request, like fibroblasts, where cristae have a less homogenous distribution and occupy 30-50% of the matrix space. (D) Electron microscopy magnification of a mitochondrion in which the outer mitochondrial membrane (OMM) is highlighted in yellow, the Inner Boundary Membrane (IBM) in light blue, Cristae Membranes (CMs) in green and cristae junctions (CJs) in red [adapted from Quintana-Cabrera R. et al., 2018].

The stability and maintenance of cristae membranes are ensured by a large number of proteins, such as the mitochondrial contact site and cristae organizing system (MICOS), F_1F_0 -ATP synthase and Optic Atrophy 1 (OPA1).

The MICOS complex, which consists of at least 7 to 8 different subunits in mammalian cells, is enriched at cristae junctions and it is the main responsible of the stability and the structural maintenance of this mitochondrial region (*Figure 1.2*). Each component has a specific function on the modulation of the inner membrane shape, especially MIC60, the core of the MICOS complex [*Harner M.E. et al., 2011; Kozjak-Pavlovic V, 2017; Wollweber F., 2017*].

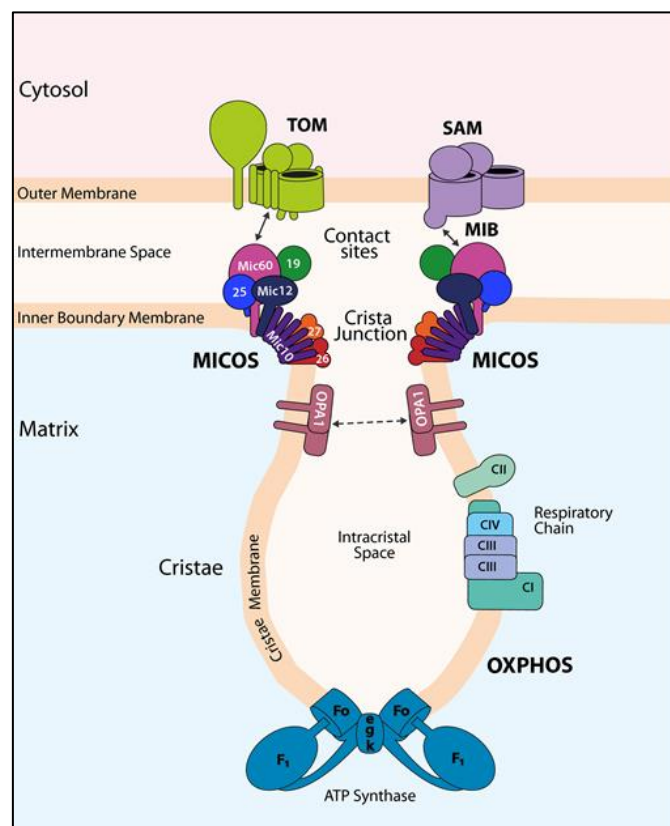


Figure 1.2. Structural factors implicated in mitochondrial cristae architecture and dynamics. The MICOS complex (which comprises the subunits MIC10, MIC60, MIC19, MIC25, MIC13, MIC26 and MIC27) is involved in the stabilization of cristae junctions. Through its components, it ensures the curvature of the inner membrane and it establishes contact sites with outer membrane protein complexes. The mitochondrial F_1F_0 -ATP synthase, due to its dimerization through subunits e, g and k, is responsible of the curvature of cristae rims. The dynamin-related GTPase OPA1 is involved in fusion of the inner membrane and play a key role in cristae biogenesis and maintenance. OXPHOS, oxidative phosphorylation system; CI, CII, CIII, CIV, complexes of the mitochondrial respiratory chain; SAM, sorting and assembly machinery; TOM, translocase of the outer mitochondrial membrane; MIB, mitochondrial intermembrane space bridging complex [*from Colina-Tenorio L. et al., 2020*].

MIC60, also known as mitofilin, is the largest component of MICOS and, in addition to its role in the maintenance of cristae junctions and membrane bending, it is involved in a dynamic series of interactions with a series of proteins and protein complexes of the outer membrane, such as the translocase of the outer membrane (TOM) or the sorting and assembly machinery (SAM), with which it associates in a stable supercomplex called mitochondrial intermembrane space bridging complex (MIB) [Ott C. *et al.*, 2012; von der Malsburg K. *et al.*, 2011; Ding C. *et al.*, 2015; Huynen M.A. *et al.*, 2016]. The interactions between MIC60 and the proteins of the outer membrane constitute a series of contact sites between the two mitochondrial membranes which seem to play a crucial role in the stability of cristae junctions.

Differently from MICOS, F_1F_0 -ATP synthase is mainly localized at cristae rims and it ensures, through its dimerization and oligomerization, an appropriate curvature of the inner membrane in this spatial site. In contrast to MIC60, which favors the negative curvature of the inner membrane, ATP synthase acts in an antagonistic way, allowing the positive curvature of the membrane, promoting cristae tightening and preventing their branching [Paumard P. *et al.*, 2002; Strauss M. *et al.*, 2008; Davies K.M. *et al.*, 2011]. In addition to its physiological role in the oxidative phosphorylation, F_1F_0 -ATP synthase exerts in this way a structural role in the complex trim of mitochondrial architecture [Walker J.E., 2013; Kühlbrandt W., 2019].

A crucial function in the cristae biogenesis and maintenance of cristae junctions is carried out by OPA1, a dynamin-related GTPase which localizes in the inner mitochondrial membrane and faces the intermembrane space [Meeusen S. *et al.*, 2006; Frezza C. *et al.*, 2006; Ishihara N. *et al.*, 2006; Cogliati S. *et al.*, 2013; Cogliati S. *et al.*, 2016]. In addition to its well-known role in the process of mitochondrial inner membrane fusion and, in general, in the mitochondrial dynamics, OPA1 is also involved in the energetic efficiency and in the maintenance of mitochondrial DNA (mtDNA) [Jones B.A. *et al.*, 1992; Shepard K.A. & yaffe M.P., 1999]; the disruption of OPA1 oligomers arrangement is strictly linked to the release of cytochrome *c* from the intracristal space subsequently to an apoptotic *stimulus* [Cipolat S. *et al.*, 2006; Yamaguchi R. *et al.*, 2008].

The physical interaction between OPA1 and MIC60, as demonstrated in mammalian cells [Barrera M. *et al.*, 2016; Glytsou C. *et al.*, 2016], and the reciprocal stabilizing effect between OPA1 and ATP synthase [Quintana-Cabrera R. *et al.*, 2018], shed light on the close connection of the molecular components involved in shaping the morphology of inner mitochondrial membrane. Defects in

mitochondrial morphology, as a consequence of their genetic alterations, can result in a series of severe human pathologies which mainly affect the cardiac and the nervous system. Therefore, the complex network of interactions and crosstalk among the membrane-shaping factors need a tight regulation and could have a relevant impact on mitochondrial and cell pathophysiology, as it will be described in detail in the next chapter.

While the outer mitochondrial membrane and the inner boundary membrane are mainly involved in a synergic interplay with other subcellular cytosolic compartments, such as the endoplasmatic reticulum (ER) or lysosomes and peroxisomes, cristae are essentially the spatial region responsible for the mitochondrial bioenergetic function. Indeed, the oxidative phosphorylation (OXPHOS), *i.e.* the coupled processes of mitochondrial respiration and ATP production, takes place in cristae membranes where the complexes of the respiratory chain and F₁F₀ - ATP synthase are localized (*Figure 1.2*); the cristae morphological display itself, with its deep invaginations and increased membrane surface, is optimized to harbour larger quantities of respiratory chain complexes and consequently to improve the overall respiratory efficiency.

1.2 Oxidative Phosphorylation

To provide a comprehensive understanding of mitochondrial bioenergetics, in 1961 the British scientist Peter Mitchell proposed the chemiosmotic theory [*Mitchell P., 1961*]. According to this model, the free energy resulting from the oxidation of organic nutrients guarantees the generation of an electrochemical gradient, pumping of protons out of the mitochondrial matrix, from one side to the other side of the mitochondrial membrane; the ATP synthase, through the back translocation of these protons from the intermembrane space towards the matrix, promotes the synthesis of ATP (*Figure 1.3*).

The electrochemical gradient, due to the cationic concentration difference (ΔpH) and the membrane potential difference ($\Delta\Psi$), is coupled to the passage of electrons from reducing equivalents through a series of enzymes which are embedded in the inner mitochondrial membrane and that constitutes the so-called electron transport chain (ETC).

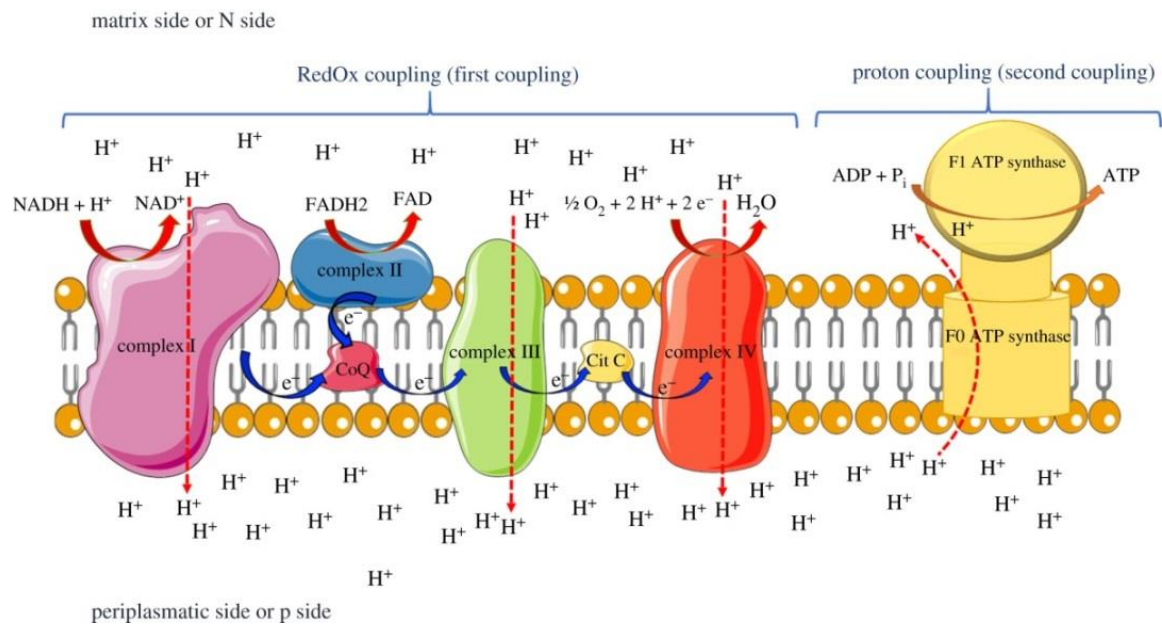


Figure 1.3. Schematic representation of the chemiosmotic theory and the oxidative phosphorylation. The entire process could be divided into two phases: the “RedOx coupling” (or “first coupling”), in which the translocation of protons is promoted by the electron transport chain, and the “proton coupling” (or “second coupling”), in which the proton movement is associated with the synthesis of ATP by the action of ATP synthase [from Morelli A.M. et al., 2019].

1.2.1 Respiratory Chain Complexes

The electron transport chain is composed of four multienzymatic complexes and two small diffusible and mobile carriers, *i.e.* ubiquinone (or coenzyme Q, CoQ) and cytochrome *c*, that shuttle electrons between them (Figure 1.3).

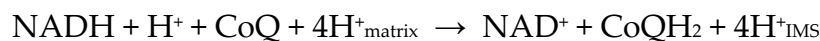
The respiratory chain consists of complex I (CI or NADH:ubiquinone oxidoreductase), complex II (CII or succinate:ubiquinone oxidoreductase), complex III (CIII or ubiquinol:cytochrome *c* reductase) and complex IV (CIV or cytochrome *c* oxidase). With the exception of complex II, whose subunits are encoded only by nuclear DNA, the subunits of complexes I, III and IV are encoded by both nuclear and mitochondrial genomes. As explained in more detail in the next chapter, genetic mutations in these subunits, as well as in the assembly factors that promote their association into mature complexes, could lead to a series of dysfunctions which are commonly referred as mitochondrial diseases, highlighting the central role of the respiratory chain complexes in the context of the mitochondrial functionality [Vercellino I. & Sazanov L.A., 2021].

1.2.1.1 Complex I or NADH:Ubiquinone Oxidoreductase

Respiratory complex I, also known as NADH:ubiquinone oxidoreductase, is the first enzyme of the electron transport chain and, with its molecular weight of about 1 MDa, it is the largest component of the OXPHOS system [for comprehensive reviews, see *Hirst J., 2013* and *Sazanov L.A., 2015*].

Complex I oxidizes NADH which is mainly produced in the mitochondrial matrix through the tricarboxylic acid (TCA) cycle and the β -oxidation of fatty acids; the two electrons arising from the oxidation of NADH to NAD^+ are used to reduce ubiquinone (CoQ) to ubiquinol (CoQH_2) in the inner mitochondrial membrane and to start the process of electron transfer through the respiratory chain until the reduction of molecular oxygen to water.

The potential energy released during this oxidoreductive process is used to transfer four protons from the mitochondrial matrix to the intermembrane space, giving a predominant contribution to the proton-motive force used to synthesize ATP. The entire process promoted by complex I is the following:



(Rxn. 1.1)

Although various structures of bacterial and mitochondrial complex I have been determined by X-ray crystallography [*Baradan R. et al., 2013*; *Zickermann V. et al., 2015*] and cryo-EM [*e.g. Agip A.A. et al., 2018*; *Parey K. et al., 2019*], the molecular details about the catalytic mechanism have not been completely understood yet.

Complex I from different organisms share a common L-shaped form in which it is possible to distinguish three different functional modules: the NADH oxidation module (N module), the ubiquinone reduction module (Q module) and the proton translocation module (P module) which could be further subdivided into two regions, proximal and distal (P_P and P_D , respectively). While the P module, where protons are pumped from matrix to intermembrane space, belongs to the inner mitochondrial membrane and constitutes the hydrophobic domain, the Q and N modules protrude towards the matrix and, together, they constitute the hydrophilic, water-soluble domain of the complex (*Figure 1.4*).

Currently, 45 subunits have been identified for human complex I; among them, 14 subunits are highly conserved across species and represent the functional core of the enzyme being necessary and sufficient for energy transduction. The remaining 31 subunits, defined as supernumerary or accessory subunits,

contribute to the assembly, stability and functional regulation of the enzyme, although they are not strictly required for the catalytic function. The hydrophobic domain contains seven core subunits (ND subunits) which are encoded by the mitochondrial DNA; the other seven core subunits, which belong to the matrix arm, are encoded by the nuclear genome and are imported to the mitochondrion, as well as all the accessory subunits.

Different coenzymes are also present in the complex: the hydrophilic domain contains the primary electron acceptor flavin mononucleotide (FMN) and a chain of iron-sulfur clusters (ISCs) which transfers electrons from the NADH oxidation site to the binding site for ubiquinone, this last localized in the membrane arm. The reduction of ubiquinone to ubiquinol induces protein conformational changes in the P module, promoting the translocation of the four protons across the membrane.

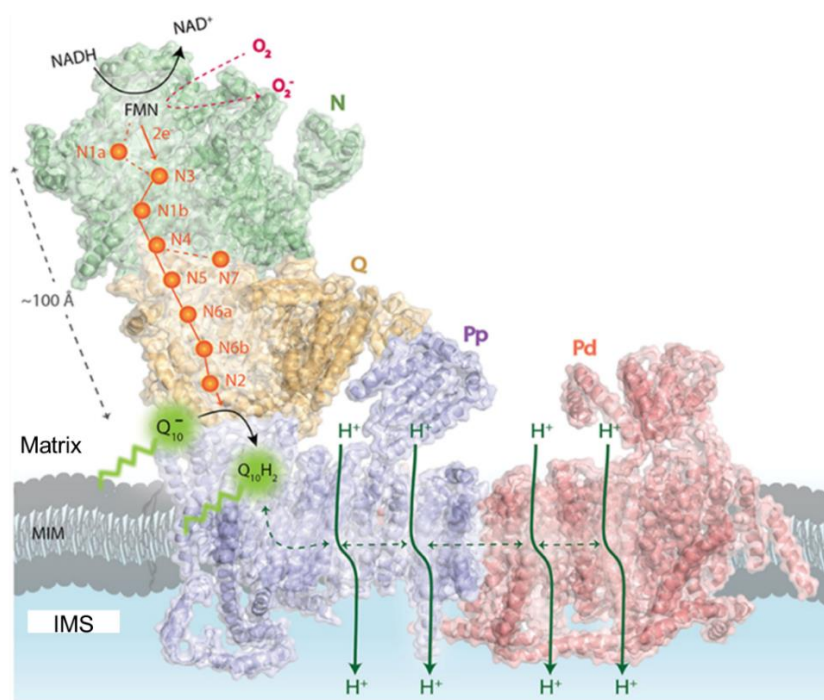


Figure 1.4. Overview of the mitochondrial complex I architecture. Representation based on the bovine heart cryo-EM structure of mitochondrial complex I (PDB ID: 4UQ8). The N-module, depicted in green, is the site for the oxidation of NADH promoted by a flavin mononucleotide (FMN). The two electrons derived from the redox reaction are transferred across a chain of iron-sulfur clusters (highlighted as orange spheres) up to the ubiquinone Q_{10} , (bound in the Q-module, colored in gold), which gets reduced to ubiquinol $Q_{10}H_2$. The reduced FMN cofactor, reacting with molecular oxygen, is a source of reactive oxygen species ROS (in red). The two P-modules of the hydrophobic membrane domain involved in the protons translocation are highlighted in violet (P_P , proximal P module) and salmon (P_D , distal P module). MIM, mitochondrial inner membrane; IMS, intermembrane space [from Giachin G. et al., 2016].

Mitochondrial complex I, representing the main entry point for electrons to the respiratory chain, plays a central role for the energetic metabolism of the cell; furthermore, due to its redox activity, it contributes in a large extent to the cellular production of reactive oxygen species (ROS) [Sugioka K. *et al.*, 1988; Turrens J. F. & Boveris A., 1980], chemical species which have important functions in different signalling pathways.

1.2.1.2 Complex II or Succinate:Ubiquinone Oxidoreductase

Complex II, or succinate:ubiquinone oxidoreductase or succinate dehydrogenase (SDH), is the second enzyme of the mitochondrial respiratory chain and the second entry point for the electrons. This enzyme, which also takes part to the TCA cycle catalyzing the oxidation of succinate to fumarate, promotes the reduction of ubiquinone to ubiquinol. Complex II consists of four subunits, all encoded by nuclear DNA: two of them, SDHA and SDHB, protrude towards the mitochondrial matrix and constitute the catalytic domain of the enzyme; the other two subunits, SDHC and SDHD, are embedded in the inner mitochondrial membrane and form the hydrophobic domain where ubiquinone gets reduced to ubiquinol (Figure 1.5).

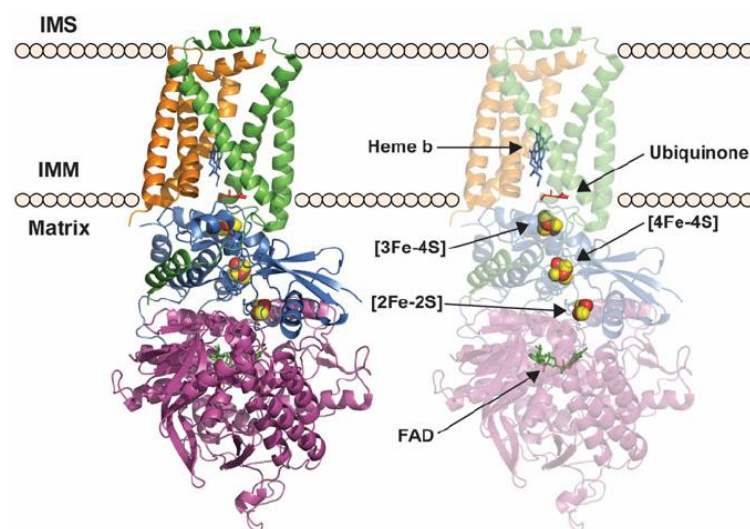
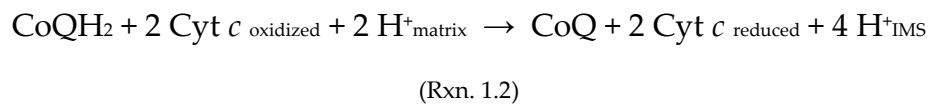


Figure 1.5. Mitochondrial complex II and its cofactors. Representation of the porcine mitochondrial complex II (PDB ID: 1ZOY). The four subunits of the enzyme are SDHA (purple), SDHB (blue), SDHC (green) and SDHD (orange). The cofactors belonging to the enzyme are FAD (green stick), three iron-sulfur clusters (red and yellow sphere), Ubiquinone (red stick) and heme b (blue stick). IMS, intermembrane space; IMM, inner mitochondrial membrane [from Van Vranken J. G. *et al.*, 2014].

While SDHA contains a flavin adenine dinucleotide (FAD) cofactor and the succinate binding site, SDHB contains three iron-sulfur clusters whose function relies on transferring the electrons from the flavin to the ubiquinone reduction site. Among its prosthetic groups, complex II contains also a heme center which seems not directly involved in the reduction of ubiquinone and whose function has not been completely clarified yet.

1.2.1.3 Complex III or Ubiquinol:Cytochrome *c* Reductase

Complex III, alternatively known as ubiquinol:cytochrome *c* reductase, plays a central role in the mitochondrial respiratory chain catalyzing the transfer of electrons from ubiquinol to the soluble carrier cytochrome *c* (Figure 1.3); the oxidoreductive reaction is coupled to the translocation of protons from the matrix to the intermembrane space:



Crystal structures for complex III have been resolved from different species and they share a common structure [Xia D. *et al.* 1997; Iwata S. *et al.*, 1998; Zhang Z. *et al.*, 1998; Lange C. & Hunte C., 2002], a homodimeric assembly in which each monomer presents several subunits, eleven in mammals, all encoded by nuclear genome, with the exception for cytochrome *b* subunit. Three of them are involved in the electron transfer: cytochrome *b*, which contains two hemes (*b_L*, or low potential heme, and *b_H*, or high potential heme), cytochrome *c₁*, which contains heme *c₁*, and the Rieske iron-sulfur protein (UQCRFS1 subunit or Rip1), which contains one iron-sulfur cluster (Figure 1.6).

Differently from complex I and complex IV, in complex III the protons are carried across the membrane by ubiquinone itself and the mechanism which is actually accepted to explain the catalytic action of the enzyme is called “proton-motive Q cycle” [Trumpower B., 1990], as depicted in Figure 1.6B.

Within the mitochondrial respiratory chain, complex III is the second major site for the production of reactive oxygen species together complex I.

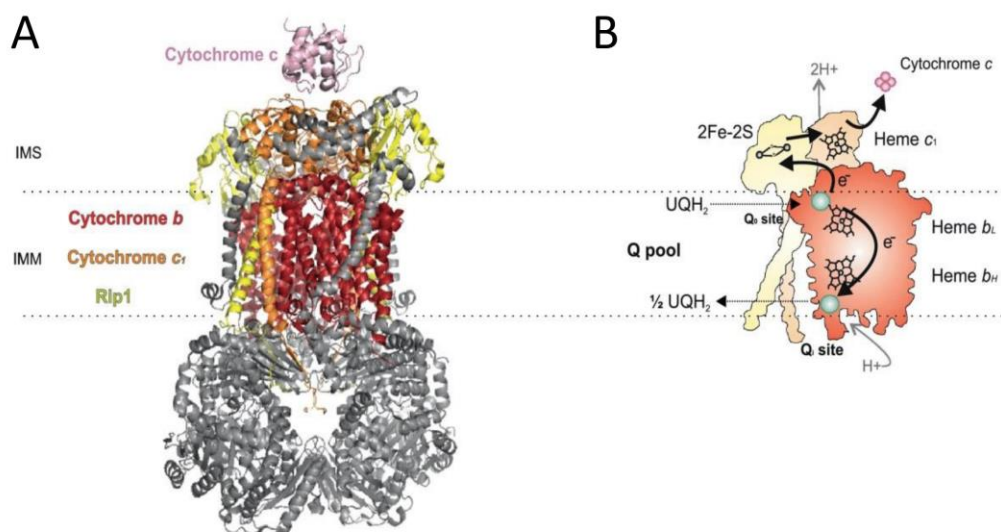
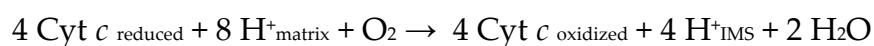


Figure 1.6. Architecture and catalytic mechanism of ubiquinol:cytochrome c reductase. (A) Crystal structure of *Saccharomyces cerevisiae* complex III (PDB ID: 3CX5). The subunits involved in the catalytic function are cytochrome b (in red), cytochrome c₁ (in orange) and Rieske iron-sulfur protein (Rip1, in yellow). The carrier cytochrome c is highlighted in pink. (B) Representation of the Q cycle. One of the two electrons derived from the oxidation of ubiquinol (UQH₂) at Q_o site is transferred to the cluster of Rieske protein (Rip1) and subsequently to heme c₁, in order to reduce cytochrome c as final step. The second electron reaches the Q_i site through hemes b_H and b_L, reducing ubiquinone (UQ) to ubiquinol (UQH₂) [from Ndi M. et al., 2018].

1.2.1.4 Complex IV or Cytochrome c Oxidase

Mitochondrial complex IV, or cytochrome c oxidase (COX), is the last enzyme of the respiratory chain, promoting the electrons transfer from the reduced cytochrome c to molecular oxygen and with the production of H₂O [Ostermeier C. et al., 1996; Kadenbach B., 2021]. In the enzymatic process catalyzed by complex IV, four protons from the mitochondrial matrix are used to synthesize two molecules of water while other four protons are translocated toward the intermembrane space, contributing to the generation of the electrochemical gradient used by ATP synthase to synthesize ATP. The overall reaction could be summarized as follows:



(Rxn. 1.3)

All the subunits of the complex belong to the inner mitochondrial membrane; for human COX, which has a total of 13 subunits (plus the recent debatable attribution of a fourteenth subunit [Zong S. *et al.*, 2018]), ten subunits are encoded by nuclear DNA, while the other three, which are directly involved in the catalytic function, are encoded by the mitochondrial genome.

As cofactors, mitochondrial complex IV contains two hemes, a cytochrome *a* and cytochrome *a₃*, and two copper centers, the CuA and CuB centers, together with phospholipid molecules (Figure 1.7). Cytochrome *a₃* and CuB form a binuclear center which is the site where oxygen reduction takes place. Starting from cytochrome *c*, previously reduced by mitochondrial complex III, electrons will be transferred to the oxygen reduction site *a₃*-CuB through cytochrome *a* and CuA and, coupling this process to the proton pumping across the mitochondrial membrane, molecules of water are produced.

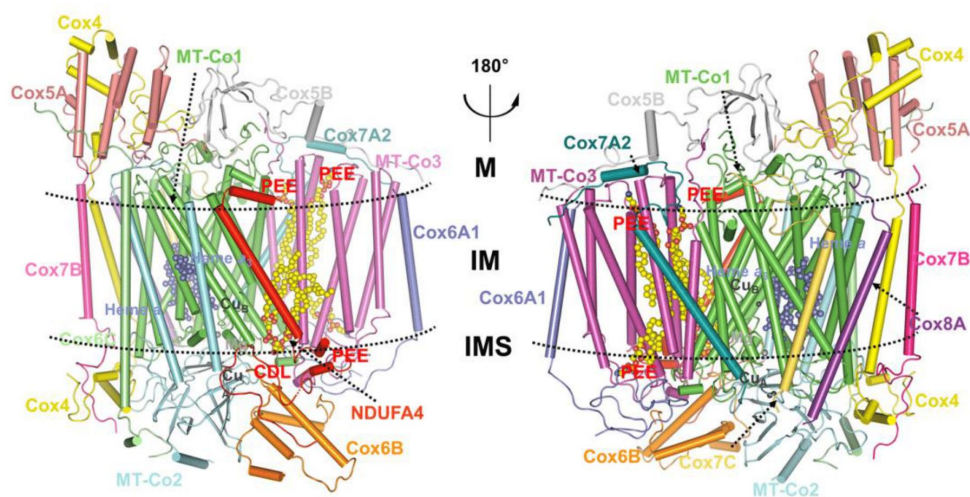


Figure 1.7. Structure of human cytochrome *c* oxidase, shown in two rotated views along the inner mitochondrial membrane. The 14 identified subunits are labeled and highlighted with different colors. The metal cofactors (CuA, CuB, heme *a* and heme *a₃*) and phospholipids cardiolipin (CDL) and phosphatidylethanolamine (PEE) are shown as spheres. M, matrix; IM, inner membrane; IMS, intermembrane space [adapted from Zong S. *et al.*, 2018].

1.2.2 Respiratory Chain Supercomplexes

The OXPHOS system represents the core of the mitochondrial bioenergetic function and the structural organization of the mitochondrial respiratory complexes is intimately linked to its role.

There are different models, widely debated, which describe how the complexes organize in the mitochondrial inner membrane. In the first model, introduced in 1947 by Keilin and Hartree [Keilin D. & Hartree E.F., 1947], the components of the respiratory chain have been considered to be:

“more or less rigidly held together in a framework that ensures their mutual accessibility and a consequent high catalytic activity”

Therefore, the “solid model” describes the complexes as closely packed, organized in bigger structures to provide an enhancement of electron transport and efficiency of the process. This model has been gradually replaced by the “fluid model” where the four complexes are considered to be randomly distributed within the inner mitochondrial membrane and the electrons could flow from a complex to another thanks to the mobile carriers ubiquinone and cytochrome *c*. As described by Hackenbrock [Hackenbrock C.R. et al., 1986]:

*“The mitochondrial inner membrane is a fluid-state rather than a solid-state membrane and...all membrane proteins and redox components which catalyze electron transport and ATP synthesis are in constant and independent diffusional motion.... We present five fundamental postulates upon which the random collision model of mitochondrial electron transport is founded: (1) All redox components are independent lateral diffusants; (2) cytochrome *c* diffuses primarily in three dimensions; (3) electron transport is a diffusion-coupled kinetic process; (4) electron transport is a multicollisional, obstructed, long-range diffusional process; (5) the rates of diffusion of the redox components have a direct influence on the overall kinetic process of electron transport and can be rate limiting, as in diffusion control”*

Although accepted for a long time, the fluid model has been later replaced by a more articulate vision of the system, when Schägger and Pfeiffer proposed a reformulation of the solid model with their “plasticity model” [Schägger H. & Pfeiffer K., 2000]:

“...we present data that fundamentally change the paradigm of how the yeast and mammalian system of oxidative phosphorylation is organized. The complexes are not randomly distributed within the inner mitochondrial membrane, but assemble into supramolecular structures”

According to this model, the respiratory chain complexes could organize into supramolecular assemblies, called respiratory supercomplexes (RSCs), which guarantee a more efficient and quick transfer of electrons and an enhancement of the overall mitochondrial respiration.

For the experimental approach used to prove their existence, supercomplexes have been questioned for a long time; indeed, Schagger and Pfeiffer observed the co-migration of the respiratory complexes using blue native polyacrylamide gel electrophoresis (BN-PAGE), a technique which necessarily requires the solubilization of the membrane with mild detergents to preserve the native interactions and assemblies between proteins and macromolecules [Schagger H. & von Jagow G., 1991]. Figure 1.8 reports the diversified pattern of mitochondrial supercomplexes as revealed by BN-PAGE, with their approximate molecular weights and their relative structures. Although initially criticized as artifacts of detergent solubilization, the existence of supercomplexes as real physical entities has been later unequivocally demonstrated [Davied K.M. et al., 2011].

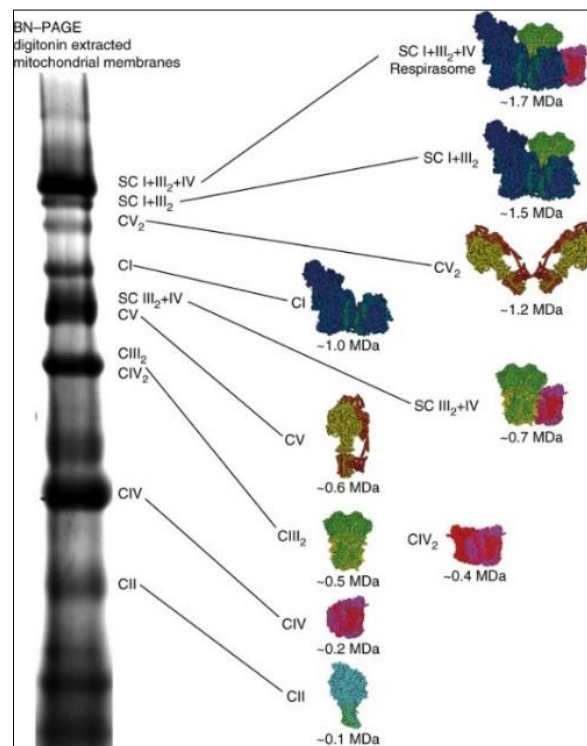


Figure 1.8. BN-PAGE analysis of mitochondrial membranes from ovine heart solubilized with the mild detergent digitonin. The respiratory chain supercomplexes, with their approximate molecular weights and structure, are reported on the right. The attribution of the bands to the correspondent supercomplexes has been done on the basis of the molecular weight and comparison to proteomic and western blot analysis [from Letts J.A. & Sazanov L.A., 2017].

The association of individual complexes into supercomplexes has been observed in different organisms including mammals [Schägger H. & Pfeiffer K., 2000; Schägger H. & Pfeiffer K., 2001], yeast [Schägger H. & Pfeiffer K., 2000], plants [Eubel H. et al., 2003], algae [Miranda-Astudillo H. et al., 2018] and some bacteria [Stroh A. et al., 2004]. It has been estimated that most of mammalian complex I (85%-100%), partly of complex III (55%-65%) and only a small extent of complex IV (15%-25%) are found to be associated into supercomplexes [Schägger H. & Pfeiffer K., 2001; Greggio C. et al., 2017]; on the contrary, complex II has not been observed to be part of a stable supramolecular assembly with other respiratory complexes. Moreover, complex I, complex III and complex IV associate with different composition and stoichiometry (including, for instance, $CI/CIII_2$, $CI/CIII_2/CIV_{1-4}$ and $CIII_2/CIV_{1-2}$) and the structures of several supramolecular assemblies have been also resolved by electron and cryo-electron microscopy [Althoff T. et al., 2011; Dudkina N.V. et al., 2011; Mileykovskaya E. et al., 2012; Letts J.A. et al., 2016]. Among the different and possible combinations, RSCs containing complex I in simultaneous association with complex III and complex IV are considered the most relevant: this supramolecular assembly, in the presence of mobile carriers ubiquinone and cytochrome *c*, is capable of independent respiration and, for this reason, is commonly referred as respirasome (Figure 1.9) [Schägger H. & Pfeiffer K., 2000; Acín-Pérez R. et al., 2008; Enriquez J.A., 2016].

Recently, it has been also proposed that mammalian OXPHOS complexes are able to associate into a higher supramolecular assembly, the respiratory megacomplex $CI_2CIII_2CIV_2$, providing new insight into the organization of the electron transport chain and new perspectives on the study of its functional mechanisms [Guo R. et al., 2017].

Differently from ATP synthase which, as previously stated, is mainly localized in the cristae rims and modulates the curvature of the inner membrane, each component of the OXPHOS system is predominantly localized on the planar cristae surfaces, as well as the respiratory supercomplexes and megacomplexes [Vogel F. et al., 2006; Davies et al., 2011; Wilkens V., 2013]; accordingly, ATP synthase has never been demonstrated to be associated with respiratory supercomplexes and cryo-EM map of the respirasome $CI_1CIII_2CIV_1$ and megacomplex $CI_2CIII_2CIV_2$ show a spatial arrangement where the cytosolic surfaces of CI, CIII and CIV are in the same plane, therefore constituting a disc-like structure (Figure 1.10) [Gu J. et al., 2016; Letts J.A. et al., 2016; Guo R. et al., 2017].

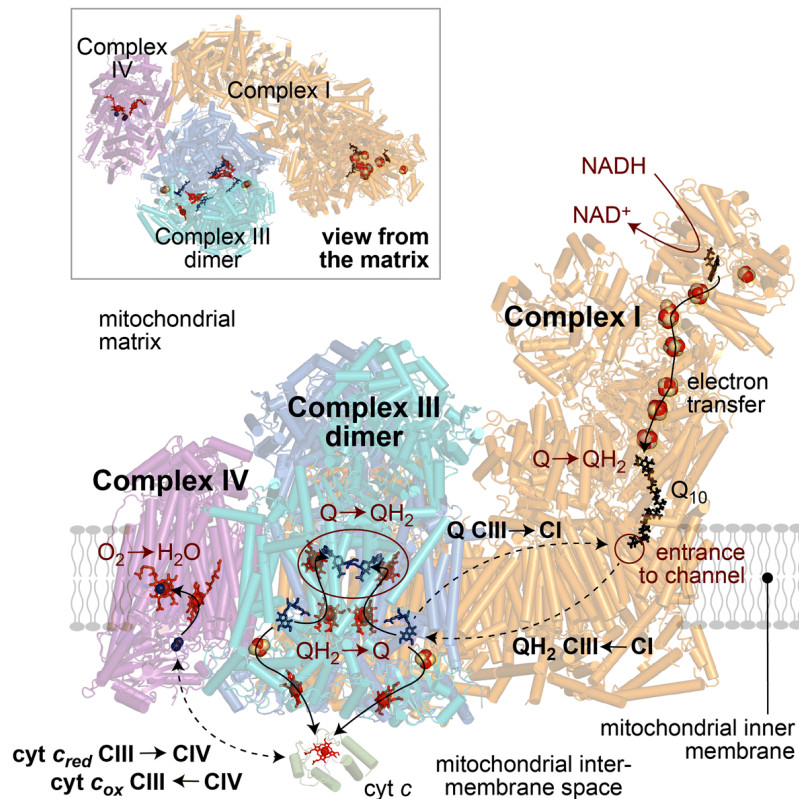


Figure 1.9. The respirasome. The principal and functional mitochondrial supercomplex is constituted by complex I associated with a dimer of complex III and with a monomer of complex IV. Complex I catalyzes the oxidation of NADH to NAD⁺ with the reduction of ubiquinone Q to ubiquinol QH₂. Complex III catalyzes the oxidation/reduction of ubiquinol/ubiquinone, according to the Q cycle mechanism. Complex IV oxidizes cytochrome c and promotes the reduction of O₂ to H₂O [from Hirst J., 2018].

The morphology of the inner mitochondrial membrane and, especially, of the cristae, has a deep impact on the stabilization of respirasomes; indeed, it has been observed that a reshape of the orthodox topology of the inner mitochondrial membrane, as a cause or a consequence of an impairment of the organelle's functionality, could have a relevant effect on the assembly of supercomplexes. The disruption of MICOS system, as well as the genetic ablation of OPA1, has a relevant effect on the respiratory chain assembly: the disorganization of the cristae morphology due to the modulation of mitochondria-shaping proteins causes defects in the structure/function of the supercomplexes and consequently leads to an impairment of the respiratory efficiency and, in general, of the bioenergetic functions [Cogliati S. et al., 2013; Cogliati S. et al., 2016].

Furthermore, the lipid composition of the inner mitochondrial membrane seems to be crucial for the formation of supercomplexes, as well as for their stabilization and function: for instance, in Barth syndrome, the defective remodeling of

cardiolipin, the main constituent of inner membrane, induces a decrease in the levels of RSCs, shedding light on a possible effect of cardiolipin in the stability of respirasomes [McKenzie M. *et al.*, 2006].

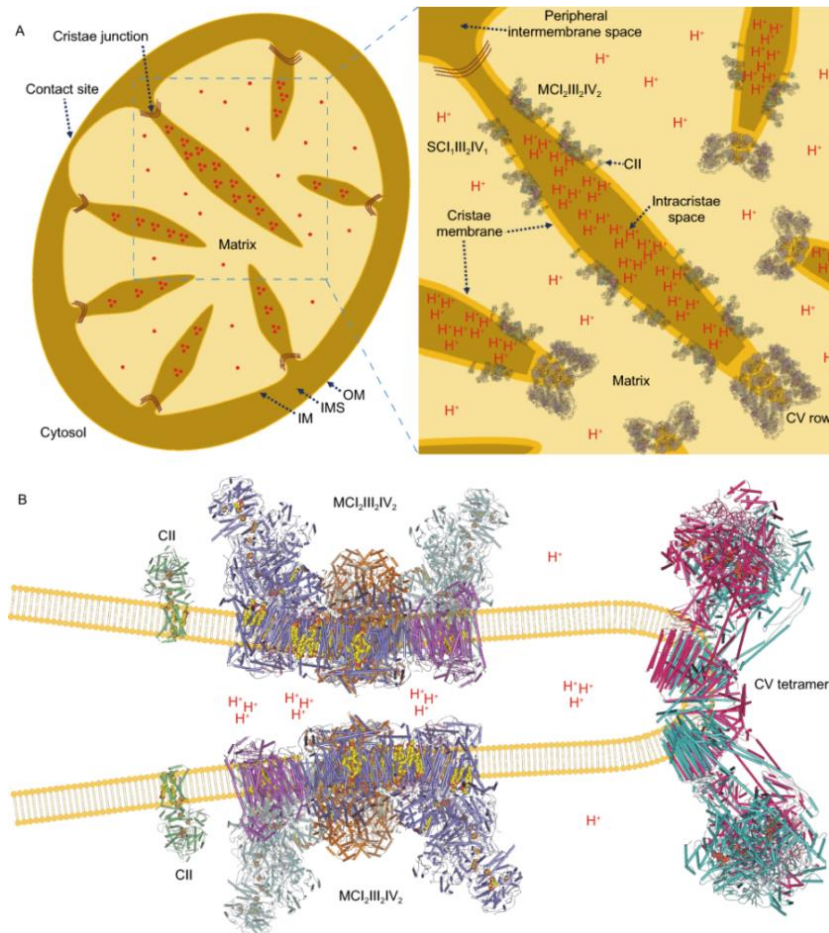


Figure 1.10. Organization and topological distribution of respiratory chain complexes in mitochondria. (A) Mitochondrial structural morphology (on the left) and its relative enlargement (on the right) with the distribution of the OXPHOS complexes and their supramolecular association in mitochondrial membrane. The concentration gradient of protons is represented with red notes. OM: outer membrane; IMS: intermembrane space; IM: inner membrane. (B) Distribution of complex II (CII), megacomplex MCI₂III₂IV₂ and ATP synthase (Complex V, CV) tetramer on mitochondrial cristae. Cofactors of the complexes are shown as spheres. CII PDB ID: 1Z0Y; megacomplex MCI₂III₂IV₂ PDB ID 5XTI; supercomplex SCI₁III₂IV₁ PDB ID 5XTH; ATP synthase PDB ID: 6J5K [from Wu M. *et al.*, 2020].

Among the possible roles hypothesized for RSCs, it has been speculated that the functional advantage of the association into supercomplexes is to guarantee structural stabilization of the individual complexes and, especially, to provide an

optimized condition for the assembly and activation of complex I. Although different other roles have been proposed for supercomplexes, such as increasing the efficiency of electron transfer through substrate channeling, enhancing the catalytic activities of the respiratory enzymes and/or preventing the generation of ROS through the regulation of reactive intermediates, the precise reason why supercomplexes exist is still under debate; anyhow, it is generally accepted that the structural organization of respiratory complexes into supercomplexes could exert a relevant role in the mitochondrial physiology; therefore, alterations to RSCs formation could be an important hallmark of pathological conditions [Enríquez J.A, 2016; Novack G.V., 2020; Ramírez-Camacho I., 2020; Javadov S. et al., 2021; Protasoni M. & Zeviani M., 2021].

Chapter 2

Mitochondrial Diseases

Mitochondrial diseases represent a large group of disorders characterized by a progressive dysfunction of oxidative phosphorylation and, in general, of mitochondrial functionality. For their heterogeneity in clinical manifestations, mitochondrial disorders are very difficult to diagnose and manage, representing a challenge for the scientific community of the new century. As described in the previous chapter, mitochondria have a crucial role in several metabolic processes: an impairment of their physiological *status* may have deleterious consequences on their functions and, for extension, on the biochemical pathways of a cell. In this chapter a brief overview of disorders which affect mitochondria is reported, focusing on their pathophysiological mechanisms and clinical phenotypes.

2.1 Pathophysiology of Human Mitochondrial Diseases

Mitochondrial diseases, also known as mitochondriopathies, are *de facto* caused by mutations in genes of the mitochondrial or nuclear genome that encode proteins whose functions are pivotal for the metabolism of the organelle [Scheibye-Knudsen M. et al., 2015; Gorman G.S. et al., 2016; Russell O.M. et al., 2020; Protasoni M. & Zeviani M., 2021]. Over about 1500 proteins are involved in the maintenance and correct functionality of mitochondria: among them, thirteen are encoded by human mtDNA while the remaining are encoded by nuclear DNA (nDNA), translated in the cytoplasm and subsequently translocated into the organelle through a fine regulated mechanism of import [Calvo S.E. & Mootha V.K., 2010]. Several pathogenic mutations in mtDNA and nDNA have been shown to cause disease: up to now, is known that 11% of the disease genes are mitochondrial DNA encoded (36 genes) while 89% are encoded by nuclear genome (302 genes) (Figure 2.1) [Stenton S.L. & Prokisch H., 2020]. Since genetic mutations could occur in both mtDNA and/or nDNA, mitochondrial diseases can present any pattern of inheritance, *i.e.* maternal, autosomal-dominant, autosomal-recessive and X-linked [Koopman W.J. et al., 2012]; it has been also reported that *de*

In the majority of cases, pathogenic mutations in the human mtDNA are heteroplasmic, a condition which occurs when an individual cell carries a mixture of wild type and mutated mitochondrial genome [Larsson N.G. & Clayton D.A., 1995]. The level of heteroplasmy, *i.e.* the relative proportion of mutant to normal mtDNA, is critical for the arise of cellular dysfunctions and, consequently, for the disease onset. Furthermore, the percentage of mutated mtDNA usually needs to exceed specific threshold values to cause biochemical defects and these values strongly depend on the mtDNA specific mutation, on the cell type and could also vary for the same mutation in different patients [Schlieben L.D. & Prokisch H., 2020].

As previously stated, the thirteen proteins encoded by mtDNA are structural subunits of the respiratory chain; additionally, mtDNA encodes twenty-four molecules of RNA (2 ribosomal RNAs and 22 transfer RNAs) that are fundamental for the translation of these proteins inside mitochondria. The polypeptides encoded by mtDNA are essential for the correct functioning of the oxidative phosphorylation process: seven of them are the core subunits of the hydrophobic domain of mitochondrial complex I (subunits MT-ND1–6 and ND4L), one is a subunit of complex III (subunit MT-CYB), three belong to complex IV (subunits MT-CO1–3) and two are the subunits of ATP synthase (MT-ATP6 and MT-ATP8). A relevant number of mutations in all of these genes and mtDNA rearrangements have been shown to induce pathological conditions, leading to dysfunctions of the OXPHOS system and, more in general, to a severe impairment of the mitochondrial bioenergetics. The majority of mitochondrial proteome is encoded by nuclear DNA and several point mutations have been found to cause a large number of mitochondrial disorders [Fernandez-Vizarra E. & Zeviani M., 2021]. Pathological mutations occur in genes coding for the structural subunits of the OXPHOS complexes, as well as for the assembly factors involved in their biogenesis. These factors are proteins which promote a correct and appropriate maturation of the complexes, stabilizing possible assembly intermediates, assisting the insertion of specific subunits or guaranteeing the biosynthesis and/or incorporation of the cofactors required for their catalytic activity. The severity of pathophysiological effects caused by mutations in genes coding for complexes subunits and/or assembly factors is highly variable, depending on the type of mutations and on the biosynthetic pathways which are directly involved. It is worth to note that pathogenic mutations in nuclear DNA can not only affect genes encoding proteins of the OXPHOS system but also proteins involved in many other mitochondrial functions, such as mitochondrial

dynamics and quality control, as well as mitochondrial morphology and cristae shaping, homeostasis and substrates/cofactors metabolism *et cetera* [Stenton S.L. & Prokisch H., 2018]. Mitochondria are complex systems where each molecular component is strictly connected to the others: this strong interdependency is relevant in the context of mitochondrial diseases, because a genetic mutation which occurs in an individual component has usually a drastic impact on the entire organelle's functionality.

2.2 Occurrence, Clinical Features and Syndromes

Mitochondrial diseases represent the most common group of inherited disorders whose large variety of clinical features and high genotype-phenotype heterogeneity makes them difficult to be recognized and treated.

Defects on nuclear genome have shown to be the principal cause of childhood mitochondrial disease while genetic mutations in mtDNA are more frequent in adult cases. The onset of mitochondrial disorders is characterized by a bimodal distribution: a peak in the first three years of life and a second broader peak between adolescence and forty years of life (adult-onset disorders) [Gorman G.S. *et al.*, 2016]. The prevalence of childhood-onset mitochondrial disorders (<16 years of age, indicatively) has been evaluated to range from 5 to 15 cases per 100 000 individuals [Skladal D. *et al.*, 2003; Ryan E. *et al.*, 2006]; in adults, the occurrence for mitochondrial diseases caused by mutations in nDNA and mtDNA have been estimated to be 9.6 and 2.9 cases per 100 000 of the population, respectively [Gorman G.S. *et al.*, 2015].

Since mitochondria are present in almost all nucleated cells, mitochondrial disorders could potentially affect every organ or tissue; however, as expected, they have a deeper impact on cells with high energetic demands (*i.e.* myocytes and neurons) leading to an impairment of organs like heart, brain and skeletal muscles. Mitochondrial human dysfunctions can cause a large spectrum of neurological and non-neurological symptoms, as schematically summarized in Figure 2.2 [McFarland R. *et al.*, 2010; Gorman G.S. *et al.*, 2016; Russell O.M. *et al.*, 2020].

Commonly, childhood-onset diseases are characterized by a series of typical symptoms such as generalized weakness, hypotonia, encephalopathy, fatigue and vomiting. Adult-onset disorders are generally less severe and they present

clinical manifestations like chronic progressive external ophthalmoplegia, diabetes, deafness and, in some cases, neurodegenerative episodes.

Although they generally manifest as multisystemic disorders, cases of mitochondrialopathies in which single organs are involved are possible: for instance, in Leber hereditary optic neuropathy (LHON) syndrome, a disease characterized by mutations in the *ND1*, *ND4* and *ND6* genes and consequent deficiency in complex I, leads young people to have problems circumscribed only to the visual apparatus [Jurkute N. & Yu-Wai-Man P., 2017].

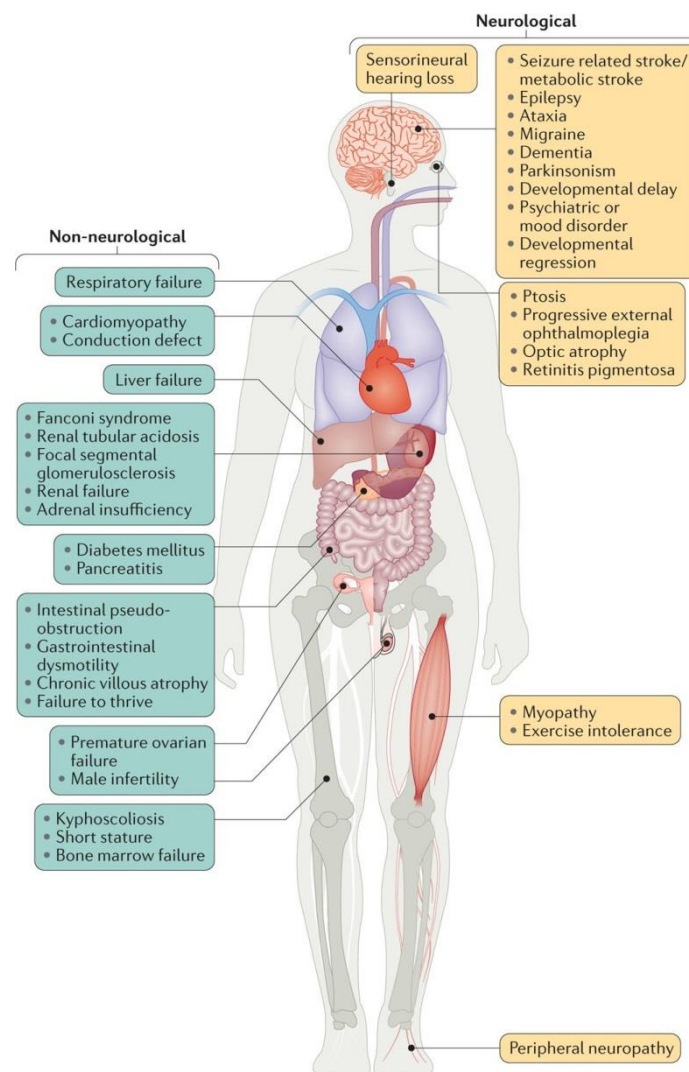


Figure 2.2. Clinical manifestations of human mitochondrial diseases. Disorders which involve mitochondrial functionality can be characterized by a series of neurological and non-neurological symptoms. The clinical presentations are usually multi-systemic involving different organs and tissues and they depend on several factors, such as the specific mutations on mtDNA or nDNA, heteroplasmy or the age of onset [from Gorman G. S. et al., 2016].

The most severe childhood mitochondrial disease is Leigh syndrome, a progressive neurodegenerative disorder which, being associated with defects in more than 90 different genes in mtDNA and nDNA, well represents the genetic heterogeneity of mitochondrial diseases [Rahman J. et al., 2017]. Patients affected by Leigh syndrome usually die in infancy or early childhood due to the rapidity of the neurodegenerative progression. Other childhood disorders are Alpers-Huttenlocher disease, characterized by epilepsy, liver disease and psychomotor regression, and Pearson syndrome, characterized by lactic acidosis, anemia and pancreatic insufficiency [Saneto R.P. et al., 2013; Rötig A. et al., 1995]. Adult-onset mitochondrial disorders include the previously mentioned LHON syndrome, the progressive cardio-encephalomyopathy Kearns-Sayre disease, the myopathy, encephalopathy, lactic acidosis and stroke-like episodes (MELAS) syndrome and the neurogenic muscle weakness, ataxia and retinitis pigmentosa (NARP) neurodegenerative disorder [see Gorman G.S. et al., 2016 for a comprehensive review]. Additionally, several other diseases have shown to be caused by mutation in genes coding for proteins involved in mitochondrial dynamics, such as in *MFN2* and *OPA1*, leading to Charcot-Marie-Tooth neuropathy type 2A and optic atrophy 1, respectively [Verhoeven K. et al., 2006; Hudson G. et al., 2008].

Currently, diagnostic methods used to evaluate a mitochondrial disease are essentially based on genetic and genomic screening, generally providing a prompt treatment of the pathology. Nowadays, therapeutic approaches are mostly symptomatic and organ-specific; although they guarantee an improvement of the life quality and expectancy, they do not provide a definitive resolution to the problem. With new advances in diagnostic techniques and omic sciences, great efforts have been made to understand the molecular mechanisms of mitochondrial pathologies, thereby providing new hope for the development of curative treatments [Stenton S.L. & Prokisch H., 2020]. In the complexity of this scenario, it is noteworthy that mitochondrial dysfunctions could be also critical for the pathogenic mechanisms that characterize some common neurological disorders, such as Parkinson's disease (PD), Alzheimer's disease (AD), Huntington's disease, prion diseases and amyotrophic lateral sclerosis; it is therefore clear that modulation and manipulation of mitochondrial functionalities could be crucial for the control and decreasing of the progression of these disorders [Murphy M.P. & Hartley R.C., 2018]. Friedreich's ataxia, a mitochondrial neurodegenerative disease, is described in detail in the next chapter.

Chapter 3

Friedreich's Ataxia

In 1863, the German neurologist and pathologist Nikolaus Friedreich (1825-1882) described for the first time a form of inherited disease characterized by early onset ataxia, kyphoscoliosis, fatty degeneration of the heart, defects of the dorsal columns and dorsal roots [Friedreich N., 1863]. His scientific work was not properly acknowledged during his lifetime and only thirty years later the French neurologist Pierre Marie (1853-1940) realized the importance of Friedreich's scientific studies [Marie P., 1893]. His eponymous disease, Friedreich's ataxia, is actually recognized as a rare disease and the most common inherited ataxia. Despite the identification of the pathogenic gene, more than twenty years ago, and the great efforts to understand the pathophysiological mechanisms of the disease, a cure is not yet available. In this chapter, the clinical, biochemical and genetic aspects of Friedreich's ataxia will be described and the main therapeutic strategies currently adopted for mitigate symptoms and slowing down the progression of the disease will be briefly reported.

3.1 Phenotypic Traits

Friedreich's ataxia (FA or FRDA; OMIM # 229300) is the most common inherited ataxia in Caucasian population [Cossée M. *et al.*, 1997]. Epidemiological studies highlight large regional differences in Europe, ranging from 1 in 20 000 in south-west (especially in North of Spain, South of France and Ireland) and 1 in 250 000 in the north and east of the continent [Vankan P., 2013]. Additionally, the estimated carrier frequency varies between 1:50 to 1:100 in European, Middle Eastern, North African and Indian people [Koeppen A.H., 2011]. The onset of symptoms is usually in middle to late childhood and adolescence, between the age of 6 and 18 ("classical" FRDA); the outbreak of the disease in adult and middle age is possible, although less common: late-onset (LOFA) and very late-onset (VLOFA) Friedreich's ataxia represent "atypical" forms of the disease, developing after the ages of 25 and 40 years, respectively [Bürk K., 2017; Cook A. & Giunti P., 2017]. In these cases, the phenotypic manifestations are milder and

less severe, showing a slower disease progression and more heterogeneous symptoms. On the contrary, early-onset FRDA represents a condition where the symptoms of the disease develop before the age of 5; these cases are rare and they are generally characterized by a more severe phenotype and a faster progression of the disease [Parkinson M.H. et al., 2013]. FRDA is slowly progressive and multisystemic, affecting both the central and peripheral nervous systems, as well as the musculoskeletal system, the heart and the endocrine pancreas; in most cases, it is characterized by progressive ataxia of limbs and gait, dysarthria, hypertrophic cardiomyopathy and *diabetes mellitus* [Harding A.E. & Hewer R.L., 1983; Delatycki M.B. & Corben L.A., 2012; Cook A. & Giunti P., 2017]. With regard to neuropathological phenotype, dorsal root ganglia, dentate nuclei of the cerebellum, peripheral nerves, posterior columns, spinocerebellar tracts and corticospinal tracts of the spinal cord are the main affected sites [Koeppen A.H., 2011]. Among the musculoskeletal defects, FRDA patients commonly suffer from scoliosis and foot deformities, such as *pes cavus* and *talipes equinovarus*. The later stages are characterized by pyramidal weakness, muscular contractures and spasticity which confine patients to a wheelchair by the age of forty; other concomitant clinical manifestations like dysphagia, oculomotor abnormalities and sensorineural hearing loss could also occur [Cook A. & Giunti P., 2017]. Diabetes, whose prevalence in FRDA patients varies between 8% and 49%, is generally a late event of Friedreich's ataxia but its manifestation may generally worsen the health *status* of the patient [Finocchiaro G. et al. 1988; Dürr A. et al., 1996]. The most common cause of death for FRDA patients is associated to cardiac dysfunction, in particular to arrhythmic manifestations; nevertheless, aspiration pneumonia, diabetic coma, stroke, ischemic heart disease and *trauma sequelae* are reported as other typical causes of death [De Michele G. et al., 1996; Leone M. et al., 1988]. Although the average age at death is reported to be approximately 40 years [Tsou A.Y. et al., 2011], life quality has considerably improved thanks to the advancement in the study of the pathophysiological mechanisms of the disease and the development of new therapeutic strategies.

3.2 Genetics and Molecular Basis of the Disease

In 1996 Friedreich's ataxia was identified as an autosomal recessive inherited disease, caused by an unstable guanine-adenine-guanine (GAA) triplet expansion

in the first intron of *FXN* gene on the positive strand of chromosome 9q21.11 [Campuzano V. et al., 1996].

The majority of FRDA patients (approximately 96%) are homozygous for the GAA expansion while the remaining 4% of the cases present a heterozygous phenotype with an expansion in one allele and a mutation in the other, including nonsense, missense, insertion and deletions [Cossée M. et al., 1999].

Whilst in normal chromosomes the number of GAA repeats is generally less than 40, in FRDA patients the number of repeats is commonly between 600 and 900 with a pathological threshold that is reported to be 70 (Figure 3.1) [Cook A. & Giunti P., 2017]. The GAA triplet expansion is also unstable during life because it could increase or decrease with a maternal passage while it usually decreases when inherited from father to child [Monros E. et al., 1997].

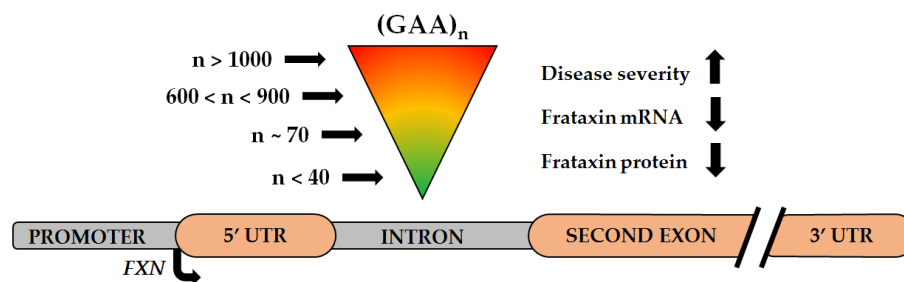


Figure 3.1. Genetic cause of Friedreich's ataxia. An aberrant expansion of GAA triplet in the first intron of *FXN* gene blocks the transcription of *FXN* mRNA leading to reduced levels of frataxin protein. The number (n) of GAA expansions correlates with disease severity.

Longer GAA expansions are usually associated with a more severe phenotype with earlier symptoms onset and faster progression of the disease, and an inverse correlation between the number of GAA triplets in the smaller allele and the age of symptoms onset, as well as disease complications like *diabetes mellitus* or *cardiomyopathy*, has been also observed in FRDA patients. Nevertheless, the number of repeats is not the only aspect which determines the variability of the age of onset; somatic mosaicism, modifier genes and the instability of the GAA expansion are only some other aspects which could contribute to that [Delatycki M.B. et al., 1999; Dürr A. et al., 1996; Filla A. et al., 1996; Montermini L. et al., 1997]. From a genetic point of view, the primary consequence of the abnormal GAA triplet repeat is the transcriptional silencing of *FXN*, gene which encodes the mitochondrial protein frataxin (FXN).

The molecular mechanisms which bring to *FXN* gene silencing have been extensively studied and some evidence indicates that the *FXN* transcriptional deficiency is due to the formation of non-canonical DNA/RNA structures, like “sticky DNA” triplexes and R-loops. The formation of heterochromatin (*i.e.* repressive chromatin), along with other aberrant epigenetic mechanism like DNA methylation, histone modifications (acetylation/deacetylation and methylation/demethylation) and noncoding RNAs, have a deep impact on the transcriptional process of the gene and, consequently, on the expression of frataxin (Figure 3.2) [Sakamoto N. *et al.*, 1999; Sandi C. *et al.*, 2013; Cook A. & Giunti P., 2017].

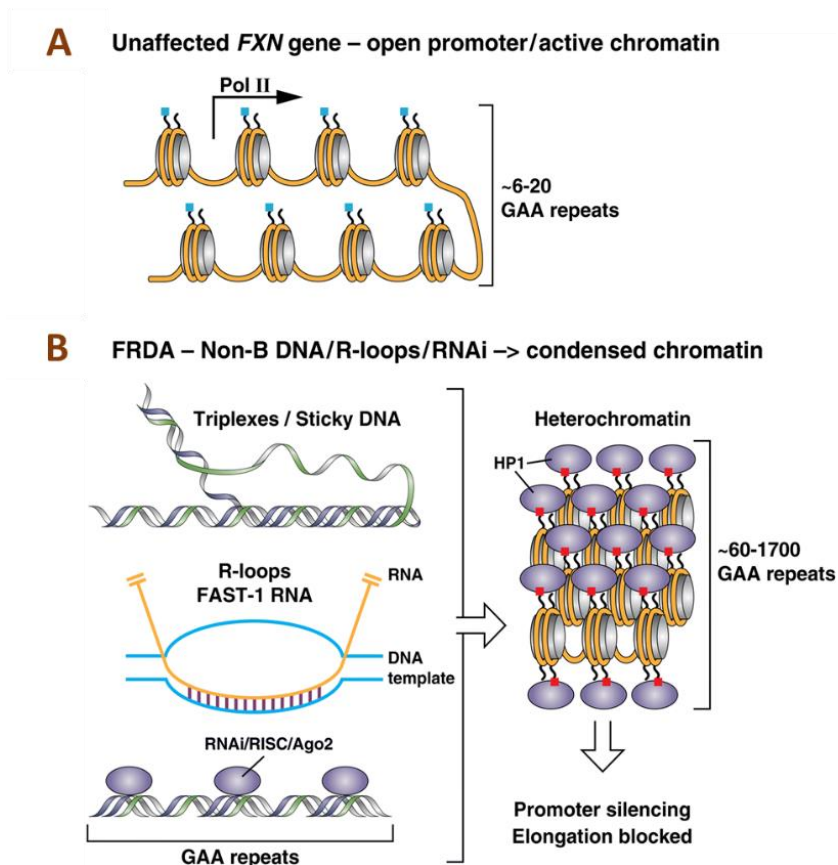


Figure 3.2. Proposed mechanisms of *FXN* gene silencing. (A) In healthy conditions, where the number of GAA repeats is less than 40, the *FXN* gene is packaged in open chromatin; RNA polymerase II (Pol II) has access to the promoter, proceeding with the elongation. Blue marks indicated acetylated histones on nucleosomes. (B) In FRDA conditions, where the number of GAA repeats is more than 40, the *FXN* gene is packaged in condensed heterochromatin (the histone methylation marks, shown in red, are the binding sites for HP1, the protein involved in the heterochromatin condensation). Some factors which induce heterochromatinization, such as triplexes and/or sticky DNA, R-loops, short RNA transcripts or FAST-1 (an antisense transcript of *FXN*), are reported [from Gottesfeld J.M. *et al.*, 2019].

In FRDA patients, frataxin levels are in fact reduced by 5-30% while, in asymptomatic carriers, protein levels are about 50% if compared to healthy unaffected individuals; therefore, a correlation between the amount of residual frataxin in FRDA patients and the onset of pathological mechanisms of the disease is likely [Campuzano V. et al., 1997; Chutake Y.K. et al., 2014; Lazaropoulos M. et al., 2015; Delatycki M.B. & Bidichandani S.I., 2019]. Frataxin deficiency mainly affects the organs and tissues where the protein is highly expressed, *i.e.* dorsal root ganglia, spinal cord, cerebellar dentate nuclei and cerebral cortex, as well as in heart, pancreas, liver and skeletal muscle [Campuzano V. et al., 1996; Campuzano V. et al., 1997] and this correlates with the sites mainly involved in FRDA pathology [Koeppen A.H., 2011]. Furthermore, the complete loss of frataxin in cells results in embryonic lethality, both in mammals [Cossée M. et al., 2000] and in plants [Vazzola V. et al. 2007], suggesting that frataxin plays a key role as a protein essential for organisms' development and survival. Since frataxin depletion has a deep impact on the mitochondrial functionalities, Friedreich's ataxia has been effectively classified as a mitochondrial disease.

3.3 Mitochondrial Pathophysiology

As described in the previous chapter, alterations in mitochondrial functionalities have a predominant role in neurodegenerative disorders. Defects in mitochondrial energy production and in oxidative stress mechanisms, as well as alterations in mitochondrial quality control, network dynamics and communication of mitochondria with other organelles, are all phenotypic traits that have been reported for FRDA pathology [González-Cabo P. & Palau F., 2013].

In particular, the imbalance of iron metabolism, which commonly characterizes neurodegenerative diseases, is a distinctive feature of Friedreich's ataxia [Lamarche J.B. et al., 1980; Bradley J.L. et al., 2000; Harding I.H. et al., 2016]. The biochemical alteration of mitochondrial and cellular iron physiology due to frataxin deficiency have been associated with mitochondrial iron overload and iron deposits, as observed in FRDA patients [Ramirez R.L. et al., 2012] and in different models of frataxin depletion such as mouse [Whitnall M. et al., 2012], yeast [Babcock M. et al., 1997] and *Caenorhabditis elegans* [González-Cabo P. et al., 2011]. In this regard, mitochondria play a central role in the maintenance of cellular iron homeostasis [Richardson D.R. et al., 2010]; iron levels need to be finely regulated because a possible imbalance at mitochondrial level can lead to the

generation of reactive oxygen species and consequent deleterious effects for the cell. In mitochondria, iron is mainly used in the biosynthesis of iron-sulfur clusters and heme centers, prosthetic groups that are responsible of the enzymatic activities of several proteins such as the complexes of electron transport chain and enzymes of Krebs cycle. Defects in iron-sulfur clusters biogenesis with the consequent deficit of Fe-S proteins lead to an increasing iron accumulation and mitochondrial iron overload [Lill R. *et al.*, 2012], as observed in Friedreich's ataxia etiology [Rötig A. *et al.*, 1997; Chiabrando D. *et al.*, 2020].

In addition to defects in iron-sulfur cluster biosynthesis and mitochondrial iron accumulation, the third main biochemical features of FRDA cells is an increased susceptibility to oxidative stress [Schulz J.B. *et al.*, 2000; Schmucker S. & Puccio H., 2010]. Increases in reactive oxygen species, in some cases associated with iron deposits, have been observed in several cellular and animal models with a depletion of frataxin (mouse [Puccio H. *et al.*, 2001; Simon D. *et al.* 2004; Al-Mahdawi S. *et al.*, 2006], yeast [*e.g.* Babcock M. *et al.*, 1997 and Wilson R.B. & Roof D.M., 1997], *Drosophila melanogaster* [Llorens J.V. *et al.*, 2007] and *C. elegans* [Vazquez-Manrique R.P. *et al.*, 2007]), as well as in fibroblasts, cerebellum and heart biopsies from FRDA patients [Garcia-Gimenez J.L. *et al.*, 2011; Waldvogel D. *et al.*, 1999; Rötig A. *et al.* 1997]. ROS imbalance is also intimately linked to the impairment of iron-sulfur protein. The complexes of the respiratory chain, especially complex I and complex III, are the primary source of endogenous reactive oxygen species; an imbalance in their activity and, for extension, in the coupling efficiency of the electron transport chain, promotes an increase in ROS levels and in oxidative stress susceptibility. In a vicious circle, a modification in physiological redox balance could bring to the activation of cellular defense mechanisms such as autophagic processes. Autophagy is a degradative cellular process responsible for the removal of damaged organelles, misfolded or aggregated proteins and intracellular pathogens, playing a key role in balancing sources of energy as an adaptive mechanism of starvation. In some cases, when autophagic mechanisms are not able to control the oxidative injuries, apoptotic pathways could be activated. In neurodegenerative diseases autophagy has been shown to be crucial for the neuronal survival; when autophagic mechanisms are not able to control the oxidative injuries, apoptotic pathways can be activated leading to cellular death. Although the correlation between frataxin depletion and apoptosis is strongly dependent on the type of cell, some evidence has pointed out classical autophagic patterns in FRDA pathology models [Simon D. *et al.*, 2004; Schiavi A. *et al.*, 2013], as well as the activation of apoptotic mechanisms

[Cossée M. *et al.*, 2000; Palomo G.M. *et al.*, 2011]. It is worth noting that the biochemical features in Friedreich's ataxia described above show a differential pattern depending on the type of tissues or organs (*Figure 3.3*); moreover, these phenotypic traits are not universal: ROS imbalance, as well as deficiencies in iron-sulfur cluster proteins or mitochondrial iron accumulation, are not always manifest or coexistent events in FRDA cells, highlighting the complexity of mitochondrial pathophysiology in Friedreich's ataxia.

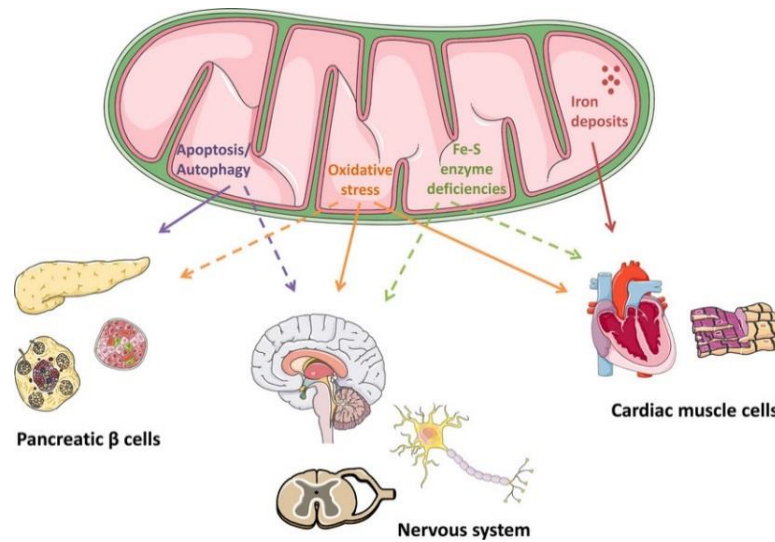


Figure 3.3. Altered biochemical pathways in Friedreich's ataxia pathology as a consequence of frataxin depletion in mitochondria. Iron deposits, deficiencies in enzymes containing iron sulfur clusters, imbalance in oxidative stress and activation of autophagic/apoptotic mechanisms are the main biochemical features that characterize FRDA patients' cells. The three principal organs affected are heart, nervous system and pancreas. Continuous arrows and dashed arrows indicate that the specific biochemical feature taken into account in the specific organ or tissue has always been reported or not, respectively [from González-Cabo P. & Palau F., 2013].

3.3 Therapeutic Approaches

Although Friedreich's ataxia has been unequivocally associated to frataxin depletion, a clear cause-effect relationship has not been clarified yet. As it will be discussed in the next chapter, different physiological roles have been proposed for frataxin, especially on the basis of the biochemical features of FRDA patients' cells; however, the precise function of frataxin is still elusive, as well as its specific contribution to the pathology onset and progression of both classical and atypical FRDA.

Since an effective and resolute therapy is not currently available, the main therapeutic and pharmacological strategies are aimed to mitigate the clinical symptoms of FRDA and slowing down the progression rate of the disease. As reported above, frataxin deficiency leads to an imbalance in iron metabolism associated with mitochondrial iron overload, an impaired enzymatic activity of Fe-S proteins and an increase in oxidative stress. On the basis of these biochemical evidence, the current therapeutic approaches are mainly based on the administration of iron chelators, drugs to decrease oxidative stress and drugs that increase frataxin expression.

3.3.1 Antioxidants and Enhancer of Energy Metabolism

Several studies highlight the beneficial use of antioxidant and mitoprotective agents in the management of FRDA disease aimed to decrease oxidative stress and increase mitochondrial functions [Pallardò F.V. et al., 2021].

Among them, the most studied antioxidants are *coenzyme Q₁₀* (CoQ₁₀), its structural analogue *idebenone*, *vitamin E* and *omaveloxolone*. *Coenzyme Q*, which is an essential component of mitochondrial respiratory chain, has a protective role against oxidative damages and acts as a compound able to restore optimal levels of energy production. Although poorly reabsorbed from the gut for its hydrophobic properties, CoQ₁₀, in combination with *vitamin E*, seems to have some positive effects on heart and skeletal muscle of FRDA patients, as well as in the slowdown of neurological symptoms progression [Cooper J.M. et al., 2008]. *Idebenone*, although combining an increased bioavailability with antioxidant properties of CoQ, has not been shown to have strong positive effects in the management of the disease [Delatycki M.B. & Bidichandani S.I., 2019]. Instead, a promising drug in the treatment of FRDA pathology appears to be *Omaveloxolone*, which has been shown to improve mitochondrial function, restore redox balance and reduce inflammation in several models of FRDA disease [Lynch D.R. et al., 2018; Lynch D.R. et al., 2021].

3.3.2 Iron Chelators

Due to the evidence of iron deposits as a biochemical consequence of frataxin depletion, iron sequestering agents are currently one of the main therapeutic

approaches adopted in the management of the disease. Among them, *deferroxamine* and *deferiprone* are the most common [Bürk K., 2017; Alsina D. et al., 2018]. Although largely used, the main problems of iron chelators are associated to their poor permeability of biological membranes and to their lack of selectivity. In fact, iron chelators act also sequestering the physiological iron, causing extracellular depletion of the metal with the risk of increasing the overall imbalance of iron metabolism. For this reason, a chelating compound able to relocate the metal from mitochondrial iron accumulations to the cytosolic compartment would be optimal, instead of non-selective chelators that indiscriminately remove iron from all the body sites.

3.3.3 Frataxin Increase and Gene Therapy

An interesting strategy in Friedreich's ataxia therapy is aimed at increasing the levels of frataxin: since heterozygous FRDA carriers with 50% level of *FXN* transcript are asymptomatic and phenotypically normal, a slight increase in frataxin levels for affected FRDA patients could be relevant to have significant clinical effects.

It has been demonstrated, both in cellular and animal models of FRDA, that frataxin levels could be increased with the use of *resveratrol*, a natural polyphenol which simultaneously acts as an antioxidant agent [Yiu E.M. et al., 2015], or *erythropoietin* [Mariotti C. et al., 2013], as well as the immune modulator *interferon gamma* [Seyer L. et al., 2015; Vavla M, et al., 2020]. The same effect may be achieved with the administration of *ubiquitin-competing molecules (UCM)*, a class of small molecules which selectively block the ubiquitination and degradation of frataxin promoted by the ubiquitin/proteasome system and guarantee the accumulation of *FXN* protein in cells [Rufini A. et al., 2015]. *Etravirine*, an antiretroviral drug currently used for the treatment of human immunodeficiency virus (HIV), has recently turned out to be a promising therapeutic for Friedreich's ataxia; in fact, *etravirine* has shown to enhance frataxin mRNA translation as well as to promote a significant increase in frataxin levels in cells from FRDA patients, allowing to restore Fe-S clusters biogenesis and conferring resistance to oxidative stress [Alfedi G. et al., 2018].

Frataxin supplementation could be also achieved by two different approaches, *i.e.* by protein replacement therapy, through a direct delivery of the protein, or by gene replacement therapy, through a delivery of a wild-type *FXN* gene [Delatycki

M.B. & Bidichandani S.I., 2019]. A direct delivery of frataxin inside cells could be carried out with the use of *TAT-frataxin fusion proteins*, chimeric proteins resulting from the fusion of frataxin with the trans-activator of transcription (TAT) domain, a cell penetrating peptide. It has been demonstrated, in FRDA mouse models, that TAT-frataxin allows an efficient delivery of the protein inside the cell and leads to a rescue of the phenotype, increasing lifespan and improving cardiac functions [Britti E. et al., 2018; Vyas P.M. et al., 2012].

New perspectives, although still at early stages, are directed to genetic therapy which could solve the upstream events of FRDA pathology. Recently, CRISPR-Cas9 system has been shown as a promising tool for genome editing and it has started to be widely applied in several preclinical trials, also for Friedreich's ataxia [e.g. Rocca C.J. et al., 2020]. However, although encouraging, gene therapy presents several problems as target delivery, genotoxicity and controlled expression [Bürk K., 2017]; for these reason, frataxin replacement or improvements in oxidative stress are currently the preferred strategies for the treatment of the disease. As an alternative approach, epigenetic therapy has been recently developed in FRDA management. The epigenetic therapy is aimed at searching for drugs and compounds which specifically target enzymes directly involved in the epigenetic changes of specific genes. In the case of Friedreich's ataxia, reversing the epigenetic modifications with, for instance, histone deacetylase inhibitors (like *pimelic 2-aminobenzamide HDAC-inhibitors*, *nicotinamide*, *sirtinol* or *splitomicin*) or DNA demethylating agents, could be a potential therapeutic tool to upregulate the expression of frataxin [Sandi C. et al., 2013].

Chapter 4

Frataxin

Among the transition metals which regulate biological processes in living systems, iron plays a role of primary importance. Iron metabolism is one of the most complex and finely regulated mechanism that characterize all life forms, from bacteria to humans. The exceptional peculiarity of this element is due to its chemical versatility which is the reason why nature selected iron in so many life processes. Several proteins are involved in iron homeostasis, from the storage and transfer of the metal to its integration as a constituent part of enzymatic cofactor. Among them, frataxin seems to play a key role in the biogenesis of Fe-S clusters, a highly complex mechanism which occurs in mitochondria. Frataxin is a mitochondrial protein whose deficiency, as described in the previous chapter, is the cause of Friedreich's ataxia. Based on the biochemical phenotypic traits of FRDA pathophysiology, several functions have been proposed for frataxin: in addition to its involvement in iron metabolism, frataxin seems to act as a pleiotropic protein taking part in other biochemical pathways, such as in cellular oxidative stress regulation or in mitochondrial bioenergetics.

In the present chapter, the current knowledge about the molecular aspects of frataxin's structure and function will be summarized, highlighting its potential capability to interact with iron, its close involvement in mitochondrial iron metabolism regulation and its role in Fe-S clusters biogenesis.

4.1 Frataxin Sequence Conservation

Frataxin is a small protein, ubiquitously found in prokaryotes and eukaryotes and highly conserved among the organisms, from bacteria and mammals to fungi and plants [Gibson T.J. *et al.*, 1996; Adinolfi S. *et al.*, 2002].

The sequence alignment of the frataxin family highlights two distinct regions, a N-terminal block of about 70 – 90 residues, poorly conserved among eukaryotes and totally absent in prokaryotes, and a C-terminal region of about 100 – 130 residues, which is highly conserved among different species (*Figure 4.1*). The sequence identity of the C-terminus is approximately 25% while the sequence

similarity corresponds to 40 – 70%, indicating that this is the functional region of the protein [Pandolfo M. & Pastore A., 2009]. It is worth to note that the sequence conservation mainly involves three tryptophan residues and a semi-conserved series of negatively charged residues, suggesting that these could have an important role in the structure and/or function of the protein.

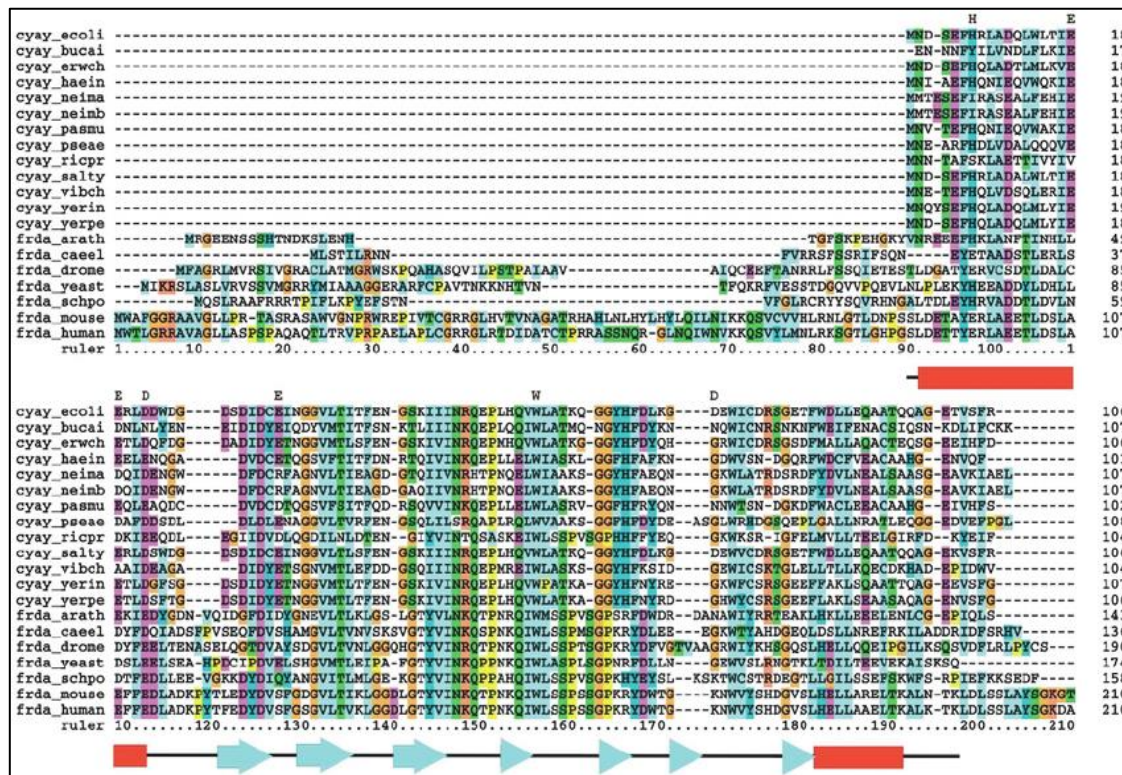


Figure 4.1. Multiple sequence alignment of frataxin proteins. Sequence alignment of some frataxin orthologues displayed with software program ClustalX (European Bioinformatics Institute, Cambridge, UK) and with the standard colour coding scheme. The red boxes and light blue arrows indicate the positions of the secondary structure motif, i.e. alpha helices and beta strands respectively [from Adinolfi S. et al., 2002].

4.2 Cellular Localization and Mitochondrial Maturation

In eukaryotes, frataxin is encoded in the nucleus, synthesized in the cytoplasm and subsequently imported into mitochondria. At first, the mitochondrial localization of frataxin was suggested by the identification of a mitochondrial targeting sequence in the N-terminal of mouse and yeast homologues, as well as by the observation of an impairment of mitochondrial function caused by the disruption of the yeast frataxin gene [Koutnikova H. et al., 1997]. This hypothesis

was unequivocally confirmed by tagging experiments that demonstrated the co-localization of human frataxin with mitochondrial cytochrome *c* oxidase [Koutnikova H. *et al.*, 1997].

The human *FXN* gene encodes a polypeptide of 210 amino acids which represents the precursor form of the protein, recently characterized *in vitro* in terms of stability, conformation and function [Castro I.H. *et al.*, 2018]. The additional N-terminal tail contains a mitochondrial import signal which delivers frataxin to the mitochondrion. Inside the organelle, frataxin is proteolytically processed by mitochondrial processing peptidase (MPP) to its final, mature, soluble and fully functional form.

The maturation process has been a matter of debate for a long time. Among different proposals [Koutnikova H. *et al.*, 1998; Cavadini P. *et al.*, 2000; Gordon D.M. *et al.*, 2001], Cavadini and coworkers proposed a two-step process: in the first step, human frataxin precursor is cleaved between residues G41 and L42, generating an intermediate form of 19 kDa (residues 42-210); a second cleavage occurs between residues A55 and S56, giving rise to a 17 kDa form (residues 56-210) [Cavadini P. *et al.*, 2000]. In addition to these two steps, a subsequent proteolytic cleavage between residues K80 and S81, generating a 14 kDa protein (residues 81-210), has been also identified. This last form, constituted of 130 amino acids, is currently recognized as the major form of mature frataxin inside human cells, both in healthy individuals and in FRDA patients [Condò I. *et al.*, 2007; Schmucker S. *et al.*, 2008; Gakh O. *et al.*, 2010].

4.3 Folding and Structure

By means of X-ray crystallography and NMR spectroscopy, several structural studies have been carried out for the yeast (Yfh1), human (Hfxn) and bacterial (CyaY) frataxin orthologues [Cho S.J. *et al.*, 2000; Dhe-Paganon S. *et al.*, 2000; Lee M.G. *et al.*, 2000; Musco G. *et al.*, 2000; Nair M. *et al.*, 2004; He Y. *et al.*, 2004]. A comparison of their tridimensional structures highlights a strong folding similarity (Figure 4.2A), which directly reflects the high degree of amino acid sequence conservation and suggests a common function.

The peculiarity of frataxin fold is due to a planar α - β sandwich motif: two terminal α -helices and five antiparallel β -strands constitutes two structural planes, and one or two additional β -strands intersect them, giving rise to the final globular and slightly elongated structure.

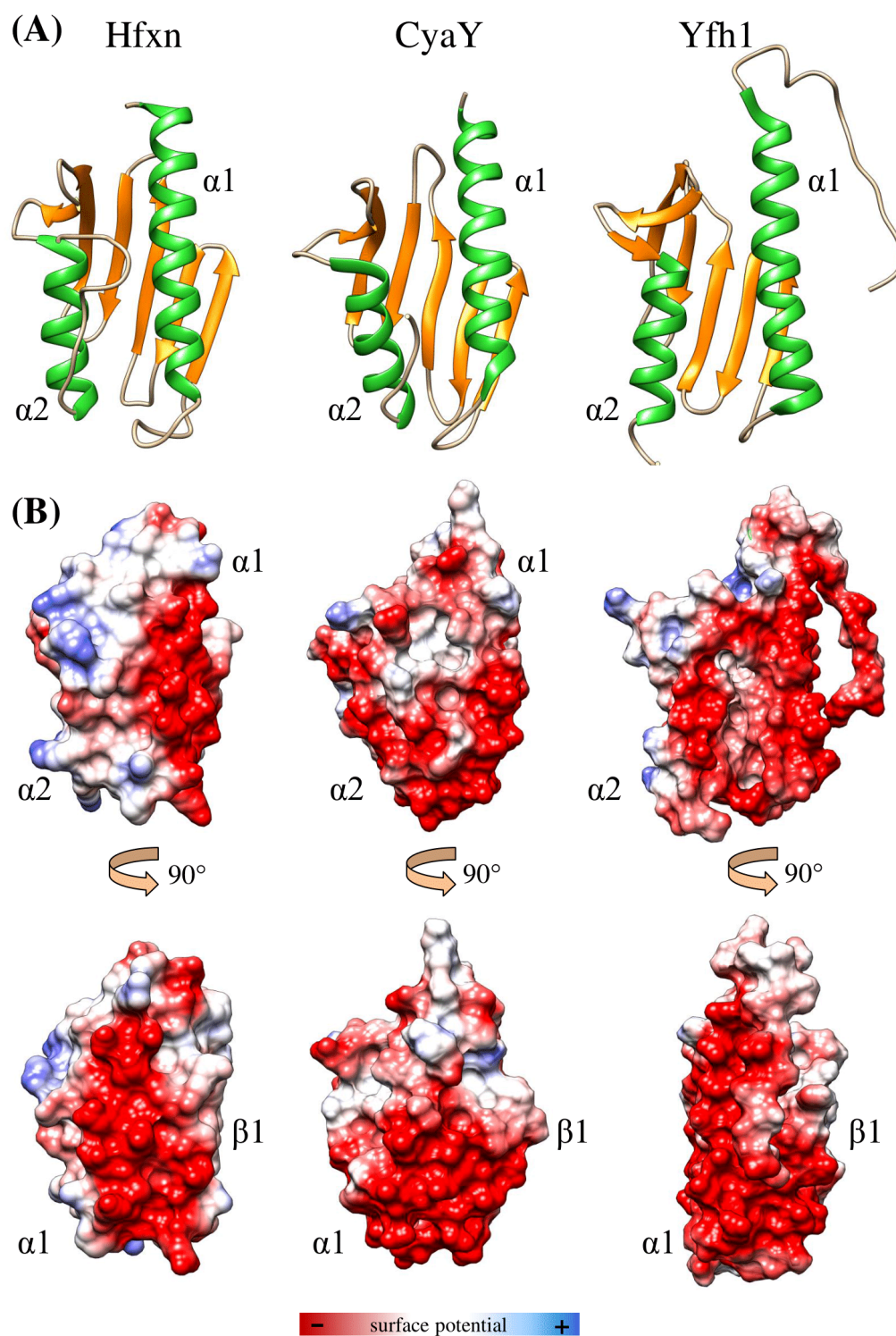


Figure 4.2. Solution structure of three frataxin orthologues and their electrostatic surfaces. (A) Ribbon structures for human (Hfxn), yeast (Yfh1) and bacterial (CyaY) frataxin. All the proteins shared a common structure characterized by two alpha-helices (in green) and 6/7 beta-sheets (in orange) following an $\alpha1\beta1\beta2\beta3\beta4\beta5\beta6(\beta7)\alpha2$ topology. (B) Electrostatic surfaces of human (Hfxn), yeast (Yfh1) and bacterial (CyaY) frataxin placed in the same orientation as in (A) on the top and rotated of 90 degrees around the y -axis on the bottom. (Structure figures and electrostatic plots have been elaborated with UCSF Chimera using PDB ID: 1LY7 for Hfxn, PDB ID: 2GA5 for Yfh1 and PDB ID: 1SOY for CyaY).

For human frataxin, the N-terminal tail which comprises residues 81-92 has been shown to be predominately unstructured and intrinsically unfolded [Musco *et al.*, 2000; Prischi F. *et al.*, 2009], justifying the frequent use of the truncated 90-210 form for the *in vitro* studies. Despite their high structural similarity, human, yeast and bacterial frataxins have also different thermodynamic stabilities [Pastore A. *et al.*, 2007] and several factors have been shown to influence frataxin fold as, for instance, the length of the C-terminal region [Adinolfi S. *et al.*, 2004].

As previously stated, the structural similarity between frataxin orthologues is the result of a high similarity in amino acid sequence. Among the most conserved and semi-conserved residues, a series of aspartates and glutamates are located in the N-terminal region of the protein covering in large part the $\alpha 1$ and $\beta 1$ secondary structural motifs. The enrichment in these residues confers acidity to frataxin, which presents an isoelectric point of around 4.5 [Adinolfi S. *et al.*, 2004]. The comparison of the electrostatic potential plots of yeast, human and bacterial frataxins (Figure 4.2B) highlights a conserved negatively charged surface distributed along the first alpha helix and the beta sheet, approximately covering a quarter of the protein total accessible surface [Dhe-Paganon *et al.*, 2000]; the conservation of this protein dipole among frataxin from different organisms suggests the potential involvement of this specific protein patch in molecular interactions with other ligands or proteins.

4.3.1 The Effect of Point Mutations on Protein Structure

As described in the previous chapter, most of the FRDA patients are homozygous for a GAA repeat expansion in the first intron of the *FXN* gene while about 4% of FRDA patients carry one GAA expansion in one allele and a truncating or missense mutation in the other. More than 40 different mutations have been reported, including insertion, deletion and/or point mutations [Cossée M. *et al.*, 1999; De Castro M. *et al.*, 2000]. Interestingly, all clinically relevant mutations have been shown to affect highly conserved residues [Cossée M. *et al.*, 1999]; for this reason, a closer inspection of these mutations have been done to provide new insights into frataxin function. Unlike the homozygous condition, which leads to a reduction of frataxin levels, the missense mutations are directly involved in alteration of the activity, folding and/or structural properties of the expressed protein, as suggested by several *in vitro* studies [Correia A.R. *et al.*, 2006; Correia A.R. *et al.*, 2008]. Using recombinant mutant proteins, it has been demonstrated

that, under physiological conditions, some of these point mutations do not affect the native protein folding but influence the thermodynamic stability, as well as protein dynamics, tendency towards aggregation and susceptibility to proteolytic digestion. For this reason, it has been suggested that the FRDA etiological manifestations in heterozygous patients could result from the combined effects of a reduced folding efficiency and an acceleration in protein degradation, leading to lower frataxin cellular levels [Pastore A. & Puccio H., 2013].

Among the most frequent pathological point mutations, D122Y, G130V, I154F, N146K, W155R and R165C could result either in the classical FRDA phenotype or in atypical clinal manifestation [Cossée M. et al., 1999; Gellera C. et al., 2007; Galea C.A. et al., 2016]. It is worth to note that the most recurrent point mutations could be clustered into two groups with common features (Figure 4.3). The first group is composed by residues which belong to the hydrophobic core of the protein and pack against each other, suggesting that their mutations could have an impact on the stabilization of protein fold (residues L106, I154, L156, W173, L182 and H183).

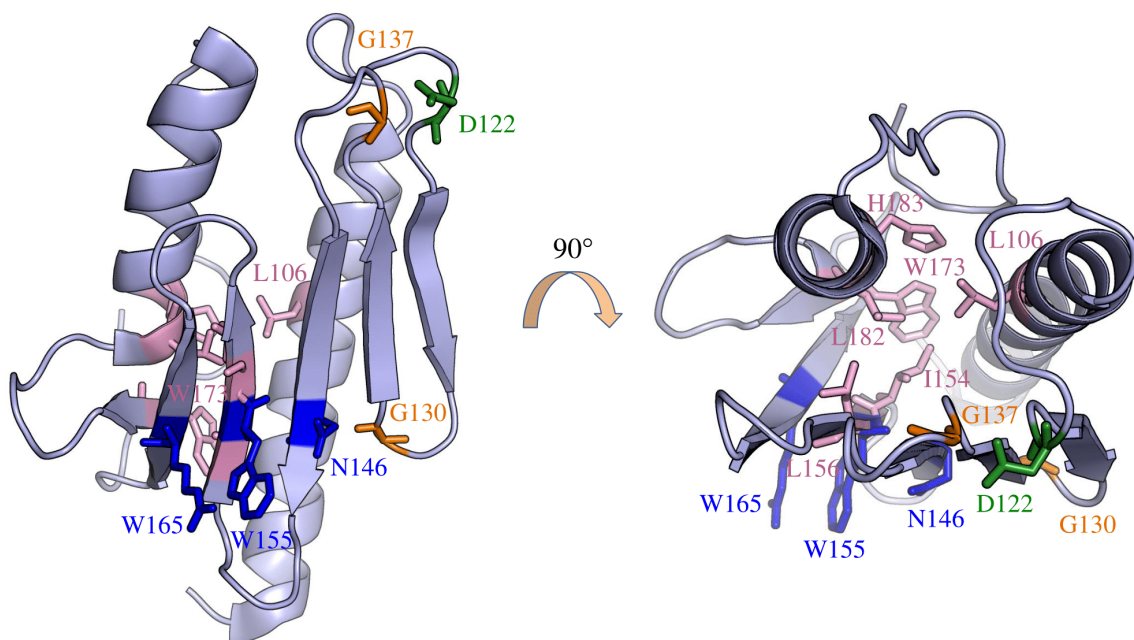


Figure 4.3. Ribbon representation of the structure of human mature frataxin and main FRDA-pathological point mutations. The side chains of mutated residues are shown as sticks and colored on the basis of the group to which they belong. In blue are highlighted the three exposed residues (N146, W155 and W165) while the buried residues of the hydrophobic core (L106, I154, L156, W173, L182 and H183) are depicted in pink and explicited in the structure rotated of 90 degrees around the x-axis. The two glycine residues (G130 and G137) are in orange while D122 is highlight in green. The structure figures have been made with PyMol using PDB ID: 1EKG for human frataxin.

The second group is represented by exposed residues located on the β -sheet, *i.e.* the conserved tryptophan W155, the arginine R165 and the asparagine N146. Other relevant point mutations affect the negatively charged aspartate in position 122 and two glycine residues in position 130 and 137 which are placed at the beginning of the β 1 β 2 turn and at the end of β 2 strand, respectively. The two glycine-to-valine mutations of G130 and G137, due to the steric hindrance with neighboring residues caused by the bulkier side chain of valine, have been shown to strongly destabilize the protein fold [Cavadini P. *et al.*, 2000; Faggianelli N. *et al.*, 2015].

Interestingly, it has been also demonstrated that some disease-related missense mutations impair the cellular localization of frataxin as well as the interaction with mitochondrial protein peptidase, with consequences on the correct protein maturation processing inside mitochondria [Clark E. *et al.*, 2017].

4.3.2 Iron-Binding Properties

The acidic patch of frataxin N-terminal domain, corresponding to the first α -helix and the first β -strand, has been suggested to confer to the protein the capability to bind cationic species. In particular, the presence of aspartates and glutamates, which are chemically proper to act as ligands for metallic ions, indicated a possible involvement of frataxin in metal binding.

NMR studies on yeast, human and bacterial frataxin orthologues pointed out the capability of the protein to chelate, although with low specificity and affinity, divalent and trivalent cationic species including Ca^{2+} , Mn^{2+} , Co^{2+} , Cu^{2+} , and various lanthanide ions [Nair M. *et al.*, 2004; Pastore C. *et al.*, 2007]. However, since one of the biochemical traits of FRDA pathophysiology is an impairment in cellular iron homeostasis, a plethora of spectroscopic studies have been performed to investigate the potential capability of the protein to bind iron. Although widely debated over the years, frataxin has been unequivocally recognized as an iron-binding protein, albeit as an unusual member of this family [Adamec J. *et al.*, 2000; Adinolfi S. *et al.*, 2002; Cavadini P. *et al.*, 2002; Yoon T. & Cowan J.A. 2003; Yoon T. & Cowan J.A., 2004; Bou-Abdallah F. *et al.*, 2004; Cook J.D. *et al.*, 2006; Bellanda M. *et al.*, 2019]. Frataxin has in fact a completely different structure if compared to classical iron-binding proteins: in iron-carrying proteins, such as transferrin, the binding sites for the metal are localized in buried pockets protected by globular domains, while in other iron-binding proteins, such as

ferritin, these sites are hidden in hydrophilic cavities. Furthermore, among the residues which are generally involved in the iron-binding, there are often cysteines, which can be in turn assisted by the coordination promoted by histidines and carboxylate groups. On the contrary, mature frataxin does not possess cysteine residues in its amino acid sequence and the putative region of iron-binding is exposed on the protein surface, suggesting that the monomeric protein could have a weak and labile tendency to bind the metal, and that a stable binding or storage functions may require the joint action of several frataxin monomers.

X-ray absorption spectroscopy (XAS) and X-ray absorption fine structure (EXAFS) have been used to characterize iron-binding to yeast and human frataxin [Cook J.D. *et al.*, 2006], and NMR spectroscopy clearly provided frataxin residues which are directly involved in the interaction with the metal [Musco G. *et al.*, 1999; Nair M. *et al.*, 2003; He Y. *et al.*, 2004].

Several independent studies demonstrated the capability of the monomeric protein to bind both ferrous and ferric ions. By means of isothermal titration calorimetry (ITC), bacterial CyaY and yeast Yfh1 were shown to bind two Fe²⁺ ions at micro-molar range and, although with comparable dissociation constant (K_d), they bind iron in a different manner: while for CyaY both binding sites have $K_d \approx 4.0 \mu\text{M}$ [Bou-Abdallah F. *et al.*, 2004], in Yfh1 the two metal binding sites for Fe²⁺ are independent with nearly identical binding affinities ($K_{d1} = 3.0 \mu\text{M}$ and $K_{d2} = 2.0 \mu\text{M}$ for the two sites, respectively) [Cook J.D. *et al.*, 2006]. Moreover, the capability of monomeric CyaY to bind six ferric ions in oxidative conditions has been demonstrated. This eventually leads to the interaction with 25-26 Fe³⁺/monomer and to an increased oligomerization tendency [Bou-Abdallah F. *et al.*, 2004]. For human frataxin, greater uncertainty concerns the stoichiometry, affinity and type of metal coordination in iron-binding. By means of ITC and fluorescence spectroscopy, it was found that human mature frataxin binds six to seven Fe²⁺/Fe³⁺ ions per monomer with $K_d(\text{Fe}^{2+}) = 55.0 \mu\text{M}$ and $K_d(\text{Fe}^{3+}) = 10.2 \mu\text{M}$ [Yoon T. & Cowan J.A., 2003]. Differently, through a combination of NMR, fluorescence, and mass spectrometry, a binding stoichiometry of only three equivalents was reported for the binding of both ferrous and ferric ions [Gentry L.E. *et al.*, 2013]. Making more controversial this issue, a recent NMR study pointed out that frataxin binds only one Fe²⁺ equivalent and has no binding affinity for Fe³⁺ [Cai K. *et al.*, 2018].

Although the large number of discrepancies regarding its iron-binding properties, it is widely accepted that frataxin, directly binding iron, could be

involved in the maintenance of cellular metabolism and homeostasis of this metal; for this reason, various hypotheses about its possible roles *in vivo* have been advanced, as described in the next section.

4.4 Frataxin, a Moonlighting Protein

As described in the previous chapter, the precise physiological function of frataxin is still elusive. Different roles have been supposed, based on the phenotype of FRDA patients' cells and on frataxin iron-binding properties. Among them, frataxin seems to take part in different pathways, all related to iron metabolism, as an iron chaperone and/or allosteric modulator in Fe-S clusters and heme biogenesis, as an iron-storage protein during condition of iron overload, or as a modulator in the oxidative stress and protection against oxidative damage. Furthermore, there are other cellular processes in which a direct involvement of frataxin has been suggested, from mitochondrial energy conversion and oxidative phosphorylation to cellular signaling, from mechanism of autophagy to apoptosis and ferroptosis. All these roles are however interdependent, suggesting how frataxin could take part simultaneously in more than a single process: to all intents and purposes frataxin can be considered a moonlighting protein, performing multiple physiological roles in the context of mitochondrial functionality.

4.4.1 The Involvement in Iron Metabolism as an Iron-Storage Protein

Isaya and co-workers were the first to suggest a physiological function for frataxin, observing the capability of the yeast Yfh1 to encapsulate iron in spheroidal oligomeric structures in a ferritin-like manner [Adamec J. *et al.*, 2000]. Later studies demonstrated that the tendency to form large oligomeric assemblies distinguishes also bacterial CyaY but not mature Hfxn: while in the absence of iron all three frataxin orthologues retain a highly soluble monomeric form *in vitro*, only CyaY and Yfh1 assemble into oligomeric structure, in the presence of large excess of iron and under aerobic conditions [Cook *et al.*, 2006; Adinolfi *et al.*, 2009; Cook *et al.*, 2010]. Although confuted later [Yoon T. *et al.*, 2007], human frataxin demonstrates a tendency to oligomerize only in its (56-210) form, in an

iron-independent manner and under extreme conditions [O'Neill H.A. *et al.*, 2005]. Frataxin oligomerization has been deeply investigated for Yfh1, highlighting the tendency of the protein to assemble into trimers, hexamers, 12-mers, 24-mers up to 48-mers, with the trimer as a basic unit, in an iron-dependent manner (Figure 4.4A). The capability to form spheroidal structures with iron storage properties led to hypothesize for frataxin a ferritin-like storage function (Figure 4.4B); this was also supported by the evidence that mitochondrial ferritin can partially complement the absence of frataxin, both in yeast and in human cells [Campanella A. *et al.*, 2004; Zanella I. *et al.*, 2008].

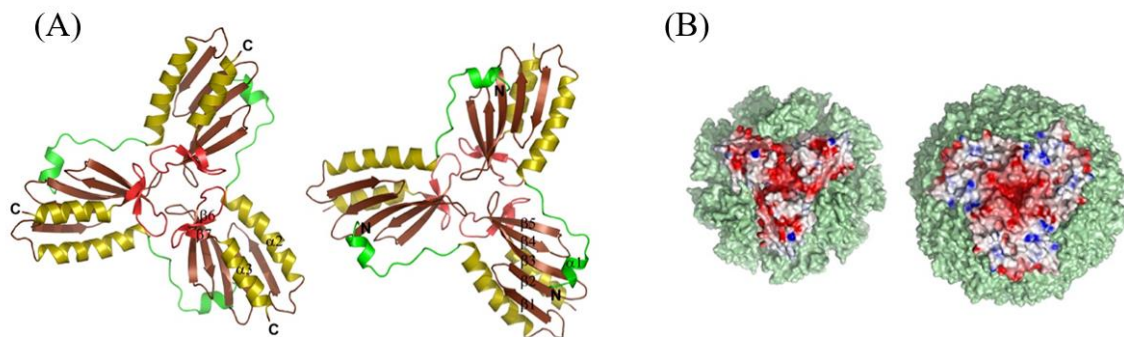
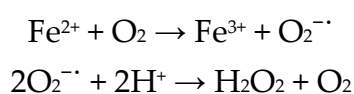


Figure 4.4. Architecture of the yeast frataxin trimer and 24-meric oligomer. (A) On the left, proposed outer surface of the trimer and, on the right, its inner surface, in ribbon representation. Loops, α -helices and β -strands are shown in brown, yellow and red, respectively. The N-terminal, which is colored in green, contributes to the stabilization of the assembly. (B) Comparison of surface representation of yeast frataxin (on the left) and horse-spleen ferritin (on the right) 24-meric oligomers in the same scale. Trimers which constitute the oligomers are represented in accordance with their electrostatic surface potential. [Adapted from Karlberg T. *et al.*, 2006].

However, experimental studies performed with Yfh1 and CyaY suggested that this should not be the major function of frataxin since, at physiological concentrations of magnesium or calcium salts within mitochondria, these proteins are in a monomeric state and the tendency to oligomerization is discouraged [Adinolfi S. *et al.*, 2002]. Moreover, iron storage function for frataxin could be a redundant role in mammals where a specialized mitochondrial ferritin (MtF) fulfills this function; the expression of human mitochondrial ferritin in frataxin-deficient yeast cells prevented the development of mitochondrial iron overload and restored the impaired mitochondrial functionality, showing that MtF can substitute for most frataxin functions in yeast [Campanella A. *et al.*, 2004].

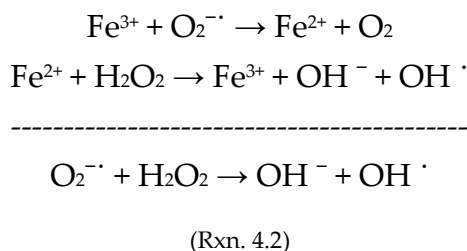
4.4.2 The Role in the Oxidative Stress

As described in the previous chapter, susceptibility to oxidative stress is one of the central features of FRDA disease. An altered iron metabolism associated with intracellular iron deposits, as observed in FRDA patients' cells as well as in different frataxin-deficiency models, remarkably contributes to cellular oxidative damage [e.g. Babcock M. et al., 1997; Rötig A. et al. 1997; Puccio H. et al., 2001; Llorens J.V. et al., 2007]. The chemical versatility of iron, which relies on the ability to cycle between the ferrous (Fe^{2+}) and ferric (Fe^{3+}) oxidation states, is the reason why the metal has been chosen by Nature to take part in several biological processes. Nevertheless, at the same time, iron redox chemistry needs to be finely regulated because, if unbalanced, it can promote a series of collateral reactions which lead to the increase the cellular concentration levels of ROS, molecules which have deleterious effects on cell membranes and other cellular components such as proteins, lipids, and nucleic acids. ROS include superoxide radical anions (O_2^-), hydroxyl radicals (OH^\cdot) and hydrogen peroxide (H_2O_2), that can easily lead to free radical reactions in living organisms. At low concentrations, ROS are particularly important in cells, playing a pivotal role as messengers in cell signaling, as a support in cell proliferation and as key regulators in survival pathways [Ray P.D. et al., 2012]. On the other hand, a very high concentration of ROS creates an imbalance between ROS formation and cellular antioxidant capacity; in this case, the cell turns into a condition of oxidative stress and the antioxidant system is not able to overcome it [Schieber M. & Chandel N.S., 2014]. The cellular antioxidant defenses include detoxifying specific enzymes, as well as small molecules which directly react with ROS as glutathione, ascorbic acid or NADPH. Among the enzymes which take part in the response to oxidative stress there are superoxide dismutases (SODs), which catalyze the dismutation of the superoxide radical into molecular oxygen and hydrogen peroxide, and glutathione peroxidase and catalase, which catalyze the decomposition of H_2O_2 to water and oxygen. With a closer inspection to iron biological chemistry, ferrous iron is extremely prone to react with molecular oxygen, leading to the formation of superoxide radical anion and hydrogen peroxide:

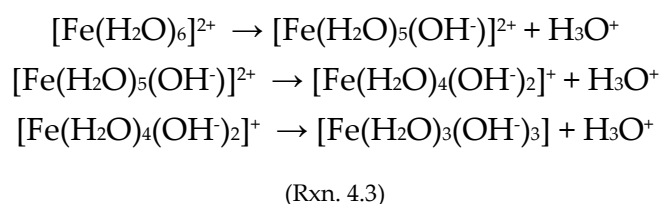


(Rxn. 4.1)

In the Haber Weiss reaction, ferric iron can be reduced to Fe²⁺ by superoxide radical anion and, subsequently, ferrous iron can react with hydrogen peroxide promoting the generation of highly reactive hydroxyl radicals according to Fenton reaction [Kehrer J.P. 2000; Aisen P. et al., 2001]. The overall Haber Weiss reaction can be summarized as follows:



In an oxidative environment, like that of the mitochondrial matrix, free Fe²⁺ ion is rapidly oxidized to Fe³⁺ and, under physiological conditions, ferric ions undergo hydrolysis process with the subsequent formation of insoluble species:



In biological systems, different mechanisms have been developed in order to prevent the iron oxidation and keep it in a soluble form, from specialized chaperones for the metal delivery (e.g. transferrin) to efficient systems for its storage (e.g. ferritin). In this context, it has been suggested that frataxin, for its iron-binding properties, could modulate iron–redox chemistry: according to a ferritin-like model, frataxin could bind Fe²⁺ and oxidize it to Fe³⁺ through a ferroxidase chemistry and eventually keep iron in a bio-available form due to its oligomerization capability [Park S. et al., 2003]. Ferroxidase activity has been observed for yeast Yfh1 [Park S. et al., 2002] and human frataxin [O'Neill H.A. et al., 2005]; oligomers of iron-loaded human frataxin showed in fact a protective effect on DNA against oxidative damage in presence of hydrogen peroxide, highlighting a possible role of the protein in the modulation of cellular oxidative stress [O'Neill H.A. et al., 2005; Gakh O. et al., 2006].

Accordingly, it has been demonstrated that, in a *Drosophila* model, frataxin overexpression improved the cellular resistance to oxidative stress and to iron accumulation, supporting the hypothesis of frataxin as a protector against

mitochondrial oxidative damage [Runko A.P. *et al.*, 2008]. However, the mechanisms through which frataxin could exert this role are not completely understood yet. In particular, although a strict relationship between frataxin deficiency and oxidative stress is clear, it is not likewise evident whether frataxin could act as an active participant in the cellular antioxidant machinery. A recent study demonstrated a direct involvement of human frataxin and yeast orthologue Yfh1 in the antioxidant defense, showing that both proteins are able to regulate the detoxifying enzymatic mechanisms and to inhibit the ROS production [Uceda A.B. *et al.*, 2021]. In support of the hypothesis which suggests frataxin as a player in the intracellular antioxidant machinery, it has been shown that frataxin from yeast is able to interact *in vitro* with superoxide dismutases and guarantee an enhancement of their enzymatic activities [Han T.H.L. *et al.*, 2019]. Interestingly, it has been also demonstrated that mature frataxin interacts not only with mitochondrial SOD2 but also with cytosolic SOD1, supporting a previous evidence which showed that extramitochondrial frataxin plays a regulatory function in the cytoplasmatic oxidative balance [Condò I. *et al.*, 2006]. Although the mechanism by which frataxin participates in the antioxidant machinery is far to be completely clarified, it is commonly accepted that, in Friedreich's ataxia, oxidative stress is intimately linked to the impairment of iron-sulfur clusters biogenesis [Pandolfo M. & Pastore A., 2009]. In this regard, the alteration of the ISC-containing OXPHOS complexes leads to a defective respiratory chain causing, as direct consequence, the leakage of electrons within the mitochondrial membrane. Thus, the direct addition of electrons to molecular oxygen leads to an increase in superoxide anions which are converted to H₂O₂ by SOD2 and hydrogen peroxide, reacting with iron according to Fenton reaction, eventually contributes to the oxidative damage.

4.4.3 The Participation in the Biosynthesis of Iron Cofactors

Among the different functions attributed to frataxin, it has been suggested that the protein plays a key role in the biogenesis of iron-sulfur clusters and in the biosynthesis of heme centers [Huynen M.A. *et al.*, 2001]. Several studies unequivocally demonstrated a direct involvement of frataxin in these metabolic pathways, providing new insights into the specific linkage between frataxin and cellular iron metabolism. In this paragraph the experimental evidence and the molecular details of the participation of frataxin in these processes will be

discussed, with a brief insight into the chemical and biochemical features of heme and iron-sulfur clusters.

4.4.3.1 Chemistry and Biochemistry of Heme and Iron-Sulfur Clusters

Heme centers and iron-sulfur clusters are ubiquitous prosthetic groups, widely diffused in almost all living beings, from prokaryotes to eukaryotes, from archaea to mammals. In biological systems, they are essential for several fundamental cellular processes including electron transport, enzymatic catalysis and metabolic regulation [Padmanaban G., 1989; Ponka P., 1999; Beinert H. & Kiley P.J., 1999]. The functional versatility of heme and iron-sulfur clusters derived from the protein environment in which they are inserted: the distribution of polar and charged groups around them, the extent of their burial inside the protein, the number and nature of protein-donated ligands to iron and the structural features of their binding site have a deep impact on their chemical properties and, consequently, on their functions [Barupala D.P. et al., 2016].

In eukaryotes three types of heme exist: heme *a*, heme *b* and heme *c* (Figure 4.5) [Kim H.J. et al., 2012]. Heme *b*, also known as protoheme IX, is the precursor of the other two types of heme and it consists of iron, two vinyl side chains, four methyl groups and two propionic acid side chains on a conjugated tetrapyrrole ring.

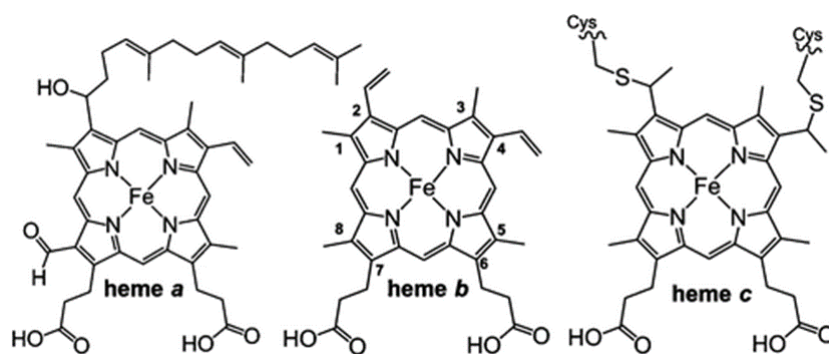


Figure 4.5. Chemical structures of protoheme IX (heme b), heme a and heme c. Heme b binds non-covalently to protein while heme c is covalently bound through two thioether bonds between cysteine side chains of the protein and the heme vinyl groups at positions 2 and 4, according to Fisher numbering system. Heme a presents a higher structural complexity, requiring two chemical modifications from protoheme, i.e. farnesylation and addition of a formyl group to position 8 of protoheme. In cytochromes, iron is either penta- or hexa-coordinate: in addition to the four coordination positions filled by the nitrogen atoms of the porphyrin ring, appropriate ligands are positioned below the heme plane and, in most cases, also above the heme plane [adapted from Liu J. et al., 2014].

Heme *a* and heme *c* are structurally similar to protoheme IX, with modifications that derive from their insertion into each specific protein: heme *c* is covalently bound to the protein through two (rarely one) thioether bonds to cysteine side-chains; heme *a* has an isoprenoid tail substituted on one of the vinyl groups and a formyl which replaced a methyl group on the porphyrin ring. Examples of proteins which contains heme *b* are hemoglobin, catalase and mitochondrial complexes II and III. Heme *c* is present in cytochrome *c* and in the subunit cytochrome *c*₁ of mitochondrial complex III, while heme *a*, with heme *a*₃, occurs in mitochondrial complex IV. In cytochromes, hemes catalyze the electrons transfer through the reversible oxidation and reduction of iron and the redox potential of the system, which dictate the direction of electron flow, is modulated by the synergic effects of the protein environment, the solvent exposure and the chemical nature of the out-of-plane ligands on the heme center.

Similarly to heme, iron-sulfur clusters (ISCs) are fundamental redox-active cofactors and they are essential components of proteins involved in many cellular processes, such as respiration, photosynthesis, metabolism and nitrogen fixation [Maio N. & Rouault T.A., 2020]. Due to their versatile chemical properties, ISCs have been shown to play a key role in many other biochemical processes like enzyme catalysis, cofactor biosynthesis, DNA replication and repair, tRNA modification and gene expression regulation [Beinert H. et al., 1997; Maio N. & Rouault T.A., 2020]. From a chemical point of view, Fe-S clusters are composed by iron (Fe²⁺/Fe³⁺) coordinated to inorganic sulphide (S²⁻); as cofactors, they are inserted into proteins typically, but not exclusively, through coordination of the iron ions by cysteinyl sulfhydryl side chains of the protein backbone. The rhombic [2Fe-2S] and the cubane [4Fe-4S] clusters are the simplest and the most common: the [2Fe-2S] cluster is formed by two tetrahedrally coordinated iron atoms with two bridging sulphides while the [4Fe-4S], as well as clusters with higher complexity (for instance with stoichiometries [3Fe-4S], [6Fe-6S], [7Fe-8S], [8Fe-7S] or [8Fe-8S]), can be conceptualized as an elaboration of the basic [2Fe-2S] moiety [Beinert H., 1997; Rees D.C. & Howard J.B., 2003] (Figure 4.6). Furthermore, among the different types of ISCs, it is worthy to note the Rieske iron-sulfur cluster in which one of the two Fe atoms of the [2Fe-2S] cofactor is coordinated by two histidine residues rather than two cysteine residues; Rieske centers are the key cofactors of several biological systems, such as mitochondrial complex III and chloroplast cytochrome *b₆f* complex. Proteins which contain ISCs as cofactors present a broad range of reduction potentials, ranging from -700 mV to 400 mV [Beinert H., 2000]; for this reason, in addition to cytochromes, they are among the

most important electron carriers in biological systems: in mitochondrial respiratory chain, the presence of up to 12 different iron-sulfur clusters is pivotal for the electron transfer between complexes I, II and III [Schultz B.E. & Chan S.I., 2001]. Furthermore, the ability of ISCs to coordinate ligands guarantees, for instance, their participation of substrate binding and catalysis: in mitochondrial aconitase, an enzyme of the TCA cycle, the substrate citrate can be converted to isocitrate, and *vice versa*, when its hydroxyl group is ligated to an iron atom of the [4Fe-4S] center [Beinert H., 2000; Rees D.C., 2002].

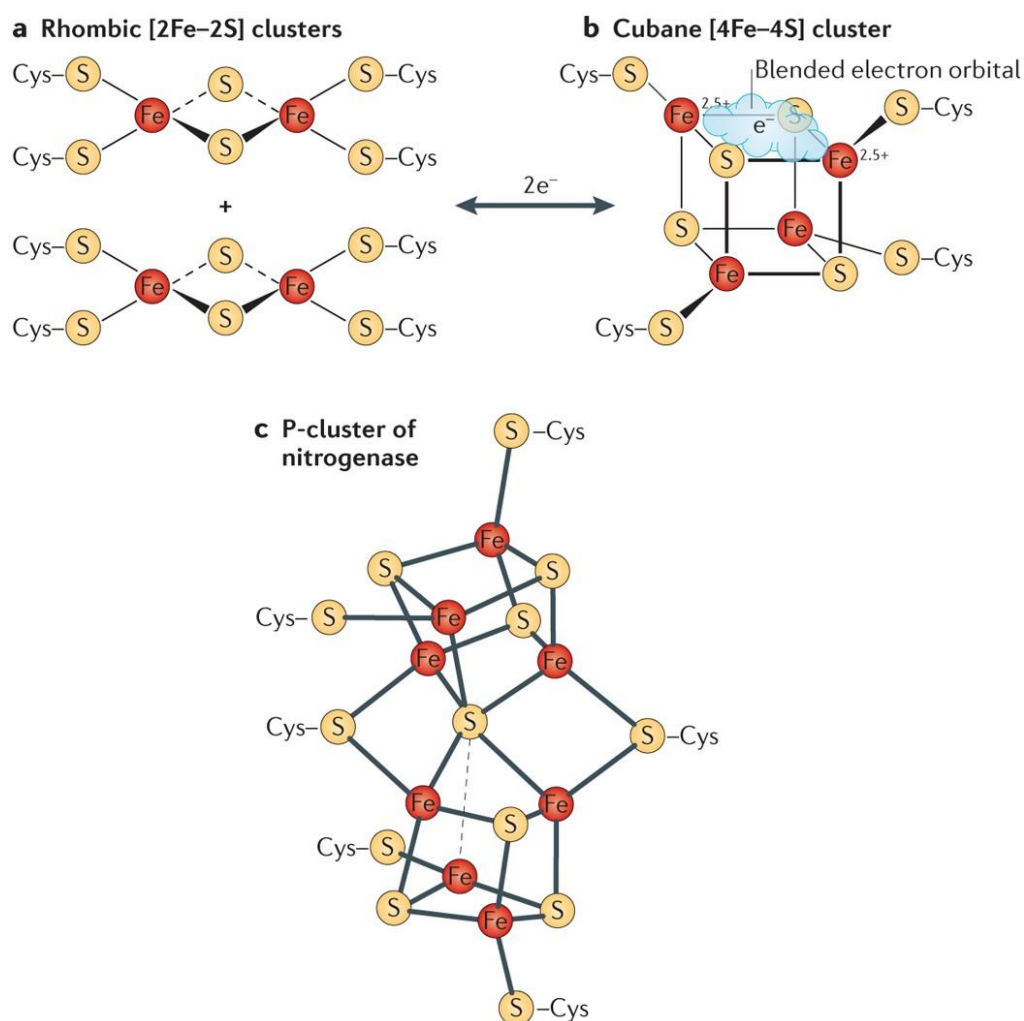


Figure 4.6. Examples of the most common Fe-S clusters found in iron-sulfur proteins. (a) The rhombic [2Fe-2S] cluster and (b) the tetranuclear or cubane [4Fe-4S] cluster which derives by reductive coupling of two [2Fe-2S] clusters and the addition of two electrons. In [4Fe-4S] clusters, the delocalization of electrons between iron sites is depicted by the cloud-like frame. (c) The [8Fe-7S] cluster (also known as P-cluster) which occurs in nitrogenase is reported as an example of a more complex structure which can be however considered as an elaboration of [2Fe-2S] as a basic unit [from Rouault T.A., 2014].

Besides their involvement in electron transfer and enzymatic catalysis, ISCs act also as important regulatory sensors: for their sensitivity towards reactive oxygen species like H_2O_2 , superoxide O_2^- and nitric oxide NO, iron-sulfur clusters are susceptible to oxidative stress and to intracellular iron levels both in bacteria [Kiley P.J. & Beinert H., 2003] and mammals [Bouton C. & Drapier J.C., 2003]. ROS could promote the oxidation of clusters leading to their interconversion and/or disassembly, as well as to conformational and activity modifications to the proteins containing them [Rouault T.A. & Tong W.H., 2005]; for instance, cytosolic iron regulatory protein-1 (IRP1) is a bifunctional enzyme, acting as an aconitase when containing a [4Fe-4S] cluster and as a regulator of cytosolic iron homeostasis when the cluster is absent as a result of iron depletion or ROS damage [Rouault T. & Klausner R., 1997; Pantopoulos K., 2004].

The biosynthesis of heme centers and iron-sulfur clusters takes place inside mitochondria, within the matrix. These processes require the assimilation of mitochondrial-imported iron with protoporphyrin IX or with atoms of sulfur, respectively [Beinert H. et al., 1997; Taketani S., 2005]. A defective biosynthesis of heme and ISCs cause a direct accumulation of iron in mitochondria, reducing its bioavailability and impairing its homeostasis, as well as increasing oxidative stress and compromising mitochondrial functionalities [Atamna H. et al., 2002].

4.4.3.2 The Interaction with Ferrochelatase in Heme Biogenesis

The hypothesis of an involvement of frataxin in heme biogenesis was suggested by the evidence of a severe deficiency of cytochromes *a*, *a3*, *b* and *c* in yeast cells lacking *YFH1* gene [Lesuisse E. et al., 2003] and of a decrease in mitochondrial complex IV activity in frataxin deleted yeast strains [Foury F. & Cazzalini O., 1997]. Furthermore, functional and biochemical alterations of the heme pathway and cytochrome oxidase were also observed in frataxin-deficient murine models and in human cells derived from FRDA patients [Schoenfeld R.A. et al., 2005].

Heme biosynthesis is a multi-step process which occurs in eight sequential steps, each of them assisted by a different enzyme and employing several substrates: the first and last three steps of the biosynthetic pathway occur in mitochondria while the remaining four occur in the cytosol (Figure 4.7). The enzyme which attends the terminal step of heme biosynthesis is ferrochelatase (FECH), which catalyzes the incorporation of ferrous iron into the tetrapyrrole ring of

protoporphyrin IX and ensures the production of a functional heme prosthetic group [Taketani S., 2005].

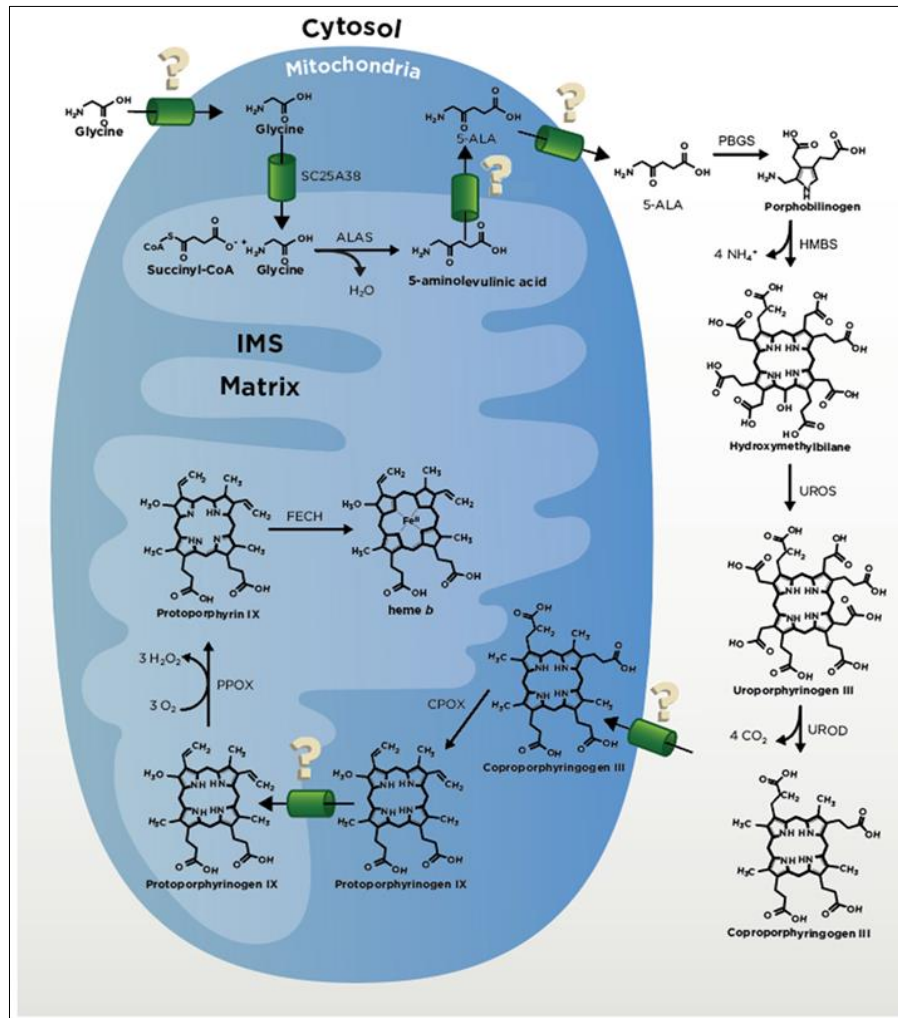


Figure 4.7. The heme biosynthetic pathway. The process starts with the transport of glycine inside mitochondria and its subsequent delivery across the inner mitochondrial membrane (IMM) by SLC25A38. The reaction between glycine and succinyl-CoA catalyzed by ALA synthase (ALAS) leads to the production of 5-aminolevulinic acid (5-ALA) which is subsequently transported outside the mitochondria to the cytosol through an unknown mechanism. In the cytoplasm, four subsequent reactions occur, involving porphobilinogen synthase (PBGS), hydroxymethylbilane synthase (HMBS), uroporphyrinogen synthase (UROS) and uroporphyrinogen decarboxylase (UROD) as enzymes. The intermediate product coproporphyrinogen III is transported into the mitochondrial intermembrane space (IMS) where is converted to protoporphyrinogen IX by CPgen oxidase (CPOX). Protoporphyrinogen IX is then oxidized into protoporphyrin IX by PPgen oxidase (PPOX). In the final step, which occurs in mitochondrial matrix, ferrochelatase (FECH) catalyzes the synthesis of heme b with the insertion of Fe²⁺ into the porphyrin ring of protoporphyrin IX [from Swenson S.A. et al., 2020].

In prokaryotes, ferrochelatase has been shown to localize within the cytoplasm or associated to the plasmatic membrane [Dailey H.A. *et al.*, 2000] while in eukaryotic cells the enzyme results associated with the inner mitochondrial membrane and oriented with its active site facing the matrix, ensuring in this way the uptake of the poorly soluble porphyrin and the release of heme [Ferreira G.C. *et al.* 1995]. To complete heme assembly, ferrochelatase needs ferrous iron as substrate [Taketani S., 2005]; this suggests the requirement of an iron chaperone that donates the metal to ferrochelatase which could subsequently insert it into the porphyrin ring. Several studies supported the idea of frataxin as the iron donor protein that delivers Fe^{2+} to ferrochelatase and that directly assists the biosynthesis of heme [Lesuisse E. *et al.*, 2003; Park S. *et al.* 2003]. Using surface plasmon resonance, Dancis and co-workers demonstrated that recombinant yeast frataxin Yfh1 interacts with yeast ferrochelatase with a high binding affinity ($K_d = 40$ nM), suggesting the involvement of frataxin in the final step of heme biosynthesis [Lesuisse E. *et al.*, 2003]. Accordingly, by mean of ITC and fluorescence spectroscopy, the formation of an *in vitro* complex between human frataxin and ferrochelatase has been also observed, although only in the presence of iron [Yoon T. & Cowan J.A., 2004]. Furthermore, it has been demonstrated that ferrochelatase enzymatic activity increases in the presence of frataxin, resulting optimal at a stoichiometric ratio of one frataxin monomer per ferrochelatase dimer [Yoon T. & Cowan J.A., 2004]. These evidences corroborate the hypothesis that frataxin can recruit ferrous ion and deliver it to ferrochelatase, acting as an iron donor and as an important player in the biogenesis of heme.

Spectroscopic analysis and modeling studies have been also used to predict how frataxin may interact with ferrochelatase [Bencze K.Z. *et al.*, 2006; Bencze K.Z. *et al.*, 2007]. A model of the complex Yfh1-ferrochelatase has been proposed, where ferrochelatase dimer is prone to interact with a trimeric yeast frataxin; in this model, the two proteins are spatially arranged to create a path for Fe^{2+} transfer from the iron-binding site of frataxin to the active site of ferrochelatase and optimizing the delivery of the metal [Söderberg C. *et al.*, 2016]. Using recombinant yeast frataxin and ferrochelatase, it has been also shown that the rate of heme production by FECH is highly dependent on the oligomerization *status* of Yfh1 *in vitro*, resulting higher in the presence of frataxin monomers and trimers and reduced in the presence of larger frataxin oligomers [Söderberg C. *et al.*, 2016]; this suggested not only that the tendency of frataxin to oligomerize in the presence of iron is linked to the potential capability of iron storage but also that this could be

crucial for the interplay with its interacting partners, as in the case of ferrochelatase.

It is worth to note that mammalian ferrochelatases, as well as yeast and some bacterial forms of the enzyme, contain a [2Fe-2S] prosthetic group which is required for enzyme activity [Ferreira G.C. *et al.* 1999]. The heme biosynthetic pathway is therefore particularly interesting in the study of the pathophysiology of FRDA disease since the terminal step of the process involves not only the delivery of iron but also the interaction with an iron-sulfur protein, supporting once again that frataxin may have a direct or indirect role on the proteins containing Fe-S clusters.

4.4.3.3 The Role in Iron-Sulfur Cluster Biogenesis

As previously described, iron-sulfur clusters are ancient and ubiquitous cofactors, widely spread in almost every life form. Their existence and prevalence in Nature rely on the spontaneous ability of iron and sulfur to self-associate into cluster assemblies, although under strictly anaerobic conditions. Since these prosthetic groups can be easily oxidized with a consequent impairment of their structure and function, different and tightly regulated biosynthetic pathways have been developed for their assembly during the evolutionary shift from anaerobic to aerobic Earth's atmosphere, both in prokaryotes and in eukaryotes [Lill R. & Mühlenhoff U., 2008; Lill R., 2009]. Although with some differences, these processes share a general action strategy which could be subdivided into two main steps, *i.e.* the assembly of the cluster on a scaffold protein and the subsequent transfer of the cofactor from the scaffold to the acceptor protein [Braymer J.J. *et al.*, 2021]. In prokaryotic organisms, three different pathways are employed to produce ISCs: the nitrogen fixation pathway (NIF), the sulfur mobilization pathway (SUF) and the iron-sulfur cluster (ISC) assembly pathway [Outten F.W., 2015; Baussier C. *et al.*, 2020]. In eukaryotes, the assembly of iron-sulfur clusters is supported by two processes, the bacteria-derived mitochondrial iron-sulfur cluster (ISC) pathway and the cytosolic iron-sulfur cluster assembly (CIA) pathway [Lill R. & Freibert S.A., 2020]. The latter, which assists the biosynthesis of ISCs utilized outside mitochondria, is strongly dependent from the ISC pathway; for this reason, the mitochondrial iron-sulfur cluster pathway appears as the pivotal mechanism for providing iron-sulfur clusters throughout the entire eukaryotic cell, in a direct or indirect manner [Lill R. & Freibert S.A., 2020].

In striking contrast to the chemical simplicity of ISCs, the biosynthesis of Fe-S proteins *in vivo* appears to be a rather complex and coordinated process, involving several proteins and cofactors that interact with each other in a synergic manner [Ciofi-Baffoni S. et al., 2018; Maio N. & Rouault T.A., 2020; Lill R. & Freibert S.A., 2020; Braymer J.J. et al., 2021; Courtney J.C. et al., 2021]. Mitochondrial iron-sulfur protein biogenesis can be conceptualized as the result of three major consecutive steps: a *de novo* synthesis of a [2Fe-2S] cluster on a scaffold protein, the transfer of the [2Fe-2S] cluster to mitochondrial [2Fe-2S] target apoproteins and the conversion of the [2Fe-2S] into [4Fe-4S] cluster with the final insertion into the apoprotein (Figure 4.8).

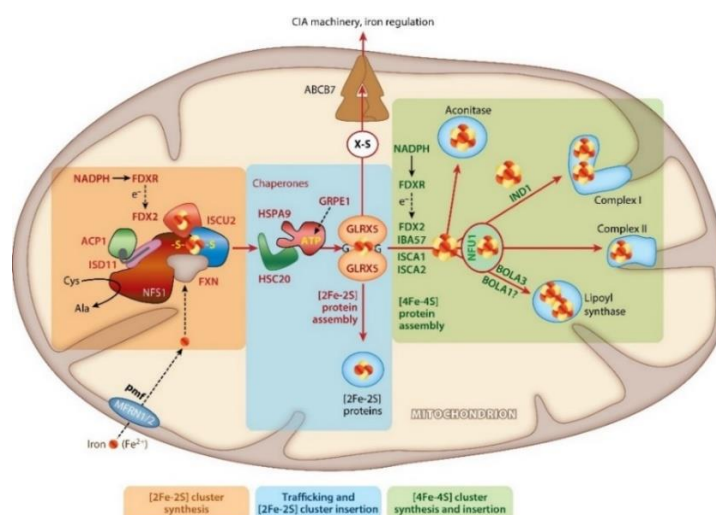


Figure 4.8. Schematic representation of mitochondrial iron-sulfur protein biogenesis. The entire process takes place within mitochondrial matrix and can be subdivided into three major steps. In the initial step (orange box) a *de novo* [2Fe-2S] cluster is synthesized. The ISC assembly machinery is constituted by the cysteine desulfurase complex NFS1-ISD11-ACP, by the scaffold ISCU2 (in the main text simply referred as ISCU) and by frataxin (FXN). Electrons (e⁻) required for the process are transferred from NADPH to ferredoxin reductase FDXR and provided by ferredoxin FDX2. The carrier protein mitoferrin MFRN1/2 and a proton motive force (pmf) are required for the import of Fe²⁺ used in the ISCs synthesis. In the second step (blue box) the chaperone system HSPA9/HSC20/GRPE1 promotes the transfer of the [2Fe-2S] cluster from ISCU2 to the monothiol glutaredoxin GLRX5 through which the cluster is delivered to target mitochondrial [2Fe-2S] proteins, converting them from apo to holo form. The [2Fe-2S] cluster can be also exported out of the mitochondria as an unknown sulfur-containing (X-S) moiety through the ATP binding cassette ABCB7 and used by the cytosolic iron-sulfur protein assembly (CIA) machinery. The third step (green box) involves the synthesis of [4Fe-4S] clusters by the transfer of [2Fe-2S] cluster from GLRX5 to ISCU2/ISCA1/ISCA2/IBA57/FDX2 system and their subsequent insertion in target proteins (e.g. respiratory complexes I and II, aconitase, lipoyl synthase) by dedicated delivery proteins (e.g. NFU1, IND1 and BOLA proteins) [from Lill R. & Freibert S.A., 2020].

Focusing on the first step of the overall process, the central component of the ISC assembly machinery is the cysteine desulfurase NFS1, a pyridoxal 5'-phosphate (PLP)-dependent enzyme that catalyzes, through a β -elimination reaction, the conversion of L-cysteine to L-alanine and sulfane sulfur via the formation of an enzyme-bound persulfide intermediate on a conserved cysteine residue [Boniecki M.T. *et al.*, 2017; Cai K. *et al.*, 2018; Cai K. & Markley J.L., 2018; Fox N.G. *et al.* 2019]. In eukaryotes, the activation/regulation and the stabilization of NFS1 are ensured by the presence of the accessory protein ISD11 and the acyl-carrier protein ACP1 [Van Vranken J.G. *et al.*, 2016; Cory S.A. *et al.*, 2017; Herrera M.G. *et al.*, 2019]. NFS1, ISD11 and ACP1 constitute the NFS1/ISD11/ACP1 (NIA) protein complex which is the core of the ISCs assembly machinery. The protein that acts as a platform for the assembly of the nascent cluster is ISCU, which receives persulfide sulfur from the NIA complex and ferrous ion, from an iron donor and in a way that are not yet fully understood. The electrons used for the reduction of the persulfide sulfur to sulfide are provided by the mitochondrial ferredoxin FDX2 which transiently binds and leaves the NIA-ISCU complex according to an oxidative/reductive cycle mechanism (Figure 4.9) [Webert H. *et al.*, 2014; Gervason S. *et al.*, 2019].

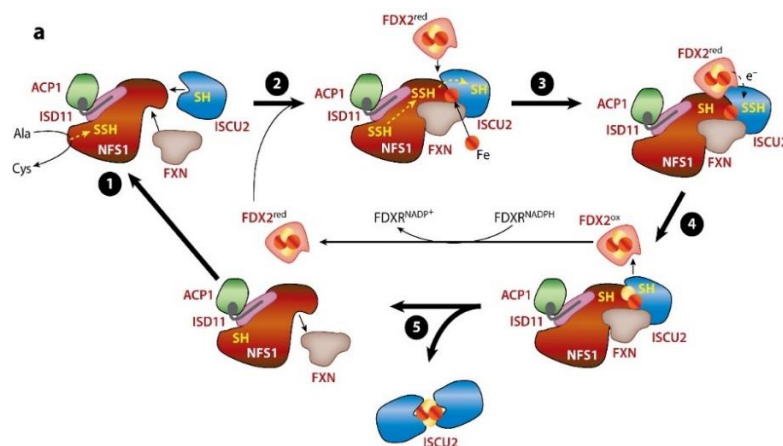


Figure 4.9. Hypothetical mechanism of the *de novo* [2Fe-2S] cluster synthesis. The process can be divided into five reactions. In the first reaction (reaction 1), the desulfurase NFS1 catalyzes the conversion of free cysteine to alanine with the generation of persulfide (-SSH) on its conserved Cys residue. In the second reaction (reaction 2), the persulfide is transferred from the catalytic site to the surface of NFS1 through the allosteric modulation promoted by FXN. In the third step (reaction 3), the persulfide sulfur is transferred from NFS1 to one of the conserved cysteine residues of ISCU2 after iron-binding of ISCU2 itself. In the reaction 4, the mitochondrial reduced ferredoxin (FDX2^{red}) transiently binds to NFS1-ISCU2 promoting the reduction of persulfide sulfur to sulfide (S²⁻) used for the [2Fe-2S] synthesis. Finally (reaction 5), the mitochondrial oxidized ferredoxin (FDX2^{ox}) leaves the complex and it is reduced by ferredoxin reductase FDR and NADPH [adapted from Lill R. & Freibert S.A., 2020].

For its iron-binding properties and for the evidence which correlates the impairment of Fe-S proteins to its cellular depletion, frataxin was originally proposed to be the iron donor in the ISC pathway [Mühlenhoff U. *et al.*, 2002; Yoon T. & Cowan J.A., 2003]. This hypothesis was also corroborated by the solved crystallographic structure of the ISCs assembly machinery, where frataxin results as a constitutive and stable component of the complex, binding at the tips of the two NIA monomers together with ISCU (Figure 4.10) [Fox N.G. *et al.* 2019]. However, a closer inspection of the cryo-EM structure of the human NFS1-ISD11-ACP1-ISCU-FXN (NIAUF) complex reveals that the iron-binding α -helix of frataxin is not proximal to the active site of [2Fe-2S] cluster biosynthesis, ruling out a direct role of frataxin for the loading, delivery and release of iron to ISCU.

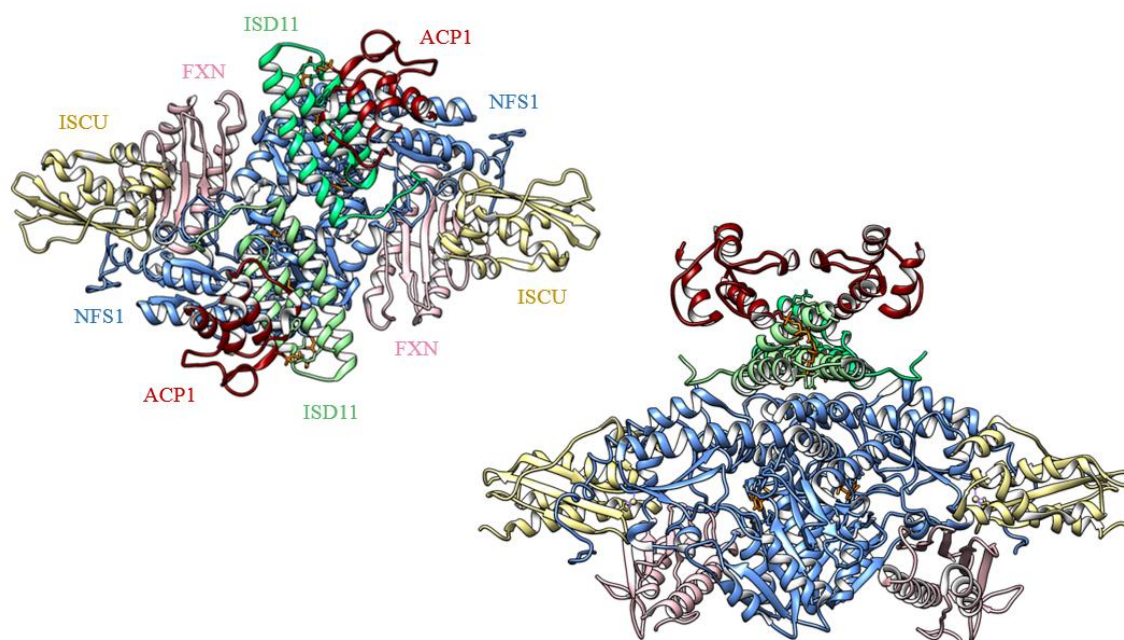


Figure 4.10. Crystal structure of the human iron-sulfur cluster assembly machinery. The symmetrical shape of the complex (reported here in two different views) is essentially determined by the dimeric nature of NFS1 (in light blue). The direct interacting partners of NFS1 are ISD11 (in green) and ACP1 (in red). The ligands (PLP and the acyl group) are colored in orange. FXN (in pink) and ISCU (in light yellow) interact with the two NFS1 monomers in a pairwise fashion with each other (structure figures made with PyMol using PDB ID: 6NZU).

Moreover, independent studies demonstrated a direct interaction between frataxin and the proteins belonging to the ISCs assembly machinery [Gerber J. *et al.*, 2003; Shan Y. *et al.*, 2007; Leidgens S. *et al.*, 2010; Schmucker S. *et al.*, 2011; Colin

F. et al., 2013; Cai K. et al., 2018]. Currently, it is widely accepted that frataxin acts as an allosteric modulator for the ISCs biogenesis rather than as an iron chaperone of the machinery [*Maio N. et al., 2020*]: several biochemical and structural studies suggest that frataxin may be directly involved in the sulfur transfer reaction, assisting the movement of the highly flexible cysteine loop of NFS1 involved in the catalytic mechanism from the site of persulfide generation toward the active site of ISCU [*Tsai C.L. & Barondeau D.P., 2010; Bridwell-Rabb J. et al., 2014; Fox N.G. et al., 2015; Gervason S. et al., 2019*]. This assumption was mainly suggested by the evidence that the binding of FXN to NFS1-ISD11 in the presence of ISCU stimulates the rate of the sulfur transfer *in vitro* [*Parent A. et al., 2015*]. Interestingly, it was also shown that the presence of ferrous iron enhances the capability of frataxin to stimulate the sulfide production, shedding light on a possible regulatory effect of frataxin iron-binding on modulating the correct orientation of the persulfide for its subsequent transfer to ISCU [*Tsai C.L. & Barondeau D.P., 2010*].

It is worth to note that in the NIAUF complex frataxin interacts with NFS1 and ISCU mainly through its β -sheet surface [*Schmucker S. et al., 2011; Fox N.G. et al., 2019*]; as previously described, many residues of this region are highly conserved and common pathological mutations involve some of them. For instance, the point mutations N146K and W155R have been shown to drastically affect the modulatory effect of FXN on the cysteine desulfurase activity of NFS1/ISD11 complex *in vitro* [*Tsai C.L. et al., 2011; Bridwell-Rabb J. et al., 2011; Bellanda M. et al., 2019*], suggesting that these residues may play a crucial role in the ability of frataxin to interact with NFS1. At the same time, mutations involving residues important for the folding/stability of frataxin (*e.g.* G130V, I154F) or for its iron-binding properties (*e.g.* D122Y) may have a deep impact on desulfurase NFS1 activity since a general destabilization of the protein structure and/or function could indirectly affect its capability to interact with the ISCs assembly machinery [*Campbell C.J. et al., 2021*].

However, although it is well established that FXN plays a key role in the biogenesis of iron-sulfur clusters through its simultaneous interactions with NFS1 and ISCU, there are still unclarified points concerning the molecular mechanism by which the ISCs assembly machinery operates.

4.4.4 Existence and Functions of Extramitochondrial Isoforms of Frataxin

As previously described, human frataxin is synthesized as a precursor protein and imported inside mitochondria where, through two distinct and subsequent proteolytic cleavages, it is converted to its mature functional form [Cavadini P. *et al.*, 2000; Condò I. *et al.*, 2007]. Interestingly, a pool of extramitochondrial mature frataxin has been also detected in different human cell types [Acquaviva F. *et al.*, 2005; Condò I. *et al.*, 2006; Lu C. & Cortopassi G., 2007]. Condò *et al.* observed that a cytosolic mature frataxin is able to promote cell survival, contributing to the resistance against oxidative damage and conferring protection against apoptosis [Condò I. *et al.*, 2006]. The same authors provided also the first evidence for a physiological role of an extramitochondrial mature frataxin, unraveling a direct physical interaction between frataxin and cytosolic aconitase/iron regulatory protein-1 (IRP1) protein [Condò I. *et al.*, 2010]; these data are in agreement with the general consensus which considers the involvement of frataxin not only in the biogenesis of Fe-S clusters, but also in the regulation of the enzymatic activity of the ISC-containing proteins.

Although the mitochondrial frataxin is prevalent in human cells, the existence of other isoforms with different cellular distribution and putative physiological functions has been recently recognized [Xia H. *et al.*, 2012; Pérez-Luz S. *et al.*, 2015; Guo L. *et al.*, 2018]. For instance, FXN II and FXN III isoforms, both lacking the mitochondrial import sequence, have been found in cytoplasm and nucleus, respectively; these isoforms are tissue-specific, with FXN II mainly found in the cerebellum and FXN III mainly localized in the heart [Xia H. *et al.*, 2012]. Although a possible involvement of FXN II and FXN III in the biogenesis of Fe-S clusters and in their protection against oxidative damage has been hypothesized [Xia H. *et al.*, 2012], the physiological relevance of these additional frataxin isoforms remains elusive.

Chapter 5

EPR Spectroscopy

in the Study of Biological Systems

Electron Paramagnetic Resonance (EPR), otherwise known as Electron Spin Resonance (ESR), is a spectroscopic technique that allows to detect and investigate molecular species containing one or more unpaired electrons as, for example, organic radicals, photoexcited triplet states, metal ions and some metal complexes. Since its inception, EPR spectroscopy has proven to be an important tool for the study of biological systems as well as the molecular mechanisms in which these systems are involved. Among them, metalloproteins containing one or more paramagnetic centers, like Fe-S clusters or heme, or biological radicals resulting as intermediates of biological reactions, are the most studied. Nevertheless, the technique is also widely used for the investigation of macromolecules which are intrinsically non-paramagnetic through the introduction of appropriate exogenous probes, added to the system (spin probes) or incorporated through covalent bonds (spin labels).

There are many different EPR techniques, from basic to the most advanced approaches, that ensure to obtain different information on the investigated system. In this chapter the principles of EPR spectroscopy will be briefly described and the specific EPR applications used in this Ph.D. thesis will be reported.

5.1 Basic Introduction to EPR Theory

EPR spectroscopy is based on the interaction between the magnetic dipole ($\vec{\mu}_e$) associated to the spin angular momentum of the electron, and an external magnetic field (B_0) applied to the system. The energy of this interaction, known as *electron Zeeman interaction*, is given by:

$$E = -\vec{\mu}_e \cdot \vec{B}_0$$

(Eq. 5.1)

where the magnetic dipole $\vec{\mu}_e$ is defined as:

$$\vec{\mu}_e = -g\mu_B\vec{S}$$

(Eq. 5.2)

In this equation, g is the *electron factor*, a dimensionless quantity that relates the observed magnetic moment to its angular momentum (for a free electron, $g = g_e = 2.0023$) and $\mu_B = e\hbar/2m_e = 9.274 \cdot 10^{-24} \text{ JT}^{-1}$ is the electron Bohr magneton, a constant which depends on the charge e and the mass m_e of the electron.

The spin angular momentum \vec{S} is related to the spin quantum number S and, since for the electron $S = 1/2$, \vec{S} can only assume one value corresponding to $|\vec{S}| = \sqrt{S(S+1)}\hbar = 3/2\hbar$. The projection of \vec{S} on the cartesian axis parallel to the magnetic field B_0 (conventionally, the z axis), assumes only two possible values depending on the spin magnetic quantum number m_s : since $S_z = m_s\hbar$ and $m_s = +1/2 ; -1/2$, the corresponding values are $S_z = +1/2$ and $S_z = -1/2$ (in \hbar units).

Therefore, the interaction between the magnetic dipole of the electron and the external magnetic field B_0 , according to Eq. 5.1, leads to the generation of two energy levels (in \hbar units), corresponding to the α and β states:

$$E_\alpha = +\frac{1}{2}g\mu_B B_0$$
$$E_\beta = -\frac{1}{2}g\mu_B B_0$$

(Eq. 5.3)

The presence of B_0 allows to remove the degeneracy of the states (*Zeeman effect*) and the energy difference between them is proportional to the intensity of the applied magnetic field, *i.e.*:

$$\Delta E = E_\alpha - E_\beta = g\mu_B B_0$$

(Eq. 5.4)

The simplest EPR experiment consists in irradiating the sample, inserted in the static magnetic field B_0 , with an oscillating electromagnetic radiation B_1 (*continuous wave* EPR, or CW EPR). In CW EPR, the magnetic field B_0 is swept and when there is a match between the frequency (ν) of the B_1 field and the energy

level separation (ΔE), a transition between the two energy levels occurs. According to *Planck's relation*:

$$\Delta E = h\nu = g\mu_B B_0 \rightarrow \nu = g \frac{\mu_B}{h} B_0$$

(Eq. 5.5)

To increase the signal to noise ratio, a modulation of the magnetic field and phase-sensitive detection are required; for this reason, the typical EPR signal is collected as the first derivative of the absorption, as shown in *Figure 5.1*. Most EPR experiments are performed with magnetic fields of 0.3 – 0.8 T, corresponding to a frequency of about 9.5 – 9.7 GHz (X band, range of the microwaves).

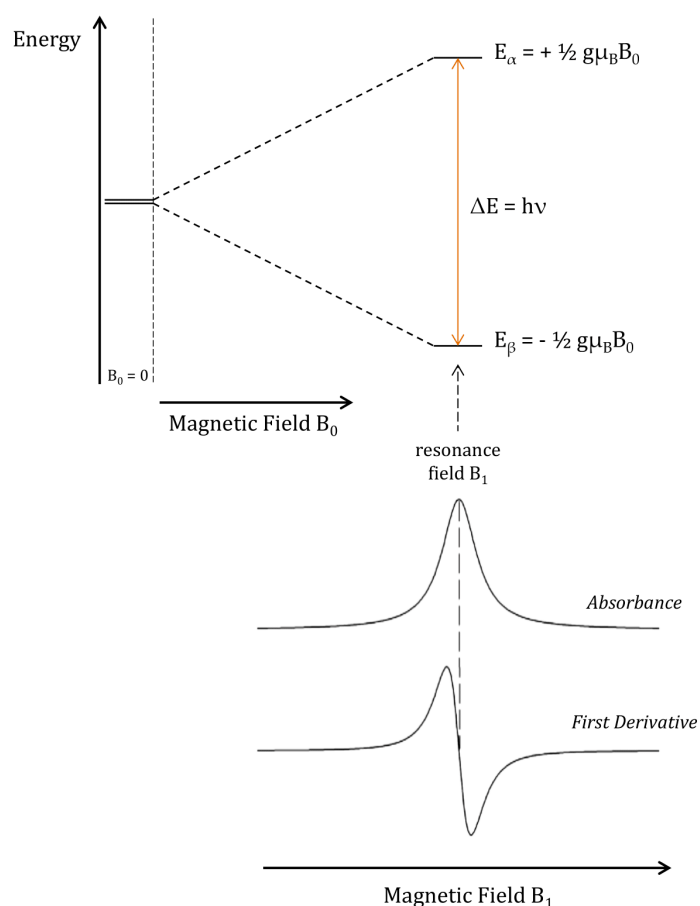


Figure 5.1. Energy levels scheme for a system with $S = 1/2$ as a function of applied magnetic field B_0 . The resonance conditions are achieved when the frequency of the electromagnetic radiation (B_1) perfectly matches the difference in energy of the two states α and β . This gives rise to the EPR spectrum, shown both in absorbance and first derivative forms.

The ratio of the populations of two spin states N_α and N_β is given according to the *Boltzmann distribution*:

$$\frac{N_\alpha}{N_\beta} = e^{-\frac{\Delta E}{k_B T}}$$

(Eq. 5.6)

where k_B is the Boltzmann's constant ($k_B = 1.38 \cdot 10^{-23} \text{ JK}^{-1}$). This ratio depends on the difference in energy of the two states (ΔE) at a given temperature T . At room temperature, the spin population in the lower energy level is slightly larger than the spin population of the higher energy level, therefore a net resonance absorption will occur. The applied microwaves tend to equalize the two populations, leading the system to saturation conditions. Nevertheless, this situation is prevented by relaxation phenomena due to interactions of spins with the molecular environment (or lattice) and interactions between spin themselves, restoring in this way the thermal equilibrium. These processes are characterized by two time constants, T_1 (*spin-lattice relaxation time*) and T_2 (*spin-spin relaxation time*), which are specific for the system under investigation and generally increase decreasing the temperature. For instance, as it will be described below, EPR signals that derive from $[4\text{Fe-4S}]^-$ clusters are characterized by extremely short relaxation time(s) at room temperature; for this reason, their EPR spectra are detectable only at low temperatures, *i.e.* below 20 K. On the contrary, nitroxides used as spin labels are characterized by long relaxation times, thus allowing to acquire EPR spectra at room temperature without losing signals.

It is worth to note that for an electron in a molecular system, the g factor can assume values significantly different from 2.0023, representing therefore an important parameter in the characterization of the paramagnetic species. Deviations from g_e value depend on the spin-orbit coupling, *i.e.* the coupling between the magnetic moment and the one attributed to the orbital motion. This contribution becomes more and more relevant with the increase of the atomic number of the atom in which the electron resides and this justifies the fact that, for example, paramagnetic molecular systems containing atoms with low atomic number, such as organic radical molecules, present an effective g (g_{eff}) very close to 2.0023, while for systems with one or more electrons in orbitals of heavy atoms, such as some transition metals, the g_{eff} can deviate significantly from this value.

The g factor is better represented by a tensor (\mathbf{g}) that in its principal axes system (XYZ) assumes a diagonal form:

$$\mathbf{g} = \begin{pmatrix} g_{XX} & 0 & 0 \\ 0 & g_{YY} & 0 \\ 0 & 0 & g_{ZZ} \end{pmatrix}$$

(Eq. 5.7)

The interactions between the magnetic field B_0 and the electron spin are therefore anisotropic, so they strongly depend on the orientation of the system with respect to a particular chosen spatial direction. The elements and orientation of the tensor relative to the molecular skeleton can be extrapolated by the analysis of EPR spectra of oriented species, such as ordered systems like crystals; alternatively, it is possible to derive the diagonal values of the tensor from the analysis of spectra of polycrystalline powders, disordered systems in which molecules assume orientations that are all statistically equiprobable. In liquid solution, however, the motions of molecular reorientation are very fast and the overall effect is the mediation of the \mathbf{g} tensor on all possible orientations. As a direct consequence, the spectrum will give an isotropic g -factor value, *i.e.* the average of the three main values of the diagonal tensor:

$$g_{iso} = \frac{(g_{XX} + g_{YY} + g_{ZZ})}{3}$$

(Eq. 5.8)

As for unpaired electrons, some nuclei have not null spin angular moment (\vec{I}), leading to a generation of an associated magnetic dipole moment $\vec{\mu}_n$:

$$\vec{\mu}_n = g_N \mu_N \vec{I}$$

(Eq. 5.9)

In this equation, g_N is the *nuclear factor*, a value which is specific for a certain nucleus, and $\mu_N = e\hbar/2m_p = 5.05 \cdot 10^{-27} \text{ JT}^{-1}$ is the *nuclear magneton*, a constant which depends on the charge e and the mass m_p of the proton.

Also for the nuclear spin, in the presence of the magnetic field, there is an energy of interaction (*nuclear Zeeman interaction*) which results as:

$$E = -\vec{\mu}_n \cdot \vec{B}_0 = -g_N \mu_N \vec{I} \cdot \vec{B}_0$$

(Eq. 5.10)

The nuclear Zeeman interaction generates a number of states with different energies on the basis of the quantum number I , typical of the nucleus under examination. The coupling between the electronic spin and the nuclear spin, a phenomenon known as *hyperfine interaction*, significantly modifies the resonance conditions for the electronic transitions leading to $2I+1$ observed peaks (or $2nI+1$ in the case of coupling with n equivalent nuclei). The energy of the system will be then expressed as follows:

$$H = \mu_B g \vec{S} \cdot \vec{B}_0 - g_N \mu_N \vec{I} \cdot \vec{B}_0 + \vec{S} \mathbf{A} \vec{I}$$

(Eq. 5.11)

where the contribution of hyperfine interaction, represented by the term $\vec{S} \mathbf{A} \vec{I}$, has been added to the electronic and nuclear Zeeman interactions. \mathbf{A} is the hyperfine coupling tensor which, in its principal axes system, assumes a diagonal form:

$$\mathbf{A} = \begin{pmatrix} A_{XX} & 0 & 0 \\ 0 & A_{YY} & 0 \\ 0 & 0 & A_{ZZ} \end{pmatrix}$$

(Eq. 5.12)

The hyperfine interaction is composed of two contributions, *i.e.* the *Fermi contact interaction* and the *dipolar interaction*. The Fermi contact interaction is:

$$E_{Fermi} = a_{iso} \vec{S} \cdot \vec{I}$$

(Eq. 5.13)

where a_{iso} is the isotropic hyperfine coupling constant resulting from the trace of the tensor \mathbf{A} . The dipolar interaction can be expressed as follow:

$$E_{dip} = \vec{S} \mathbf{T} \vec{I}$$

(Eq. 5.14)

Where \mathbf{T} is the dipolar tensor and has a null trace ($\text{Tr}(\mathbf{T}) = 0$). The hyperfine coupling tensor \mathbf{A} can then be expressed in this way:

$$\mathbf{A} = a_{iso} \begin{pmatrix} 1 & 0 & 0 \\ 0 & 1 & 0 \\ 0 & 0 & 1 \end{pmatrix} + \mathbf{T}$$

(Eq. 5.15)

As in the case of the \mathbf{g} tensor, it is possible to determine all elements of the tensor \mathbf{A} by analyzing EPR spectra of crystal samples. However, with samples in liquid solution, the fast molecular tumbling results in rapid orientational mediation leading to a complete average of the tensor \mathbf{A} . Since the dipolar tensor \mathbf{T} has a null trace, the hyperfine coupling tensor will result equivalent to a_{iso} .

Then, in a liquid solution, the energy of the system can be expressed as follow (in the high-field approximation):

$$E = g_{iso}\mu_B\vec{S}_z \cdot \vec{B}_0 - g_N\mu_N\vec{I}_z \cdot \vec{B}_0 + a_{iso}\vec{S}_z \cdot \vec{I}_z$$

(Eq. 5.16)

In this regard, it is useful to analyze the particular case of a nitroxide radical, a molecule in which the unpaired electron is delocalized between the atoms of the N-O bond and that is found to magnetically interact with ^{14}N , the nitrogen isotope with quantum number $I = 1$. For a molecular system with $S = 1/2$ and $I = 1$, as for a nitroxide spin system, the resolution of Eq. 5.16 allows to derive, on the basis of the electronic spin quantum number m_s and the nuclear spin quantum number m_I , six distinct spin states, whose energies (E_{m_s, m_I}) are:

$$E_{\pm\frac{1}{2}, +1} = \pm\frac{1}{2}g_{iso}\mu_B B_0 - g_N\mu_N B_0 \pm\frac{1}{2}a_{iso}$$

$$E_{\pm\frac{1}{2}, 0} = \pm\frac{1}{2}g_{iso}\mu_B B_0$$

$$E_{\pm\frac{1}{2}, -1} = \pm\frac{1}{2}g_{iso}\mu_B B_0 + g_N\mu_N B_0 \mp\frac{1}{2}a_{iso}$$

(Eq. 5.17)

For the selection rules, the oscillating field B_1 induces transitions only between states with different quantum number m_s but with the same quantum number m_l ($\Delta m_s = \pm 1$ and $\Delta m_l = 0$); therefore, the allowed transitions are three and there will be three distinct peaks of equal intensity in the EPR spectrum, separated from each other by the a_{iso} value (Figure 5.2).

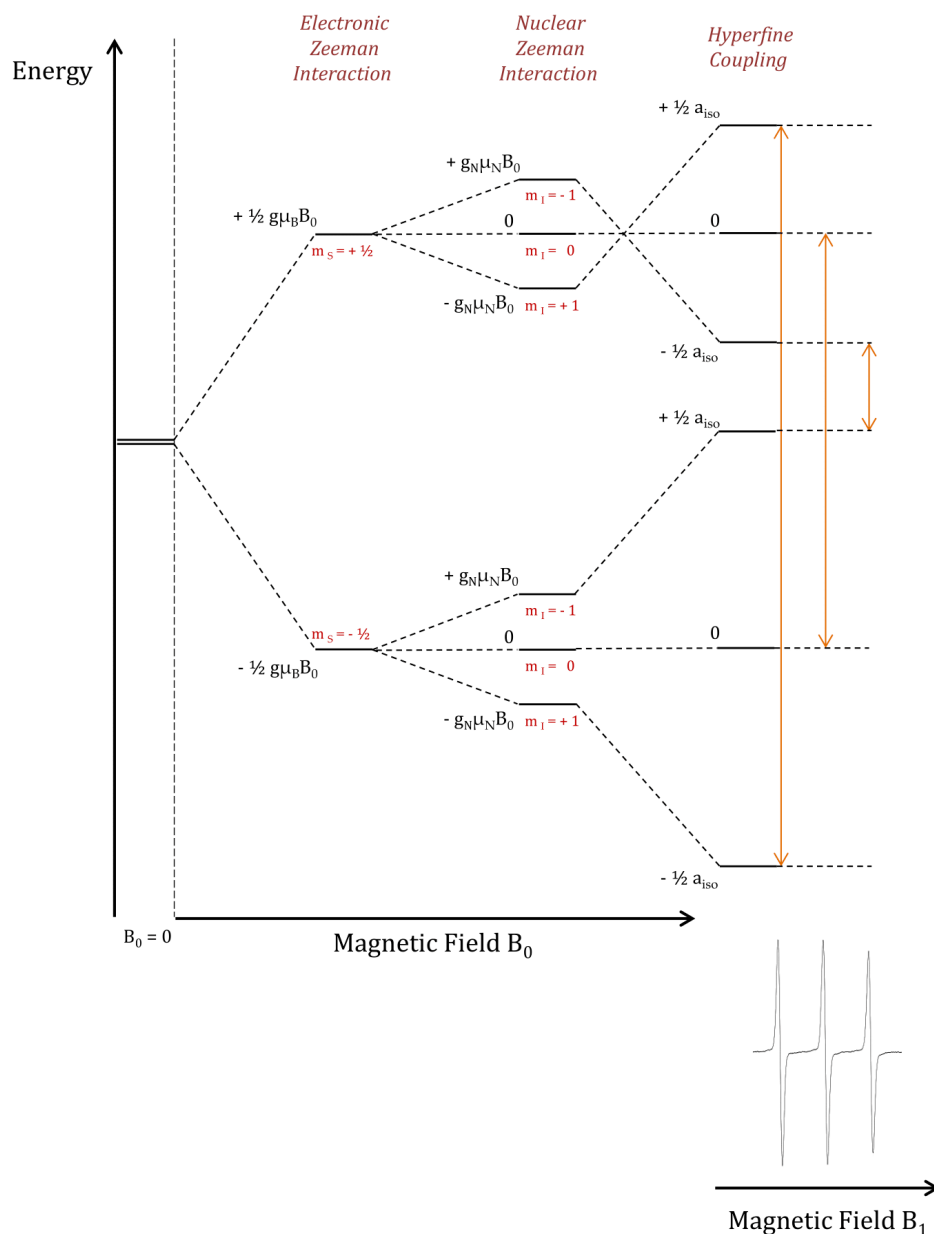


Figure 5.2. Schematic representation of the energetic levels for s system with $S = \frac{1}{2}$ and $I = 1$. Only the isotropic hyperfine contribution has been taken into account. Double-headed arrows indicate the allowed transitions between the energetic states ($\Delta m_s = \pm 1$ and $\Delta m_l = 0$).

5.2 Site-Directed Spin Labeling

Site-Directed Spin Labeling (SDSL) is a technique which consists in the introduction of one or more paramagnetic probes in specific positions of a biological macromolecule in order to study its structural and conformational features by EPR spectroscopy. Spin labeling is mainly used for the investigation of soluble and membrane proteins, but it finds application also in the study of other biomolecules, such as nucleic acids or peptides. In the case of proteins, small organic radical molecules are generally chosen as probes which could be chemically bound to the protein backbone via reaction with the thiol group of cysteine residues, natively present in the protein or inserted via site-directed mutagenesis. To perform a selective labeling, it is necessary to have the target cysteine residue only in a specific site of the protein; this condition is achieved replacing all the native cysteines with structurally similar residues, such as alanines or serines [Bordignon E. & Steinhoff H.J., 2007].

The most used spin labels are nitroxides, paramagnetic molecules that presents an unpaired electron on their NO \cdot group and that are characterized by a certain degree of chemical stability. Among them, MTSSL ((1-oxy-2,2,5,5-tetramethylpyrrolidin-3-methyl) methane sulfonate) is the most widely used due to its high affinity for the cysteine thiol group with which it reacts forming a disulfide bridge (Figure 5.3); furthermore, the volume of its side chain, comparable to that of a tryptophan or a phenylalanine residue, does not generally compromise the structural stability of the protein as well as its biological functionality [Czogalla A. et al., 2007]. Other nitroxide spin labels commonly used are, for instance, IAP (3-(2-iodoacetamido)-proxyl), MSL (4-maleimido-TEMPO) and IASL (4-(2-iodoacetamido)-TEMPO), which differ from each other in terms of steric hindrance, length of the chain and mobility.

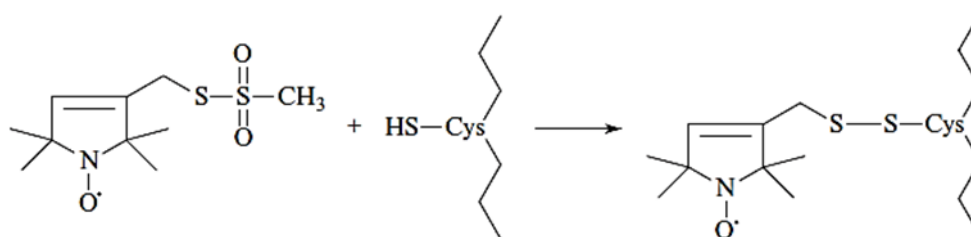


Figure 5.3. Cysteine labeling with MTSSL. The chemical reaction between the nitroxide MTSSL and the thiol group of a cysteine residue belonging to the backbone of a protein.

The importance of the SDSL-EPR technique relies on the fact that the analysis of the EPR spectrum of the labelled system allows to obtain information on [Steinhoff H.J., 2002]:

- *molecular dynamics and mobility*, since the spectral shape of the nitroxide is strongly dependent on the local environment in which it is located and on the restrictions on free motion that this imposes;
- *solvent accessibility*, through the analysis of the collisional frequency of the nitroxide side chain with apolar (such as molecular oxygen) or polar (such as $\text{Cr}(\text{C}_2\text{O}_4)^{3-}$) paramagnetic molecules;
- *molecular distances*, through the study of the dipolar interaction between two spin labels inserted in different positions of the macromolecule.

5.2.1 Spin Label and Mobility

Through the analysis of the EPR spectrum of the labelled protein, it is possible to acquire information about the mobility of the nitroxide and, consequently, on the structural and conformational features of the specific site of the protein where the spin label has been inserted.

At room temperature, the EPR spectrum highly depends on the mobility of the nitroxide and different mobilities lead to different degrees of averaging of the \mathbf{g} and \mathbf{A} tensors, the magnetic parameters which describe the system. The overall mobility of the nitroxide, conventionally described by the rotational correlation time τ_c , results as a sum of three different contributions: the mobility of the nitroxide side chain, the motions of the protein backbone in which the nitroxide is located, and the tumbling of the protein itself. Since the first two contributions have comparable timescales and longer than the third, they are referred to be “local” motions. The latter contribution is negligible in the case of large proteins (*i.e.* with molecular weight higher than 200 kDa) and for which correlation times are greater than 60 ns; however, in the case of small proteins, this contribution leads to the averaging of the tensors \mathbf{g} and \mathbf{A} in any particular condition of local mobility of the nitroxide, losing information about the nitroxide mobility itself. In these cases, it could be useful to modify the viscosity of the sample adding glycerol, sucrose or other thickening agents (*e.g.* Ficoll, a synthetic glucose

polymer) in order to slow down the reorientational motion of the entire macromolecule without altering in a significant way the local mobility of the nitroxide.

On the basis of the EPR spectrum, it is therefore possible to distinguish different mobility regimes, varying from fast motion regime ($\tau_c < 0.1$ ns) to slow motion regime ($\tau_c > 100$ ns). If the nitroxide has a completely unrestrained mobility, the complete time averaging of both tensors \mathbf{g} and \mathbf{A} occurs: as a result, the EPR spectrum will consist in three narrow peaks, centered at g_{iso} , and spaced by the hyperfine coupling constant a_{iso} . When the mobility of the nitroxide decreases, a significant variation in the spectrum shape occurs, with a global broadening of the spectral lineshape due to the incomplete averaging of the \mathbf{g} and \mathbf{A} tensors. When the tumbling slows down to a large extent, the EPR spectrum becomes indistinguishable from that of a powder or frozen solution (Figure 5.4).

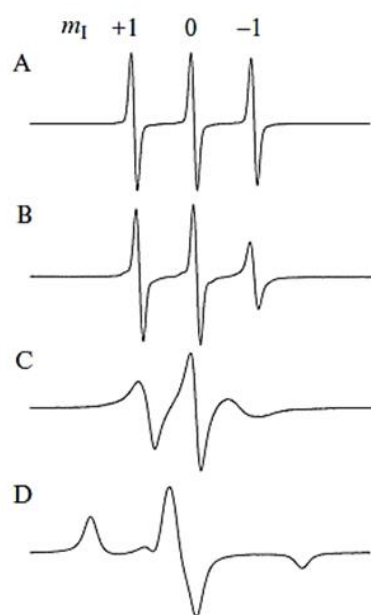


Figure 5.4. EPR spectra for MTSSL nitroxide under different rotational mobility conditions. The spectrum (A) refers to the free spin label in solution where the motion is completely isotropic. In (B) the situation where MTSSL is bound to a small, unstructured peptide of 15 amino acids in aqueous solution is represented. Spectrum (C) depicts the case in which the same peptide is labelled with nitroxide but structured in α -helix. The last spectrum (D) is related to the spin label bound to the same peptide but in frozen solution [from Klug C.S. & Feix J.B., 2008].

Although spectroscopic analysis can be quite complex in describing the overall nitroxide mobility, some qualitative considerations can be easily done by the

simple inspection of the EPR spectral profile. For instance, if the nitroxide is located on the surface of the protein or in interconnecting loops, its mobility is high and the resulting EPR spectrum will present three narrow and intense peaks; if the spin label is constrained in buried sites or at the interface with another interacting protein, the steric hindrance could lead the nitroxide to be poorly mobile, thus giving an EPR spectrum in which the peaks are broadened and less intense.

Moreover, if the labelled protein has two or more possible conformations which affect the nitroxide mobility, the registered spectrum will consist in the weighed sum of the spectrum of each conformation with its particular nitroxide mobility condition (*Figure 5.5*). Since the spectral lineshape is strongly dependent on the structural features of the protein region in which the nitroxide is located, a change in the components of the spectrum as a result of an external solicitation, such as the addition of a substrate or effector, may be indicative of a conformational change in the protein.

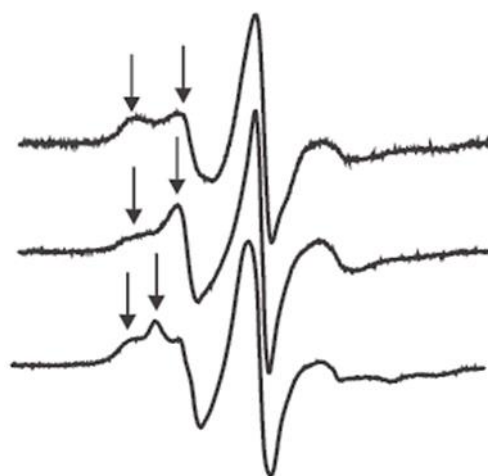


Figure 5.5. Multi-component EPR spectra. EPR spectra in which multiple components with different mobility are present (indicated by arrows) [from Klug C.S. & Feix J.B., 2008].

Distinction of multiple components and a more quantitative understanding of the experimental data can be made by simulation of the EPR spectra, whenever possible. With the support of computational models, it is possible to obtain information about the dynamics of the protein backbone to which the spin label is bound. Among those proposed, the MOMD (*Microscopic Order Macroscopic Disorder*) model has been developed considering that the spin label molecular

motion has not a free diffusion, but it is limited by the protein structure (*microscopic order*); however, the macromolecules adopt all the possible orientations with respect to the external magnetic field (*macroscopic disorder*) [Budil D.E. et al., 1996]. The MOMD model allows to describe the spin label mobility through two main parameters: the rotational correlation time τ_c and the order parameter S . The rotational correlation time is related to the isotropic rotational diffusion coefficient D_R because $\tau_c = 1/6D_R$, implying that lower nitroxide mobility corresponds to longer rotational correlation times. The coefficient D_R results from the averaging of the diffusion tensor \mathbf{D} , which for an axial diffusion symmetry tensor, as for elongated proteins, has two equal diagonal elements, according to:

$$\mathbf{D} = \begin{pmatrix} D_{\parallel} & 0 & 0 \\ 0 & D_{\perp} & 0 \\ 0 & 0 & D_{\perp} \end{pmatrix}$$

(Eq. 5.18)

In this case, the rotational correlation time of a protein with an axial diffusion symmetry is calculated as:

$$\tau_c = \frac{1}{6\sqrt[3]{(D_{\parallel}D_{\perp}D_{\perp})}}$$

(Eq. 5.19)

However, in a more general case, it is possible that the motion of nitroxide is anisotropic and therefore it must be described by a rotational diffusion tensor whose main axis system is not necessarily coincident with the magnetic one.

The mobility of a spin label can be modeled as its rotation within an ideal cone built around the z axis of the reference system for the rotational diffusion tensor. The width of this cone is a function of the angle ϑ of deviation from that axis, so that the order parameter can be expressed as:

$$S = \frac{(3\langle \cos^2\vartheta \rangle - 1)}{2}$$

(Eq. 5.20)

where $\langle \cos^2\theta \rangle$ is the average value on the molecular orientational distribution. The order parameter S represents therefore a measure for the nitroxide mobility constraint: it can assume values comprised between 0 (no order, all the orientations of the spin label side chain with respect to the protein backbone are present), and 1 (total order, only a single orientation of the spin label side chain is possible). To conclude, through the MOMD model, it is possible to evaluate if the nitroxide mobility can be described as an isotropic or anisotropic motion and to understand if more than one mobility component is necessary to reproduce the experimental spectrum, describing each of them with the parameters τ_c and S .

5.3 The Study of Mitochondrial Diseases by EPR Spectroscopy

As mentioned before, EPR spectroscopy has proved to be an important tool for the structural and functional analysis of biological molecules. Among them, the most studied systems are proteins containing one or more metallic centers, as well as small radical molecules involved in the biochemical pathways of the cell. Mitochondrial respiratory chain complexes are characterized by a large variety of redox-active cofactors, such as iron-sulfur clusters, heme, copper ions, flavines and quinones; in the investigation of a biological sample, be it an organic tissue or whole cells, the predominant EPR signals are mainly given by them. Additionally, relevant spectral contribution could also derive from other cellular components such as ferriheme, transferrin, aconitase and catalase, although to a lower extent. It is worth to note that, although Fe-S clusters are molecular systems characterized by complex magnetic interactions between the Fe nuclei, in the majority of cases iron-sulfur clusters belonging to the mitochondrial respiratory complexes can be simply described as systems with an effective $S = \frac{1}{2}$ in their reduced state [Hagen W.R., 2018]. Moreover, most of the electrons in Fe-S clusters are mainly localized in the $3d$ molecular orbitals of iron, thereby leading to a significant deviation of the g factor from that of a free electron and being indicative of the interactions between the spin system with the molecular environment [Ohnishi T., 1998].

Although the g factors differ from one spin system to another, one of the main practical problems in the study of biological samples is the multiple signal overlap: in fact, each redox center is characterized by a distinct EPR signal which is, however, in the same region of the other EPR-active centers. Nevertheless, a deconvolution of the overall spectral lineshape by means of computational

simulations and a direct assignment of the individual contributions have been extensively done in the past by the comparison of EPR signals from tissues like liver, muscles or heart, with those derived from purified proteins, fractionated extracts, or isolated mitochondria (Figure 5.6) [Beinert H., 1978; Haddy A. & Smith G., 1999; Kalyanaraman B. et al., 2019].

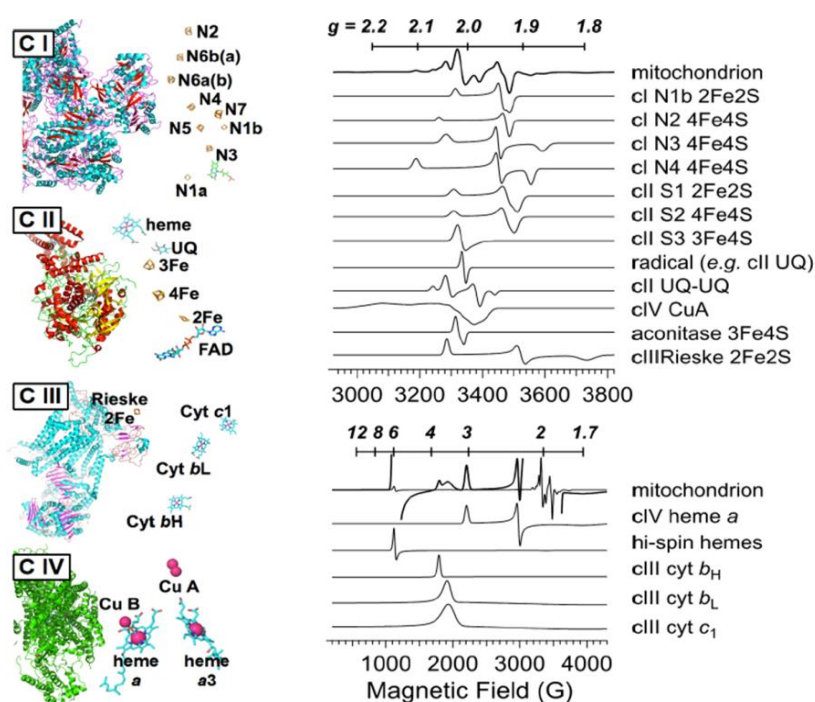


Figure 5.6. EPR spectra of mitochondrial redox centers. Redox cofactors belonging to the four mitochondrial respiratory chain complexes (CI, CII, CIII and CIV, on the left) and the relative computational simulation of their EPR signals observed in whole, unprocessed, frozen tissue (on the right). The g values and resonant fields at 9.5 GHz are reported on the top scale and on the bottom scale, respectively. In order to appreciate each contributory signal, the EPR spectrum of the whole mitochondrion is shown at two different amplitudes [adapted from Bennett B., 2020].

Among the complexes belonging to the respiratory chain, complex I is the one that contributes the most. It provides the richest array of EPR signals due to the large number of iron-sulfur clusters, both as [2Fe-2S] and [4Fe-4S], which are all EPR-detectable in their reduced state. The direct assignment for EPR signals of Fe-S clusters from mammalian complex I is, however, still controversial [Yakovlev G. et al., 2007; Ohnishi T. & Nakamaru-Ogiso E., 2008]. Nevertheless, the most informative clusters in complex I are also the best-resolved in the EPR spectrum and they correspond to the [2Fe-2S] cluster N1b ($g \approx 1.92$) and the three [4Fe-4S]

clusters N2, N3 and N4 ($g \approx 1.92$, $g = 1.86$ and $g = 1.88$, respectively) [Roeslter M.M. et al., 2010; Bennett B. et al., 2020]. There are three signals arising from the iron-sulfur clusters of mitochondrial complex II: two are due to [2Fe-2S] cluster S1 and the [4Fe-4S] cluster S2, both centered at $g \approx 1.92$ and overlapping the signal of complex I, and the third derives from an oxidized [3Fe4S] (cluster S3) whose signal is at $g \approx 2.02$ [Beinert H. et al., 1975; Maguire J.J. et al., 1985; Johnson M.K. et al., 1985; Bennett B., 2020]. For complex III, the only signal which is usually attributed is the one ascribed to reduced [2Fe-2S] cluster of the Rieske protein; it is characterized by a sharp resonance at $g = 2.03$, a derivative peak at $g = 1.90$ (usually not distinguishable by the overlap of the EPR signals at $g = 1.92$) and a distinctive very broad signal at $g = 1.78$ [Rieske J.S. et al., 1964; Orme-Johnson N.R. et al., 1974; Trumpower B.L. et al., 1979; Bennett B. et al., 2016]. Unfortunately, the signals ascribed to the other cofactors of complex III, *i.e.* cytochromes c_L , b_L and b_H , are generally very weak and difficult to be detected and characterized, also because their resonance positions and line widths strongly depend on the environment and the specific sample under investigation [Orme-Johnson N.R. et al., 1974; Siedow J.N. et al., 1978]. In the case of complex IV, the main recognizable signal derives from the low-spin heme a ($g \approx 3.0$ and $g \approx 2.2$) and, in some cases, from the dinuclear $S = 1/2$ CuA center ($g \approx 2.18$ and $g \approx 2.0$) [Aasa R. et al., 1976; Kroneck P.M. et al., 1990].

In addition to the aforementioned problem concerning the overlap of signals and the consequent difficulty in the interpretation of the spectra, there are two other problems concerning the study of iron-sulfur biological clusters by EPR, both related to sensitivity: the low concentrations of Fe-S clusters in the biological samples and the temperatures at which EPR spectra are acquired [Hagen W.R., 2018]. With purified proteins or synthetic model systems, EPR studies related to iron-sulfur clusters are not constrained by concentration limits; in the case of biological samples, the lower concentrations, ranging from micromolar to sub-micromolar, hamper the spectroscopic survey, requiring an increase of the sample concentration (whenever possible) or adopting some additional experimental tricks, although limiting the EPR to the basic continuous-wave X-band experiment. The second problem, related to temperature, is not trivial: cofactors like Fe-S clusters, semiquinones, semiflavines and heme can be detected in mitochondria and quantified only at cryogenic temperatures, close to that of liquid helium. This is mainly due to the relaxation kinetics of the EPR signals arising from iron-sulfur clusters, which are characterized by short and/or extremely short relaxation times; a temperature of 12-15 K is frequently chosen in

the X-band studies, since it represents a good compromise for the detection of both fast relaxing [4Fe-4S] clusters and the slow relaxing [2Fe-2S] clusters [Hagen W.R., 2018]. Acquiring EPR spectra at different temperatures, for instance at 15 K and 40 K, is usually sufficient to ensure an adequate interpretation of experimental data [Bennett B., 2016].

From a general point of view, the mitochondrial EPR-active cofactors can exist in different oxidation states and the modulation of their *status* is determined by several factors, such as the mitochondrial and cellular redox environment, the functionality of the individual respiratory complexes and the electron transfer process, the integrity of the mitochondrial membrane and/or an imbalance in the physiological levels of reactive oxygen species. As previously described, mitochondrial complexes are pivotal to sustain cellular energetic demands. In general, an alteration of the functionality of mitochondrial respiratory chain is a common feature shared by all mitochondrial diseases. The application of cryogenic electron paramagnetic resonance spectroscopy on cells and flash-frozen tissues turns out to be a promising tool for the investigation of cellular dysfunction *in situ* and, especially, for the characterization of mitochondrial diseases [Bennett B. et al., 2016; Bennett B., 2020]. In support of the classical biochemical investigation methods, this approach could provide new clues on the pathophysiology of mitochondrial disorders and, in a long-term perspective, novel molecular targets for effective pharmacological action.

Aim of the Thesis

Friedreich's ataxia (FRDA) is a cardio- and neuro-degenerative disease, caused by an abnormal expanded GAA triplet repeat in the first intron of the nuclear *FXN* gene which leads to a transcriptional silencing of *FXN* and to a reduced expression of frataxin, a ubiquitous and highly conserved mitochondrial protein. Several roles have been proposed for frataxin, essentially based on the structural/functional features of the protein. Genetic and biochemical studies carried out on several orthologues support a role of frataxin as a multifunction protein involved in different aspects of intracellular iron metabolism, ranging from biogenesis of Fe-S clusters and heme, to iron-binding/storage and iron chaperone activity. All these proposed functions are in agreement with the cardinal downstream biochemical features of FRDA cells, *i.e.* a deficit of Fe-S proteins, associated to mitochondrial iron overload and a consequent increased sensitivity to oxidative stress.

Although the depletion of frataxin is crucial for the disease onset and progression, the precise function of frataxin in the cell (patho)physiology is still elusive and a definite relationship between frataxin decrease, Fe-S clusters assembly dysregulation, iron homeostasis and mitochondrial bioenergetics impairment has not been established yet.

Based on this background, my Ph.D. project has been based on a multidisciplinary approach ranging from *in vitro* biochemistry and advanced biophysical analysis on isolated proteins, to mitochondrial physiology and cell imaging, to explore how frataxin deficiency could be involved in FRDA pathogenesis.

My research has been developed in two main parallel working lines. In the first one (Part II, *Chapter 1*), I have explored if and how the cellular deficiency of frataxin is involved in the upstream events leading to Fe-S clusters assembly impairment and bioenergetics defects; in this regard, I have investigated the mitochondrial phenotype of cells derived from FRDA patients, assessing the cellular respiration, the mitochondrial morphology and ultrastructure, the activity and structural stability of individual respiratory chain complexes as well as their association in supercomplexes. In light of these studies, a potential functional relationship between frataxin and mitochondrial respiratory chain was further explored.

In the second part of my research (Part II, *Chapter 2*) the focus has been on the iron-binding properties of human frataxin by means of different spectroscopic techniques; in particular, I took advantage of an approach never used before in the study of frataxin, *i.e.* Site Directed Spin Labeling (SDSL) technique coupled to Electron Paramagnetic Resonance (EPR). This approach has been exploited to have a precise picture of the structural and conformational changes of frataxin *in vitro*, not only as response to the iron-binding to the isolated protein, but also in the interplay with the mitochondrial superoxide dismutase, a key enzyme belonging to the intracellular antioxidant machinery.

The combination of these studies, performed with both purified recombinant proteins and intact cells, have been aimed to understand the molecular mechanisms underlying the upstream pathophysiological effects of frataxin deficiency in mitochondria and, consequently, to gain new insights into the role of frataxin in the cell.

Part II
Experimental
Section

Chapter 1

Deciphering the Role of Frataxin in Mitochondrial Pathophysiology of Friedreich’s Ataxia

Friedreich’s ataxia (FRDA) is a cardio-neurodegenerative disease resulting from a severe decrease of frataxin (FXN), a mitochondrial protein involved in the biogenesis of iron-sulfur clusters. Most patients carry a GAA repeat expansion in both alleles of the FXN gene, whereas a small fraction of them are compound heterozygous for the expansion and a point mutation in the other allele. A distinctive feature of all FRDA patients’ cells is an impaired cellular respiration, likely due to a deficit of Fe-S clusters and heme, key redox cofactors working as electrons shuttles through the complexes of the respiratory chain. However, a definite relationship between frataxin levels, iron-sulfur clusters assembly dysregulation and bioenergetics failure has not been established. In this work, we made a comparative analysis of the mitochondrial phenotype of lymphoblastoid cell lines from FRDA patients, either homozygous for the expansion or compound heterozygotes for the G130V mutation. We disclosed defects in respiratory supercomplexes assembly, reduced maximal respiration and spare respiratory capacity in all FRDA cell lines. Taking advantage of cryo-EPR, we identified a severe impairment of the redox centers belonging to the respiratory chain in FRDA cells. Furthermore, we found that in healthy cells FXN and two key proteins of the Fe-S cluster assembly machinery, i.e. NFS1 and ISCU, are enriched in mitochondrial cristae, the dynamic subcompartment housing the respiratory chain. On the other hand, FXN widely redistributes to the matrix in FRDA cells with an altered respiratory function. We propose that this could be relevant for the early mitochondrial defects afflicting FRDA cells and that perturbation of mitochondrial morphodynamic could in turn be critical in terms of disease mechanisms. The hypothesis of a functional interaction between frataxin and the respiratory chain has been further investigated by means of in situ proximity ligation assay (PLA) in human healthy fibroblasts and iPSC-derived cardiomyocytes. Taken together, our findings suggest that frataxin could act as a bridge between iron-sulfur clusters biogenesis and the oxidative phosphorylation system.

This chapter has been adapted from:

Doni D., Rigoni G., Palumbo E., Baschiera E., Peruzzo R., De Rosa E., Caicci F., Passerini L., Bettio D., Russo A., Szabò I., Soriano M.E., Salviati L., Costantini P. – *The displacement of frataxin from the mitochondrial cristae correlates with abnormal respiratory supercomplexes formation and bioenergetic defects in cells of Friedreich ataxia patients* – The FASEB Journal (2021); 35(3): e21362 - [doi: 10.1096/fj.202000524RR]

Introduction

As described in Part I, the cardinal downstream biochemical feature of frataxin deficiency in FRDA cells is a severely affected mitochondrial physiology, associated to deficit of Fe-S proteins, impairment of energy production, iron overload and increased sensitivity to oxidative stress [Rötig A. *et al.*, 1997; Schulz J.B. *et al.*, 2000; Puccio H. *et al.*, 2001; Schmucker S. & Puccio H., 2010]. However, although several roles have been hypothesized, ranging from heme and Fe-S clusters biogenesis [Huynen M.A. *et al.*, 2001; Yoon T. & Cowan J.A., 2004] to iron-chaperone and binding/storage activities [Cavadini P. *et al.*, 2002; Yoon T. & Cowan J.A., 2003], the precise physiological function of frataxin remains unclear. All the potential functions proposed are in agreement with the impaired mitochondrial phenotype of FRDA cells; however, due to the tight link between these crucial cellular pathways, it is difficult to identify with certainty the upstream event(s) leading to the disease onset and progression and to define which metabolic consequences primarily occur after frataxin depletion. It is worth noting that in disorders associated to dysfunctions of Fe-S clusters biogenesis, such as FRDA, mitochondria have to be considered as double-sided: on the one hand, their primary function in energy production relies on Fe-S clusters (respiratory complexes I, II and III) and heme (respiratory complex IV) as prosthetic groups; on the other hand, the biogenesis of Fe-S clusters itself takes place in mitochondria, which contain the specific assembly machinery responsible for the biosynthesis of these cofactors. According to an involvement in the Fe-S clusters biogenesis, human frataxin was shown to interact *in vitro* with multiple core components of this machinery, although its exact molecular function at this level remains elusive [Gerber J. *et al.*, 2003; Shan Y. *et al.*, 2007; Schmucker S. *et al.*, 2011; Bridwell-Rabb J. *et al.*, 2014; Parent A. *et al.*, 2015]. This assembly system is also essential to all extra-mitochondrial Fe-S proteins [Martelli A. *et al.*, 2007], putting mitochondria physiology more in general at the core of the metabolic pathways involving Fe-S proteins [Lill R. & Mühlhoff U., 2008; Lill R., 2009].

Most, if not all functions of mitochondria are closely linked to their morphology: mitochondria are highly dynamic organelles which continually fuse, divide and remodel the cristae to adapt their morphology and ultrastructure to the cell energy demand, and to participate in several processes besides bioenergetics, including organelle distribution during cell proliferation, calcium homeostasis, apoptosis, autophagy [Pernas L. & Scorrano L., 2016]. In the complex architecture

of a mitochondrion, cristae have a remarkable structural variability [Colina-Tenorio L. et al., 2020] and are considered a functional subcompartment, since in addition to hosting many key processes, such as protein translocation, metabolite exchange and protein assembly and degradation [Vogel F. et al., 2006], they house the assembled respiratory complexes and supercomplexes, quaternary structures which in healthy cells increase the electron flow channeling and the overall mitochondrial respiratory efficiency [Schägger H. & Pfeiffer K., 2000; Schägger H. & Pfeiffer K., 2001]. Cristae shape and their dynamic remodeling are therefore fundamental for the complexes and supercomplexes formation, and ultimately for the performance of the electron transport chain [Cogliati S. et al., 2013; Cogliati S. et al., 2016]. Energy-intensive cells, such as neurons and skeletal/cardiac myocytes, are particularly vulnerable to mitochondrial dysfunctions and several neurodegenerative pathologies are caused by mutations in genes directly involved in mitochondrial dynamics [Pernas L. & Scorrano L., 2016; Chan D.C., 2020]. Moreover, other neurological disorders, including Parkinson's and Huntington's diseases, have been associated with defects in these processes, even if the link in this case is less direct and the potential causative role remains to be determined [Pernas L. & Scorrano L., 2016; Chan D.C., 2020].

Interestingly, it has been shown that in *Saccharomyces cerevisiae* some of the proteins of the Fe-S cluster assembly machinery, *i.e.* the NFS1 desulfurase and its chaperonine ISD11, are closely attached to the mitochondrial inner membrane and enriched in the cristae, as assessed by quantitative immuno-electron microscopy of intact cells [Vogel F. et al., 2006]; more recently, an association of these two proteins with the respiratory chain supercomplexes of *S. cerevisiae* was found [Böttinger L. et al., 2018], and this could be instrumental to drive the coordination of Fe-S cluster assembly with the respiratory activity. Such an association has not yet been shown in mammalian mitochondria, however large-scale protein interactome studies point to an interaction of human NFS1 with complex I [Floyd B.J. et al., 2016; Huttlin E.L. et al., 2017]. Furthermore, some evidences suggest that frataxin itself could interact with the proteins belonging to the respiratory chain [Gonzalez-Cabo P. et al., 2005; Vázquez-Manrique R.P. et al., 2006]; in this regard, it has been shown that, in yeast, frataxin is able to interact with succinate dehydrogenase, indicating that FXN may have a direct involvement in the electron transport chain [Gonzalez-Cabo P. et al., 2005].

In this work we therefore thoroughly explore the mitochondrial phenotype of three cell lines from FRDA patients, two homozygous for the GAA triplet expansion and the third heterozygous for the GAA expansion on one *FXN* allele

and for the G130V point mutation in the other, which is one of the most frequently found in affected patients. We found that in healthy cells frataxin as well as some key components of the Fe-S cluster assembly machinery are enriched in the mitochondrial cristae and we propose that the decrease of frataxin in this functional subcompartment is associated with lower levels of respiratory chain supercomplexes, which could be in turn a crucial factor in the mitochondrial respiratory defects afflicting FRDA patient cells. On the basis of our results, we hypothesized that frataxin could have a role on the stability and/or activity of mitochondrial (super)complexes through a functional interaction with the respiratory complex I.

Materials & Methods

Cell Lines and Culture Conditions

Lymphoblastoid cell lines (LCLs) were obtained from the Coriell Institute for Medical Research (NJ, USA) and cultured in RPMI 1640 (GIBCO Life Technologies), supplemented with 15% (v/v) Fetal Bovine Serum (FBS) (GIBCO Life Technologies), 2 mM L-glutamine, 100 U/mL penicillin and 100 µg/mL streptomycin, under 5% CO₂ at 37°C. FRDA LCLs were from three unrelated clinically affected patients: GM04079 (homozygous for the GAA expansion in the *FXN* gene, with alleles carrying 541 and 420 repeats at sampling), GM16227 (homozygous for the GAA expansion in the *FXN* gene, with alleles carrying 630 and 830 repeats at sampling) and GM21542 (with one *FXN* allele carrying 900-950 GAA repeats, as determined in this work by long-range PCR, and the second carrying a G130V point mutation and a normal number of repeats). Control LCL was from one clinically unaffected and unrelated subject, *i.e.* GM07533 (with both *FXN* alleles in the normal range of GAA repeats); a second control cell line (GM15849, with one *FXN* allele carrying 920 GAA repeats and the second allele in the normal range) was used in the comparative analysis of the *FXN* transcription for the LCLs used in this work. GM04079 and GM16227 are indicated throughout the text as FRDA 1 and FRDA 2, respectively. Cytogenetic analysis was performed on the lymphoblastoid cell lines used for the experiments, according to standard laboratory procedures. This analysis was kindly provided by Dr. Daniela Bettio of the Clinical Genetic Unit of the Department of Women’s and Children’s Health, University of Padova. A normal karyotype was observed in all the 20 Q-banded metaphases analyzed for each case (*Figure 1.1*).

Healthy and FRDA human immortalized fibroblasts were used as *in vitro* models for the immunofluorescence experiments reported in this thesis. FRDA fibroblasts were obtained from the Coriell Institute for Medical Research (NJ, USA) and were from a clinically affected patient (GM04078), homozygous for the GAA expansion in the *FXN* gene with alleles of approximately 541 and 420 repeats. Fibroblast cells were cultured in DMEM (Dulbecco’s Modified Eagle’s Medium, GIBCO Life Technologies) supplemented with 100 mM Sodium Pyruvate (100X solution, GIBCO Life Technologies), 10% (v/v) FBS (GIBCO Life

Technologies), 100 U/mL penicillin G, 100 µg/mL streptomycin and 1% non-essential amino acids (100X solution; GIBCO Life Technologies) under 5% CO₂ at 37°C. For cell passaging, fibroblasts were washed with Phosphate Buffered Saline (PBS), trypsinized with 0.25% trypsin/EDTA (GIBCO Life Technologies) and supplemented with fresh growth medium.

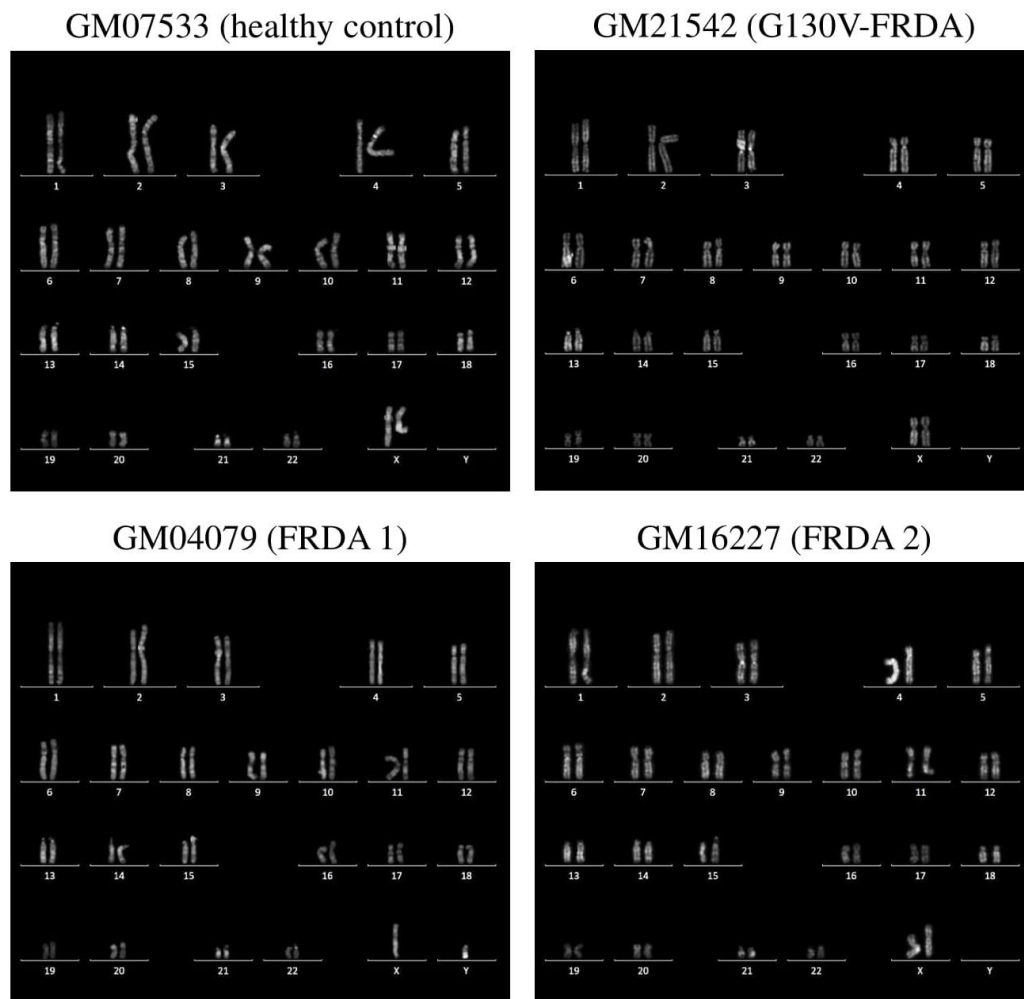


Figure 1.1. Normal karyotypes obtained from healthy control, FRDA 1 and 2 and G130V FRDA LCL.

Genotyping and RT-PCR

Four million cells from each lymphoblastoid cell line were harvested, sedimented, washed twice with PBS and resuspended in lysis buffer (10 mM Tris-HCl pH 8.0, 1 mM EDTA pH 8.0, 0.1% SDS, 400 µg/mL Proteinase K). Samples were incubated at 50°C overnight. Genomic DNA was purified with

phenol : chloroform : isoamyl-alcohol (25 : 24 : 1) according to standard procedures. For *FXN* expression analysis, total RNA was isolated from 3×10^6 cells using the RNeasy mini kit (Qiagen). DNA and RNA samples were quantified using ND-1000 spectrophotometer (Nanodrop, Wilmington, DE, USA). The genotype of all cell lines employed in this work was verified by long-range PCR. In the case of GM21542, derived from the compound heterozygote carrying the G130V mutation and one expanded allele of unknown length, we found that the GAA expansion consists of 900-950 repeats (*Figure 1.2*).

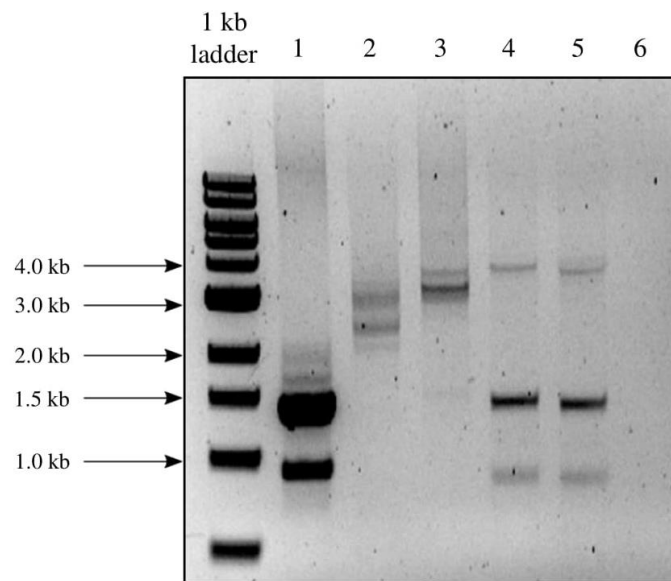


Figure 1.2. The length of *FXN* alleles for the six LCLs was assessed by long-range PCR. Lane 1: GM 07533 (healthy control); lane 2: GM 04079 (homozygous FRDA 1); lane 3: GM 16227 (homozygous FRDA 2) lane 4: GM 21542 (heterozygous G130V-FRDA) lane 5: GM 15849 (healthy carrier); lane 6: no template control. Molecular weight of the 1kb ladder bands of interest is indicated by an arrow. Amplicon length is calculated as follow: amplicon length (bp) = 1350 + 3n GAA (n = number of GAA repeats).

An amount of 50 ng of each DNA sample were amplified with the QIAGEN LongRange PCR Kit (Qiagen) according to manufacturer’s instructions using a primer set specific for the amplification of the expanded GAA-repeat:

forward: 5'-GGAGGGATCCGTCTGGGCAAAGG-3'
reverse: 5'-CAATCCAGGACAGTCAGGGCTT-3'
amplicon length: 1350 + 3n GAA

2 µg of RNA was retrotranscribed (EuroScript M-MLW Reverse Transcriptase RNase H-, Euroclone) and 2 ng of cDNA were used as template in the quantitative real-time PCR (qRT-PCR) using the following primer pairs:

FXN forward: 5'-CCTTGCAGACAAGCCATACA-3'

FXN reverse: 5'-GGTCCACTGGATGGAGAAGA-3'

GAPDH forward: 5'-CCTCAACGACCACTTTGTCA-3'

GAPDH reverse: 5'-TTCCTCTTGCTCTTGCTG-3'

qRT-PCR was performed using an Applied Biosystems 7500 Fast Real-Time PCR System according to the following amplification protocol: 95°C for 10 min, 95°C for 15 sec, 60°C for 60 sec (40 cycles). qRT-PCR reactions were always performed in triplicates amplifying the cDNA deriving from two independent reverse transcription reactions. Amplification efficiency of *FXN* and *GAPDH* genes was verified using the standard curve method. *FXN* expression was normalized to that measured in the non-mutated cell line (GM07533), using the comparative delta CT method ($2^{-\Delta\Delta CT}$) implemented in the 7500 Real Time System software.

SDS-PAGE and Protein Immunoblotting

Five million cells from each lymphoblastoid cell line were harvested, sedimented, washed once with cold PBS and lysed for 30 min on ice in 1 mL of RIPA lysis buffer (50 mM Tris-HCl pH 7.5, 150 mM NaCl, 1% NP-40, 100 µM phenylmethylsulfonyl fluoride (PMSF), 1 µg/mL aprotinin, 1 µg/mL leupeptin, 1 µg/mL pepstatin). Lysates were sedimented at full speed in a microcentrifuge for 30 min at 4°C, the supernatants transferred to clean tubes and the protein concentration determined by the Bradford assay (Bradford Reagent, Sigma-Aldrich). Equal protein amounts were solubilized in Laemmli gel sample buffer (Tris-HCl 62.5 mM, SDS 2%, glycerol 10%, β-mercaptoethanol 5%, bromophenol blue 0.1%, pH 6.8) and separated electrophoretically by SDS-PAGE on 4%-20% polyacrylamide gels (GenScript® ExpressPlus™ PAGE), except for the analyses of OPA1 in which the gels were 8%. Proteins were then transferred on nitrocellulose membranes (0.45 µm, LifeScience) through a semi-dry Trans-Blot® Turbo™ Transfer System (BioRad). Membranes have been then blocked with 10% milk in Tris-Buffered Saline (TBS) for 1 hour at room temperature and subsequently incubated with primary antibodies diluted in Tris-Buffered Saline

with 0.05% Tween20 (TBS-T) (the list of antibodies and the experimental conditions of their use are reported in *Table 1*). After incubation with secondary Horseradish Peroxidase-Conjugated (HRP) antibodies at room temperature for 1 hour, the proteins were visualized using Immobilon® Forte Western HRP Substrate (Millipore) by Imager CHEMI Premium Detector (VWR). Reaction product levels were quantified by scanning densitometry using ImageJ software and normalized to those of β -actin or the mitochondrial protein TOM20.

Blue Native Gel Electrophoresis (BNGE)

For BN extraction, 40×10^6 cells from each lymphoblastoid cell line were collected, sedimented and washed once with cold PBS. Cell pellets were homogeneously resuspended in 200 μ L of PBS and 200 μ L of a freshly prepared solution of 8 mg/mL digitonin (SIGMA) were added. After incubation for 10 min in ice, 1 mL of cold PBS was added to each sample to be then centrifuged at $9.600 \times g$, 10 min, 4°C. Pre-treated cells were washed once with cold PBS and sedimented again at $9.600 \times g$, 10 min, 4°C in order to remove the excess of residual digitonin. After centrifugation, the pellets containing the mitochondrial fraction were solubilized in 100 μ L of Loading Native Buffer 1X containing Protease Inhibitor Cocktails (PIC, 1:100) and 10 μ L of a freshly prepared solution of digitonin 10%. After 5 min of incubation in ice, samples were centrifuged at maximal speed in a microcentrifuge, 25 min, 4°C, and the supernatant containing mitochondrial complexes was collected. In the final step, 5 μ L of 5% Coomassie Blue G-250 (Invitrogen) were added to each sample. The electrophoresis in native conditions was performed by loading 20 μ L of each sample in a precast native Bis-Tris gel 3-12% (Invitrogen). A first electrophoretic run was done at 150 V in the presence of Anode buffer and Dark cathode buffer (Invitrogen), 45 min, 4°C. The Dark buffer was then replaced with Light buffer (Invitrogen) and a second run was done at 250 V, 90 min, 4°C. Then, a part of the gel was stained with Coomassie Blue (40% methanol, 10% acetic acid, 0.25 g of Coomassie Brilliant Blue R-250) and the other part, containing the replicates, was blotted onto a PVDF membrane at 33 V, overnight, 4°C. After transfer, the membrane was fixed with acetic acid 8% for 15 min, washed with water and let it dry. The membrane was then re-activated for 1 min in pure methanol and incubated with the antibodies of interest (*Table 1.1*). Protein bands were visualized as described above.

Table 1.1. List of antibodies used in western blotting analyses and experimental conditions adopted for their usage.

Antibody	Supplier	Condition of use
Anti – β -actin	Merck; MAB1501	1 : 20 000 in TBST 1X 5% milk – 3h, RT
Anti – TOM20	Santa Cruz; SC-11415	1 : 1000 in TBST 1X 5% milk – 3h, RT
Anti – Frataxin	proteintech; 14147-1-AP	1 : 500 in TBST 1X 5% milk – O/N, 4°C
Anti – NFS1	LSBio; LS-C482672	1 : 1000 in TBST 1X – O/N, 4°C
Anti – ISCU	LSBio; LS-C157839	1 : 500 in TBST 1X – O/N, 4°C
Anti – NDUFA9	Abcam; ab14713	1 : 1000 in TBST 1X 5% milk – O/N, 4°C
Anti – NDUFS1	Abcam; ab157221	1:1000 in TBST 1X – O/N, 4°C
Anti – NDUFS8	Santa Cruz; SC-515527	1:500 in TBST 1X – O/N, 4°C
Anti – NDUFV2	Santa Cruz; SC-271620	1:500 in TBST 1X – O/N, 4°C
Anti – NDUFS2	Santa Cruz; SC-390596	1:500 in TBST 1X – O/N, 4°C
Anti – NDUFS3	Invitrogen; 459130	1:1000 in TBST 1X – O/N, 4°C
Anti – NDUFS4	Santa Cruz; SC-514002	1:500 in TBST 1X – O/N, 4°C
Anti – SDHA	Abcam; ab14715	1 : 8000 in TBST 1X – O/N, 4°C
Anti – SDHB	Santa Cruz; SC-59688	1:1000 in TBST 1X – O/N, 4°C
Anti – UQCRC1	Santa Cruz; SC-65238	1 : 1000 in TBST 1X 5% milk – O/N, 4°C
Anti – UQCRC1	Santa Cruz; SC-271609	1:500 in TBST 1X – O/N, 4°C
Anti – MTCO1	Abcam; ab14705	1 : 1000 in TBST 1X 5% milk – O/N, 4°C
Anti – ACO2	Santa Cruz; SC-517651	1:500 in TBST 1X – O/N, 4°C
Anti – OPA1	BD Biosciences; 612607	1 : 1000 in TBST 1X 5% milk – O/N, 4°C
Anti – Mitofilin	proteintech; 10179-1-AP	1 : 1000 in TBST 1X 5% milk – O/N, 4°C
Anti – Vinculin	Sigma Aldrich; V9264-25UL	1:1000 in TBST 1X – O/N, 4°C
Anti – ATP5A	Abcam; ab14748	1:4000 in TBST 1X 5% milk – O/N, 4°C
Anti – Lamin B1	Santa Cruz; SC-6216	1:1000 in TBST 1X 5% milk – O/N, 4°C
Anti – mouse peroxidase	Sigma Aldrich; A4416	1 : 10 000 in TBST 1X – 1h, RT
Anti – rabbit peroxidase	Sigma Aldrich; A0545	1 : 20 000 in TBST 1X – 1h, RT
Anti – goat peroxidase	Sigma Aldrich; A5420	1:80 000 in TBST 1X – 1h, RT

Biochemical Analysis of Respiratory Complexes

The activities of the mitochondrial electron transport chain (ETC) complexes were measured according to the protocol described by Spinazzi *et al.* [Spinazzi M. *et al.*, 2012]. Briefly, 50×10^6 cells from each lymphoblastoid cell line were harvested, sedimented, washed twice with PBS (pH 7.6) and pellets were frozen in liquid nitrogen and stored at -80°C before proceeding with mitochondrial extraction. To obtain the mitochondrial-enriched fraction, each pellet was kept in ice and resuspended in 1 mL of 10 mM ice-cold hypotonic Tris buffer (pH 7.6); cells were homogenized with a precooled 2-mL glass/Teflon tissue grinder kept on ice through 20 slow up-down strokes at 1800 r.p.m.. The cell homogenate was then transferred to a clean tube and 200 μL of a 1.5 M sucrose solution was added and thoroughly mixed. The suspension was centrifuged at $600 \times g$, 10 min, 2°C and the supernatant was subsequently centrifuged at $14\,000 \times g$ for 10 min at 2°C . The supernatant was then removed and the mitochondrial pellet was resuspended with 500 μL of 10 mM ice-cold hypotonic Tris buffer (pH 7.6). Each mitochondrial suspension was subjected to three cycles of snap-freezing / thawing at 37°C in order to disrupt the mitochondrial membranes and the mitochondrial lysates were kept on ice. Protein content of each sample was then quantified according to the Bradford method and the activity of respiratory chain complexes I-IV and citrate synthase (CS) was measured by means of a single-wavelength multicuvette spectrophotometer (Varian Cary UV-Vis 100) at 37°C . Activities of the mitochondrial OXPHOS complexes were normalized to CS activity.

Oxygen Consumption Studies

Cells from each lymphoblastoid cell line were collected, sedimented and resuspended in DMEM without serum and sodium bicarbonate, supplemented with 10 mM sodium pyruvate and 2 mM glutamine; 2.5×10^5 cells/well were then seeded into a Seahorse plate after pre-coating with Cell Tak reagent (Corning), following the protocol described by the manufacturer. The plate was then centrifuged for 2 min at $600 \times g$ to ensure cells adhesion to the bottom of the wells. The oxygen consumption rate (OCR) was measured with an extracellular flux analyzer (Seahorse) at fixed time points and after the addition of the following compounds: oligomycin (2 $\mu\text{g}/\text{mL}$), carbonyl cyanide *p*-

(trifluoromethoxy)phenylhydrazine (FCCP) (400 nM), antimycin A (1 μ M). At the end of each experiment, every plate well was directly observed using an optic microscope, to exclude wells with a massive detachment of cells from the analysis. To assess mitochondrial functionality, bioenergetic parameters were calculated as follows: ATP-linked respiration is the difference between OCR before and after the addition of oligomycin; proton leak is the difference between OCR measured after the treatment with oligomycin and after the treatment with antimycin; maximal respiration was obtained by subtracting the OCR value measured after the addition of antimycin from the OCR value observed upon the addition of FCCP; spare respiratory capacity is the difference between the respiration obtained after the addition of FCCP and basal respiration; non-mitochondrial respiration is OCR value of cells incubated with antimycin.

Isolation of Mitochondria for EPR Samples

Mitochondrial enriched fractions for EPR experiments were obtained starting from 700×10^6 cells for each lymphoblastoid cell line. Cells were collected, sedimented and washed twice with cold PBS (pH 7.6) and pellets were instantly frozen in liquid nitrogen and stored at -80°C before proceeding with mitochondrial extraction. To obtain the mitochondrial-enriched fraction, each pellet was kept in ice and resuspended with cold PBS in a total volume of 20 mL. Cells were homogenized with a precooled 30-mL glass/Teflon tissue grinder kept on ice through 20 slow up-down strokes at 1800 r.p.m.. The cell homogenate was then transferred to a clean tube and 4 mL of a 1.5 M sucrose solution was added and thoroughly mixed. The suspension was then centrifuged at $600 \times g$, 10 min, 2°C and the supernatant, containing both the cytosolic and mitochondrial fractions, was subsequently centrifuged at $14000 \times g$ for 10 min at 2°C . The supernatant was carefully removed and the mitochondrial pellet was gently resuspended with 50 μL of a 50% (v/v) glycerol solution in PBS. The mitochondrial suspension was kept on ice and 200 μL and then transferred to a 3 mm (i.d.) \times 4 mm (o.d.) EPR quartz tube. The samples in the EPR tubes were immediately frozen in liquid nitrogen and stored in liquid nitrogen until spectroscopic analysis. The total protein concentration of each mitochondrial fraction was determined by the BCA assay (PierceTM BCA Protein Assay Kit). Each step of subcellular fractionations was checked by western blotting analysis using antibodies directed against lamin B1, vinculin and ATP5A as markers for

nuclear, cytoplasmic and mitochondrial fractions, respectively (see Table 1.1). Protein bands were visualized as previously described.

EPR Measurements

EPR experiments were performed at the Department of Chemical Sciences of University of Padova with an ELEXSYS E580 spectrometer equipped with a SHQ cavity (both from Bruker, Germany). For cryogenic measurements, the spectrometer was equipped with an Oxford ESR900 cryostat and an Oxford ITC4 variable-temperature controller.

Spectra were obtained using the following parameters: temperature, 15 K, 40 K and 100 K (the parameters that have been used exclusively for 100 K experiments are reported in parentheses); microwave frequency, 9.38 GHz, *i.e.* X-band; number of scans, 25; microwave power, 5 mW (0.02 mW); modulation amplitude, 0.7 mT; modulation frequency, 100 kHz; time constant, 41 ms; conversion time, 41 ms; scan width, 100 mT (12 mT); points, 1024. The microwave power was chosen to maximize signal intensity while limiting signal saturation. The magnetic field was calibrated using a 2,2-Diphenyl-1-Picrylhydrazyl radical (DPPH) sample ($g = 2.0036$). EPR spectra were corrected for the blank baseline, obtained using an EPR sample tube filled with the buffer used for mitochondria resuspension (50% glycerol in PBS), and for the baseline contributions resulting from the small amounts of frozen oxygen in the sample tube. The resulting spectra were then normalized dividing them by the total protein concentration (between 25 $\mu\text{g}/\mu\text{L}$ and 37 $\mu\text{g}/\mu\text{L}$) and the effective sample volume.

Immunogold Staining and Electron Microscopy

Cells were fixed in a 24 wells plate with 4% PFA (freshly prepared) in PBS (pH 7.4) for 30 min at room temperature. After fixation, cells were washed 5 times with PBS (5 min each), blocked and permeabilized with 5% normal goat serum and 0.1% saponin in PBS for 30 min, and then incubated 2 hours at room temperature with the primary antibody of interest in PBS, 5% normal goat serum and 0.05% saponin. After five washes with PBS (5 min each), cells were incubated 1 hour at room temperature with the secondary antibody Nanogold Fab GAR Ultra Small (Aurion). After 5 washes, cells were fixed with 2% glutaraldehyde in

PBS for 30 min. After 5 washes with water (5 min each) cells were incubated with Gold Enhancer (Nanoprobes), washed with water and prepared as for classical electron microscopy sample. Briefly, samples were postfixed with 1% osmium tetroxide/1% ferrocyanide in 0.1 M sodium cacodylate buffer for 1 hour at 4°C; after three water washes, samples were dehydrated in a graded ethanol series and embedded in an epoxy resin (Sigma-Aldrich). Ultrathin sections (60-70 nm) were obtained with an Ultratome V (LKB) ultramicrotome, counterstained with uranyl acetate and lead citrate and finally examined under a Tecnai G2 (FEI) transmission electron microscope operating at 100 kV at the electron microscopy facility of the Department of Biology, University of Padova. Images were captured with a Veleta (Olympus Soft Imaging System) digital camera. Antibody used for immunogold analyses were anti-frataxin, anti-NFS1 and anti-ISCU. Controls for specificity of immunolabeling were made by omitting the primary antibodies.

Morphometric Analysis of Mitochondria

The mitochondrial ultrastructure was analyzed using ImageJ Fiji software. For each mitochondrion, two morphological parameters were assessed in 2D: i) mitochondria length, evaluated as the longest distance between any two points of the selected mitochondrion (Feret's maximum diameter); ii) cristae width, evaluated as the widest point of the selected crista. For each cell line, TEM micrographs ranging from 30 to 150 (mitochondrial length) and from 165 to 600 (cristae width) were analyzed, as specified in the figure legends. For both morphological descriptors, frequency distribution and fitting analysis were performed using Origin. Briefly, the relative frequencies, expressed as percentage of mitochondria, were fitted by a nonlinear regression as singular or sum of gaussian functions, according to the data distribution.

Immunofluorescence

For immunofluorescence experiments, 15.000 fibroblast cells/well were seeded on 13 mm diameter cover glasses in 24-well plates, to reach approximately 60% final confluence. Cells, 24 hours after seeding, were gently washed with PBS, fixed with paraformaldehyde (PFA) 3.8% in PBS for 15 minutes, permeabilized with

0,2% Triton-X 100 (Sigma) in PBS for 10 minutes and saturated with Bovine Serum Albumin (BSA) (Sigma Aldrich) 2% in PBS, at room temperature for 1 hour, in order to prevent non-specific binding of primary and secondary antibodies. Samples were subsequently incubated overnight at 4°C with primary antibodies and for 1 hour at room temperature with secondary antibodies (the list of antibodies and the experimental conditions of their use are reported in *Table 1.2*). The incubations with both primary and secondary antibodies were performed in a humidified chamber. Finally, cover slides were extensively washed, dried and mounted with DAPI mounting media (Sigma). Images were acquired at 40X magnification by means of Leica SP5 confocal microscope and LAS-AF Software at the Imaging facility of the Department of Biology, University of Padova, and ultimately processed with ImageJ Fiji software.

Proximity Ligation Assay (PLA)

To perform Proximity Ligation Assay (PLA), Duolink® *In Situ* Red Starter Kit Mouse/Rabbit (DUO92101, Sigma Aldrich) has been used. A number of 15.000 fibroblast cells/well were seeded on 13 mm diameter cover glasses in 24-well plates, to reach approximately 60% final confluence. 24 hours after seeding, cells were fixed with PFA 3.8% for 15 minutes and permeabilized with 0,2% Triton-X 100 in PBS for 10 minutes. Samples were then saturated with BSA 2% in PBS, at room temperature for 1 hour, and incubated overnight at 4°C with primary antibodies diluted at suitable concentrations in a humidified chamber (*Table 2*).

Cells were washed twice with Buffer A® (DUO82046), for 5 min each at room temperature, and subsequently incubated for 1 h at 37 °C in a pre-heated humidified chamber with secondary antibodies conjugated with complementary oligonucleotides, *i.e.* anti-rabbit PLUS® (DUO82002) and anti-mouse MINUS® (DUO82004), properly diluted 1:5 in the Duolink® Antibody Diluent (DUO82008). After three washes in Buffer A® (5 min each, at room temperature), cells were incubated with DNA Ligase (DUO82029) properly diluted 1:5 in Ligation Buffer (DUO82009), for 30 min at 37 °C in a pre-heated humidified chamber. Subsequently, cells were washed three times in Buffer A® (5 min each, at room temperature) and incubated for 100 min at 37 °C with DNA Polymerase (DUO82030) diluted 1:5 in Amplification Buffer (DUO82011) containing red fluorescent-labeled oligonucleotides, for 100 min at 37 °C in a pre-heated humidified chamber and in the dark. Cells were washed twice with 1X Buffer B®

(DUO82048) for 10 min and eventually once with 0.01X Buffer B® for 1 min protecting them from light. The slides were then mounted using Duolink *In Situ* Mounting Medium containing DAPI (DUO82040) and stored at -20°C. Images were acquired under identical conditions at 40X magnification by means of Leica SP5 confocal microscope and LAS-AF Software at the Imaging facility of the Department of Biology, University of Padova. Images were ultimately processed with ImageJ Fiji software to assess the number of PLA dots/cell.

Immunofluorescence and PLA experiments were also preliminary performed on iPSC (induced Pluripotent Stem Cell)-derived cardiomyocytes, kindly provided by Dr. Milena Bellin of the Department of Biology of University of Padova.

Table 1.2. List of antibodies used in immunofluorescence and proximity ligation assay. The experimental conditions adopted for their usage are reported.

Antibody	Supplier	Condition of use
Anti – Frataxin	proteintech; 14147-1-AP	1 : 50 in BSA 1% (v/v) / 0.1% (v/v) Tween20 in PBS – O/N, 4°C
Anti – NFS1	Santa Cruz; SC-365308	1 : 50 in BSA 1% (v/v) / 0.1% (v/v) Tween20 in PBS – O/N, 4°C
Anti – MTND1	Invitrogen; 43-8800	1 : 500 in BSA 1% (v/v) / 0.1% (v/v) Tween20 in PBS – O/N, 4°C
Anti – SDHB	Invitrogen; 45-9230	1 : 100 in BSA 1% (v/v) / 0.1% (v/v) Tween20 in PBS – O/N, 4°C
Anti – UQCRFS1	Santa Cruz; SC-271609	1 : 10 in BSA 1% (v/v) / 0.1% (v/v) Tween20 in PBS – O/N, 4°C
Anti – Cyt c	BD Pharmingen; 556432	1 : 200 in BSA 1% (v/v) / 0.1% (v/v) Tween20 in PBS – O/N, 4°C
Anti – mouse	Invitrogen; Alexa Fluor™ 568	1 : 500 in 0.1% (v/v) Tween20 in PBS –1h, RT
Anti – rabbit	Invitrogen; Alexa Fluor™ 488	1 : 500 in 0.1% (v/v) Tween20 in PBS –1h, RT

Statistical Analysis

All numerical data, analyzed by GraphPad Prism, are expressed as mean ± SEM. Statistical analysis and significance were performed and assessed as specified in the figure legends, with $p \leq 0.05$ accepted as statistically significant.

Results

Comparative Analysis of Frataxin in FRDA Patients’ Cells

We evaluated *FXN* transcription by qRT-PCR in five lymphoblastoid cell lines (LCLs). Three of them were derived from FRDA patients, two homozygous for the GAA expansion (FRDA 1 and FRDA 2) and the other carrying the G130V point mutation and an expanded allele (G130V-FRDA). The other LCLs were derived from a clinically unaffected control with two unexpanded alleles and from a healthy carrier, heterozygous for the GAA expansion.

We detected the lowest levels of *FXN* mRNA in the homozygous FRDA cell lines, while *FXN* expression was similar in the G130V-FRDA and in the heterozygous carrier (*Figure 1.3A*). Frataxin protein levels were then analyzed by western blotting in whole-cell extracts. Frataxin is synthesized in the cytosol as a full-length precursor (*i.e.* FXN^{1-210}) and then imported into the mitochondria, where it undergoes to a two-step proteolytic processing resulting in the mature, shorter form (*i.e.* FXN^{81-210}) [Koutnikova H. *et al.*, 1998; Condò I. *et al.*, 2007; Schmucker S. *et al.*, 2008]. *Figure 1.3B* shows that the amount of mature frataxin is reduced in the three FRDA patients’ cells when compared to the control. The lowest protein levels were found in LCLs from the G130V-FRDA heterozygous patient. Clark and colleagues showed that G130V mutation impairs the frataxin processing from FXN^{42-210} to FXN^{81-210} in FRDA patients’ fibroblasts [Clark E. *et al.*, 2017]. *Figure 1.3C* indicates that $FXN^{42-210}/FXN^{81-210}$ ratio is increased also in the G130V-FRDA LCLs used in our experiments and, on the other hand, that the amount of the intermediate FXN^{42-210} has the same trend of the mature FXN^{81-210} , as they are both strongly reduced.

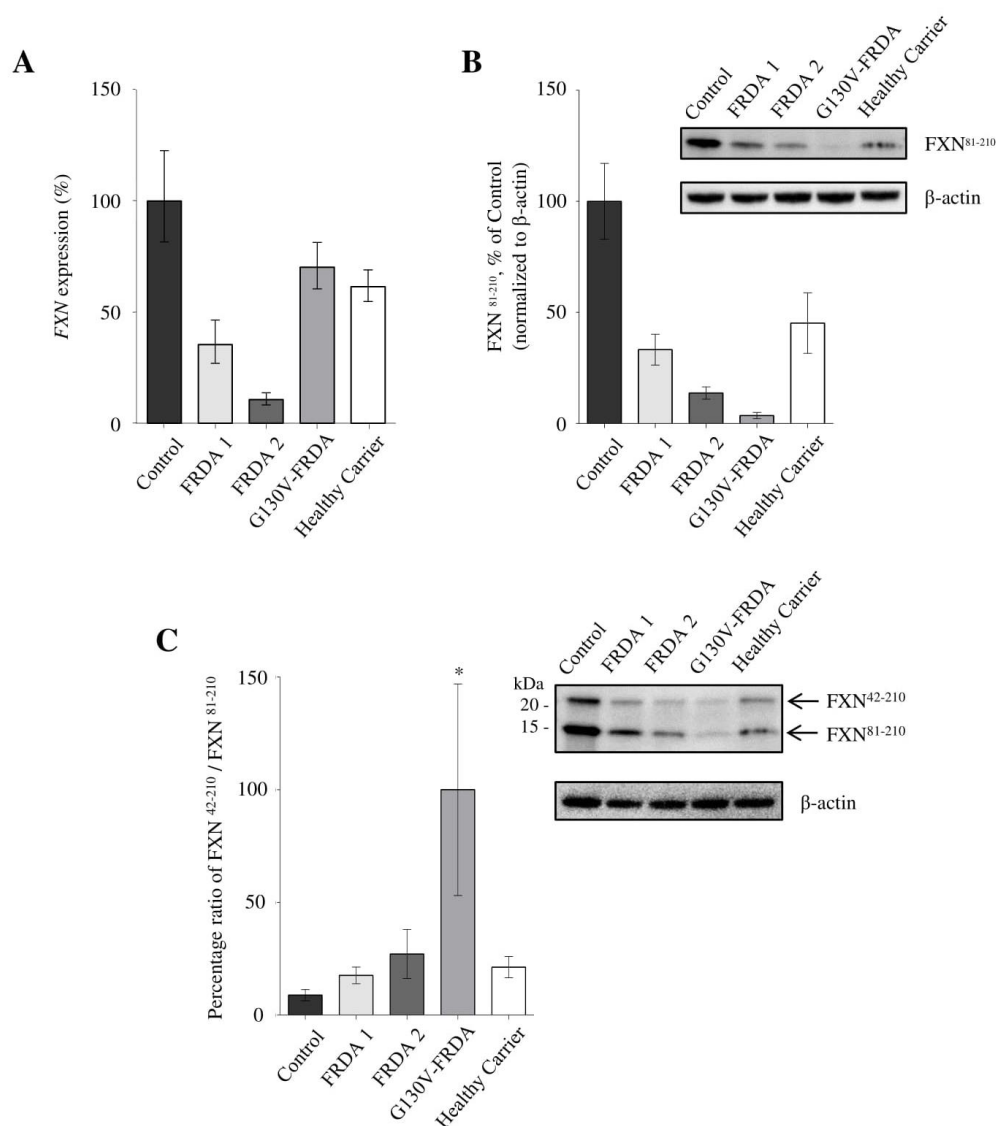


Figure 1.3. Comparative analysis of frataxin in healthy control, homozygous FRDA and heterozygous G130V-FRDA LCLs. (A) FXN expression measured by qRT-PCR in unaffected control, FRDA (1 and 2), G130V-FRDA and healthy carrier LCLs. FXN expression levels are normalized to those detected in the non-mutated control cell line, expressed as 100%. Error bars represent gene expression range calculated according to the standard deviation of the $\Delta\Delta CT$ value. (B) Western blotting analysis of FXN protein (mature form) in whole cell extracts from unaffected control, FRDA (1 and 2), G130V-FRDA and healthy carrier LCLs. Equal amounts of protein (i.e. 60 μ g) were loaded in each lane. β -actin was used as loading control. Protein levels were quantified after normalization with β -actin and expressed as a percentage of control level. Reported data result from the mean of four independent experiments \pm SEM. (C) Impaired frataxin processing from FXN⁴²⁻²¹⁰ to FXN⁸¹⁻²¹⁰ in lymphoblasts from G130V-FRDA patient. Equal amounts of protein (i.e. 60 μ g) were loaded in each lane. β -actin was used as loading control. FXN⁴²⁻²¹⁰ and FXN⁸¹⁻²¹⁰ were detected by western blot. FXN levels were quantified and expressed as ratio of FXN⁴²⁻²¹⁰ to FXN⁸¹⁻²¹⁰. Reported data result from the mean of four independent experiments \pm SEM. Statistical significance was determined using One-way ANOVA with Dunnett's post-hoc test (* $p \leq 0.05$, compared to control).

Figure 1.5 shows that the levels of some structural subunits, *i.e.* NDUFA9 (complex I), SDHA (complex II), UQCRC1 (complex III) and MTCO1 (complex IV), are comparable in LCLs from healthy and FRDA patient cells. Protein levels were quantified after normalization with β -actin and, as a further control, with TOM20 as a mitochondrial housekeeping protein.

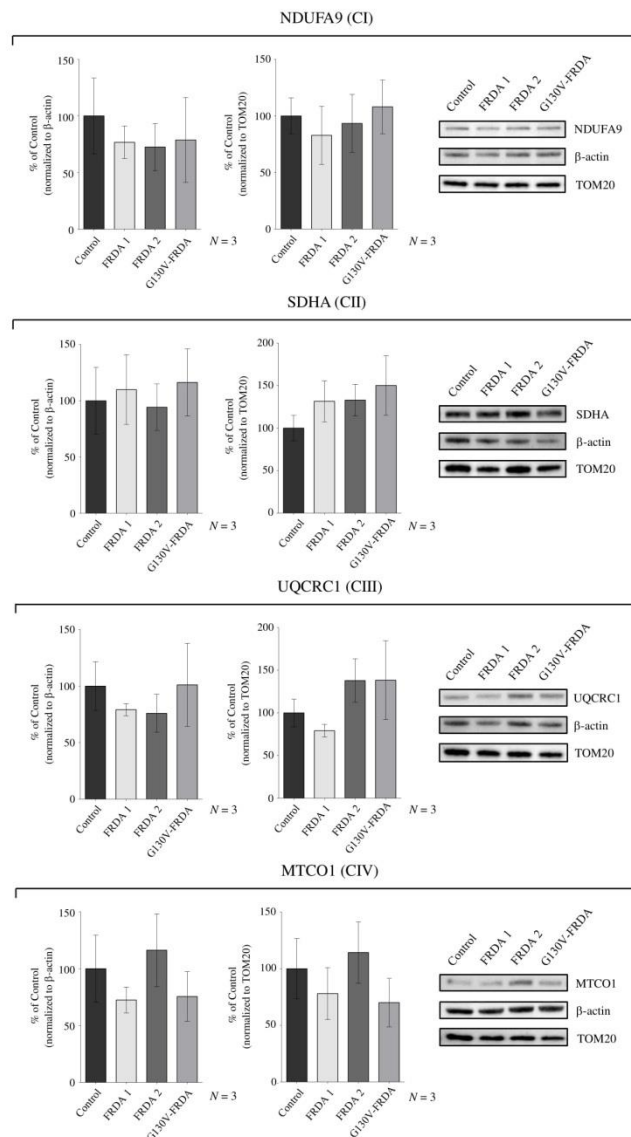


Figure 1.5. Comparative analysis of mitochondrial respiratory complexes structural subunits in healthy control, homozygous FRDA and heterozygous G130V-FRDA LCLs. Western blotting analysis of respiratory complexes structural subunits, *i.e.* NDUFA9 (complex I), SDHA (complex II), UQCRC1 (complex III) and MTCO1 (complex IV) in whole cell extracts from FRDA 1, FRDA 2, G130V-FRDA and unaffected control LCLs. Equal amounts of protein (*i.e.* 25 μ g) were loaded in each lane. Protein levels were quantified after normalization with β -actin and TOM20 and expressed as percentage of control level. Reported data result from the mean of N independent experiments \pm SEM. Statistical significance was determined using One-way ANOVA with Dunnett's post-hoc test.

Different results have been obtained analyzing the subunits containing Fe-S clusters. For complex I, six subunits were analyzed, all belonging to the hydrophilic domain. Three of them, *i.e.* NDUF51, NDUF58 and NDUFV2, contain three, two, and one Fe-S clusters, respectively; subunits NDUF52, NDUF53, and NDUF54, do not contain iron-sulfur centers but belong to the Fe-S cluster domain of the complex. The comparative analysis of the protein levels for NDUF51, NDUF58 and NDUFV2 is reported in *Figure 1.6*, while *Figure 1.7* shows the levels of NDUF52, NDUF53 and NDUF54 in the four lymphoblastoid cell lines, normalized on both β -actin and TOM20 as loading controls.

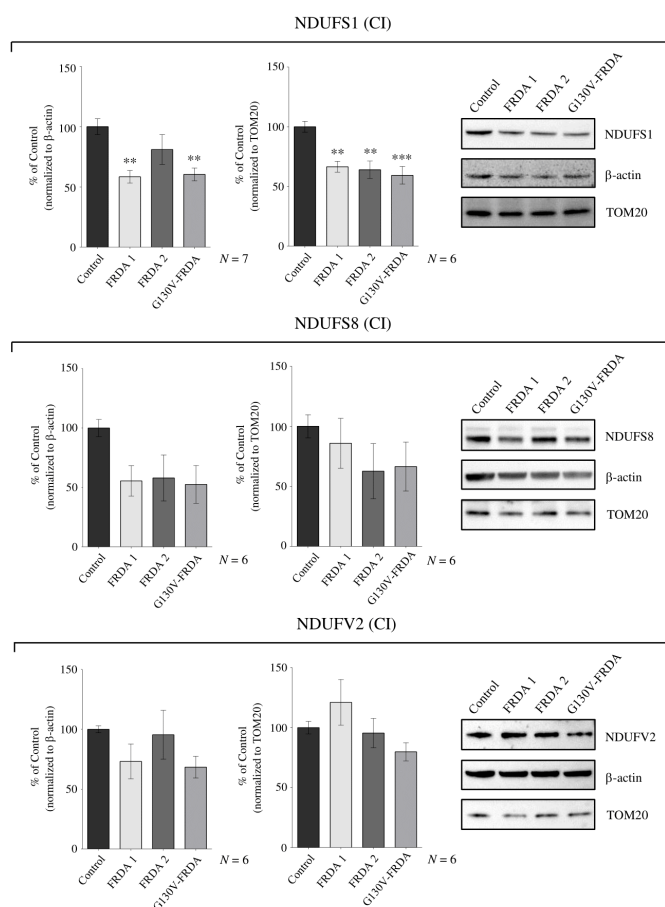


Figure 1.6. Comparative analysis of mitochondrial respiratory complex I Fe-S subunits in healthy control, homozygous FRDA and heterozygous G130V-FRDA LCLs. Western blotting analysis of some of respiratory complex I Fe-S cluster-containing subunits (*i.e.* NDUF51, NDUF58, NDUFV2) in whole cells extracts from FRDA 1, FRDA 2, G130V-FRDA and unaffected control LCLs. Equal amounts of protein (*i.e.* 25 μ g) were loaded in each lane. β -actin and TOM20 was used as loading control. Protein levels were quantified after normalization with β -actin and TOM20 and expressed as a percentage of control level. Reported data result from the mean of N independent experiments \pm SEM. Statistical significance was determined using One-way ANOVA with Dunnett’s post-hoc test (* $p \leq 0.05$, ** $p \leq 0.01$, compared to control).

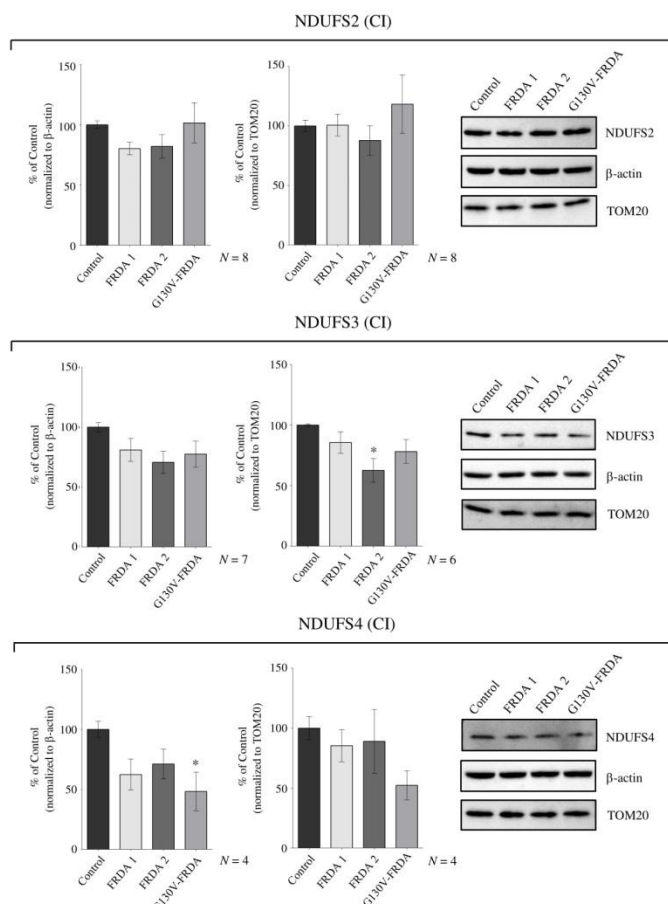


Figure 1.7. Comparative analysis of some subunits belonging to the Fe-S clusters domain of mitochondrial respiratory complex I in healthy control, homozygous FRDA and heterozygous G130V-FRDA LCLs. Western blotting analysis of some of respiratory complex I subunits NDUF2, NDUF3 and NDUF4 in whole cells extracts from FRDA 1, FRDA 2, G130V-FRDA and unaffected control LCLs. Equal amounts of protein (i.e. 25 μ g) were loaded in each lane. Protein levels were quantified after normalization with β -actin and TOM20 and expressed as a percentage of control level. Reported data result from the mean of N independent experiments \pm SEM. Statistical significance was determined using One-way ANOVA with Dunnett's post-hoc test (* $p \leq 0.05$, compared to control).

The results indicate that NDUF1, NDUF8, NDUF3, and NDUF4 are reduced in the three FRDA cell lines, although in a variable way; on the contrary, the levels of the NDUF2 and NDUFV2 subunits remain almost unaltered if compared to the control. Interestingly, only NDUF1 subunit, which contains three Fe-S clusters, results significantly reduced in all three FRDA cell lines.

For complex II and complex III we analyzed SDHB and UQCRC1, respectively; Figure 1.8 shows that the levels of these subunits were unaltered in the FRDA LCLs compared to healthy control, with the exception of SDHB which appears to

be slightly reduced in the FRDA cell lines characterized by the lowest levels of frataxin (*i.e.* FRDA 2 and G130V-FRDA).

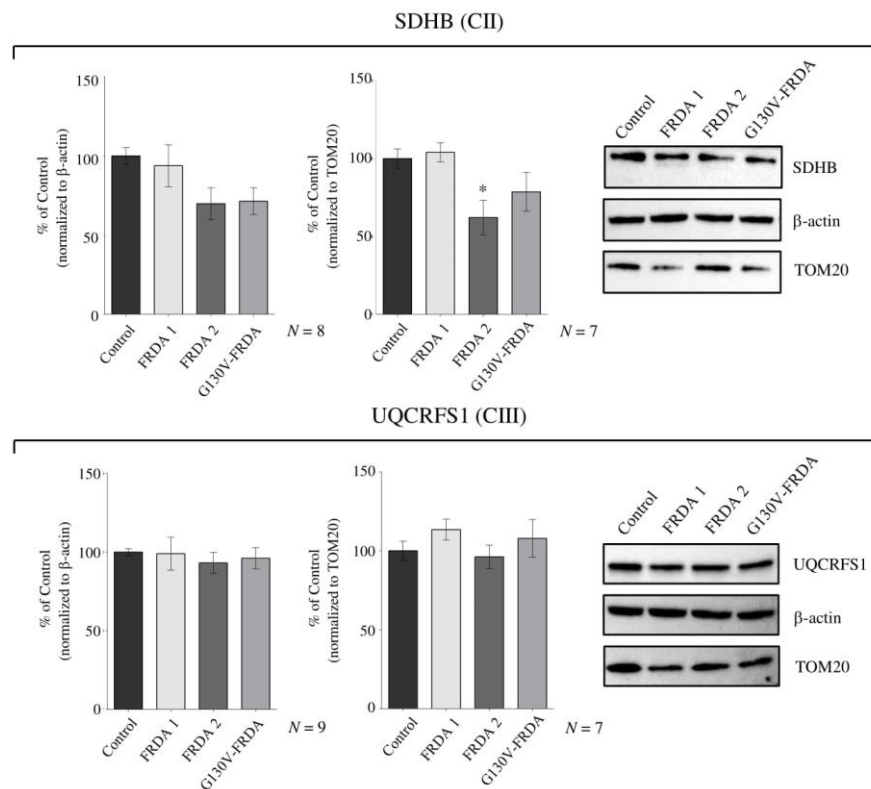


Figure 1.8. Comparative analysis of Fe-S subunits in mitochondrial respiratory complexes II and III in healthy control, homozygous FRDA and heterozygous G130V-FRDA LCLs. Western blotting analysis of Fe-S cluster-containing subunits of respiratory complex II (SDHB) and respiratory complex III (UQCRFS1) in whole cell extracts from FRDA (1 and 2), G130V-FRDA and unaffected control LCLs. Equal amounts of protein (*i.e.* 25 μ g) were loaded in each lane. Protein levels were quantified after normalization with β -actin and TOM20 and expressed as percentage of control level. Reported data result from the mean of N independent experiments \pm SEM. Statistical significance was determined using One-way ANOVA with Dunnett’s post-hoc test (* $p \leq 0.05$, compared to control).

To assess the possible impairment of other Fe-S proteins, we further analyzed the protein levels of mitochondrial aconitase ACO2, an iron-sulfur enzyme involved in the TCA cycle which catalyzes the reversible isomerization of citrate to isocitrate via *cis*-aconitate. In this regard, it has been demonstrated that frataxin is able to interact with mitochondrial aconitase, modulating its enzymatic activity and acting as an iron chaperone [Bulteau A.L. *et al.*, 2004]; furthermore, a deficiency in frataxin has been shown to impair its enzymatic activity [Rötig A. *et al.*, 1997; Bradley J.L. *et al.*, 2000; Condò I. *et al.*, 2010]. Western blotting analysis in

whole-cell extracts showed that, ACO2 levels in FRDA LCLs are not significantly altered respect to the control, although slightly reduced in G130V-FRDA cell line (Figure 1.9).

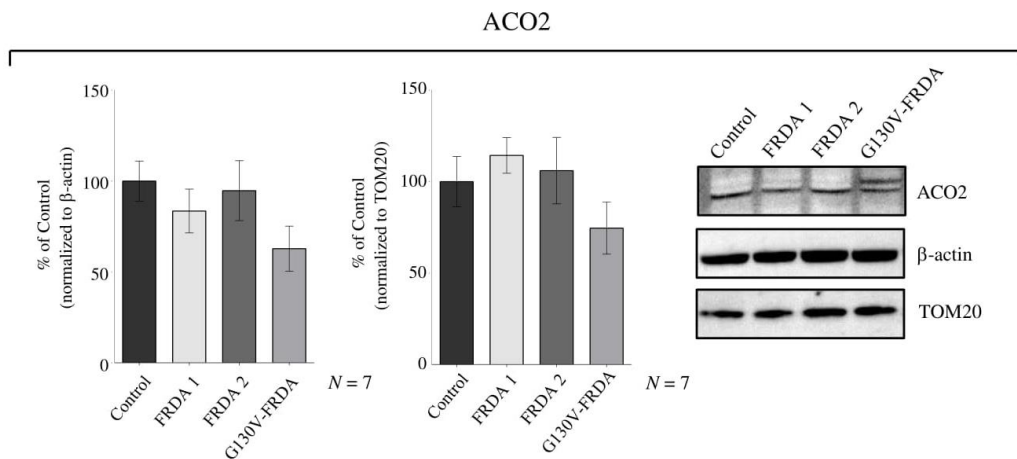


Figure 1.9. Comparative analysis of mitochondrial aconitase ACO2 in healthy control, homozygous FRDA and heterozygous G130V-FRDA LCLs. Western blotting analysis of ACO2 in whole cell extracts from FRDA 1, FRDA 2, G130V-FRDA and unaffected control LCLs. Equal amounts of protein (i.e. 25 μ g) were loaded in each lane. Protein levels were quantified after normalization with β -actin and TOM20 and expressed as percentage of control level. Reported data result from the mean of N independent experiments \pm SEM. Statistical significance was determined using One-way ANOVA with Dunnett's post-hoc test.

Biochemical and Functional Analyses of Mitochondrial Respiratory Complexes in FRDA and G130V-FRDA Patients' Cells

The individual activities of respiratory complexes in control, FRDA 1, FRDA 2 and G130V-FRDA LCLs were measured by spectrophotometric assays (Figure 1.10). Results were variable: the FRDA 1 and FRDA 2 cells displayed essentially a partial reduction of complex III, while other complexes were only mildly decreased (complex I), or unaffected (complex II). The cells from patient with the G130V mutation had a partial reduction of complexes I and IV, while complex II was only mildly affected, and complex III was normal. Complex IV does not contain Fe-S clusters and the observed reduction of its activity could be explained by the involvement of frataxin in the biosynthesis of heme [Yoon T. & Cowan J.A., 2004; Schoenfeld R.A. et al., 2005], an essential cofactor of this complex.

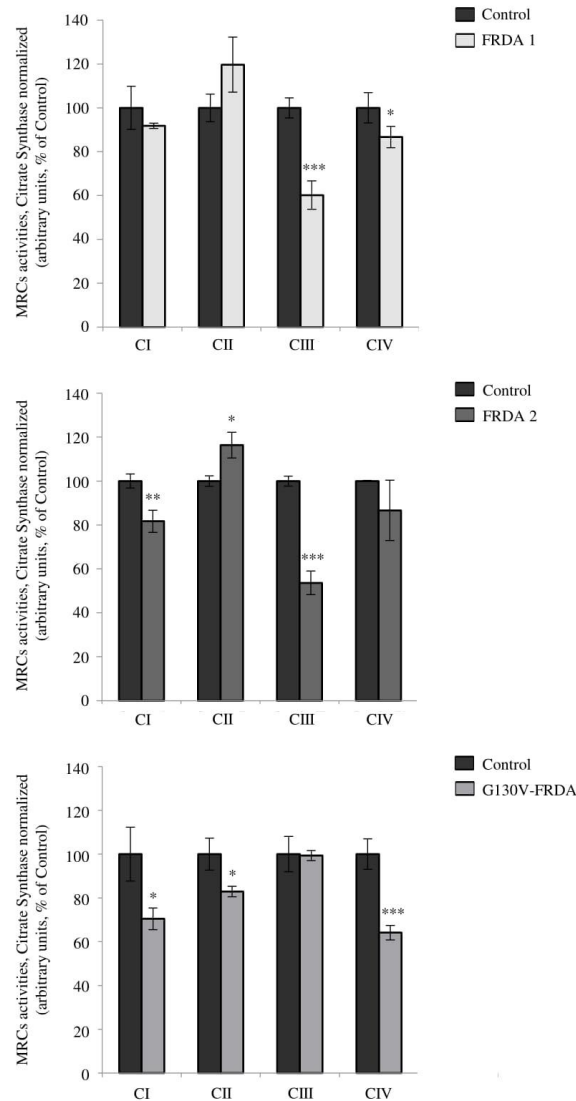


Figure 1.10. Biochemical analysis of mitochondrial respiratory complexes in healthy control, homozygous FRDA and heterozygous G130V-FRDA LCLs. Complex I-IV individual activities (nmol / min · mg of protein) in control, FRDA 1, FRDA 2 and G130V-FRDA LCLs. All activity values were normalized to citrate synthase and expressed as percentage of control activity. Reported data result from the mean of four independent experiments ± SEM. Statistical significance was determined using unpaired t-test (* $p \leq 0.05$, ** $p \leq 0.01$, *** $p \leq 0.001$, compared to control).

We next measured the oxygen consumption rate of LCLs by means of a Seahorse flux analyzer. We found that, compared to healthy control, homozygous FRDA 1 and FRDA 2 and G130V-FRDA LCLs have decreased maximal respiration and spare respiratory capacity, with no difference both in basal and in ATP-linked respiration (Figure 1.11). This result could indicate an impaired capability of FRDA cells to increase mitochondrial oxygen consumption rate in conditions of increased energy demand.

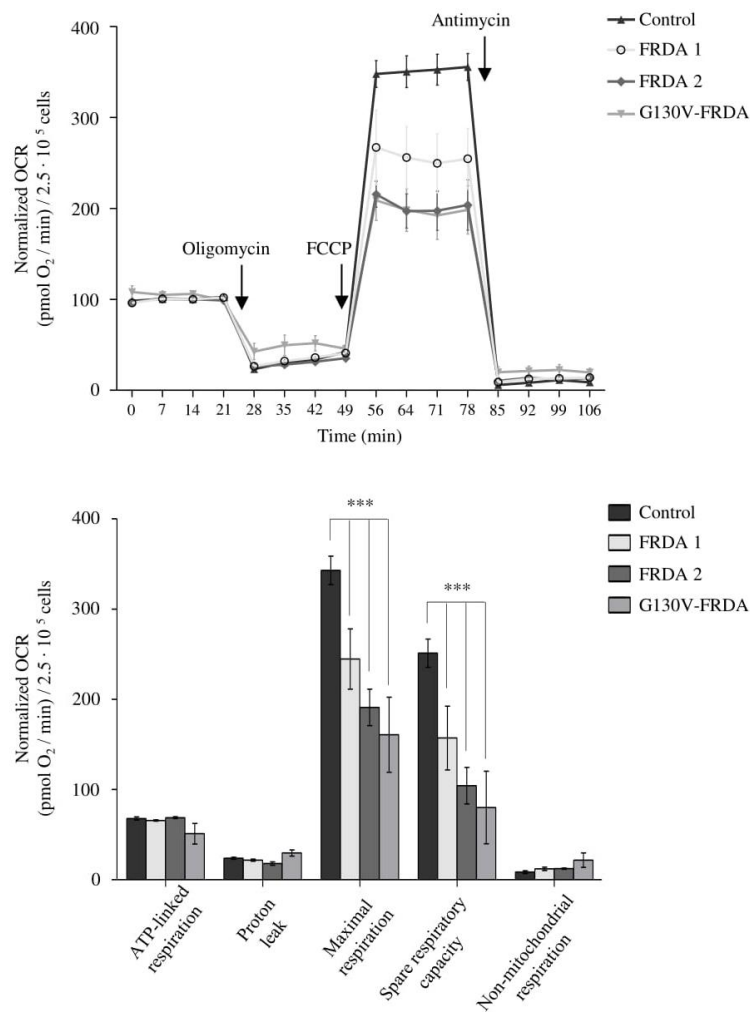


Figure 1.11. Oxygen consumption studies in healthy control, homozygous FRDA and heterozygous G130V-FRDA LCLs. Oxygen consumption rates (OCR) of cells were measured in real time under basal conditions and after injection of oligomycin, FCCP and antimycin as indicated in the figure. Values were normalized with respect to basal respiration which was considered as 100%. OCR values at basal condition were 275.9 ± 26.9 , $281.5.3 \pm 33.5$, 247.8 ± 14.5 and 250.3 ± 50.9 (pmol O_2 /min)/ $2.5 \cdot 10^5$ cells in control, FRDA 1, FRDA 2 and G130V-FRDA LCLs respectively. Bioenergetic parameters were calculated as described in Materials & Methods. Reported data result from the mean of three independent experiments \pm SEM. Statistical significance was determined using Two-way ANOVA with Bonferroni's post-hoc test (***) $p \leq 0.001$, compared to control).

Since in healthy cells individual stability and function of the mitochondrial respiratory complexes are improved by their organization in supercomplexes (SCs), we next wondered if a defective formation of these supramolecular structures could contribute to the differences in the respiratory activity described

above. Respiratory SCs of different composition and stoichiometry have been described; the most functionally relevant are SCs [I+III], [I+III+IV] and [III-IV], while the association of complex II in supercomplexes has not been reported yet [Schägger H. & Pfeiffer K., 2000; Schägger H. & Pfeiffer K., 2001; Acín-Pérez R. et al., 2008; Enriquez J.A., 2016]. To get additional insights into the impaired respiratory phenotype of FRDA LCLs compared to healthy control, we therefore analyzed the pattern of SCs assembly. To this end, cells were solubilized using the mild detergent digitonin to maintain the integrity of respiratory complexes, which were then separated by blue-native gel electrophoresis (BN-PAGE). Following electrophoresis, the gels were transblotted and proteins immunodetected with antibodies against complex I (*i.e.* subunit NDUFA9) and complex II (*i.e.* subunit SDHA). *Figure 1.12* indicates that the relative abundance of higher molecular-weight CI-containing supercomplexes, among which the respirasome, is decreased in FRDA LCLs compared to healthy control cells. On the contrary, the relative levels of CII in FRDA LCLs are comparable to those of control. This is in accordance with the lower individual enzymatic activities of respiratory complexes I, III and IV (*Figure 1.10*), as well as with the reduced maximal respiration and reserve capacity of FRDA LCLs (*Figure 1.11*).

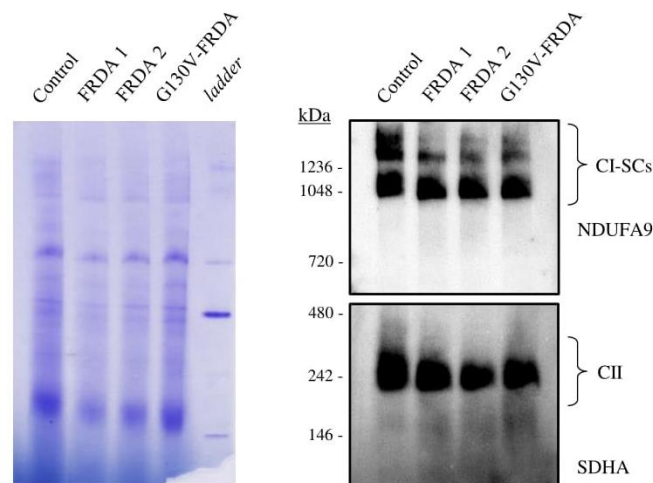


Figure 1.12. Blue native PAGE and western blotting analyses of the mitochondrial supercomplexes in healthy control, homozygous FRDA and heterozygous G130V-FRDA LCLs. On the left, BN-PAGE, followed by Coomassie staining and destaining, of the control, FRDA 1, FRDA 2 and G130V-FRDA LCLs treated with digitonin. 5 μ L of native protein marker (ladder) was loaded in the gel to estimate the molecular weight of the bands. On the right, western blotting after BN-PAGE of CI-containing SCs and CII from digitonin-treated control, FRDA 1, FRDA 2 and G130V-FRDA LCLs. The blot was immunodecorated with an antibody against NDUFA9 (complex I) and, subsequently, the same membrane was incubated with an antibody against SDHA (complex II).

EPR Measurements on Isolated Mitochondria from FRDA Cells

The association of mitochondrial complexes into supercomplexes is pivotal to enhance their catalytic activities as well as to increase the efficiency of electron transfer. As previously stated, the electron channeling relies on Fe-S clusters and heme centers belonging to the respiratory complexes; altered enzymatic activities of the respiratory complexes, along with impaired respiratory efficiency, could be due to an impairment of these prosthetic groups. For this reason, we explored the redox centers in FRDA LCLs used in this study taking advantage of EPR spectroscopy at cryogenic temperatures as investigative tool.

Firstly, to overcome the problem of sensitivity related to this technique, we optimized a protocol to obtain highly enriched mitochondrial fractions in a buffer suitable for EPR analysis; starting from a high number of lymphoblastoid cells from each line (around 700×10^6 cells), we isolated mitochondria through a subcellular fractionation, as described in detail in Materials & Methods. Samples from each step of the extraction were assessed by western blotting analysis. The results obtained with the mitochondrial extraction of the control cell line are reported as an example in *Figure 1.13*; western blot highlights how the final sample used for EPR experiments is highly enriched in mitochondria and relatively pure, despite the presence of a residual cytosolic fraction which, however, was considered negligible for the purposes of the spectroscopic experiments. Similar patterns were obtained with the subcellular fractionations for the three FRDA cell lines (data not shown), confirming the validity of the protocol.

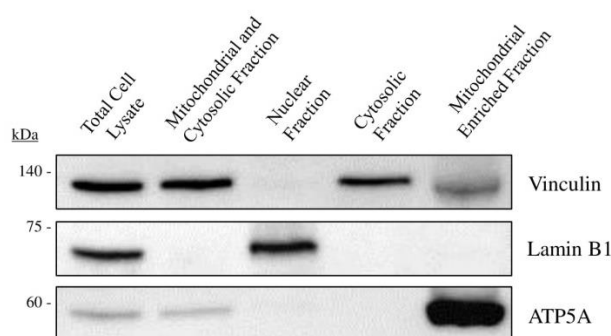


Figure 1.13. Western blotting analysis for the subcellular fractionation of lymphoblastoid cells. Cells were fractionated to nuclear, cytosolic and mitochondrial fractions by sequential centrifugation. For each fractionation step, an identical volume has been resuspended in Laemmli buffer and equal amounts of the samples (5 μ L) were loaded onto the gel. Vinculin, lamin B1 and ATP5A have been respectively chosen as cytosolic, nuclear and mitochondrial markers for the western blot analysis. The reported western blot refers to the subcellular fractionation of the healthy control lymphoblastoid cell line used in this work.

Isolated mitochondria from each cell line have been transferred in EPR tubes and subsequently flash frozen in liquid nitrogen to proceed with the acquisition of EPR measurements at three different temperatures, *i.e.* at 100, 40 and 15 K. The choice of acquiring EPR spectra at different temperatures has been made with the aim of obtaining as much information as possible on the redox cofactors belonging to mitochondrial respiratory chain. *Figure 1.14* shows the spectra acquired at 100 K for the mitochondrial fractions from the four LCLs. At this temperature, the only detectable species are radicals coming mostly from semiquinones (SQ) and semiflavins (SF). SQ radicals derive mainly from the partial reduction of CoQ in complex I and complex II while SF radicals typically derive from the partial reduction of FMN in complex I. Although SQ and SF radicals have slightly different *g* tensors, in our experimental conditions they are characterized by an unresolved isotropic *g* value of 2.005.

An inspection of the spectra reveals that the healthy control is characterized by more intense radical signals, while those arising from FRDA LCLs are less intense, confirming a higher respiratory activity in healthy control than in FRDA cells.

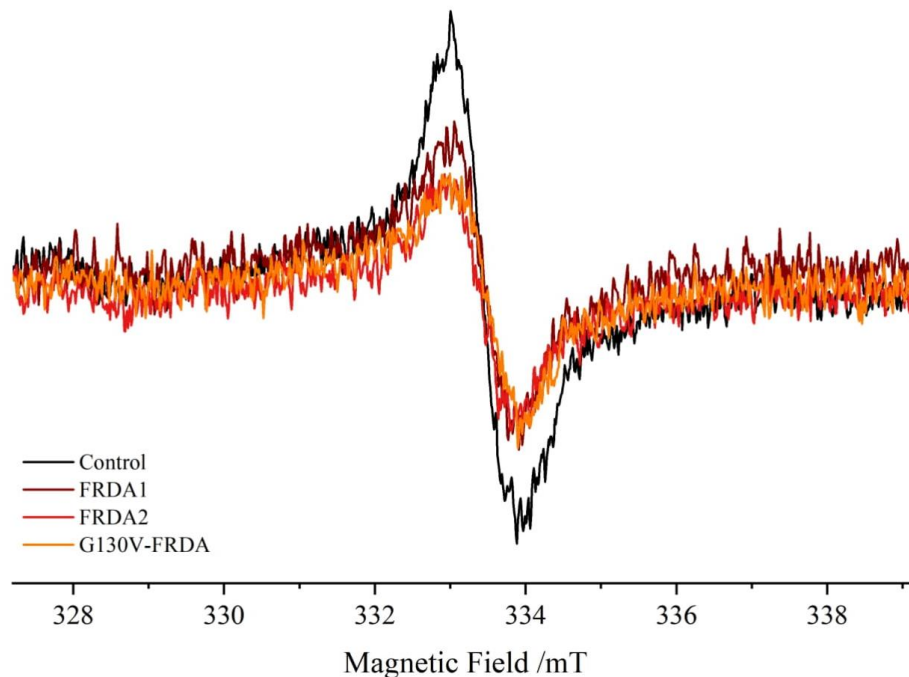


Figure 1.14. EPR spectra acquired at 100 K on isolated mitochondria from healthy control, homozygous FRDA and heterozygous G130V-FRDA LCLs. The spectra show the $g=2.0$ spectral region. The superimposed spectra are reported with a different color for each LCLs: black, healthy control; brown, FRDA 1; dark red, FRDA 2; orange, G130V-FRDA. The spectra were normalized to the total protein concentration of each corresponding mitochondrial fractions.

Lowering the temperature, signals arising from Fe-S clusters of the respiratory chain complexes can be observed; in particular, at 15 K, it is possible to detect both fast relaxing [4Fe-4S] and [3Fe-4S] centers and, to a lesser extent, the slow relaxing [2Fe-2S] clusters, in addition to other cofactors of the respiratory chain, such as the copper center of Complex IV (CuA). *Figure 1.15* reports the spectra acquired at 15 K for the healthy control and the three FRDA LCLs.

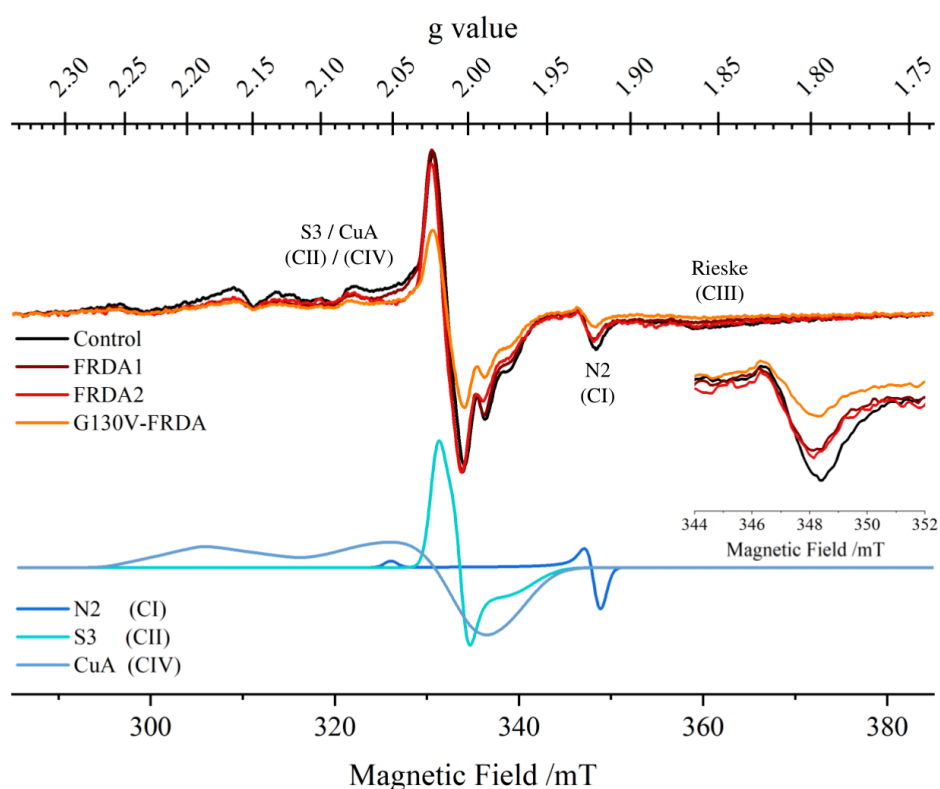


Figure 1.15. EPR spectra acquired at 15 K on isolated mitochondria from healthy control, homozygous FRDA and heterozygous G130V-FRDA LCLs. The superimposed spectra are reported with a different color for each LCLs: black, healthy control; brown, FRDA 1; dark red, FRDA 2; orange, G130V-FRDA. The spectra were normalized to the total protein concentration of each corresponding mitochondrial fractions. The attribution of the peaks of the redox centers is indicated in the figure; for more clarity, the reference simulated EPR signals of N2 [4Fe4S] cluster, S3 [3Fe-4S] cluster and CuA copper center are reported in sky blue, cyan and steel blue, respectively. The inset on the right refers to the region of the signal of N2 [4Fe-4S] cluster of complex I.

A comparative analysis between the EPR spectra deriving from mitochondria of FRDA cells and that originating from the healthy control highlights different spectroscopic responses, reflecting in turn a different mitochondrial physiological *status*. In particular, G130V-FRDA cell line, which is characterized by the lowest level of frataxin among the LCLs used in this study (*Figure 1.3B*), shows strongly

reduced signals across the whole range, while the healthy control has the strongest signals overall. The diagnostic peak of N2 [4Fe-4S] ($g \approx 1.92$, see the inset in *Figure 1.15*), the cluster located in the NDUFS7 subunit of the hydrophilic domain of complex I (see *Figure 1.4*) and at the end of the electron transport chain that directly donates electrons to the ubiquinone, is far less intense in the FRDA cell lines. The signals arising from the S3 [3Fe-4S] cluster of the complex II, along with that arising from CuA center of the complex IV, are overall reduced in FRDA LCLs when compared to control. On the contrary, no differences have been detected for the broad signal typical of the Rieske [2Fe-2S] cluster belonging to complex III. This observation was further confirmed by the acquisition of EPR spectra at 40 K (*Figure 1.16*), condition in which only the [2Fe-2S] clusters are detectable; in fact, all LCLs are characterized by comparable spectroscopic signals in the region of mitochondrial Fe-S clusters, indicating almost no changes for the Rieske [2Fe-2S] (complex III) and the N1b [2Fe-2S] (complex I). The spectra at 40 K do not give any further insights, since they are dominated by the multiple EPR signals from Mn^{2+} ions, which are ubiquitously present in biological systems.

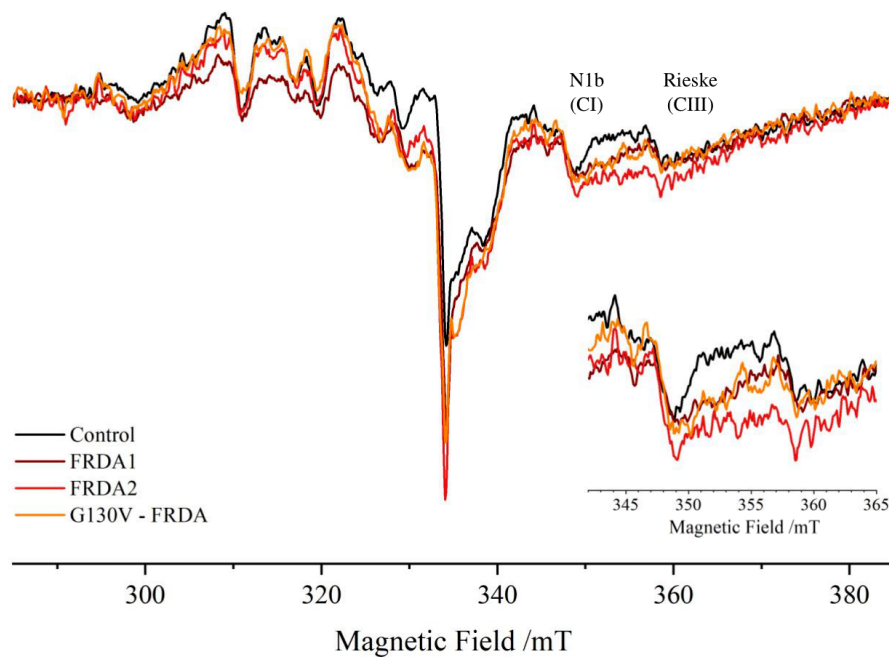


Figure 1.16. EPR spectra acquired at 40 K on isolated mitochondria from healthy control, homozygous FRDA and heterozygous G130V-FRDA LCLs. The superimposed spectra are reported with a different color for each LCLs: black, healthy control; brown, FRDA 1; dark red, FRDA 2; orange, G130V-FRDA. The spectra were normalized to the total protein concentration of each corresponding mitochondrial fractions. The attribution of the peaks to the correspondent redox center is indicated in the figure. The inset refers to the region of the signal of N1b [2Fe-2S] cluster of complex I and Rieske [2Fe-2S] cluster of complex III.

Frataxin Co-localizes with the Fe-S Clusters Assembly Machinery in the Mitochondrial Cristae in Healthy Cells and Redistributes to the Matrix in FRDA Cells

Frataxin has been claimed to play a role in the biogenesis of Fe-S clusters, and it was previously shown that in *S. cerevisiae* two other proteins involved in this pathway (*i.e.* NFS1, the sulfur donor to the assembly machinery, and the accessory protein ISD11) are closely attached to the mitochondrial inner membrane and enriched in the cristae [Vogel F. *et al.*, 2006].

Therefore, we investigated if the Fe-S cluster assembly machinery is localized in the cristae also in the human LCLs used in our work. We addressed this issue by immunogold-labeling, in control cells and in the three FRDA LCLs, the proteins NFS1 and ISCU (*i.e.* the scaffold upon which the Fe-S cluster is synthesized), as described in detail Material & Methods. Both proteins are expressed in control and FRDA cells with any significant difference, as assessed by the western blotting analyses (Figure 1.17).

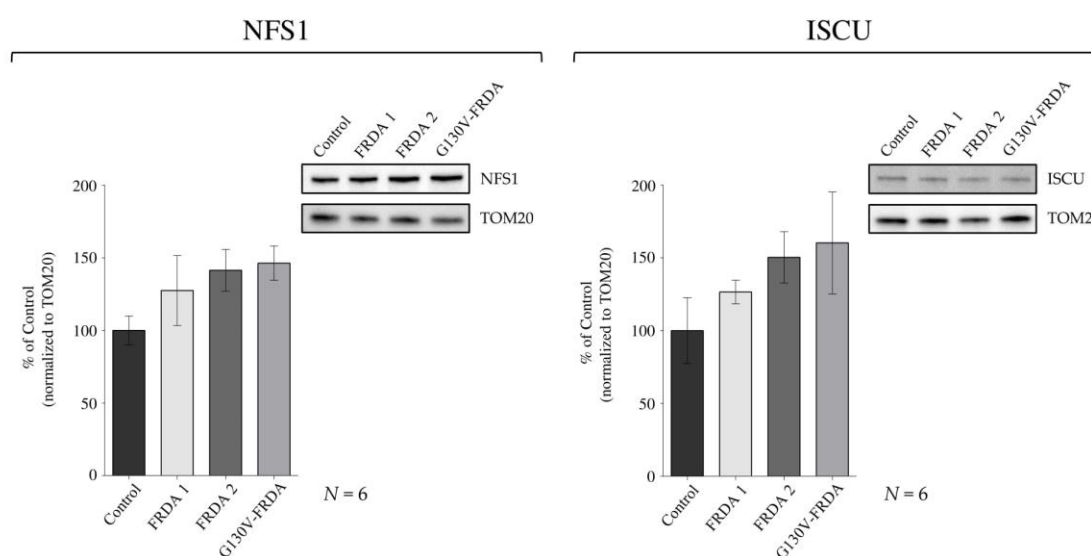


Figure 1.17. Comparative analysis of NFS1 and ISCU in healthy control, homozygous FRDA and heterozygous G130V-FRDA LCLs. Western blotting analyses of NFS1 and ISCU proteins in whole cell extracts from FRDA (1 and 2), G130V-FRDA and unaffected control LCLs. Equal amounts of protein (*i.e.* 25 μ g) were loaded in each lane. TOM20 was used as mitochondrial loading control. Protein levels were quantified after normalization with TOM20 and expressed as percentage of control level. Reported data result from the mean of six independent experiments \pm SEM. One-way ANOVA with Dunnett's post hoc test was used for statistical analysis.

Figure 1.18 shows that in the four LCLs NFS1 and ISCU are mostly localized in the cristae.

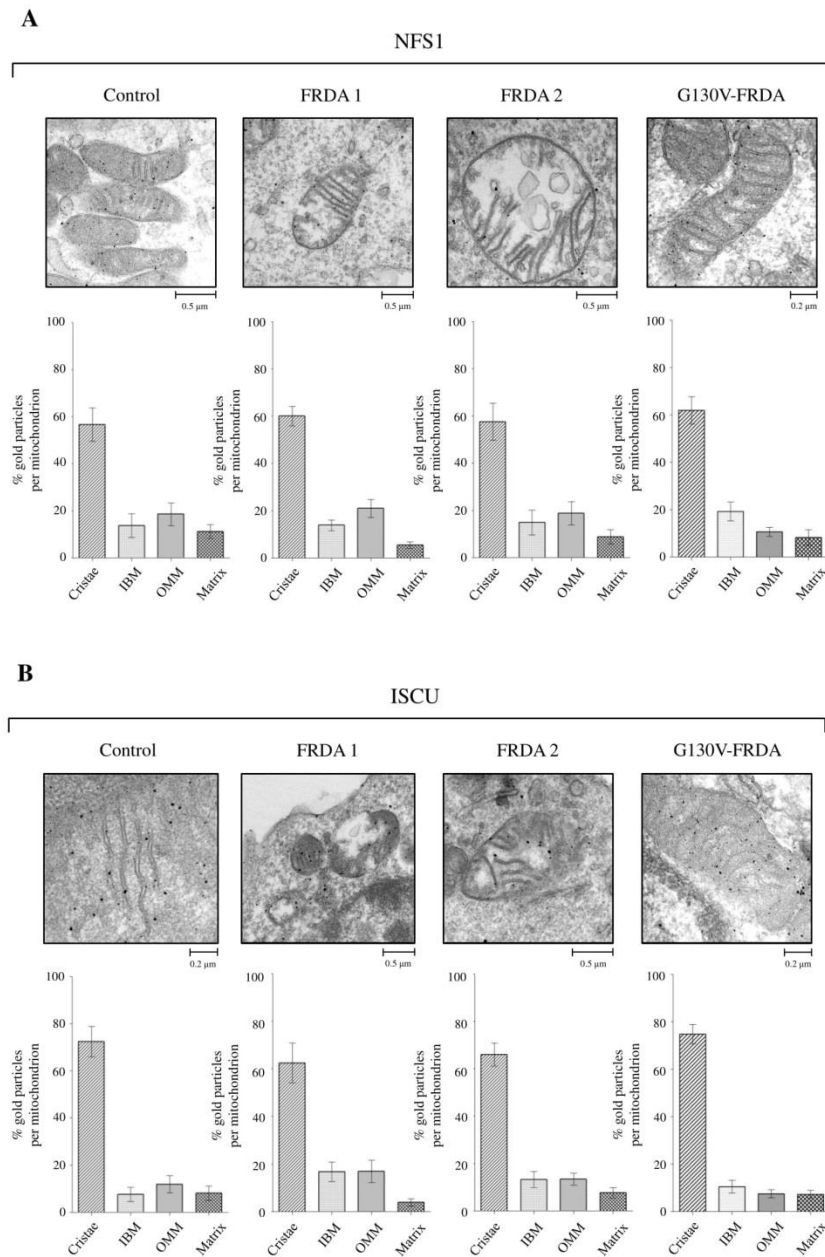


Figure 1.18. The NFS1 desulfurase and ISCU scaffold proteins of the mitochondrial FeS-cluster assembly machinery are closely associated to the cristae membranes of healthy control, FRDA and G130V-FRDA LCLs. Panel A refers to NFS1, Panel B refers to ISCU. In both panels: top, representative images of the immunogold-labeling coupled to electron microscopy; bottom, quantitative analyses of the gold particles distribution in different mitochondrial subcompartments, expressed as percentage of particles per mitochondrion. Reported data result from the mean of three independent experiments \pm SEM. Mitochondria from 20-45 cells were analyzed. IBM, inner boundary membrane; OMM, outer mitochondrial membrane. Scale bars are indicated in the figure.

We next explored the sublocalization of frataxin in mitochondria of healthy control and FRDA LCLs by the same immunogold-labeling approach. It is clearly visible in *Figure 1.19* that in healthy LCLs frataxin is in fact enriched in the cristae.

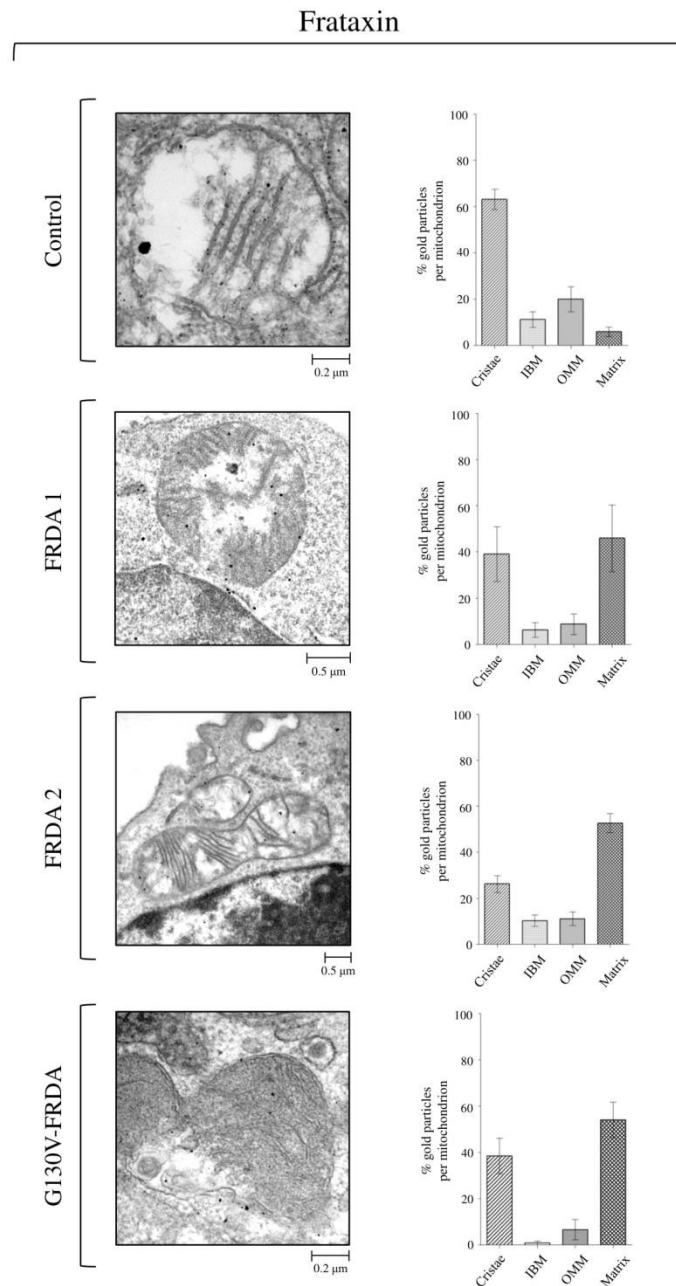


Figure 1.19. Frataxin is enriched in the mitochondrial cristae of healthy control and moves to the matrix in FRDA LCLs. Left, representative images of the immunogold-labeling coupled to electron microscopy of control, FRDA (1 and 2) and G130V-FRDA LCLs; right, quantitative analyses of the gold particles distribution in different mitochondrial subcompartments, expressed as percentage of particles per mitochondrion. Reported data result from the mean of three independent experiments \pm SEM. Mitochondria from 20-45 cells were analyzed. IBM, inner boundary membrane; OMM, outer mitochondrial membrane. Scale bars are indicated in the figure.

Frataxin levels are strongly reduced in the three FRDA patient LCLs used in this work (Figure 1.3B), nevertheless we were able to detect immunogold particles both in homozygous FRDA and in the heterozygous G130V-FRDA LCLs, albeit at a smaller extent (Figure 1.19).

Some gold particles are also present at the inner boundary and outer membranes and likely label the full-length precursor of frataxin (*i.e.* FXN¹⁻²¹⁰), which is synthesized in the cytosol and then imported into the mitochondria, where it undergoes to a two-step proteolytic processing resulting in the mature, shorter form (*i.e.* FXN⁸¹⁻²¹⁰). Interestingly, a close inspection of mitochondria of FRDA LCLs revealed that their residual frataxin is partially redistributed to the matrix even in the presence of intact cristae (Figure 1.19). Negative controls experiments, performed in parallel in absence of primary antibodies (Figure 1.20), did not show electron-dense deposits in the cristae, supporting the specificity of the approach.

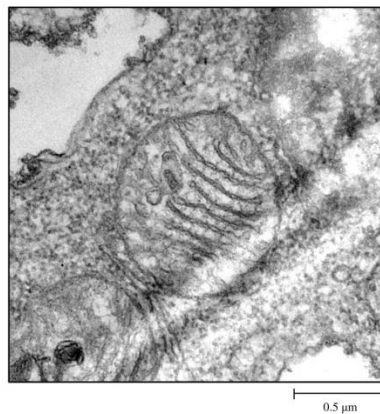


Figure 1.20. Negative control for the immunogold-labeling experiments with LCLs. Control cells were fixed and prepared for immunogold staining exactly as described in Materials and Methods except for the rabbit primary antibody (against human NFS1, ISCU or FXN proteins), which was omitted.

Mitochondrial Cristae Morphology in FRDA Patient’s Cells

Cristae morphology as well as their dynamic remodeling are crucial to keep the respiratory complexes properly assembled and functional [Cogliati S. *et al.*, 2013; Cogliati S. *et al.*, 2016] and in the same way they could be relevant to keep in site the Fe-S cluster biogenesis machinery and frataxin.

We therefore analyzed by transmission electron microscopy the mitochondrial ultrastructure of healthy control and FRDA LCLs. In all LCLs used in this work, mitochondria are mostly localized near the plasma membrane and inside the

nuclear invagination that is typically present in lymphoblasts. On the other hand, while mitochondria of healthy cells have an overall architecture with groups of parallel cristae extending through the entire body of the organelle, those of FRDA 1, FRDA 2 and G130V-FRDA cells are reduced in length and contain cristae significantly shorter and wider than healthy control (*Figure 1.21*).

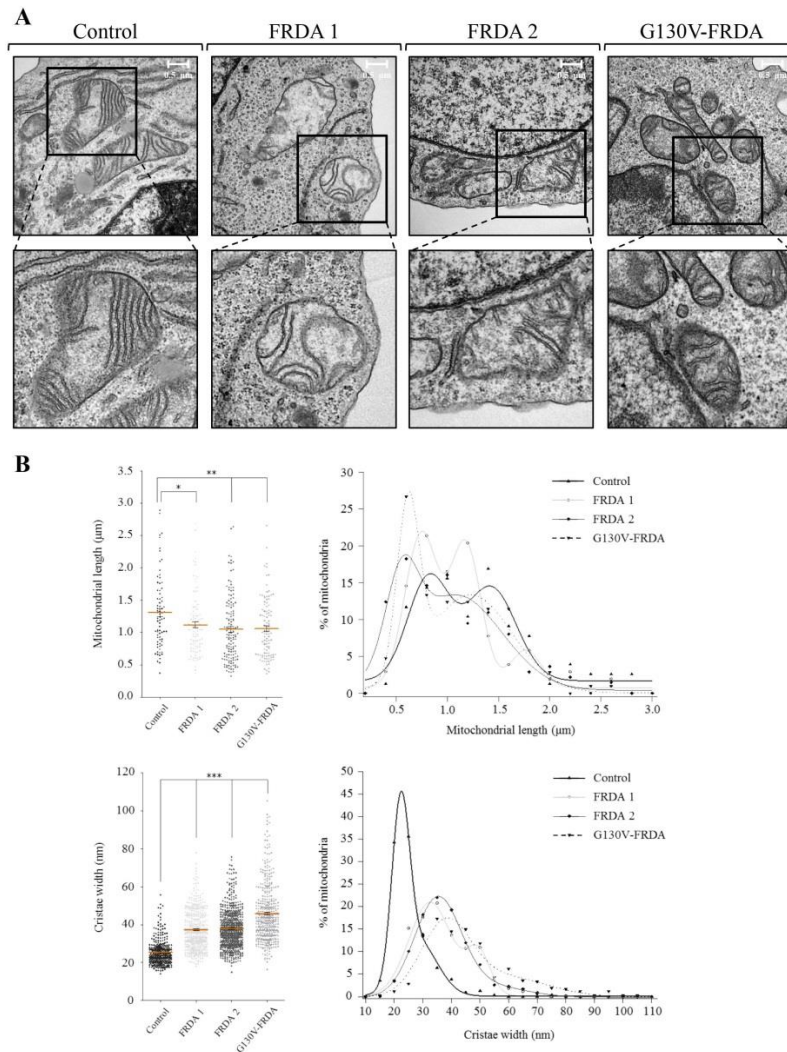


Figure 1.21. Cristae morphology is altered in mitochondria of FRDA LCLs. Panel A. Representative electron micrographs of control, FRDA (1 and 2) and G130V-FRDA LCLs. Cells were fixed and TEM images of randomly selected fields were acquired. Scale bars: 0.5 μm. Boxed areas represent a 4X magnification. **Panel B.** Morphometric analysis. To estimate mitochondrial length, 80 to 150 mitochondria were analyzed in each experiment; to estimate cristae width, 300 to 600 cristae were analyzed in each experiment. Data represent mean ± SEM of three independent experiments. Statistical significance was determined using One-way ANOVA with Dunnett’s post-hoc test (*p ≤ 0.05, **p ≤ 0.01, ***p ≤ 0.001, compared to control). For each morphological parameter, the frequency distribution plot of the experimental data is reported on the right. Symbols represent the relative frequencies expressed as percentage of mitochondria and lines represent the gaussian fit curves for each individual data set.

Frataxin is a free-soluble protein devoid of any transmembrane domains [Musco G. et al., 2000; Dhe-Paganon S. et al., 2000] and this morphological change could be relevant for its partial loss from the cristae membranes. Because cristae shape could have *per se* an impact in the mitochondrial phenotype of the three FRDA LCLs used in our work, to exclude an upstream defect in the mitochondrial-shaping proteins background, we next analyzed the expression levels of two proteins involved in the formation and maintenance of the cristae, *i.e.* mitofilin and OPA1. Mitofilin is a key component of the protein complex MICOS while OPA1 has a fundamental role in cristae architecture and exists in eight tissue-specific isoforms, which are proteolytically processed to form several long and short forms [Cogliati S. et al., 2016]. The western blotting analysis reported in Figure 1.22 indicates that healthy control and FRDA LCLs have comparable levels of mitofilin and share a similar pattern of the detected long/short forms of OPA1, except for the smallest, which is slightly increased in all FRDA LCLs, as expected in cells with respiratory defects [Duvezin-Caubet S. et al., 2006].

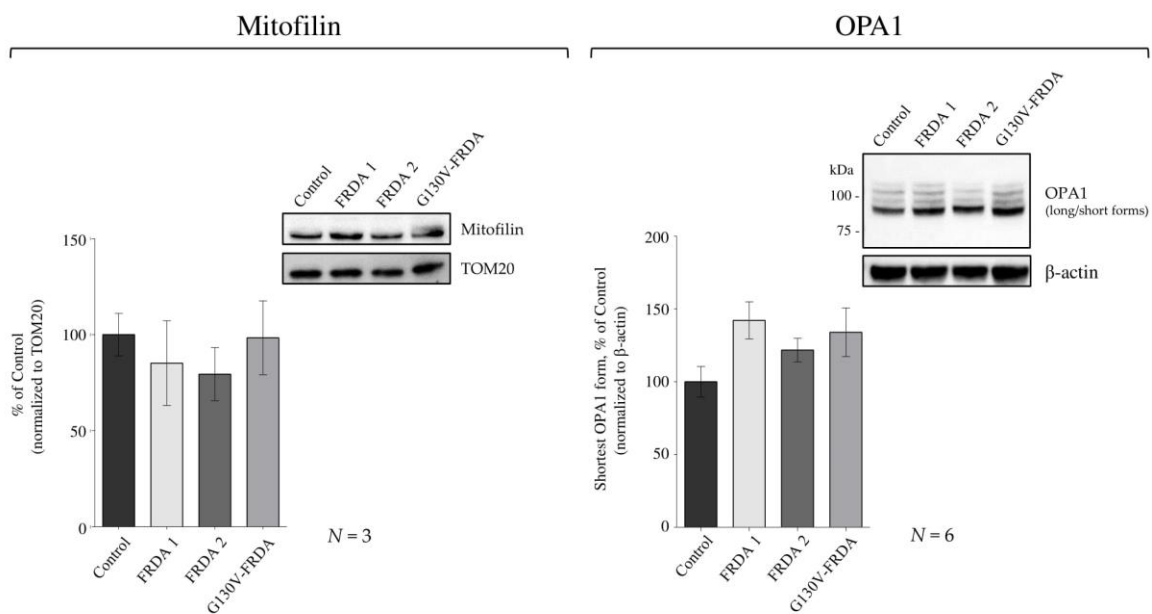
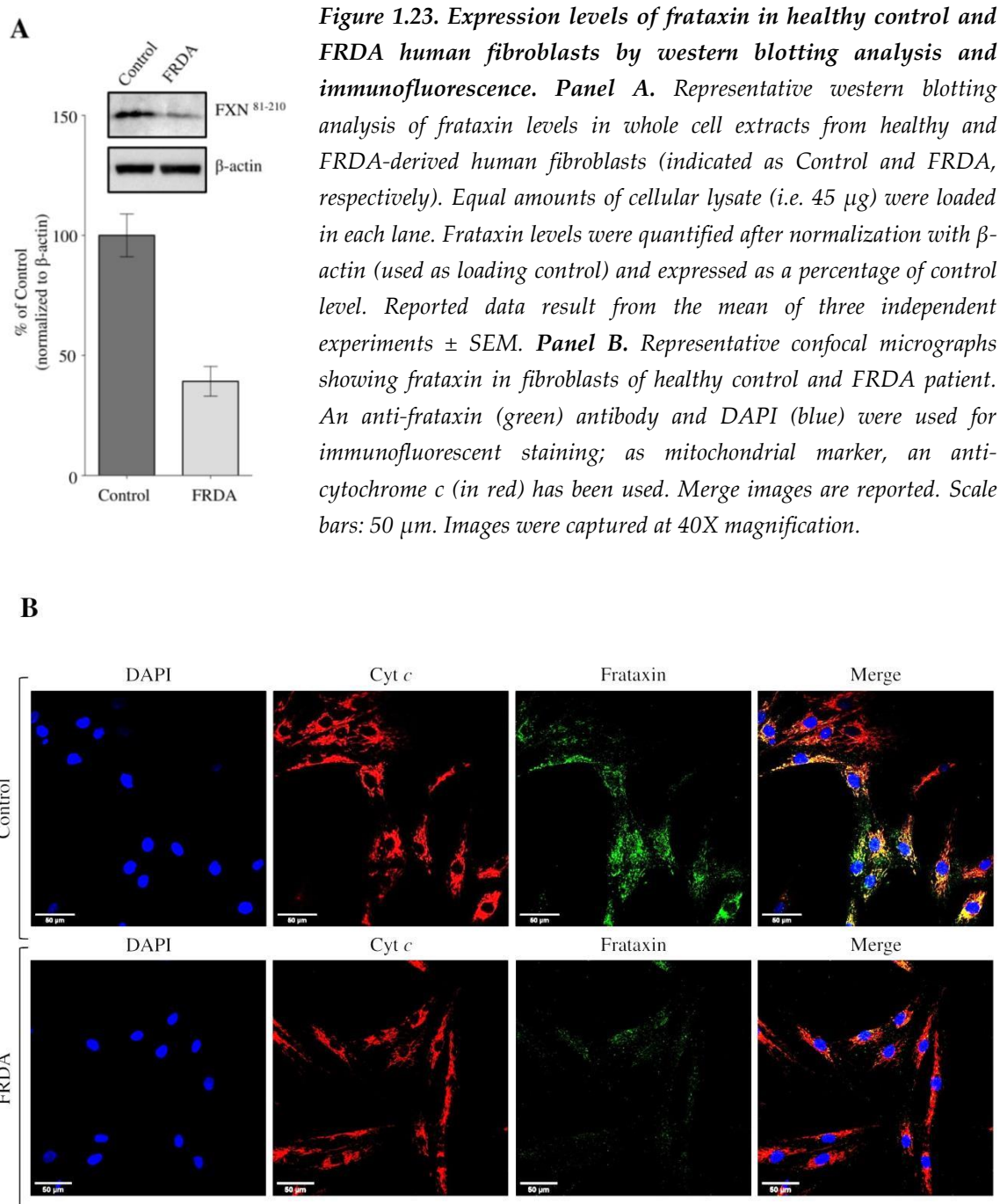


Figure 1.22. Comparative analysis of mitofilin and OPA1 in healthy control, homozygous FRDA and heterozygous G130V-FRDA LCLs. Western blotting analyses of mitofilin and OPA1 in whole cell extracts from FRDA (1 and 2), G130V-FRDA and unaffected control LCLs. Equal amounts of protein (*i.e.* 25 μ g) were loaded in each lane. β -actin and TOM20 were used as loading controls. Protein levels were quantified after normalization with β -actin or TOM20 and expressed as percentage of control level. Reported data result from the mean of N independent experiments \pm SEM. One-way ANOVA with Dunnett's post hoc test was used for statistical analysis.

Frataxin is in Close Proximity with Mitochondrial Respiratory Chain in Human Cells

Immunogold-labeling experiments have shown that, in healthy cells, frataxin co-localizes in the mitochondrial cristae with two proteins belonging to the Fe-S cluster assembly machinery (*i.e.* the sulphur donor NFS1 and the scaffold protein ISCU) and that in FRDA cells, characterized by wider cristae and defects in respiratory efficiency as well as in formation/stabilization of supercomplexes, only frataxin moves to the matrix. As previously stated, mitochondrial cristae play a crucial role for the cellular bioenergetics since they host the complexes of the respiratory chain, whose functionality relies on Fe-S clusters as prosthetic groups. Therefore, we wondered if frataxin could have a role in the stabilization of supercomplexes through a spatial and functional proximity with the individual complexes belonging to the electron transport chain. The hypothesis of a functional interaction between frataxin and respiratory (super)complexes has been investigated by Proximity Ligation Assay (PLA), an immunofluorescence technique which allows to detect *in situ* physical closeness of proteins and potential protein-protein interactions with high specificity and sensitivity, also at endogenous protein expression levels [Fredriksson S. *et al.*, 2002; Söderberg O. *et al.*, 2006]. The general principles of PLA technique are reported in *Figure 1.25A* (see below). Briefly, this method requires to use antibodies that specifically recognize the two proteins of interest; if they are closer than 40 nm, based on the operating mode of the assay, proximity between the two proteins results in fluorescent spots that can be visualized and quantified by confocal microscopy.

PLA experiments have been conducted on healthy human fibroblasts, along with fibroblasts derived from a FRDA patient (*i.e.* GM04078, see Materials & Methods). As preliminary investigation, a comparative analysis of frataxin levels in the two fibroblast cell lines was performed. Western blot analysis in whole-cell extracts showed a residual amount of frataxin in FRDA cells corresponding to about 40% of the frataxin levels in the healthy control (*Figure 1.23A*). This evaluation was also confirmed by immunofluorescence analysis carried out on the two cell lines using an anti-frataxin antibody, since a strong decrease of fluorescence was observed in FRDA cells if compared to the control (*Figure 1.23B*); furthermore, the fluorescence signal is localized exclusively in mitochondria as suggested by the co-localization of frataxin with cytochrome *c* (*Figure 1.23B*), thus indicating that the primary antibody used against frataxin is highly specific for the protein of interest and then suitable for PLA experiments.



As positive control for PLA assay, we firstly address the physical closeness of frataxin towards NFS1, which is considered its putative functional interacting partner [Gerber J. et al., 2003; Schmucker S. et al., 2011; Fox N.G. et al., 2019]. In healthy fibroblasts, frataxin and NFS1 perfectly co-localized in mitochondria (Figure 1.24).

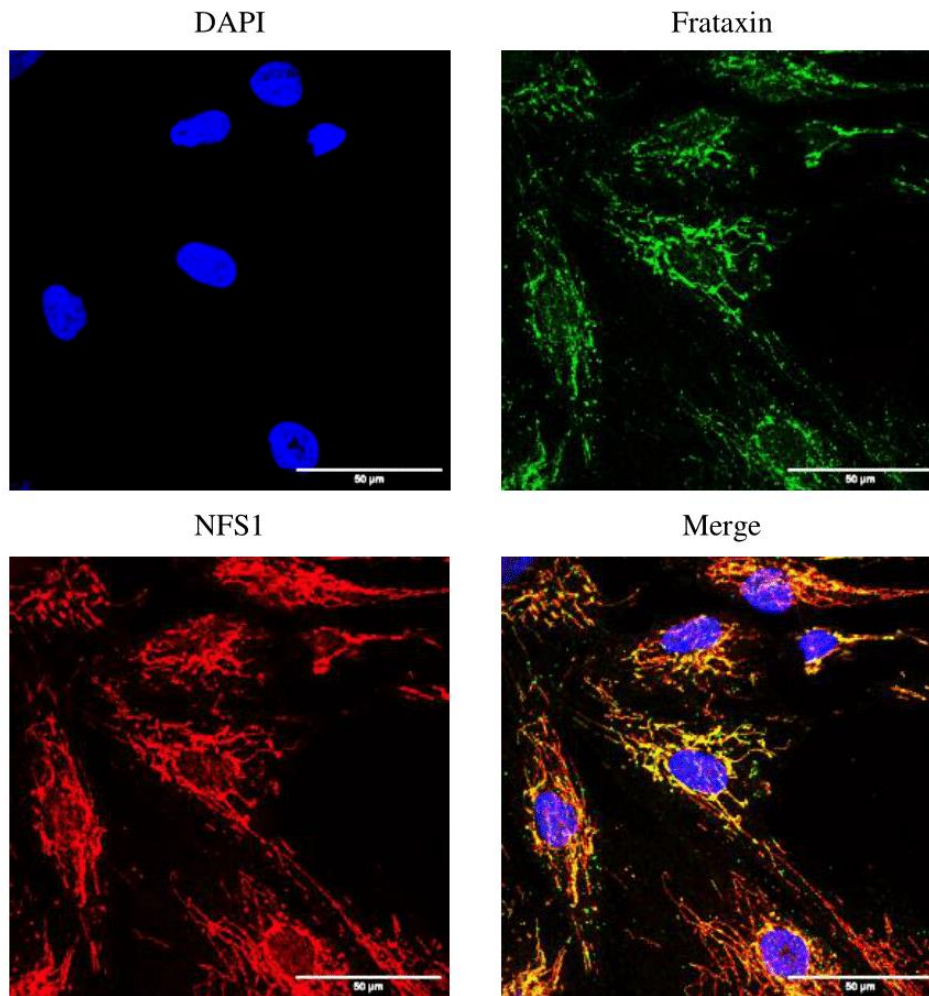


Figure 1.24. Mitochondrial co-localization of frataxin with NFS1 in healthy human fibroblasts cells. Double immunofluorescence staining was performed in human healthy fibroblasts using an anti-frataxin antibody (in green) and an anti-NFS1 (in red) as a second antibody. The nuclei were counterstained with DAPI (in blue). In yellow, overlap of red and green which show the mitochondrial co-localization of frataxin with NFS1. Scale bars: 50 µm. Images were captured at 40X magnification.

In situ PLA between the two proteins provided positive signals (red dots) (Figure 1.25B). The specificity of the assay was further confirmed by the qualitative decrease of the number of fluorescent spots in FRDA fibroblasts (Figure 1.25B) in which frataxin levels are severely reduced (Figure 1.23). To detect possible unspecific signal, we performed PLA in absence of primary antibodies or secondary antibodies as negative controls; in both cases, no PLA dots were observed (Figure 1.25B), confirming the specificity of the technique.

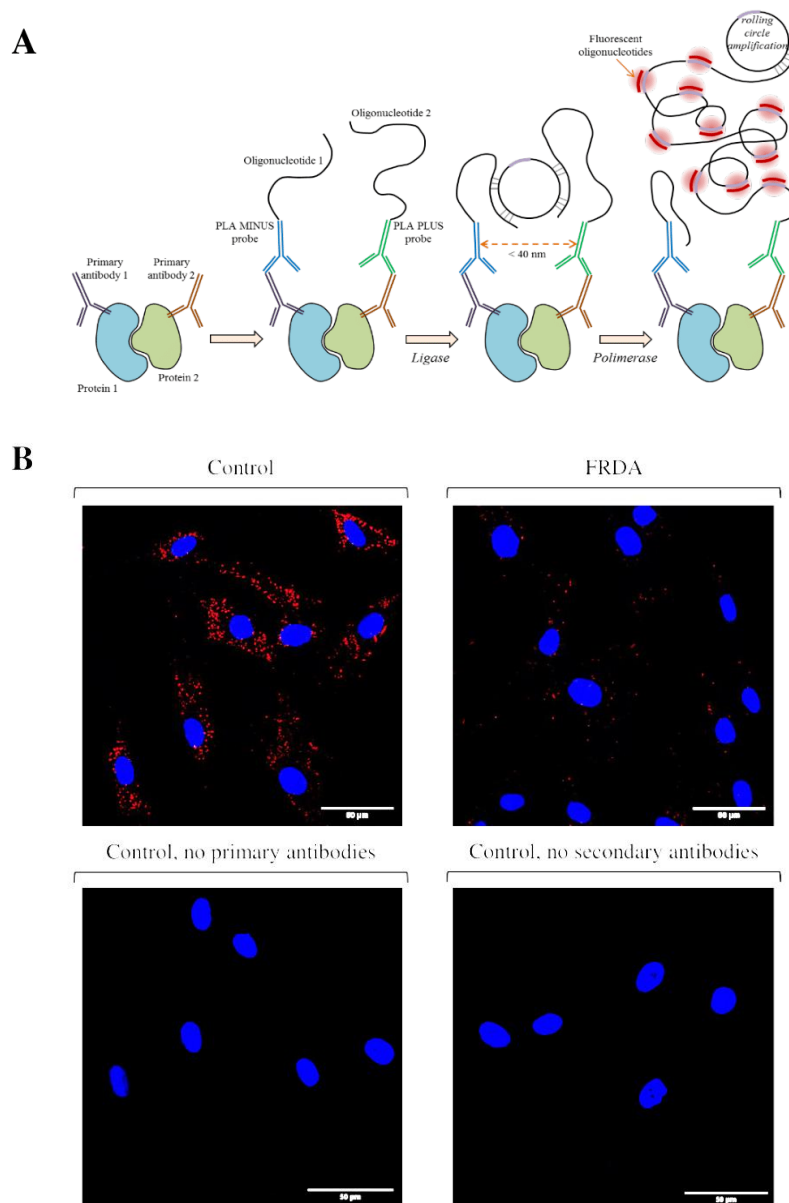


Figure 1.25. Frataxin and NFS1 are in close proximity in human fibroblasts. Panel A. Principles of PLA. Two primary antibodies raised in different species are used to recognize the two proteins of interest; a pair of secondary antibodies (PLA probes), each conjugated to a short oligonucleotide that is complementary to the other, bind the primary antibodies; if in close proximity (less than 40 nm), the oligonucleotides hybridize and an added DNA ligase forms a closed circle DNA template required for rolling circle amplification. Then, the addition of a DNA polymerase promotes the formation of a long DNA product which remains covalently attached to one of the PLA probes. In the last step, fluorescent-labelled oligonucleotides hybridize to the complementary sequences resulting as distinct fluorescent spots that can be detected and quantified by confocal microscopy. **Panel B.** Representative confocal images of in situ PLA between frataxin and NFS1 performed in human healthy control and FRDA, using an anti-frataxin antibody in combination with an antibody against NFS1. Evidence of proximity between frataxin and NFS1 is indicated by the presence of red spots. Confocal images for negative controls, where the primary or secondary antibodies were omitted, are reported. Nuclei were counterstained with DAPI (in blue). Scale bar: 50 μm . Images were captured at 40X magnification.

As previously observed in healthy LCLs, we verified by means of immunogold-labeling that also in healthy fibroblasts frataxin is enriched in mitochondrial cristae, as suggested by the distribution of gold particles in the representative micrographs reported in *Figure 1.26*.

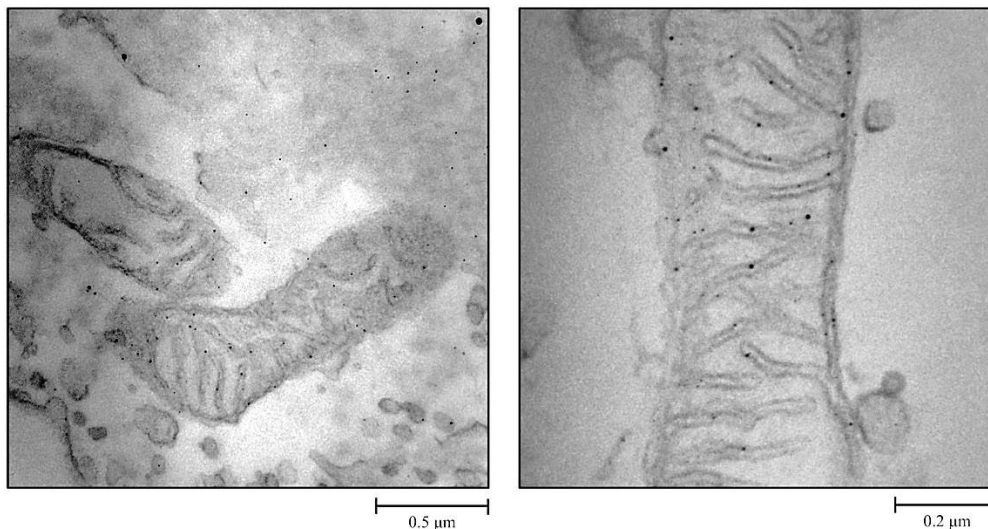


Figure 1.26. Frataxin is enriched in the mitochondrial cristae of healthy control fibroblasts. Representative images at two different magnitudes of the immunogold-labeling coupled to electron microscopy of healthy control fibroblasts. Scale bars are indicated in the figure.

We then investigated, by means of PLA, whether frataxin may also be found in close proximity to the complexes of the electron transport chain, focusing on the mitochondrial complexes containing Fe-S clusters as cofactors.

As preliminary control, we checked the specificity of the selected primary antibodies against respiratory complexes I, II and III. *Figure 1.27* clearly shows that frataxin co-localizes in mitochondria with all complexes, thus allowing to proceed with PLA experiments. *Figure 1.28* reports the results of *in situ* proximity ligation assay performed with frataxin and the complexes of respiratory chain, both in healthy fibroblasts and in FRDA fibroblasts. PLA puncta are detected in all cases, suggesting a physical closeness between frataxin and mitochondrial respiratory chain; as expected, the number of fluorescent dots decreases in FRDA fibroblasts, accordingly with the reduced levels of frataxin in comparison to the healthy control. Interestingly, a different number of PLA signals has been detected in all cases, with the highest number observed for frataxin with complex I and the lowest number of dots detected for frataxin with complex II (*Figure 1.28*).

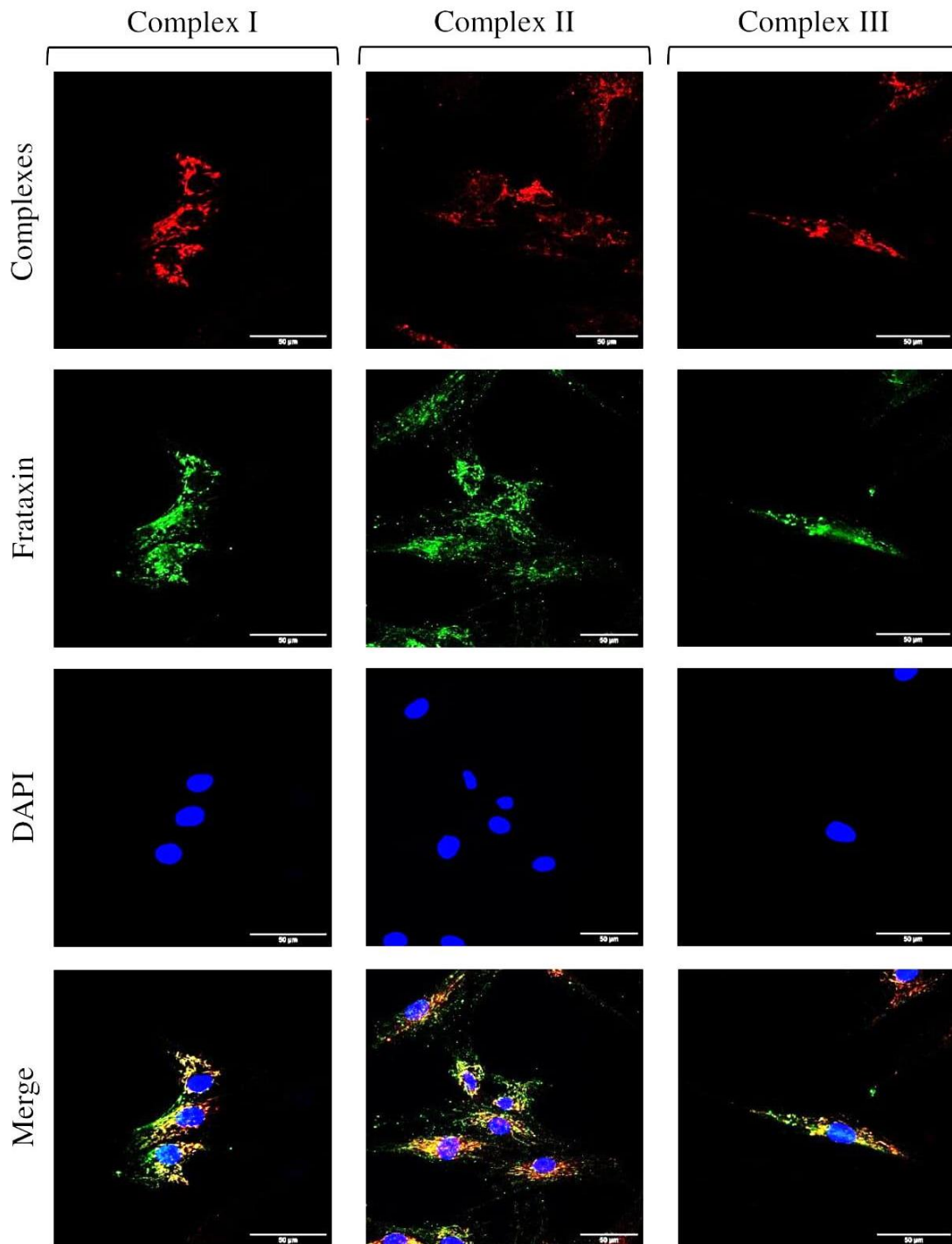


Figure 1.27. Mitochondrial co-localization of frataxin and respiratory complexes I-II-III in human healthy fibroblasts. Double immunofluorescence staining was performed in human healthy fibroblasts using an anti-frataxin antibody (in green) and an anti-complex I, II, or III (in red) as a second antibody. The antibodies recognizing the complexes are against ND1 subunit for complex I, against SDHB subunit for complex II and against UQCRCF1 subunit for complex III. The nuclei were counterstained with DAPI (in blue). In yellow, overlap of red and green which show the co-localization of frataxin with each of the complexes of the respiratory chain. Scale bars: 50 μm. Images were captured at 40X magnification.

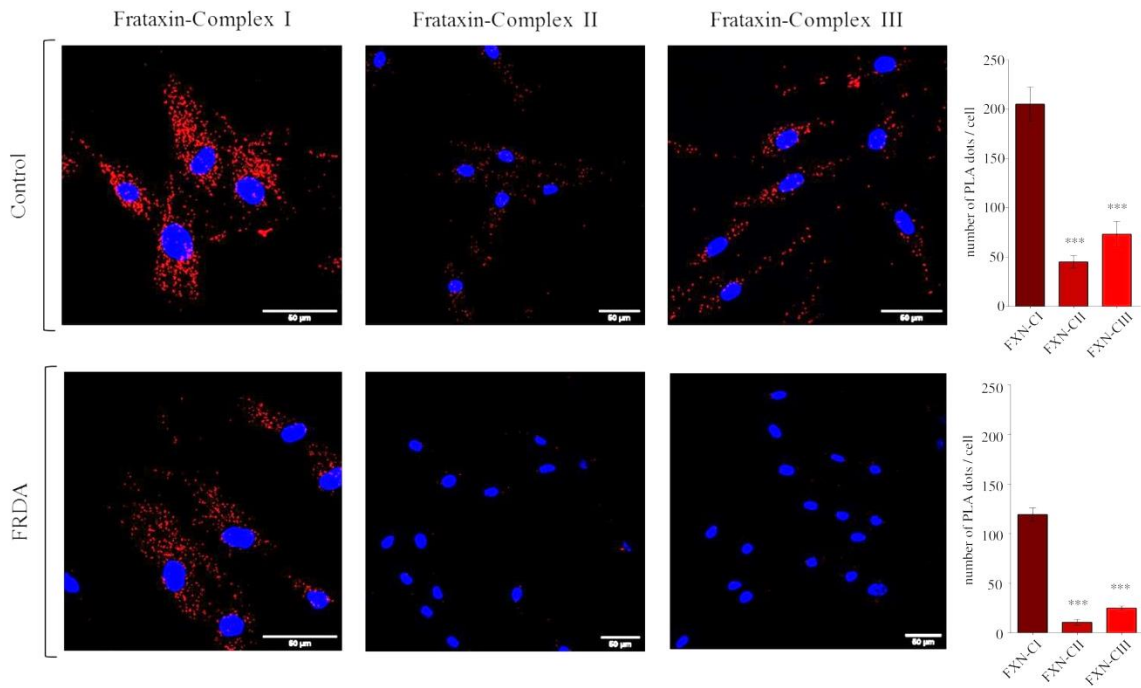


Figure 1.28. Detection of physical closeness between frataxin and mitochondrial respiratory chain in healthy control and FRDA human fibroblasts by *in situ* PLA. On the left, representative confocal images of *in situ* proximity ligation assay performed in human healthy and FRDA fibroblasts (indicated as Control and FRDA, respectively), using an anti-frataxin antibody in combination with antibodies against the respiratory chain complexes I, II or III (anti-ND1 subunit for complex I, anti-SDHB subunit for complex II and anti- UQCRFS1 subunit for complex III). Evidence of proximity between frataxin and the targeted proteins is indicated by the presence of red spots. Nuclei were counterstained with DAPI (in blue). Scale bar: 50 μ m. Images were captured at 40X magnification. On the right, quantitative analyses expressed as number of PLA dots per cell. Different images for each condition have been acquired and an average number of 50 cells have been analyzed for the quantification. Reported data result from the mean of three independent experiments \pm SEM. Statistical significance was determined using One-way ANOVA with Bonferroni's post-hoc test multiple comparison test (** $p \leq 0.001$).

To validate these results, negative control experiments were performed in parallel in the absence of primary or secondary antibodies (data not shown); in all cases, no red dots were observed, confirming the specificity of the technique. The same pattern of PLA signals was also qualitatively observed in iPSC (induced Pluripotent Stem Cell)-derived cardiomyocytes, which have been chosen as a model of choice to interpret the experimental data in the context of FRDA disease. As expected, a close proximity between frataxin and NFS1 was detected (Figure 1.29); PLA dots have been also observed for frataxin with the respiratory complexes and, notably, to a greater extent with complex I (Figure 1.29).

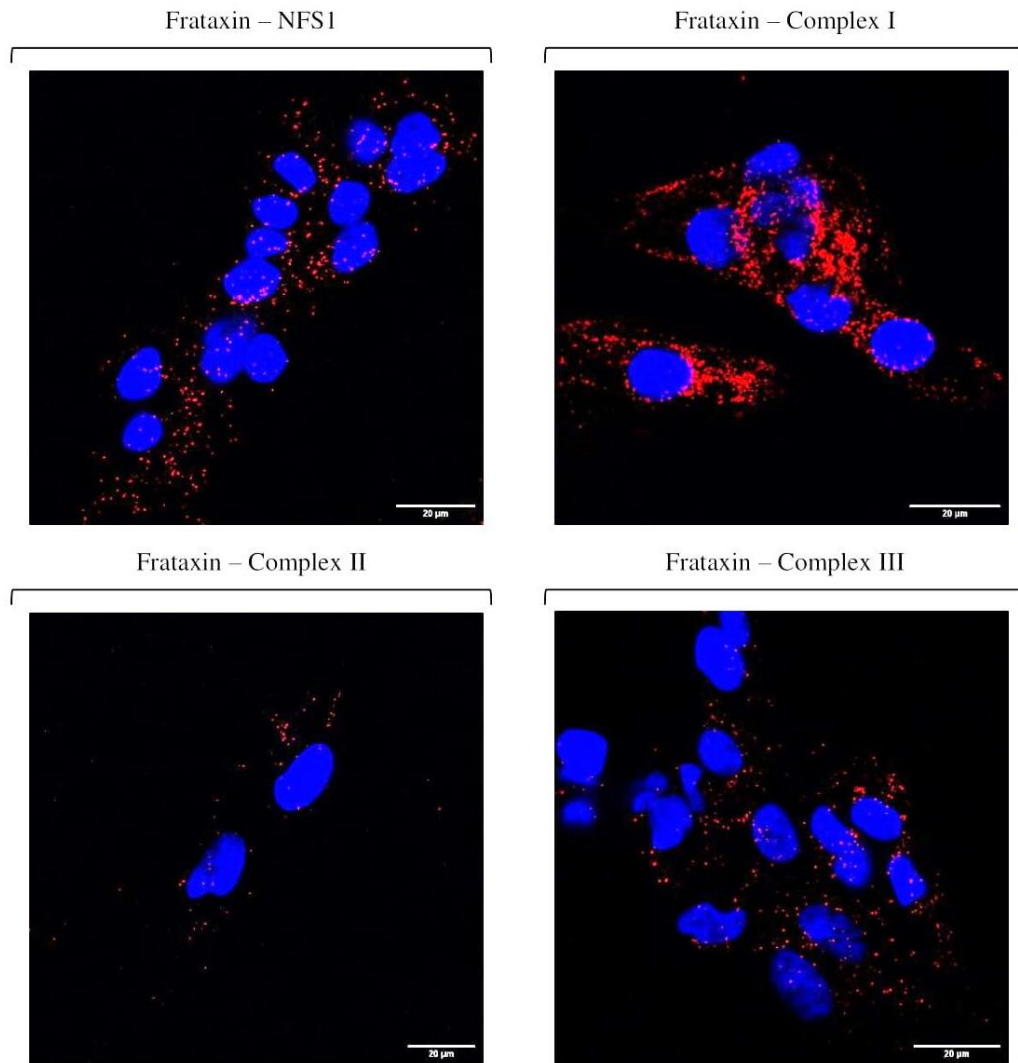


Figure 1.29. Detection of proximity between frataxin, iron-sulfur clusters assembly machinery and mitochondrial respiratory chain in iPSC-derived by *in situ* PLA. Representative confocal images of *in situ* proximity ligation assay performed in iPSC (induced Pluripotent Stem Cell)-derived cardiomyocytes using an anti-frataxin antibody in combination with antibodies against cysteine desulfurase NFS1 or the respiratory chain complex I, II or III (anti-ND1 subunit for complex I, anti-SDHB subunit for complex II and anti-UQCRCF1 subunit for complex III). Evidence of proximity (distance < 40 nm) between FXN and the targeted proteins is indicated by the presence of red spots. Nuclei were counterstained with DAPI (in blue). Scale bar: 50 µm. Images were captured at 40X magnification.

Discussion & Conclusions

In the present study, we report a comparative analysis of the mitochondrial phenotype of lymphoblastoid cell lines derived either from two “classic” Friedreich’s ataxia patient (homozygous for the GAA triplet expansion in the *FXN* gene) or from a compound heterozygous patient harboring the expansion on one *FXN* allele and a G130V point mutation on the other. The GAA expansion, that is present in at least one allele in virtually all patients, causes a transcriptional repression of the gene, resulting in the production of reduced amounts of otherwise normal frataxin [Campuzano V. *et al.*, 1996; Lazaropoulos M. *et al.*, 2015], an iron-binding protein able to functionally interact with the Fe-S cluster assembly machinery [Gerber J. *et al.*, 2003; Shan Y. *et al.*, 2007; Schmucker S. *et al.*, 2011; Bridwell-Rabb J. *et al.*, 2014; Parent A. *et al.*, 2015; Boniecki M.T. *et al.*, 2017]. The G130V point mutation, frequently found in heterozygous patients with a severe frataxin deficiency [Lazaropoulos M. *et al.*, 2015], has been reported to alter the protein conformation, leading to a higher tendency towards aggregation *in vitro* [Correia A.R. *et al.*, 2006; Correia A.R. *et al.*, 2008; Faggianelli N. *et al.*, 2015; Bellanda M. *et al.*, 2019]. Accordingly, we found the lowest levels of residual frataxin in the G130V-FRDA LCLs (Figure 1.3B). This point mutation has been shown to impair the frataxin processing from FXN⁴²⁻²¹⁰ to FXN⁸¹⁻²¹⁰ in FRDA patients’ fibroblasts [Clark E. *et al.*, 2017]. In fact, we found an increased FXN⁴²⁻²¹⁰/FXN⁸¹⁻⁸¹⁰ ratio in the G130V-FRDA lymphoblastoid cells, confirming the previous observation. On the other hand, in these cells the amount of the intermediate FXN⁴²⁻²¹⁰ has the same trend of the mature FXN⁸¹⁻²¹⁰, as they are both strongly reduced compared not only to healthy control but also to the homozygous FRDA cells (Figure 1.3C). Therefore, the alterations of the mitochondrial phenotype that we observe in G130V-FRDA LCLs are likely due to a decrease of overall frataxin levels, as in homozygous FRDA cells.

Deficiencies in oxidative phosphorylation and alteration of respiratory complexes have been observed in FRDA patients’ cells [Rötig A. *et al.*, 1997; Salehi M.H. *et al.* 2014] and in the cerebellum of a frataxin-deficient FRDA mouse model (KIKO mouse) [Lin H. *et al.*, 2017]. We found that the assembly of higher molecular weight respiratory supercomplexes and the spare respiratory capacity are also decreased in the FRDA LCLs analyzed in our work (Figure 1.12 and Figure 1.11), indicating that lymphoblastoid cells with a severe frataxin depletion are unable to boost the respiratory function in response to an increase in energy demands.

The role of frataxin in the mitochondrial phenotype of FRDA cells could be related to an impaired assembly of the Fe-S clusters [Huynen M.A. *et al.*, 2001], key prosthetic groups involved in the transfer of electrons (such as in respiratory complexes I, II and III) or in the catalytic activity of several enzymes (*e.g.* aconitase). Accordingly, EPR experiments performed on isolated mitochondria have highlighted different spectroscopic responses for the LCLs used in this work (Figure 1.14 and Figure 1.15), indicating a general impairment of the redox centers, including Fe-S clusters, belonging to the electron transport chain in FRDA cells.

Although the specific contribution of frataxin to the Fe-S clusters biogenesis has not been yet definitively clarified, an emerging role is that it could act as an allosteric activator of cysteine binding to the NFS1 desulfurase and ensuing sulfur transfer to the ISCU scaffold protein [Tsai C.L. & Barondeau D.P., 2010; Colin F. *et al.*, 2013; Bridwell-Rabb J. *et al.*, 2014; Parent A. *et al.*, 2015]. This relies on its transient binding to multiple core components of the assembly machinery, which has been confirmed by several independent experiments *in vitro* using purified recombinant proteins [Gerber J. *et al.*, 2003; Schmucker S. *et al.*, 2011; Fox N.G. *et al.*, 2019]. A relevant novel finding of the present work is that in healthy cells mitochondrial cristae, which house the respiratory complexes, are enriched of frataxin as well as of NFS1 and ISCU, as assessed by immunogold-labeling coupled to electron microscopy (Figure 1.18, Figure 1.19 and Figure 1.26). The localization of some proteins of the Fe-S cluster assembly complex in the mitochondrial cristae was previously found in the yeast *S. cerevisiae* [Vogel F. *et al.*, 2006] and it would be therefore an evolutionary conserved feature essential to drive an efficient biogenesis of these key redox cofactors. An indication that frataxin localizes at or near the inner mitochondrial membrane was previously obtained by Campuzano and colleagues in transfected HeLa cells overexpressing a recombinant full-length FXN¹⁻²¹⁰ [Campuzano V. *et al.*, 1997]. To the best of our knowledge, our data provide the first direct evidence that in healthy cells endogenous frataxin is mostly associated with the mitochondrial cristae. This subcompartmentalization would put the Fe-S cluster biogenesis complex in close proximity with frataxin, enabling key structural and functional interactions, and with the respiratory chain complexes, which rely on these cofactors for their redox activity. Interestingly, we found that a significant proportion of residual frataxin moves towards the matrix in FRDA LCLs, while NFS1 and ISCU proteins are mostly associated to the mitochondrial cristae as in control cells (Figure 1.18 and Figure 1.19). This could in turn prevent or decrease its binding to the Fe-S

cluster assembly machinery. The frataxin expressed by heterozygous G130V-FRDA cells is expected to be a mixture of wild type and mutant proteins, which are both recognized by the antibody used in the immunogold-labeling experiments, so we cannot rule out the possibility that the point mutation itself could have an impact in the localization of residual frataxin in the cristae. In any case this would lead to a poor structural stability and contribute to a further decrease of the protein at this level. In a previous work, we showed that the G130V-frataxin retains the capability to interact with the scaffold protein ISCU, to enhance the NFS1 desulfurase activity and to bind iron *in vitro* [Bellanda M. *et al.*, 2019]. Therefore, the pathological phenotype of G130V-FRDA cells is likely related to the instability of the mutant protein.

The transient nature of the interactions between frataxin and the proteins belonging to the Fe-S cluster assembly machinery could explain the reason why only frataxin has the tendency to redistribute from the cristae to the matrix in FRDA cells with wider mitochondrial cristae. In fact, this machinery is a stable supramolecular complex composed of NFS1, ISCU and the accessory proteins ISD11 and ACP (Acyl Carrier Protein). Frataxin binding to this core complex is dynamic and this makes the reconstitution of the whole complex very challenging. The only FXN-bound complex structure known to date, from any organism, has been solved by Fox and colleagues, by cryo-electron microscopy using recombinant human proteins [Fox N.G. *et al.*, 2019]. Based on this structure, frataxin would transiently and dynamically bind at the interface of two NFS1 and one ISCU subunits, stabilizing key conformations of these two proteins and promoting sulfur transfer from NFS1 to ISCU.

Taken together, our evidences support a major role of frataxin enrichment in the mitochondrial cristae of healthy cells as a key factor to allow an efficient biogenesis of Fe-S clusters and in turn a proper assembly of functional respiratory complexes. It is worth noting that in mitochondria of healthy mammalian cells almost all complex I, the major entry point of electrons in the respiratory chain, is usually found to be associated with supercomplexes, and this increases its stability [Schägger H. & Pfeiffer K., 2000; Schägger H. & Pfeiffer K., 2001; Acín-Pérez R. & Enriquez J.A. 2014]. We also found a defect in respirasome formation in FRDA cells (Figure 1.12); to the best of our knowledge, this is the first experimental evidence that respiratory chain supercomplexes are destabilized in cells with a severe deficiency of frataxin.

Our results allow us to speculate that frataxin could simultaneously and synergically interacts with the ISCs assembly machinery and the electron

transport chain, acting as a bridge between the two molecular systems and promoting the biogenesis and/or the incorporation of Fe-S clusters into the respiratory complexes, as well as ensuring their stability.

Evidence of a functional relationship between frataxin and the mitochondrial respiratory chain was previously described in literature. In fact, it was shown that in *S. cerevisiae* frataxin is able to physically interact with complex II [Gonzalez-Cabo P. et al., 2005]: frataxin, interacting with the FAD binding domain of the SDHA subunit and the iron-sulfur-containing subunit SDHB, may regulate the entry of electrons in the electron transport chain, at least via complex II, and/or that could contribute to the stability or the assembly of the respiratory complex. To date, however, no evidence of a possible interaction of frataxin with the complex I and complex III has been reported.

On the basis of these premises, we addressed the hypothesis of a potential functional interaction between frataxin and respiratory (super)complexes by means of Proximity Ligation Assay (PLA), a highly-specific and sensitive technique which allow to detect stable and transient protein-protein interactions *in situ*. Our data showed a close proximity between frataxin and the respiratory complexes I, II and III in two different cellular models, *i.e.* fibroblasts (*Figure 1.28*) and iPSC-derived cardiomyocytes (*Figure 1.29*). Interestingly, in both cellular models, we disclosed the strongest proximity signal between frataxin and complex I and the weakest one with complex II, suggesting that frataxin could preferentially interact with mitochondrial complex I rather than complex II and complex III. According to this hypothesis, a closer inspection of the EPR spectra deriving from mitochondria of FRDA LCLs (*Figure 1.15* and *Figure 1.16*) revealed that the strongest signal decrease concerns the Fe-S clusters belonging to complex I, while the signals arising from the iron-sulfur clusters of the other two complexes are slightly decreased (complex II) or superimposable (complex III) relatively to the healthy control. The EPR results are also fully consistent with the protein expression of the individual respiratory complexes in FRDA LCLs: western blot analysis indicates that, while the levels of Fe-S-containing subunits of complex II and complex III do not vary significantly (*Figure 1.8*), some specific Fe-S subunits of complex I are reduced in FRDA cells (*Figure 1.6* and *Figure 1.7*). Additionally, no relevant differences in protein levels have been observed for mitochondrial aconitase (*Figure 1.9*), an iron-sulfur enzyme belonging to the TCA cycle whose deficiency is reported to be a frequent hallmark of FRDA disease [Rötig A. et al., 1997; Bradley J.L. et al., 2000; Condò I. et al., 2010]. Trivially, it is possible that we disclosed defects mainly on complex I because, among the

respiratory chain complexes and, in general, among the Fe-S proteins, it is the one containing the highest number of iron-sulfur clusters, hence resulting the most affected. However, an interesting finding corroborates our hypothesis of a direct functional interaction between frataxin and complex I, going beyond this mere evaluation. In fact, the solved crystallographic structure of the hydrophilic domain of the complex I of *Thermus thermophilus* [Sazanov L.A. & Hinchliffe P., 2006; Hinchliffe P. et al., 2006] highlights the presence of a subunit, i.e. Nqo15, characterized by a frataxin-like structure, with a folding and topology highly similar to those of frataxin (Figure 1.30). Furthermore, a closer inspection of the structure of the bacterial complex I shows that Nqo15 is closely proximal to Nqo3 subunit, the equivalent of human NDUF51 (Figure 1.30). In this regard, it is worth to note that NDUF51 is the only Fe-S subunit which is severely and significantly reduced in the FRDA LCLs analyzed in our work (Figure 1.6). The presence of a putative iron-binding channel at the interface between Nqo15 and its binding surface to bacterial complex I suggests that Nqo15 may promote the incorporation of iron to the Fe-S subunits and/or prevent and repair iron-sulfur cofactors from their damage; since there are no current available crystallographic structures or experimental evidences which highlight a stable binding between frataxin and mammalian complex I, it could be hypothesized that, in mammals, frataxin may interact transiently with complex I in order to perform an analogue function.

Interestingly, it was shown that, in *E. coli*, although the frataxin homologue CyaY is not a structural component of complex I, its deletion has an effect on reducing the total contents of complex I as well as of complex II [Pohl T. et al., 2007]. This evidence was ascribed to an impaired biogenesis or a destabilized repairing process of the Fe-S clusters belonging to the respiratory complexes, suggesting that a transient interaction between CyaY and the electron transport chain could take place [Pohl T. et al., 2007]. Furthermore, it was demonstrated that a silencing of frataxin in NSC34 motoneuronal cells specifically affects mitochondrial complex I among the respiratory chain complexes, strongly reducing its enzymatic activity and impairing its structural stability more than its assembly [Carletti B. et al., 2014].

A deficiency of frataxin could be then crucial for the stability of the respiratory complex I, whose structural and functional integrity is pivotal for the organization of the entire electron transport chain and, consequently, for the overall respiratory efficiency. In fact, a dysfunctional complex I could critically impair the organization of respiratory complexes into supercomplexes since

supercomplexes formation starts and is ensured only with a complex I fully assembled and structurally intact [Guerrero-Castillo S. *et al.*, 2017].

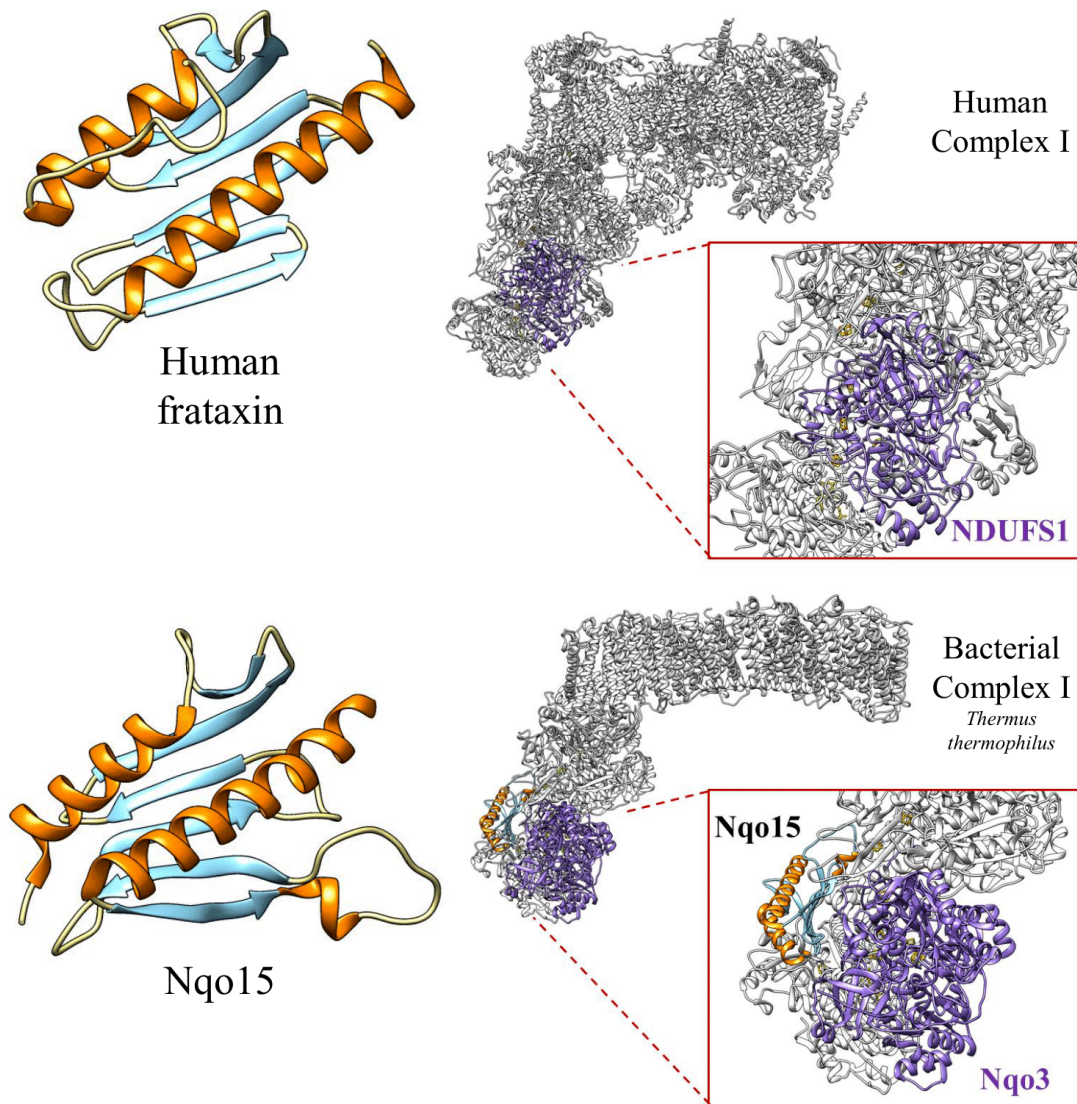


Figure 1.30. Similarity between human frataxin and Nqo15 subunit of bacterial complex I from *Thermus thermophilus*. On the left, comparison of the structures of human frataxin (PDB ID: 1EKG) and Nqo15 subunit belonging to the hydrophilic domain of complex I of the bacterium *Thermus thermophilus* (PDB ID: 6Y11). Secondary structure motifs are highlighted with the same colors in the two structures (α -helices in orange, β -strands in light blue). On the right, structures of the human respiratory complex I (PDB ID: 5XTD) and complex I from *Thermus thermophilus* (PDB ID: 6Y11). Nqo3 and the equivalent human subunit NDUFS1 are highlighted in purple. In the complex I from *Thermus thermophilus* is also highlighted the Nqo15 subunit with α -helices in orange and β -sheet in light blue. In both structures, the sulphur and iron atoms of the Fe-S clusters are colored in yellow and dark orange, respectively. Figures of structures have been elaborated with UCSF Chimera.

Interestingly, in the scenario of the assembly pathway of respiratory complex I, it has been shown that the subunits NDUFS1, NDUFV1 and NDUFV2 are added only at the final stages of the assembly process [Guerrero-Castillo S. et al., 2017]; since NDUFS1 is the subunit mostly affected in the FRDA LCLs analyzed in the present work, we are prompted to speculate that reduced levels of frataxin could have a downstream effect in the assembly and/or stability of complex I, impairing its structural integrity and its association into supercomplexes.

Nevertheless, the relationship between frataxin depletion and the reduced ability to assemble functional respiratory supercomplexes observed in FRDA patients’ cells requires additional experiments to be completely clarified.

To date, we still do not know exactly which metabolic consequences primarily occur after frataxin depletion and would be most relevant for early FRDA therapy strategies. Our finding that beside housing respiratory (super)complexes cristae are also enriched in proteins of the Fe-S cluster assembly machinery, including frataxin, is relevant because it opens up a new working perspective aimed at addressing if and how the perturbation of mitochondrial morphology and dynamics are involved in the events leading to bioenergetic defects in cells from FRDA patients. The redistribution of frataxin in mitochondrial subcompartments upon changes of the cell physiological state defines a novel framework to address the pathogenesis of Friedreich’s ataxia and to explore if manipulation of mitochondria shaping-proteins could correct the bioenergetic defects afflicting patient cells, as in other mitochondrial disease [Varanita T. et al., 2015; Civiletto G. et al., 2015].

Chapter 2

Insight into the Iron-Binding Properties of Human Frataxin and its Interaction with Mitochondrial Superoxide Dismutase

Frataxin (FXN) is a highly conserved mitochondrial protein whose deficiency causes Friedreich's ataxia, a cardio-neurodegenerative disease. The precise physiological function of FXN is still elusive, but several evidences point out its direct involvement in the iron-sulphur clusters (ISCs) and heme biosynthetic pathways, as well as in iron homeostasis and antioxidant defense.

In this work, we combined different spectroscopic techniques to explore the ferric and ferrous iron-binding properties of human frataxin in vitro. We found that the human protein binds both iron forms, displaying different behaviors. By means of fluorescence spectroscopy and Site-Directed Spin Labeling coupled to Electron Paramagnetic Resonance (SDSL-EPR) we showed that ferric iron causes reversible aggregation in a concentration-dependent fashion and that ferrous iron binds without inducing either aggregation or altering the protein conformation. The use of a spin label resistant to reduction and the comparison of the binding effect of Fe²⁺ in wild type frataxin and in a pathological variant carrying a point mutation in the iron-binding region (i.e. D122Y), allowed us to characterize the ferrous binding properties of different protein sites. Furthermore, the involvement of frataxin in the redox imbalance suggests that FXN could interact with mitochondrial superoxide dismutase (SOD2), an enzyme which plays a key role in antioxidant cellular defense. Taking advantage of SDSL-EPR and fluorescence quenching experiments, we explored the interaction between human FXN and SOD2 in vitro to point out this issue. Spectroscopic data were combined with rigid body protein-protein docking to assess the potential structure of the FXN-SOD2 complex, which leaves the metal binding region of FXN accessible to the solvent. We provide evidence that human FXN interacts with human SOD2 in vitro and that the complex is in fast exchange. This interaction could be relevant during the assembly of Fe-S clusters and/or their incorporation in proteins, when Fe-S clusters are potentially susceptible to oxidative damage by reactive oxygen species (ROS).

This chapter has been adapted from:

Doni D., Passerini L., Audran G., Marque S.R.A., Schulz M., Santos J., Costantini P., Bortolus M., Carbonera D. – *Effects of Fe²⁺/Fe³⁺ binding to human frataxin and its D122Y variant, as revealed by Site Directed Spin labelling (SDSL) EPR complemented by Fluorescence and Circular Dichroism spectroscopies* – *Int. J. Mol. Sci.*, 21, 9619, (2020) - [doi: 10.3390/ijms21249619]

and

Doni D., Meggiolaro M., Santos J., Audran G., Marque S.R.A., Costantini P., Bortolus M., Carbonera D. – *A combined spectroscopic and in silico approach to evaluate the interaction of human frataxin with mitochondrial superoxide dismutase* – *Biomedicines*, 9(12):1763 (2021) – [doi: 10.3390/biomedicines9121763]

Introduction

The main biochemical trait characterizing cells from FRDA patients is a severe impairment of proteins containing Fe-S clusters as cofactors; however, frataxin deficiency is also associated with dysregulation of iron homeostasis and to a marked increase in mitochondrial iron overload and increased levels of oxidative stress [Rötig A. *et al.* 1997; Schulz J.B. *et al.*, 2000; Puccio H. *et al.*, 2001; Chiabrando D. *et al.*, 2020].

The C-terminal region of the protein is highly conserved and considered the most important part for its function(s) [Huynen M.A. *et al.*, 2001]. On the contrary, the N-terminal region, corresponding to residues 81–92, is intrinsically unfolded and poorly conserved [Musco G. *et al.*, 2000]; for this reason, the N-terminal region is often truncated to obtain FXN^{90–210} for *in vitro* studies. As described in detail in Part I, despite its simplicity, the structure of the folded portion of mature human FXN is relatively rare and consists of an alpha-beta-alpha motif, where two α -helices pack against a contiguous anti-parallel β -sheet. Furthermore, FXN folding is remarkably stable, and the secondary structure has limited dynamics, as demonstrated by the high level of similarity between NMR [Musco G. *et al.*, 2000] and X-ray crystallography [Dhe-Paganon S. *et al.*, 2000] structures.

As pointed out in the general introduction, several roles have been proposed for frataxin, essentially based on its capability to bind iron: FXN has been claimed to participate in the Fe-S clusters biogenesis as iron donor [Mühlhoff U. *et al.*, 2002; Yoon T. & Cowan J.A., 2003], as well as to be a key regulator of iron homeostasis [Alsina D. *et al.*, 2018] and ferroptosis [Cotticelli M.G. *et al.*, 2019; Du J. *et al.*, 2020], a recently identified iron-dependent form of cell death [Stockwell B.R. *et al.*, 2020]. These functions highlight the critical importance of the interaction between iron ions and frataxin. This interaction has been investigated through a wide range of chemical and biochemical techniques, but so far, literature on this topic is often controversial and some incongruities among the collected data remain. Using fluorescence spectroscopy and calorimetry titrations with both Fe²⁺ and Fe³⁺, it was found that human FXN^{81–210} binds 6–7 ferrous/ferric ions [Yoon T. & Cowan J.A., 2003]. Differently, through a combination of fluorescence, NMR, and mass spectrometry, a binding stoichiometry of only 3 equivalents was reported for Fe²⁺/Fe³⁺ and Co²⁺ ions [Gentry L.E. *et al.*, 2013]. A NMR study proposed that FXN binds only one Fe(II) equivalent and does not bind Fe(III) [Cai K. *et al.*, 2018]. In a previous paper, using EPR and NMR spectroscopies we showed that FXN is able

to bind both iron forms [Bellanda M. et al., 2019]. Another controversial feature of FXN is the tendency to aggregate in presence of ferrous or ferric ions. Mature human FXN⁸¹⁻²¹⁰, as well as yeast and bacterial orthologues (*i.e.* Yfh1 and CyaY, respectively) do not aggregate *in vitro* when overexpressed and purified. However, only human FXN was reported to retain the monomeric form when added with ferrous ions, while the orthologues show a clear tendency to aggregation [Cavadini P. et al., 2002; Bou-Abdallah F. et al., 2004]. While human FXN aggregation in the presence of ferric ions has been alternatively dismissed [Yoon T. et al., 2007] or confirmed [Ahlgren E.C. et al., 2017], Yfh1 and CyaY show tendency to aggregate [Adinolfi S. et al., 2002]. Since aggregation may affect the iron-binding properties, it is important to determine its threshold in terms of protein concentration and compare it to those commonly employed for the experimental determination of iron affinity.

The capability of frataxin to bind iron appears to be an important issue to investigate in the context of FRDA disease. Indeed, in biological systems, iron homeostasis requires a fine regulation since an imbalance in the metabolic processes and biochemical reactions in which iron takes part could be critically relevant for the onset of an oxidative stress condition. Frataxin has been claimed to work in the protection against the oxidative damage which is, in fact, a common hallmark characterizing FRDA disease. In this regard, it has been shown that yeast FXN is able to interact with superoxide dismutases (SODs) [Han T.H.L. et al., 2019], an ubiquitous class of antioxidant enzymes that play a crucial role in the response to oxidative stress catalyzing the dismutation of superoxide radicals into molecular oxygen and hydrogen peroxide. SODs are considered the first line of defense against reactive oxygen species (ROS), whose unbalanced concentration within the cell can dramatically contribute to the pathophysiological mechanisms of several diseases [Fukai T. & Ushio-Fukai M., 2011]. To date, three different SOD isoforms have been identified in mammals: two of them, SOD1 (or Cu/Zn-SOD) and SOD2 (or Mn-SOD), are localized inside the cells, while the third isoform, SOD3 (or EC-SOD), is in the extracellular spaces [Zelko I.N. et al., 2002]. SOD1 is mainly localized in the cytoplasm, although it is partially present in the mitochondrial intermembrane space [Fukai T. & Ushio-Fukai M., 2011]. SOD2, a homotetrameric enzyme containing one Mn³⁺ ion (in the resting state) per monomer as a cofactor, is localized exclusively in the mitochondria and exerts a pivotal role in the defense against superoxide radicals produced by electron transport chain complexes, the major source of ROS in cells.

In this work, we firstly address the iron-binding properties of the mature human frataxin (FXN⁹⁰⁻²¹⁰) and its D122Y variant, the only pathological point mutation identified so far in the iron-binding region. We used the Site-Directed Spin Labelling (SDSL) technique coupled to electron paramagnetic resonance (EPR), a powerful tool which, as described in detail in Part I (*Chapter 5*) of this Thesis, is generally used for detecting changes in structure, dynamics, and oligomerization in proteins; taking advantage of SDSL-EPR, we got information on the frataxin structural changes following the ferrous/ferric iron-binding using two different spin labels, MTSSL and the reduction-resistant M-TETPO, to work with Fe(III) and Fe(II), respectively.

Based on the previous *in vitro* work by Han *et al.* on the interactions between yeast FXN and SODs [Han T.H.L. *et al.*, 2019], we explored the potential interaction between human mature FXN and human SOD2 using the same spectroscopic approach. Since human and yeast FXN show a good degree of homology, the interaction is likely to be conserved, and we use human proteins not only to confirm the interaction but also to gain a deeper molecular insight into the interface of the complex with a combined *in vitro* and *in silico* approach. The EPR investigation were completed by endogenous tryptophan fluorescence experiments and, based on the experimental data, we performed a guided protein-protein docking between FXN and SOD2 to identify the interface region and suggest a possible structure for the FXN/SOD2 complex.

Materials & Methods

Materials

The spin label MTSSL ((1-Oxyl-2,2,5,5-tetramethyl- Δ^3 -pyrroline-3-methyl) Methanethiosulfonate), was purchased from Toronto Research Chemicals. M-TETPO (1-Oxyl-3-(maleimidomethyl)-2,2,5,5-tetraethyl-1-pyrrolidine) was kindly provided by Prof. Gérard Audran and Prof. Sylvain R.A. Marque of Institut de Chimie Radicale de Aix-Marseille University, France. A comparison between the chemical structures of MTSSL and M-TETPO is reported in *Figure 2.1*.

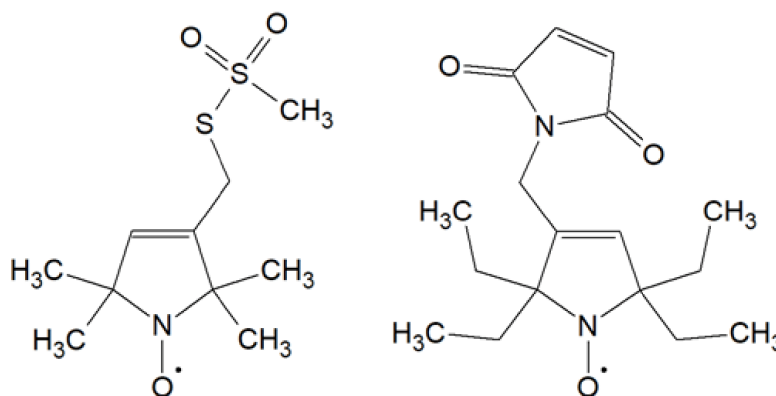


Figure 2.1. Chemical structures of the nitroxide spin labels used in this work. On the left, MTSSL; on the right, M-TETPO. M-TETPO is resistant to reduction thanks to a good steric hindrance formed by ethyl groups on the pyrroline ring.

Unless otherwise specified, the buffer composition for spectroscopic experiments was 25 mM HEPES (pH 7.0), 50 mM KCl. Ferrous iron solutions were prepared in anaerobic atmosphere in degassed deionized water slightly acidified starting from (NH₄)₂Fe(SO₄)₂·6H₂O (Mohr's Salt, >99% Fe²⁺ content). Ferric iron solutions were prepared from FeCl₃·6H₂O in HCl at pH = 0.8. Ficoll® PM 70 stock solution was prepared dissolving the polymer in degassed buffer at a 35% w/w concentration, under anaerobic atmosphere. 1,10-Phenanthroline monohydrate (PHEN) was dissolved in dilute buffer. Human mitochondrial superoxide dismutase (SOD2) was purchased as a His-tag recombinant protein from Technical Novusbio; the SOD2 buffer was 20 mM Tris HCl (pH 8.0) and

containing 20% glycerol. Unless otherwise specified, chemicals were purchased from Merck and used without further purification.

Heterologous Expression and Purification of Human Wild Type and Frataxin Mutants

A plasmid containing the coding sequence of human wild type (WT) mature FXN, *i.e.* pET-9b/FXN⁹⁰⁻²¹⁰, was kindly provided by Prof. Javier Santos of the Departamento de Química Biológica of University of Buenos Aires, Argentina. The plasmid pET-9b (Novagen) confers resistance to kanamycin and contains the phage T7 promoter; the coding sequence for frataxin has been inserted using BamHI and NdeI restriction sites. In order to select bacteria transformed with the plasmid, kanamycin (Sigma-Aldrich) has been added in concentration 50 µg/mL to the culture media. Frataxin mutants were obtained through site-directed mutagenesis with the QuickChange® II Site-Directed Mutagenesis Kit (from Agilent Technologies) using as template the pET-9b/FXN⁹⁰⁻²¹⁰ plasmid and the couples of primers listed in *Table 2.1*, with the exception of frataxin mutants H177C and S202C that were obtained with Q5® Site-Directed Mutagenesis Kit (from New England Biolabs) and the couples of primers listed in *Table 2.1*. Each sequence was checked by DNA sequencing (at GATC Biotech, Germany).

E. coli BL21 (DE3) cells (genotype F⁻, ompT gal dcm lon hsdSB (rB-mB-) λ, (DE3 [lacI lacUV5-T7 gene 1 ind1 sam7 non5])) were chemically transformed with the plasmid of interest, and positive clones were selected by antibiotic resistance. For the transformation, about 2-5 µL of the plasmid has been added to competent bacteria and the suspension was incubated for 30 minutes in ice. To ensure the internalization of the DNA, heat shock was performed incubating the solution for 1 minute at 42°C and transferring it on ice for 1 minute. After the addition of 300 µL of Luria Bertani liquid medium (LB), the culture has been incubated for one hour at 37°C under shaking. Then, the bacteria have been plated in solid media LB + Agar (with kanamycin 50 µg/mL) and incubated overnight at 37°C to promote the bacterial growth. Bacteria have been then inoculated in LB media with kanamycin 50 µg/mL, starting from a small-volume pre-culture previously grown to saturation at 37°C overnight. The bacterial culture was incubated under shaking at 37°C until reaching an optical density at 600 nm (OD_{600nm}) between 0.4 and 0.6. Expression of the wild-type and mutant proteins was induced by adding 1 mM isopropyl-β-thiogalactopyranoside (IPTG) in LB medium and incubating

the bacteria cultures at 30°C overnight under constant stirring. Cells were then harvested by centrifugation at 5000 × g and 4°C for 20 min, resuspended in lysis buffer (25 mM HEPES, pH 7.0) supplemented with protease inhibitors (1 µg/mL pepstatin A, 1 µg/mL leupeptin, 1 µg/mL antipain, 100 µM PMSF) and lysed by French Press (from Constant Systems Limited, Daventry, UK). The supernatant fractions were isolated from cell debris by centrifugation at 17 000 × g and 4°C for 15 min and incubated with 10 mM EDTA for 1 hour at 4°C under gentle agitation.

Proteins were purified by combining Anionic Exchange Chromatography (AEC) and Size Exclusion Chromatography (SEC). The first chromatographic step was performed using a cationic DEAE (Diethylaminoethyl) Sepharose column using 25 mM HEPES (pH 7.0) as the buffer of equilibration and 25 mM HEPES (pH 7.0), 1 M KCl as the elution gradient buffer. The fractions containing frataxin, as assessed by SDS PAGE, were collected, pooled together, concentrated by centrifugal filters (Amicon Ultra Centrifugal Filter, 3000 NMWL, from Merck Millipore, Burlington, MA, USA), and purified by SEC. For FXN mutants containing cysteines, incubation with 1 mM of dithiothreitol (DTT) was performed for 1 h at 4 °C after cationic exchange.

The second purification step was performed on a Superdex 200 GL 10–300 column (from GE Healthcare, Chicago, IL, USA) equilibrated in a buffer containing 25 mM HEPES (pH 7.0) and 50 mM KCl. To estimate the molecular weight of the protein samples, the column was equilibrated in the same buffer and calibrated with the standards thyroglobulin (669 kDa), ferritin (440 kDa), β-amylase (200 kDa), bovine serum albumin (67 kDa), carbonic anhydrase (29 kDa), and cytochrome *c* (12 kDa). The eluted fractions containing frataxin proteins were finally pooled together and the molar concentration of the protein samples was determined spectroscopically with an UV-Vis spectrophotometer (Perkin Elmer Lambda Bio-40) using $\epsilon_{280\text{nm}} = 26930 \text{ M}^{-1}\text{cm}^{-1}$ for all mutants and $\epsilon_{280\text{nm}} = 28420 \text{ M}^{-1}\text{cm}^{-1}$ for those containing D122Y point mutation (as evaluated by ExPASy ProtParam tool).

For each FXN protein (wild type and mutants), expression, purification steps and integrity were checked by 15% SDS-PAGE and Coomassie blue staining (see below). *Figure 2.2A* of the next paragraph reports, as an example, the SDS-PAGE gel showing the different steps of expression and purification of recombinant human FXN⁹⁰⁻²¹⁰ wild type. Similar results were obtained with the other FXN mutants (data not shown). Purified proteins were stored at – 20°C.

Table 2.1. List of primer sequences for human mature FXN⁹⁰⁻²¹⁰ mutants used in the present work.

FXN mutant	Primer	Primer sequence
FXN_D122Y	FXN_D122Y_for	5' - GCCATACACGTTTGAGTACTATGATGTCTCCTTTGG - 3'
	FXN_D122Y_rev	5' - CCAAAGGAGACATCATAGTACTCAAACGTGTATGGC - 3'
FXN_A99C	FXN_A99C_for	5' - GAGACCACCTATGAAAGACTATGCGAGGAAACGCTGGACTC - 3'
	FXN_A99C_rev	5' - GAGTCCAGCGTTTCCTCGCATAGTCTTTCATAGGTGGTCTC - 3'
FXN_A114C	FXN_A114C_for	5' - CAGAGTTTTTTGAAGACCTTTGCGACAAGCCATACACGTTTGAG - 3'
	FXN_A114C_rev	5' - CTCAAACGTGTATGGCTTGTGCGAAAGGTCTTCAAAAACTCTG - 3'
FXN_T133C	FXN_T133C_for	5' - TCCTTTGGGAGTGGTGTCTTATGTGTCAAACCTGGGTGG - 3'
	FXN_T133C_rev	5' - CCACCCAGTTTGACACATAAGACACCACTCCCAAAGGA - 3'
FXN_H177C	FXN_H177C_for	5' - GGACTTGTCTTGCTTGGCCTATT - 3'
	FXN_H177C_rev	5' - CAGTTTTTCCCAGTCCAGTC - 3'
FXN_A183C	FXN_A183C_for	5' - CGGCGTGTCCCTCTGTGAGCTGCTGGCC - 3'
	FXN_A183C_rev	5' - GGCCAGCAGCTCACAGAGGGACACGCCG - 3'
FXN_H193C	FXN_H193C_for	5' - GGCCGCAGAGCTCACTAAATGCTTAAAAACCAAACCTGGAC - 3'
	FXN_H193C_rev	5' - GTCCAGTTTGGTTTTTAAGCATTTAGTGAGCTCTGCGGCC - 3'
FXN_S202C	FXN_S202C_for	5' - GGTGTACTCCTGCGACGGCGTGT - 3'
	FXN_S202C_rev	5' - AGTTTGGTTTTTAAGGCTTTAGTG - 3'

SDS-PAGE Electrophoresis and Western Blot Analysis

Protein expression, purity and integrity were assessed by SDS-PAGE and Coomassie blue staining, prior to any spectroscopic experiment reported in this work. Samples of each step of FXN expression and purification and a small aliquot of recombinant SOD2 have been solubilized in Laemmli gel sample buffer (Tris-HCl 62.5 mM, SDS 2%, glycerol 10%, β -mercaptoethanol 5%, bromophenol blue 0.1%, pH 6.8) and further denatured at 95°C for 10 min on a heating block. Samples were then loaded into precast 4-20% polyacrylamide gel (GenScript® ExpressPlus™ PAGE). The run has been done at 100 volts in Tris-MOPS-SDS Running Buffer Powder GenScript® as running buffer. At the end of the run, the

gel has been incubated with the Coomassie Brilliant Blue dye and subsequently destained using a solution of acetic acid 7.5% - methanol 10%. The correct separation and molecular weights of proteins have been estimated using a marker of molecular weight (PM2610 ExcelBand™ Enhanced 3-color High Range Protein Marker, SMOBiO Technology). For SOD2 and purified FXN proteins, an immunoblot assay has been performed to assess their identities (Figure 2.2).

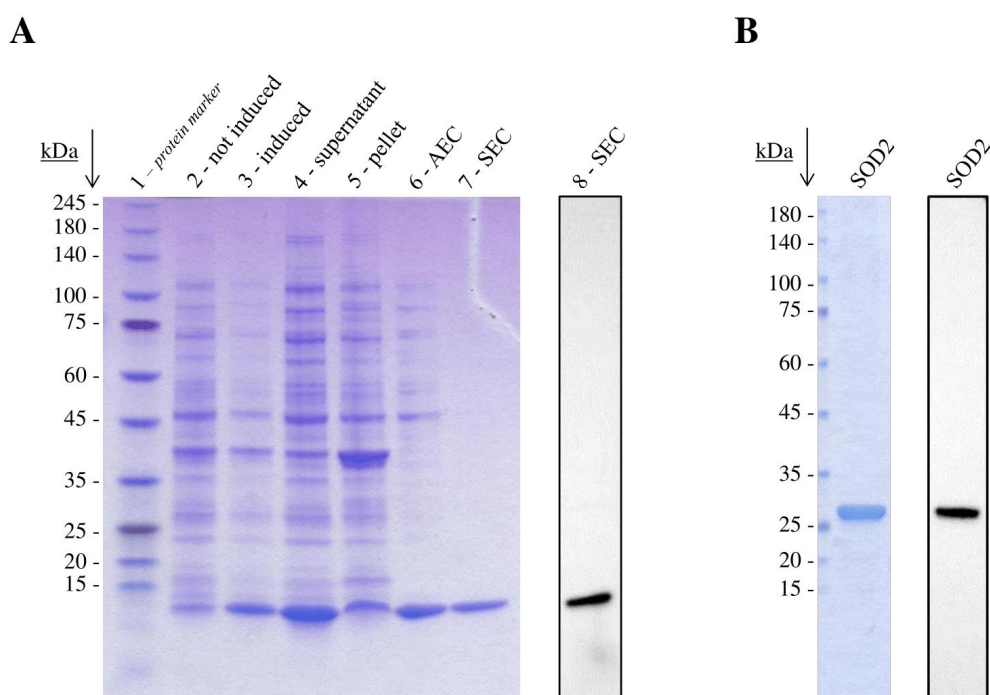


Figure 2.2. SDS-PAGE and western blotting analyses for recombinant human FXN⁹⁰⁻²¹⁰ and SOD2. **(A)** SDS-PAGE followed by Coomassie Brilliant Blue staining for the expression and purification steps of recombinant human wild type FXN⁹⁰⁻²¹⁰. Lane (1): protein marker (5 μ L). Lanes (2) and (3): bacterial culture before and after the induction with IPTG, respectively (10 μ L of sample loaded in the correspondent lane). Lane (4) and (5): soluble and insoluble fractions of the total cellular lysate (5 μ L of sample). Lane (6): protein pool after the first purification step performed by Anionic Exchange Chromatography AEC (5 μ L). Lane (7): protein pool after the second purification step performed by Size Exclusion Chromatography SEC (10 μ L). The identity of the recombinant human FXN⁹⁰⁻²¹⁰ was further confirmed by western blotting analysis using an anti-FXN antibody (lane 8). **(B)** SDS-PAGE gel (on the left) and western blot analysis (on the right) of recombinant human SOD2. The SDS-PAGE gel shows that recombinant SOD2 is present in high purity, and the western blot confirmed the identity of the protein.

After the electrophoretic run, the gel was transferred to a nitrocellulose membrane (Life Science) through a semi-dry Trans-Blot® Turbo™ Transfer System (BioRad). The membranes were then blocked with 10% milk in Tris-

buffered Saline (TBS) for 1 hour at room temperature and subsequently incubated at 4°C overnight with primary antibodies (anti-SOD2 - HPA001814, Sigma / anti-FXN 14147-1-AP, proteintech) diluted 1:1000 for anti-SOD2 and 1:500 for anti-FXN in Tris-buffered Saline with 0.05% Tween20 (TBS-T) and 5% milk. After incubation with anti-rabbit IgG HRP-conjugate antibody (A0545, Sigma Aldrich) diluted 1:20000 at room temperature for 1 hour, the protein was visualized using Immobilon® Forte Western HRP Substrate (Millipore) by Imager CHEMI Premium Detector (VWR).

Spin Labeling

Protein samples were labeled with MTSSL or M-TETPO for EPR experiments. Samples labeled with MTSSL were obtained by adding to the purified protein (at a concentration of about 150 μM) a seven-fold molar excess of spin label (dissolved in DMSO) and incubating the protein at 4 °C overnight in the dark and gentle stirring. Excess of non-ligated spin label was removed by PD10 desalting column (GE Healthcare) using 25 mM HEPES (pH 7.0), 50 mM KCl as final buffer. For the experiments with Fe^{2+} , in order to avoid possible oxidation of iron, anaerobic conditions have been adopted in the labeling with M-TETPO and all steps were performed under a glove box (MBRAUN MB 200B).

For the labeling with M-TETPO, purified proteins (at a concentration of 50 μM) were previously incubated with DTT in a molar ratio of 1:100 at 4 °C for 30 min in slow agitation. The excess of DTT was removed from the samples by PD10 desalting column (GE Healthcare) using 25 mM HEPES (pH 7.0) and 50 mM KCl as elution buffer. Proteins were labeled with a tenfold molar excess of M-TETPO (dissolved in acetonitrile) and incubated at 4 °C for 2 hours in the dark and slow agitation. Labeled protein samples were concentrated by centrifugal filters (Amicon Ultra Centrifugal Filter, 3000 NMWL, from Merck Millipore, Burlington, MA, USA) and the excess of spin label was then removed by gel filtration using a Superdex 200 GL 10 300 column (from GE Healthcare) and 25 mM HEPES (pH 7.0), 50 mM KCl as elution buffer. MTSSL/M-TETPO-labeled proteins were finally concentrated by centrifugal filters to a volume suitable for EPR spectroscopic analysis, and their concentration determined by UV-Vis spectroscopy as previously described.

Labelled proteins were stored at -80°C and in anaerobic conditions for those labelled with M-TETPO.

EPR Spectroscopy

EPR spectra were recorded on an ELEXSYS E580 spectrometer equipped with a SHQ cavity, both from Bruker, Germany. The experiments with Fe²⁺ and Fe³⁺ were performed at room temperature, using the following parameters: microwave frequency 9.87 GHz, microwave power 10 mW (attenuation 12 dB), sweep width 150 mT, center field 352 mT, conversion time 164 ms, time constant 82 ms, modulation amplitude 1.6 mT, 1024 points, 3–25 averages (depending on protein concentration). Samples were prepared thoroughly mixing 32 µL of Ficoll PM70 stock solution (or buffer when needed), 7 µL of protein stock solution, and 1 µL of Fe²⁺ or Fe³⁺ solution; the resulting solution was put in glass capillary (internal diameter 0.8 mm) and measured under nitrogen gas flow. The final protein concentration was typically 50 or 10 µM for Fe²⁺ or Fe³⁺ respectively, save for when differently stated. The different FXN: Fe²⁺ or Fe³⁺ molar ratios were prepared from an appropriate dilution of a concentrated stock solution.

The experiments with SOD2 were performed at room temperature, using the following parameters: microwave frequency 9.86 GHz, microwave power 19 mW (attenuation 9 dB), sweep width 150 mT, center field 351.4 mT, conversion time 164 ms, time constant 82 ms, modulation amplitude 1.6 mT, 1024 points, 25 averages. Samples were prepared thoroughly mixing 18 µL of SOD2 buffer or SOD2 protein stock solution (both in 20% v/v glycerol) with 2 µL of FXN stock solution for a final FXN concentration of 10 µM; the resulting solution was put in glass capillary (internal diameter 0.8 mm) and measured under nitrogen gas flow. The experiments testing the effect of Fe³⁺ on the interaction between FXN and SOD2 were performed adding 1 µL of Fe³⁺ stock solution to the EPR samples containing FXN and SOD2.

Simulation of EPR Spectra

The simulation of the EPR spectra allows getting quantitative information on the mobility of the spin label and eventually pointing out the presence of multiple components. To perform the simulations, it is necessary to know or estimate the nitroxide g-tensor (*g*) and hyperfine tensor (*A*) and then adopt a model of the spin label motion based on the stochastic Liouville equation, Microscopic Order Macroscopic Disorder (MOMD) being the one used most often [Budil D.E. *et al.*, 1996]. As described in Part I (*Chapter 5*), the MOMD model allows to describe the

spin label mobility in terms of the diffusion tensor \mathbf{D} and the order parameter S . The mobility is often discussed in terms of the rotational correlation time τ_c , which is derived from the diffusion tensor. To perform the simulations, we used the MultiComponentEPR827.vi program by Christian Altenbach. The program is written in LabVIEW (National Instruments) and can be freely downloaded from the following website: <http://www.biochemistry.ucla.edu/Faculty/Hubbell/>.

Fluorescence Spectroscopy

Fluorescence experiments were performed on a FLS 1000 UV/Vis/NIR photoluminescence spectrometer by Edinburgh Instruments with a 450 W Xenon Arc lamp for excitation at 285 nm and a PMT-980 detector. The Peltier controlled holder allowed measuring at 288 K under stirring. The sample compartment was under constant nitrogen flow to avoid condensation on the windows and keeping an anaerobic atmosphere. Experiments were conducted using a fluorescence cuvette (117104F-10-40 from Hellma, Mülheim, Germany) with 10 × 4 mm optical path length and gas tight screw cap with a silicon septum for addition of the ferrous/ferric iron solutions via a gas tight microsyringe (from Hamilton Company, Reno, NV, USA) under anaerobic atmosphere. For the experiments with iron (Fe^{2+} and Fe^{3+}), FXN proteins were used at 1.4 μM concentration and the buffer was 25 mM HEPES (pH 7.0), 50 mM KCl. The titration curves of FXN with Fe^{2+} have been analyzed according to the method reported in [Sawyer W.H. & Winzor D.J., 1999]. For the fluorescence experiment with SOD2, the buffer was a mix of the SODs buffer (910 μL of 20 mM TRIS-HCl, pH 8.0) and FXN buffer (90 μL of 25 mM HEPES, pH 7.0, 50 mM KCl) to mimic the composition of the buffer in EPR experiments. The final concentrations of the proteins were: FXN, 1.4 μM ; SOD2, 1.9 μM .

Circular Dichroism (CD) Spectroscopy

CD measurements were performed with a Jasco J-1500 spectropolarimeter. Experiments were performed at 298 K using a Jasco PTC-423 Peltier cell holder connected to a Jasco PTC-423S Peltier controller. Far-UV CD spectra were collected using a cylindrical cell (121-0.20-40 from Hellma) with 0.2 mm optical path length using 50 μL of protein solution. Data were acquired at a scan speed

of 20 nm/min and at least three scans were averaged. FXN proteins were used at a concentration of 50 μM , in a 0.5 mM Tris-HCl pH 7.0, 1 mM KCl buffer. For experiments with Fe^{2+} , the cuvette was filled and sealed under anaerobic atmosphere in a glove box; the compartment of the CD spectropolarimeter is anaerobic since it is constantly under nitrogen flow.

Protein-Protein Docking

The molecular docking simulations were performed using three docking software packages freely available as webservers, all of them allow the input of one or more residues to be considered for the interface: ClusPro [Kozakov D. *et al.*, 2017], ZDOCK [Pierce B.G. *et al.*, 2014], GRAMM-X [Tovchigrechko A. & Vakser I.A., 2006], PatchDock [Schneidman-Duhovny D. *et al.*, 2005; Andrusier N. *et al.*, 2007]. The generation of the docking poses, the potential energy function that evaluates the energy of each docking pose, and the additional steps performed to rank the final docking poses all depend on the individual program, for the details we refer to the relative references. ZDOCK, GRAMM-X, and ClusPro are based on an FFT approach to probe a fine grid for the generation of the docking poses. PatchDock adopts a different approach to accelerate the generation of the possible docking poses, matching the surface of the two proteins based on geometric complementarity. All programs perform additional steps to score the docking poses, each characterized by a different function. Therefore, to compare the results, the top solutions of each program were pooled together and re-ranked using a common scoring function.

Among the different possibilities, we chose to adopt CONStrank, a freely available webserver that allows to easily score at the same time the solutions from all programs, without only minimal formatting on the output files [Oliva R. *et al.*, 2013; Vangone A. *et al.*, 2013; Chermak E. *et al.*, 2015]. The re-ranking is based on the frequency of inter-residue contacts that appear in the solutions. Visualization, analysis, and plotting of the docking models were performed using the UCSF Chimera software, developed by the Resource for Biocomputing, Visualization, and Informatics at the University of California, San Francisco, with support from NIH P41-GM103311 [Pettersen E.F. *et al.*, 2004].

Results

Structural Remarks, Choice of Labelling Sites and Molecular Dynamics of Frataxin

The physiological role of human FXN is still uncertain, as mentioned in the introduction, but its ability to bind iron in its ferrous and ferric oxidation states, along with other ions, seems to be a key part of its function. The iron-binding region of WT human FXN and that of its pathological variants has been previously studied [Huang J. *et al.*, 2008; Bellanda M. *et al.*, 2019]: FXN uses Asp and Glu residues to bind iron via chelation by carboxylate groups. The long α -helix, located towards the N-terminal portion of the mature protein, as well as the following loop region, are rich in negatively charged residues and constitute the main iron-binding region. FXN-D122Y is the only pathological variant currently known that carries a mutation in the iron-binding region (shown in brown in stick representation in *Figure 2.3*); in a previous work, we showed that this mutation affects the conformation of the loop region and influences iron-binding [Bellanda M. *et al.*, 2019].

The spectroscopic study of human FXN reported so far have taken advantage of the three native Trp residues (W155, W168, W173) for fluorescence experiments; the Trp are shown in bright green in stick representation in *Figure 2.3*. The W155 residue is in the β -sheet region, exposed to the solution: this Trp is involved in the interface of the FXN/ISCU/NFS1 complex [Fox N.G. *et al.*, 2019], and the W155R variant is one of the known pathological mutations [Galea C.A. *et al.*, 2016]. The other two Trp are spatially close together, W168 and W173 are separated by about 0.6 nm, while W155 is more distant (1.4/1.7 nm to W168/172 respectively); W168 is partially exposed to the solution, while W173 is buried. The fluorescence probably comes from one or two of them since they are very close to each other and homo-FRET (Fluorescence Resonance Energy Transfer) can easily occur. Mature FXN has no native cysteine residues, and thus for SDSL-EPR studies, cysteine mutants must be designed and expressed to place the spin label in the desired position. Five protein sites (namely A99, A114, T133, H183, A193, see *Figure 2.3*) were chosen with the aim of mapping possible changes in the protein structure and dynamics upon ferrous/ferric iron addition, probing the response of different protein regions.

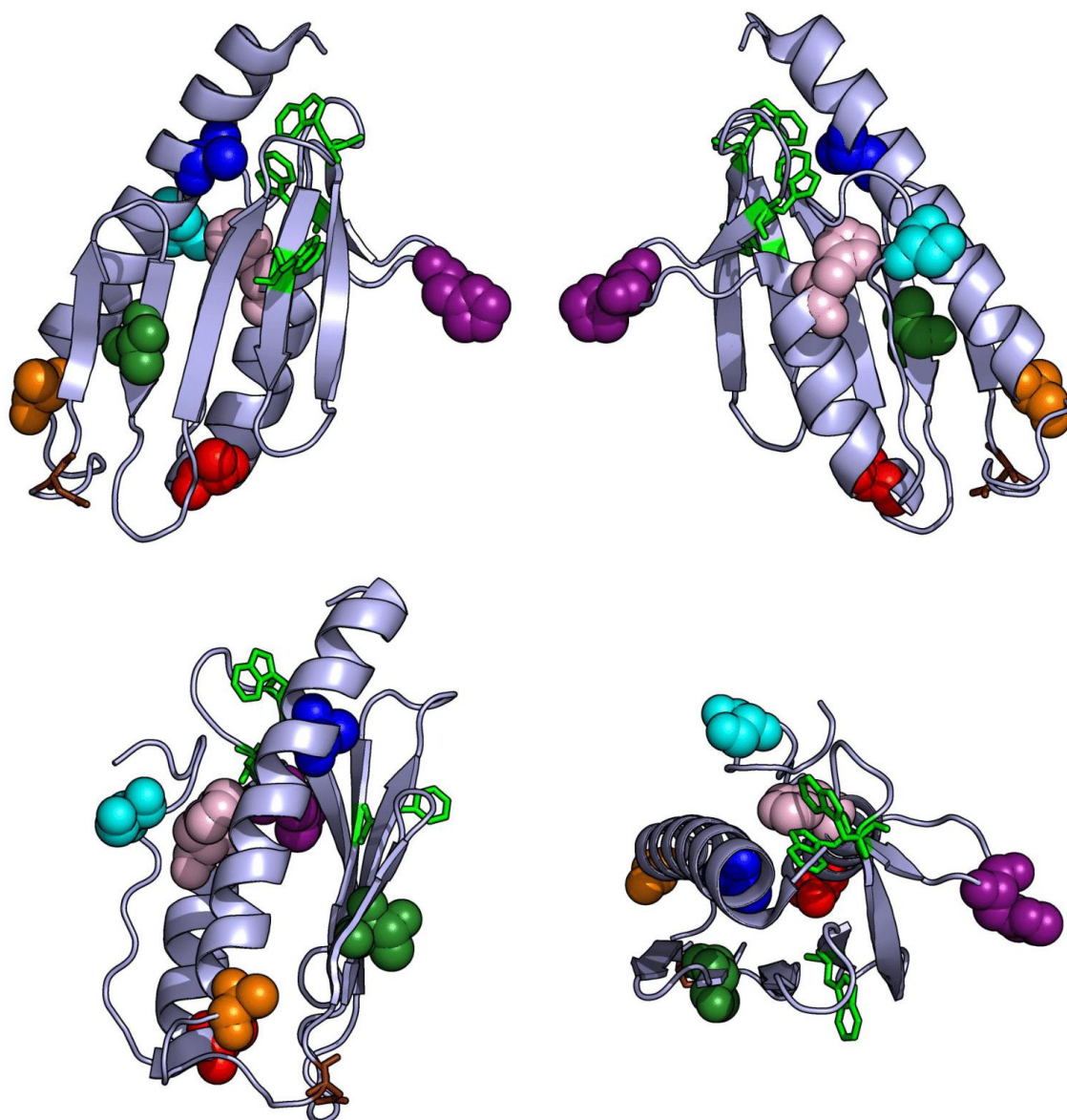


Figure 2.3. Structure of human mature FXN viewed from different angles. The three native Trp residues are shown in stick representation and colored in bright green. The D122 residue is shown in stick representation and highlighted in brown. The spin labelling sites - A99 (blue), A114 (dark orange), T133 (dark green), H177 (deep purple), H183 (pink), A193 (red), S202 (cyan) - are shown in sphere representation. The structure figures were elaborated with PyMol using PDB ID: 1EKG for human mature frataxin.

The A99 site is a buried site located at the beginning of the long α -helix, close to the iron-binding region; A114 is close to iron-binding sites and located to the end of the long α -helix; T133 belongs to the β -sheet region involved in the interaction with the complex with ISCU/NFS1 [Fox N.G. *et al.*, 2019]; H183 is located at the beginning of the second α -helix, not involved either in the iron-binding or the

complex with ISCU/NFS1; A193 is located at the end of the second α -helix, spatially close to the iron-binding region. These sites have been individually mutated to Cys for the subsequent coupling reaction with nitroxide spin probes. For its particular position, the A114 site has been investigated by SDSL-EPR both in wild type frataxin and in the pathological variant D122Y. It is worth to note that the A99 position has a very limited solvent accessibility; therefore, it showed low labeling efficiency (about 10%) and was thus viable only for the analysis with Fe^{2+} at higher concentration.

The same FXN mutants were also used to investigate the possible interaction between FXN and SOD2; for this analysis, we produced two additional mutants to map the loop region between the β -sheet and the short α -helix (*i.e.* H177C) and the C-terminal portion of the protein (*i.e.* S202C) (in *Figure 2.3*, H177 and S202 are highlighted in deep purple and cyan, respectively). The local mobility of the residues, together with the tumbling of the protein, is reflected in the lineshapes of the EPR spectra of the spin probes. Then, the internal motions of the WT frataxin were studied by all-atom molecular dynamics (MD) simulations (nanosecond timescale) to investigate the mobility of the labeled positions. This analysis was kindly performed by Prof. Javier Santos of the University of Buenos Aires. The results are reported in *Figure 2.4*, showing the root mean square fluctuations (RMSF) along the protein chain; the mutated sites are colored using the same color code as in *Figure 2.3*. The MD simulations clearly show that the H177 and S202 positions are more mobile than the rest of the labeled positions. Furthermore, H177 is part of a flexible stretch of the protein.

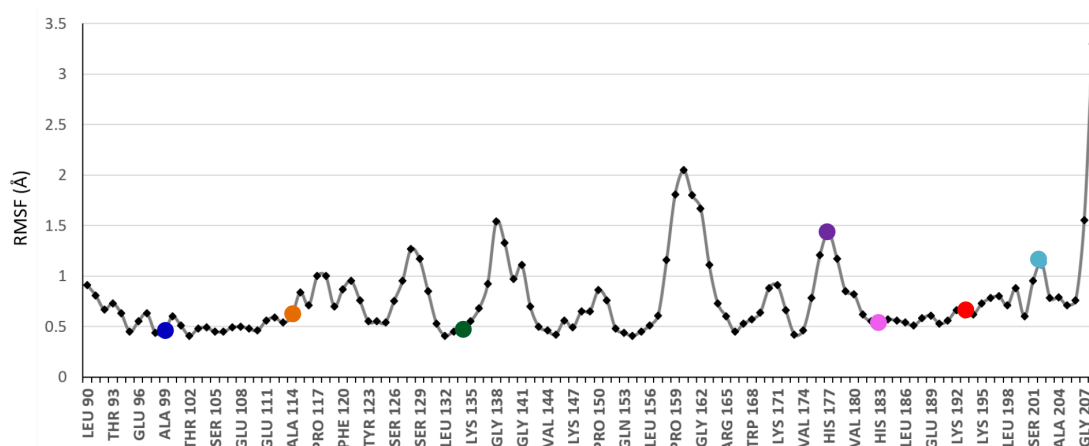


Figure 2.4. Root-mean-square fluctuations (RMSF) along the protein chain determined from the MD simulations on WT FXN⁹⁰⁻²¹⁰. The spin labelling sites are shown as colored dots: A99 (blue), A114 (dark orange), T133 (dark green), H177 (deep purple), H183 (pink), A193 (red), S202 (cyan).

Since FXN is a small protein (MW = 13.64 kDa), its reorientation in aqueous solutions, at room temperature, is very rapid. This motion would mask any local contribution to the EPR spectral lineshape proper of the spin label; therefore, as described in detail in Part I (*Chapter 5*), it is necessary to slow down the protein tumbling (quantified by the rotational correlation time, τ_c) performing the EPR experiments in viscous solution. Ficoll PM70, a synthetic glucose polymer, at a 28% w/w concentration, was suggested as one of the best thickening agents [López C.J. *et al.*, 2009]. We calculated the FXN rotational correlation time τ_c , on the basis of the protein structure, at the viscosity of a buffer solution ($\eta_{\text{Water}} = 8.94 \times 10^{-4}$ Pa·s) and at the viscosity of a 28% w/w Ficoll solution ($\eta_{\text{Ficoll}} = 1.92 \times 10^{-2}$ Pa·s) using the program by M. Zerbetto *et al.* [Barone V. *et al.*, 2009]: in buffer, $\tau_{c, \text{Water}}$ was 5.6 ns, which is on a timescale comparable with that of the motions of the spin label side chain; in Ficoll, $\tau_{c, \text{Ficoll}}$ was 122 ns, slow enough to observe an EPR spectral shape influenced exclusively by the spin probe and backbone mobility, rather than the protein tumbling.

Human Frataxin & Iron

- EPR Spectra of FXN Interacting with Fe³⁺

The EPR spectra of FXN mutants in a 28% w/w Ficoll solution, were recorded at increasing protein:Fe³⁺ molar ratios and at different FXN concentrations, to explore both the effects of iron-binding and the influence of protein concentration on the binding equilibrium. The spectra of all mutants at 10 μM concentration, labelled with MTSSL, are reported in *Figure 2.5*. As previously assessed, mutant A99C showed very limited labeling efficiency (about 10%) that made it impossible to record EPR spectra at 10 μM concentration.

In the absence of iron, each mutant shows a characteristic spin label mobility proper of the site, which confirms that the protein molecular tumbling has been slowed enough by the Ficoll solution; this allows distinguishing spectral differences due to the specific local motion of the spin probe. Among these mutants, A193C showed the least restrained mobility, suggesting that the secondary structure of the WT FXN is not very rigid at the edge of its second α -helix. On the contrary, A114C, which is in a similar position at the end of FXN long α -helix, has a more restrained mobility indicating a stable helical terminal.

The other two labelled sites show a mobility that is intermediate between those two; in the A114C-D122Y mutant, MTSSL shows instead minimal differences in the spectra compared to the WT form.

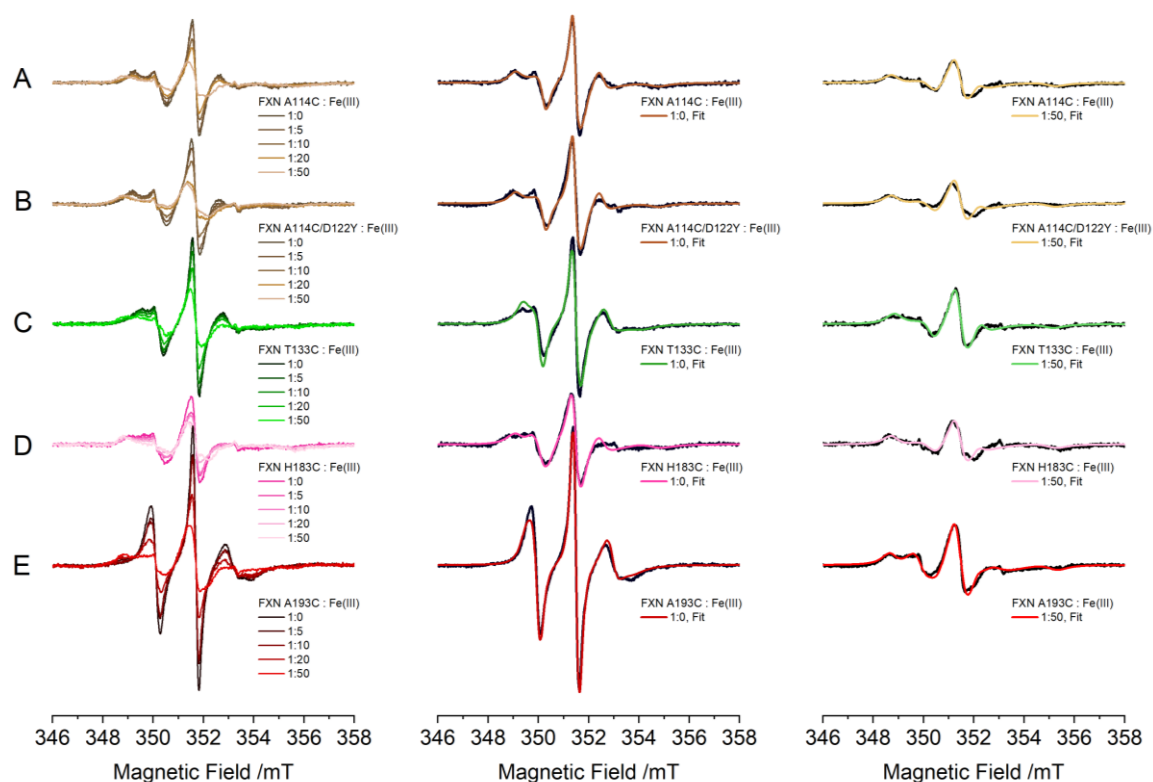


Figure 2.5. EPR spectra of FXN mutants at increasing protein: Fe^{3+} molar ratios from 1:0 to 1:50; protein concentration 10 μM , MTSSL label. The colors are the same of the positions highlighted in figure 2.3: (A) A114C – dark orange; (B) A114C/D122Y – dark orange; (C) T133C – dark green; (D) H183C – pink; (E) A193C – red. Central & Right panels: EPR spectra (black) and simulations (color) of FXN mutants at protein: Fe^{3+} molar ratios 1:0 (central) and 1:50 (right).

Upon addition of increasing amounts of Fe^{3+} , all the labelled positions show a progressively restrained mobility both for the WT and the D122Y variant. In fact, the spectral broadening proceeds until an almost complete spin label immobilization is observed, at all labelled sites, as shown by the spectra at a FXN: Fe^{3+} 1:50 ratio in Figure 2.5. The onset of the immobilization, at a protein concentration of 10 μM , can be observed after the addition of about 5 equivalents of ferric iron. The rotational correlation time, determined from the simulations of the spectra, increases more than 2-fold going from a 1:0 to a 1:50 ratio and, concurrently, the order parameter increases for all positions as shown in Table

2.2: this indicates that the motion of the labelled sites becomes slower and more constricted, consistent with the formation of a new interfacial contact hindering the probe mobility.

Table 2.2. The rotational correlation times of the different FXN labelled positions in 28% w/w Ficoll solution. The g tensor principal components are: $g_{xx} = 2.0088$, $g_{yy} = 2.0070$, $g_{zz} = 2.0030$. The hyperfine tensor principal components are: $A_{xx} = 0.79$ mT; $A_{yy} = 0.54$ mT; $A_{zz} = 3.68$ mT. The spectrum of A193C at a FXN:Fe³⁺ 1:50 ratio is characterized by two components. In the table, for each component, are reported the orientation angle β_D and the order parameter S .

Position	FXN:Fe ³⁺ 1:0		FXN:Fe ³⁺ 1:50	
	S	τ_c	S	τ_c
A114C	0.44	0.7 ns	0.53	5.3 ns
A114C / D122Y	0.44	0.7 ns	0.53	5.3 ns
T133C	0.36	0.9 ns	0.53	3.8 ns
H183C	0.44	3.9 ns	0.53	8.4 ns
A193C	0.44	1.8 ns	0.53	3.6 ns
			0	2.2 ns

The immobilization of the protein depends not only on the protein:iron ratio, but also on the absolute protein concentrations. The dependence of the immobilization on protein concentration and pH has been explored using the A193C mutant, that has the highest sensitivity to immobilization since it is the one that changes its mobility most dramatically; the zoom of the left shoulders of the EPR spectra are shown in *Figure 2.6A*. It is worth to note that ferric iron at neutral pH is not present in solution as a free isolated ion, and the main species are colloidal oxo-hydroxo suspensions. The formation of these complexes upon addition of Fe³⁺ stock solution has a very strong acidifying effect on the sample solution, and even small additions of Fe³⁺ lead to a drop in pH. Therefore, we checked the effective pH as a function of Fe³⁺ concentration, as shown in *Figure 2.6B*, right axis: in our buffering conditions, nominal Fe³⁺ concentrations of 1 mM and above steadily drop the pH below 6.5. Since FXN isoelectric point is IP = 4.94, Fe³⁺ concentrations of 1.5 mM and above will cause protein aggregation by acidic

denaturation rather than by a specific iron effect. Note that EPR, fluorescence and CD experiments detailed in the text are all performed at $\text{pH} \geq 6.8$.

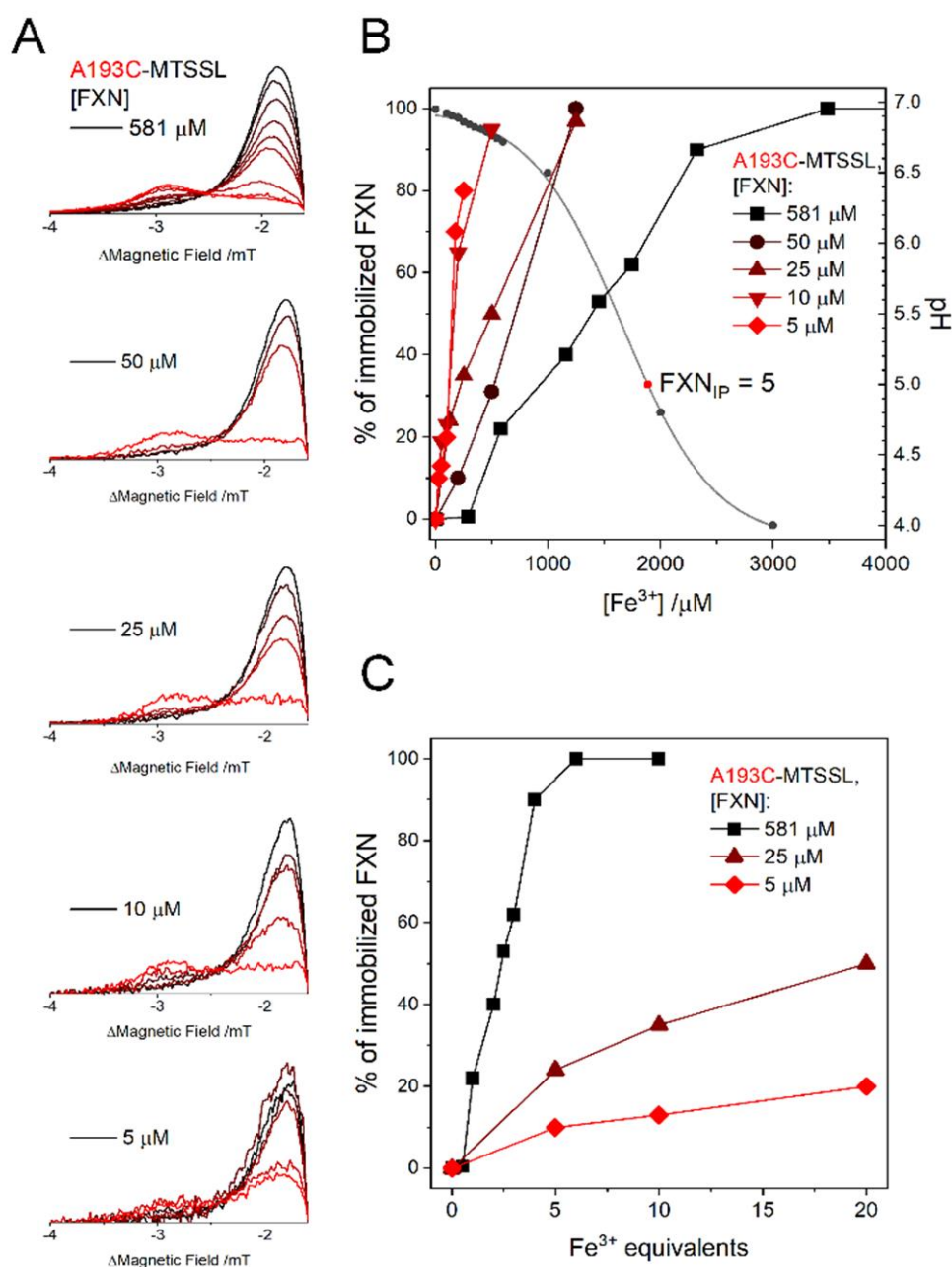


Figure 2.6. Effects of concentration and pH on FXN immobilization. (A) From top to bottom, the left shoulder of the EPR spectrum of the A193C mutant labelled with MTSSL at progressively lower protein concentrations, the lighter the color the higher the FXN: Fe^{3+} ratio. (B) The percentage of immobilized protein (left axis, big dots) or the pH (right axis, small dots) vs the nominal ferric iron concentration for different protein concentrations (C) the percentage of immobilized protein vs the FXN: Fe^{3+} molar ratio for three protein concentrations.

The gradual spectral changes may be analyzed and reconstructed as combination of two “pure” contributions: 1) the initial, more mobile, nitroxide lineshape and 2) the final immobilized one, which does not change upon further Fe^{3+} addition. Importantly, the spectral analysis suggests that there are no further intermediate conformational states at significant concentration. The obtained percentage of immobilized protein (*Figure 2.6B*, left axis) has been plotted as a function of ferric iron nominal concentration concurrently with the effective pH of the solution (*Figure 2.6B*, right axis). Note that irrespective of the final pH value, the immobilized shape is always the same, suggesting that high amounts of ferric iron lead to a denatured and/or strongly aggregated protein. The immobilization starts at progressively lower FXN: Fe^{3+} ratios as the protein concentration gets higher, as shown by the plot in *Figure 2.6C*. At the lowest concentration that we explored, *i.e.* 5 μM , the immobilization starts at 25 μM Fe^{3+} , but the spectra are only partially immobilized (< 20%) even at a 1:20 FXN: Fe^{3+} molar ratio. Detection of the EPR spectra in buffered aqueous solution without the addition of Ficoll was also performed in labelled FXN A193C. The EPR spectra have been detected both in the absence of iron and in the presence of Fe^{3+} . In the absence of iron, the spectra show three sharp peaks in agreement with the averaging effect on the spectra exerted by the protein tumbling, due to the small size of the protein. Upon addition of Fe^{3+} , the spectral broadening occurs as it was observed for the samples in Ficoll; however, the effect is much less noticeable since the intensity is dominated by the sharper mobile component (*Figure 2.7*). Centrifugation of the sample, followed by EPR analysis of the supernatant, showed that the protein fraction that is immobilized precipitates along with the colloidal iron, leaving behind the fraction that showed no motional broadening (*Figure 2.7*).

These results confirm that Fe^{3+} addition promotes protein oligomerization [Ahlgren E.C. *et al.*, 2017], slowing down the molecular tumbling due to the bigger size of the Fe^{3+} -FXN formed complexes. Similar results were obtained in centrifugation experiments performed in Ficoll solutions (not shown), however they are less clear cut, since a density gradient is formed.

The reversibility of the immobilization effect has been checked by adding EDTA in a three-fold excess relative to Fe^{3+} to remove the bound iron ions (*Figure 2.8*). After a one-hour incubation, the amount of immobilized component decreases, suggesting that the aggregation is at least partially reversible.

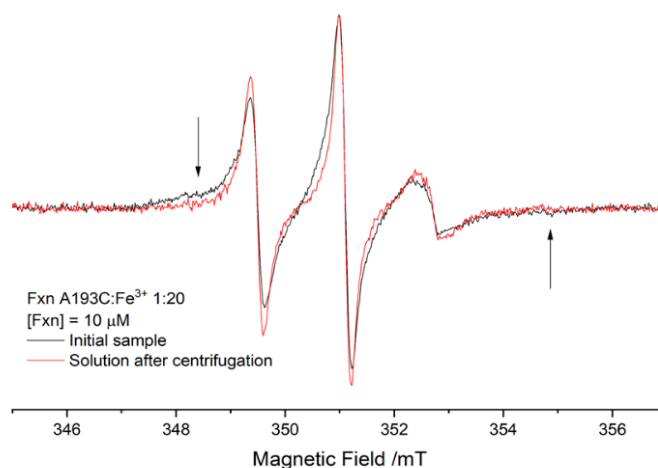


Figure 2.7. EPR spectra of FXN A193C in buffer solution at a FXN:Fe³⁺ 1:20 ratio, [FXN] = 10 μM. The figure shows the spectrum before (black) and after (red) centrifugation. The lineshape shows a partial averaging of the different components relative to the sample in Ficoll, as expected from the fast tumbling of FXN. Nevertheless, the immobilized component is visible as indicated by the arrows (black spectrum). Upon centrifugation of the sample, the EPR spectrum of the supernatant shows only the mobile component, indicating that the immobilized component has been precipitated.

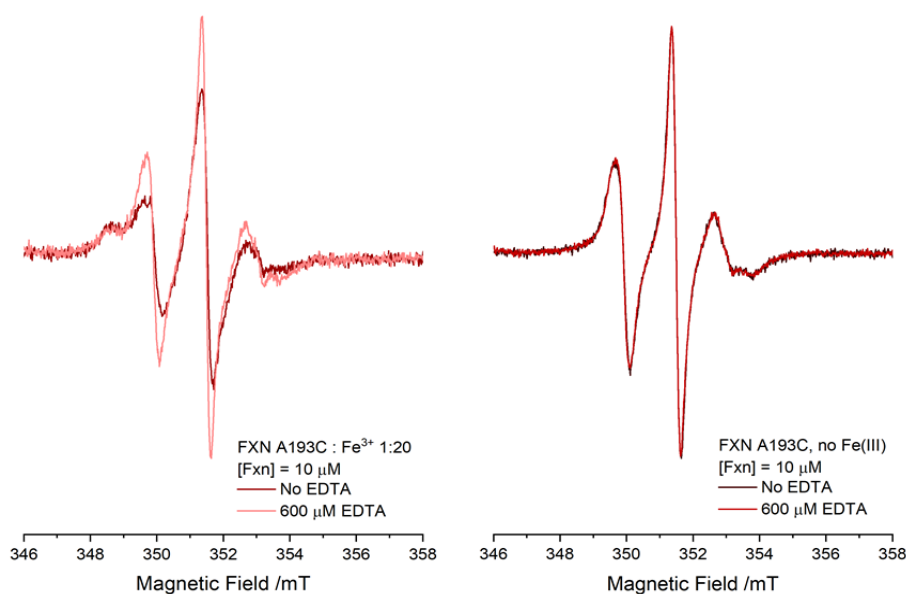


Figure 2.8. Reversibility of Fe³⁺ aggregation via chelation by EDTA. The reversibility of FXN aggregation was checked by incubating the sample with A193C at a 1:20 FXN:Fe³⁺ molar ratio, taking the EPR spectrum before (red) and after (pink) incubation of the sample with a three-fold molar excess of EDTA relative to iron (on the left). The lineshape partially reverts to the one in the absence of Fe³⁺, showing that aggregation is at least partially reversible. To confirm that EDTA does not perturb the protein, the spectra of the protein with/without EDTA in the absence of Fe³⁺ (on the right) are reported.

- EPR Spectra of FXN Interacting with Fe²⁺

EPR spectra have been collected for the different FXN mutants after addition of increasing amounts of Fe²⁺ to the samples, to investigate possible conformational changes induced by the binding of the divalent ion, which could be relevant for protein function. To prevent iron oxidation, the proteins have been prepared in strictly anaerobic conditions from the labeling stage, and samples capillaries were prepared in an anaerobic glove box and sealed with wax at both ends.

We observed a very rapid signal loss in FXN labelled with MTSSL following the addition of Fe²⁺. The reason lies in the quick reduction of the MTSSL nitroxide function to the EPR-silent nitroxylamine with concurrent oxidation of Fe²⁺ to Fe³⁺: this unwanted reaction not only results in signal loss, but also makes it impossible to separate the spectral changes induced by Fe²⁺ from those induced by Fe³⁺. For this reason, we changed the spin label to M-TETPO, a non-commercial spin label designed to be resistant to the cellular reducing environment [Karthikeyan G. *et al.*, 2018]. Indeed, we verified that M-TETPO is also resistant to the reduction by Fe²⁺ in solution, making it the ideal probe in EPR studies of Fe²⁺ binding.

The EPR spectra of FXN mutants labelled with M-TETPO in the presence of ferrous iron are reported in *Figure 2.9* (samples in Ficoll, protein concentration 50 μM). The spectra recorded at 10 μM protein concentration were identical to those reported here, except for the worse signal to noise ratio. When iron is not present, the spectra show a reduced mobility compared to FXN labelled with MTSSL, indicating that the side chain of M-TETPO has less degrees of freedom than the one of MTSSL. Unlike MTSSL, M-TETPO differentiates the A114C-D122Y mutant from the WT counterpart, since the spectra of the former reveal a faster mobility which indicates a change in the local structure of the D122Y FXN around residue 114. The difference between the labels is determined by the different conformers and mobility of their sidechain.

Once ferrous iron is added to the solution, we observe that the spectra of the sites located far from the iron-binding region are unchanged even at a 1:50 FXN: Fe²⁺ ratio (T133, H183, A193, *Figure 2.9B,D,F*), while those close to the iron-binding sites show an EPR intensity that gets progressively lower at higher iron content (A99, A114, A114-D122Y, *Figure 2.9A,C,E*). The signal loss is less marked for the D122Y pathological variant than for the WT: at a 1:50 FXN:Fe²⁺ ratio, the signal loss for A114C-D122Y (and for A99C) is 40%, while that for A114C raises to 65%.

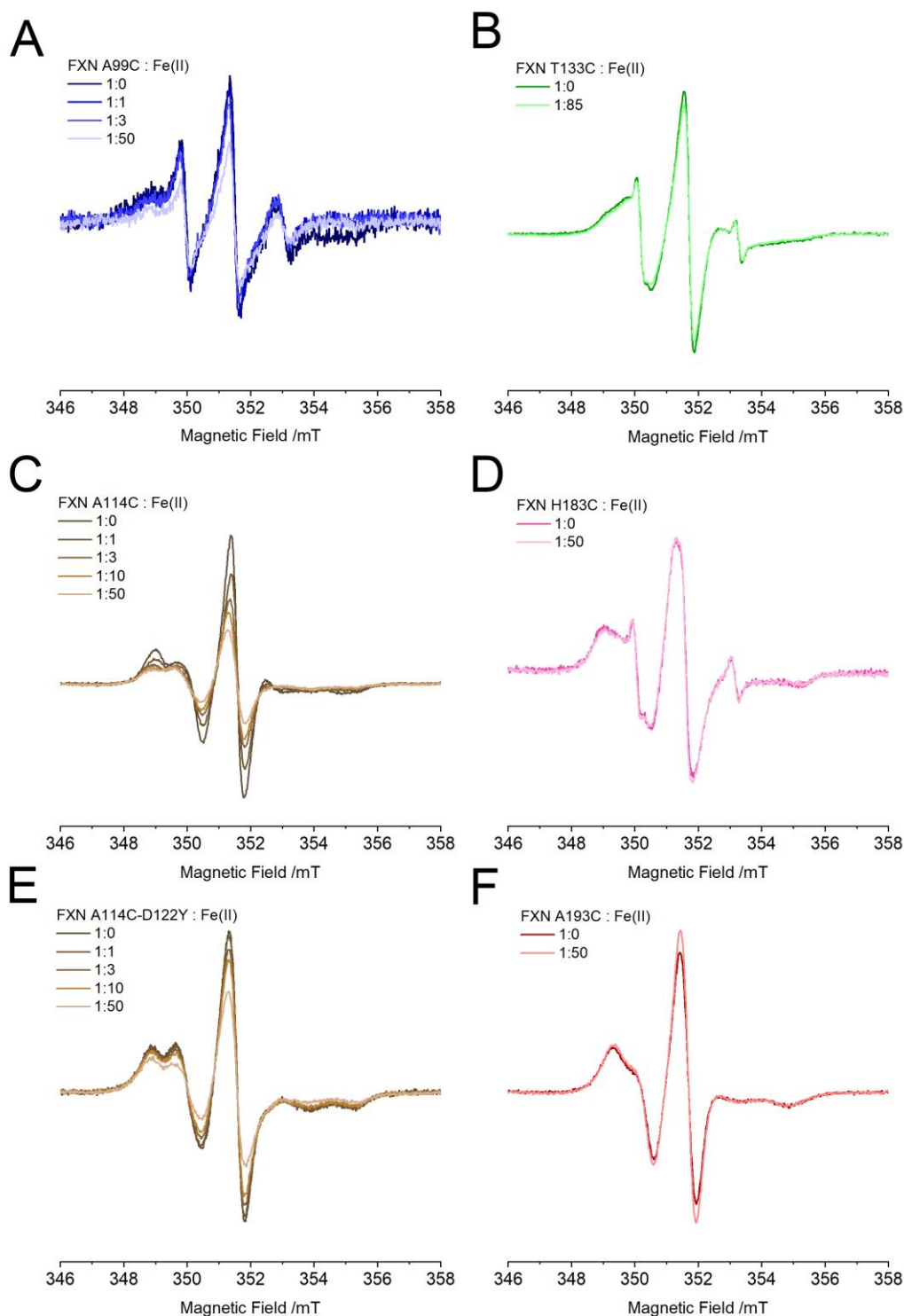


Figure 2.9. EPR spectra of FXN mutants at increasing protein:Fe²⁺ molar ratios from 1:0 to 1:50; protein concentration 50 μ M, M-TETPO label. The colors are the same of the positions highlighted in figure 2.3: (A) A99C – blue; (B) T133C – dark green; (C) A114C – dark orange; (D) H183C – pink; (E) A114C/D122Y – dark orange; (F) A193C – red.

For the A114 position, the signal loss is accompanied by a change in shape, whereas no change is observed for the A99 position: this difference arises from the intrinsic mobility of the probe sidechain in the two positions. The signal loss is independent of the presence of Ficoll (data not shown), and we verified that it is caused by a redox reaction of the M-TETPO nitroxide with Fe^{2+} as observed for MTSSL. To test this hypothesis, we removed protein-bound Fe^{2+} by treatment with 1,10-phenanthroline (PHEN), which forms a strongly colored red complex with Fe^{2+} . Treating the sample with a three-fold molar excess of PHEN relative to iron leads to quantitative removal of Fe^{2+} from FXN, as evaluated spectrophotometrically by UV-Vis under anaerobic conditions from the absorption band at $\lambda_{\text{max}} = 508 \text{ nm}$ [Brateman P.S. *et al.*, 1992]. When stripping Fe^{2+} from FXN by PHEN, the solution turns red but the EPR signal is not restored (Figure 2.10), confirming that an irreversible reduction of the nitroxide has taken place.

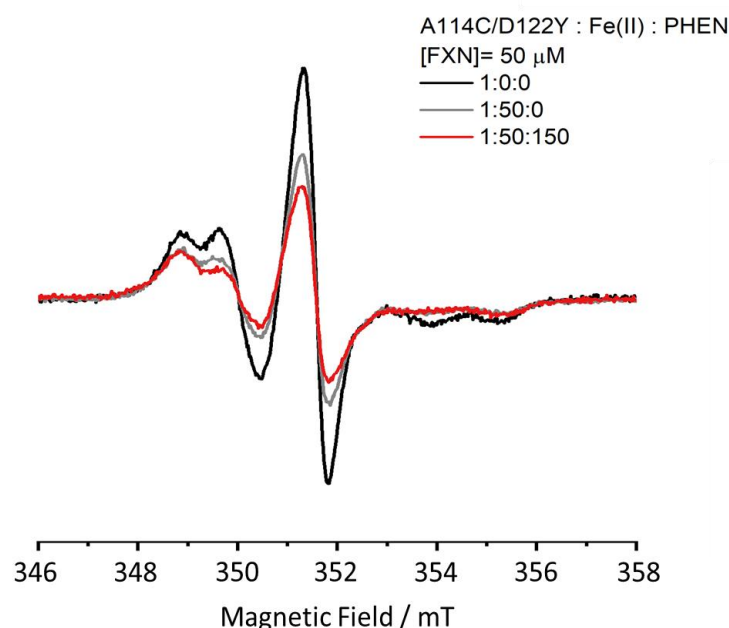


Figure 2.10. Removal of Fe^{2+} bound to FXN via chelation by PHEN. The presence of an irreversible redox reaction of the M-TETPO nitroxide with Fe^{2+} , as observed for MTSSL, via chelation of the protein-bound Fe^{2+} by treatment with 1,10-phenanthroline (PHEN) was verified. Here we report the EPR spectra of A114C/D122Y alone (black), at a FXN: Fe^{2+} 1:50 ratio (grey), and at a FXN: Fe^{2+} :PHEN 1:50:150 ratio (red); $[\text{FXN}] = 50 \mu\text{M}$. Upon PHEN addition to a sample of the A114C/D122Y mutant - 1:50 FXN: Fe^{2+} molar ratio, the spectral intensity does not recover, even though Fe^{2+} has been chelated as verified by the solution turning red.

We can then hypothesize that the signal loss is directly correlated with the presence of a nearby Fe^{2+} binding site. Indeed, signal loss does not originate from Fe^{2+} free in solution, as confirmed by the lack of effect in the three mutants labelled at positions far away from the iron-binding region. When a ferrous iron is close to the nitroxide of the spin label, the redox reduction can be favored by the closeness of the redox partners, and nearby amino-acid residues might also favor the electron transfer kinetics. The exact mechanism will be tested in the next future, nevertheless the redox reaction is a clear sign of proximity and this makes M-TETPO an interesting probe, able to detect nearby Fe^{2+} binding sites.

- *Fluorescence Spectra of FXN Interacting with Fe^{3+}*

The quenching effect upon Fe^{3+} addition to the fluorescence emission of the three Trp residues of wild type and FXN D122Y proteins was explored. We worked at low protein concentration ($[\text{FXN}] = 1.4 \mu\text{M}$) and with a focus on the sub-stoichiometric region, since, as shown by the EPR experiments reported above, aggregation starts to occur when adding more than few equivalents. The fluorescence signals and their quenching are shown in *Figure 2.11*; quenching is reported as $(F-F_0)/F_0$, where F is the fluorescence intensity at the maximum of emission and at a given amount of quencher and F_0 is the intensity in the absence of quenchers. The normalized signal shape of the WT and the FXN D122Y are identical, as expected (*Figures 2.11E,F*). In addition, the normalized emission profiles in the absence of iron and at 9.5 equivalents of iron do not show any difference neither in the position of the maxima nor in the shape of the band, indicating that the three Trp residues are equally quenched by the presence of Fe^{3+} . The quenching of Trp fluorescence by Fe^{2+} and Fe^{3+} is likely due to an energy transfer mechanism, which is a distance dependent process [*Ilari A. et al., 2005*]. Due to the short distance between Trp residues and to the homo-FRET, the observed quenching of the fluorescence could be due only to iron ions close to any of the Trp residues. The signal decreases sharply in the sub-stoichiometric region, levels off somewhat around 1.5 equivalents of Fe^{3+} and then falls off more sharply again at six equivalents and beyond. Visual inspection of the cuvette revealed no visible precipitate in the sub-stoichiometric region, but substantial precipitate already at six equivalents. It is therefore impossible to reliably assess a binding constant for Fe^{3+} with human FXN using fluorescence, due to the presence of Fe^{3+} -induced FXN aggregates (in agreement with the EPR results

reported above). The WT protein and the D122Y variant show almost no difference in the quenching profile.

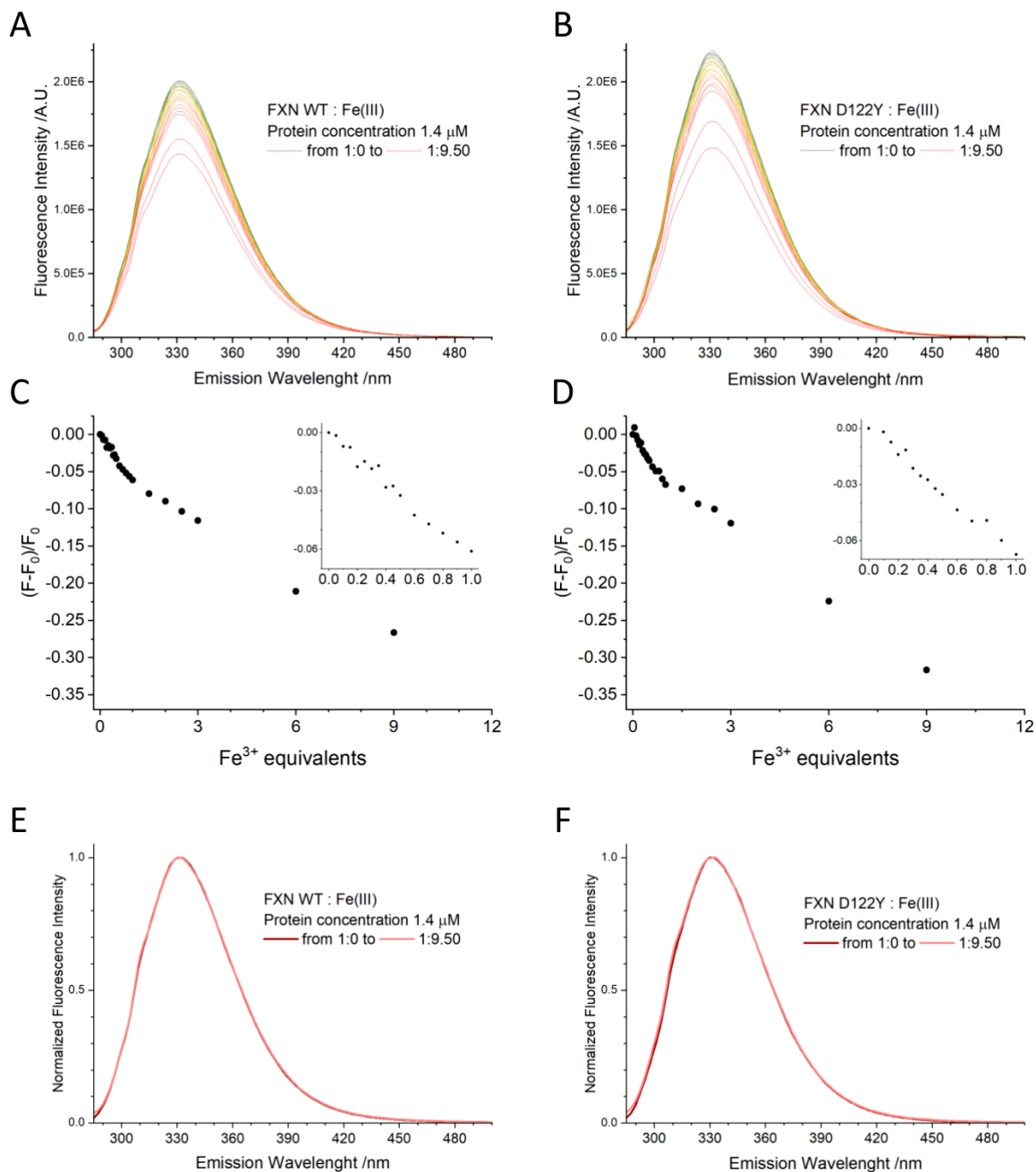


Figure 2.11. Tryptophan fluorescence spectra of WT FXN and D122Y variant at increasing amounts of Fe³⁺. Protein concentration 1.4 μM , 288 K, $\lambda_{\text{exc}} = 280 \text{ nm}$, $\lambda_{\text{max}} = 332 \text{ nm}$. (A) and (B) fluorescence of FXN WT & D122Y with Fe(III), respectively; (C) and (D) fluorescence quenching by Fe³⁺ calculated at λ_{max} for FXN WT and D122Y, respectively; in the inset, a zoom of the sub-stoichiometric region. (E) and (F) normalized fluorescence spectra of WT and D122Y FXN with Fe(III), respectively.

▪ Fluorescence Spectra of FXN Interacting with Fe²⁺

The quenching effect of Fe²⁺ addition on the fluorescence emission of WT and D122Y FXN was explored using strictly anaerobic solutions at low concentration ([FXN] = 1.4 μM) and focusing on the sub-stoichiometric region. To ensure that the Fe²⁺ is not oxidized during the experiment, both the iron stock solution and the cuvette were filled under nitrogen atmosphere and closed with silicon septa. The experimental compartment was flushed with nitrogen at all times. Fe²⁺ was injected into the cuvette through the septum using a Hamilton syringe flushed with nitrogen before any addition. The absorption of a stock solution of Fe²⁺ was checked and we found that it does not contribute significantly in the experimental conditions ($\lambda_{\text{exc}} = 280 \text{ nm}$).

The fluorescence signals and their quenching, expressed as $(F-F_0)/F_0$, are reported in *Figure 2.12*. As discussed above, the quenching by Fe²⁺ has the same mechanism as the one by Fe³⁺, *i.e.* through an energy transfer from a bound iron ion to the nearest of the three Trp residues. The normalized spectra (*Figure 2.12E,F*) show that Fe²⁺ does not alter the shape of the emission profiles even at 20 equivalents, indicating that all three Trp residues are equally quenched as for the case of Fe³⁺.

The signal decreases sharply in the sub-stoichiometric region, levels off somewhat around 2.2 equivalents of Fe²⁺, and then does not further decrease reaching a *plateau*. The absence of further quenching indicates that either Fe²⁺ populates only one binding site, or that the other binding sites are too far from the Trp to further quench them, as further discussed below. This is true only in rigorously anaerobic conditions: in a control experiment in the presence of oxygen, quick conversion of Fe²⁺ to Fe³⁺ leads to a progressively increasing quenching (data not shown).

The WT protein shows a markedly more intense quenching than the D122Y variant, the $(F-F_0)/F_0$ being -0.08 vs -0.06 at the 20 equivalents. The absolute quenching by Fe²⁺ in the sub-stoichiometric region is comparable for ferrous and ferric iron (about -0.08 for both oxidation states). Proceeding with the titration, at 10 equivalents the $(F-F_0)/F_0$ for the WT protein is -0.08 for Fe²⁺, much lower than the quenching observed for Fe³⁺, -0.27.

The titration curves have been analyzed according to the method of Sawyer and Winzor [*Sawyer W.H. & Winzor D.J., 1999*]; we obtained $K_D = 4.2 \cdot 10^{-7}$ for the WT protein and $K_D = 7.8 \cdot 10^{-7}$ for the D122Y variant, and for both a stoichiometry of one strongly bound Fe²⁺. These values must be considered only indicative, due to

the low concentration used for the experiments which introduces a 10% error in the estimate.

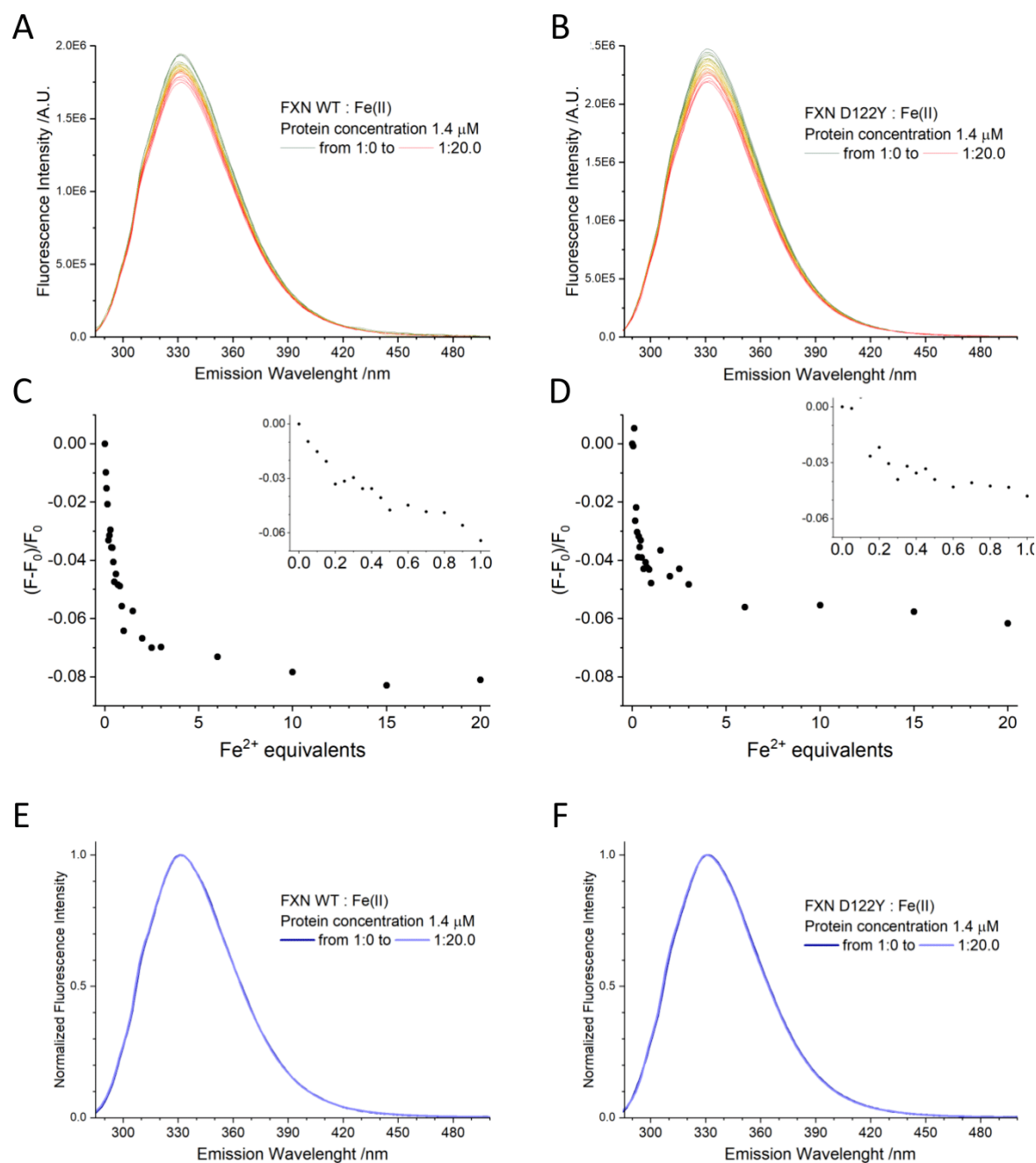


Figure 2.12. Tryptophan fluorescence spectra of WT FXN and D122Y variant at increasing amounts of Fe^{2+} . Protein concentration 1.4 μM , 288 K, $\lambda_{\text{exc}} = 280 \text{ nm}$, $\lambda_{\text{max}} = 332 \text{ nm}$. (A) and (B) fluorescence of FXN WT & D122Y with Fe(II), respectively; (C) and (D) fluorescence quenching by Fe^{2+} calculated at λ_{max} for FXN WT and D122Y, respectively; in the inset, a zoom of the sub-stoichiometric region. (E) and (F) normalized fluorescence spectra of WT and D122Y FXN with Fe(II), respectively.

▪ Circular Dichroism Spectra of FXN Interacting with Fe^{3+} and Fe^{2+}

The effects of iron-binding on the secondary structure of wild type and D122Y FXN proteins were evaluated by circular dichroism spectroscopy, as reported in Figure 2.13. In the absence of iron, the CD spectra for both WT and D122Y FXN are identical and show the typical shape of a mixed alpha-beta secondary structure [Faraj S.E. et al., 2016].

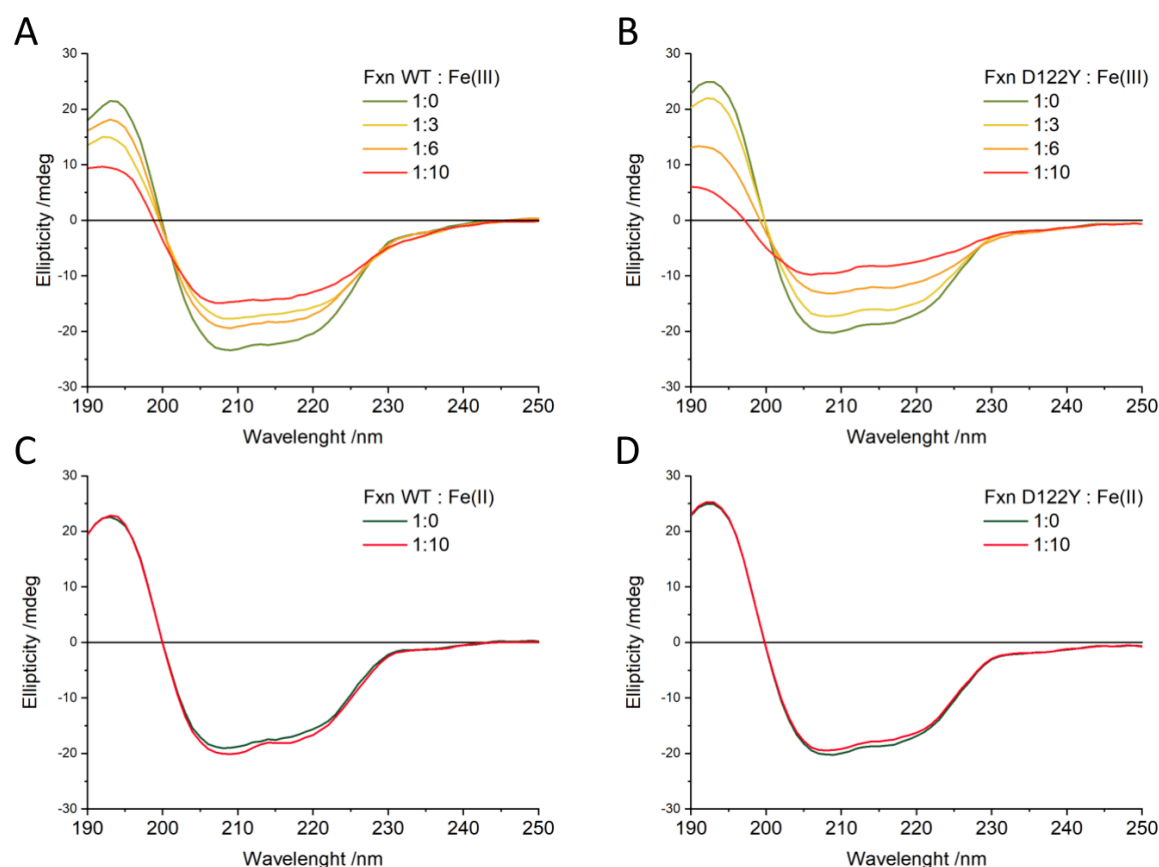


Figure 2.13. CD spectra of FXN of WT FXN and D122Y variant with either Fe^{3+} or Fe^{2+} . Protein concentration $50 \mu\text{M}$. (A) WT FXN with increasing amounts of Fe^{3+} ; (B) FXN D122Y with increasing amounts of Fe^{3+} ; (C) WT FXN with Fe^{2+} ; (D) FXN D122Y with Fe^{2+} .

Increasing addition of Fe^{3+} leads to a progressive loss of ellipticity across the whole spectral range for both proteins (Figure 2.13A,B). There are no marked changes in spectral shape and no well-defined isodichroic point can be observed; in addition, at high Fe^{3+} amounts, the low wavelength region shows signs of increased scattering. It was previously shown that a peptide derived from the

main helix of FXN can bind one Fe³⁺ ion through its acidic residues and gains alpha-helical structure upon binding [Vazquez D.S. et al., 2015]. All these observations suggest that the loss of ellipticity cannot be interpreted as a loss of structure, but only as a sign of protein aggregation/precipitation, as already proven by EPR spectroscopy.

On the contrary, additions of up to ten equivalents of Fe²⁺ do not change the CD spectra of WT and D122Y FXN (Figure 2.13C,D). Therefore, Fe²⁺ binding to FXN does not induce either significant secondary structure changes or protein aggregation.

Human Frataxin & SOD2

▪ EPR Spectra of FXN Interacting with SOD2

To investigate the potential interaction between human frataxin and mitochondrial superoxide dismutase, we performed EPR experiments on FXN spin-labeled in different regions to try to pinpoint the interface formed by FXN with SOD2. The formation of an interface in the position where the nitroxide probe is located would result in a marked slowdown of the side-chain motion, leading to a broader EPR spectrum. We performed the experiments in 20% v/v glycerol, which slows down the FXN tumbling enough to observe an EPR spectral shape influenced not only by the protein tumbling but also by the mobility of the spin probe sidechain and the backbone mobility.

The EPR spectra of FXN mutants at 10 μM concentration, in the absence or presence of SOD2 at 40 μM concentration for a final 1:1 FXN:(SOD2)₄ molar ratio, are reported in Figure 2.14. In the absence of SOD2, each mutant shows a characteristic spin label mobility, which confirms that the addition of glycerol, as previously seen in the presence of Ficoll, slows the molecular tumbling of the protein enough for the spectrum to report both local and general mobility. Based on the EPR spectra, the mobility of the two additional sites taken into account in this survey, i.e. H177 and S202, faithfully reflects the high mobility of the native residues. H177 is positioned in the loop between the β-sheet and the short α-helix (see above in Figure 2.3), it has the highest mobility among the studied residues, favored by little crowding by nearby sidechains, and accordingly it shows an EPR spectrum typical of very fast motion. S202 is in a relatively rigid part of the

C-terminal region (residues 196-210) (see above in *Figure 2.3*), but it has a larger mobility relative to neighboring residues and its EPR spectrum indicates a mobility that is faster than that of all other positions other than H177.

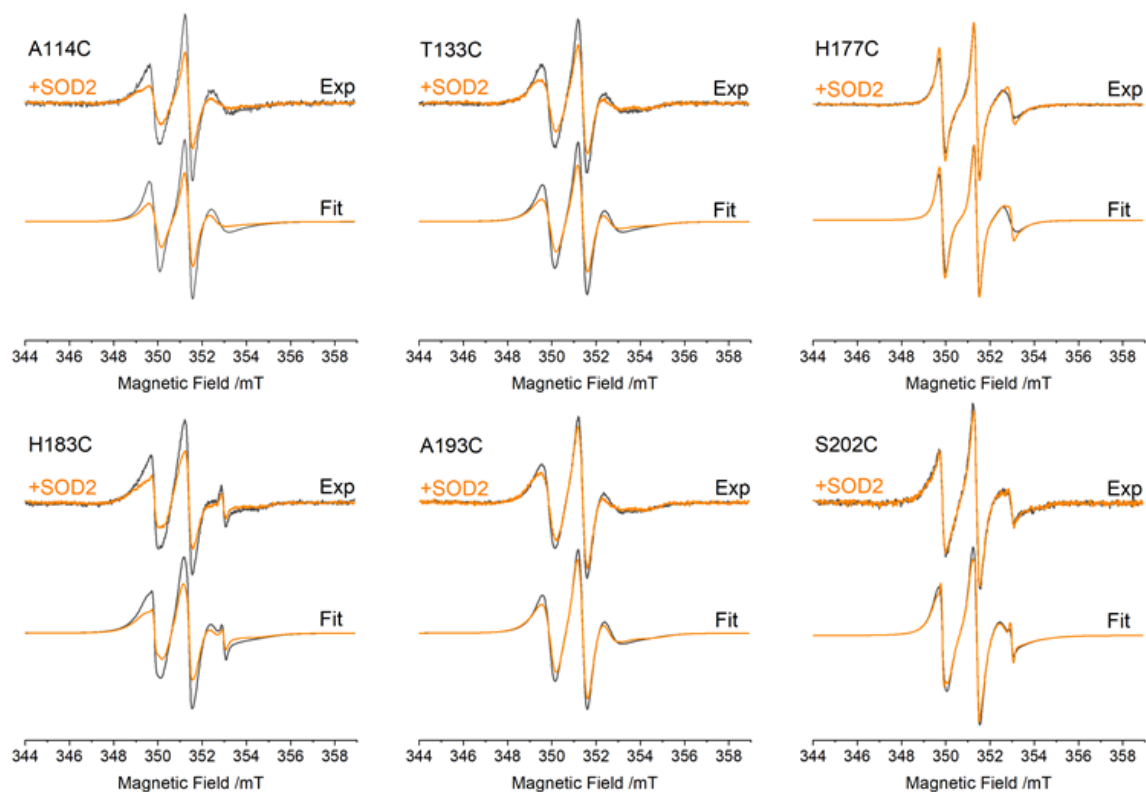


Figure 2.14. EPR spectra of FXN mutants (10 μM) in the absence (dark grey) and in the presence (orange) of SOD2 (40 μM); molar ratio FXN:(SOD2)₄ 1:1. For each mutant: top, experimental spectra; bottom, fitting. All spectra have been normalized to the same number of spins to compare the spectral shape in terms of spin probe mobility.

Upon addition of an equimolar quantity of tetrameric SOD2, all positions are affected similarly except for H177 and S202, for which the effect is almost null. Similar, albeit slightly less pronounced effects were obtained with a FXN:(SOD2)₄ 1:0.5 ratio (*Figure 2.15*), closer to the one used in fluorescence experiments reported below. The spectral changes clearly indicate that there is an interaction between FXN and SOD2.

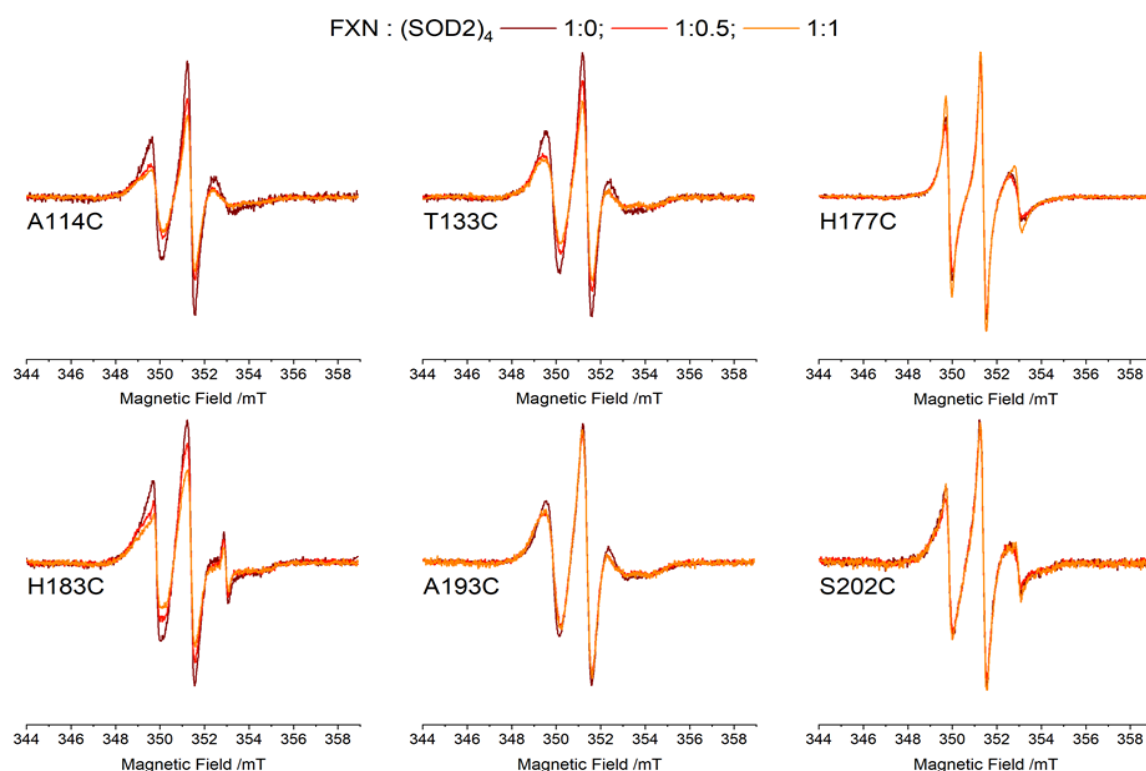


Figure 2.15. EPR spectra of FXN mutants in the absence (dark red) and in the presence of (SOD2)₄ at a 1:0.5 (red) and 1:1 (orange) molar ratio. All spectra have been normalized to the same number of spins to compare the spectral shape in terms of spin probe mobility. The spectra show a progressive slowdown at all spin label positions, but the spectral shape does not significantly change, a sign that most of the proteins are already involved in the complex.

To better quantify the effects of SOD2 on FXN, we fitted the EPR spectra obtaining the rotational correlation time, τ_c (the fittings are reported in Figure 2.14 as grey and orange lines). The slow motion of the EPR probe was assumed to be isotropic: this simple model captures the spectral variations induced by SODs quite well and makes it easy to discuss the spectral variations in terms of the changes in the rotational correlation times (τ_c), reported in Table 2.3 as the difference between τ_c in the presence of SOD (τ_c^{+SOD}) minus the one in its absence (τ_c^{-SOD}).

Table 2.3. Isotropic rotational correlation times for FXN mutants alone (τ_c^{-SOD}), in the presence of 1:1 tetrameric SOD (τ_c^{+SOD}), and their variation ($\Delta\tau_c$) obtained from the fitting of the EPR spectra. The g tensor principal components are: $g_{xx} = 2.0088$, $g_{yy} = 2.0070$, $g_{zz} = 2.0030$. The hyperfine tensor principal components are: $A_{xx} = 0.79$ mT; $A_{yy} = 0.54$ mT; $A_{zz} = 3.68$ mT.

Mutant	τ_c^{-SOD}	τ_c^{+SOD}	$\Delta\tau_c (\tau_c^{+SOD} - \tau_c^{-SOD})$
A114C	2.52 ns	2.96 ns	0.44 ns
T133C	2.70 ns	3.10 ns	0.40 ns
H177C	1.13 ns	1.24 ns	0.11 ns
H183C	2.77 ns	3.33 ns	0.56 ns
A193C	2.77 ns	3.18 ns	0.41 ns
S202C	2.30 ns	2.47 ns	0.16 ns

A homogeneous reduction in dynamics τ_c is observed for four sites (A114, T133, H183, A193) that are spread over a large region of the protein: the observed change likely reflects the slowdown in protein tumbling following the formation of the complex with bulky SOD2. In particular, H183, being an internal residue with limited sidechain and backbone dynamics, has the lowest mobility (*i.e.* the highest τ_c) of all sites and almost purely reflects the protein tumbling. Given that the changes in protein tumbling are the dominant effect on spin label mobility, we cannot exclude that one or more of the exposed sites (A114, T133, A193) are located at the interface between the two proteins. On the other hand, τ_c indicates that the mobility of H177 and S202 remains almost unchanged upon addition of SOD2. Their mobility is always dominated by the fast backbone and sidechain motions (lowest τ_c), making them insensitive to the protein tumbling changes. This excludes that these latter residues partake on the protein-protein interface: they would be at the interface, their sidechain motion would be strongly reduced, bringing down their τ_c to that characteristic of the protein tumbling (*i.e.* that of the internal site H183). Another important aspect that emerges from the simulation of the EPR spectra is that only one motional component is present in all spectra, even after SOD2 addition, suggesting that the interaction between the proteins is in the fast exchange regime. Previously, we showed that the addition of excess Fe(III) slows the FXN motion by inducing its aggregation at all positions. Here, we tested the effects of Fe³⁺ addition in the presence of SOD2, performing EPR experiments at FXN:(SOD2)₄:Fe³⁺ 1:0.5:20 ratio. The spectra,

reported in *Figure 2.16*, clearly show that the presence of SOD2 has no effect on FXN aggregation at this molar ratio.

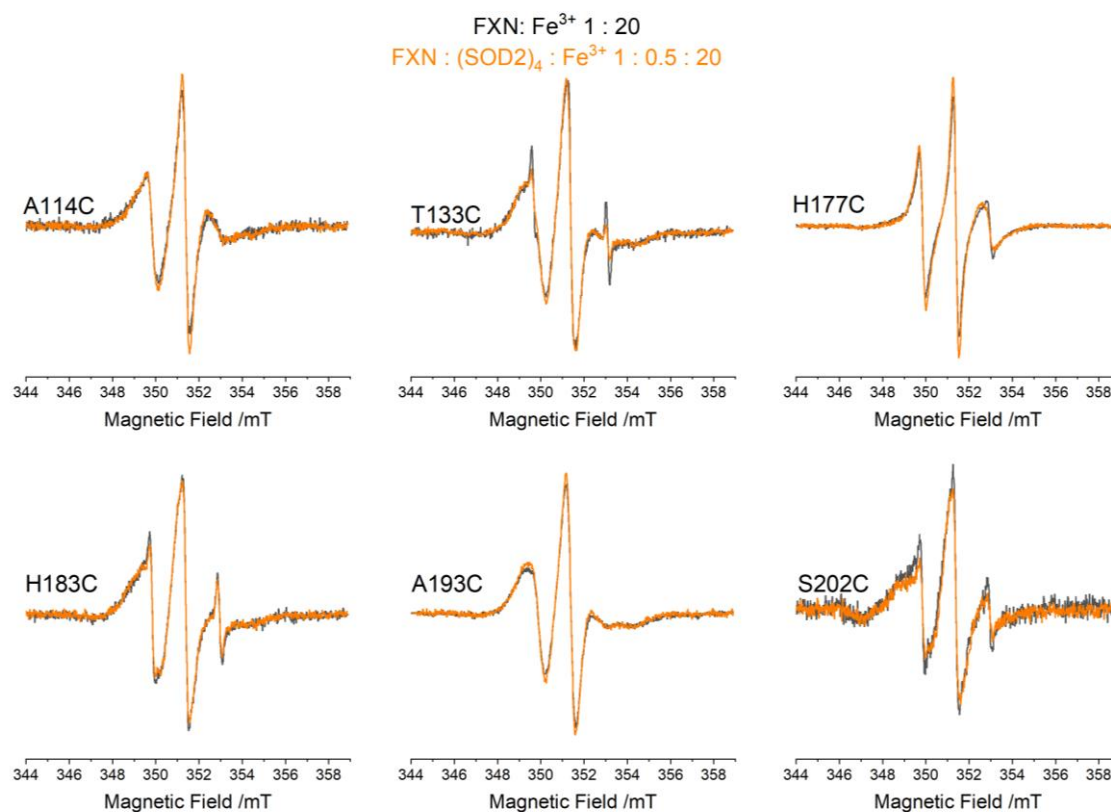


Figure 2.16. EPR spectra of FXN mutants with Fe^{3+} in the absence (black) and in the presence (orange) of SOD2. $[\text{FXN}] = 10 \mu\text{M}$; $[\text{SOD2}] = 0/20 \mu\text{M}$; $[\text{Fe}^{3+}] = 200 \mu\text{M}$. Black, $\text{FXN}:(\text{SOD2})_4:\text{Fe}^{3+} 1:0:20$; orange, $\text{FXN}:(\text{SOD2})_4:\text{Fe}^{3+} 1:0.5:20$. FXN and SOD2 have been mixed, and then Fe^{3+} has been added. All spectra have been normalized to the same number of spins to compare the spectral shape in terms of spin probe mobility.

- Fluorescence Spectra of FXN Interacting with SOD2

The interaction between FXN and SOD2 was tested following the fluorescence emission of the tryptophan residues, by comparing the fluorescence of the individual proteins with the fluorescence of the mixed solution. The results are reported in *Figure 2.17*. We must note that the spectra show at 310 nm the Raman scattering peak of the buffer (corresponding to a Raman shift $\bar{\nu} = 3456 \text{ cm}^{-1}$).

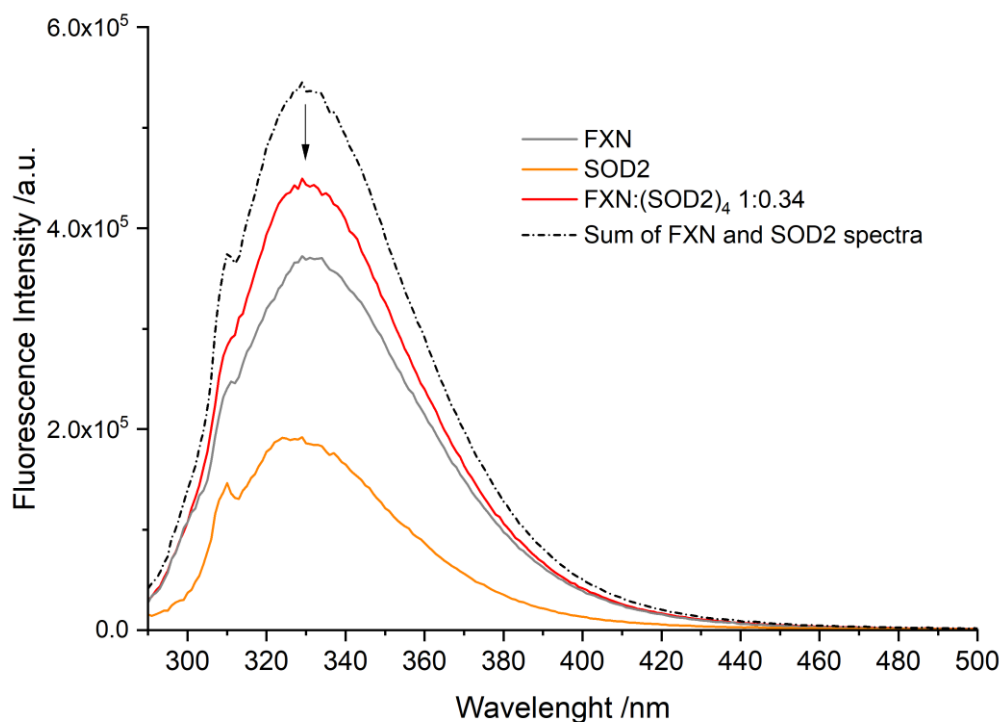


Figure 2.17. Tryptophan fluorescence spectra of WT FXN (1.4 μM) and SOD2 (1.9 μM). Temperature 288 K, $\lambda_{\text{exc}} = 280 \text{ nm}$. FXN alone, grey; SOD2 alone, orange; SOD2 and FXN (molar ratio FXN:(SOD2)₄ 1:0.34), red; sum of the individual fluorescence spectra of SOD2 and FXN, black dashed line. The peak at 310 nm is the Raman peak of the buffer.

FXN has three native Trp residues (W155, W168, W173; the Trp are shown in bright green in stick representation in *figure 2.3*). While the W155 residue is in the beta sheet region and exposed to the solution, W168 is partially exposed and W173 is completely buried. It should be noted that all three Trp residues are spatially close together and therefore interact with each other via energy transfer, affecting the overall fluorescence in a complex way. W155, being the only fully exposed Trp residue, is likely the most sensitive to the presence of quenchers in solution. We must note here that we previously verified that fluorescence experiments based on Trp quenching may be not fully reliable when the quencher binds far away from the Trp region. For frataxin, the fluorescence spectrum therefore results in a maximum at 332 nm (grey line in *Figure 2.17*).

Human SOD2 has six Trp residues per protein chain (W78, W123, W125, W161, W181, and W186) mostly buried inside the protein and in proximity to each other, either in the same chain or in neighboring chains in the tetramer with only W181 and W186 exposed to the solution. SOD2 fluorescence is largely self-

quenched, and the limited solvent exposition leads to it being blue-shifted relative to FXN with a maximum at 328 nm (orange line in *Figure 2.17*).

The fluorescence spectrum of the mixed FXN:(SOD2)₄ solution in a molar ratio of 1:0.34 (red line in *Figure 2.17*) shows a marked quenching relative to the sum of the experimental spectra of the individual proteins (17% less fluorescence, black dashed line in *Figure 2.17*). The quenching, highlighted by the arrow in the figure, suggests that the two proteins come in contact and that the exposed Trp residues are close to the interaction surface, leading to a quench in fluorescence. We propose that the quenching stems from the energy transfer from the exposed W155 (or possibly also W168) in FXN to the tryptophan network in SOD2 through the solvent exposed W181/W186 residues.

- Protein-Protein Docking of FXN and SOD2

To complement the experimental data and gain further insight into the interaction, we decided to model the structure of the FXN:(SOD2)₄ 1:1 complex using protein-protein molecular docking. We performed both blind docking simulations and simulations using the site-specific information from SDSL-EPR and fluorescence as restraints. The structures used for the docking calculations were: FXN, PDB ID: 1EKG [*Dhe-Paganon S. et al., 2000*]; SOD2, PDB ID: 5VF9 [*Azadmanesh J. et al., 2017*].

The top fifteen models obtained from the blind docking simulations were analyzed collectively to identify which residues of FXN and SODs are most often found at the interface of the protein complex. The full details of the docking simulations are reported in Materials & Methods; briefly, the docking protocol has been performed in three steps: 1) docking simulations using four programs freely available as webserver (ClusPro [*Kozakov D. et al., 2017*], ZDOCK [*Pierce B.G. et al., 2014*], GRAMM-X [*Tovchigrechko A. et al., 2006*], PatchDock [*Schneidman-Duhovny D. et al., 2005; Andrusier N. et al., 2007*]); 2) re-ranking of the solutions using a common scoring function with CONSRank; 3) analysis of the interface regions in the top 15 re-ranked docking poses using PDBePISA. The normalized frequency with which each residue appears at the interface in the top 15 models has been represented as a histogram and then mapped on the protein surface; the results for the blind docking are shown in *Figure 2.18*. In this set of simulations, FXN interacts with a single monomer of SOD2, contacting only a second monomer close to the interface.

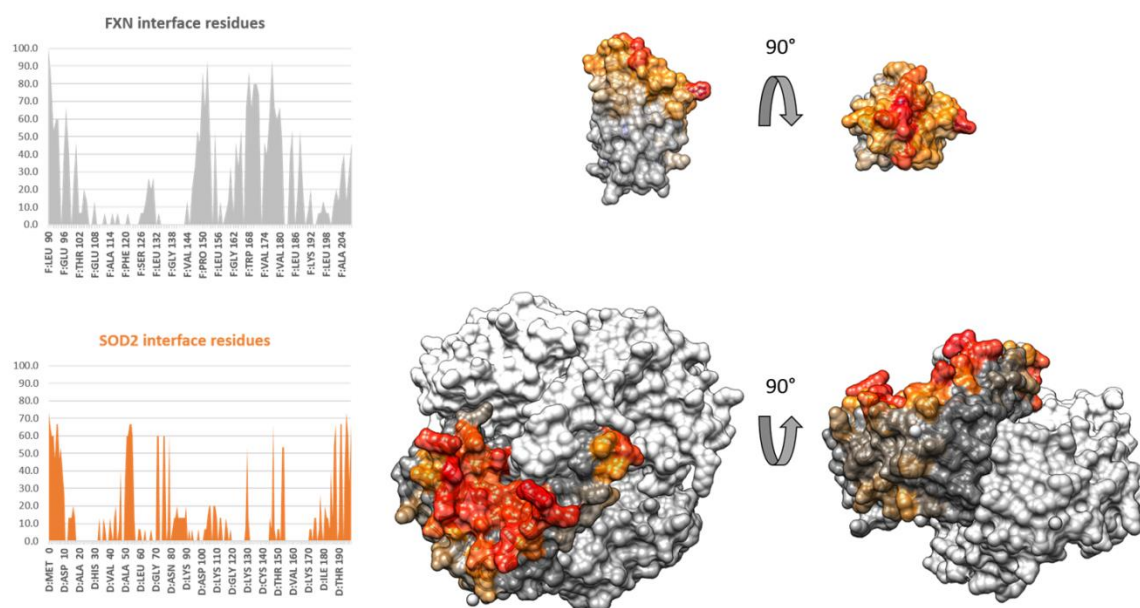


Figure 2.18. Blind docking simulations FXN/(SOD2)₄. Left - histogram of the normalized frequency of appearance of each amino acid at the interface: grey, FXN; orange, SOD2. Right - surface mapping of the frequency of appearance at the interface: the frequency with which an individual residue is involved in the interaction lowers going from red to orange; grey residues are never involved in an interaction. SOD2 has only one monomer mapped. FXN is represented showing the β -sheet to the reader on the left image.

The SOD2 region involved in the interaction is the hollow region on top of the N and C-terminal tails of the protein, on the other side of the active site that faces the inner tetrameric cavity. The interaction region for FXN is concentrated mostly around the top part of the protein comprising the N- and C-terminal regions, leaving the beta-sheet region exposed to the solution. These models show a good surface complementarity, and several hydrogen bonds and salt bridges are possible; however, they contrast with the experimental evidence. First, a site that is almost always found at the interface is H177 (present in more than 90% of the models), in marked contrast to the EPR experimental results which show limited effects of the complex formation on H177 mobility. Furthermore, the exposed Trp residues of SOD2 are also relatively far away from the interface, as is W155 from FXN, while the other FXN Trp residues are close to the interaction region. Overall, since the Trp residues of the two proteins are far from each other and do not change their solvent exposition, the obtained docking poses make it hard to justify the observed fluorescence quenching. Given that the blind-docking analysis did not respect the observations from the spectroscopic data, the

docking simulations were also performed using the data as restraints. We chose not to exclude any residue from the interface, even if H177 and S202 could be excluded based on the EPR results. Instead, we opted to locate only W181 and/or W186 from SOD2 close to the binding interface if possible, as Trp fluorescence was strongly affected. No Trp residue from FXN was chosen, since, while W155 is the only Trp residue fully solvent exposed, W168 is also sufficiently close to the surface to potentially act as a conduit for quenching. In this set of calculations, we specified as restraints the Trp residues belonging to a single SOD2 chain: this is reasonable since the exposed Trp of SOD2 are located far away from the tetramer interfaces and FXN, being smaller than a SOD2 monomer, would be unable to reach the other SOD2 monomers when interacting with the Trp region. The best docking model of the restrained simulations is reported in *Figure 2.19*, from two different angles.

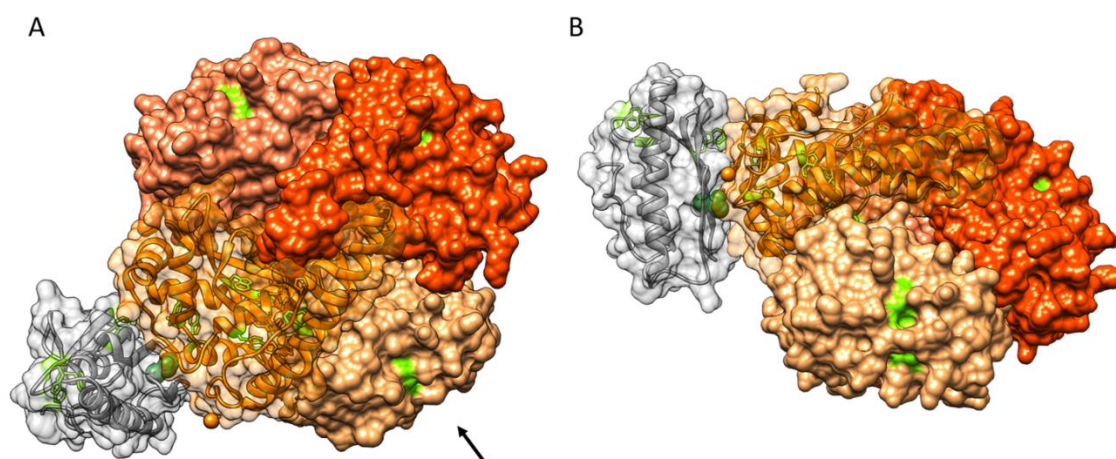


Figure 2.19. Docking model of FXN:(SOD2)₄ 1:1 complex. FXN in grey; SOD2 in shades of orange, one shade per protein chain. Tryptophan residues in light green, stick representation; T133 in dark green, sphere representation. The protein chains involved in the interaction are represented with a partially transparent surface. (A) SOD2 viewed in the same orientation as in figure 2.17; (B) the complex as viewed from the direction of the arrow to better highlight the orientation of FXN.

The structure of this complex involves a different region from the blind docking simulations, as expected. The active site of SOD2 is still accessible, as is the iron-binding region of FXN. Although the complementarity of the surface is reduced relative to the blind-docking simulations, and the specific interactions are limited

to two hydrogen bonds, this structure satisfies both the fluorescence and the EPR data. FXN is now contacting SOD2 using the beta sheet region, bringing W155 close to the exposed Trp of SOD2: the closest inter-atom distance between W155 and W186 is only 0.8 nm. Additionally, both H177 and S202 are now far from the region of interaction, which justifies the smaller changes in mobility for these two residues according to the EPR data. The full accessibility of the iron-binding region is also in line with the experiments in the presence of Fe³⁺.

Discussion & Conclusions

FXN has been proposed to have several physiological roles: allosteric regulator of ISCs biogenesis [Maio N. *et al.*, 2020], the iron source for building iron-sulfur clusters [Cai K. *et al.*, 2018], regulator of iron homeostasis [Alsina D. *et al.*, 2018] and ferroptosis [Du J. *et al.*, 2020]. All these potential roles involve iron ions; therefore, it is of key importance to understand the effects of ferrous and ferric iron on the structure and function of FXN. In the first part of this work, the response of human FXN, both WT and D122Y variant (*i.e.* the only pathological variant with a mutation in the iron-binding region), was investigated in the presence of ferrous and ferric ions using the SDSL-EPR technique, which has never been used on FXN before, and the results were combined with those obtained by fluorescence and circular dichroism.

Ferrous iron binds human FXN without causing any large secondary structure changes, as shown by CD, even at a 10-fold excess (*Figure 2.13C*). On the other hand, EPR clearly indicates that Fe²⁺ binding does not alter local backbone dynamics of regions that are not involved in iron-binding, as revealed by the lack of mobility changes of the spin probes at all the sites investigated (*Figure 2.9*). Moreover, no FXN oligomerization occurs in the presence of Fe²⁺, which is in agreement with previous results [Cavadini P. *et al.*, 2002]. The M-TETPO probe that we adopted, was liable to reduction by Fe²⁺ bound in close proximity (at sites A99 and A114), thus proving that Fe²⁺ binds to both ends of the long α -helix, in accordance with previous reports [Huang J. *et al.*, 2008; Gentry L.E. *et al.*, 2013; Bellanda M. *et al.*, 2019]. The majority of the EPR probe reduction takes place in the first three iron equivalents. The EPR data also put the results of fluorescence quenching into context. Fluorescence analysis leads to the conclusion that at least one strongly bound iron ion can be located in the long α -helix containing many Asp and Glu residues, close to W168/W173 (note that W155 is located in a region where putative Fe²⁺ binding sites are absent). This would be the site that reduces the spin label at position 99 (which is close to these two Trp). Conversely, the fluorescence measurements are not sensitive to binding of the Fe²⁺ ions in regions which are far from the Trp. Indeed, the Fe²⁺ binding site at the end of the α -helix suggested by the EPR spectra of A114C may escape fluorescence detection being out of range of the energy transfer Trp quenching mechanism. In conclusion, the number and the position of Fe²⁺ binding sites cannot be easily determined based on fluorescence quenching only, due to the presence of multiple Trp emitters

spatially close to each other, and our results explain the apparent conflict in the number of iron-binding sites reported in the literature.

In contrast to ferrous iron, ferric iron-binding promotes FXN aggregation when few equivalents are added, as shown by EPR and CD experiments, while the initial binding events at sub-stoichiometric ratios do not induce it. The WT protein exhibited a loss of ellipticity upon Fe^{3+} addition (*Figure 2.13A*), and centrifugation of EPR samples showed the precipitation of the immobilized portion of the sample (*Figure 2.7*). We observed immobilization at sites placed not only in the long acidic α -helix, which is the major putative iron-binding region, but also in the second β -strand and in the shorter α -helix. Thus, the interactions between monomers involve all the secondary structure elements and a large surface area is interested in the aggregation induced by iron-binding: as such, it is likely that FXN does not form dimers, rather oligomers, and these would be arranged in a globular fashion, without a preferential interface. Immobilization is the result of the constraint of the local motion of the labels, arising from new contacts between different protein monomers upon aggregation. Fe^{3+} -mediated oligomerization was previously suggested using SAXS, light scattering, and electron microscopy, at least at high FXN concentrations (150–700 μM), with EM images suggesting that at least a portion of the aggregates are present as ring tetramers [*Ahlgren E.C. et al., 2017*]. This was in contrast to previous reports, according to which human frataxin showed no tendency towards oligomerization, while the yeast and *E. coli* orthologues aggregate in the presence of both Fe^{2+} and Fe^{3+} [*Adinolfi S. et al., 2002*]. Since Fe^{3+} promotes the formation of FXN aggregates, also at relatively low protein concentration, it is impossible to evaluate the dissociation constant of Fe^{3+} using fluorescence or calorimetry since the quenching or heat, respectively, have dominant contributions from aggregation and precipitation phenomena. Based on our results, the data previously reported for the dissociation constants and binding stoichiometry of human FXN with Fe^{3+} [*Yoon T. & Cowan J.A., 2003*] need to be critically reconsidered.

Our results may have some implication in the context of the physiological behavior of FXN. The lack of perturbation of the structure of FXN by Fe^{2+} suggests that ferrous iron might easily bind/unbind FXN without any change in structure and dynamics. Therefore, FXN might partake in the ISCs assembly machinery while exchanging Fe^{2+} from the solution to the complex. With respect to the aggregation induced by Fe^{3+} , we showed that it is strongly dependent on FXN concentration, and therefore large oligomers are not expected to be present

at the low physiological concentrations of FXN in normal physiological states (FXN mitochondrial concentration is estimated to be between 0.1–1.0 μM in *S. cerevisiae*, by combining literature data [Garber Morales J, et al., 2010; Seguin A. et al., 2010]). However, in FRDA patients, a significant iron imbalance was observed [Lamarche J.B. et al., 1980; Bradley J.L. et al., 2000; Harding I.H. et al., 2016], and pathological conditions are likely to trigger oligomerization. It seems then unlikely that the interaction of FXN with Fe^{3+} has no physiological function and only reflects a non-specific electrostatic effect. Indeed, a recent report linked FXN deficiency to cell death by ferroptosis [Du J. et al., 2020]. Therefore, in conditions of an excess of ferric iron, a contribution of FXN to iron scavenging could be important, substantiating the function of FXN as a ‘ferritin-like’ scavenger helping iron homeostasis by keeping iron in a nontoxic, soluble and more bio-available form [Zanella I. et al., 2008]. In this context, it is important to note that, as demonstrated by the effects of EDTA (Figure 2.8), the aggregation is reversible: therefore, once the imbalances in cell physiology that are responsible for the increase in ferric iron are overcome, FXN can potentially return monomeric.

Finally, the use of SDSL-EPR allowed us to highlight differences in iron-binding between the WT and the D122Y variant. A lower iron affinity of the FXN D122Y has been previously related to a higher intrinsic mobility of the protein iron-binding region [Correia A.R. et al., 2008]. Indeed, an increased mobility of FXN D122Y in comparison with WT FXN is proved by the M-TETPO spin probe at the A114 position. The D122Y variant shows lower EPR signal loss in the presence of Fe^{2+} relative to the WT (Figure 2.9C,E), and reduced fluorescence quenching (Figure 2.12C,D), confirming a lower Fe^{2+} affinity. In addition, since the M-TETPO probe is sensitive to bound Fe^{2+} in the vicinity, the lower signal loss observed in the D122Y variant implies that the aspartate side chain in position 122 is directly involved in ferrous iron-binding. In contrast, in the sub-stoichiometric region, the effects of Fe^{3+} on the fluorescence quenching show no difference between the WT protein and the D122Y variant. The differences in fluorescence quenching by Fe^{3+} that were previously observed [Correia A.R. et al., 2008; Bellanda M. et al., 2019] are referred especially to the region dominated by precipitation, and as such depend strongly on the protein concentration as already described. Overall, the different binding affinity with ferrous, but not ferric, iron likely arises from a combination of variations in the structural dynamics of the region and loss of the aspartate partaking in iron-binding. Since it was previously observed that D122Y variant retains some capability to enhance the desulfurase activity *in vitro* [Bellanda M. et al., 2019], it is likely that the pathological nature of D122Y mutation lies in a

combination of lowered ability of the variant to participate in Fe²⁺ trafficking and less than optimal conformation hampering the interaction with the other proteins in the Fe-S cluster biogenesis complex.

Taken together, the results obtained through the combination of SDSL-EPR, fluorescence and CD spectroscopies prove that human FXN interacts with Fe²⁺ and Fe³⁺ with a markedly different outcome. Fe³⁺ causes aggregation in a concentration-dependent fashion, starting when adding few equivalents, and this makes it difficult to evaluate the exact binding stoichiometry. Fe²⁺, the physiological form of iron in cells, simply binds without affecting FXN conformation or inducing aggregation. We suggest that both ions might be relevant in the context of the proposed FXN physiological functions. A role as a regulator of iron homeostasis and ferroptosis might be exerted by sequestering the excess of ferric iron through a concentration-dependent reversible aggregation. The absence of structural and dynamic effects of Fe²⁺ binding suggests that FXN would be able to partake in ferrous iron trafficking even while bound to the ISCs assembly machinery, possibly intercepting the iron from the labile pool in solution and passing it to ISCU during cluster formation. The different binding affinity with ferrous, but not ferric, iron in D122Y pathological shows that the aspartate side chain in position 122 is directly involved in ferrous iron-binding and that the mobility of the protein in the vicinity of the mutated site is increased compared to the WT. Both the effects may be related to the pathological nature of D122Y. As future perspective, it would be interesting to explore the effects of Fe²⁺/Fe³⁺ on FXN structure and dynamics in the presence of the other partners of the ISC cluster assembly machinery, ISCU, NFS1 and the accessory proteins. We will use the currently available spin labeled sites plus new others strategically chosen in light of the available structure of the complex.

For the second part reported in this chapter, we have taken into account a previous work by Han *et al.* [Han T.H.L. *et al.*, 2019], which reported on the interaction between yeast FXN and SODs (bovine and human, in that work). To give full meaning to the results, however, the question of whether the same interaction could be detected between human FXN and human SODs must be addressed. We therefore investigated the interaction between the mature form of FXN and mitochondrial SOD2, since Han and coworkers excluded that at physiological concentrations a complex between FXN and SOD1 could be formed within mitochondria [Han T.H.L. *et al.*, 2019]. Furthermore, since SOD1 is primarily a cytosolic protein, it would probably interact with the immature form of FXN or with the extramitochondrial pool of mature FXN which has been

shown to play a role in preventing oxidative damage and suppressing apoptosis [Condò I. *et al.*, 2006]. EPR experiments suggest that human SOD2 interacts with mature FXN: all positions report a slowdown in dynamics upon the addition of SOD2, which is likely the result of the large increase in the hydrodynamic radius (Figure 2.14 and Table 2.3). We did not observe two different spectral populations, suggesting that the proteins are in fast exchange in solution, and therefore the kinetics of association/dissociation are fast, in the order of tens of nanoseconds. The results of the fluorescence experiments confirm an interaction with SOD2: when both proteins are present, the fluorescence is reduced by 17% relative to the sum of the individual contributions (Figure 2.17). Interestingly, Han *et al.* observed a fluorescence enhancement by about 13% mixing yeast FXN with human SOD2, as opposed to the quenching that we observed, suggesting that the details of the interaction between human proteins are significantly different from those of the mixed-species system. Together, our experimental results suggest a definite interaction between human FXN and SOD2 *in vitro*. A quantitative estimation of the K_D would require additional experiments and it is under way. Several experimental works point to a possible direct or indirect role of FXN in SOD2 activity, giving a potential physiological relevance for the *in vitro* interaction that we observed. The two proteins are located in the same mitochondrial compartment. In the previous chapter of this thesis it has been shown that FXN is enriched in the mitochondrial cristae and an involvement of frataxin in stabilizing the organization of respiratory chain has been hypothesized. Interestingly, recent cryo-EM studies showed that SOD2 is associated with respiratory supercomplexes in both mycobacteria [Gong H. *et al.*, 2018] and *Caenorhabditis elegans* [Suthammarak W. *et al.*, 2013], and this provides local protection against ROS damage. FXN and SOD2 are both involved in the biochemical hallmarks of FRDA pathophysiology, *i.e.* increased susceptibility to oxidative stress, iron overload, and a deficit in ISC biogenesis. FXN deficiency correlates with a lower antioxidant capacity of the cell, especially for SOD2 [Chantrel-Groussard K., 2001; Jiralerspong S. *et al.*, 2001]. In the yeast model of FRDA, SOD2 is overexpressed but shows a lower activity, that can be recovered by manganese supplementation [Irazusta V. *et al.*, 2006]. Furthermore, iron overload plays a role in the inactivation of SOD2, since it can compete with manganese for binding to SOD2, inactivating the enzyme [Yang M. *et al.*, 2006; Irazusta V. *et al.*, 2010]. In this context, we can propose two hypotheses on the physiological relevance of the FXN/SOD2 interaction, but we cannot exclude that the link between FXN and SOD2 discussed above is more a consequence of their

common involvement in mitochondrial function than the result of a direct interaction. One possibility is that the interaction between the two proteins acts as a modulator of antioxidant mechanisms in the vicinity of respiratory complexes, given their localization and involvement in oxidative stress. A second possibility is that in pathological conditions of excess iron, FXN transiently interacts with SOD2, lowering the local iron concentration, since one FXN can bind several Fe²⁺/Fe³⁺ ions, thus preventing manganese substitution with the consequent inactivation of SOD2. The structure of the complex that we proposed (*Figure 2.19*), in which the iron-binding region of FXN is exposed to the solution and does not block the active site of SOD2, could be in line with both hypotheses. In conclusion, the results obtained in the second part of this work through the combination of SDSL-EPR, fluorescence and molecular docking prove that mature human FXN interacts with human SOD2 *in vitro*. Considering the increasing amount of evidence that both proteins are present in the region around the respiratory chain complexes and that iron interacts with both, we deem that the observed interaction deserves additional investigations to better frame it in the context of the uncertain physiological role of FXN and of the molecular mechanisms of FRDA.

References

- Aasa R., Albracht P.J., Falk K.E., Lanne B., Vännngard T. - *EPR signals from cytochrome c oxidase* - *Biochim. Biophys. Acta* (1976); 422(2):260-272, [doi: 10.1016/0005-2744(76)90137-6].
- Acín-Pérez R. & Enriquez J.A. - *The function of the respiratory supercomplexes: the plasticity model* - *Biochim. Biophys. Acta* (2014); 1837(4):444-450, [doi: 10.1016/j.bbabi.2013.12.009].
- Acín-Pérez R., Fernández-Silva P., Peleato M.L., Pérez-Martos A., Enriquez J.A. - *Respiratory active mitochondrial supercomplexes* - *Mol. Cell* (2008); 32(4):529-539, [doi: 10.1016/j.molcel.2008.10.021].
- Acquaviva F., De Biase I., Nezi L., Ruggiero G., Tatangelo F., Pisano C., Monticelli A., Garbi C., Acquaviva A.M., Coccozza S. - *Extra-mitochondrial localisation of frataxin and its association with IscU1 during enterocyte-like differentiation of the human colon adenocarcinoma cell line Caco-2* - *J. Cell. Sci.* (2005); 118(Pt 17):3917-24, [doi: 10.1242/jcs.02516].
- Adamec J., Rusnak F., Owen W.G., Naylor S., Benson L.M., Gacy A.M., Isaya G. - *Iron-dependent self-assembly of recombinant yeast frataxin: implications for Friedreich ataxia* - *Am. J. Hum. Genet.* (2000); 67(3):549-562, [doi: 10.1086/303056].
- Adinolfi S., Iannuzzi C., Prischi F., Pastore C., Iametti S., Martin S.R., Bonomi F., Pastore A. - *Bacterial frataxin CyaY is the gatekeeper of iron-sulfur cluster formation catalyzed by IscS* - *Nat. Struct. Mol. Biol.* (2009); 16(4):390-396, [doi: 10.1038/nsmb.1579].
- Adinolfi S., Trifuoggi M., Politou A.S., Martin S., Pastore A. - *A structural approach to understanding the iron-binding properties of phylogenetically different frataxins* - *Hum. Mol. Genet.* (2002); 11(16):1865-1877, [doi: 10.1093/hmg/11.16.1865].
- Agip A.A., Blaza J.N., Bridges H.R., Viscomi C., Rawson S., Muench S.P., Hirst J. - *Cryo-EM structures of complex I from mouse heart mitochondria in two biochemically defined states* - *Nat. Struct. Mol. Biol.* (2018); 25(7):548-556, [doi: 10.1038/s41594-018-0073-1].
- Ahlgren E.C., Fekry M., Wiemann M., Söderberg C.A., Bernfur K., Gakh O., Rasmussen M., Højrup P., Emanuelsson C., Isaya G., Al-Karadaghi S. - *Iron-induced oligomerization of human FXN81-210 and bacterial CyaY frataxin and the effect of iron chelators* - *PLoS One* (2017); 12(12):e0188937, [doi: 10.1371/journal.pone.0188937].
- Aisen P., Enns C., Wessling-Resnick M. - *Chemistry and biology of eukaryotic iron metabolism* - *Int. J. Biochem. Cell Biol.* (2001); 33(10):940-959, [doi: 10.1016/s1357-2725(01)00063-2].

- Alfedì G., Luffarelli R., Condò I., Pedini G., Mannucci L., Massaro D.S., Benini M., Toschi N., Alaimo G., Panarello L., Pacini L., Fortuni S., Serio D., Malisan F., Testi R., Rufini A. - *Drug repositioning screening identifies etravirine as a potential therapeutic for friedreich's ataxia* - *Mov. Disord.* (2019); 34(3):323-334, [doi: 10.1002/mds.27604].
- Al-Mahdawi S., Pinto R.M., Varshney D., Lawrence L., Lowrie M.B, Hughes S., Webster Z., Blake J., Cooper J.M., King R., Pook M.A. - *GAA repeat expansion mutation mouse models of Friedreich ataxia exhibit oxidative stress leading to progressive neuronal and cardiac pathology* - *Genomics* (2006); 88(5):580-590, [doi: 10.1016/j.ygeno.2006.06.015].
- Alsina D., Purroy R., Ros J., Tamarit J. - *Iron in Friedreich Ataxia: A Central Role in the Pathophysiology or an Epiphenomenon?* - *Pharmaceuticals* (2018); 11(3):89, [doi: 10.3390/ph11030089].
- Althoff T., Mills D.J., Popot J.L., Kühlbrandt W. - *Arrangement of electron transport chain components in bovine mitochondrial supercomplex I₁III₂IV₁* - *EMBO J.* (2011); 30(22):4652-4664, [doi: 10.1038/emboj.2011.324].
- Andrusier N., Nussinov R., Wolfson H.J. - *FireDock: fast interaction refinement in molecular docking* - *Proteins* (2007); 69(1):139-159, [doi: 10.1002/prot.21495].
- Atamna H., Walter P.B., Ames B.N. - *The role of heme and iron-sulfur clusters in mitochondrial biogenesis, maintenance, and decay with age* - *Arch. Biochem. Biophys.* (2002); 397(2):345-353, [doi: 10.1006/abbi.2001.2671].
- Azadmanesh J., Trickle S.R., Borgstahl G.E.O. - *Substrate-analog binding and electrostatic surfaces of human manganese superoxide dismutase* - *J. Struct. Biol.* (2017); 199(1):68-75, [doi: 10.1016/j.jsb.2017.04.011].
- Babcock M., de Silva D., Oaks R., Davis-Kaplan S., Jiralerspong S., Montermini L., Pandolfo M., Kaplan J. - *Regulation of mitochondrial iron accumulation by Yfh1p, a putative homolog of frataxin* - *Science* (1997); 276(5319):1709-1712, [doi: 10.1126/science.276.5319.1709].
- Baradaran R., Berrisford J.M., Minhas G.S., Sazanov L.A. - *Crystal structure of the entire respiratory complex I* - *Nature* (2013); 494(7438):443-448, [doi: 10.1038/nature11871].
- Barone V., Zerbetto M., Polimeno A. - *Hydrodynamic modeling of diffusion tensor properties of flexible molecules* - *J. Comput. Chem.* (2009); 30(1):2-13, [doi: 10.1002/jcc.21007].
- Barrera M., Koob S., Dikov D., Vogel F., Reichert A.S. - *OPA1 functionally interacts with MIC60 but is dispensable for crista junction formation* - *FEBS Lett.* (2016); 590(19):3309-3322, [doi: 10.1002/1873-3468.12384].

- Barupala D.P., Dzul S.P., Riggs-Gelasco P.J., Stemmler T.L. - *Synthesis, delivery and regulation of eukaryotic heme and Fe-S cluster cofactors* - Arch. Biochem. Biophys. (2016); 592:60-75, [doi: 10.1016/j.abb.2016.01.010].
- Baussier C., Fakroun S., Aubert C., Dubrac S., Mandin P., Py B., Barras F. - *Making iron-sulfur cluster: structure, regulation and evolution of the bacterial ISC system* - Adv. Microb. Physiol. (2020); 76:1-39, [doi: 10.1016/bs.ampbs.2020.01.001].
- Beinert H. - *EPR spectroscopy of components of the mitochondrial electron-transfer system* - Methods Enzymol. (1978); 54:133-150, [doi: 10.1016/s0076-6879(78)54014-7].
- Beinert H. - *Iron-sulfur proteins: ancient structures, still full of surprises* - J. Biol. Inorg. Chem. (2000); 5(1):2-15, [doi: 10.1007/s007750050002].
- Beinert H., Ackrell B.A., Kearney E.B., Singer T.P. - *Iron-sulfur components of succinate dehydrogenase: stoichiometry and kinetic behavior in activated preparations* - Eur. J. Biochem. (1975); 54(1):185-194, [doi: 10.1111/j.1432-1033.1975.tb04128.x].
- Beinert H., Holm R.H., Münck E. - *Iron-sulfur clusters: nature's modular, multipurpose structures* - Science (1997); 277(5326):653-659, [doi: 10.1126/science.277.5326.653].
- Beinert H. & Kiley P.J. - *Fe-S proteins in sensing and regulatory functions* - Curr. Opin. Chem. Biol. (1999); 3(2):152-157, [doi: 10.1016/S1367-5931(99)80027-1].
- Bellanda M., Maso L., Doni D., Bortolus M., De Rosa E., Lunardi F., Alfonsi A., Noguera M.E., Herrera M.G., Santos J., Carbonera D., Costantini P. - *Exploring iron-binding to human frataxin and to selected Friedreich ataxia mutants by means of NMR and EPR spectroscopies* - Biochim. Biophys. Acta Proteins Proteom. (2019); 1867(11):140254, [doi: 10.1016/j.bbapap.2019.07.007].
- Bencze K.Z., Kondapalli K.C., Cook J.D., McMahon S., Millán-Pacheco C., Pastor N., Stemmler T.L. - *The structure and function of frataxin* - Crit. Rev. Biochem. Mol. Biol. (2006); 41(5):269-291, [doi: 10.1080/10409230600846058].
- Bencze K.Z., Yoon T., Millán-Pacheco C., Bradley P.B., Pastor N., Cowan J.A., Stemmler T.L. - *Human frataxin: iron and ferroxidase binding surface* - Chem. Commun. (2007); (18):1798-1800, [doi: 10.1039/b703195e].
- Bennett B. - *Cryogenic electron paramagnetic resonance spectroscopy of flash-frozen tissue for characterization of mitochondrial disease* - J. Transl. Genet. Genom. (2020); 4:36-49, [doi: 10.20517/jtgg.2020.17].
- Bennett B., Helbling D., Meng H., Jarzembowski J., Geurts A.M., Friederich M.W., Van Hove J.L.K., Lawlor M.W., Dimmock D.P. - *Potentially diagnostic electron paramagnetic resonance spectra elucidate the underlying mechanism of mitochondrial dysfunction in the*

deoxyguanosine kinase deficient rat model of a genetic mitochondrial DNA depletion syndrome - Free Radic. Biol. Med. (2016); 92:141-151, [doi: 10.1016/j.freeradbiomed.2016.01.001].

- Boniecki M.T., Freibert S.A., Mühlenhoff U., Lill R., Cygler M. - *Structure and functional dynamics of the mitochondrial Fe/S cluster synthesis complex* - Nat. Commun. (2017); 8(1):1287, [doi: 10.1038/s41467-017-01497-1].
- Bordignon E. & Steinhoff H.J. - *Membrane protein structure and dynamics studied by site-directed spin labeling ESR* - Hemminga M.A. and Berliner L.J. (eds). ESR Spectroscopy in Membrane Biophysics. Springer Science and Business Media, New York, 129-164 (2007).
- Böttinger L., Mårtensson C.U., Song J., Zufall N., Wiedemann N., Becker T. - *Respiratory chain supercomplexes associate with the cysteine desulfurase complex of the iron-sulfur cluster assembly machinery* - Mol. Biol. Cell (2018); 29(7):776-785, [doi: 10.1091/mbc.E17-09-0555].
- Bou-Abdallah F., Adinolfi S., Pastore A., Laue T.M., Dennis Chasteen N. - *Iron binding and oxidation kinetics in frataxin CyaY of Escherichia coli* - J. Mol. Biol. (2004); 341(2):605-615, [doi: 10.1016/j.jmb.2004.05.072].
- Bouton C. & Drapier J.C. - *Iron regulatory proteins as NO signal transducers* - Sci. STKE (2003); 2003(182):pe17, [doi: 10.1126/stke.2003.182.pe17].
- Bradley J.L., Blake J.C., Chamberlain S., Thomas P.K., Cooper J.M., Schapira A.H. - *Clinical, biochemical and molecular genetic correlations in Friedreich's ataxia* - Hum. Mol. Genet. (2000); 9(2):275-282, [doi: 10.1093/hmg/9.2.275].
- Braterman P.S., Song J.I., Peacock R.D. - *Electronic Absorption Spectra of the Iron(II) Complexes of 2, 2'-Bipyridine, 2, 2'-Bipyrimidine, 1, 10-Phenanthroline, and 2, 2':6',2''-Terpyridine and Their Reduction Products* - Inorg. Chem. (1992); 31:555-559, [doi: 10.1021/ic00030a006].
- Braymer J.J., Freibert S.A., Rakwalska-Bange M., Lill R. - *Mechanistic concepts of iron-sulfur protein biogenesis in Biology* - Biochim. Biophys. Acta Mol. Cell. Res. (2021); 1868(1):118863, [doi: 10.1016/j.bbamcr.2020.118863].
- Bridwell-Rabb J., Fox N.G., Tsai C.L., Winn A.M., Barondeau D.P. - *Human frataxin activates Fe-S cluster biosynthesis by facilitating sulfur transfer chemistry* - Biochemistry (2014); 53(30):4904-4913, [doi: 10.1021/bi500532e].
- Bridwell-Rabb J., Winn A.M., Barondeau D.P. - *Structure-function analysis of Friedreich's ataxia mutants reveals determinants of frataxin binding and activation of the Fe-S assembly complex* - Biochemistry (2011); 50(33):7265-7274, [doi: 10.1021/bi200895k].

- Britti E., Delaspre F., Feldman A., Osborne M., Greif H., Tamarit J., Ros J. - *Frataxin-deficient neurons and mice models of Friedreich ataxia are improved by TAT-MTScs-FXN treatment* - J. Cell. Mol. Med. (2018); 22(2):834-848, [doi: 10.1111/jcmm.13365].
- Budil D.E., Sanghyuk L., Saxena S., Freed J.H. - *Nonlinear-Least-Squares Analysis of Slow-Motion EPR Spectra in One and Two Dimensions Using a Modified Levenberg-Marquardt Algorithm* - J. Magn. Reson. Ser. A (1996), 120, 155-189.
- Bulteau A.L., O'Neill H.A., Kennedy M.C., Ikeda-Saito M., Isaya G., Szwedda L.I. - *Frataxin acts as an iron chaperone protein to modulate mitochondrial aconitase activity* - Science (2004); 305(5681):242-245, [doi: 10.1126/science.1098991].
- Bürk K. - *Friedreich Ataxia: current status and future prospects* - Cerebellum & Ataxias (2017), 4(1):4, [doi: 10.1186/s40673-017-0062-x].
- Cai K., Frederick R.O., Dashti H., Markley J.L. - *Architectural Features of Human Mitochondrial Cysteine Desulfurase Complexes from Crosslinking Mass Spectrometry and Small-Angle X-Ray Scattering* - Structure (2018); 26(8):1127-1136.e4, [doi: 10.1016/j.str.2018.05.017].
- Cai K., Frederick R.O., Tonelli M., Markley J.L. - *Interactions of iron-bound frataxin with ISCU and ferredoxin on the cysteine desulfurase complex leading to Fe-S cluster assembly* - J. Inorg. Biochem. (2018); 183:107-116, [doi: 10.1016/j.jinorgbio.2018.03.007].
- Cai K. & Markley J.L. - *NMR as a Tool to Investigate the Processes of Mitochondrial and Cytosolic Iron-Sulfur Cluster Biosynthesis* - Molecules (2018); 23(9):2213, [doi: 10.3390/molecules23092213].
- Calvo S.E. & Mootha V.K. - *The mitochondrial proteome and human disease* - Annu. Rev. Genomics Hum. Genet. (2010); 11:25-44, [doi: 10.1146/annurev-genom-082509-141720].
- Campanella A., Isaya G., O'Neill H.A., Santambrogio P., Cozzi A., Arosio P., Levi S. - *The expression of human mitochondrial ferritin rescues respiratory function in frataxin-deficient yeast* - Hum. Mol. Genet. (2004); 13(19):2279-2288, [doi: 10.1093/hmg/ddh232].
- Campbell C.J., Pall A.E., Naik A.R., Thompson L.N., Stemmler T.L. - *Molecular Details of the Frataxin-Scaffold Interaction during Mitochondrial Fe-S Cluster Assembly* - Int. J. Mol. Sci. (2021); 22(11):6006, [doi: 10.3390/ijms22116006].
- Campuzano V., Montermini L., Lutz Y., Cova L., Hindelang C., Jiralerspong S., Trottier Y., Kish S.J., Faucheux B., Trouillas P., Authier F.J., Dürr A., Mandel J.L., Vescovi A., Pandolfo M., Koenig M. - *Frataxin is reduced in Friedreich ataxia patients and is associated with mitochondrial membranes* - Hum. Mol. Genet. (1997); 6(11):1771-1780, [doi: 10.1093/hmg/6.11.1771].

- Campuzano V., Montermini L., Moltò M.D., Pianese L., Cossée M., Cavalcanti F., Monros E., Rodius F., Duclos F., Monticelli A., Zara F., Cañizares J., Koutnikova H., Bidichandani S.I., Gellera C., Brice A., Trouillas P., De Michele G., Filla A., De Frutos R., Palau F., Patel P.I., Di Donato S., Mandel J.L., Coccozza S., Koenig M., Pandolfo M. - *Friedreich's ataxia: autosomal recessive disease caused by an intronic GAA triplet repeat expansion* - Science (1996); 271(5254):1423-1427, [doi: 10.1126/science.271.5254.1423].
- Carletti B., Piermarini E., Tozzi G., Travaglini L., Torraco A., Pastore A., Sparaco M., Petrillo S., Carrozzo R., Bertini E., Piemonte F. - *Frataxin silencing inactivates mitochondrial Complex I in NSC34 motoneuronal cells and alters glutathione homeostasis* - Int. J. Mol. Sci. (2014); 15(4):5789-5806, [doi: 10.3390/ijms15045789].
- Castro I.H., Ferrari A., Herrera M.G., Noguera M.E., Maso L., Benini M., Rufini A., Testi R., Costantini P., Santos J. - *Biophysical characterisation of the recombinant human frataxin precursor* - FEBS Open Bio. (2018); 8(3):390-405, [doi: 10.1002/2211-5463.12376].
- Cavadini P., Adamec J., Taroni F., Gakh O., Isaya G. - *Two-step processing of human frataxin by mitochondrial processing peptidase. Precursor and intermediate forms are cleaved at different rates* - J. Biol. Chem. (2000); 275(52):41469-41475, [doi: 10.1074/jbc.M006539200].
- Cavadini P., O'Neill H.A., Benada O., Isaya G. - *Assembly and iron-binding properties of human frataxin, the protein deficient in Friedreich ataxia* - Hum. Mol. Genet. (2002); 11(3):217-227, [doi: 10.1093/hmg/11.3.217].
- Chan D.C. - *Mitochondrial Dynamics and Its Involvement in Disease* - Annu. Rev. Pathol. (2020); 15:235-259, [doi: 10.1146/annurev-pathmechdis-012419-032711].
- Chantrel-Groussard K., Geromel V., Puccio H., Koenig M., Munnich A., Rötig A., Rustin P. - *Disabled early recruitment of antioxidant defenses in Friedreich's ataxia* - Hum. Mol. Genet. (2001); 10(19):2061-2067, [doi: 10.1093/hmg/10.19.2061].
- Chermak E., Petta A., Serra L., Vangone A., Scarano V., Cavallo L., Oliva R. - *CONSRANK: a server for the analysis, comparison and ranking of docking models based on inter-residue contacts* - Bioinformatics (2015); 31(9):1481-1483, [doi: 10.1093/bioinformatics/btu837].
- Chiabrando D., Bertino F., Tolosano E. - *Hereditary Ataxia: A Focus on Heme Metabolism and Fe-S Cluster Biogenesis* - Int. J. Mol. Sci. (2020); 21(11):3760, [doi: 10.3390/ijms21113760].
- Cho S.J., Lee M.G., Yang J.K., Lee J.Y., Song H.K., Suh S.W. - *Crystal structure of Escherichia coli CyaY protein reveals a previously unidentified fold for the evolutionarily conserved frataxin family* - Proc. Natl. Acad. Sci. U. S. A. (2000); 97(16):8932-8937, [doi: 10.1073/pnas.160270897].

- Chutake Y.K., Lam C., Costello W.N., Anderson M., Bidichandani S.I. - *Epigenetic promoter silencing in Friedreich ataxia is dependent on repeat length* - *Ann. Neurol.* (2014); 76(4):522-528, [doi: 10.1002/ana.24249].
- Ciofi-Baffoni S., Nasta V., Banci L. - *Protein networks in the maturation of human iron-sulfur proteins* - *Metallomics* (2018); 10(1):49-72, [doi: 10.1039/c7mt00269f].
- Cipolat S., Rudka T., Hartmann D., Costa V., Serneels L., Craessaerts K., Metzger K., Frezza C., Annaert W., D'Adamio L., Derks C., Dejaegere T., Pellegrini L., D'Hooge R., Scorrano L., De Strooper B. - *Mitochondrial rhomboid PARL regulates cytochrome c release during apoptosis via OPA1-dependent cristae remodeling* - *Cell* (2006); 126(1):163-175, [doi: 10.1016/j.cell.2006.06.021].
- Civiletto G., Varanita T., Cerutti R., Gorletta T., Barbaro S., Marchet S., Lamperti C., Viscomi C., Scorrano L., Zeviani M. - *Opa1 overexpression ameliorates the phenotype of two mitochondrial disease mouse models* - *Cell Metab.* (2015); 21(6):845-854, [doi: 10.1016/j.cmet.2015.04.016].
- Clark E., Butler J.S., Isaacs C.J., Napierala M., Lynch D.R. - *Selected missense mutations impair frataxin processing in Friedreich ataxia* - *Ann. Clin. Transl. Neurol.* (2017); 4(8):575-584, [doi: 10.1002/acn3.433].
- Cogliati S., Enriquez J.A., Scorrano L. - *Mitochondrial Cristae: Where Beauty Meets Functionality* - *Trends Biochem. Sci.* (2016); 41(3):261-273, [doi: 10.1016/j.tibs.2016.01.001].
- Cogliati S., Frezza C., Soriano M.E., Varanita T., Quintana-Cabrera R., Corrado M., Cipolat S., Costa V., Casarin A., Gomes L.C., Perales-Clemente E., Salviati L., Fernandez-Silva P., Enriquez J.A., Scorrano L. - *Mitochondrial cristae shape determines respiratory chain supercomplexes assembly and respiratory efficiency* - *Cell* (2013); 155(1):160-171, [doi: 10.1016/j.cell.2013.08.032].
- Colin F., Martelli A., Clémancey M., Latour J.M., Gambarelli S., Zeppieri L., Birck C., Page A., Puccio H., Ollagnier de Choudens S. - *Mammalian frataxin controls sulfur production and iron entry during de novo Fe₄S₄ cluster assembly* - *J. Am. Chem. Soc.* (2013); 135(2):733-740, [doi: 10.1021/ja308736e].
- Colina-Tenorio L., Horten P., Pfanner N., Rampelt H. - *Shaping the mitochondrial inner membrane in health and disease* - *J. Intern. Med.* (2020); 287(6):645-664, [doi: 10.1111/joim.13031].
- Condò I., Malisan F., Guccini I., Serio D., Rufini A., Testi R. - *Molecular control of the cytosolic aconitase/IRP1 switch by extramitochondrial frataxin* - *Hum. Mol. Genet.* (2010); 19(7):1221-1229, [doi: 10.1093/hmg/ddp592].

- Condò I., Ventura N., Malisan F., Rufini A., Tomassini B, Testi R. - *In vivo maturation of human frataxin* - Hum. Mol. Genet. (2007); 16(13):1534-1540, [doi: 10.1093/hmg/ddm102].
- Condò I., Ventura N., Malisan F., Tomassini B., Testi R. - *A pool of extramitochondrial frataxin that promotes cell survival* - J. Biol. Chem. (2006); 281(24):16750-16756, [doi: 10.1074/jbc.M511960200].
- Cook J.D., Bencze K.Z., Jankovic A.D., Crater A.K., Busch C.N., Bradley P.B., Stemmler A.J., Spaller M.R., Stemmler T.L. - *Monomeric yeast frataxin is an iron-binding protein* - Biochemistry (2006); 45(25):7767-7777, [doi: 10.1021/bi060424r].
- Cook A. & Giunti P. - *Friedreich's ataxia: clinical features, pathogenesis and management* - Br. Med. Bull. (2017); 124(1): 19-30, [doi: 10.1093/bmb/ldx034].
- Cook J.D., Kondapalli K.C., Rawat S., Childs W.C., Murugesan Y., Dancis A., Stemmler T.L. - *Molecular details of the yeast frataxin-Isu1 interaction during mitochondrial Fe-S cluster assembly* - Biochemistry (2010); 49(40):8756-8765, [doi: 10.1021/bi1008613].
- Cooper J.M., Korlipara L.V., Hart P.E., Bradley J.L., Schapira A.H. - *Coenzyme Q10 and vitamin E deficiency in Friedreich's ataxia: predictor of efficacy of vitamin E and coenzyme Q10 therapy* - Eur. J. Neurol. (2008); 15(12):1371-1379, [doi: 10.1111/j.1468-1331.2008.02318.x].
- Correia A.R., Adinolfi S., Pastore A., Gomes C.M. - *Conformational stability of human frataxin and effect of Friedreich's ataxia-related mutations on protein folding* - Biochem. J. (2006); 398(3):605-611, [doi: 10.1042/BJ20060345].
- Correia A.R., Pastore C., Adinolfi S., Pastore A., Gomes C.M. - *Dynamics, stability and iron-binding activity of frataxin clinical mutants* - FEBS J. (2008); 275(14):3680-3690, [doi: 10.1111/j.1742-4658.2008.06512.x].
- Cory S.A., Van Vranken J.G., Brignole E.J., Patra S., Winge D.R., Drennan C.L., Rutter J., Barondeau D.P. - *Structure of human Fe-S assembly subcomplex reveals unexpected cysteine desulfurase architecture and acyl-ACP-ISD11 interactions* - Proc. Natl. Acad. Sci. U. S. A. (2017); 114(27):E5325-E5334, [doi: 10.1073/pnas.1702849114].
- Cossée M., Dürr A., Schmitt M., Dahl N., Trouillas P., Allinson P., Kostrzewa M., Nivelon-Chevallier A., Gustavson K.H., Kohlschütter A., Müller U., Mandel J.L., Brice A., Koenig M., Cavalcanti F., Tammara A., De Michele G., Filla A., Coccozza S., Labuda M., Montermini L., Poirier J., Pandolfo M. - *Friedreich's ataxia: point mutations and clinical presentation of compound heterozygotes* - Ann. Neurol. (1999); 45(2):200-206, [doi: 10.1002/1531-8249(199902)45:2<200::aid-ana10>3.0.co;2-u].
- Cossée M., Puccio H., Gansmuller A., Koutnikova H., Dierich A., LeMeur M., Fischbeck K., Dollé P., Koenig M. - *Inactivation of the Friedreich ataxia mouse gene leads to early*

embryonic lethality without iron accumulation - Hum. Mol. Genet. (2000); 9(8):1219-1226, [doi: 10.1093/hmg/9.8.1219].

- Cossée M., Schmitt M., Campuzano V., Reutenauer L., Moutou C., Mandel J.L., Koenig M. - *Evolution of the Friedreich's ataxia trinucleotide repeat expansion: Founder effect and premutations* - Proc. Natl. Acad. Sci. U.S.A. (1997), 94, 7452-7457, [doi: 10.1073/pnas.94.14.7452].
- Cotticelli M.G., Xia S., Lin D., Lee T., Terrab L., Wipf P., Huryn D.M., Wilson R.B. - *Ferroptosis as a Novel Therapeutic Target for Friedreich's Ataxia* - J. Pharmacol. Exp. Ther. (2019); 369(1):47-54, [doi: 10.1124/jpet.118.252759].
- Czogalla A., Pieciul A., Jezierski A., Sikorski A.F. - *Attaching a spin to a protein - site - directed spin labeling in structural biology* - Acta Biochim. Pol. (2007); 54(2):235-244.
- Dailey H.A., Dailey T.A., Wu C.K., Medlock A.E., Wang K.F., Rose J.P., Wang B.C. - *Ferrochelatase at the millennium: structures, mechanisms and [2Fe-2S] clusters* - Cell. Mol. Life Sci. (2000); 57(13-14):1909-1926, [doi: 10.1007/pl00000672].
- Davies K.M., Strauss M., Daum B., Kief J.H., Osiewacz H.D., Rycovska A., Zickermann V., Kühlbrandt W. - *Macromolecular organization of ATP synthase and complex I in whole mitochondria* - Proc. Natl. Acad. Sci. U. S. A. (2011); 108(34):14121-14126, [doi: 10.1073/pnas.1103621108].
- De Castro M., García-Planells J., Monrós E., Cañizares J., Vázquez-Manrique R., Vilchez J.J., Urtasun M., Lucas M., Navarro G., Izquierdo G., Moltó M.D., Palau F. - *Genotype and phenotype analysis of Friedreich's ataxia compound heterozygous patients* - Hum. Genet. (2000); 106(1):86-92, [doi: 10.1007/s004399900201].
- De Michele G., Perrone F., Filla A., Mirante E., Giordano M., De Placido S., Campanella G. - *Age of onset, sex, and cardiomyopathy as predictors of disability and survival in Friedreich's disease: a retrospective study on 119 patients* - Neurology (1996), 47(5) 1260-1264, [doi: 10.1212/WNL.47.5.1260].
- Delatycki M.B. & Bidichandani S.I. - *Friedreich ataxia- pathogenesis and implications for therapies* - Neurobiol. Dis. (2019), 132:104606, [doi: 10.1016/j.nbd.2019.104606].
- Delatycki M.B., Corben L.A. - *Clinical features of Friedreich ataxia* - J. Child Neurol. (2012) ;27(9):1133-1137, [doi: 10.1177/0883073812448230].
- Delatycki M.B., Paris D.B., Gardner R.J., Nicholson G.A., Nassif N., Storey E., MacMillan J.C., Collins V., Williamson R., Forrest S.M. - *Clinical and genetic study of Friedreich ataxia in an Australian population* - Am. J. Med. Genet. (1999); 87(2):168-174, [doi:10.1002/(sici)1096-8628(19991119)87:2<168::aid-ajmg8>3.0.co;2-2].

- Dhe-Paganon S., Shigeta R., Chi Y.I., Ristow M., Shoelson S.E. - *Crystal structure of human frataxin* - J. Biol. Chem. (2000); 275(40):30753-6, [doi: 10.1074/jbc.C000407200].
- Dimauro S., Tay S., Mancuso M. - *Mitochondrial encephalomyopathies: diagnostic approach* - Ann. N. Y. Acad. Sci. (2004); 1011:217-231, [doi: 10.1196/annals.1293.022].
- Ding C., Wu Z., Huang L., Wang Y., Xue J., Chen S., Deng Z., Wang L., Song Z., Chen S. - *Mitofilin and CHCHD6 physically interact with Sam50 to sustain cristae structure* - Sci. Rep. (2015); 5:16064, [doi: 10.1038/srep16064].
- Du J., Zhou Y., Li Y., Xia J., Chen Y., Chen S., Wang X., Sun W., Wang T., Ren X., Wang X., An Y., Lu K., Hu W., Huang S., Li J., Tong X., Wang Y. - *Identification of Frataxin as a regulator of ferroptosis* - Redox. Biol. (2020); 32:101483, [doi: 10.1016/j.redox.2020.101483].
- Dudkina N.V., Kudryashev M., Stahlberg H., Boekema E.J. - *Interaction of complexes I, III, and IV within the bovine respirasome by single particle cryoelectron tomography* - Proc. Natl. Acad. Sci. U. S. A. (2011); 108(37):15196-15200, [doi: 10.1073/pnas.1107819108].
- Dürr A., Cossee M., Agid Y., Campuzano V., Mignard C., Penet C., Mandel J.L., Brice A., Koenig M. - *Clinical and genetic abnormalities in patients with Friedreich's ataxia* - N. Engl. J. Med. (1996); 335(16):1169-1175, [doi: 10.1056/NEJM199610173351601].
- Duvezin-Caubet S., Jagasia R., Wagener J., Hofmann S., Trifunovic A., Hansson A., Chomyn A., Bauer M.F., Attardi G., Larsson N.G., Neupert W., Reichert A.S. - *Proteolytic processing of OPA1 links mitochondrial dysfunction to alterations in mitochondrial morphology* - J. Biol. Chem. (2006); 281(49):37972-37979, [doi: 10.1074/jbc.M606059200].
- Enríquez J.A. - *Supramolecular Organization of Respiratory Complexes* - Annu. Rev. Physiol. (2016); 78:533-561, [doi: 10.1146/annurev-physiol-021115-105031].
- Eubel H., Jansch L., Braun H.P. - *New insights into the respiratory chain of plant mitochondria. Supercomplexes and a unique composition of complex II* - Plant Physiol. (2003); 133(1):274-86, [doi: 10.1104/pp.103.024620].
- Faggianelli N., Puglisi R., Veneziano L., Romano S., Frontali M., Vannocci T., Fortuni S., Testi R., Pastore A. - *Analyzing the Effects of a G137V Mutation in the FXN Gene* - Front. Mol. Neurosci. (2015); 8:66, [doi: 10.3389/fnmol.2015.00066].
- Faraj S.E., González-Lebrero R.M., Roman E.A., Santos J. - *Human Frataxin Folds Via an Intermediate State. Role of the C-Terminal Region* - Sci. Rep. (2016); 6:20782, [doi: 10.1038/srep20782].
- Fernandez-Vizarra E. & Zeviani M. - *Mitochondrial disorders of the OXPHOS system* - FEBS Lett. (2021); 595(8):1062-1106, [doi: 10.1002/1873-3468.13995].

- Ferreira G.C. – *Ferrochelatase* - Int. J. Biochem. Cell Biol. (1999); 31(10):995-1000, [doi: 10.1016/s1357-2725(99)00066-7].
- Ferreira G.C., Franco R., Lloyd S.G., Moura I., Moura J.J., Huynh B.H. - *Structure and function of ferrochelatase* - J. Bioenerg. Biomembr. (1995); 27(2):221-229, [doi: 10.1007/BF02110037].
- Filla A., De Michele G., Cavalcanti F., Pianese L., Monticelli A., Campanella G., Coccozza S. - *The relationship between trinucleotide (GAA) repeat length and clinical features in Friedreich ataxia* - Am. J. Hum. Genet. (1996); 59(3):554-560.
- Finocchiaro G., Baio G., Micossi P., Pozza G., di Donato S. - *Glucose metabolism alterations in Friedreich's ataxia* - Neurology (1988); 38(8):1292-1296, [doi: 10.1212/wnl.38.8.1292].
- Floyd B.J., Wilkerson E.M., Veling M.T., Minogue C.E., Xia C., Beebe E.T., Wrobel R.L., Cho H., Kremer L.S., Alston C.L., Gromek K.A., Dolan B.K., Ulbrich A., Stefely J.A., Bohl S.L., Werner K.M., Jochem A., Westphall M.S., Rensvold J.W., Taylor R.W., Prokisch H., Kim J.P., Coon J.J., Pagliarini D.J. - *Mitochondrial Protein Interaction Mapping Identifies Regulators of Respiratory Chain Function* - Mol. Cell (2016); 63(4):621-632, [doi: 10.1016/j.molcel.2016.06.033].
- Foury F. & Cazzalini O. - *Deletion of the yeast homologue of the human gene associated with Friedreich's ataxia elicits iron accumulation in mitochondria* - FEBS Lett. (1997); 411(2-3):373-377, [doi: 10.1016/s0014-5793(97)00734-5].
- Fox N.G., Das D., Chakrabarti M., Lindahl P.A., Barondeau D.P. - *Frataxin Accelerates [2Fe-2S] Cluster Formation on the Human Fe-S Assembly Complex* - Biochemistry (2015); 54(25):3880-3889, [doi: 10.1021/bi5014497].
- Fox N.G., Yu X., Feng X., Bailey H.J., Martelli A., Nabhan J.F., Strain-Damerell C., Bulawa C., Yue W.W., Han S. - *Structure of the human frataxin-bound iron-sulfur cluster assembly complex provides insight into its activation mechanism* - Nat. Commun. (2019); 10(1):2210, [doi: 10.1038/s41467-019-09989-y].
- Fredriksson S., Gullberg M., Jarvius J., Olsson C., Pietras K., Gústafsdóttir S.M., Ostman A., Landegren U. - *Protein detection using proximity-dependent DNA ligation assays* - Nat. Biotechnol. (2002); 20(5):473-477, [doi: 10.1038/nbt0502-473].
- Frezza C., Cipolat S., Martins de Brito O., Micaroni M., Beznoussenko G.V., Rudka T., Bartoli D., Polishuck R.S., Danial N.N., De Strooper B., Scorrano L. - *OPA1 controls apoptotic cristae remodeling independently from mitochondrial fusion* - Cell (2006); 126(1):177-189, [doi: 10.1016/j.cell.2006.06.025].
- Friedreich N. - *Über degenerative Atrophie der spinalen Hinterstränge* - Virchow's Arch. Pathol. Anat. (1863), 26:391–419, [doi: 10.1007/BF01930976].

- Fukai T. & Ushio-Fukai M. - *Superoxide dismutases: role in redox signaling, vascular function, and diseases* - *Antioxid. Redox Signal.* (2011); 15(6):1583-1606, [doi: 10.1089/ars.2011.3999].
- Gakh O., Bedekovics T., Duncan S.F., Smith D.Y. 4th, Berkholtz D.S., Isaya G. - *Normal and Friedreich ataxia cells express different isoforms of frataxin with complementary roles in iron-sulfur cluster assembly* - *J. Biol. Chem.* (2010); 285(49):38486-38501, [doi: 10.1074/jbc.M110.145144].
- Gakh O., Park S., Liu G., Macomber L., Imlay J.A., Ferreira G.C., Isaya G. - *Mitochondrial iron detoxification is a primary function of frataxin that limits oxidative damage and preserves cell longevity* - *Hum. Mol. Genet.* (2006); 15(3):467-479, [doi: 10.1093/hmg/ddi461].
- Galea C.A., Huq A., Lockhart P.J., Tai G., Corben L.A., Yiu E.M., Gurrin L.C., Lynch D.R., Gelbard S., Durr A., Pousset F., Parkinson M., Labrum R., Giunti P., Perlman S.L., Delatycki M.B., Evans-Galea M.V. - *Compound heterozygous FXN mutations and clinical outcome in friedreich ataxia* - *Ann. Neurol.* (2016); 79(3):485-495, [doi: 10.1002/ana.24595].
- Garber Morales J., Holmes-Hampton G.P., Miao R., Guo Y., Münck E., Lindahl P.A. - *Biophysical characterization of iron in mitochondria isolated from respiring and fermenting yeast* - *Biochemistry* (2010); 49(26):5436-5444, [doi: 10.1021/bi100558z].
- García-Giménez J.L., Gimeno A., González-Cabo P., Dasí F., Bolinches-Amorós A., Mollá B., Palau F., Pallardó F.V. - *Differential expression of PGC-1 α and metabolic sensors suggest age-dependent induction of mitochondrial biogenesis in Friedreich ataxia fibroblasts* - *PLoS One* (2011); 6(6):e20666, [doi: 10.1371/journal.pone.0020666].
- Gellera C., Castellotti B., Mariotti C., Mineri R., Seveso V., Didonato S., Taroni F. - *Frataxin gene point mutations in Italian Friedreich ataxia patients* - *Neurogenetics.* (2007); 8(4):289-299, [doi: 10.1007/s10048-007-0101-5].
- Gentry L.E., Thacker M.A., Doughty R., Timkovich R., Busenlehner L.S. - *His86 from the N-terminus of frataxin coordinates iron and is required for Fe-S cluster synthesis* - *Biochemistry* (2013); 52(35):6085-6096, [doi: 10.1021/bi400443n].
- Gerber J., Mühlenhoff U., Lill R. - *An interaction between frataxin and Isu1/Nfs1 that is crucial for Fe/S cluster synthesis on Isu1* - *EMBO Rep.* (2003); 4(9):906-911, [doi: 10.1038/sj.embor.embor918].
- Gervason S., Larkem D., Mansour A.B., Botzanowski T., Müller C.S., Pecqueur L., Le Pavec G., Delaunay-Moisan A., Brun O., Agramunt J., Grandas A., Fontecave M, Schünemann V., Cianférani S., Sizun C., Tolédano M.B., D'Autréaux B. - *Physiologically relevant reconstitution of iron-sulfur cluster biosynthesis uncovers persulfide-processing functions of ferredoxin-2 and frataxin* - *Nat. Commun.* (2019); 10(1):3566, [doi: 10.1038/s41467-019-11470-9].

- Giachin G., Bouverot R., Acajjaoui S., Pantalone S., Soler-López M. - *Dynamics of Human Mitochondrial Complex I Assembly: Implications for Neurodegenerative Diseases* - *Front. Mol. Biosci.* (2016); 3:43, [doi: 10.3389/fmolb.2016.00043].
- Giacomello M., Pyakurel A., Glytsou C., Scorrano L. - *The cell biology of mitochondrial membrane dynamics* - *Nat. Rev. Mol. Cell. Biol.* (2020); 21(4):204-224, [doi: 10.1038/s41580-020-0210-7].
- Gibson T.J., Koonin E.V., Musco G., Pastore A., Bork P. - *Friedreich's ataxia protein: phylogenetic evidence for mitochondrial dysfunction* - *Trends Neurosci.* (1996); 19(11):465-468, [doi: 10.1016/S0166-2236(96)20054-2].
- Glytsou C., Calvo E., Cogliati S., Mehrotra A., Anastasia I., Rigoni G., Raimondi A., Shintani N., Loureiro M., Vazquez J., Pellegrini L., Enriquez J.A., Scorrano L., Soriano M.E. - *Optic Atrophy 1 Is Epistatic to the Core MICOS Component MIC60 in Mitochondrial Cristae Shape Control* - *Cell Rep.* (2016); 17(11):3024-3034, [doi: 10.1016/j.celrep.2016.11.049].
- Gong H., Li J., Xu A., Tang Y., Ji W., Gao R., Wang S., Yu L., Tian C., Li J., Yen H.Y., Man Lam S., Shui G., Yang X., Sun Y., Li X., Jia M., Yang C., Jiang B., Lou Z., Robinson C.V., Wong L.L., Guddat L.W., Sun F., Wang Q., Rao Z. - *An electron transfer path connects subunits of a mycobacterial respiratory supercomplex* - *Science* (2018); 362(6418):eaat8923, [doi: 10.1126/science.aat8923].
- González-Cabo P., Bolinches-Amorós A., Cabello J., Ros S., Moreno S., Baylis H.A., Palau F., Vázquez-Manrique R.P. - *Disruption of the ATP-binding cassette B7 (ABTM-1/ABC7) induces oxidative stress and premature cell death in *Caenorhabditis elegans** - *J. Biol. Chem.* (2011); 286(24):21304-21314, [doi: 10.1074/jbc.M110.211201].
- González-Cabo P. & Francesc Palau F. - *Mitochondrial pathophysiology in Friedreich's ataxia* - *J. Neurochem.* (2013), 126 (Suppl. 1), 53-64, [doi: 10.1111/jnc.12303].
- González-Cabo P., Vázquez-Manrique R.P., García-Gimeno M.A., Sanz P., Palau F. - *Fra1axin interacts functionally with mitochondrial electron transport chain proteins* - *Hum. Mol. Genet.* (2005); 14(15):2091-2098, [doi: 10.1093/hmg/ddi214].
- Gordon D.M., Kogan M., Knight S.A., Dancis A., Pain D. - *Distinct roles for two N-terminal cleaved domains in mitochondrial import of the yeast fra1axin homolog, *Yfh1p** - *Hum. Mol. Genet.* (2001); 10(3):259-269, [doi: 10.1093/hmg/10.3.259].
- Gorman G.S., Chinnery P.F., DiMauro S., Hirano M., Koga Y., McFarland R., Suomalainen A., Thorburn D.R., Zeviani M., Turnbull D.M. - *Mitochondrial diseases* - *Nat. Rev. Dis. Primers* (2016); 2:16080, [doi: 10.1038/nrdp.2016.80].

- Gorman G.S., Schaefer A.M., Ng Y., Gomez N., Blakely E.L., Alston C.L., Feeney C., Horvath R., Yu-Wai-Man P., Chinnery P.F., Taylor R.W., Turnbull D.M., McFarland R. - *Prevalence of nuclear and mitochondrial DNA mutations related to adult mitochondrial disease* - *Ann. Neurol.* (2015); 77(5):753-759, [doi: 10.1002/ana.24362].
- Gottesfeld J.M. - *Molecular Mechanisms and Therapeutics for the GAA·TTC Expansion Disease Friedreich Ataxia* - *Neurotherapeutics* (2019) ;16(4):1032-1049, [doi: 10.1007/s13311-019-00764-x].
- Gu J., Wu M., Guo R., Yan K., Lei J., Gao N., Yang M. - *The architecture of the mammalian respirasome* - *Nature* (2016); 537(7622):639-643, [doi: 10.1038/nature19359].
- Guerrero-Castillo S., Baertling F., Kownatzki D., Wessels H.J., Arnold S., Brandt U., Nijtmans L. - *The Assembly Pathway of Mitochondrial Respiratory Chain Complex I* - *Cell Metab.* (2017); 25(1):128-139, [doi: 10.1016/j.cmet.2016.09.002].
- Guo L., Wang Q., Weng L., Hauser L.A., Strawser C.J., Mesaros C., Lynch D.R., Blair I.A. - *Characterization of a new N-terminally acetylated extra-mitochondrial isoform of frataxin in human erythrocytes* - *Sci. Rep.* (2018); 8(1):17043, [doi: 10.1038/s41598-018-35346-y].
- Guo R., Zong S., Wu M., Gu J., Yang M. - *Architecture of Human Mitochondrial Respiratory Megacomplex I₂III₂IV₂* - *Cell* (2017); 170(6):1247-1257.e12., doi: 10.1016/j.cell.2017.07.050.
- Hackenbrock C.R., Chazotte B., Gupte S.S. - *The random collision model and a critical assessment of diffusion and collision in mitochondrial electron transport* - *J. Bioenerg. Biomembr.* (1986); 18(5):331-368, [doi: 10.1007/BF00743010].
- Haddy A. & Smith G. - *Transition metal and organic radical components of carp liver tissue observed by electron paramagnetic resonance spectroscopy* - *Comparative Biochem. Physiol. B Comparative Biochem.* (1999); 123:407-415, [doi: 10.1016/S0305-0491(99)00087-5].
- Hagen W.R. - *EPR spectroscopy of complex biological iron-sulfur systems* - *J. Biol. Inorg. Chem.* (2018); 23(4):623-634, [doi: 10.1007/s00775-018-1543-y].
- Han T.H.L., Camadro J.M., Barbault F., Santos R., El Hage Chahine J.M., Ha-Duong N.T. - *In Vitro interaction between yeast frataxin and superoxide dismutases: Influence of mitochondrial metals* - *Biochim. Biophys. Acta Gen. Subj.* (2019); 1863(5):883-892, [doi: 10.1016/j.bbagen.2019.02.011].
- Harding A.E. & Hewer R.L. - *The heart disease of Friedreich's ataxia: a clinical and electrocardiographic study of 115 patients, with an analysis of serial electrocardiographic changes in 30 cases* - *Q. J. Med.* (1983); 52(208):489-502.
- Harding I.H., Corben L.A., Storey E., Egan G.F., Stagnitti M.R., Poudel G.R., Delatycki M.B., Georgiou-Karistianis N. - *Fronto-cerebellar dysfunction and dysconnectivity underlying*

cognition in friedreich ataxia: The IMAGE-FRDA study - Hum. Brain Mapp. (2016); 37(1):338-350, [doi: 10.1002/hbm.23034].

- Harner M., Körner C., Walther D., Mokranjac D., Kaesmacher J., Welsch U., Griffith J., Mann M., Reggiori F., Neupert W. - *The mitochondrial contact site complex, a determinant of mitochondrial architecture* - EMBO J. (2011); 30(21):4356-4370, [doi: 10.1038/emboj.2011.379].
- He Y., Alam S.L., Proteasa S.V., Zhang Y., Lesuisse E., Dancis A., Stemmler T.L. - *Yeast frataxin solution structure, iron binding, and ferroxidase interaction* - Biochemistry (2004); 43(51):16254-16262, [doi: 10.1021/bi0488193].
- Herrera M.G., Noguera M.E., Sewell K.E., Agudelo Suárez W.A., Capece L., Klinke S., Santos J. - *Structure of the Human ACP-ISD11 Heterodimer* - Biochemistry (2019); 58(46):4596-4609, [doi: 10.1021/acs.biochem.9b00539].
- Hinchliffe P., Carroll J., Sazanov L.A. - *Identification of a novel subunit of respiratory complex I from Thermus thermophilus* - Biochemistry (2006); 45(14):4413-4420, [doi: 10.1021/bi0600998].
- Hirst J. - *Mitochondrial complex I* - Annu. Rev. Biochem. (2013); 82:551-575, [doi: 10.1146/annurev-biochem-070511-103700].
- Hirst J. - *Open questions: respiratory chain supercomplexes-why are they there and what do they do?* - BMC Biol. (2018); 16(1):111, [doi: 10.1186/s12915-018-0577-5].
- Huang J., Dizin E., Cowan J.A. - *Mapping iron binding sites on human frataxin: implications for cluster assembly on the ISU Fe-S cluster scaffold protein* - J. Biol. Inorg. Chem. (2008); 13(5):825-836, [doi: 10.1007/s00775-008-0369-4].
- Hudson G., Amati-Bonneau P., Blakely E.L., Stewart J.D., He L., Schaefer A.M., Griffiths P.G., Ahlqvist K., Suomalainen A., Reynier P., McFarland R., Turnbull D.M., Chinnery P.F., Taylor R.W. - *Mutation of OPA1 causes dominant optic atrophy with external ophthalmoplegia, ataxia, deafness and multiple mitochondrial DNA deletions: a novel disorder of mtDNA maintenance* - Brain (2008); 131(Pt 2):329-337, [doi: 10.1093/brain/awm272].
- Huttlin E.L., Bruckner R.J., Paulo J.A., Cannon J.R., Ting L., Baltier K., Colby G., Gebreau F., Gygi M.P., Parzen H., Szpyt J., Tam S., Zarraga G., Pontano-Vaites L., Swarup S., White A.E., Schweppe D.K., Rad R., Erickson B.K., Obar R.A., Guruharsha K.G., Li K., Artavanis-Tsakonas S., Gygi S.P., Harper J.W. - *Architecture of the human interactome defines protein communities and disease networks* - Nature (2017); 545(7655):505-509, [doi: 10.1038/nature22366].
- Huynen M.A., Snel B., Bork P., Gibson T.J. - *The phylogenetic distribution of frataxin indicates a role in iron-sulfur cluster protein assembly* - Hum. Mol. Genet. (2001); 10(21):2463-2468, [doi: 10.1093/hmg/10.21.2463].

- Ilari A., Latella M.C., Ceci P., Ribacchi F., Su M., Giangiacomo L., Stefanini S., Chasteen N.D., Chiancone E. - *The unusual intersubunit ferroxidase center of Listeria innocua Dps is required for hydrogen peroxide detoxification but not for iron uptake. A study with site-specific mutants* - *Biochemistry* (2005); 44(15):5579-5587, [doi: 10.1021/bi050005e].
- Irazusta V., Cabisco E., Reverter-Branchat G., Ros J., Tamarit J. - *Manganese is the link between frataxin and iron-sulfur deficiency in the yeast model of Friedreich ataxia* - *J. Biol. Chem.* (2006); 281(18):12227-12232, [doi: 10.1074/jbc.M511649200].
- Irazusta V., Obis E., Moreno-Cermeño A., Cabisco E., Ros J., Tamarit J. - *Yeast frataxin mutants display decreased superoxide dismutase activity crucial to promote protein oxidative damage* - *Free Radic. Biol. Med.* (2010); 48(3):411-420, [doi: 10.1016/j.freeradbiomed.2009.11.010].
- Ishihara N., Fujita Y., Oka T., Mihara K. - *Regulation of mitochondrial morphology through proteolytic cleavage of OPA1* - *EMBO J.* (2006); 25(13):2966-2977, [doi: 10.1038/sj.emboj.7601184].
- Iwata S., Lee J.W., Okada K., Lee J.K., Iwata M., Rasmussen B., Link T.A., Ramaswamy S., Jap B.K. - *Complete structure of the 11-subunit bovine mitochondrial cytochrome bc1 complex* - *Science* (1998); 281(5373):64-71, [doi: 10.1126/science.281.5373.64].
- Javadov S., Jang S., Chapa-Dubocq X.R., Khuchua Z., Camara A.K. - *Mitochondrial respiratory supercomplexes in mammalian cells: structural versus functional role* - *J. Mol. Med.* (2021); 99(1):57-73, [doi: 10.1007/s00109-020-02004-8].
- Jiralerspong S., Ge B., Hudson T.J., Pandolfo M. - *Manganese superoxide dismutase induction by iron is impaired in Friedreich ataxia cells* - *FEBS Lett.* (2001); 509(1):101-105, [doi: 10.1016/s0014-5793(01)03140-4].
- Johnson M.K., Morningstar J.E., Bennett D.E., Ackrell B.A., Kearney E.B. - *Magnetic circular dichroism studies of succinate dehydrogenase. Evidence for [2Fe-2S], [3Fe-xS], and [4Fe-4S] centers in reconstitutively active enzyme* - *J. Biol. Chem.* (1985); 260(12):7368-78.
- Jones B.A. & Fangman W.L. - *Mitochondrial DNA maintenance in yeast requires a protein containing a region related to the GTP-binding domain of dynamin* - *Genes Dev.* (1992); 6(3):380-9, [doi: 10.1101/gad.6.3.380].
- Jurkute N. & Yu-Wai-Man P. - *Leber hereditary optic neuropathy: bridging the translational gap* - *Curr. Opin. Ophthalmol.* (2017); 28(5):403-409, [doi: 10.1097/ICU.0000000000000410].
- Kadenbach B. - *Complex IV - The regulatory center of mitochondrial oxidative phosphorylation* - *Mitochondrion* (2021); 58:296-302, [doi: 10.1016/j.mito.2020.10.004].

- Kalyanaraman B., Cheng G., Zielonka J., Bennett B. - *Low-Temperature EPR Spectroscopy as a Probe-Free Technique for Monitoring Oxidants Formed in Tumor Cells and Tissues: Implications in Drug Resistance and OXPHOS-Targeted Therapies* - Cell Biochem. Biophys. (2019); 77(1):89-98, [doi: 10.1007/s12013-018-0858-1].
- Karlberg T., Schagerlöf U., Gakh O., Park S., Ryde U., Lindahl M., Leath K., Garman E., Isaya G., Al-Karadaghi S. - *The structures of frataxin oligomers reveal the mechanism for the delivery and detoxification of iron* - Structure (2006); 14(10):1535-1546, [doi: 10.1016/j.str.2006.08.010].
- Karthikeyan G., Bonucci A., Casano G., Gerbaud G., Abel S., Thomé V., Kodjabachian L., Magalon A., Guigliarelli B., Belle V., Ouari O., Mileo E. - *A Bioresistant Nitroxide Spin Label for In-Cell EPR Spectroscopy: In Vitro and In Oocytes Protein Structural Dynamics Studies* - Angew. Chem. Int. Ed. Engl. (2018); 57(5):1366-1370, [doi: 10.1002/anie.201710184].
- Kehrer J.P. - *The Haber-Weiss reaction and mechanisms of toxicity* - Toxicology (2000); 149(1):43-50, [doi: 10.1016/s0300-483x(00)00231-6].
- Keilin D. & Hartree E.F. - *Activity of the cytochrome system in heart muscle preparations* - Biochem. J. (1947); 41(4):500-502, [doi: 10.1042/bj0410500].
- Kiley P.J & Beinert H. - *The role of Fe-S proteins in sensing and regulation in bacteria* - Curr Opin Microbiol. (2003); 6(2):181-185, [doi: 10.1016/s1369-5274(03)00039-0].
- Kim H.J., Khalimonchuk O., Smith P.M., Winge D.R. - *Structure, function, and assembly of heme centers in mitochondrial respiratory complexes* - Biochim. Biophys. Acta (2012); 1823(9):1604-1616, [doi: 10.1016/j.bbamcr.2012.04.008].
- Klug C.S. & Feix J.B. - *Methods and applications of site-directed spin labeling EPR spectroscopy* - Methods Cell. Biol. (2008); 84:617-658, [doi: 10.1016/S0091-679X(07)84020-9].
- Koeppen A.H. - *Friedreich's ataxia: pathology, pathogenesis, and molecular genetics* - J. Neurol. Sci. (2011), 303(1-2):1-12, [doi: 10.1016/j.jns.2011.01.010].
- Koopman W.J., Willems P.H., Smeitink J.A. - *Monogenic mitochondrial disorders* - N. Engl. J. Med. (2012); 366(12):1132-1141, [doi: 10.1056/NEJMra1012478].
- Kozjak-Pavlovic V. - *The MICOS complex of human mitochondria* - Cell Tissue Res. (2017); 367(1):83-93, [doi: 10.1007/s00441-016-2433-7].
- Koutnikova H., Campuzano V., Foury F., Dollé P., Cazzalini O., Koenig M. - *Studies of human, mouse and yeast homologues indicate a mitochondrial function for frataxin* - Nat. Genet. (1997); 16(4):345-351, [doi: 10.1038/ng0897-345].

- Koutnikova H., Campuzano V., Koenig M. - *Maturation of wild-type and mutated frataxin by the mitochondrial processing peptidase* - Hum. Mol. Genet. (1998); 7(9):1485-1489, [doi: 10.1093/hmg/7.9.1485].
- Kozakov D., Hall D.R., Xia B., Porter K.A., Padhorney D., Yueh C., Beglov D., Vajda S. - *The ClusPro web server for protein-protein docking* - Nat. Protoc. (2017); 12(2):255-278, [doi: 10.1038/nprot.2016.169].
- Kroneck P.M., Antholine W.E., Kastrau D.H., Buse G., Steffens G.C., Zumft W.G. - *Multifrequency EPR evidence for a bimetallic center at the CuA site in cytochrome c oxidase* - FEBS Lett. (1990); 268(1):274-276, [doi: 10.1016/0014-5793(90)81026-k].
- Kühlbrandt W. - *Structure and Mechanisms of F-Type ATP Synthases* - Annu. Rev. Biochem. (2019); 88:515-549, [doi: 10.1146/annurev-biochem-013118-110903].
- Lamarche J.B., Côté M., Lemieux B. - *The cardiomyopathy of Friedreich's ataxia morphological observations in 3 cases* - Can. J. Neurol. Sci. (1980); 7(4):389-396, [doi: 10.1017/s0317167100022927].
- Lange C. & Hunte C. - *Crystal structure of the yeast cytochrome bc1 complex with its bound substrate cytochrome c* - Proc. Natl. Acad. Sci. U. S. A. (2002); 99(5):2800-2805, [doi: 10.1073/pnas.052704699].
- Larsson N.G. & Clayton D.A. - *Molecular genetic aspects of human mitochondrial disorders* - Annu. Rev. Genet. (1995); 29:151-178, [doi: 10.1146/annurev.ge.29.120195.001055].
- Lazaropoulos M., Dong Y., Clark E., Greeley N.R., Seyer L.A., Brigatti K.W., Christie C., Perlman S.L., Wilmot G.R., Gomez C.M., Mathews K.D., Yoon G., Zesiewicz T., Hoyle C., Subramony S.H., Brocht A.F., Farmer J.M., Wilson R.B., Deutsch E.C., Lynch D.R. - *Frataxin levels in peripheral tissue in Friedreich ataxia* - Ann. Clin. Transl. Neurol. (2015); 2(8):831-842, [doi: 10.1002/acn3.225].
- Lee M.G., Cho S.J., Yang J.K., Song H.K., Suh S.W. - *Crystallization and preliminary X-ray crystallographic analysis of Escherichia coli CyaY, a structural homologue of human frataxin* - Acta Crystallogr. D Biol. Crystallogr. (2000); 56(Pt 7):920-921, [doi: 10.1107/s0907444900005916].
- Leidgens S., De Smet S., Foury F. - *Frataxin interacts with Isu1 through a conserved tryptophan in its beta-sheet* - Hum. Mol. Genet. (2010); 19(2):276-286, [doi: 10.1093/hmg/ddp495].
- Leone M., Rocca W.A., Rosso M.G., Mantel N., Schoenberg B.S., Schiffer D. - *Friedreich's disease: survival analysis in an Italian population* - Neurology (1988), 38 (9) 1433, [doi: 10.1212/WNL.38.9.1433].

- Lesuisse E., Santos R., Matzanke B.F., Knight S.A., Camadro J.M., Dancis A. - *Iron use for haeme synthesis is under control of the yeast frataxin homologue (Yfh1)* - Hum. Mol. Genet. (2003); 12(8):879-889, [doi: 10.1093/hmg/ddg096].
- Letts J.A., Fiedorczuk K., Sazanov L.A. - *The architecture of respiratory supercomplexes* - Nature (2016); 537(7622):644-648, [doi: 10.1038/nature19774].
- Letts J.A. & Sazanov L.A. - *Clarifying the supercomplex: the higher-order organization of the mitochondrial electron transport chain* - Nat. Struct. Mol. Biol. (2017); 24(10):800-808, [doi: 10.1038/nsmb.3460].
- Lill R. - *Function and biogenesis of iron-sulphur proteins* - Nature (2009); 460(7257):831-838, [doi: 10.1038/nature08301].
- Lill R. & Freibert S.A. - *Mechanisms of Mitochondrial Iron-Sulfur Protein Biogenesis* - Annu. Rev. Biochem. (2020); 89:471-499, [doi: 10.1146/annurev-biochem-013118-111540].
- Lill R., Hoffmann B., Molik S., Pierik A.J., Rietzschel N., Stehling O., Uzarska M.A., Webert H., Wilbrecht C., Mühlhoff U. - *The role of mitochondria in cellular iron-sulfur protein biogenesis and iron metabolism* - Biochim. Biophys. Acta (2012); 1823(9):1491-1508, [doi: 10.1016/j.bbamcr.2012.05.009].
- Lill R. & Mühlhoff U. - *Maturation of iron-sulfur proteins in eukaryotes: mechanisms, connected processes, and diseases* - Annu. Rev. Biochem. (2008); 77:669-700, [doi: 10.1146/annurev.biochem.76.052705.162653].
- Lin H., Magrane J., Rattelle A., Stepanova A., Galkin A., Clark E.M., Dong Y.N., Halawani S.M., Lynch D.R. - *Early cerebellar deficits in mitochondrial biogenesis and respiratory chain complexes in the KIKO mouse model of Friedreich ataxia* - Dis. Model. Mech. (2017); 10(11):1343-1352, [doi: 10.1242/dmm.030502].
- Liu J., Chakraborty S., Hosseinzadeh P., Yu Y., Tian S., Petrik I., Bhagi A., Lu Y. - *Metalloproteins containing cytochrome, iron-sulfur, or copper redox centers* - Chem. Rev. (2014); 114(8):4366-4469, [doi: 10.1021/cr400479b].
- Llorens J.V., Navarro J.A., Martínez-Sebastián M.J., Baylies M.K., Schneuwly S., Botella J.A., Moltó M.D. - *Causative role of oxidative stress in a Drosophila model of Friedreich ataxia* - FASEB J. (2007); 21(2):333-344, [doi: 10.1096/fj.05-5709com].
- López C.J., Fleissner M.R., Guo Z., Kusnetzow A.K., Hubbell W.L. - *Osmolyte perturbation reveals conformational equilibria in spin-labeled proteins* - Protein Sci. (2009); 18(8):1637-1652, [doi: 10.1002/pro.180].

- Lu C. & Cortopassi G. - *Frataxin knockdown causes loss of cytoplasmic iron-sulfur cluster functions, redox alterations and induction of heme transcripts* - Arch. Biochem. Biophys. (2007); 457(1):111-22, [doi: 10.1016/j.abb.2006.09.010].
- Lynch D.R., Chin M.P., Delatycki M.B., Subramony S.H., Corti M., Hoyle J.C., Boesch S., Nachbauer W., Mariotti C., Mathews K.D., Giunti P., Wilmot G., Zesiewicz T., Perlman S., Goldsberry A., O'Grady M., Meyer C.J. - *Safety and Efficacy of Omaveloxolone in Friedreich Ataxia (MOXIe Study)* - Ann. Neurol. (2021); 89(2):212-225, [doi: 10.1002/ana.25934].
- Lynch D.R., Farmer J., Hauser L., Blair I.A., Wang Q.Q., Mesaros C., Snyder N., Boesch S., Chin M., Delatycki M.B., Giunti P., Goldsberry A., Hoyle C., McBride M.G., Nachbauer W., O'Grady M., Perlman S., Subramony S.H., Wilmot G.R., Zesiewicz T., Meyer C. - *Safety, pharmacodynamics, and potential benefit of omaveloxolone in Friedreich ataxia* - Ann. Clin. Transl. Neurol. (2018) ; 6(1):15-26, [doi: 10.1002/acn3.660].
- Maguire J.J., Johnson M.K., Morningstar J.E., Ackrell B.A., Kearney E.B. - *Electron paramagnetic resonance studies of mammalian succinate dehydrogenase. Detection of the tetranuclear cluster S2* - J. Biol. Chem. (1985); 260(20):10909-12.
- Maio N., Jain A., Rouault T.A. - *Mammalian iron-sulfur cluster biogenesis: Recent insights into the roles of frataxin, acyl carrier protein and ATPase-mediated transfer to recipient proteins* - Curr. Opin. Chem. Biol. (2020); 55:34-44, [doi: 10.1016/j.cbpa.2019.11.014].
- Maio N. & Rouault T.A. - *Outlining the Complex Pathway of Mammalian Fe-S Cluster Biogenesis* - Trends Biochem. Sci. (2020); 45(5):411-426, [doi: 10.1016/j.tibs.2020.02.001].
- Marie P. - *Sur l'hérédité-ataxie cérébelleuse* - Sem Med. (1893); 13:444-447.
- Mariotti C., Nachbauer W., Panzeri M., Poewe W., Taroni F., Boesch S. - *Erythropoietin in Friedreich ataxia* - J. Neurochem. (2013); 126 Suppl 1:80-87, [doi: 10.1111/jnc.12301].
- Martelli A., Wattenhofer-Donzé M., Schmucker S., Bouvet S., Reutenauer L., Puccio H. - *Frataxin is essential for extramitochondrial Fe-S cluster proteins in mammalian tissues* - Hum. Mol. Genet. (2007); 16(22):2651-2658, [doi: 10.1093/hmg/ddm163].
- McFarland R., Taylor R.W., Turnbull D.M. - *A neurological perspective on mitochondrial disease* - Lancet Neurol. (2010); 9(8):829-840, [doi: 10.1016/S1474-4422(10)70116-2].
- McKenzie M., Lazarou M., Thorburn D.R., Ryan M.T. - *Mitochondrial respiratory chain supercomplexes are destabilized in Barth Syndrome patients* - J. Mol. Biol. (2006); 361(3):462-469, [doi: 10.1016/j.jmb.2006.06.057].
- Meeusen S., DeVay R., Block J., Cassidy-Stone A., Wayson S., McCaffery J.M., Nunnari J. - *Mitochondrial inner-membrane fusion and crista maintenance requires the dynamin-related GTPase Mgm1* - Cell (2006); 127(2):383-395, [doi: 10.1016/j.cell.2006.09.021].

- Mileykovskaya E., Penczek P.A., Fang J., Mallampalli V.K., Sparagna G.C., Dowhan W. - *Arrangement of the respiratory chain complexes in Saccharomyces cerevisiae supercomplex III₂IV₂ revealed by single particle cryo-electron microscopy* - J. Biol. Chem. (2012); 287(27):23095-23103, [doi: 10.1074/jbc.M112.367888].
- Miranda-Astudillo H., Colina-Tenorio L., Jiménez-Suárez A., Vázquez-Acevedo M., Salin B., Giraud M.F., Remacle C., Cardol P., González-Halphen D. - *Oxidative phosphorylation supercomplexes and respirasome reconstitution of the colorless alga Polytomella sp* – Biochim. Biophys. Acta Bioenerg. (2018); 1859(6):434-444, [doi: 10.1016/j.bbabi.2018.03.004].
- Mitchell P. - *Coupling of phosphorylation to electron and hydrogen transfer by a chemi-osmotic type of mechanism* - Nature (1961); 191:144-148 [doi: 10.1038/191144a0].
- Monrós E., Moltó M.D., Martínez F., Cañizares J., Blanca J., Vilchez J.J., Prieto F., de Frutos R., Palau F. - *Phenotype correlation and intergenerational dynamics of the Friedreich ataxia GAA trinucleotide repeat* - Am. J. Hum. Genet. (1997); 61(1):101-10, [doi: 10.1086/513887].
- Montermini L., Richter A., Morgan K., Justice C.M., Julien D., Castellotti B., Mercier J., Poirier J., Capozzoli F., Bouchard J.P., Lemieux B., Mathieu J., Vanasse M., Seni M.H., Graham G., Andermann F., Andermann E., Melançon S.B., Keats B.J., Di Donato S., Pandolfo M. - *Phenotypic variability in Friedreich ataxia: role of the associated GAA triplet repeat expansion* – Ann. Neurol. (1997); 41(5):675-682, [doi: 10.1002/ana.410410518].
- Morelli A.M., Ravera S., Calzia D., Panfoli I. - *An update of the chemiosmotic theory as suggested by possible proton currents inside the coupling membrane* - Open Biol. (2019); 9(4):180221, [doi: 10.1098/rsob.180221].
- Mühlhoff U., Richhardt N., Ristow M., Kispal G., Lill R. - *The yeast frataxin homolog Yfh1p plays a specific role in the maturation of cellular Fe/S proteins* - Hum. Mol. Genet. (2002); 11(17):2025-36, [doi: 10.1093/hmg/11.17.2025].
- Mukherjee I., Ghosh M., Meinecke M. - *MICOS and the mitochondrial inner membrane morphology - when things get out of shape* - FEBS Lett. (2021); 595(8):1159-1183, [doi: 10.1002/1873-3468.14089].
- Murphy M.P. & Hartley R.C. - *Mitochondria as a therapeutic target for common pathologies* - Nat. Rev. Drug Discov. (2018); 17(12):865-886, [doi: 10.1038/nrd.2018.174].
- Musco G., de Tommasi T., Stier G., Kolmerer B., Bottomley M., Adinolfi S., Muskett F.W., Gibson T.J., Frenkiel T.A., Pastore A. - *Assignment of the 1H, 15N, and 13C resonances of the C-terminal domain of frataxin, the protein responsible for Friedreich ataxia* - J. Biomol. NMR (1999); 15(1):87-88, [doi: 10.1023/a:1008398832619].

- Musco G., Stier G., Kolmerer B., Adinolfi S., Martin S., Frenkiel T., Gibson T., Pastore A. - *Towards a structural understanding of Friedreich's ataxia: the solution structure of frataxin* - Structure (2000); 8(7):695-707, [doi: 10.1016/s0969-2126(00)00158-1].
- Nair M., Adinolfi S., Kelly G., Frenkiel T.A., Pastore A. - *NMR assignment of the 1H, 15N and 13C resonances of the E. coli frataxin orthologue, CyaY* – J. Biomol. NMR (2003); 27(4):403-404, [doi: 10.1023/a:1025845513018].
- Nair M., Adinolfi S., Pastore C., Kelly G., Temussi P., Pastore A. - *Solution structure of the bacterial frataxin ortholog, CyaY: mapping the iron binding sites* - Structure (2004); 12(11):2037-2048, [doi: 10.1016/j.str.2004.08.012].
- Ndi M., Marin-Buera L., Salvatori R., Singh A.P., Ott M. - *Biogenesis of the bc1 Complex of the Mitochondrial Respiratory Chain* - J. Mol. Biol. (2018); 430(21):3892-3905, [doi: 10.1016/j.jmb.2018.04.036].
- Novack G.V., Galeano P., Castaño E.M., Morelli L. - *Mitochondrial Supercomplexes: Physiological Organization and Dysregulation in Age-Related Neurodegenerative Disorders* - Front. Endocrinol. (2020); 11:600, [doi: 10.3389/fendo.2020.00600].
- Ohnishi T. - *Iron-sulfur clusters/semiquinones in complex I* - Biochim. Biophys. Acta (1998); 1364(2):186-206, [doi: 10.1016/s0005-2728(98)00027-9].
- Ohnishi T. & Nakamaru-Ogiso E. - *Were there any "misassignments" among iron-sulfur clusters N4, N5 and N6b in NADH-quinone oxidoreductase (complex I)?* – Biochim. Biophys. Acta (2008); 1777(7-8):703-710, [doi: 10.1016/j.bbabi.2008.04.032].
- Oliva R., Vangone A., Cavallo L. - *Ranking multiple docking solutions based on the conservation of inter-residue contacts* - Proteins (2013); 81(9):1571-1584, [doi: 10.1002/prot.24314].
- O'Neill H.A., Gakh O., Isaya G. - *Supramolecular assemblies of human frataxin are formed via subunit-subunit interactions mediated by a non-conserved amino-terminal region* - J. Mol. Biol. (2005); 345(3):433-439, [doi: 10.1016/j.jmb.2004.10.074].
- Orme-Johnson N.R., Hansen R.E., Beinert H. - *Electron paramagnetic resonance-detectable electron acceptors in beef heart mitochondria. Ubihydroquinone-cytochrome c reductase segment of the electron transfer system and complex mitochondrial fragments* - J. Biol. Chem. (1974); 249(6):1928-1939.
- Ostermeier C., Iwata S., Michel H. - *Cytochrome c oxidase* - Curr. Opin. Struct. Biol. (1996); 6(4):460-466, [doi: 10.1016/s0959-440x(96)80110-2].
- Ott C., Ross K., Straub S., Thiede B., Götz M., Goosmann C., Krischke M., Mueller M.J., Krohne G., Rudel T., Kozjak-Pavlovic V. - *Sam50 functions in mitochondrial intermembrane*

space bridging and biogenesis of respiratory complexes - Mol. Cell Biol. (2012); 32(6):1173-1188, [doi: 10.1128/MCB.06388-11].

- Outten F.W. - *Recent advances in the Suf Fe-S cluster biogenesis pathway: Beyond the Proteobacteria* - Biochim. Biophys. Acta (2015); 1853(6):1464-1469, [doi: 10.1016/j.bbamcr.2014.11.001].
- Padmanaban G, Venkateswar V, Rangarajan P.N. - *Haem as a multifunctional regulator* - Trends Biochem. Sci. (1989); 14(12):492-496, [doi: 10.1016/0968-0004(89)90182-5].
- Palade G.E. - *An electron microscope study of the mitochondrial structure* - J. Histochem. Cytochem. (1953); 1(4):188-211, [doi: 10.1177/1.4.188].
- Pallardó F.V., Pagano G., Rodríguez L.R., González-Cabo P., Lyakhovich A., Trifuoggi M. - *Friedreich Ataxia: current state-of-the-art, and future prospects for mitochondrial-focused therapies* - Transl. Res. (2021); 229:135-141, [doi: 10.1016/j.trsl.2020.08.009].
- Palomo G.M., Cerrato T., Gargini R., Diaz-Nido J. - *Silencing of frataxin gene expression triggers p53-dependent apoptosis in human neuron-like cells* - Hum. Mol. Genet. (2011); 20(14):2807-2822, [doi: 10.1093/hmg/ddr187].
- Pandolfo M. & Pastore A. - *The pathogenesis of Friedreich ataxia and the structure and function of frataxin* - J. Neurol. (2009); 256 Suppl 1:9-17, [doi: 10.1007/s00415-009-1003-2].
- Pantopoulos K. - *Iron metabolism and the IRE/IRP regulatory system: an update* - Ann. N. Y. Acad. Sci. (2004); 1012:1-13, [doi: 10.1196/annals.1306.001].
- Parent A., Elduque X., Cornu D., Belot L., Le Caer J.P., Grandas A., Toledano M.B., D'Autréaux B. - *Mammalian frataxin directly enhances sulfur transfer of NFS1 persulfide to both ISCU and free thiols* - Nat. Commun. (2015); 6:5686, [doi: 10.1038/ncomms6686].
- Parey K., Haapanen O., Sharma V., Köfeler H., Züllig T., Prinz S., Siegmund K., Wittig I., Mills D.J., Vonck J., Kühlbrandt W., Zickermann V. - *High-resolution cryo-EM structures of respiratory complex I: Mechanism, assembly, and disease* - Sci. Adv. (2019); 5(12):eaax9484, [doi: 10.1126/sciadv.aax9484].
- Park S., Gakh O., Mooney S.M., Isaya G. - *The ferroxidase activity of yeast frataxin* - J. Biol. Chem. (2002); 277(41):38589-38595, [doi: 10.1074/jbc.M206711200].
- Park S., Gakh O., O'Neill H.A., Mangravita A., Nichol H., Ferreira G.C., Isaya G. - *Yeast frataxin sequentially chaperones and stores iron by coupling protein assembly with iron oxidation* - J Biol Chem. (2003); 278(33):31340-51 [doi: 10.1074/jbc.M303158200].

- Parkinson M.H., Boesch S., Nachbauer W., Mariotti C., Giunti P. - *Clinical features of Friedreich's ataxia: classical and atypical phenotypes* - J. Neurochem. (2013); 126 Suppl 1:103-117, [doi: 10.1111/jnc.12317].
- Pastore A., Martin S.R., Politou A., Kondapalli K.C., Stemmler T., Temussi P.A. - *Unbiased cold denaturation: low- and high-temperature unfolding of yeast frataxin under physiological conditions* - J. Am. Chem. Soc. (2007); 129(17):5374-5375, [doi: 10.1021/ja0714538].
- Pastore A. & Puccio H. - *Frataxin: a protein in search for a function* - J. Neurochem. (2013); 126 Suppl 1:43-52, [doi: 10.1111/jnc.12220].
- Paumard P., Vaillier J., Couлары B., Schaeffer J., Soubannier V., Mueller D.M., Brèthes D., di Rago J.P., Velours J. - *The ATP synthase is involved in generating mitochondrial cristae morphology* - EMBO J. (2002); 21(3):221-230, [doi: 10.1093/emboj/21.3.221].
- Pérez-Luz S., Gimenez-Cassina A., Fernández-Frías I., Wade-Martins R., Díaz-Nido J. - *Delivery of the 135 kb human frataxin genomic DNA locus gives rise to different frataxin isoforms* - Genomics (2015); 106(2):76-82, [doi: 10.1016/j.ygeno.2015.05.006].
- Pernas L. & Scorrano L. - *Mito-Morphosis: Mitochondrial Fusion, Fission, and Cristae Remodeling as Key Mediators of Cellular Function* - Annu. Rev. Physiol. 2016; 78:505-531, [doi: 10.1146/annurev-physiol-021115-105011].
- Pettersen E.F., Goddard T.D., Huang C.C., Couch G.S., Greenblatt D.M., Meng E.C., Ferrin T.E. - *UCSF Chimera-a visualization system for exploratory research and analysis* - J. Comput. Chem. (2004); 25(13):1605-1612, [doi: 10.1002/jcc.20084].
- Pierce B.G., Wiehe K., Hwang H., Kim B.H., Vreven T., Weng Z. - *ZDOCK server: interactive docking prediction of protein-protein complexes and symmetric multimers* - Bioinformatics (2014); 30(12):1771-1773, [doi: 10.1093/bioinformatics/btu097].
- Pohl T., Walter J., Stolpe S., Soufo J.H., Grauman P.L., Friedrich T. - *Effects of the deletion of the Escherichia coli frataxin homologue CyaY on the respiratory NADH:ubiquinone oxidoreductase* - BMC Biochem. (2007); 8:13, [doi: 10.1186/1471-2091-8-13].
- Ponka P. - *Cell biology of heme* - Am. J. Med. Sci. (1999); 318(4):241-256, [doi: 10.1097/00000441-199910000-00004].
- Prischi F., Giannini C., Adinolfi S., Pastore A. - *The N-terminus of mature human frataxin is intrinsically unfolded* - FEBS J. (2009); 276(22):6669-6676, [doi: 10.1111/j.1742-4658.2009.07381.x].
- Protasoni M. & Zeviani M. - *Mitochondrial Structure and Bioenergetics in Normal and Disease Conditions* - Int. J. Mol. Sci. (2021); 22(2):586, [doi: 10.3390/ijms22020586].

- Puccio H., Simon D., Cossée M., Criqui-Filipe P., Tiziano F., Melki J., Hindelang C., Matyas R., Rustin P., Koenig M. - *Mouse models for Friedreich ataxia exhibit cardiomyopathy, sensory nerve defect and Fe-S enzyme deficiency followed by intramitochondrial iron deposits* - Nat. Genet. (2001); 27(2):181-186, [doi: 10.1038/84818].
- Quintana-Cabrera R., Mehrotra A., Rigoni G., Soriano M.E. - *Who and how in the regulation of mitochondrial cristae shape and function* - Biochem. Biophys. Res. Commun. (2018); 500(1):94-101, [doi: 10.1016/j.bbrc.2017.04.088].
- Quintana-Cabrera R., Quirin C., Glytsou C., Corrado M., Urbani A., Pellattiero A., Calvo E., Vázquez J., Enríquez J.A., Gerle C., Soriano M.E., Bernardi P., Scorrano L. - *The cristae modulator Optic atrophy 1 requires mitochondrial ATP synthase oligomers to safeguard mitochondrial function* - Nat. Commun. (2018); 9(1):3399, [doi: 10.1038/s41467-018-05655-x].
- Rahman J., Noronha A., Thiele I., Rahman S. - *Leigh map: A novel computational diagnostic resource for mitochondrial disease* - Ann. Neurol. (2017); 81(1): 9-16, [doi: 10.1002/ana.24835].
- Ramirez R.L., Qian J., Santambrogio P., Levi S., Koeppen A.H. - *Relation of cytosolic iron excess to cardiomyopathy of Friedreich's ataxia* - Am. J. Cardiol. (2012); 110(12):1820-1827, [doi: 10.1016/j.amjcard.2012.08.018].
- Ramírez-Camacho I., García-Niño W.R., Flores-García M., Pedraza-Chaverri J., Zazueta C. - *Alteration of mitochondrial supercomplexes assembly in metabolic diseases* - Biochim. Biophys. Acta Mol. Basis Dis. (2020); 1866(12):165935, [doi: 10.1016/j.bbadis.2020.165935].
- Ray P.D., Huang B.W., Tsuji Y. - *Reactive oxygen species (ROS) homeostasis and redox regulation in cellular signaling* - Cell Signal. (2012); 24(5):981-990, [doi: 10.1016/j.cellsig.2012.01.008].
- Rees D.C. - *Great metalloclusters in enzymology* - Annu. Rev. Biochem. (2002); 71:221-246, [doi: 10.1146/annurev.biochem.71.110601.135406].
- Rees D.C. & Howard J.B. - *The interface between the biological and inorganic worlds: iron-sulfur metalloclusters* - Science (2003); 300(5621):929-931, [doi: 10.1126/science.1083075].
- Richardson D.R., Lane D.J., Becker E.M., Huang M.L., Whitnall M., Suryo Rahmanto Y., Sheftel A.D., Ponka P. - *Mitochondrial iron trafficking and the integration of iron metabolism between the mitochondrion and cytosol* - Proc. Natl. Acad. Sci. U.S.A. (2010); 107(24):10775-10782, [doi: 10.1073/pnas.0912925107].
- Rieske J.S., MacLennan D.H., Coleman R. - *Isolation and properties of an iron-protein from the (reduced coenzyme Q)-cytochrome C reductase complex of the respiratory chain* - Biochem. Biophys. Res. Commun. (1964); 15:338-344, [doi: 10.1016/0006-291X(64)90171-8].

- Rocca C.J., Rainaldi J.N., Sharma J., Shi Y., Haquang J.H., Luebeck J., Mali P., Cherqui S. - *CRISPR-Cas9 Gene Editing of Hematopoietic Stem Cells from Patients with Friedreich's Ataxia* - Mol. Ther. Methods Clin. Dev. (2020); 17:1026-1036, [doi: 10.1016/j.omtm.2020.04.018].
- Roessler M.M., King M.S., Robinson A.J., Armstrong F.A., Harmer J., Hirst J. - *Direct assignment of EPR spectra to structurally defined iron-sulfur clusters in complex I by double electron-electron resonance* - Proc. Natl. Acad. Sci. U. S. A. (2010); 107(5):1930-1935, [doi: 10.1073/pnas.0908050107].
- Rötig A., Bourgeron T., Chretien D., Rustin P., Munnich A. - *Spectrum of mitochondrial DNA rearrangements in the Pearson marrow-pancreas syndrome* - Hum. Mol. Genet. (1995); 4(8):1327-1330, [doi: 10.1093/hmg/4.8.1327].
- Rötig A., de Lonlay P., Chretien D., Foury F., Koenig M., Sidi D., Munnich A., Rustin P. - *Aconitase and mitochondrial iron-sulphur protein deficiency in Friedreich ataxia* - Nat. Genet. (1997); 17(2):215-217, [doi: 10.1038/ng1097-215].
- Rouault T.A. - *Mammalian iron-sulphur proteins: novel insights into biogenesis and function* - Nat. Rev. Mol. Cell Biol. (2015); 16(1):45-55, [doi: 10.1038/nrm3909].
- Rouault T. & Klausner R. - *Regulation of iron metabolism in eukaryotes* - Curr. Top. Cell. Regul. (1997); 35:1-19, [doi: 10.1016/s0070-2137(97)80001-5].
- Rouault T.A. & Tong W.H. - *Iron-sulphur cluster biogenesis and mitochondrial iron homeostasis* - Nat. Rev. Mol. Cell Biol. (2005); 6(4):345-351, [doi: 10.1038/nrm1620].
- Rufini A., Cavallo F., Condò I., Fortuni S., De Martino G., Incani O., Di Venere A., Benini M., Massaro D.S., Arcuri G., Serio D., Malisan F., Testi R. - *Highly specific ubiquitin-competing molecules effectively promote frataxin accumulation and partially rescue the aconitase defect in Friedreich ataxia cells* - Neurobiol. Dis. (2015); 75:91-99, [doi: 10.1016/j.nbd.2014.12.011].
- Runko A.P., Griswold A.J., Min K.T. - *Overexpression of frataxin in the mitochondria increases resistance to oxidative stress and extends lifespan in Drosophila* - FEBS Lett. (2008); 582(5):715-719, [doi: 10.1016/j.febslet.2008.01.046].
- Russell O.M., Gorman G.S., Lightowers R.N., Turnbull D.M. - *Mitochondrial Diseases: Hope for the Future* - Cell (2020); 181(1):168-188, [doi: 10.1016/j.cell.2020.02.051].
- Ryan E., King M.D., Rustin P., Mayne P.D., Brown G.K., Monavari A.A., Walsh R., Treacy E.P. - *Mitochondrial cytopathies, phenotypic heterogeneity and a high incidence* - Ir. Med. J. (2006); 99(9):262-264.
- Sakamoto N., Chastain P.D., Parniewski P., Ohshima K., Pandolfo M., Griffith J.D., Wells R.D. - *Sticky DNA: self-association properties of long GAA.TTC repeats in R.R.Y triplex*

structures from Friedreich's ataxia – Mol. Cell (1999); 3(4):465-475, [doi: 10.1016/s1097-2765(00)80474-8].

- Salehi M.H., Kamalidehghan B., Houshmand M., Yong Meng G., Sadeghizadeh M., Aryani O., Nafissi S. - *Gene expression profiling of mitochondrial oxidative phosphorylation (OXPHOS) complex I in Friedreich ataxia (FRDA) patients* - PLoS One (2014); 9(4):e94069, [doi: 10.1371/journal.pone.009406].
- Sandi C., Al-Mahdawi S., Pook M.A. - *Epigenetics in Friedreich's Ataxia: Challenges and Opportunities for Therapy* - Genet. Res. Int. (2013), 852080, [doi: 10.1155/2013/852080].
- Saneto R.P., Cohen B.H., Copeland W.C., Naviaux R.K. - *Alpers-Huttenlocher syndrome* - Pediatr. Neurol. (2013); 48(3):167-178, [doi: 10.1016/j.pediatrneurol.2012.09.014].
- Sawyer W.H. & Winzor D.J. - *Theoretical aspects of the quantitative characterization of ligand binding* - Curr. Protoc. Protein Sci. (1999), 19, 1-40.
- Sazanov L.A. - *A giant molecular proton pump: structure and mechanism of respiratory complex I* - Nat. Rev. Mol. Cell Biol. (2015); 16(6):375-388, [doi: 10.1038/nrm3997].
- Sazanov L.A. & Hinchliffe P. - *Structure of the hydrophilic domain of respiratory complex I from *Thermus thermophilus** - Science (2006); 311(5766):1430-1436, [doi: 10.1126/science.1123809].
- Schägger H. & Pfeiffer K. - *Supercomplexes in the respiratory chains of yeast and mammalian mitochondria* - EMBO J. (2000); 19(8):1777-1783, [doi: 10.1093/emboj/19.8.1777].
- Schägger H & Pfeiffer K. - *The ratio of oxidative phosphorylation complexes I-V in bovine heart mitochondria and the composition of respiratory chain supercomplexes* - J. Biol. Chem. (2001); 276(41):37861-37867, [doi: 10.1074/jbc.M106474200].
- Schägger H. & von Jagow G. - *Blue native electrophoresis for isolation of membrane protein complexes in enzymatically active form* - Anal. Biochem. (1991); 199(2):223-231, [doi: 10.1016/0003-2697(91)90094-a].
- Scheibye-Knudsen M., Fang E.F., Croteau D.L., Wilson D.M. III, Bohr V.A. - *Protecting the mitochondrial powerhouse* - Trends Cell Biol. (2015); 25(3):158-170, [doi: 10.1016/j.tcb.2014.11.002].
- Schiavi A., Torgovnick A., Kell A., Megalou E., Castelein N., Guccini I., Marzocchella L., Gelino S., Hansen M., Malisan F., Condò I., Bei R., Rea S.L., Braeckman B.P., Tavernarakis N., Testi R., Ventura N. - *Autophagy induction extends lifespan and reduces lipid content in response to frataxin silencing in *C. elegans** - Exp. Gerontol. (2013); 48(2):191-201, [doi: 10.1016/j.exger.2012.12.002].

- Schieber M., Chandel N.S. - *ROS function in redox signaling and oxidative stress* - *Curr Biol.* (2014); 24(10):R453-462, [doi: 10.1016/j.cub.2014.03.034].
- Schlieben L.D. & Prokisch H. - *The Dimensions of Primary Mitochondrial Disorders* - *Front. Cell Dev. Biol.* (2020); 8:600079, [doi: 10.3389/fcell.2020.600079].
- Schmucker S., Argentini M., Carelle-Calmels N., Martelli A., Puccio H. - *The in vivo mitochondrial two-step maturation of human frataxin* - *Hum. Mol. Genet.* (2008); 17(22):3521-3531, [doi: 10.1093/hmg/ddn244].
- Schmucker S., Martelli A., Colin F., Page A., Wattenhofer-Donzé M., Reutenauer L., Puccio H. - *Mammalian frataxin: an essential function for cellular viability through an interaction with a preformed ISCU/NFS1/ISD11 iron-sulfur assembly complex* - *PLoS One* (2011); 6(1):e16199, [doi: 10.1371/journal.pone.0016199].
- Schmucker S. & Puccio H. - *Understanding the molecular mechanisms of Friedreich's ataxia to develop therapeutic approaches* - *Hum. Mol. Genet.* (2010); 19(R1):R103-110, [doi: 10.1093/hmg/ddq165].
- Schneidman-Duhovny D., Inbar Y., Nussinov R., Wolfson H.J. - *PatchDock and SymmDock: servers for rigid and symmetric docking* - *Nucleic Acids Res.* (2005); 33(Web Server issue):W363-367, [doi: 10.1093/nar/gki481].
- Schoenfeld R.A., Napoli E., Wong A., Zhan S., Reutenauer L., Morin D., Buckpitt A.R., Taroni F., Lonnerdal B., Ristow M., Puccio H., Cortopassi G.A. - *Frataxin deficiency alters heme pathway transcripts and decreases mitochondrial heme metabolites in mammalian cells* - *Hum. Mol. Genet.* (2005); 14(24):3787-3799, [doi: 10.1093/hmg/ddi393].
- Schultz B.E. & Chan S.I. - *Structures and proton-pumping strategies of mitochondrial respiratory enzymes* - *Annu. Rev. Biophys. Biomol. Struct.* (2001); 30:23-65, [doi: 10.1146/annurev.biophys.30.1.23].
- Schulz J.B., Dehmer T., Schöls L., Mende H., Hardt C., Vorgerd M., Bürk K., Matson W., Dichgans J., Beal M.F., Bogdanov M.B. - *Oxidative stress in patients with Friedreich ataxia* - *Neurology* (2000); 55(11):1719-1721, [doi: 10.1212/wnl.55.11.1719].
- Seguin A., Sutak R., Bulteau A.L., Garcia-Serres R., Oddou J.L., Lefevre S., Santos R., Dancis A., Camadro J.M., Latour J.M., Lesuisse E. - *Evidence that yeast frataxin is not an iron storage protein in vivo* - *Biochim. Biophys. Acta.* (2010); 1802(6):531-538, [doi: 10.1016/j.bbadis.2010.03.008].
- Seyer L., Greeley N., Foerster D., Strawser C., Gelbard S., Dong Y., Schadt K., Cotticelli M.G., Brocht A., Farmer J., Wilson R.B., Lynch D.R. - *Open-label pilot study of interferon gamma-1b in Friedreich ataxia* - *Acta Neurol. Scand.* (2015); 132(1):7-15, [doi: 10.1111/ane.12337].

- Shan Y., Napoli E., Cortopassi G. - *Mitochondrial frataxin interacts with ISD11 of the NFS1/ISCU complex and multiple mitochondrial chaperones* - Hum. Mol. Genet. (2007); 16(8):929-941, [doi: 10.1093/hmg/ddm038].
- Shepard K.A. & Yaffe M.P. - *The yeast dynamin-like protein, Mgm1p, functions on the mitochondrial outer membrane to mediate mitochondrial inheritance* - J. Cell Biol. (1999); 144(4):711-720, [doi: 10.1083/jcb.144.4.711].
- Siedow J.N., Power S., de la Rosa F.F., Palmer G. - *The preparation and characterization of highly purified, enzymically active complex III from baker's yeast* - J. Biol. Chem. (1978); 253(7):2392-2399.
- Simon D., Seznec H., Gansmuller A., Carelle N., Weber P., Metzger D., Rustin P., Koenig M., Puccio H. - *Friedreich ataxia mouse models with progressive cerebellar and sensory ataxia reveal autophagic neurodegeneration in dorsal root ganglia* - J. Neurosci. (2004); 24(8):1987-1995, [doi: 10.1523/JNEUROSCI.4549-03.2004].
- Skladal D., Halliday J., Thorburn D.R. - *Minimum birth prevalence of mitochondrial respiratory chain disorders in children* - Brain (2003); 126(Pt 8):1905-12, [doi: 10.1093/brain/awg170].
- Söderberg C., Gillam M.E., Ahlgren E.C., Hunter G.A., Gakh O., Isaya G., Ferreira G.C., Al-Karadaghi S. - *The Structure of the Complex between Yeast Frataxin and Ferrochelatase: characterization and pre-steady state reaction of ferrous iron delivery and heme synthesis* - J. Biol. Chem. (2016); 291(22):11887-11898, [doi: 10.1074/jbc.M115.701128].
- Söderberg O., Gullberg M., Jarvius M., Ridderstråle K., Leuchowius K.J., Jarvius J., Wester K., Hydbring P., Bahram F., Larsson L.G., Landegren U. - *Direct observation of individual endogenous protein complexes in situ by proximity ligation* - Nat. Methods (2006); 3(12):995-1000, [doi: 10.1038/nmeth947].
- Spinazzi M., Casarin A., Pertegato V., Salviati L., Angelini C. - *Assessment of mitochondrial respiratory chain enzymatic activities on tissues and cultured cells* - Nat. Protoc. (2012); 7(6):1235-1246, [doi: 10.1038/nprot.2012.058].
- Steinhoff H.J. - *Methods for study of protein dynamics and protein-protein interaction in protein-ubiquitination by electron paramagnetic resonance spectroscopy* - Front. Biosci. (2002); 7:c97-110, [doi: 10.2741/A763].
- Stenton S.L. & Prokisch H. - *Advancing genomic approaches to the molecular diagnosis of mitochondrial disease* - Essays Biochem. (2018); 62(3):399-408, [doi: 10.1042/EBC20170110].

- Stenton S.L. & Prokisch H. - *Genetics of mitochondrial diseases: Identifying mutations to help diagnosis* - *EbioMedicine* (2020); 56:102784, [doi: 10.1016/j.ebiom.2020.102784].
- Stockwell B.R., Jiang X., Gu W. - *Emerging Mechanisms and Disease Relevance of Ferroptosis* - *Trends Cell. Biol.* (2020); 30(6):478-490, [doi: 10.1016/j.tcb.2020.02.009].
- Strauss M., Hofhaus G., Schröder R.R., Kühlbrandt W. - *Dimer ribbons of ATP synthase shape the inner mitochondrial membrane* - *EMBO J.* (2008); 27(7):1154-1160, [doi: 10.1038/emboj.2008.35].
- Stroh A., Anderka O., Pfeiffer K., Yagi T., Finel M., Ludwig B., Schägger H. - *Assembly of respiratory complexes I, III, and IV into NADH oxidase supercomplex stabilizes complex I in *Paracoccus denitrificans** - *J. Biol. Chem.* (2004); 279(6):5000-5007, [doi: 10.1074/jbc.M309505200].
- Sugioka K., Nakano M., Totsune-Nakano H., Minakami H., Tero-Kubota S., Ikegami Y. - *Mechanism of O₂⁻ generation in reduction and oxidation cycle of ubiquinones in a model of mitochondrial electron transport systems* - *Biochim. Biophys. Acta* (1988); 936(3):377-385, [doi: 10.1016/0005-2728(88)90014-x].
- Suthammarak W., Somerlot B.H., Opheim E., Sedensky M., Morgan P.G. - *Novel interactions between mitochondrial superoxide dismutases and the electron transport chain* - *Aging Cell* (2013); 12(6):1132-1140, [doi: 10.1111/accel.12144].
- Swenson S.A., Moore C.M., Marcero J.R., Medlock A.E., Reddi A.R., Khalimonchuk O. - *From Synthesis to Utilization: The Ins and Outs of Mitochondrial Heme* - *Cells* (2020); 9(3):579, [doi: 10.3390/cells9030579].
- Taketani S. - *Aquisition, mobilization and utilization of cellular iron and heme: endless findings and growing evidence of tight regulation* - *Tohoku J. Exp. Med.* (2005); 205(4):297-318, [doi: 10.1620/tjem.205.297].
- Tovchigrechko A. & Vakser I.A. - *GRAMM-X public web server for protein-protein docking* - *Nucleic Acids Res.* (2006); 34(Web Server issue):W310-4, [doi: 10.1093/nar/gkl206].
- Trumpower B.L. - *The protonmotive Q cycle. Energy transduction by coupling of proton translocation to electron transfer by the cytochrome bc₁ complex* - *J. Biol. Chem.* (1990); 265(20):11409-12.
- Trumpower B.L. & Edwards C.A. - *Purification of a reconstitutively active iron-sulfur protein (oxidation factor) from succinate cytochrome c reductase complex of bovine heart mitochondria* - *J. Biol. Chem.* (1979); 254(17):8697-8706.

- Tsai C.L. & Barondeau D.P. - *Human frataxin is an allosteric switch that activates the Fe-S cluster biosynthetic complex* - *Biochemistry* (2010); 49(43):9132-9139, [doi: 10.1021/bi1013062].
- Tsai C.L., Bridwell-Rabb J., Barondeau D.P. - *Friedreich's ataxia variants I154F and W155R diminish frataxin-based activation of the iron-sulfur cluster assembly complex* - *Biochemistry* (2011); 50(29):6478-6487, [doi: 10.1021/bi200666h].
- Tsou A.Y., Paulsen E.K., Lagedrost S.J., Perlman S.L., Mathews K.D., Wilmot G.R., Ravina B., Koeppen A.H., Lynch D.R. - *Mortality in Friedreich ataxia* - *J. Neurol. Sci.* (2011); 307(1-2):46-49, [doi: 10.1016/j.jns.2011.05.023].
- Turrens J.F. & Boveris A. - *Generation of superoxide anion by the NADH dehydrogenase of bovine heart mitochondria* - *Biochem. J.* 1980; 191(2):421-427, [doi: 10.1042/bj1910421].
- Uceda A.B., Donoso J., Frau J., Vilanova B., Adrover M. - *Frataxins Emerge as New Players of the Intracellular Antioxidant Machinery* - *Antioxidants* (2021); 10(2):315, [doi: 10.3390/antiox10020315].
- Van Vranken J.G., Jeong M.Y., Wei P., Chen Y.C., Gygi S.P., Winge D.R., Rutter J. - *The mitochondrial acyl carrier protein (ACP) coordinates mitochondrial fatty acid synthesis with iron sulfur cluster biogenesis* - *Elife* (2016); 5:e17828, [doi: 10.7554/eLife.17828].
- Van Vranken J.G., Na U., Winge D.R., Rutter J. - *Protein-mediated assembly of succinate dehydrogenase and its cofactors* - *Crit. Rev. Biochem. Mol. Biol.* (2015); 50(2):168-180, [doi: 10.3109/10409238.2014.990556].
- Vangone A., Cavallo L., Oliva R. - *Using a consensus approach based on the conservation of inter-residue contacts to rank CAPRI models* - *Proteins* (2013); 81(12):2210-2220, [doi: 10.1002/prot.24423].
- Vankan P. - *Prevalence gradients of Friedreich's ataxia and R1b haplotype in Europe co-localize, suggesting a common Palaeolithic origin in the Franco-Cantabrian ice age refuge* - *J. Neurochem.* (2013); 126 Suppl 1:11-20, [doi: 10.1111/jnc.12215].
- Varanita T., Soriano M.E., Romanello V., Zaglia T., Quintana-Cabrera R., Semenzato M., Menabò R., Costa V., Civiletto G., Pesce P., Viscomi C., Zeviani M, Di Lisa F., Mongillo M., Sandri M., Scorrano L. - *The OPA1-dependent mitochondrial cristae remodeling pathway controls atrophic, apoptotic, and ischemic tissue damage* - *Cell Metab.* (2015); 21(6):834-844, [doi: 10.1016/j.cmet.2015.05.007].
- Vavla M., D'Angelo M.G., Arrigoni F., Toschi N., Peruzzo D., Gandossini S., Russo A., Diella E., Tirelli S., Salati R., Scarpazza P., Luffarelli R., Fortuni S., Rufini A., Condò I., Testi R., Martinuzzi A. - *Safety and efficacy of interferon γ in friedreich's ataxia* - *Mov. Disord.* (2020); 35(2):370-371, [doi: 10.1002/mds.27979].

- Vazquez D.S., Agudelo W.A., Yone A., Vizioli N., Arán M., González Flecha F.L., González Lebrero M.C., Santos J. - *A helix-coil transition induced by the metal ion interaction with a grafted iron-binding site of the CyaY protein family* - Dalton Trans. (2015); 44(5):2370-2379, [doi: 10.1039/c4dt02796e].
- Vázquez-Manrique R.P., González-Cabo P., Ros S., Aziz H., Baylis H.A., Palau F. - *Reduction of Caenorhabditis elegans frataxin increases sensitivity to oxidative stress, reduces lifespan, and causes lethality in a mitochondrial complex II mutant* - FASEB J. (2006); 20(1):172-174, [doi: 10.1096/fj.05-4212fje].
- Vazzola V., Losa A., Soave C., Murgia I. - *Knockout of frataxin gene causes embryo lethality in Arabidopsis* - FEBS Lett. (2007); 581(4):667-672, [doi: 10.1016/j.febslet.2007.01.030].
- Verhoeven K., Claeys K.G., Züchner S., Schröder J.M., Weis J., Ceuterick C., Jordanova A., Nelis E., De Vriendt E., Van Hul M., Seeman P., Mazanec R., Saifi G.M., Szigeti K., Mancias P., Butler I.J., Kochanski A., Ryniewicz B., De Bleecker J., Van den Bergh P., Verellen C., Van Coster R., Goemans N., Auer-Grumbach M., Robberecht W., Milic Rasic V., Nevo Y., Tournev I., Guergueltcheva V., Roelens F., Vieregge P., Vinci P., Moreno M.T., Christen H.J., Shy M.E., Lupski J.R., Vance J.M., De Jonghe P., Timmerman V. - *MFN2 mutation distribution and genotype/phenotype correlation in Charcot-Marie-Tooth type 2 - Brain* (2006); 129(Pt 8):2093-2102, [doi: 10.1093/brain/awl126].
- Vogel F., Bornhövd C., Neupert W., Reichert A.S. - *Dynamic subcompartmentalization of the mitochondrial inner membrane* - J. Cell. Biol. (2006); 175(2):237-247, [doi: 10.1083/jcb.200605138].
- Von der Malsburg K., Müller J.M., Bohnert M., Oeljeklaus S., Kwiatkowska P., Becker T., Loniewska-Lwowska A., Wiese S., Rao S., Milenkovic D., Hutu D.P., Zerbes R.M., Schulze-Specking A., Meyer H.E., Martinou J.C., Rospert S., Rehling P., Meisinger C., Veenhuis M., Warscheid B., van der Klei I.J., Pfanner N., Chacinska A., van der Laan M. - *Dual role of mitofilin in mitochondrial membrane organization and protein biogenesis* - Dev. Cell (2011); 21(4):694-707, [doi: 10.1016/j.devcel.2011.08.026].
- Vyas P.M., Tomamichel W.J., Pride P.M., Babbey C.M., Wang Q., Mercier J., Martin E.M., Payne R.M. - *A TAT-frataxin fusion protein increases lifespan and cardiac function in a conditional Friedreich's ataxia mouse model* - Hum. Mol. Genet. (2012); 21(6):1230-1247, [doi: 10.1093/hmg/ddr554].
- Waldvogel D., van Gelderen P., Hallett M. - *Increased iron in the dentate nucleus of patients with Friedreich's ataxia* - Ann. Neurol. (1999); 46(1):123-125, [doi: 10.1002/1531-8249(199907)46:1<123::aid-ana19>3.0.co;2-h].
- Walker J.E. - *The ATP synthase: the understood, the uncertain and the unknown* - Biochem. Soc. Trans. (2013); 41(1):1-16, [doi: 10.1042/BST20110773].

- Weibert H., Freibert S.A., Gallo A., Heidenreich T., Linne U., Amlacher S., Hurt E., Mühlhoff U., Banci L., Lill R. - *Functional reconstitution of mitochondrial Fe/S cluster synthesis on Isu1 reveals the involvement of ferredoxin* - Nat. Commun. (2014); 5:5013, [doi: 10.1038/ncomms6013].
- Whitnall M., Suryo Rahmanto Y., Huang M.L., Saletta F., Lok H.C., Gutiérrez L., Lázaro F.J., Fleming A.J., St Pierre T.G., Mikhael M.R., Ponka P., Richardson D.R. - *Identification of nonferritin mitochondrial iron deposits in a mouse model of Friedreich ataxia* - Proc. Natl. Acad. Sci. U. S. A. (2012); 109(50):20590-20595, [doi: 10.1073/pnas.1215349109].
- Wilkens V., Kohl W., Busch K. - *Restricted diffusion of OXPHOS complexes in dynamic mitochondria delays their exchange between cristae and engenders a transitory mosaic distribution* - J. Cell Sci. (2013); 126(Pt 1):103-116, [doi: 10.1242/jcs.108852].
- Wilson R.B. & Roof D.M. - *Respiratory deficiency due to loss of mitochondrial DNA in yeast lacking the frataxin homologue* - Nat. Genet. (1997); 16(4):352-357, [doi: 10.1038/ng0897-352].
- Wollweber F., von der Malsburg K., van der Laan M. - *Mitochondrial contact site and cristae organizing system: A central player in membrane shaping and crosstalk* - Biochim. Biophys. Acta Mol. Cell Res. (2017); 1864(9):1481-1489, [doi: 10.1016/j.bbamcr.2017.05.004].
- Wu M., Gu J., Zong S., Guo R., Liu T., Yang M. - *Research journey of respirasome* - Protein Cell (2020); 11(5):318-338, [doi: 10.1007/s13238-019-00681-x].
- Xia D., Yu C.A., Kim H., Xia J.Z., Kachurin A.M., Zhang L., Yu L., Deisenhofer J. - *Crystal structure of the cytochrome bc1 complex from bovine heart mitochondria* - Science (1997); 277(5322):60-66, [doi: 10.1126/science.277.5322.60].
- Xia H., Cao Y., Dai X., Marelja Z., Zhou D., Mo R., Al-Mahdawi S., Pook M.A., Leimkühler S., Rouault T.A., Li K. - *Novel frataxin isoforms may contribute to the pathological mechanism of Friedreich ataxia* - PLoS One (2012); 7(10):e47847, [doi: 10.1371/journal.pone.0047847].
- Yakovlev G., Reda T., Hirst J. - *Reevaluating the relationship between EPR spectra and enzyme structure for the iron sulfur clusters in NADH:quinone oxidoreductase* - Proc. Natl. Acad. Sci. U. S. A. (2007); 104(31):12720-12725, [doi: 10.1073/pnas.0705593104].
- Yamaguchi R., Lartigue L., Perkins G., Scott R.T., Dixit A., Kushnareva Y., Kuwana T., Ellisman M.H., Newmeyer D.D. - *Opa1-mediated cristae opening is Bax/Bak and BH3 dependent, required for apoptosis, and independent of Bak oligomerization* - Mol. Cell (2008); 31(4):557-569, [doi: 10.1016/j.molcel.2008.07.010].

- Yang M., Cobine P.A., Molik S., Naranuntarat A., Lill R., Winge D.R., Culotta V.C. - *The effects of mitochondrial iron homeostasis on cofactor specificity of superoxide dismutase 2* - EMBO J. (2006); 25(8):1775-1783, [doi: 10.1038/sj.emboj.7601064].
- Yiu E.M., Tai G., Peverill R.E., Lee K.J., Croft K.D., Mori T.A., Scheiber-Mojdehkar B., Sturm B., Prashberger M., Vogel A.P., Rance G., Stephenson S.E., Sarsero J.P., Stockley C., Lee C.Y., Churchyard A., Evans-Galea M.V., Ryan M.M., Lockhart P.J., Corben L.A., Delatycki M.B. - *An open-label trial in Friedreich ataxia suggests clinical benefit with high-dose resveratrol, without effect on frataxin levels* - J. Neurol. (2015); 262(5):1344-1353, [doi: 10.1007/s00415-015-7719-2].
- Yoon T. & Cowan J.A. - *Iron-sulfur cluster biosynthesis. Characterization of frataxin as an iron donor for assembly of [2Fe-2S] clusters in ISU-type proteins* - J. Am. Chem. Soc. (2003); 125(20):6078-6084, [doi: 10.1021/ja027967i].
- Yoon T., Cowan J.A. - *Frataxin-mediated iron delivery to ferrochelatase in the final step of heme biosynthesis* - J. Biol. Chem. (2004); 279(25):25943-25946, [doi: 10.1074/jbc.C400107200].
- Yoon T., Dizin E., Cowan J.A. - *N-terminal iron-mediated self-cleavage of human frataxin: regulation of iron binding and complex formation with target proteins* - J. Biol. Inorg. Chem. (2007); 12(4):535-542, [doi: 10.1007/s00775-007-0205-2].
- Zanella I., Derosas M., Corrado M., Cocco E., Cavadini P., Biasiotto G., Poli M., Verardi R., Arosio P. - *The effects of frataxin silencing in HeLa cells are rescued by the expression of human mitochondrial ferritin* - Biochim. Biophys. Acta (2008); 1782(2):90-98, [doi: 10.1016/j.bbadis.2007.11.006].
- Zelko I.N., Mariani T.J., Folz R.J. - *Superoxide dismutase multigene family: a comparison of the CuZn-SOD (SOD1), Mn-SOD (SOD2), and EC-SOD (SOD3) gene structures, evolution, and expression* - Free Radic. Biol. Med. (2002); 33(3):337-349, [doi: 10.1016/s0891-5849(02)00905-x].
- Zhang Z., Huang L., Shulmeister V.M., Chi Y.I., Kim K.K., Hung L.W., Crofts A.R., Berry E.A., Kim S.H. - *Electron transfer by domain movement in cytochrome bc1* - Nature (1998); 392(6677):677-684, [doi: 10.1038/33612].
- Zickermann V., Wirth C., Nasiri H., Siegmund K., Schwalbe H., Hunte C., Brandt U. - *Structural biology. Mechanistic insight from the crystal structure of mitochondrial complex I* - Science (2015); 347(6217):44-49, [doi: 10.1126/science.1259859].
- Zong S., Wu M., Gu J., Liu T., Guo R., Yang M. - *Structure of the intact 14-subunit human cytochrome c oxidase* - Cell Res. (2018); 28(10):1026-1034, [doi: 10.1038/s41422-018-0071-1].

Part III
List of
Publications

The published papers in which I gave my contribution during my Ph.D. are reported hereafter in their entire version. The first three papers of the following list have not been discussed in this thesis work as they belong to side projects in which I have taken part.

- Bortolus M., Costantini P., **Doni D.**, Carbonera D. – *Overview of the Maturation Machinery of the H-Cluster of [FeFe]-Hydrogenases with a Focus on HydF* – Int. J. Mol. Sci., 19(10): 3118, (2018), [doi: 10.3390/ijms19103118].
- Bellanda M., Maso L., **Doni D.**, Bortolus M., De Rosa E., Lunardi F., Alfonsi A., Noguera M.E., Herrera M.G., Santos J., Carbonera D., Costantini P. – *Exploring iron-binding to human frataxin and to selected Friedreich ataxia mutants by means of NMR and EPR spectroscopies* – Biochim. Biophys. Acta Proteins Proteom., 1867(11): 140254, (2019), [doi: 10.1016/j.bbapap.2019.07.007].
- Castro I.H., Bringas M., **Doni D.**, Noguera M.E., Capece L., Aran M., Blaustein M., Costantini P., Santos J. – *Relationship Between Activity and Stability: Design and Characterization of Stable Variants of Human Frataxin* – Arch. Biochem. Biophys., 691, 108491 (2020), [doi: 10.1016/j.abb.2020.108491].
- **Doni D.**, Passerini L., Audran G., Marque S.R.A., Schulz M., Santos J., Costantini P., Bortolus M., Carbonera D. – *Effects of Fe²⁺/Fe³⁺ binding to human frataxin and its D122Y variant, as revealed by Site Directed Spin labelling (SDSL) EPR complemented by Fluorescence and Circular Dichroism spectroscopies* – Int. J. Mol. Sci., 21, 9619, (2020), [doi: 10.3390/ijms21249619].
- **Doni D.**, Rigoni G., Palumbo E., Baschiera E., Peruzzo R., De Rosa E., Caicci F., Passerini L., Bettio D., Russo A., Szabò I., Soriano M.E., Salviati L., Costantini P. – *The displacement of frataxin from the mitochondrial cristae correlates with abnormal respiratory supercomplexes formation and bioenergetic defects in cells of Friedreich ataxia patients* – The FASEB Journal, 35(3): e21362 (2021), [doi: 10.1096/fj.202000524RR].
- **Doni D.**, Meggiolaro M., Santos J., Audran G., Marque S.R.A., Costantini P., Bortolus M., Carbonera D. – *A combined spectroscopic and in silico approach to evaluate the interaction of human frataxin with mitochondrial superoxide dismutase* – Biomedicines, 9(12): 1763 (2021), [doi: 10.3390/biomedicines9121763].



Review

Overview of the Maturation Machinery of the H-Cluster of [FeFe]-Hydrogenases with a Focus on HydF

Marco Bortolus ^{1,*}, Paola Costantini ^{2,*}, Davide Doni ² and Donatella Carbonera ¹

¹ Department of Chemical Sciences, University of Padova, Via F. Marzolo 1, 35131 Padova, Italy; donatella.carbonera@unipd.it

² Department of Biology, University of Padova, Viale G. Colombo 3, 35131 Padova, Italy; davide.doni.2@phd.unipd.it

* Correspondence: marco.bortolus@unipd.it (M.B.); paola.costantini@unipd.it (P.C.); Tel.: +39-049-827-5123 (M.B.); +39-049-827-6323 (P.C.)

Received: 14 September 2018; Accepted: 6 October 2018; Published: 11 October 2018



Abstract: Hydrogen production in nature is performed by hydrogenases. Among them, [FeFe]-hydrogenases have a peculiar active site, named H-cluster, that is made of two parts, synthesized in different pathways. The cubane sub-cluster requires the normal iron-sulfur cluster maturation machinery. The [2Fe] sub-cluster instead requires a dedicated set of maturase proteins, HydE, HydF, and HydG that work to assemble the cluster and deliver it to the apo-hydrogenase. In particular, the delivery is performed by HydF. In this review, we will perform an overview of the latest knowledge on the maturation machinery of the H-cluster, focusing in particular on HydF.

Keywords: hydrogenases; [FeFe]-hydrogenases; HydF; HydG; HydE; maturases

1. Introduction

Hydrogen metabolism is one of the most ancient processes of life, and today it is at the center of growing attention in the field of bioenergy (or bio-inspired) production technologies [1–5]. Hydrogenases are the enzymes responsible for the biological production or consumption of hydrogen in all domains, Archaea, Bacteria, and Eukarya [6,7]. They are divided into three classes based on their metal cofactors [7,8]: [Fe]-hydrogenases [9]; [NiFe]-hydrogenases [10]; [FeFe]-hydrogenases [11]; [NiFeSe]-hydrogenases [12]. [Fe]-hydrogenases, found only in methanogenic Archaea, are the smallest group and are restricted to a single function, they catalyze reversible reaction of methenyltetrahydromethanopterin with H₂ to methylenetetrahydromethanopterin and H⁺. [NiFe]-hydrogenases are widespread among all bacteria families, including archaea, eubacteria and cyanobacteria. [FeFe]-hydrogenases have been found in some unicellular green algae, such as *Chlamydomonas reinhardtii*, as well as in strict anaerobes, fungi and protists. For the most part, hydrogenases likely function either in recycling reduced electron carriers that accumulate during anaerobic fermentation through proton reduction or in coupling H₂ oxidation to energy yielding processes. Indeed, both [NiFe]- and [FeFe]-hydrogenases catalyze the reversible conversion of protons into hydrogen $2\text{H}^+ + 2\text{e}^- \rightleftharpoons \text{H}_2$ in conditions of strict anaerobiosis; [FeFe]-hydrogenases are usually involved in the forward reaction, while [NiFe]-hydrogenases in the backward reaction, although there are a number of exceptions [13,14]. Both classes of enzymes are oxygen sensitive, and hydrogen production is strongly inhibited by aerobic conditions, whereas [FeFe]-hydrogenases are irreversibly inactivated during catalysis by trace amounts of O₂, in most cases [NiFe]-hydrogenases react reversibly with O₂, giving rise to a mixture of inactivated states [15–18]. This sensitivity to molecular oxygen is one of the most critical drawbacks that have seriously limited the use of recombinant hydrogenases as

biotechnological tools so far, and several recent studies aim at overcoming this problem from different angles [2,19–21]. In fact, growing interest in exploiting particularly robust and more O₂-tolerant enzymes has become a major driving force for understanding the hydrogenases biogenesis and catalytic mechanisms, in vivo and in vitro. An additional problem for potential technical applications of biomimetic catalysis aimed at H₂ production by artificial hydrogenases is linked to the synthesis of their active site in a functional form [22,23]: recent advances have shown that in vitro activation of the recombinant enzymes using synthetic precursors is feasible [24]. It is worth noting that among all hydrogenases, [FeFe]-hydrogenases (HydA) show an unsurpassed H₂ release activity of up to 8.000 μmol H₂ min⁻¹ mg⁻¹ [25]: this efficiency is based on the unique and peculiar design of the cofactor responsible for their catalytic activity, the so-called H-cluster, which requires a dedicated protein machinery to be assembled [26]. As discussed in detail below, to date this maturation pathway is still incompletely characterized. Figure 1 shows that this site is a complex organometallic center composed of two halves, a standard cubane (called [4Fe-4S]_H) anchored to the protein backbone via four cysteine residues, one of which acts as the linker for the other half, a complex cluster (called [2Fe]_H) in which two Fe atoms are coordinated each by a CO and a CN⁻ and bridged by a third CO and an aza-dithiolate moiety, the nature of which had been long debated [27,28]. As soon as structural and functional details of the [FeFe]-hydrogenases active site were known, production of bioinspired catalysts for hydrogen production became a major goal in the field and this prompted the molecular studies of the H-cluster assembly. As for other FeS-proteins, the maturation process allowing the assembly of the H-cluster follows some basic common biosynthetic rules (reviewed in [29]), and can be divided in two main coordinated steps, i.e., the synthesis of a cluster precursor on a scaffold protein and the accurate delivery of this precursors to the target apoprotein, which culminates with its assembly into the polypeptide chain. The biosynthesis of the H-cluster is further complicated by the existence of the unusual non-protein ligands, CO, CN⁻ and dithiolate, and by its composite double iron, unique in nature. It is not surprising that, whereas several systems for the biogenesis of more conventional [4Fe-4S] and [2Fe-2S] clusters have been thoroughly characterized in bacteria as well as in different eukaryotic intracellular compartments [29], despite crucial advancements made in recent years, important gaps remain in the understanding of the molecular pathway leading to the assembly of the [FeFe]-hydrogenase H-cluster, and eventually allowing the enzyme activation. Three highly conserved proteins, at first found in *C. reinhardtii* and then in all microorganisms containing a [FeFe]-hydrogenase [30], have been shown to form the minimal synthetic machinery for the assembly of this site: HydE, HydG and HydF. Based on several in vitro experimental evidences, it has been proposed that the whole HydE/HydF/HydG maturation machinery would be dedicated to the synthesis and insertion of the [2Fe] subcluster, with its ligands, into a hydrogenase containing a [4Fe-4S] unit that would be performed by a housekeeping FeS clusters biogenesis system [31]. In fact, the division of the H-cluster in two sub-clusters is also reflected by their different synthetic paths: [4Fe-4S]_H is assembled and inserted into the hydrogenase by the general iron-sulfur clusters assembly machinery in a first step, while the [2Fe]_H is assembled by the three specific maturase proteins, as outlined in Figure 1 [30,32,33]. All three maturases are essential for the maturation of HydA, as shown by the lack of hydrogen production in the absence of one of the three proteins [30,34]. HydF is a homodimeric GTPase belonging to the family of the P-loop NTPases [35] and containing a FeS cluster binding consensus sequence [30], and is the core of the H-cluster biogenesis pathway, since it plays a dual role in the maturation process acting as scaffold upon which the final form of the [2Fe]_H cluster is assembled and as carrier to insert it into the hydrogenase [36,37]. HydG and HydE, both monomeric radical-SAM (*S*-adenosyl-*L*-methionine) proteins, synthesize different parts of the H-cluster and interact with HydF to assemble it. While many details of these maturation proteins have been elucidated in recent years, the exact sequence of events and intermediates of the maturation process is still unknown.

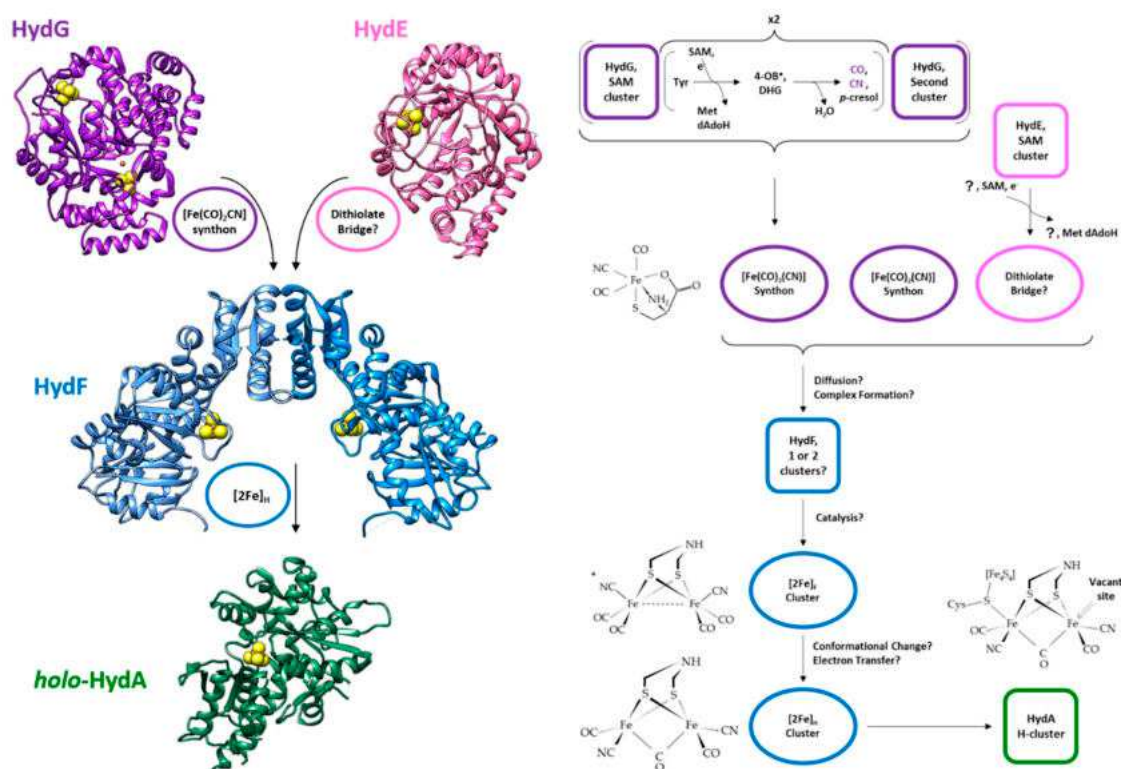


Figure 1. Scheme of the maturation process of the $[2\text{Fe}]_{\text{H}}$ sub-cluster of $[\text{FeFe}]$ hydrogenase. On the left side, we show the structures and active sites of the enzymes involved in the maturation: purple, HydG from *T. italicus* (pdb.id 4WCX) with the first active site, the SAM cluster on top, and the second active site on the bottom; pink, HydE from *T. maritima* (pdb.id 3CIW); blue, HydF from *T. melaniensis* (pdb.id 5KH0); green, HydA, from *C. reinhardtii* (pdb.id 3LX4), without the complete active site. On the right side, a more detailed scheme of the reactions involved in the process. The enzymes are indicated as squares (the color scheme is conserved); the products of the enzymes are shown as ovals of the same color of the enzymes producing them. Some relevant chemical structures are reported, from top to bottom: the synthon; the $[2\text{Fe}]_{\text{F}}$ cluster; the $[2\text{Fe}]_{\text{H}}$ cluster; and the active site of the holo-HydA with the full H-cluster. The question mark denotes unknown substrates/products; the asterisk denotes the attachment point of the $[2\text{Fe}]_{\text{F}}$ sub cluster to HydF. For the acronyms, please refer to the abbreviation section.

The principal methods that have been used to characterize hydrogenases and their active sites are crystallography, fourier-transform infrared spectroscopy (FT-IR), electron paramagnetic resonance spectroscopy (EPR). Crystallography beside providing the molecular structures of the enzymes, also helped in the identification of the molecular mechanisms through co-crystallization experiments with putative substrates. However, most of the information on the mechanisms of action of the hydrogenases and on their maturation process, has been obtained through spectroscopic methods, mainly EPR methodologies and FT-IR, often coupled together. Conventional EPR spectroscopy (i.e., continuous-wave EPR) provides a wealth of information on FeS clusters of the enzymes: different kinds of FeS clusters have different EPR spectra. Additionally, since EPR is only sensitive to paramagnetic states, it can help to define the oxidation state of the metal centers in different conditions. When coupled to isotopic labeling or mutagenesis experiments, pulsed EPR methods allow to identify the residues bound to the metal centers of the active site in the different functional states through the detection of the electron-nuclei hyperfine coupling. Finally, EPR has been coupled to the site-directed spin labeling method (SDSL) to study the changes in structure and dynamics of the enzymes in solution. FT-IR resulted to be unique in its ability to differentiate both the nature of the H-cluster ligands, and their mode of binding. By a careful analysis of the molecular stretching modes, the CO and CN^-

ligands and their orientation have been defined. In addition, the stretching modes sensitive to the iron oxidation state have allowed to identify the EPR-silent cluster states.

In this work, we will review the updated knowledge on the maturation machinery of the H-cluster, highlighting the questions that are still open, focusing in particular on the structure and catalytic mechanisms of HydF. A first section will be devoted to the individual enzymes and a second one to the discussion of the overall process.

2. The maturases

2.1. HydE

HydE is the least characterized of the three maturation enzymes, while its structure has been solved and HydE has been assigned to the radical SAM superfamily of enzymes, its substrates and products are still uncertain. While the exact role of HydE in the maturation process is not well-defined, it has been suggested to provide the bridging di (thiomethyl) amine ligand of the H cluster [38].

The structure of HydE has been solved only for the enzyme from *Thermotoga maritima* (pdb.id 3CIW) [39], see Figure 2. HydE from *T. maritima* adopts a distorted triose-phosphate isomerase (TIM)-barrel fold, where 8 α -helices and 8 parallel β -strands (shown in dark pink and green, respectively, in Figure 2) alternate along the peptide backbone, these last forming a large internal cavity where a molecule of SAM and additional substrates can be accommodated. Relative to the standard TIM-barrel fold, HydE has additional helices at the N-terminus and an additional strand at the C-terminus (shown in pale pink and dark blue, respectively, in Figure 2). The protein hosts one [4Fe-4S] cluster in the N-terminal part which is highly conserved and has been identified as the active site; this cluster faces the internal cavity of the enzyme, and it is coordinated by a SAM molecule in the crystal structure. A secondary [FeS] cluster binding site is present, about 2 nm away from the SAM cluster, but this secondary site does not seem to be essential for the maturation process, the cysteines of the secondary site are shown as spheres in Figure 2. The stoichiometry of the secondary cluster is not exactly defined in the crystal structures, varying from [2Fe-2S] to [4Fe-4S] [40], and EPR spectroscopy data have shown that full cluster reconstitution leads to two [4Fe-4S] clusters in the enzyme [38].

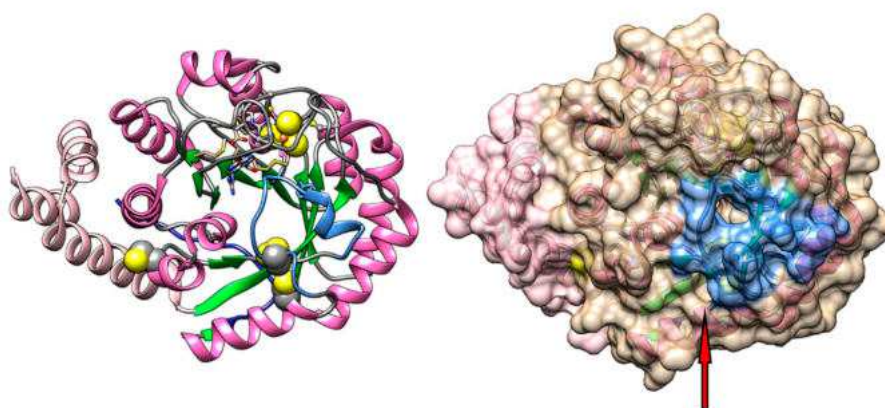


Figure 2. HydE (pdb.id 3CIW) from *T. maritima*. Left, cartoon representation of the protein, showing the protein from the top of the internal cavity. In magenta (helix) and green (strand) the TIM-barrel fold; in pale pink the N-terminal helices; in dark blue (on the other side of the protein) the C-terminal loop; in light blue the putative “lid” region governing the access to the active site; the [4Fe-4S] cluster forming the active site is in sphere representation; and the cysteine residues not binding the cluster are also in sphere representation. Right, same view as before but with the surface shown: the accesses to the internal cavity are in the center of the light blue zone and close to the two cysteines as shown by the red arrow.

Based on the crystal structure, the access to the internal cavity has been hypothesized to be regulated by a region of the protein directly above the active site, a loop-helix-loop structure acting as a “lid” (shown in light blue in Figure 2) with a strictly conserved aromatic motif, YXXY. The protein surface on this region shows one main access point in the “lid” region and a second one that is open in the absence of the secondary cluster (indicated by the red arrow in Figure 2). Both accesses are narrow, but, combined with dynamic conformational fluctuations of the protein in solution, could allow substrates and products to diffuse to the active site. A third access to the internal cavity, closed in the static protein structure, rests on the other side of the cavity relative to the active site, covered by the C-terminal loop.

While it is certain that the dithiolate bridge comes from HydE, the exact substrates and products of HydE are unknown. HydE belongs, like HydG, to the radical SAM superfamily of enzymes, which perform a homolytic cleavage of the C5'-Sδ bond of SAM at a [4Fe-4S] cluster, to yield a reactive 5'-deoxyadenosyl radical species (5'-dA●), used to usually extract a hydrogen atom from a substrate, thus generating a highly reactive carbon centered radical which is used in further synthetic steps. At variance with the general mechanism, it has been shown that HydE can react directly on a sulfur atom to form a C-S bond without passing through the hydrogen abstraction [41]. However, without knowledge of the actual substrate, it is unclear if this unusual reaction is part of the physiological mechanism involved in the maturation process. Nevertheless, it has been suggested that the substrate of HydE contains a thiol functional group [38]. Additionally, the SAM chemistry is performed on the main cluster, but the role of the secondary, less conserved, cluster in the function of the enzyme is still unknown.

2.2. HydG

HydG has been well-characterized, its crystal structure has been solved for different organisms and its function has been recently established in detail. HydG, belonging as HydE to the radical-SAM superfamily, is a bifunctional enzyme performing the synthesis of a Fe-containing complex with CO and CN⁻ ligands that acts as a synthon of the [2Fe]_H cluster.

The structure of HydG has been solved for two organisms, *Carboxydotherrmus hydrogenoformans* (pdb.id 4RTB) [42] and *Thermoanaerobacter italicus* (pdb.id 4WCX) [43], the latter shown in Figure 3. HydG, similarly to HydE, has a distorted TIM-barrel fold, 8 α-helices and 8 β-strands (shown in dark pink and green, respectively, in Figure 3), with additional helical domains at the N-terminus and C-terminus (about 80 amino acids long, shown in pale pink and dark blue, respectively, in Figure 3). It has a large internal cavity at the edge of which two distinct active sites, both iron-sulfur clusters, are present. The first is a [4Fe-4S] cluster with the conserved structural motif of a radical-SAM active site, and it is located at the top of the cavity of the TIM-barrel fold. The second site is a peculiar [4Fe-4S] cluster bridged by a μ₂ sulfide ion (or a non-proteic Cys) to a labile dangling Fe atom, and it is located at the bottom of the TIM-barrel cavity about 2.4 nm away from the first cluster, bound to the additional helical domain at the C-terminus. The second cluster is the site at which a Fe(CO)₂CN synthon is assembled (see the next paragraph). The internal cavity of HydG is connected to the protein surface by a channel through which the products and substrates are thought to diffuse, shaded in light blue in Figure 3. The opening/closing of the channel located at the top of the cavity, close to the SAM active site, is thought to be governed by a loop region with a conserved Arg residue that partakes in Tyr binding, and is analogous to *Streptomyces actuosus* tryptophan lyase [42,43].

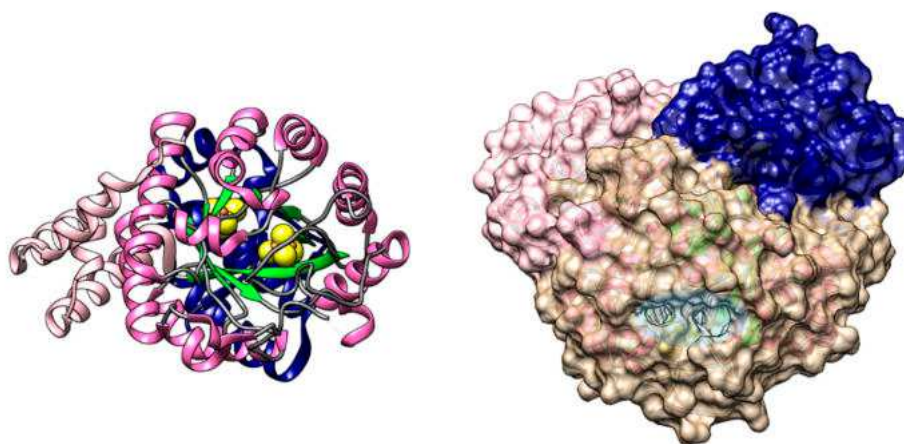


Figure 3. HydG (pdb.id 4WCX) from *T. italicus*. Left, cartoon representation of the protein, in the figure we show the protein from the top of the internal cavity. In magenta (helix) and green (strand) the TIM-barrel fold; in pale pink the N-terminal helices; in dark blue (on the other side of the protein) the C-terminal domain; and the [4Fe-4S] and [5Fe-4S] clusters forming the two active sites at the opposite sides of the cavity are in sphere representation. Right, a rotated view of the protein with the surface shown: the access to the internal cavity is in the center shaded in light blue.

HydG has long been recognized to provide the CO and CN^- ligands of the $[\text{2Fe}]_{\text{H}}$ cluster. Recently, mostly through a combination of isotopic labeling and pulsed EPR experiments the role of HydG in the maturation pathway has been further expanded [41,44–47]: it has been shown to synthesize the synthon of the $[\text{2Fe}]_{\text{H}}$ cluster, a low-spin iron complex, $\text{Fe}(\text{CO})_2(\text{CN})\text{Cys}$. The assembly of the synthon is a multi-step process involving both active sites of the enzyme. The first active site utilizes the radical-SAM mechanism similarly to HydE (see above) to cleave a tyrosine into *p*-cresol, one molecule of CO, and one of CN^- via a dehydroglycine intermediate. *p*-cresol migrates out of the protein cavity following the opening of the active site, while the other products migrate to the bottom of the cavity at the second active site. The second active site assembles the synthon: the dangling Fe atom, initially coordinated by a free cysteine, water, and histidine from the backbone, is coordinated by two CO and one CN^- produced at the first active site while the second CN^- cleaves the formed synthon from the [4Fe-4S] cluster. Note that in the proposed mechanism the stoichiometry of the overall formation of the synthon involves the conversion of two molecules of tyrosine at the first site to produce all the necessary ligands.

2.3. HydF

HydF holds a central role in the maturation pathway, but while its homodimeric structure has been crystallized, and its dual role, as a scaffold upon which the $[\text{2Fe}]_{\text{H}}$ cluster is assembled and carrier of the cluster into the apo-HydA, is universally recognized, a detailed knowledge of its mechanisms of action is still missing.

The structure of a recombinant HydF from *Thermotoga neapolitana* (pdb.id 3QQ5) has been solved without the [4Fe-4S] cluster [48], which is known to be part of the holo-protein as derived by EPR of the protein in solution-state [37,49–55], and more recently complete with the cluster from *Thermosipho melaniensis* (pdb.id 5KH0, used for Figure 4) and from *T. maritima* (pdb.id 5LAD) [56]. HydF is a homodimeric protein with three domains per monomer. The N-terminus holds the GTPase domain, the central domain is the dimerization domain, and the C-terminus holds the [4Fe-4S] cluster-binding domain. While HydE and HydG are globular, the homodimeric structure of HydF adopts an open fold with a skewed inverted V shape, with the two GTPase domains located at the outermost part of the dimer and twisting away from the plane formed by the other two domains (as shown in Figure 4). This fold creates a large open “cavity” just below the dimerization interface with the active [4Fe-4S] cluster site of each monomer in its center. The cluster is solvent-exposed as befits an active site that needs to interact with several different proteins, as shown in Figure 4.

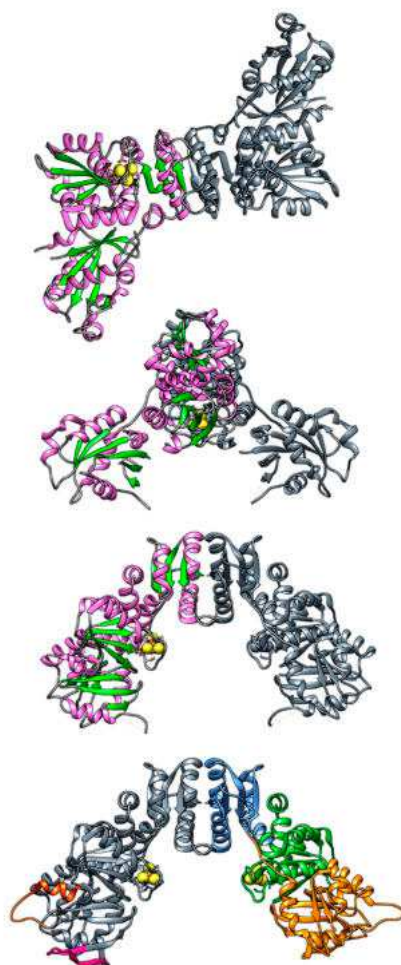


Figure 4. Top, HydF (pdb.id 5KH0) from *T. melaniensis* viewed from three angles (bottom of the cavity, and two views of the sides rotated 90° one relative to the other). To highlight the homodimeric assembly of the protein only one monomer has been colored according to secondary structure: in magenta the α -helices, in green the β -strands, the [4Fe-4S] cluster is in sphere representation. Bottom, reconstruction of the whole protein structure in the absence of GTP based on HydF from *T. melaniensis* (see text) including the missing amino-acid stretches. The left monomer has the reconstructed stretches colored in purple (switch 1 region) and dark orange (switch 2 region). The right monomer has been colored to highlight the three protein domains: GTPase domain in orange, dimerization domain in blue, and cluster-binding domain in green.

2.3.1. GTPase Domain

The GTPase domain at the N-terminus (orange in Figure 4), is the least resolved in the crystal structures, it has high B factors, and is not stabilized in the crystal by direct contact with other molecules [56]. Its fold is similar to that of other GTPases: six β -strands, five parallel and one anti-parallel, assemble into a large sheet, with three α -helices flanking this sheet on one side and two α -helices on the other. Recently, through sequence and structure analysis, it has been shown that the GTPase domain has a high homology to analogous domains of other small K^+ -dependent GTPases, and as such it should act as a molecular switch triggering a conformational change [57]. Two regions have been identified as switch regions: switch 1 (residues 31–46, located directly above the nucleotide binding site) not solved in any crystal structure, and switch 2 (residues 68–86), solved only for HydF from *T. neapolitana*. Switch 1 is the most conserved in function and sequence among different K^+ -dependent GTPases. Upon GTP binding, the switch 1 region of K^+ -dependent GTPases exhibits a change from a β -sheet to a structured loop region with specific interactions with K^+ and Mg^{2+} ions mediated by conserved Asn residues [58]. This structural change is highly conserved, and likely adopted by HydF as well. On the other hand, the switch 2 region, which in HydF comprises a loop ending in an α -helix, has a high variability among the proteins belonging to different species and thus the structure adopted by HydF in the presence of GTP is not easily predicted starting from that resolved in the absence of GTP. Based on these considerations, we here present a model of the whole protein in the absence of GTP constructed with the UCSF Chimera package [59]. The model is based on the structure of HydF from *T. melaniensis*, pdb.id 5KH0, on top of which the two switch regions have been modeled. The switch 2 region was taken from the structure from HydF from *T. neapolitana* (pdb.id 3QQ5) where it is resolved. The switch 1 region was taken from the GDP-bound soluble N-terminal domain of FeoB from *Streptococcus thermophilus* (pdb.id 3LX8), a membrane protein that imports Fe^{2+} [60], taken as the reference structure of a K^+ -activated GTPase. The two reconstructed regions are highlighted in Figure 4 (bottom): switch 1 (residues 31–46) in purple and switch 2 (residues 68–86) in dark orange.

2.3.2. Dimerization Domain

The second domain in the sequence is responsible for the formation of the HydF dimer (blue in Figure 4). An extended stretch of residues, about thirteen amino-acids long, connects the dimerization to the GTPase domain. The domain is composed of four parallel β -strands and three α -helices. The four-stranded parallel β -sheets of each monomer are coupled in an antiparallel way to form a continuous eight-stranded β -sheet. Additional stabilization comes from the interactions between the neighboring α -helices and the loop regions, to a degree that depends on the species. Note that, so far, it is not clear why HydF needs to be dimeric to partake in cluster maturation, since a single [4Fe-4S] cluster is potentially sufficient to anchor the [2Fe]_H cluster. On the other hand, a close look at the HydF structure indicates that the total buried surface due to the dimerization is large enough to support the existence of a stable physiological dimer, which assumes a sort of left-handed helical shape leaving both the putative FeS cluster and GTP-binding sites exposed to the solvent and giving a large protein surface for contacts with possible partners, such as the other two maturases and/or the apo-[FeFe]-hydrogenase. Thus, the dimer could be essential to provide the central open cavity to bind alternatively HydE, HydG, or the domain of HydA containing the H-cluster. This issue will be discussed in greater detail below.

2.3.3. Cluster Binding Domain

The C-terminal domain hosts the putative enzyme active site, where the [4Fe-4S] cluster is predicted to act as an anchor for the [2Fe]_H assembly and delivery (green in Figure 4). The domain is composed of four β -strands and five α -helices arranged in a complex way to bring the three highly conserved Cys residues belonging to the highly conserved iron-sulfur cluster-binding motif (CxHx46-53HCxxC) spatially close [48,56]. Site-specific mutagenesis analysis coupled to EPR spectroscopy have shown that while cysteine residues are essential for the cluster assembly of HydF, the conserved histidines are not, and do not belong to the cluster coordination sphere [52]. However, the histidines are essential for the [2Fe]_H cluster assembly, possibly partaking in this process via hydrogen bonding to the synthons. The crystal structure of HydF from *T. melaniensis* revealed that the fourth ligand of the cluster in the absence of the synthon comes from a highly conserved acidic residue (Glu in this organism) coordinating via the carboxylate [56]. HYSORE spectroscopy studies had already shown that the fourth ligand is an oxygen in a variety of organisms and that this ligand is easily exchangeable, as expected since the fourth position is the one where the [2Fe]_H cluster is anchored [52,54,55]; to date, the only known exception coming from the cluster of *Clostridium acetobutylicum*, where a nitrogen was found, however the possibility that the His-tag at the N-terminus of the recombinant protein, which is located spatially close to the cluster, interferes with the natural coordination must be taken into account. The putative binding pocket of the [2Fe]_H cluster is located in a cleft at the interface between the second and third domains and is characterized by a positively charged surface. The loop that holds the fourth ligand likely changes conformation upon de-coordination of the acidic residue for the binding of the synthon, a model has been proposed comparing the two existing crystal structures, with and without the cluster [56].

In addition to the [4Fe-4S] cluster, there is evidence from EPR spectroscopy that as-isolated and chemically reconstituted HydF can also host a [2Fe-2S] cluster [61–65], which is otherwise lacking in all solved HydF crystal structures [48,56]. Given this discrepancy, it is still unclear whether the presence of a [2Fe-2S] cluster represents a physiological state, a state of partial cluster maturation, or simply arises from an incomplete reconstitution due to the *in vitro* conditions. Since there are no other binding motifs in HydF, and its relaxation properties suggest that the [2Fe-2S] cluster is located at least 2.5 nm away from the main cluster, it is likely bound in the same binding site in a different monomer, with a mixed occupancy of the sites in the two monomers, or a subset of proteins binding only a single type of cluster [62]. Finally, while there is a consensus about the role of the [4Fe-4S] cluster as the anchor for the [2Fe]_H cluster, the role of [2Fe-2S] cluster is completely undefined.

The role of HydF as a scaffold and carrier in the maturation process is widely accepted based on both structural and functional studies [24,36,48,66], but several unclear points on its function are still present.

2.3.4. Tetrameric Form

HydF adopts in the crystal structures and in the purification process a tetrameric form (or more precisely forms a dimer of dimers), less abundant than the native dimeric form. The quaternary structure of the tetramer is uncertain since in the three available crystal structures the tetrameric assembly differs greatly and it is likely influenced by the crystal packing [56]. It is possible to separate the two forms in the recombinant protein via chromatographic methods, but the dimer and tetramer are in dynamic equilibrium [64]. A regulatory role has been attributed to the tetrameric form of HydF, acting as a switched-off state of the enzyme, since the tetrameric fractions are much less active in assembling the cluster [62].

2.3.5. [2Fe]_H Cluster Precursor

In a recent work [65], the precursor to the [2Fe]_H cluster present in HydF (called [2Fe]_F cluster) has been suggested to be structurally different from the one present in HydA, based on FT-IR data (see Figure 1 for its structure). [2Fe]_F has not been detected by EPR spectroscopy suggesting it is diamagnetic. The [2Fe]_F cluster form is coordinatively saturated and bridged to the [4Fe-4S] cluster of HydF by a cyanide ligand. Relative to the [2Fe]_H cluster, the [2Fe]_F cluster would lack the bridging CO molecule and the relative orientation of the CO and CN- ligands relative to the dithiolate bridge is different, see Figure 1. Another difference that has been highlighted is the different redox state of the sub clusters, which would imply that the [4Fe-4S] cluster of HydF might be redox active and involved in the change of the redox state going from [2Fe]_F to [2Fe]_H, a step that might play a role in the transfer of the cluster to HydA.

2.3.6. Role of the GTPase Domain

Site-specific mutagenesis analysis revealed that the HydF GTPase consensus motifs are essential for the [FeFe]-hydrogenase maturation and activation [34,66]. NTPases are commonly involved in the assembly of metal cofactors of FeS proteins [67], mediating either the metal delivery to the active site or the transfer of the whole cluster to the target apoprotein. Experimental evidences excluded a role of HydF GTPase activity in the transfer of H-cluster precursor to the [FeFe]-hydrogenase [68], and an involvement of the GTPase domain in the interaction with the two other maturases has been suggested [66,68]. As reported above, the HydF crystal structures showed that this domain includes a flexible loop region which could rearrange upon GTP binding, thus facilitating the interaction with the maturation partners (see next paragraph). The changes in structure and backbone dynamics in the presence of GTP were investigated by EPR spectroscopy coupled to site-directed spin labeling (SDSL) and CD spectroscopy both in the full enzyme [57] and in the isolated domain [69]. EPR spectra in the presence of non-hydrolysable analogues and transition state mimics of GTP showed that GTP binding, and not its hydrolysis, triggers the switch. The binding of GTP causes a change in backbone dynamics diffused throughout the whole protein (Figure 5): the largest changes are in the GTPase domain (S38, V71, R88), at the interface between the GTPase and cluster-binding domain (D340), or between the GTPase and dimerization domains (I175), while they are nonexistent in the core of dimerization domain proper (V261). All buried residues that were labeled do not change spectra upon GTP addition, suggesting that they do not get exposed irrespective of the domain (A89, T164, L341). DEER (Double Electron-Electron Resonance) experiments, measuring the distances between couples of spin labels, carried on double mutants of the isolated domain [69] and in the full enzyme [57] showed that neither the folding of the GTPase domain nor the dimeric quaternary structure are largely altered by GTP addition. The secondary structure changes in the whole enzyme evidenced by CD spectroscopy were modest, showing that the overall folding does not change. Taken together, all these results suggest that GTP binding induces local conformational changes in the domain and changes in protein backbone dynamics that radiate to the active site. These subtle changes in conformation and backbone dynamics likely play a key role in the regulation of the interaction with the other maturases and/or hydrogenase. Intriguingly, it has been reported that the presence of GTP affects the EPR spectral properties of the HydF [4Fe-4S] cluster [68], suggesting a communication between the GTPase domain and the FeS cluster domain. Thus, another possibility is that the GTP-induced conformational switches could instead modulate the coordination and orientation of the [4Fe-4S] cluster, switching from the four-coordination state with the carboxylate bound to a three-coordination states ready to bind the [2Fe]_H precursors. Further work is needed to have more information on the actual mechanism.

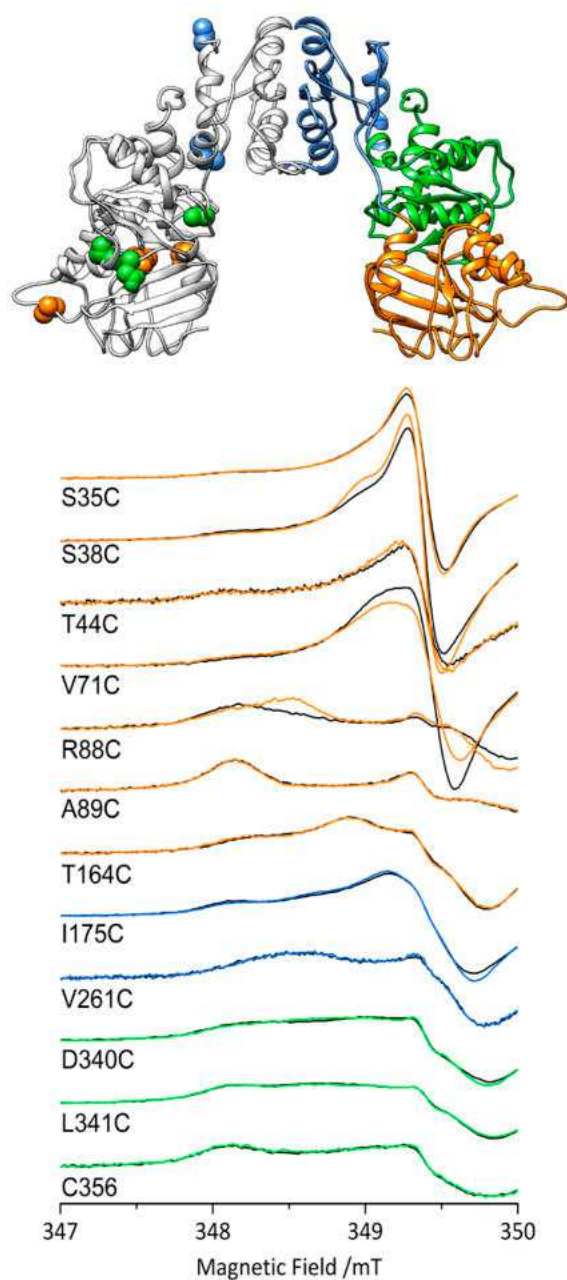


Figure 5. Top. The structure of HydF from *T. neapolitana* (pdb.id 3QQ5) with the mutated labeling sites highlighted in the same color of the domain they are located in (orange, GTPase; blue, dimerization; green, cluster binding). Bottom. EPR spectra (zoom of the low field region) of HydF from *T. neapolitana* spin labelled at the indicated positions: black, the spectra in the absence of GTP; colored lines, the spectra in the presence of GTP. The figure is based on the results reported in reference [57].

3. The Overall Process

The function of the individual maturases has been the object of extended work, and in the last few years the knowledge of HydG and HydF proteins has significantly progressed. Quite lacking, on the contrary, is the knowledge of the interactions between the different maturases, the sequence of individual steps, and both the stoichiometry and the regulatory mechanisms of the overall process. Due to the multistep nature of the molecular pathway leading to the [FeFe]-hydrogenase maturation described above, a close and coordinate network of protein interactions between several partners must be achieved. The structural features and the dynamic behavior of HydF as scaffold and carrier assign

to this protein a key role along the entire [FeFe]-hydrogenase maturation pathway and indicate its capability to establish functional interaction with all the players of this process. These binding events were at first inferred from co-purification of HydE and HydG with HydF [36] and then confirmed and quantified in vitro through a combination of Surface Plasmon Resonance and co-purification experiments using recombinant proteins from *C. acetobutylicum* [66]. The dissociation constants of HydE and HydG interacting with HydF have been determined both in the absence and in the presence of a non-hydrolysable GTP analogue. The study showed that HydE has a ten times higher affinity for HydF than HydG, both with and without GTP, and that HydG cannot interact with HydF if HydE is bound to it. This suggests that the interactions of HydE and HydG with the HydF scaffold are distinct events occurring in a precise functional order and would be fully consistent with the model proposed below. Nevertheless, the dissociation constants are relatively high, implying that the interaction of HydF with the other maturases is not very strong, as expected for a protein that acts as a scaffold for up to three other proteins (HydG, HydE, HydA). The role of GTP binding is less clear: while both proteins have slightly higher affinity for HydF when GTP is present, the difference is less than an order of magnitude. Together with the other assays used in the work, the authors suggested that HydE and HydG bind separately to HydF and not cooperatively, thereby ruling out the possibility of a ternary complex [66]. It is still unknown, however, if there is an interaction between HydG and HydE occurring before either interacts with HydF.

Since no direct evidence of the role of the cavity formed by the dimeric structure of HydF as the protein-protein interaction interface has been obtained so far, we used rigid-body molecular docking to test this hypothesis, which is relevant for the discussion of the overall maturation pathway. To perform the docking procedure, we docked together proteins from different organisms since there is no common organism for which all structures have been obtained. Note that performing the docking simulations of proteins from different organisms is meaningful since it has been shown that mixing maturases and HydA of different species still yields a functional hydrogenase [70]. For HydF, we used the reconstructed structure from *T. melaniensis* described above. Then, we chose the structures of the maturases for which the primary sequence had the highest homology with HydF from *T. melaniensis*: for HydE, the structure from *T. maritima* (pdb.id 3CIW) and for HydG, the structure from *T. italicus* (pdb.id 4WCX). For HydA, we chose the structure from *C. reinhardtii* (pdb.id 3LX4), since it has the smallest complete hydrogenase domain of the available structures. The soft rigid-body docking procedure, adapted from [71], was performed using the webservers of both PatchDock [72] (in tandem FireDock [73]) and ZDOCK [74]. The full results of these simulations will be further refined and presented in a future work, we here report the preliminary results of our analysis in Figure 6, where we chose three docking poses that show that indeed HydE, HydG, and HydA are all able to dock in the “cavity” formed by the dimer of HydF. However, these are rigid body docking simulations, dynamics are not accounted for, and some physiologically relevant docking poses, resulting from different conformations of flexible structural elements, might be lost. Additionally, we used the structure of HydF in the absence of GTP, and since the full structural changes induced by GTP binding are not known, the results might be very different in the GTP-bound state.

Based on the evidence gathered so far, we propose two speculative models of the overall process that are schematically shown in Figure 7. These models provide for a central role of HydF that receives all parts of the cluster and assembles them, with separate binding events of HydG and HydE. As shown in Figure 1, the overall maturation of the $[2Fe]_H$ cluster implies a stoichiometry for the maturases that depends on the protein: HydG needs four turnovers at the first active site and two at the second site to produce the two synthons necessary for the complete cluster, while only a single turnover is expected to be necessary for the formation of the dithiolate bridge by HydE. It seems unlikely that the reactive dithiolate bridge is delivered to HydF before a synthon is bound, therefore it is reasonable that the first step (Figure 7A) always involves the binding of HydG to HydF and the delivery of a synthon. The synthon could easily bind to the $[4Fe-4S]$ cluster of HydF via the cyanide ligand like in the complete $[2Fe]_F$ structure. It has to be noted that the only access to the inner cavity of HydG is

the single channel on top of the cavity, where both substrate and products are thought to pass, and therefore the access to the active site of HydG would be sterically impossible when it is bound to HydF. Then, the synthesis and delivery of the second synthon imply a dissociation and re-association of HydG. Following the binding of the first synthon two possibilities exist: (1) HydE delivers the dithiolate bridge (Figure 7B) before a second HydG comes to deliver the second synthon to the partially formed $[2Fe]_F$ cluster (Figure 7C); and (2) HydG binds to deliver the second synthon (Figure 7D) before HydE comes in to clip the two synthons together via the dithiolate bridge (Figure 7E). In the latter case, the second synthon could either be attached to the first one, implying a rearrangement of the ligands, or it could be delivered to the empty $[4Fe-4S]$ cluster of the other HydF monomer and then coupled by HydE. The presence of two individual synthons in the two monomers of HydF is attractive, since it would provide another justification for its homo-dimeric structure besides the presence of the central cavity where the other maturases could dock. In both cases additional regulatory mechanisms, i.e., GTP binding, changes in protein backbone dynamics, and/or a conformational change of the cluster region following the binding of the first synthon, must modulate the binding affinity of the other maturases to HydF.

A further alternative mechanism would provide for HydG and HydE to interact first, assembling the whole $[2Fe]$ sub-cluster possibly making use of the secondary cluster binding motif of HydE. Then, HydE would deliver the complete cluster to HydF. We performed docking simulations on a possible HydG-HydE complex, but the results do not show any preferential binding interface between the two proteins. However, this mechanism cannot be excluded, and experiments on HydE-HydG binding affinity would be needed to verify this hypothesis.

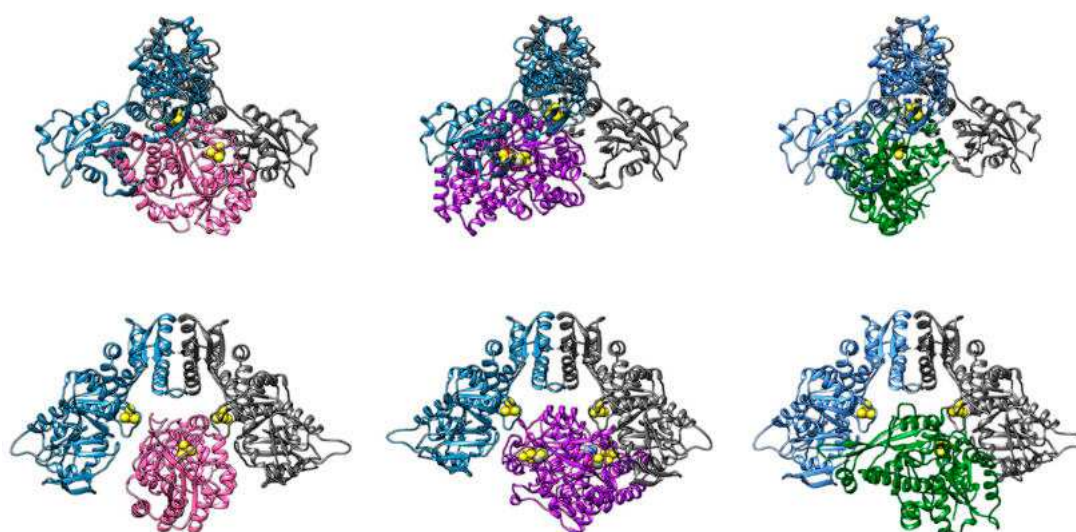


Figure 6. Molecular docking of reconstructed HydF from *T. melaniensis* (monomers in blue and grey) with: left, HydE (pink) from *T. maritima* (pdb.id 3CIW); center, HydG (purple) from *T. italicus* (pdb.id 4WCX); right, HydA (green) from *C. reinhardtii* (pdb.id 3LX4). Top and bottom show two views of the same docking pose rotated by 90° . All proteins show the active FeS clusters in sphere representation.

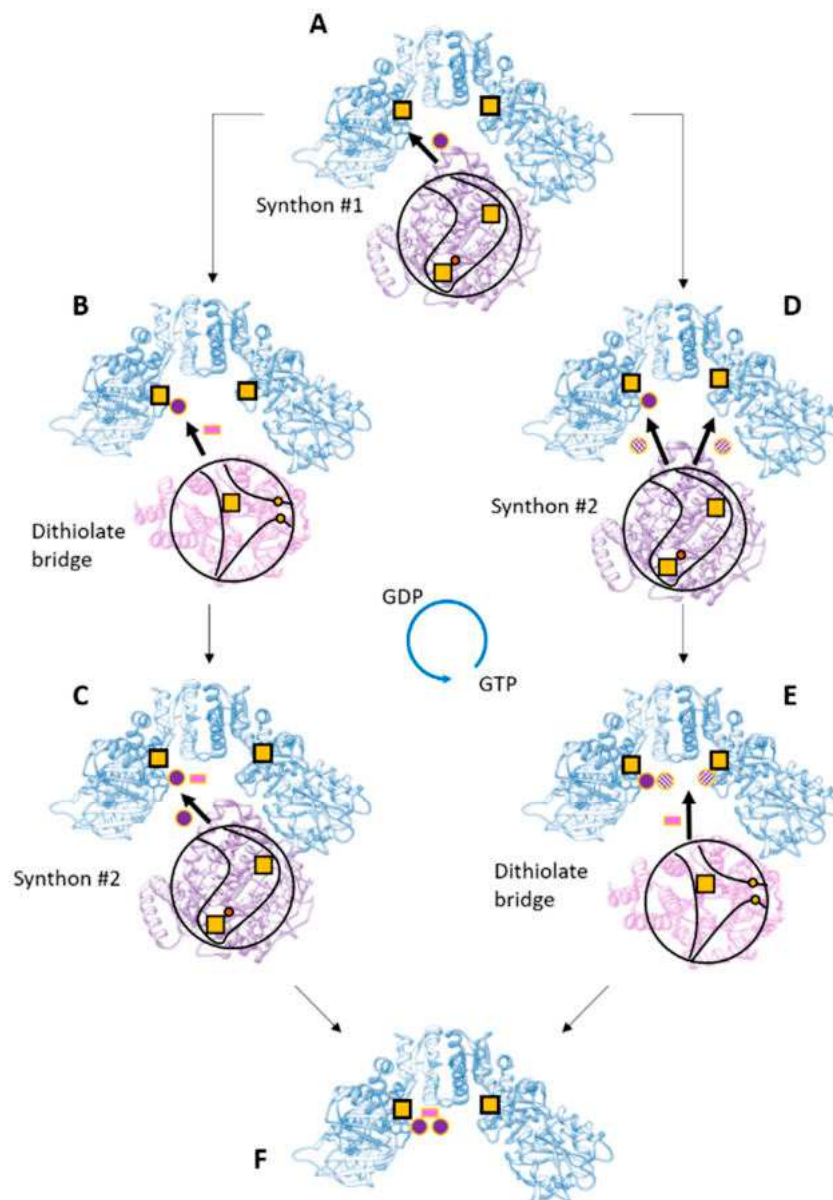


Figure 7. Possible sequence of events leading to the $[2Fe]_H$ cluster assembly. In this hypothesis, HydG (purple) and HydE (pink) bind to HydF (blue) in separate steps. For the description of the steps please refer to the text. The cavities of HydE and HydG are shown schematically in black lines with the inner cavities outlined and the putative access points shown; yellow squares, $[4Fe-4S]$ clusters; yellow dots, the cysteines of HydE; orange dot, the labile iron in HydG; purple dots, the synthon; pink rectangle, the dithiolate bridge.

Funding: This research was funded by the PRAT project CPDA149178/14 from University of Padova to P.C., CARIPARO Foundation M3PC project to D.C., and CARIPARO Starting Grants to M.B.

Conflicts of Interest: The authors declare no conflict of interest. The funders had no role in the design of the study; in the collection, analyses, or interpretation of data; in the writing of the manuscript, or in the decision to publish the results.

Abbreviations

EPR	Electron Paramagnetic Resonance
GTP	Guanosine-5'-Triphosphate
GDP	Guanosine-5'-Diphosphate
SAM	S-adenosyl-L-Methionine
TIM	Triose-Phosphate Isomerase
DHG	Dehydroglycine
dAdoH	5'- Deoxyadenosine
4OB•	4-Oxidobenzyl Radical

References

1. McPherson, I.J.; Vincent, K.A. Electrocatalysis by Hydrogenases: Lessons for Building Bio-Inspired Devices. *J. Braz. Chem. Soc.* **2014**, *25*, 1–15. [[CrossRef](#)]
2. Morra, S.; Valetti, F.; Gilardi, G. [FeFe]-hydrogenases as biocatalysts in bio-hydrogen production. *Rend. Lincei* **2017**, *28*, 183–194. [[CrossRef](#)]
3. Khan, M.A.; Ngo, H.H.; Guo, W.; Liu, Y.; Zhang, X.; Guo, J.; Chang, S.W.; Nguyen, D.D.; Wang, J. Biohydrogen production from anaerobic digestion and its potential as renewable energy. *Renew. Energy* **2018**, *129*, 754–768. [[CrossRef](#)]
4. Reeve, H.A.; Ash, P.A.; Park, H.; Huang, A.; Posidias, M.; Tomlinson, C.; Lenz, O.; Vincent, K.A. Enzymes as modular catalysts for redox half-reactions in H₂-powered chemical synthesis: From biology to technology. *Biochem. J.* **2017**, *474*, 215–230. [[CrossRef](#)] [[PubMed](#)]
5. Esmieu, C.; Raleiras, P.; Berggren, G. From protein engineering to artificial enzymes—Biological and biomimetic approaches towards sustainable hydrogen production. *Sustain. Energy Fuels* **2017**, 724–750. [[CrossRef](#)]
6. Greening, C.; Biswas, A.; Carere, C.R.; Jackson, C.J.; Taylor, M.C.; Stott, M.B.; Cook, G.M.; Morales, S.E. Genomic and metagenomic surveys of hydrogenase distribution indicate H₂ is a widely utilised energy source for microbial growth and survival. *ISME J.* **2016**, *10*, 761–777. [[CrossRef](#)] [[PubMed](#)]
7. Vignais, P.M.; Billoud, B. Occurrence, classification, and biological function of hydrogenases: An overview. *Chem. Rev.* **2007**, *107*, 4206–4272. [[CrossRef](#)] [[PubMed](#)]
8. Lubitz, W.; Ogata, H.; Rüdiger, O.; Reijerse, E. Hydrogenases. *Chem. Rev.* **2014**, *114*, 4081–4148. [[CrossRef](#)] [[PubMed](#)]
9. Corr, M.J.; Murphy, J.A. Evolution in the understanding of [Fe]-hydrogenase. *Chem. Soc. Rev.* **2011**, *40*, 2279–2292. [[CrossRef](#)] [[PubMed](#)]
10. Ogata, H.; Lubitz, W.; Higuchi, Y. Structure and function of [NiFe] hydrogenases. *J. Biochem.* **2016**, *160*, 251–258. [[CrossRef](#)] [[PubMed](#)]
11. Mulder, D.W.; Shepard, E.M.; Meuser, J.E.; Joshi, N.; King, P.W.; Posewitz, M.C.; Broderick, J.B.; Peters, J.W. Insights into [FeFe]-hydrogenase structure, mechanism, and maturation. *Structure* **2011**, *19*, 1038–1052. [[CrossRef](#)] [[PubMed](#)]
12. Baltazar, C.S.A.; Marques, M.C.; Soares, C.M.; DeLacey, A.M.; Pereira, I.A.C.; Matias, P.M. Nickel-iron-selenium hydrogenases—An overview. *Eur. J. Inorg. Chem.* **2011**, 948–962. [[CrossRef](#)]
13. Vincent, K.A.; Parkin, A.; Armstrong, F.A. Investigating and exploiting the electrocatalytic properties of hydrogenases. *Chem. Rev.* **2007**, *107*, 4366–4413. [[CrossRef](#)] [[PubMed](#)]
14. Marques, M.C.; Coelho, R.; De Lacey, A.L.; Pereira, I.A.C.; Matias, P.M. The three-dimensional structure of [nifese] hydrogenase from *desulfovibrio vulgaris hildenborough*: A hydrogenase without a bridging ligand in the active site in its oxidised, “as-isolated” state. *J. Mol. Biol.* **2010**, *396*, 893–907. [[CrossRef](#)] [[PubMed](#)]
15. De Lacey, A.L.; Fernández, V.M.; Rousset, M.; Cammack, R. Activation and inactivation of hydrogenase function and the catalytic cycle: Spectroelectrochemical studies. *Chem. Rev.* **2007**, *107*, 4304–4330. [[CrossRef](#)] [[PubMed](#)]
16. Goldet, G.; Brandmayr, C.; Stripp, S.T.; Happe, T.; Cavazza, C.; Fontecilla-Camps, J.C.; Armstrong, F.A. Electrochemical kinetic investigations of the reactions of [FeFe]-hydrogenases with carbon monoxide and oxygen: Comparing the importance of gas tunnels and active-site electronic/redox effects. *J. Am. Chem. Soc.* **2009**, *131*, 14979–14989. [[CrossRef](#)] [[PubMed](#)]

17. Stripp, S.T.; Goldet, G.; Brandmayr, C.; Sanganas, O.; Vincent, K.A.; Haumann, M.; Armstrong, F.A.; Happe, T. How oxygen attacks [FeFe] hydrogenases from photosynthetic organisms. *Proc. Natl. Acad. Sci. USA* **2009**, *106*, 17331–17336. [[CrossRef](#)] [[PubMed](#)]
18. Lambertz, C.; Leidel, N.; Havelius, K.G.V.; Noth, J.; Chernev, P.; Winkler, M.; Happe, T.; Haumann, M. O₂ reactions at the six-iron active site (H-cluster) in [FeFe]-hydrogenase. *J. Biol. Chem.* **2011**, *286*, 40614–40623. [[CrossRef](#)] [[PubMed](#)]
19. Rodríguez-Maciá, P.; Reijerse, E.J.; Van Gastel, M.; Debeer, S.; Lubitz, W.; Rüdiger, O.; Birrell, J.A. Sulfide Protects [FeFe] Hydrogenases from O₂. *J. Am. Chem. Soc.* **2018**, *140*, 9346–9350. [[CrossRef](#)] [[PubMed](#)]
20. Oughli, A.A.; Vélez, M.; Birrell, J.A.; Schuhmann, W.; Lubitz, W.; Plumeré, N.; Rüdiger, O. Viologen-modified electrodes for protection of hydrogenases from high potential inactivation while performing H₂oxidation at low overpotential. *Dalt. Trans.* **2018**, *47*, 10685–10691. [[CrossRef](#)] [[PubMed](#)]
21. Caserta, G.; Papini, C.; Adamska-Venkatesh, A.; Pecqueur, L.; Sommer, C.; Reijerse, E.; Lubitz, W.; Gauquelin, C.; Meynial-Salles, I.; Pramanik, D.; et al. Engineering an [FeFe]-Hydrogenase: Do Accessory Clusters Influence O₂ Resistance and Catalytic Bias? *J. Am. Chem. Soc.* **2018**, *140*, 5516–5526. [[CrossRef](#)] [[PubMed](#)]
22. Apfel, U.P.; Weigand, W. Biomimetic assembly of the [FeFe] hydrogenase: Synthetic mimics in a biological shell. *ChemBioChem* **2013**, *14*, 2237–2238. [[CrossRef](#)] [[PubMed](#)]
23. Artero, V.; Berggren, G.; Atta, M.; Caserta, G.; Roy, S.; Pecqueur, L.; Fontecave, M. From Enzyme Maturation to Synthetic Chemistry: The Case of Hydrogenases. *Acc. Chem. Res.* **2015**, *48*, 2380–2387. [[CrossRef](#)] [[PubMed](#)]
24. Birrell, J.A.; Rüdiger, O.; Reijerse, E.J.; Lubitz, W. Semisynthetic Hydrogenases Propel Biological Energy Research into a New Era. *Joule* **2017**, *1*, 61–76. [[CrossRef](#)]
25. Stripp, S.T.; Happe, T. How algae produce hydrogen—News from the photosynthetic hydrogenase. *Dalt. Trans.* **2009**, *45*, 9960–9969. [[CrossRef](#)] [[PubMed](#)]
26. Haumann, M.; Stripp, S.T. The Molecular Proceedings of Biological Hydrogen Turnover. *Acc. Chem. Res.* **2018**, *51*, 1755–1763. [[CrossRef](#)] [[PubMed](#)]
27. Schilter, D.; Rauchfuss, T.B. And the winner is...azadithiolate: An amine proton relay in the [FeFe] hydrogenases. *Angew. Chem. Int. Ed.* **2013**, *52*, 13518–13520. [[CrossRef](#)] [[PubMed](#)]
28. Adamska-Venkatesh, A.; Roy, S.; Siebel, J.F.; Simmons, T.R.; Fontecave, M.; Artero, V.; Reijerse, E.; Lubitz, W. Spectroscopic Characterization of the Bridging Amine in the Active Site of [FeFe] Hydrogenase Using Isotopologues of the H-Cluster. *J. Am. Chem. Soc.* **2015**, *137*, 12744–12747. [[CrossRef](#)] [[PubMed](#)]
29. Lill, R. Function and biogenesis of iron-sulphur proteins. *Nature* **2009**, *460*, 831–838. [[CrossRef](#)] [[PubMed](#)]
30. Posewitz, M.C.; King, P.W.; Smolinski, S.L.; Zhang, L.; Seibert, M.; Ghirardi, M.L. Discovery of two novel radical S-adenosylmethionine proteins required for the assembly of an active [Fe] hydrogenase. *J. Biol. Chem.* **2004**, *279*, 25711–25720. [[CrossRef](#)] [[PubMed](#)]
31. Mulder, D.W.; Ortillo, D.O.; Gardenghi, D.J.; Naumov, A.V.; Ruebush, S.S.; Szilagyi, R.K.; Huynh, B.; Broderick, J.B.; Peters, J.W. Activation of HydAΔEFG requires a preformed [4Fe-4S] cluster. *Biochemistry* **2009**, *48*, 6240–6248. [[CrossRef](#)] [[PubMed](#)]
32. Nicolet, Y.; Fontecilla-Camps, J.C. Structure-function relationships in [FeFe]-hydrogenase active site maturation. *J. Biol. Chem.* **2012**, *287*, 13532–13540. [[CrossRef](#)] [[PubMed](#)]
33. Peters, J.W.; Schut, G.J.; Boyd, E.S.; Mulder, D.W.; Shepard, E.M.; Broderick, J.B.; King, P.W.; Adams, M.W.W. [FeFe]- and [NiFe]-hydrogenase diversity, mechanism, and maturation. *Biochim. Biophys. Acta-Mol. Cell. Res.* **2015**, *1853*, 1350–1369. [[CrossRef](#)] [[PubMed](#)]
34. King, P.W.; Posewitz, M.C.; Ghirardi, M.L.; Seibert, M.; Al, K.E.T.; Acteriol, J.B. Functional Studies of [FeFe] Hydrogenase Maturation in an Escherichia coli Biosynthetic System Functional Studies of [FeFe] Hydrogenase Maturation in an Escherichia coli Biosynthetic System. *J. Bacteriol.* **2006**, *188*, 2163–2172. [[CrossRef](#)] [[PubMed](#)]
35. Bourne, H.R.; Sanders, D.A.; McCormick, F. The GTPase superfamily: Conserved structure and molecular mechanism. *Nature* **1991**, *349*, 117–127. [[CrossRef](#)] [[PubMed](#)]

36. McGlynn, S.E.; Shepard, E.M.; Winslow, M.A.; Naumov, A.V.; Duschene, K.S.; Posewitz, M.C.; Broderick, W.E.; Broderick, J.B.; Peters, J.W. HydF as a scaffold protein in [FeFe] hydrogenase H-cluster biosynthesis. *FEBS Lett.* **2008**, *582*, 2183–2187. [[CrossRef](#)] [[PubMed](#)]
37. Czech, I.; Silakov, A.; Lubitz, W.; Happe, T. The [FeFe]-hydrogenase maturase HydF from *Clostridium acetobutylicum* contains a CO and CN-ligated iron cofactor. *FEBS Lett.* **2010**, *584*, 638–642. [[CrossRef](#)] [[PubMed](#)]
38. Betz, J.N.; Boswell, N.W.; Fugate, C.J.; Holliday, G.L.; Akiva, E.; Scott, A.G.; Babbitt, P.C.; Peters, J.W.; Shepard, E.M.; Broderick, J.B. Hydrogenase maturation: Insights into the role hyde plays in dithiomethylamine biosynthesis. *Biochemistry* **2015**, *54*, 1807–1818. [[CrossRef](#)] [[PubMed](#)]
39. Nicolet, Y.; Rubach, J.K.; Posewitz, M.C.; Amara, P.; Mathevon, C.; Atta, M.; Fontecave, M.; Fontecilla-Camps, J.C. X-ray structure of the [FeFe]-hydrogenase maturase HydE from *Thermotoga maritima*. *J. Biol. Chem.* **2008**, *283*, 18861–18872. [[CrossRef](#)] [[PubMed](#)]
40. Nicolet, Y.; Rohac, R.; Martin, L.; Fontecilla-Camps, J.C. X-ray snapshots of possible intermediates in the time course of synthesis and degradation of protein-bound Fe₄S₄ clusters. *Proc. Natl. Acad. Sci. USA* **2013**, *110*, 7188–7192. [[CrossRef](#)] [[PubMed](#)]
41. Rao, G.; Tao, L.; Suess, D.L.M.; Britt, R.D. A [4Fe–4S]-Fe(CO)(CN)-l-cysteine intermediate is the first organometallic precursor in [FeFe] hydrogenase H-cluster bioassembly. *Nat. Chem.* **2018**, 1–6. [[CrossRef](#)] [[PubMed](#)]
42. Nicolet, Y.; Pagnier, A.; Zeppieri, L.; Martin, L.; Amara, P.; Fontecilla-Camps, J.C. Crystal structure of HydG from *carboxydotherrmus hydrogenoformans*: A trifunctional [FeFe]-Hydrogenase maturase. *Chem. Biol. Chem.* **2015**, *16*, 397–402. [[CrossRef](#)] [[PubMed](#)]
43. Dinis, P.; Suess, D.L.M.; Fox, S.J.; Harmer, J.E.; Driesener, R.C.; De La Paz, L.; Swartz, J.R.; Essex, J.W.; Britt, R.D.; Roach, P.L. X-ray crystallographic and EPR spectroscopic analysis of HydG, a maturase in [FeFe]-hydrogenase H-cluster assembly. *Proc. Natl. Acad. Sci. USA* **2015**, *112*, 1362–1367. [[CrossRef](#)] [[PubMed](#)]
44. Kuchenreuther, J.M.; Myers, W.K.; Stich, T.A.; George, S.J.; Nejatjahromy, Y.; Swartz, J.R.; Britt, R.D. A Radical Intermediate in Tyrosine of FeFe Hydrogenase. *Science* **2013**, *342*, 472–475. [[CrossRef](#)] [[PubMed](#)]
45. Kuchenreuther, J.M. The HydG Enzyme Generates an. *Science* **2014**, *343*, 424. [[CrossRef](#)] [[PubMed](#)]
46. Suess, D.L.M.; Kuchenreuther, J.M.; De La Paz, L.; Swartz, J.R.; Britt, R.D. Biosynthesis of the [FeFe] Hydrogenase H Cluster: A Central Role for the Radical SAM Enzyme HydG. *Inorg. Chem.* **2016**, *55*, 478–487. [[CrossRef](#)] [[PubMed](#)]
47. Suess, D.L.M.; Pham, C.C.; Bürstel, I.; Swartz, J.R.; Cramer, S.P.; Britt, R.D. The Radical SAM Enzyme HydG Requires Cysteine and a Dangler Iron for Generating an Organometallic Precursor to the [FeFe]-Hydrogenase, H-Cluster. *J. Am. Chem. Soc.* **2016**, *138*, 1146–1149. [[CrossRef](#)] [[PubMed](#)]
48. Cendron, L.; Berto, P.; D'Adamo, S.; Vallese, F.; Govoni, C.; Posewitz, M.C.; Giacometti, G.M.; Costantini, P.; Zanotti, G. Crystal structure of HydF scaffold protein provides insights into [FeFe]-hydrogenase maturation. *J. Biol. Chem.* **2011**, *286*, 43944–43950. [[CrossRef](#)] [[PubMed](#)]
49. Shepard, E.M.; Duffus, B.R.; George, S.J.; McGlynn, S.E.; Challand, M.R.; Swanson, K.D.; Roach, P.L.; Cramer, S.P.; Peters, J.W.; Broderick, J.B. [FeFe]-Hydrogenase Maturation: HydG-Catalyzed Synthesis of Carbon Monoxide. *J. Am. Chem. Soc.* **2010**, *132*, 9247–9249. [[CrossRef](#)] [[PubMed](#)]
50. Brazzolotto, X.; Rubach, J.K.; Gaillard, J.; Gambarelli, S.; Atta, M.; Fontecave, M. The [Fe-Fe]-hydrogenase maturation protein HydF from *Thermotoga maritima* is a GTPase with an iron-sulfur cluster. *J. Biol. Chem.* **2006**, *281*, 769–774. [[CrossRef](#)] [[PubMed](#)]
51. Czech, I.; Stripp, S.; Sanganas, O.; Leidel, N.; Happe, T.; Haumann, M. The [FeFe]-hydrogenase maturation protein HydF contains a H-cluster like [4Fe4S]-2Fe site. *FEBS Lett.* **2011**, *585*, 225–230. [[CrossRef](#)] [[PubMed](#)]
52. Berto, P.; Di Valentin, M.; Cendron, L.; Vallese, F.; Albertini, M.; Salvadori, E.; Giacometti, G.M.; Carbonera, D.; Costantini, P. The [4Fe-4S]-cluster coordination of [FeFe]-hydrogenase maturation protein HydF as revealed by EPR and HYSCORE spectroscopies. *Biochim. Biophys. Acta-Bioenergy* **2012**, *1817*, 2149–2157. [[CrossRef](#)] [[PubMed](#)]

53. Berggren, G.; Garcia-Serres, R.; Brazzolotto, X.; Clemancey, M.; Gambarelli, S.; Atta, M.; Latour, J.M.; Hernández, H.L.; Subramanian, S.; Johnson, M.K.; et al. An EPR/HYSCORE, Mössbauer, and resonance Raman study of the hydrogenase maturation enzyme HydF: A model for N-coordination to [4Fe-4S] clusters. *J. Biol. Inorg. Chem.* **2014**, *19*, 75–84. [[CrossRef](#)] [[PubMed](#)]
54. Albertini, M.; Vallese, F.; Di Valentin, M.; Berto, P.; Giacometti, G.M.; Costantini, P.; Carbonera, D. The proton iron-sulfur cluster environment of the [FeFe]-hydrogenase maturation protein HydF from *Thermotoga neapolitana*. *Int. J. Hydrogen Energy* **2014**, *39*, 18574–18582. [[CrossRef](#)]
55. Albertini, M.; Galazzo, L.; Maso, L.; Vallese, F.; Berto, P.; De Rosa, E.; Di Valentin, M.; Costantini, P.; Carbonera, D. Characterization of the [FeFe]-Hydrogenase Maturation Protein HydF by EPR Techniques: Insights into the Catalytic Mechanism. *Top. Catal.* **2015**, *58*, 708–718. [[CrossRef](#)]
56. Caserta, G.; Pecqueur, L.; Adamska-Venkatesh, A.; Papini, C.; Roy, S.; Artero, V.; Atta, M.; Reijerse, E.; Lubitz, W.; Fontecave, M. Structural and functional characterization of the hydrogenase-maturation HydF protein. *Nat. Chem. Biol.* **2017**, *13*, 779–784. [[CrossRef](#)] [[PubMed](#)]
57. Galazzo, L.; Maso, L.; De Rosa, E.; Bortolus, M.; Doni, D.; Acquasaliente, L.; Filippis, V.D.V.D.; Costantini, P.; Carbonera, D. Identifying conformational changes with site-directed spin labeling reveals that the GTPase domain of HydF is a molecular switch. *Sci. Rep.* **2017**, *7*, 1–14. [[CrossRef](#)] [[PubMed](#)]
58. Ash, M.R.; Maher, M.J.; Mitchell Guss, J.; Jormakka, M. The cation-dependent G-proteins: In a class of their own. *FEBS Lett.* **2012**, *586*, 2218–2224. [[CrossRef](#)] [[PubMed](#)]
59. Pettersen, E.F.; Goddard, T.D.; Huang, C.C.; Couch, G.S.; Greenblatt, D.M.; Meng, E.C.; Ferrin, T.E. UCSF Chimera - A visualization system for exploratory research and analysis. *J. Comput. Chem.* **2004**, *25*, 1605–1612. [[CrossRef](#)] [[PubMed](#)]
60. Ash, M.R.; Guilfoyle, A.; Clarke, R.J.; Guss, J.M.; Maher, M.J.; Jormakka, M. Potassium-activated GTPase reaction in the G protein-coupled ferrous iron transporter B. *J. Biol. Chem.* **2010**, *285*, 14594–14602. [[CrossRef](#)] [[PubMed](#)]
61. Broderick, J.B.; Byer, A.S.; Duschene, K.S.; Duffus, B.R.; Betz, J.N.; Shepard, E.M.; Peters, J.W. H-Cluster assembly during maturation of the [FeFe]-hydrogenase. *J. Biol. Inorg. Chem.* **2014**, *19*, 747–757. [[CrossRef](#)] [[PubMed](#)]
62. Shepard, E.M.; Byer, A.S.; Aggarwal, P.; Betz, J.N.; Scott, A.G.; Shisler, K.A.; Usselman, R.J.; Eaton, G.R.; Eaton, S.S.; Broderick, J.B. Electron Spin Relaxation and Biochemical Characterization of the Hydrogenase Maturase HydF: Insights into [2Fe-2S] and [4Fe-4S] Cluster Communication and Hydrogenase Activation. *Biochemistry* **2017**, *56*, 3234–3247. [[CrossRef](#)] [[PubMed](#)]
63. Shepard, E.M.; Byer, A.S.; Broderick, J.B. Iron-Sulfur Cluster States of the Hydrogenase Maturase HydF. *Biochemistry* **2017**, *56*, 4733–4734. [[CrossRef](#)] [[PubMed](#)]
64. Shepard, E.M.; Byer, A.S.; Betz, J.N.; Peters, J.W.; Broderick, J.B. A redox active [2Fe-2S] cluster on the hydrogenase maturase HydF. *Biochemistry* **2016**, *55*, 3514–3527. [[CrossRef](#)] [[PubMed](#)]
65. Scott, A.G.; Szilagy, R.K.; Mulder, D.W.; Ratzlo, W.; Byer, A.S.; King, P.W.; Broderick, W.E.; Shepard, M.; Broderick, J.B. Compositional and structural insights into the nature of the H-cluster precursor on HydF. *Dalt. Trans.* **2018**. [[CrossRef](#)] [[PubMed](#)]
66. Vallese, F.; Berto, P.; Ruzzene, M.; Cendron, L.; Sarno, S.; De Rosa, E.; Giacometti, G.M.; Costantini, P. Biochemical analysis of the interactions between the proteins involved in the [FeFe]-hydrogenase maturation process. *J. Biol. Chem.* **2012**, *287*, 36544–36555. [[CrossRef](#)] [[PubMed](#)]
67. Leippe, D.D.; Wolf, Y.I.; Koonin, E.V.; Aravind, L. Classification and evolution of P-loop GTPases and related ATPases. *J. Mol. Biol.* **2002**, *317*, 41–72. [[CrossRef](#)] [[PubMed](#)]
68. Shepard, E.M.; McGlynn, S.E.; Bueling, A.L.; Grady-Smith, C.S.; George, S.J.; Winslow, M.A.; Cramer, S.P.; Peters, J.W.; Broderick, J.B. Synthesis of the 2Fe subcluster of the [FeFe]-hydrogenase H cluster on the HydF scaffold. *Proc. Natl. Acad. Sci. USA* **2010**, *107*, 10448–10453. [[CrossRef](#)] [[PubMed](#)]
69. Maso, L.; Galazzo, L.; Vallese, F.; Di Valentin, M.; Albertini, M.; De Rosa, E.; Giacometti, G.M.; Costantini, P.; Carbonera, D. A conformational study of the GTPase domain of [FeFe]-hydrogenase maturation protein HydF by PELDOR spectroscopy. *Appl. Magn. Reson.* **2015**, *46*, 465–479. [[CrossRef](#)]
70. McGlynn, S.E.; Ruebush, S.S.; Naumov, A.; Nagy, L.E.; Dubini, A.; King, P.W.; Broderick, J.B.; Posewitz, M.C.; Peters, J.W. In vitro activation of [FeFe] hydrogenase: New insights into hydrogenase maturation. *J. Biol. Inorg. Chem.* **2007**, *12*, 443–447. [[CrossRef](#)] [[PubMed](#)]

71. De Toni, L.; Guidolin, D.; De Filippis, V.; Tescari, S.; Strapazzon, G.; Rocca, M.S.; Ferlin, A.; Plebani, M.; Foresta, C. Osteocalcin and sex hormone binding globulin compete on a specific binding site of GPRC6A. *Endocrinology* **2016**, *157*, 4473–4486. [[CrossRef](#)] [[PubMed](#)]
72. Schneidman-Duhovny, D.; Inbar, Y.; Nussinov, R.; Wolfson, H.J. PatchDock and SymmDock: Servers for rigid and symmetric docking. *Nucleic Acids Res.* **2005**, *33*, 363–367. [[CrossRef](#)] [[PubMed](#)]
73. Andrusier, N.; Nussinov, R.; Wolfson, H.J. FireDock: Fast interaction refinement in molecular docking. *Proteins Struct. Funct. Genet.* **2007**, *69*, 139–159. [[CrossRef](#)] [[PubMed](#)]
74. Pierce, B.G.; Wiehe, K.; Hwang, H.; Kim, B.H.; Vreven, T.; Weng, Z. ZDOCK server: Interactive docking prediction of protein-protein complexes and symmetric multimers. *Bioinformatics* **2014**, *30*, 1771–1773. [[CrossRef](#)] [[PubMed](#)]



© 2018 by the authors. Licensee MDPI, Basel, Switzerland. This article is an open access article distributed under the terms and conditions of the Creative Commons Attribution (CC BY) license (<http://creativecommons.org/licenses/by/4.0/>).



Contents lists available at ScienceDirect

BBA - Proteins and Proteomics

journal homepage: www.elsevier.com/locate/bbapap

Exploring iron-binding to human frataxin and to selected Friedreich ataxia mutants by means of NMR and EPR spectroscopies



Massimo Bellanda^{a,1}, Lorenzo Maso^{b,1}, Davide Doni^b, Marco Bortolus^a, Edith De Rosa^{a,b}, Federica Lunardi^a, Arianna Alfonsi^a, Martín Ezequiel Noguera^{c,d}, Maria Georgina Herrera^{c,d}, Javier Santos^{c,d}, Donatella Carbonera^{a,*}, Paola Costantini^{b,*}

^a Department of Chemical Sciences, University of Padova, Via F. Marzolo 1, 35131 Padova, Italy

^b Department of Biology, University of Padova, Viale G. Colombo 3, 35131 Padova, Italy

^c Departamento de Fisiología y Biología Molecular y Celular, Facultad de Ciencia Exactas y Naturales, Universidad de Buenos Aires, Instituto de Biociencias, Biotecnología y Biomedicina (IB3), Intendente Güiraldes 2160 - Ciudad Universitaria, 1428EGA C.A.B.A., Argentina

^d Instituto de Química y Físicoquímica Biológicas, Dr. Alejandro Paladini, Universidad de Buenos Aires, CONICET, Junín 956, 1113AAD C.A.B.A., Argentina

ARTICLE INFO

Keywords:

Friedreich ataxia

Frataxin

Iron

FeS clusters assembly

ABSTRACT

The neurodegenerative disease Friedreich ataxia results from a deficiency of frataxin, a mitochondrial protein. Most patients have a GAA expansion in the first intron of both alleles of frataxin gene, whereas a minority of them are heterozygous for the expansion and contain a mutation in the other allele. Frataxin has been claimed to participate in iron homeostasis and biosynthesis of FeS clusters, however its role in both pathways is not unequivocally defined. In this work we combined different advanced spectroscopic analyses to explore the iron-binding properties of human frataxin, as isolated and at the FeS clusters assembly machinery. For the first time we used EPR spectroscopy to address this key issue providing clear evidence of the formation of a complex with a low symmetry coordination of the metal ion. By 2D NMR, we confirmed that iron can be bound in both oxidation states, a controversial issue, and, in addition, we were able to point out a transient interaction of frataxin with a N-terminal 6his-tagged variant of ISCU, the scaffold protein of the FeS clusters assembly machinery. To obtain insights on structure/function relationships relevant to understand the disease molecular mechanism(s), we extended our studies to four clinical frataxin mutants. All variants showed a moderate to strong impairment in their ability to activate the FeS cluster assembly machinery *in vitro*, while keeping the same iron-binding features of the wild type protein. This supports the multifunctional nature of frataxin and the complex biochemical consequences of its mutations.

1. Introduction

Frataxin (FXN) is a small highly conserved protein, found in both prokaryotic and eukaryotic organisms [1,2], that was originally identified based on its link to Friedreich ataxia (FRDA; OMIM 229300), a neurodegenerative disease caused by an abnormal expansion of a GAA repeat in the first intron of the *FXN* gene, leading to a severe deficiency of the protein [3,4]. FRDA is the most common inherited form of ataxia, clinically characterized by a progressive limb and gait ataxia, diabetes mellitus and hypertrophic cardiomyopathy, which is the main cause of death [5]. Although the majority of FRDA patients (*i.e.* > 95%) are homozygous for the GAA expansion, a small but significant proportion of them (*i.e.* around 4%) are compound heterozygous for the expansion

on one *FXN* allele and for a mutation on the other, including nonsense, missense, insertion and deletions [6,7]. To date, out of the 40 reported pathogenic variants of *FXN*, at least 20 different point mutations have been described, and it is worth noting that all clinically important mutations described in heterozygous FRDA patients affect highly conserved residues [6]. These patients present either the classical FRDA phenotype or an atypical, less severe clinical picture [6,8]. Contrary to the homozygous GAA expansion, which reduces *FXN* levels, these missense mutations are expected to directly affect the activity and/or structural properties of the expressed protein, as suggested by *in vitro* studies using recombinant mutant proteins [9,10]. There are currently no options to prevent or specifically treat this disease, and life expectancy of patients is reduced to ~ 40–50 years. In fact, although

* Corresponding authors.

E-mail addresses: donatella.carbonera@unipd.it (D. Carbonera), paola.costantini@unipd.it (P. Costantini).

¹ These authors contributed equally to this work.

<https://doi.org/10.1016/j.bbapap.2019.07.007>

Received 12 March 2019; Received in revised form 12 July 2019; Accepted 18 July 2019

Available online 22 July 2019

1570-9639/ © 2019 The Author(s). Published by Elsevier B.V. This is an open access article under the CC BY-NC-ND license (<http://creativecommons.org/licenses/by-nc-nd/4.0/>).

FRDA has been unequivocally associated to FXN depletion, a clear cause-effect relationship is still elusive: the precise physiological function of the protein has not been clarified, as well as its specific contribution to the pathology onset and progression of both classical and atypical FRDA. Several potential roles have been proposed for FXN (reviewed in [11,12]), essentially based on the structural/functional features of the protein. Genetic and biochemical studies carried out on several orthologues support a role of FXN as a multifunction protein involved in different (and likely related) aspects of intracellular iron metabolism, ranging from biogenesis of heme [13] and FeS clusters [14], to iron binding/storage [15] and iron chaperon activity [16]. All these possible functions of FXN are in agreement with the cardinal downstream biochemical features of FRDA cells, i.e. an impaired mitochondrial respiration, likely due to the decrease of the FeS clusters working as electrons shuttles through the respiratory chain, associated to iron overload and increased sensitivity to oxidative stress [17–19]. Some of these defects are probably secondary consequences of FeS clusters assembly defects, and a large body of data supports the idea that the complex phenotypes associated with FXN deficiency in humans as well as in other eukaryotes reflects, at least in part, an impaired capability to assemble these key cofactors (as reviewed in [20]). In fact, FXN depletion is associated with multiple deficit of FeS proteins, especially mitochondrial aconitase and respiratory chain complexes [17] but also cytosolic enzymes [21]; this is usually accompanied by a general dysregulation of cellular iron homeostasis, leading to mitochondrial iron accumulation and cytosolic iron depletion [22,23]. It is thus generally accepted that FXN is a mitochondrial protein involved in iron metabolism, however whether and how it directly participates in this pathway remains unclear and controversial.

Human FXN is a nuclear-encoded protein, ubiquitously expressed at low levels, with the higher concentrations found in tissues strongly dependent on respiratory metabolism, such as heart, dorsal root ganglia sensory neurons and spinal cord [3]. It is an acidic iron-binding protein [1], synthesized in the cytosol as a precursor of 210 amino acids and then imported to the mitochondrion, where it undergoes to proteolytic maturation by a two-step process leading to an intermediate form of 19 kDa (residues 42–210) and finally to a mature form of 14 kDa (residues 81–210) [24–26], which is widely accepted to be the most abundant species both in normal individuals and in patients. Sequence alignment of frataxins from different organisms showed two distinct regions: i) a N-terminal block of 70–90 residues, completely absent in prokaryotes and poorly conserved also among eukaryotes, with features typical of intrinsically unfolded proteins, and ii) a C-terminus encompassing a block of about 100–200 amino acids that is highly conserved in most organisms. The sequence identity of this region is as high as 25%, and the similarity is 40 to 70%, indicating that this is likely the functional portion of the protein. The three-dimensional crystal structure of a recombinant human FXN has been solved [27,28] and indicates that the protein has indeed a N-terminal tail (residues 81–92) intrinsically unfolded and highly flexible, and a C-terminal domain folded in a mixed, compact $\alpha\beta$ -sandwich, with two α -helices packing against an antiparallel β -sheet. Several highly conserved residues are buried in the protein core, consistent with a requirement for maintenance of a compact structure, whereas other are located either in a N-terminal anionic patch or within the flat, conserved external surface of the β -sheet, strongly supporting the hypothesis that these surfaces are critical for FXN function. The highly acidic N-terminal domain, corresponding to the first α -helix together with the first β -strand, has been suggested to confer to FXN the capability to bind iron, and indeed independent NMR studies on human, yeast and bacterial frataxin homologues indicated iron addition effects at or near the negatively charged residues (aspartate and glutamate) clustered on this surface acidic ridge [27,29–32]. On the other hand, there is still uncertainty with respect to the iron-stoichiometry and affinities as well as type of coordination: different constructs of human FXN were reported to bind different $\text{Fe}^{2+}/\text{Fe}^{3+}$ equivalents per monomer, with largely discrepant

dissociation constants [13,16,33], and it has been recently proposed that this protein is not able to bind ferric iron [34], making even more controversial its involvement in iron metabolism and homeostasis. Moreover, how the capability of human FXN to bind iron is related to its potential role in the FeS clusters assembly process is not completely clarified and unequivocally defined.

Based on these premises, in this work we combined different spectroscopic analyses to further characterize the iron-binding properties of human FXN, both as isolated and at the FeS clusters assembly machinery. Moreover, we extended our study to four variants found in FRDA heterozygous patients carrying clinically relevant missense mutations in highly conserved FXN residues.

2. Materials and methods

All chemicals were of the highest purity commercially available.

2.1. Heterologous expression and purification of human FXN, ISCU and NFS1/ISD11 proteins

A plasmid containing human wild type mature FXN, i.e. pET-9b/FXN(90–210), was previously obtained in our laboratory as described in [35]. FXN mutants were obtained through site-directed mutagenesis with the QuickChange® II Site-Directed Mutagenesis Kit (from Agilent Technologies), using as template the pET-9b/FXN(90–210) plasmid and the couples of primers listed in Table 1 (Supplementary material). The sequence of each mutant FXN gene was confirmed by DNA sequencing (at GATC Biotech, Germany). Human ISCU2 cDNA cloned into a pENTR223.1 vector was purchased from MyBioSource, Inc. (San Diego, CA, USA) and used as template to amplify the sequence corresponding to the mature ISCU2 variant, i.e. without mitochondrial targeting sequence, by using the couple of primers FW_{ISCU} (5'-gaattcttatcaacaagaaggtgttgat-3') and REV_{ISCU} (5'-aagctttctctctctctgxtctcc-3'). The fragment of interest was then directionally sub-cloned into a pETDuet-1 expression vector in frame with a sequence coding for a 6his-tag at the 5' terminus. The identity of the insert was confirmed by DNA sequencing (at GATC Biotech, Germany). The sequence coding for the mature ISCU2 protein was also sub-cloned in frame with the 6his-tag sequence at the 3' terminus into a pET-22b(+) expression vector, also carrying the TEV protease cleavage site sequence to remove the 6his-tag from the C-terminus of the purified protein, as described in more detail in Supplementary material. Sequences coding for mature mouse NFS1 and ISD11 proteins were cloned into the two multi-cloning sites (NFS1 in MCS1, in frame with a N-terminus 6his-tag, and ISD11 in MCS2) of a pETDuet-1 vector. *Escherichia coli* BL21 (DE3) cells were transformed with the plasmids of interest, positive clones selected by antibiotic resistance, and recombinant proteins expressed and purified as described in more detail in Supplementary material: briefly, 6his-ISCU2 by combining affinity Ni-NTA and size exclusion chromatographies, wild type and mutant FXN proteins by combining anion exchange and size exclusion chromatographies, and the NFS1/ISD11 complex by a single step of Ni-NTA affinity chromatography, exploiting the NFS1 N-terminus 6his-tag.

2.2. Cysteine desulfurase activity measurements

The enzymatic catalysis of cysteine to alanine by NFS1/ISD11 (SD) complex was measured by the production of sulfide, using slight modifications of the assay described by Leimkühler and co-workers [36]. Briefly, sulfide quantification was performed by a colorimetric reaction in which the latter is used to generate methylene blue. For the assay, a total volume of 0.4 mL was employed, containing 1 μM NFS1/ISD11, 3 μM FXN and 3 μM ISCU. The samples were also supplemented with 10 μM PLP, 2 mM DTT and 10 μM Fe^{2+} at final concentrations. Argon-purged 50 mM Tris-HCl, 200 mM NaCl, pH 8.0 was used as the reaction buffer. To initiate the reaction, 1 mM cysteine was added and

the sample was incubated at room temperature. As sulfide production is linear during the first 40 min (data not shown), 30 min were employed to generate sufficient product for the detection. The assays were stopped by the addition of 50 μ L of 20 mM *N,N*-dimethyl *p*-phenylenediamine in 7.2 M HCl and 50 μ L of 30 mM FeCl_3 in 1.2 M HCl. After letting the reaction proceed for 20 min, the samples were centrifuged for 5 min at 12000 *xg*. Then, the absorbance at 670 nm was measured. The same assay was performed for each frataxin variant, in the same concentration as the wild type. In this case, the desulfurase activity was normalized to the activity of the wild type protein.

2.3. Circular dichroism (CD)

CD measurements were performed with a Jasco J-810 spectropolarimeter. Far-UV CD spectra were collected using cells of 0.1 cm path-length. Data were acquired at a scan speed of 20 nm/min and at least three scans were averaged. Proteins were used at a concentration of 0.2 mg/mL, in a 2.5 mM Tris-HCl pH 7.0, 5 mM KCl buffer. Experiments were performed at 25 $^{\circ}$ C using a thermostated Jasco PTC-423 peltier cell holder connected to a Jasco PTC-423S peltier controller. The secondary structure content of all analyzed proteins was calculated using the CD spectrum deconvolution software CDNN (a software that calculates the secondary structure by comparison with a CD database of known protein structures) [37], and then compared with the one present in literature to confirm their correct folding state.

2.4. UV-Vis absorption and fluorescence spectroscopy

UV-Vis absorption were performed using a Cary 100 UV-Vis Spectrometer from Varian. Fluorescence spectra were detected with a FluoroMax-P Fluorimeter from Horiba Scientific, using 280 nm excitation wavelength which allows to excite tryptophan residues. Quartz cells of 1 cm path-length were used. Proteins were used at a concentration of 0.05 mg/mL (10 μ M), in a 100 mM HEPES pH 7.5, 50 mM KCl buffer. Experiments were performed at 25 $^{\circ}$ C using a thermostated cell. Fe^{3+} equivalents were added step by step starting from a concentrated stock solution of FeCl_3 in diluted HCl (pH \sim 2) by addition of few microliters each time, under constant stirring. Correction of the fluorescence spectra for the filter effect and for dilution resulted to be negligible.

2.5. Electron paramagnetic resonance (EPR) spectroscopy

EPR spectra were recorded on an ELEXSYS E580 spectrometer equipped with a rectangular cavity, ER4102ST, both from Bruker, Germany, and fitted with a cryostat (ESR900) and a variable-temperature controller (ITC503S), both from Oxford Instruments, UK. The experiments were performed using the following parameters: microwave frequency 9.38 GHz, microwave power 6.4 mW (attenuation 15 dB), sweep width 170 mT, center field 150 mT, conversion time 82 ms, time constant 41 ms, modulation amplitude 0.95 mT, 1024 points, 50 averages, temperature 10 K. Samples were prepared incubating the proteins and 2 μ L of Fe^{3+} in a FXN: Fe^{3+} 1:4 molar ratio and a final protein concentration 50 μ M, in a 25 mM HEPES pH 7.0, 5 mM KCl buffer, sample volume 100 μ L. Fe^{3+} was added from a concentrated solution stock solution of FeCl_3 in diluted HCl (pH \sim 2), [Fe^{3+}] = 10 mM. Samples were frozen in dry ice in quartz tubes (i.d. 3 mm, o.d. 4 mm). Quantitative measurements were performed for all samples using identical instrumental conditions, volume and position of the sample tube. The spectra were corrected by subtracting the baseline obtained from the spectrum of a solution of 200 μ M Fe^{3+} in buffer.

2.6. Nuclear magnetic resonance (NMR) spectroscopy

Wild type and mutant FXN ^{15}N -labeled and $^{15}\text{N}/^{13}\text{C}$ -double labeled proteins were isolated from *E. coli* cultures expressing the protein of

interest, grown in M9 minimal media supplemented with ^{15}N $\text{NH}_4\text{Cl}/^{13}\text{C}$ D-Glucose, in the same conditions described above. When Fe^{2+} was used, all samples were prepared with N_2 purged buffer (25 mM Tris-HCl pH 7.0, 50 mM KCl, and 1 mM DTT) under an anaerobic glove box (MBRAUN MB-200B) saturated with N_2 . ^{15}N labeled wild type and mutant FXN proteins had a final concentration of 45 μ M; unlabeled ISCU, when present, was at 80 μ M, taking into account that in all ISCU sample preparations a complex SEC profile was observed, indicative of the co-existence of monomeric and dimeric proteins, or of species with different degree of folding. Fe^{2+} stock solution was freshly prepared before each experiment, dissolving $(\text{NH}_4)_2\text{Fe}(\text{SO}_4)_2 \cdot 6\text{H}_2\text{O}$ in the buffer described above, into the anaerobic glove box. Fe^{3+} solution was prepared dissolving FeCl_3 in the same buffer. Both iron stock solutions had a concentration of 14 mM. Samples "FXN wild type/mutant + Fe^{2+} " (1:4 FXN: Fe ratio) and "FXN wild type/mutant + Fe^{2+} + ISCU" (1:4:2 FXN: Fe :ISCU ratio) were prepared starting from a common stock of FXN wild type/mutant + Fe^{2+} , and then diluted to the right final concentration either with buffer alone or with buffer + ISCU, in order to obtain the same FXN/ Fe ratio in all experiments. 10% D_2O was added to all samples, which were then transferred in anaerobic conditions in Shigemi NMR tubes, without the insert, and sealed with appropriate rubber septa that secured air-tightness throughout the duration of the experiments. Before and after NMR experiments, pH of all samples was strictly controlled, and, in particular after addition of Fe^{3+} , it was necessary to adjust it with 1 M NaOH. All NMR experiments were acquired at 298 K on a Bruker DMX 600 MHz spectrometer with room temperature probes. SOFAST HMQC (band-Selective Optimized Flip-Angle Short-Transient Heteronuclear Multiple Quantum Coherence) [38] was used to monitor the effect of iron and ISCU on ^{15}N labeled FXN wild type/mutants. Resonance assignment for the amides groups of FXN was achieved by comparison with data available for human FXN in the BMRB database (<http://www.bmrwisc.edu>; accession code: 4342) and confirmed by HNCA, HN(CO)CA, HNC(O), HN(CA)CO, HNCACB and HN(CO)CACB 3D heteronuclear experiments, using a sample of 1 mM doubly-labeled protein in the same buffer described above. Spectra were analyzed with NMRFAM-Sparky 1.4 [39] and CARI [40]. Normalized chemical shifts were calculated using the following equation:

$$\Delta\delta = ((\delta_{\text{HN}})^2 + (\delta_{\text{N}}/5)^2)^{0.5}$$

Residues that underwent significant chemical shift perturbations were mapped on the human FXN crystal structure (PDBID: 1EKG) using the program PyMOL [41].

3. Results and discussion

Despite the wide consensus that frataxins are iron-binding proteins involved in the mitochondrial FeS clusters assembly process, there is not a general agreement on iron stoichiometries and dissociation rates, nor on the specific role of frataxin either in the FeS clusters biogenesis or in iron homeostasis. This issue is even more complex for human FXN, for which different recombinant constructs have been shown to bind 6 to 7 iron ions per monomer, irrespective of whether they were Fe^{2+} or Fe^{3+} [16,33,42], with largely incongruous dissociation constants. It is worth noting that in many respects frataxins are quite atypical iron-binding proteins, since they are thought to achieve iron coordination solely through aspartate and glutamate residues exposed on the protein surface instead of cysteines as most of the other iron-binding proteins. An additional unusual property, which may contribute to the experimental discrepancies, is related to the apparent lack of selectivity of frataxin, which is able to coordinate most divalent cations using the same surface acidic residues used for iron [43], so that different experimental conditions could in principle affect both stoichiometries and measured dissociation constants. Moreover, although eukaryotic FXN₈₁₋₂₁₀ is widely accepted as the mitochondrial mature form and several experimental data refer to this protein, pivotal structural studies

have been performed with a shorter construct (*i.e.* FXN₉₀₋₂₁₀), which comprises only the C-terminal evolutionary conserved domain and lacks the extra stretch of residues besides the mitochondrial import sequence at the N-terminus, that is likely unfolded [16,27,29,44]. In the first part of this work, we readdressed the iron-binding properties of a recombinant human FXN₉₀₋₂₁₀ protein by means of a multidisciplinary approach in which different spectroscopic analyses have been combined to obtain new independent structural data on the controversial role of iron in frataxin function(s). Moreover, to gain new clues on potential structure-function relationships, we extended our studies to a panel of selected FXN clinical variants carrying a point mutation either in the iron-binding region itself (*i.e.* D122Y) or in the conserved external surface likely involved in the interaction with the FeS clusters assembly machinery (*i.e.* G130V, N146K and W155R). In the second part of the work, we focused on the iron effect in relation to the structural and functional interactions of these FXN constructs with the FeS clusters assembly machinery, in order to obtain additional molecular details on the involvement of FXN in this biosynthetic pathway.

3.1. Testing iron-binding to human FXN and to selected clinical variants found in FRDA patients

3.1.1. Heterologous expression and purification of different variants of human FXN₉₀₋₂₁₀

We overexpressed in *E. coli* and purified by combining an anionic exchange and a size exclusion chromatography, as described in detail in the section Materials and methods, both the wild type FXN₉₀₋₂₁₀ protein (supplementary Fig. S1) and the four clinical variants (not shown), obtained by inserting the selected point mutation into the wild type FXN₉₀₋₂₁₀ coding sequence by site-specific mutagenesis. All FXN₉₀₋₂₁₀ variants were expressed at the same extent as the wild type protein and were almost completely found in the soluble fraction after cell lysis, except for G130V mutant, which showed a higher tendency towards aggregation (supplementary Fig. S2), as previously reported by Correia and coworkers [9]. This could be explained by the position of residue G130, which is in the tight turn formed by G128, S129 and G130 itself, between strands β 1 and β 2; thus, its mutation into a valine may disturb the turn conformation, resulting in a severe local strain.

3.1.2. UV-visible and fluorescence spectroscopy

The oxidation of Fe²⁺ in the presence of FXN was estimated by following the absorbance change at a wavelength of about 296 nm, which is diagnostic of formation of oxo/hydroxo Fe³⁺ species [45], after adding Fe²⁺ to the protein in aerobic buffer, without stirring. The oxidation rate, in these conditions, depends on the Fe²⁺/protein ratio. While at low iron concentration the oxidation rate is lower than that of the auto-oxidation in buffer, at higher equivalents the oxidation occurs at rates faster. In fact, after adding 3 equivalents, corresponding to 30 μ M of Fe(II), the oxidation rate is already much faster compared to auto-oxidation of Fe²⁺ in buffer at the same iron concentration (Fig. 1). Moreover, there is a fast (within the 10–20 s) initial oxidation phase clearly observable by adding 3 or more iron equivalents, followed by a slower oxidation process. The fast oxidation is saturating already at about 3–4 Fe²⁺ equivalents, showing the same optical density change by addition of 10 equivalents. The second phase is dependent on the Fe²⁺ concentration as expected for an enzymatic reaction following the Michaelis-Menten relationship. Clearly, as the titration progresses, iron-binding sites with different reaction properties are filled. A similar behavior was reported before for CyaY from *E. coli* [45] and was ascribed to the presence of different iron-binding sites.

An indirect evidence for the iron-FXN complex formation was then provided by fluorescence quenching of the tryptophan residues emission, induced by Fe³⁺ addition to a protein solution. The effect on the fluorescence may mainly be ascribed to the energy transfer of the excitation that occurs between tryptophan residues and the oxo-complexes formed by Fe³⁺ ions with the protein upon binding, as suggested

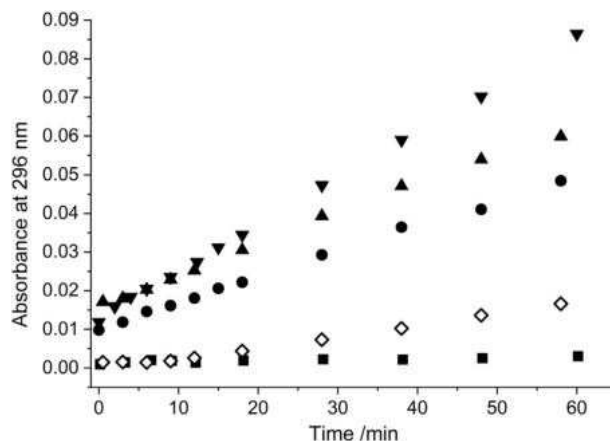


Fig. 1. Kinetics of Fe²⁺ oxidation. The oxidation of Fe²⁺ to Fe³⁺ was detected by absorbance change at 296 nm, at different FXN: Fe²⁺ molar ratios: squares, 1:0.5; circles, 1:3; up triangles, 1:4; down triangles, 1:10. In empty diamonds, the oxidation in buffer alone of Fe²⁺ 30 μ M. Protein concentration: 10 μ M. T = 298 K.

before for ferritin fluorescence quenching observed when Fe³⁺ was loaded [46]. Human FXN contains three tryptophan residues, and it is worth noting that one of them is missing in one of the four variants analyzed in this work (*i.e.* the W155R FXN). It can be seen that the fluorescence quenching due to the increasing amount of ferric ions is similar among the samples (wild type and mutants), with a more pronounced deviation for the D122Y mutant, which shows a reduced quenching (about -20%) (Fig. 2). The quenching of fluorescence produced by Fe²⁺ was almost absent (data not shown). In the case of Fe²⁺ the quenching, strongly reduced compared to that induced by Fe³⁺ addition, is expected to be due only to a paramagnetic effect rather than to energy transfer as for Fe³⁺. However, since strictly anaerobic conditions were not guaranteed, it is possible that the observed quenching derives from the trace amounts of Fe³⁺ produced by oxidation due to the residual oxygen. Our experimental data on Fe²⁺ are in disagreement with those reported by Yoon and co-workers, who observed a large fluorescence quenching following Fe²⁺ addition, similar to that observed with Fe³⁺ [13].

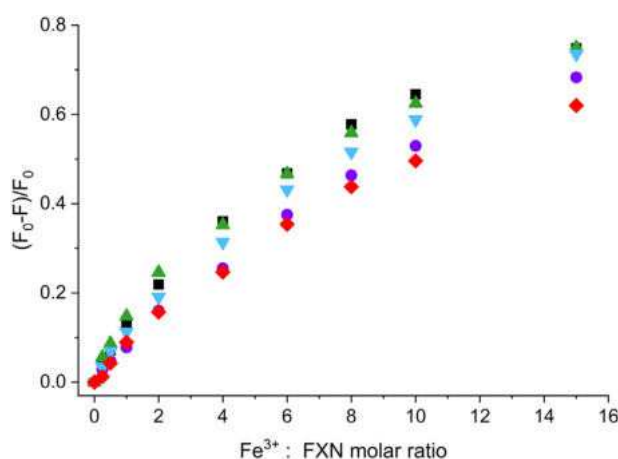


Fig. 2. Quenching of tryptophan fluorescence intensity in wild type and mutant FXN proteins after addition of increasing Fe³⁺ equivalents. The quenching was followed on the maximum of fluorescence emission at different FXN:Fe³⁺ molar ratios. Black squares, wild type FXN; red diamonds, D122Y mutant; purple circles, G130V mutant; azure down triangles, N146K mutant; green up triangles, W155R mutant. F = fluorescence intensity at the actual concentration of Fe³⁺, F₀ = fluorescence intensity in the absence of Fe³⁺. Protein concentration: 10 μ M. T = 298 K.

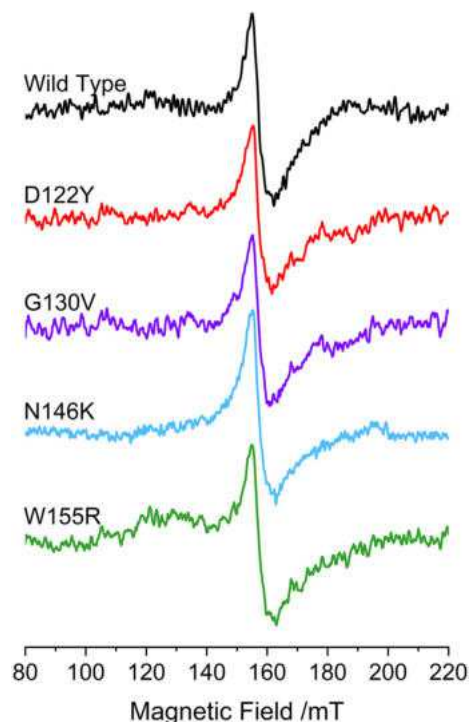


Fig. 3. EPR spectra of Fe^{3+} bound to wild type and mutant FXN proteins. The spectra show the $g = 4.3$ spectral region. Top to bottom: black, wild type FXN; red, D122Y mutant; purple, G130V mutant; azure, N146K mutant; green, W155R mutant. The samples have a 4:1 Fe^{3+} :FXN ratio. Protein concentration: 50 μM . $T = 10\text{ K}$.

The iron-binding to FXN was further addressed, for the first time, by EPR spectroscopy of wild type and mutant frataxins, as described in the following.

3.1.3. EPR spectroscopy

EPR measurements were performed at 10 K to get a direct evidence, instead of an indirect effect as probed by fluorescence spectroscopy, of the iron-binding to FXN, since EPR is able to detect bound Fe^{3+} ions and gives information on the coordination to the protein residues. A protein sample in the absence of iron does not show an EPR signal, and the signal of Fe^{3+} in HEPES buffer solution at pH 7.0 is negligible in the low-field $g = 4.3$ region and absent at higher field values (data not shown). This was expected, since i) HEPES does not coordinate iron and ii) under these experimental conditions, in terms of pH and concentration, iron precipitates as hydroxide. On the other hand, when Fe^{3+} was added to FXN, a signal centered at $g = 4.3$, ascribed to a high-spin mononuclear Fe^{3+} species in an environment of low symmetry, has been observed for all the samples, compatible with an aspartate/glutamate coordination [47], with no further signals present in other spectral regions. In Fig. 3, the EPR signals detected after addition of 4 equivalents of Fe^{3+} to 50 μM protein solutions are shown. The spectra have been normalized to unit intensity to compare their shape: no significant differences among the samples have been detected when comparing wild type and mutant frataxins. The intensity of the signal of D122Y variant was reduced with respect to that of the wild type, in agreement with the fluorescence experiments reported above. Instead, the other variants showed only slightly different signal intensities.

The EPR experiments unequivocally show that i) FXN is able to bind Fe^{3+} ions and ii) the mutations in the FXN clinical variants examined in our study do not impair the protein ability to bind iron ions. The D122Y mutant seems to be affected in this respect, but the capability of binding iron is not fully compromised. Due to the broadness of the spectral shape, it was not possible to characterize the different iron-binding sites

suggested by the absorption spectra.

We next investigated the iron-binding properties of wild type and mutant frataxins by NMR, either as isolated and in the presence of ISCU, the key scaffold protein of the FeS clusters assembly machinery.

3.1.4. 2D NMR analysis

Both the NMR spectral assignment and the structure of human FXN₉₀₋₂₁₀ have been previously achieved by Musco and coworkers [27,44], and the Fe^{2+} -binding sites were mapped onto the protein by chemical shift perturbation analysis [29]. We first confirmed these data by titrating with Fe^{2+} a ^{15}N -labeled FXN₉₀₋₂₁₀ protein and using SOFAST-HMQC NMR spectra to monitor perturbations, as described in detail in Material and methods, and we performed the same analyses with Fe^{3+} . Supplementary Fig. S3 shows the NMR spectrum of FXN with the peak assignments, whereas supplementary Fig. S4 reports the superimposition of the spectra in the absence and in the presence of Fe^{2+} (panel A) or Fe^{3+} (panel B). In these experiments we used a protein:iron ratio of 1:4 and at the relatively low FXN concentration used in our experiments we did not observe any evident precipitation upon addition of Fe^{3+} . Fig. 4, panels A and B, shows the normalized chemical shift changes, calculated as described in Materials and methods. Upon the addition of Fe^{2+} in anaerobic conditions (panel A), as previously shown [29], or of Fe^{3+} (panel B), positions and/or intensities of several peaks in NMR spectra of FXN resulted to be perturbed. As expected, the perturbed peaks mostly correspond to residues belonging to the N-terminal $\alpha 1/\beta 1$ acidic iron-binding region of FXN. Titration of FXN with Fe^{3+} showed effects qualitatively similar to those caused by Fe^{2+} , indicating that the protein binds iron ions by using essentially the same area, as previously reported for the frataxin bacterial homologue CyaY [29]. Interestingly, Fe^{2+} generally induces larger perturbations (larger shifts or higher intensity decrease of the peaks), except for residues 119 and 120, that appear more shifted upon addition of Fe^{3+} (Fig. 4, panels A and B). This is in agreement with the EPR data reported above, showing that Fe^{3+} is able to bind to FXN, and further suggests a slightly different binding mode for iron in the two oxidation states.

We next analyzed, in the same experimental conditions, the 2D NMR spectra of the four clinical FXN variants described above, either in the absence or in the presence of Fe^{2+} . The same experiment using Fe^{3+} was not performed because of the very similar effects observed on wild type FXN upon addition of iron in the two different oxidation states. In the absence of iron, the spectra of all mutants showed a good signal dispersion, compatible with folded species (supplementary Fig. S5). This was already reported for D122Y, G130V and W155R [9] but not for N146K, whose $^1\text{H}-^{15}\text{N}$ correlation spectrum is shown here for the first time. All the spectra of the mutants were partially superimposable to that of the wild type protein and, accordingly, it was possible to assign most of the resonances and to identify the regions most perturbed by the mutations (supplementary Fig. S6). When compared to the wild type protein, the NMR spectra of the four clinical FXN variants reflected local rearrangements, mostly surrounding the mutation. In all cases some peaks of residues adjacent to the mutation could not be assigned because of very large shifts when compared to the wild type protein. For mutant D122Y, the substitution induced strong perturbations in several residues facing it. Perturbed regions include residues of the terminal part of $\alpha 1$ and the beginning of $\beta 1$ together with the loop connecting them, the loop between $\beta 1$ and $\beta 2$ and the beginning of $\alpha 2$. The most significant perturbations were observed for the G130V and W155R variants, in a relatively wide region extending from the mutation that includes not only residues from the whole β -sheet but also from the N-terminal part of $\alpha 1$, as shown in supplementary Fig. S6. These results are compatible with the W155R crystal structure, in which a significant side-chain reorganization surrounding the mutation is evident when compared to the native FXN [48]. Instead, mutation N146K perturbed only few adjacent residues, mostly belonging to $\beta 3$ (where mutation is located) and $\beta 4$ strands (supplementary Fig. S6).

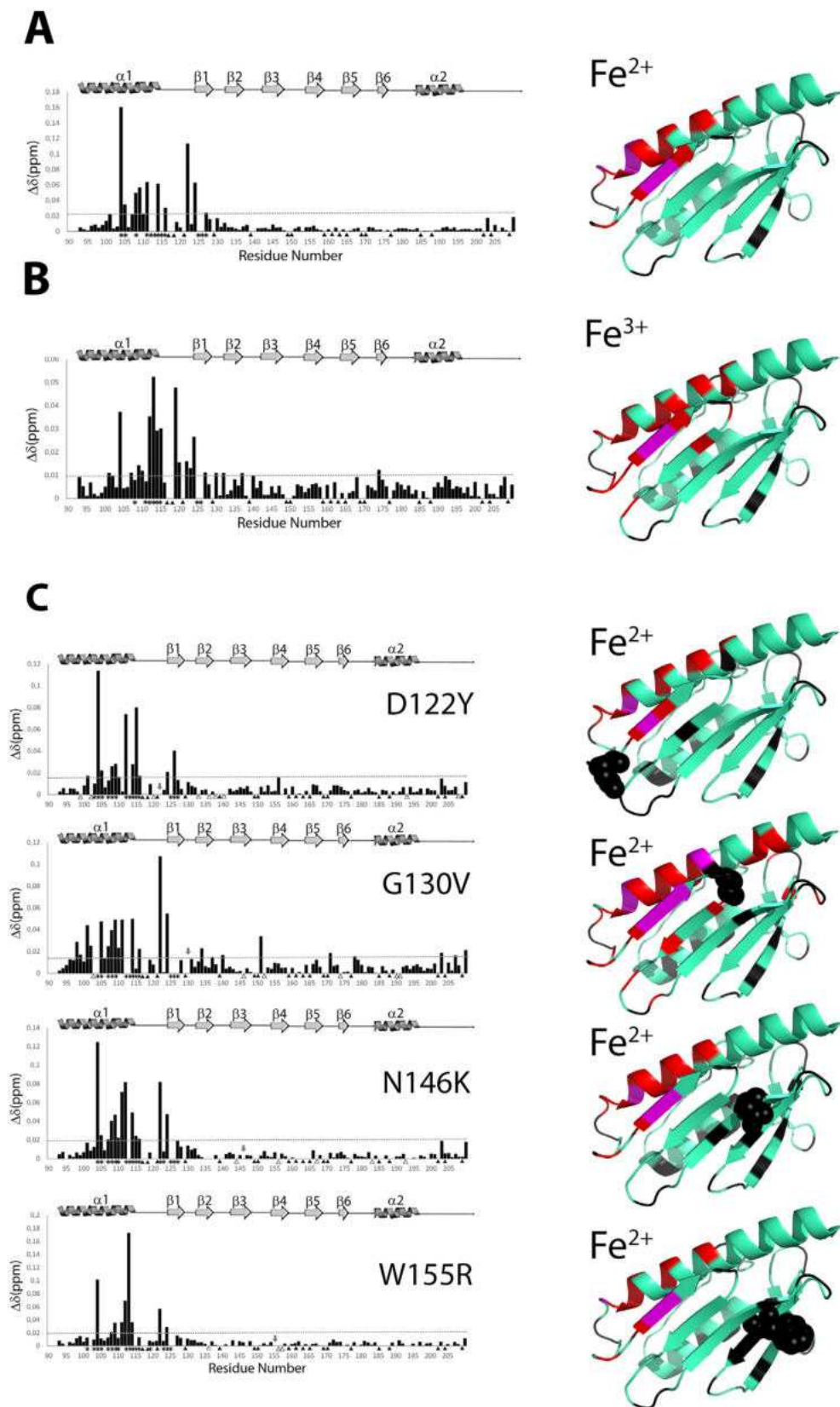


Fig. 4. Mapping the iron-binding sites of FXN by NMR chemical shift perturbation. Normalized chemical shift changes for wild type FXN with and without 4 equivalents of Fe^{2+} (A) or Fe^{3+} (B) and for the four FXN mutants with and without 4 equivalents of Fe^{2+} (C). The dotted line represents the threshold calculated as one standard deviation of the shifts. The asterisks indicate residues whose peaks disappeared or presented significantly reduced intensity in presence of iron. Prolines or residues corresponding to severe overlapped or unassigned peaks in wild type FXN are indicated with black triangles while residues which cannot be traced in the mutants are shown with empty triangles. A schematic representation of FXN secondary structure is inserted in frame with residues sequence number to facilitate the interpretation of the figure. On the right column, protein regions perturbed upon iron addition are mapped with colours on the apo-FXN structure (PDBID: 1EKG). The residues presenting, upon addition of iron, normalized chemical shift changes larger than a one standard deviation of all the shifts are coloured in red. Residues whose signal disappear upon addition of iron are coloured in magenta. The mutated residues are represented in spheres. In black are coloured prolines, residues corresponding to severe overlapped or unassigned peaks in wild type FXN and residues whose assignment could not be traced in the mutants.

This is in agreement with the crystal structure of the variant N146K (construct FXN₉₀₋₂₁₀), that shows backbone and side chain conformations similar to those of native FXN [9]. Additionally, we analyzed the temperature-induced unfolding profiles of all FXN variants (as assessed by using Sypro-orange dye that binds to the unfolded state) and found

T_m values compatible with stable tertiary structure and resistance to the temperature unfolding, *i.e.* 50.3 ± 0.3 , 57.1 ± 0.3 , 54.8 ± 0.1 , 69.4 ± 0.1 , 64.9 ± 0.2 °C for G130V, D122Y, W155R, N146K and wild type FXN, respectively (Fig. 5). Interestingly, mutation N146K may be stabilizing. On the other hand, since a difference in T_m does not

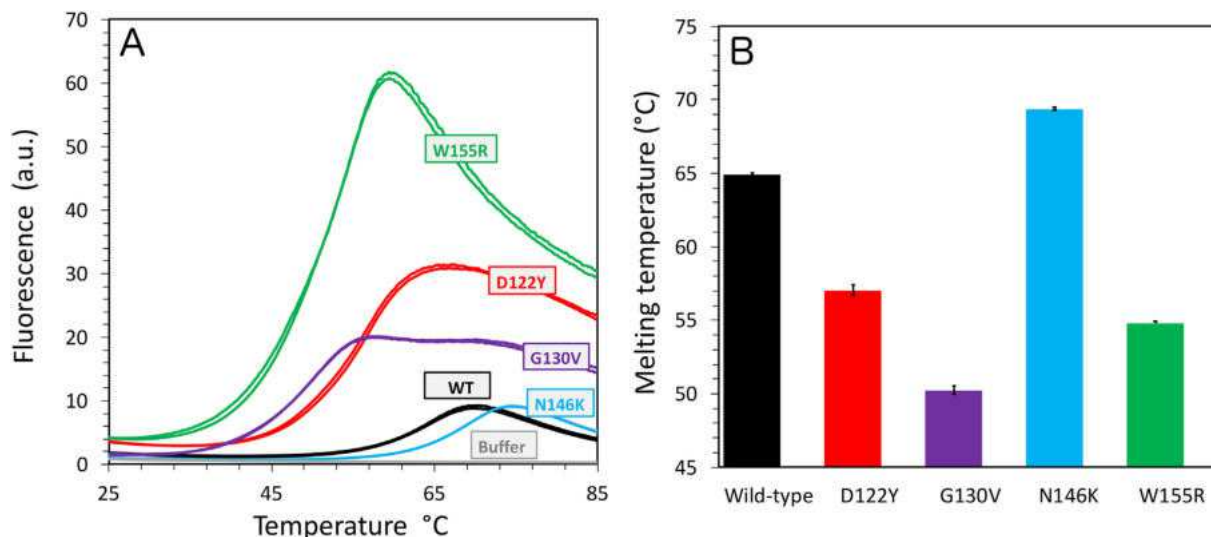


Fig. 5. Temperature-induced unfolding of FXN mutants. Unfolding of FXN mutants was followed by the change in sypro-orange dye fluorescence. (A) Unfolding profiles. (B) Melting temperatures. Data represent the mean of four replicates \pm S.D. for each variant.

necessarily imply a difference in free energy more experiments will be carried out in order to confirm these data.

We then explored by the same NMR analysis the N-terminal acidic region of these four clinical variants after addition of Fe^{2+} at a 1:4 protein:iron ratio. Notably, in these conditions, for the W155R mutant we did not observe any significant protein precipitation as was previously reported [9], most likely due to the lower protein concentrations used in our experiments. The results are shown in Fig. 4, panel C, which reports the normalized chemical shift and intensity changes (NMR spectra are in supplementary Fig. S7). When compared to the wild type protein, FXN variants showed similar behaviors in the presence of four equivalents of Fe^{2+} . The iron-binding region of mutants N146K and W155R resulted to be almost identical to that of the wild type protein, suggesting that these two mutations do not significantly impact on the iron-binding capability of FXN. Instead, the effect of Fe^{2+} on the NMR spectrum of mutant G130V involves a larger number of peaks which become very broad or shift, with additional perturbed residues surrounding the $\alpha 1/\beta 1$ acidic region. This increased perturbation in the NMR spectrum of G130V FXN variant upon addition of Fe^{2+} could reflect the lower conformational stability previously observed by Correia and coworkers [9], as discussed above, and it is in agreement with a decrease in T_m value compared to the wild type FXN ($\Delta T_m = 14.6$ °C). Surprisingly, with four Fe^{2+} equivalents, mutant D122Y does not show striking differences in the iron-binding region, where the mutation is located, when compared to the wild type protein. On the other hand, it must be underlined that residues 120 and 121 (and 122 itself) were not assigned in this mutant because of their large resonance shift; thus, possible differences in this region potentially affecting the capability of D122Y FXN variant to bind iron could not be tracked. As the EPR and fluorescence experiments reported above suggest, at least for Fe^{3+} binding, D122Y FXN shows a reduced capability to bind iron with respect to all the mutants addressed in this work. This is in agreement with the previous observation that iron-binding is only partially impaired in this mutant, which maintains the ability to bind four irons per protein.

An additional key open issue is the way by which FXN is involved in the FeS clusters assembly process; several functions have been hypothesized for FXN in this pathway, ranging from iron delivery [16,49,50] to allosteric activation of the assembly machinery [51–53]. However, a converging consensus on its specific role is still missing. We thus further investigated this issue, focusing on the structural and functional interactions of FXN with ISCU, the scaffold protein upon which the FeS clusters are assembled prior to the transfer to the target

apoproteins, as reported in the next paragraph. Although we used the mitochondrial isoform ISCU2, this protein will be simply referred as ISCU in the following.

3.2. Exploring human iron-bound FXN at the FeS cluster assembly machinery

According to an involvement in the FeS clusters biogenesis, human FXN was shown to interact with multiple core components of the assembly machinery. In eukaryotes, FeS proteins are distributed in almost every cellular compartment, especially in mitochondria, cytosol and nucleus [54]; the assembly of the FeS clusters is mainly performed by the mitochondrial ISC multiprotein machinery, which is composed of the cysteine desulfurase NFS1, the accessory proteins ISD11 and ACP (Acyl Carrier Protein), and the ISCU scaffold [55–60]. It is worth noting that although eukaryotes possess an additional cytosolic assembly system (*i.e.* CIA, Cytosolic Iron-sulfur cluster Assembly) [54], the ISC complex is also essential to all extra-mitochondrial FeS proteins [54,55], putting this machinery more in general at the core of the metabolic pathways involving FeS proteins, both in healthy cells and in human diseases caused by FeS clusters deficiencies, including Friedreich ataxia. Although evidence of an interaction between FXN and the NFS1-ISD11-ACP-ISCU complex has received many independent confirmations [34,49,53,61–64], several questions are unanswered, particularly as far as concerns its direct partner, which remains controversial as different one-to-one interactions with each component were reported [16,49,61,63,64]. It is worth noting that many residues of the FXN whole β -sheet external surface are highly conserved and have been claimed to be critical for its specific interactions with other FeS cluster assembly proteins [28,62]. Several known missense point mutations associated with compound heterozygous FRDA patients map indeed to these residues, including the four selected for our study, that belong either to the N-terminal anionic patch or to the flat, conserved external surface of the β -sheet, which is likely fundamental for the docking of protein partner(s) on FXN.

Whatever is the specific role of FXN, the general consensus is that it is iron-dependent [16,34,49], and that it relies on transient interactions with the biosynthetic core complex. Thus, by means of the same NMR analysis described above, we addressed the iron-binding to FXN in the presence of the scaffold ISCU, using either the wild type protein or the four selected pathological mutants. To this end, we heterologously expressed and purified a recombinant human mature (*i.e.* without the N-terminal mitochondrial targeting sequence) N-6his-tagged ISCU

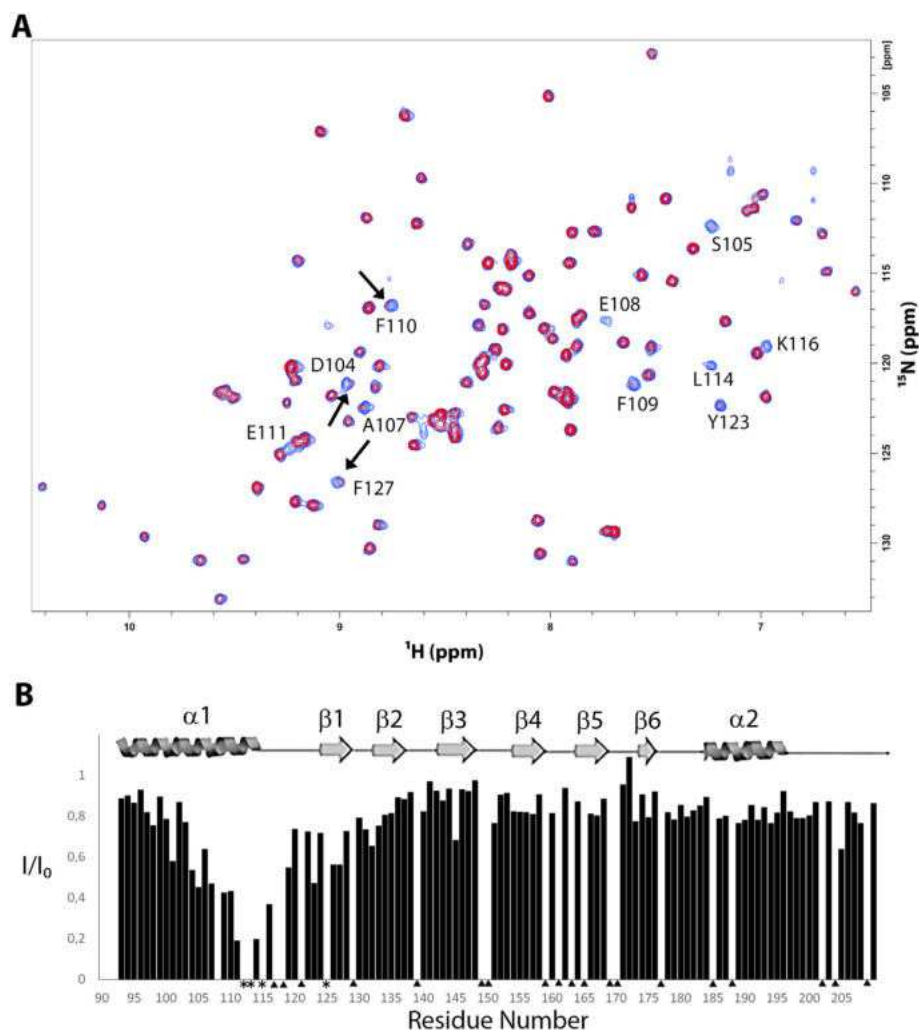


Fig. 6. Effect of N-6his-tagged ISCU on the NMR spectra of FXN in presence of four equivalents of Fe^{2+} . The superposition of the $^1\text{H}, ^{15}\text{N}$ -SOFAST-HMQC spectra of FXN in absence (blue) and in presence (red) of ISCU are shown in panel A. The ratios of the peak intensities in the spectra without (I_0) and with (I) ISCU are represented as a function of the residue number in panel B. Residues corresponding to signals which disappeared in presence of ISCU and iron are indicated with asterisks. Prolines or residues corresponding to severe overlapped or unassigned peaks in wild type FXN are marked with black triangles. A schematic representation of FXN secondary structure is inserted in frame with residues sequence number to facilitate the interpretation of the figure. The black arrows indicate peaks that, besides being broadened, are also slightly shifted upon addition of ISCU.

protein, as described in detail in Materials and methods. The purified protein showed a secondary structure content compatible with a properly folded α/β species, as assessed by far-UV circular dichroism (supplementary Fig. S8 and Table 2 in Supplementary material). Addition of unlabeled ISCU to the ^{15}N -labeled FXN protein was then performed in the presence of Fe^{2+} , in anaerobic conditions, as described in detail in Material and methods, with a 1:4:2 FXN: Fe^{2+} :ISCU ratio. In order to facilitate the interaction with FXN, ISCU was added in excess taking into account that this protein is present in solution in monomeric and dimeric states, as pointed out above. The SOFAST HMQC NMR spectrum was finally acquired to map the residues potentially affected by the presence of ISCU. We found that addition of ISCU did not cause evident chemical shift perturbation on the NMR spectrum of the iron-bound frataxin (Fig. 6), which would have indicated the formation of a binary complex interaction of this protein with ISCU, at least in the absence of the other ISC complex functional partners. Interestingly, some cross-peaks corresponding to residues located in the $\alpha 1/\beta 1$ acidic region already perturbed by iron-binding became significantly broader upon addition of N-6his-tagged ISCU. Furthermore, a close look to the NMR spectrum of the Fe^{2+} -bound FXN protein indicates that few residues present a small but significant shift in the proton dimension upon addition of ISCU (Fig. 6). In particular, the significant increase of line broadening for residues in the $\alpha 1/\beta 1$ acidic region already perturbed by iron-binding could be due to an enhancement of paramagnetic relaxation caused by existence of transient, low population of the complex between the two proteins. Moreover, we added the N-6his tagged ISCU to ^{15}N -labeled frataxin in

absence of iron and, as expected, in this case we did not observe any effect (supplementary Fig. S9), confirming that the further broadening is due to enhanced paramagnetic relaxation, which is very sensitive to protein-protein interaction. Although a strong interaction between the two proteins can be excluded, our data suggest that, even in the absence of the cysteine desulfurase complex, ISCU could interact directly with the $\alpha 1/\beta 1$ acidic region or that a transient interaction of ISCU with the $\beta 3$ - $\beta 5$ sheet of FXN, previously proposed for the interaction between the two proteins, could affect the structure and/or dynamics of the iron-binding region. Moreover, differently from what observed before by Cai and coworkers [34], the finding that upon addition of ISCU the spectrum of FXN remained very similar to that of the iron-bound protein indicates that, at least in our conditions, the transfer of iron from FXN to ISCU does not take place. Qualitatively similar results were obtained when N-6his-tagged ISCU was added to the FXN mutants studied in this work in the presence of 4 equivalents of Fe^{2+} , in anaerobic conditions. As in the case of the wild type FXN, the addition of N-6his-tagged ISCU causes changes in the NMR spectra for peaks corresponding to residues in the $\alpha 1/\beta 1$ acidic region, mostly in term of a further line broadening (Fig. 7). This was not evident in the case of G130V, where the signals that experienced the larger effect in presence of ISCU for the wild type FXN or for the mutants were already extremely broad upon iron addition. Although there are some small differences, in all cases the addition of ISCU appeared to strengthen the effects observed upon addition of iron. In particular, there are 8 peaks, corresponding to E108, E111, D112, L113, D115, V125 and S126, that disappear or become very weak upon addition of Fe^{2+} and ISCU. Interestingly, they are located in

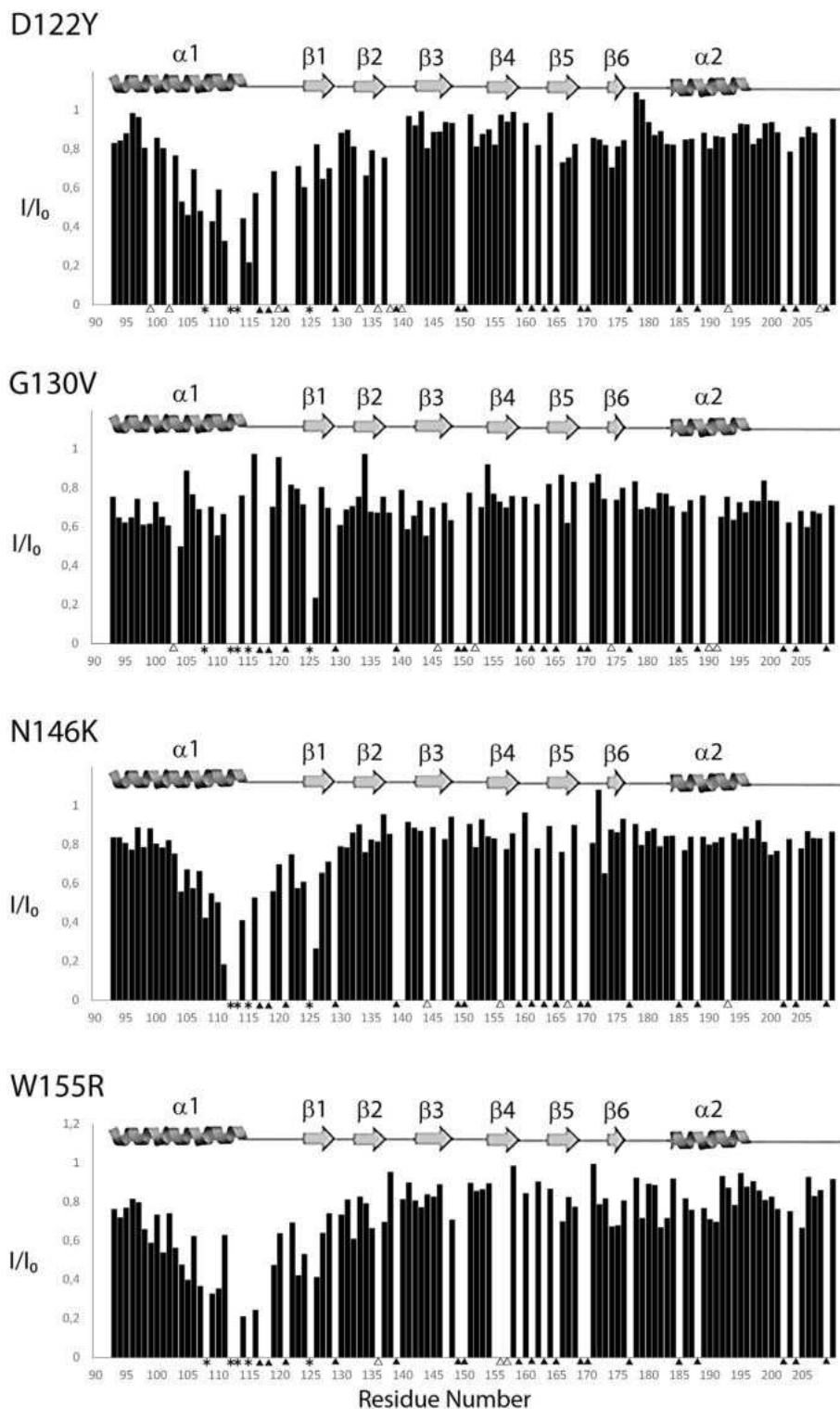


Fig. 7. Ratios of the peak intensities in the spectra without (I_0) and with (I) ISCU represented as a function of the residue number for FXN mutants. Residues corresponding to signals which disappeared in presence of ISCU and iron are indicated with asterisks. Prolines or residues corresponding to severe overlapped or unassigned peaks in wild type FXN are marked with black triangles while residues which cannot be traced in the mutants are shown with empty triangles. A schematic representation of FXN secondary structure is inserted in frame with residues sequence number to facilitate the interpretation of the figure.

the C-terminal part of $\alpha 1$ and in the residues of $\beta 1$ facing it, while the binding sites at the N-terminus of $\alpha 1$ and in the loop are much less influenced.

In order to exclude that the effect of ISCU on FXN described above may be due to an interaction of the N-terminal 6his-tag, possibly mediated by iron, we produced a novel construct allowing the

expression of a C-6his-ISCU protein, with a TEV-cleavage site to remove the tag after purification, as described in Materials and methods and in the supplementary materials. The C-6his-ISCU and untagged ISCU proteins were then used to explore potential effects on the NMR spectrum of the iron-bound ^{15}N -labeled frataxin, exactly as described above. We found that both proteins did not cause neither evident chemical

shift perturbation nor additional broadening of NMR signals, including those corresponding to the residues of the $\alpha 1/\beta 1$ acidic already perturbed by iron-binding, unlike what we observed with the N-6his-tagged ISCU protein (supplementary Fig. S10). On the other hand, the lack of effects observed with untagged or C-6his-tagged ISCU proteins suggested that the his-tag at the N-terminus should influence the structural properties of ISCU. In view of the capability of ISCU to explore different conformational states, as previously reported by different groups [65,66], it is likely that the flexible N-terminus when his-tagged promotes a shift of the equilibrium among conformations. Thus, a transient interaction between FXN and ISCU could be enhanced, allowing the changes measured in the NMR spectra. In particular, the significant increase of line broadening for residues in the $\alpha 1/\beta 1$ acidic region already perturbed by iron-binding could be due to an enhancement of paramagnetic Curie relaxation caused by existence of transient, low population of the complex between the two proteins.

Taken together, these results confirm that a binary complex interaction between FXN and ISCU, at least in the absence of the other ISC complex functional partners, is not formed, as it was pointed out by Cai and co-workers with the FXN₈₀₋₂₁₀ protein [34]. On the other hand, they suggest that the presence of a 6his-tag at the N-terminus of ISCU may promote a transient interaction with FXN, which is not mediated by a potential iron-binding to the 6his-tag.

The capability of iron-bound FXN to functionally interact with the NFS1-ISD11-ACP-ISCU complex is pivotal to drive the biogenesis of the FeS clusters at the assembly machinery. The mutations of the highly conserved residues associated with the four clinical variants analyzed in this work are all expected to have a functional impact on the FeS clusters synthesis. Since our EPR and NMR data did not point out significant differences between the wild type and the mutant proteins in terms of iron-binding and ISCU interaction, to further investigate the structure-function relationships in these variants we next evaluated their activity at the whole FeS cluster biogenesis complex. Mammalian FXN was proposed to stimulate the rate of FeS clusters assembly by enhancing the sulfide production at the NFS1-ISD11-ISCU machinery [53,67,68]. The cysteine desulfurase NFS1, which forms a functional complex with ISD11 (an essential mitochondrial matrix protein that is required for the stability and function of NFS1), catalyzes the breakdown of cysteine to alanine and produces a transient persulfide species that can be detected *in vitro* by the enzymatic assay described in detail in Materials and methods. By taking advantage of this approach, we monitored the amount of sulfide produced by NFS1/ISD11 conversion of cysteine to alanine in the presence of ISCU, with or without wild type or mutant frataxin proteins. In these experiments, sulfide production has been monitored in the presence of 1 equivalent of the NFS1/ISD11 complex, purified as described in Materials and methods, 3 equivalents of ISCU and 10 equivalents of Fe²⁺, either in the absence or in the presence of wild type FXN and of each of the four FXN variants. The results of these analyses are reported in Fig. 8 and Table 3 in Supplementary material. The mutations N146K and W155R had been previously shown to affect the capability of FXN to stimulate the NFS1/ISD11 desulfurase activity *in vitro* [48,69], whereas these data were lacking for both D122Y and G130V variants. Our results confirmed that i) wild type FXN increases the cysteine desulfurase activity of NFS1/ISD11 complex and ii) N146K and W155R variants are almost unable to further activate NFS1. We next analyzed the effects of G130V and D122Y point mutations. We found that, when compared to the wild type FXN, both variants retain a partial capability to enhance the desulfurase activity *in vitro*. Since it has been previously proposed the FXN stimulatory effect on the desulfurase activity relies on the presence of the ISCU scaffold [68], these functional data would be in accordance with the structural NMR analysis reported above. On the other hand, even though N146K may be more stable than the wild type protein, it exhibited a significant decrease of desulfurase activation. Based on the analysis of the experimental model of NFS1/ISD11-ACP-ISCU/FXN complex determined by Cai and coworkers [34], residue Asn146 of FXN

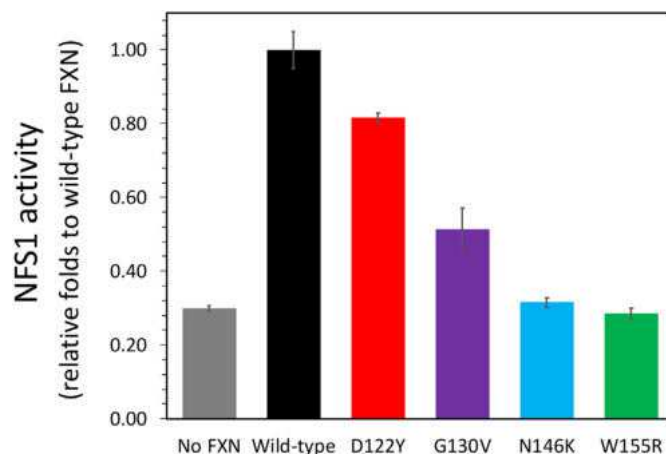


Fig. 8. Modulation of the NFS1 cysteine desulfurase activity at the FeS clusters assembly complex. Sulfide production was assessed in the presence of 1 equivalent of the NFS1/ISD11 complex, 3 equivalents of ISCU and 10 Fe²⁺ equivalents, either in the absence or in the presence of 3 equivalents of wild type FXN and each FXN mutant, as described in detail in Materials and methods. The enzymatic activity is normalized to the desulfurase activity in the presence of wild type FXN. Data represent the mean of three replicates \pm S.D.

interacts with residues Pro108 and Val109 of ISCU (supplementary Fig. S11). Thus, the mutation N146K may distort the interaction surface of ISCU-FXN subcomplex. In fact, when the residue is mutated to Lys, the N atom of the Lys146 side-chain is located near Cys44 of ISCU (*i.e.* 5.0–6.0 Å), one of the conserved Cys residues where the cluster is assembled. Therefore, the electrostatics of the active site of ISCU (residues Cys44, Cys70, His112 and Cys113) may be highly altered by the presence of a positive charge.

Taken together, these data thus indicate that iron-binding, at least to the specific FXN clinical variants selected in this work, is not univocally related to their capability to enhance sulfide production *via* binding the NFS1-ISD11-ISCU complex, one the proposed molecular functions of frataxin. The complex relationships between stability and function of FXN at the whole FeS cluster assembly machinery are currently under further investigation in our laboratory.

4. Conclusions

One of the end results of FXN decrease in cells of FRDA patients is a severe iron overload in their mitochondria, especially in nerve and cardiac tissues, associated to cellular iron dysregulation, impairment of FeS clusters assembly and increased sensitivity to oxidative stress, likely due to the mitochondrial redox-active environment. This has been suggested to play a key role in the pathogenesis of the disease and indeed pharmacological strategies based on free-radical scavengers, such as idebenone or CoQ₁₀, as well as on iron chelators, such as deferiprone, showed some cardiac and neurological improvements in FRDA mouse models and in-patient clinical trials [11,70–72]. On the other hand, to date the primary cause of the disease is still difficult to identify, and the precise physiological role of FXN remains unclear, both in iron metabolism and in the FeS clusters biogenesis. Although iron-binding to FXN has been proposed to be essential for its function(s), this important issue is still controversial in many respects, and has been readdressed in the present work in which we combined different advanced spectroscopic analyses to investigate the iron-binding properties of a recombinant human FXN. Moreover, in order to disclose potential structure-function relationships, we applied the same multidisciplinary approach to a panel of FXN variants found in FRDA heterozygous patients, with point mutations in highly conserved residues mapping either in the iron-binding acidic ridge or in the surface involved in the iron-dependent interaction of FXN with the FeS clusters assembly

machinery. EPR is an advanced spectroscopic technique of choice to investigate metalloproteins, and in this work it has been exploited for the first time to provide direct experimental evidence *in vitro* that FXN binds Fe³⁺. This was then further supported by 2D NMR experiments, which also confirmed that FXN is able to bind iron ions in both oxidation states, although with slightly different binding modes. An intriguing result was obtained by the same NMR analysis when iron-bound FXN was incubated with ISCU, the scaffold protein of the mitochondrial FeS clusters assembly machinery, providing a novel molecular insight on this complex biosynthetic pathway: indeed, our data may suggest that structural changes of the N-terminal portion of ISCU could be instrumental for the transitions between different conformational states, which have been previously claimed to be relevant, as scaffold protein, for the interactions with the functional partners of the FeS cluster assembly machinery [65,66].

Although the pathophysiological consequences of the point mutations of the selected variants are relevant, no significant differences were detected when compared to the wild type FXN, in terms of both iron-binding properties and interaction with the ISCU scaffold protein, suggesting that these are not key factors for the disease onset, at least in heterozygous patients. On the other hand, we confirmed that two out of the four FXN mutants (*i.e.* N146K and W155R) have an impaired capability to enhance the desulfurase activity *in vitro*, one of the functional roles that have been hypothesized for this protein. This indicates that FXN missense point mutations could have multiple biochemical effects, and further supports the multifunctional nature of the protein. Examining FXN mutations in the context of protein structure/function relationships is expected to increase our knowledge of FXN biology and FRDA pathology, and additional clinical mutants are thus currently under investigation in our laboratory.

Understanding the intricate pathophysiology of FXN defects is pivotal to characterize the FRDA disease molecular mechanisms and to better define the clinical outcome of both homozygous and compound heterozygous patients, which is in turn crucial to develop novel, more specific therapeutic strategies.

Supplementary data to this article can be found online at <https://doi.org/10.1016/j.bbapap.2019.07.007>.

Declaration of Competing Interest

None

Acknowledgements

This work was supported by grants COST_FINA_P14_02 to Paola Costantini from Department of Biology, University of Padova; Fondazione Cassa di Risparmio di Padova e Rovigo (CARIPARO) starting grants to Donatella Carbonera and Marco Bortolus; PICT 2016 2280 from ANPCyT (Argentina) and Friedreich's Ataxia Research Alliance (FARA) to Javier Santos. Massimo Bellanda acknowledges the financial support by grant P-DiSC #01BIRD2018-UNIPD from University of Padova. We especially thank Dr. H el ene Puccio and Dr. Benoit D'Autr eaux for kindly providing us with the *FXN* and *NFS1/ISD11* genes, respectively.

References

- [1] S. Adinolfi, M. Trifuoggi, A.S. Politou, S. Martin, A. Pastore, A structural approach to understanding the iron-binding properties of phylogenetically different frataxins, *Hum. Mol. Genet.* 11 (2002) 1865–1877.
- [2] T.J. Gibson, E.V. Koonin, G. Musco, A. Pastore, P. Bork, Friedreich's ataxia protein: phylogenetic evidence for mitochondrial dysfunction, *Trends Neurosci.* 19 (1996) 465–468.
- [3] V. Campuzano, L. Montermini, M.D. Molto, L. Pianese, M. Coss e, F. Cavalcanti, E. Monros, F. Rodius, F. Duclos, A. Monticelli, F. Zara, J. Canizares, H. Koutnikova, S.I. Bidichandani, C. Gellera, A. Brice, P. Trouillas, G. De Michele, A. Filla, R. De Frutos, F. Palau, P.I. Patel, S. Di Donato, J.L. Mandel, S. Cocozza, M. Koenig, M. Pandolfo, Friedreich's ataxia: autosomal recessive disease caused by an intronic GAA triplet repeat expansion, *Science* 271 (1996) 1423–1427.
- [4] V. Campuzano, L. Montermini, Y. Lutz, L. Cova, C. Hindelang, S. Jiralerspong, Y. Trottier, S.J. Kish, B. Faucheu, P. Trouillas, F.J. Authier, A. D urr, J.L. Mandel, A. Vescovi, M. Pandolfo, M. Koenig, Frataxin is reduced in Friedreich ataxia patients and is associated with mitochondrial membrane, *Hum. Mol. Genet.* 6 (1997) 1771–1780.
- [5] M. Pandolfo, Friedreich ataxia: the clinical picture, *J. Neurol.* 256 (2009) 3–8.
- [6] M. Coss e, A. D urr, M. Schmitt, N. Dahl, P. Trouillas, P. Allinson, M. Kostrzewa, A. Nivelon-Chevallier, K.H. Gustavson, A. Kohlsch utter, U. M uller, J.L. Mandel, A. Brice, M. Koenig, F. Cavalcanti, A. Tammaro, G. De Michele, A. Filla, S. Cocozza, M. Labuda, L. Montermini, J. Poirier, M. Pandolfo, Friedreich's ataxia: point mutations and clinical presentation of compound heterozygotes, *Ann. Neurol.* 45 (1999) 200–206.
- [7] M. De Castro, J. Garc ia-Planells, E. Monr os, J. Ca nizares, R. V azquez-Manrique, J.J. V ilchez, M. Urtasun, M. Lucas, G. Navarro, G. Izquierdo, M.D. Molt o, F. Palau, Genotype and phenotype analysis of Friedreich's ataxia compound heterozygous patients, *Hum. Genet.* 106 (2000) 86–92.
- [8] C. Gellera, B. Castellotti, C. Mariotti, R. Miner, V. Seveso, S. Di Donato, F. Taroni, Frataxin gene point mutations in Italian Friedreich ataxia patients, *Neurogenetics* 8 (2007) 289–299.
- [9] A.R. Correia, S. Adinolfi, A. Pastore, C.M. Gomes, Conformational stability of human frataxin and effect of Friedreich's ataxia related mutations on protein folding, *Biochem. J.* 398 (2006) 605–611.
- [10] A.R. Correia, C. Pastore, S. Adinolfi, A. Pastore, C.M. Gomes, Dynamics, stability and iron-binding activity of frataxin clinical mutants, *FEBS J.* 275 (2008) 3680–3690.
- [11] S. Schmucker, H. Puccio, Understanding the molecular mechanisms of Friedreich's ataxia to develop therapeutic approaches, *Hum. Mol. Genet.* 19 (2010) R103–R110.
- [12] M. Pandolfo, A. Pastore, The pathogenesis of Friedreich ataxia and the structure and function of frataxin, *J. Neurol.* 256 (Suppl. 1) (2009) 9–17.
- [13] T. Yoon, J.A. Cowan, Frataxin-mediated iron delivery to ferrocetolase in the final step of heme biosynthesis, *J. Biol. Chem.* 279 (2004) 25943–25946.
- [14] M.A. Huynen, B. Snel, P. Bork, T.J. Gibson, The phylogenetic distribution of frataxin indicates a role in iron-sulfur cluster protein assembly, *Hum. Mol. Genet.* 10 (2001) 2463–2468.
- [15] P. Cavadini, H.A. O'Neill, O. Benada, G. Isaya, Assembly and iron-binding properties of human frataxin, the protein deficient in Friedreich ataxia, *Hum. Mol. Genet.* 11 (2002) 217–227.
- [16] T. Yoon, J.A. Cowan, Iron-sulfur cluster biosynthesis. Characterization of frataxin as an iron donor for assembly of [2Fe-2S] clusters in ISU-type proteins, *J. Am. Chem. Soc.* 125 (2003) 6078–6084.
- [17] A. R otig, P. de Lonlay, D. Chretien, F. Foury, M. Koenig, D. Sidi, A. Munnich, P. Rustin, Aconitase and mitochondrial iron-sulphur protein deficiency in Friedreich ataxia, *Nat. Genet.* 17 (1997) 215–217.
- [18] H. Puccio, D. Simon, M. Coss e, P. Cricqui-Filipe, F. Tiziano, J. Melki, C. Hindelang, R. Matyas, P. Rustin, M. Koenig, Mouse models for Friedreich ataxia exhibit cardiomyopathy, sensory nerve defect and Fe-S enzyme deficiency followed by intramitochondrial iron deposits, *Nat. Genet.* 27 (2001) 181–186.
- [19] J.B. Schulz, T. Dehmer, L. Schols, H. Mende, C. Hardt, M. Vorgerd, K. Burk, W. Matson, J. Dichgans, M.F. Beal, M.B. Bogdanov, Oxidative stress in patients with Friedreich's ataxia, *Neurology* 55 (2000) 1719–1721.
- [20] R.V. Vaubel, G. Isaya, Iron-sulfur cluster synthesis, iron homeostasis and oxidative stress in Friedreich ataxia, *Mol. Cell. Neurosci.* 55 (2013) 50–61.
- [21] A. Martelli, M. Wattenhofer-Donze, S. Schmucker, S. Bouvet, L. Reutenauer, H. Puccio, Frataxin is essential for extramitochondrial Fe-S cluster proteins in mammalian tissues, *Hum. Mol. Genet.* 16 (2007) 2651–2658.
- [22] M.L. Huang, E.M. Becker, M. Whitnall, Y.S. Rahmanto, P. Ponka, D.R. Richardson, Elucidation of the mechanism of mitochondrial iron loading in Friedreich's ataxia by analysis of a mouse mutant, *Proc. Natl. Acad. Sci. U. S. A.* 106 (2009) 16381–16386.
- [23] M. Whitnall, Y.S. Rahmanto, R. Sutak, X. Xu, E.M. Becker, M.R. Mikhael, P. Ponka, D.R. Richardson, The MCK mouse heart model of Friedreich's ataxia: alterations in iron-regulated proteins and cardiac hypertrophy are limited by iron chelation, *Proc. Natl. Acad. Sci. U. S. A.* 105 (2008) 9757–9762.
- [24] H. Koutnikova, V. Campuzano, M. Koenig, Maturation of wild-type and mutated frataxin by the mitochondrial processing peptidase, *Hum. Mol. Genet.* 7 (1998) 1485–1489.
- [25] I. Cond o, N. Ventura, F. Malisan, A. Rufini, B. Tomassini, R. Testi, *In vivo* maturation of human frataxin, *Hum. Mol. Genet.* 16 (2007) 1534–1540.
- [26] S. Schmucker, M. Argentini, N. Carelle-Camels, A. Martelli, H. Puccio, The *in vivo* mitochondrial two-steps maturation of human frataxin, *Hum. Mol. Genet.* 17 (2008) 3521–3531.
- [27] G. Musco, G. Stier, B. Kolmerer, S. Adinolfi, S.R. Martin, T.A. Frenkiel, T.J. Gibson, A. Pastore, Towards a structural understanding of Friedreich's ataxia: the solution structure of frataxin, *Structure* 8 (2000) 695–707.
- [28] S. Dhe-Paganon, R. Shigetani, Y.I. Chi, M. Ristow, S.E. Shoelson, Crystal structure of human frataxin, *J. Biol. Chem.* 275 (2000) 30753–30756.
- [29] M. Nair, S. Adinolfi, C. Pastore, G. Kelly, P. Temussi, A. Pastore, Solution structure of the bacterial frataxin ortholog, CyaY: mapping the iron binding sites, *Structure* 12 (2004) 2037–2048.
- [30] Y. He, S.L. Alam, S.V. Proteasa, Y. Zhang, E. Lesuisse, A. Dancis, T.L. Stemmler, Yeast frataxin solution structure, iron binding, and ferrocetolase interaction, *Biochemistry* 43 (2004) 16254–16262.
- [31] J.D. Cook, K.Z. Bencze, A.D. Jankovic, A.K. Crater, C.N. Busch, P.B. Bradley, A.J. Stemmler, M.R. Spaller, T.L. Stemmler, Monomeric yeast frataxin is an iron-binding protein, *Biochemistry* 45 (2006) 7767–7777.

- [32] L.E. Gentry, M.A. Thacker, R. Doughty, R. Timkovich, L.S. Busenlehner, His86 from the N-terminus of frataxin coordinates iron and is required for Fe-S cluster synthesis, *Biochemistry* 52 (2013) 6085–6096.
- [33] J. Huang, E. Dizin, J. Cowan, Mapping iron binding sites on human frataxin: implications for cluster assembly on the ISCU Fe-S cluster scaffold protein, *J. Biol. Inorg. Chem.* 13 (2008) 825–836.
- [34] K. Cai, R.O. Frederick, M. Tonelli, J.L. Markley, Interactions of iron-bound frataxin with ISCU and ferredoxin on the cysteine desulfurase complex leading to Fe-S cluster assembly, *J. Inorg. Biochem.* 183 (2018) 107–116.
- [35] E.A. Roman, S.E. Faraj, M. Gallo, A.G. Salvay, D.U. Ferreira, J. Santos, Protein stability and dynamics modulation: the case of human frataxin, *PLoS One* 7 (2012) e45743.
- [36] Z. Marelja, W. Stocklein, M. Nimtz, S. Leimkühler, A novel role for human Nfs1 in the cytoplasm: Nfs1 acts as a sulfur donor for MOCS3, a protein involved in molybdenum cofactor biosynthesis, *J. Biol. Chem.* 283 (2008) 25178–25185.
- [37] G. Bohm, R. Muhr, R. Jaenicke, CDNN: quantitative analysis of protein far UV circular dichroism spectra by neural networks, *Protein Eng.* 5 (1992) 191–195.
- [38] P. Schanda, B. Brutscher, Very fast two-dimensional NMR spectroscopy for real-time investigation of dynamic events in proteins on the time scale of seconds, *J. Am. Chem. Soc.* 127 (2005) 8014–8015.
- [39] W. Lee, M. Tonelli, J.L. Markley, NMRFAM-SPARKY: enhanced software for biomolecular NMR spectroscopy, *Bioinformatics* 31 (2015) 1325–1327.
- [40] R. Keller, *The Computer Aided Resonance Assignment Tutorial*, 1st, (2004) ISBN 3-85600-112-113.
- [41] W.L. DeLano, Pymol: an open-source molecular graphics tool, *CCP4 Newsletter on Protein Crystallography* 40 (2002) 82–92.
- [42] T. Yoon, E. Dizin, J.A. Cowan, N-terminal iron-mediated self-cleavage of human frataxin: regulation of iron binding and complex formation with target proteins, *J. Biol. Inorg. Chem.* 12 (2007) 535–542.
- [43] D.J. Lane, D.R. Richardson, Frataxin, a molecule of mystery: trading stability for function in its iron-binding site, *Biochem. J.* 426 (2010) e1–e3.
- [44] G. Musco, T. DeTommasi, G. Stier, B. Kolmerer, M. Bottomley, S. Adinolfi, F. Muskett, T. Gibson, T. Frenkiel, A. Pastore, Assignment of the ¹H, ¹⁵N, and ¹³C resonances of the C-terminal domain of frataxin, the protein responsible for Friedreich ataxia, *J. Biomol. NMR* 15 (1999) 87–88.
- [45] F. Bou-Abdallah, S. Adinolfi, A. Pastore, T.M. Laue, N. Dennis Chasteen, Iron binding and oxidation kinetics in frataxin CyaY of *Escherichia coli*, *J. Mol. Biol.* 341 (2004) 605–615.
- [46] A. Ilari, M.C. Latella, P. Ceci, F. Ribacchi, M. Su, L. Giangiacomo, S. Stefanini, N.D. Chasteen, E. Chiancone, The unusual intersubunit ferroxidase center of *Listeria innocua* Dps is required for hydrogen peroxide detoxification but not for iron uptake. A study with site-specific mutants, *Biochemistry* 44 (2005) 5579–5587.
- [47] F. Bou-Abdallah, N.D. Chasteen, Spin concentration measurements of high-spin ($g' = 4.3$) rhombic iron(III) ions in biological samples: theory and application, *J. Biol. Inorg. Chem.* 13 (2008) 15–24.
- [48] C.L. Tsai, J. Bridwell-Rabb, D.P. Barondeau, Friedreich's ataxia variants I154F and W155R diminish frataxin-based activation for the iron-sulfur cluster assembly complex, *Biochemistry* 50 (2011) 6478–6487.
- [49] J. Gerber, U. Mühlenhoff, R. Lill, An interaction between frataxin and Isu1/Nfs1 that is crucial for Fe/S cluster synthesis on Isu1, *EMBO Rep.* 4 (2003) 906–911.
- [50] H. Li, O. Gakh, D.Y. Smith IV, G. Isaya, Oligomeric yeast frataxin drives assembly of core machinery for mitochondrial iron-sulfur cluster synthesis, *J. Biol. Chem.* 284 (2009) 21971–21980.
- [51] C.L. Tsai, D.P. Barondeau, Human frataxin is an allosteric switch that activates the Fe-S cluster biosynthetic complex, *Biochemistry* 49 (2010) 9132–9139.
- [52] J. Bridwell-Rabb, C. Iannuzzi, A. Pastore, D.P. Barondeau, Effector role reversal during evolution: the case of frataxin in Fe-S cluster biosynthesis, *Biochemistry* 51 (2012) 2506–2514.
- [53] A. Parent, X. Elduque, D. Cornu, L. Belot, J.-P. Le Caer, A. Grandas, M.B. Toledano, B. D'Autréaux, Mammalian frataxin directly enhances sulfur transfer of NFS1 persulfide to both ISCU and free thiols, *Nat. Commun.* 6 (2015) 5686.
- [54] R. Lill, Function and biogenesis of iron-sulphur proteins, *Nature* 460 (2009) 831–838.
- [55] R. Lill, U. Mühlenhoff, Maturation of iron-sulfur proteins in eukaryotes: mechanisms, connected processes, and diseases, *Annu. Rev. Biochem.* 77 (2008) 669–700.
- [56] J.G. Van Vranken, M.Y. Jeong, P. Wei, Y.C. Chen, S.P. Gygi, D.R. Winge, J. Rutter, The mitochondrial acyl carrier protein (ACP) coordinates mitochondrial fatty acid synthesis with iron sulfur cluster biogenesis, *Elife* 5 (2016) e17828.
- [57] S.A. Cory, J.G. Van Vranken, E.J. Brignole, S. Patra, D.R. Winge, C.L. Drennan, J. Rutter, D.P. Barondeau, Structure of human Fe-S assembly subcomplex reveals unexpected cysteine desulfurase architecture and acyl-ACP-ISD11 interactions, *Proc. Natl. Acad. Sci. U. S. A.* 114 (2017) E5325–E5334.
- [58] M.T. Boniecki, S.A. Freibert, U. Mühlenhoff, R. Lill, M. Cygler, Structure and functional dynamics of the mitochondrial Fe/S cluster synthesis complex, *Nat. Commun.* 8 (2017) 1287.
- [59] K. Cai, R.O. Frederick, H. Dashti, J.L. Markley, Architectural features of human mitochondrial cysteine desulfurase complexes from crosslinking mass spectrometry and small-angle X-ray scattering, *Structure* 26 (2018) 1127–1136.
- [60] N.G. Fox, X. Yu, X. Feng, H.J. Bailey, A. Mertelli, J.F. Nabhan, C. Strain-Damerell, C. Bulawa, W.W. Yue, S. Han, Structure of the human frataxin-bound iron-sulfur cluster assembly complex provides insight into its activation mechanism, *Nat. Commun.* 10 (2019) 2210.
- [61] A. Martelli, M. Wattenhofer-Donzè, S. Schmucker, S. Bouvet, L. Reutenauer, H. Puccio, Frataxin is essential for extramitochondrial Fe-S cluster proteins in mammalian tissues, *Hum. Mol. Genet.* 16 (2007) 2651–2658.
- [62] S. Schmucker, A. Martelli, F. Colin, A. Page, M. Wattenhofer-Donzè, L. Reutenauer, H. Puccio, Mammalian frataxin: an essential function for cellular viability through an interaction with a preformed ISCU/NFS1/ISD11 iron-sulfur assembly complex, *PLoS One* 6 (2011) e16199.
- [63] Y. Shan, E. Napoli, G. Cortopassi, Mitochondrial frataxin with ISD11 of the NFS1/ISCU complex and multiple mitochondrial chaperones, *Hum. Mol. Genet.* 16 (2007) 929–941.
- [64] S. Leidgens, S. De Smet, F. Foury, Frataxin interacts with Isu1 through a conserved tryptophan in its beta-sheet, *Hum. Mol. Genet.* 19 (2010) 276–286.
- [65] J.H. Kim, J.L. Tonelli, J.L. Markley, Disordered form of the scaffold protein IscU in the substrate for iron-sulfur cluster on cysteine desulfurase, *Proc. Natl. Acad. Sci. U. S. A.* 109 (2012) 454–459.
- [66] R. Yan, G. Kelly, A. Pastore, The scaffold protein IscU retains a structured conformation in the FeS cluster assembly complex, *ChemBioChem* 15 (2014) 1682–1686.
- [67] F. Colin, A. Martelli, M. Clémancey, J.M. Latour, S. Gambarelli, L. Zeppieri, C. Birck, A. Page, H. Puccio, S. Ollagnier de Choudens, Mammalian frataxin controls sulfur production and iron entry during *de novo* Fe4S4 cluster assembly, *J. Am. Chem. Soc.* 135 (2013) 733–740.
- [68] J. Bridwell-Rabb, N.G. Fox, C.L. Tsai, A.M. Winn, D.P. Barondeau, Human frataxin activates Fe-S cluster biosynthesis by facilitating sulfur transfer chemistry, *Biochemistry* 53 (2014) 4904–4913.
- [69] J. Bridwell-Rabb, A.M. Winn, D.P. Barondeau, Structure-function analysis of Friedreich's ataxia mutants reveals determinants of frataxin binding and activation of the Fe-S assembly complex, *Biochemistry* 50 (2011) 7265–7274.
- [70] H. Seznec, D. Simon, L. Monassier, P. Criqui-Filipe, A. Gansmuller, P. Rustin, M. Koenig, H. Puccio, Idebenone delays the onset of cardiac functional alteration without correction of Fe-S enzymes deficit in a mouse model for Friedreich ataxia, *Hum. Mol. Genet.* 13 (2004) 1017–1024.
- [71] P.E. Hart, R. Lodi, B. Rajagopalan, J.L. Bradley, J.G. Crilley, C. Turner, A.M. Blamire, D. Manners, P. Styles, A.H. Schapira, J.M. Cooper, Antioxidant treatment of patients with Friedreich ataxia: four-year follow-up, *Arch. Neurol.* 62 (2005) 621–626.
- [72] N. Bodaert, K.H. Le Quan Sang, A. Rötig, A. Leroy-Willig, S. Gallet, F. Brunelle, D. Sidi, J.C. Thalabard, A. Munnich, Z.I. Cabantchik, Selective iron chelation in Friedreich ataxia: biologic and clinical implications, *Blood* 110 (2007) 401–408.

Supplementary material

1. Methods

Heterologous expression and purification of human FXN, ISCU and NSF1/ISD11 proteins.

Bacteria cultures were grown at 37°C and 180 rpm in Luria-Bertani Broth, pH 7.5 (except for ¹⁵N/¹³C labeled proteins, see below in the paragraph describing NMR). For the expression of ISCU protein, induction was performed at OD₆₀₀=0.5 by addition of 1.0 mM isopropyl-β-thiogalactopyranoside (IPTG) and carried out over-night at 25°C and 180 rpm. For the expression of FXN (wild type and mutant proteins), induction was performed at OD₆₀₀=0.7 by addition of 1.0 mM IPTG. All bacterial cultures, except for the one expressing FXN mutant G130V, were harvested after 3.5 h of induction at 37°C and 180 rpm. For FXN mutant G130V, instead, it was necessary to perform induction at 18°C and 180 rpm over-night, to prevent high levels of protein aggregation. The expression of NFS1/ISD11 complex was induced at OD₆₀₀=0.7 by addition of 1.0 mM IPTG, carried out over-night at 16°C and 180 rpm. At the end of inductions, bacteria were centrifuged at 6,000 rpm at 4°C and the pellet stored at -20°C until cell disruption with French press (within a month).

Recombinant ISCU-6his, either N-6his or C-6his-tagged, was purified starting from 1 to 1.5 L cultures by combining affinity Ni-NTA chromatography and size exclusion chromatography (SEC). Briefly, frozen harvested cells were thawed on ice, resuspended in lysis buffer (20 mM Tris-HCl pH 8.0, 50 mM NaCl and 20 mM imidazole) supplemented with protease inhibitors (1 μg/ml pepstatin A, 1 μg/ml leupeptin, 1 μg/ml antipain, 1 mM PMSF), and lysed by French press. The supernatant fractions were isolated from cell debris by centrifugation and the proteins purified to homogeneity by double chromatography, starting from affinity chromatography (HIS-Select® Nickel Affinity Gel, from Sigma-Aldrich). Fractions eluted in the first chromatographic step, obtained with subsequent elutions with lysis buffer added with growing imidazole concentrations (from 50 to 500 mM), were evaluated by SDS-PAGE. ISCU containing fractions were pooled together and incubated 1h on ice with 10 mM EDTA to eliminate any residual metal. Then, a gel filtration chromatography was performed using a Superose 12 10/300 GL (from GE Healthcare), equilibrated in final buffer (25 mM Tris-HCl pH 7.0, 50 mM KCl, and 1 mM DTT). The eluted fractions containing ISCU (both dimeric and monomeric) were finally pooled together and concentrated by centrifugal filters (Amicon Ultra Centrifugal Filter, 3000 NMWL, from Merck Millipore), obtaining a final concentration up to 200 μM, as determined spectroscopically using $\epsilon_{280\text{nm}} = 10220 \text{ M}^{-1}\text{cm}^{-1}$. To obtain the untagged ISCU, a sample of C-6his-tagged protein purified by affinity chromatography was digested with the TEV protease (from Sigma-Aldrich) before gel filtration.

Briefly, the C-6his-tagged ISCU was incubated with TEV (50:1 w/w) overnight at 4°C, and then subjected to a further step of affinity chromatography. The flow through, containing the protein without 6his-tag, was kept and finally subjected to gel filtration as described above.

Purification of wild type and mutant FXN proteins was carried out starting from 0,5 to 1L cultures and exploiting two subsequent chromatographic steps: anion exchange chromatography and SEC. In particular, after cell disruption with French press in lysis buffer (20 mM Tris-HCl, 1 mM EDTA, pH 7.0) supplemented with protease inhibitors (1 µg/ml pepstatin A, 1 µg/ml leupeptin, 1 µg/ml antipain, 1 mM PMSF), soluble and insoluble fractions were separated by centrifugation. The soluble fraction, after 1h incubation with 10 mM EDTA, was carefully loaded onto a column packed with a weak anion exchanger resin (DEAE Sepharose Fast Flow, GE Healthcare), and eluted with a 300 mL linear gradient, from 0.0 to 1.0 M NaCl, in buffer 20 mM Tris-HCl, 1 mM EDTA, pH 7.0. Subsequently, fractions with FXN (identified by SDS-PAGE) were loaded onto a preparative HiLoad 16/600 Superdex 200 pg column (GE Healthcare), previously equilibrated with final buffer (25 mM Tris-HCl pH 7.0, 50 mM KCl, and 1 mM DTT). SEC fractions corresponding to FXN (wild type and mutant, both present exclusively as monomeric proteins) were finally pooled together and concentrated by centrifugal filters (Amicon Ultra Centrifugal Filter, 3000 NMWL, from Merck Millipore), obtaining a final concentration up to 1 mM, as determined spectroscopically using $\epsilon_{280\text{nm}} = 26930 \text{ M}^{-1}\text{cm}^{-1}$ for wild type FXN and mutants G130V and N146K, $\epsilon_{280\text{nm}} = 28420 \text{ M}^{-1}\text{cm}^{-1}$ for mutant D122Y and $\epsilon_{280\text{nm}} = 21430 \text{ M}^{-1}\text{cm}^{-1}$ for mutant W155R. To estimate the molecular weight of the analyzed samples during SEC, the columns were equilibrated in the same final buffer and calibrated with the standards thyroglobulin (669 kDa), ferritin (440 kDa), β -amylase (200 kDa), bovine serum albumin (67 kDa), carbonic anhydrase (29 kDa) and cytochrome c (12 kDa). All proteins, after the final purification step, were analyzed by SDS-PAGE.

The identity of ISCU and FXN proteins was confirmed by Western Blotting analysis, using a primary rabbit antibody anti-human ISCU (LSBio, LifeSpan Biosciences, Inc.) and a primary rabbit antibody anti-human FXN (Proteintech), respectively, and a secondary goat anti-rabbit IgG conjugated with horseradish peroxidase (Sigma-Aldrich). The ECL SuperSignal™ West Pico Chemiluminescent Substrate (Thermo Scientific) was used for final detection on HYPERFILM™ (GE Healthcare Life Sciences).

The NFS1/ISD11 complex was purified starting from 1 L cultures, and performing a single step of affinity chromatography, exploiting NFS1 N-terminus His-tag. Briefly, frozen harvested cells were thawed on ice and resuspended in lysis buffer (50 mM Tris-HCl, 300 mM NaCl, pH 8.0), and lysed by multiple cycles of sonication. The soluble fraction of lysate, separated from the insoluble

fraction through centrifugation, was loaded into a column for nickel affinity chromatography (HIS-Select® Nickel Affinity Gel, from Sigma-Aldrich). After several washes of the column with lysis buffer and lysis buffer supplemented with growing imidazole concentrations (20-50 mM), NFS1/ISD11 complex was eluted with elution buffer (50 mM Tris-HCl, 300 mM NaCl, 500 mM imidazole, pH 8.0). Fractions containing NFS1/ISD11 proteins were identified by SDS-PAGE and pooled together. Finally, the proteins pool was supplemented with pyridoxal phosphate 10 mM (PLP) and 1 mM DTT, and subsequently dialyzed over-night against dialysis buffer (50 mM Tris-HCl, 200 mM NaCl, 1 mM DTT, pH 8.0), with a 10 kDa cut-off membrane. Finally, protein concentrations were spectroscopically estimated using an $\epsilon_{280\text{nm}} = 42670 \text{ M}^{-1}\text{cm}^{-1}$.

2. Tables

Table 1. List of primers used for the mutagenesis of the human *FXN*₉₀₋₂₁₀ sequence

Primer name	Primer sequence
FXN_D122Y_for	5' - gccatacacgtttgagtactatgatgtctccttgg - 3'
FXN_D122Y_rev	5' - ccaaaggagacatcatagtactcaaacgtgtatggc - 3'
FXN_G130V_for	5' - gtctccttgggagtggtgtcttaactgtcaaactg - 3'
FXN_G130V_rev	5' - cagtttgacagttaagacaacactcccaaaggagac - 3'
FXN_N146K_for	5' - aggaacctatgtgatcaagaagcagacgccaaca - 3'
FXN_N146K_rev	5' - tgtttggcgtctgcttcttgatcacataggctcct - 3'
FXN_W155R_for	5' - gccaaacaagcaaatcaggctatcttccatcca - 3'
FXN_W155R_rev	5' - tggatggagaagatagcctgatttgcttgtttggc - 3'

Table 2. Percentages of secondary structure elements obtained from the fitting of the CD spectra of purified recombinant human ISCU expressed in *E. coli*

Secondary structure component	Percentage
α -helix	27.6%
Parallel β	14.1%
Antiparallel β	9.6%
β -turn	18.2%
Random coil	32.2%
Total	101.8%

Table 3. NFS1 sulfide production at the FeS clusters assembly complex. The activity was monitored in the absence of FXN or in the presence of wild type or mutant FXN. Activity is reported as micromoles of sulfide produced by NFS1 per micromole of NFS1 per minute. Data represent the mean of three replicates \pm S.D.

FeS clusters assembly complex	NFS1 activity (mol H ₂ S/mol NFS1/min)
no FXN	1.125 \pm 0.10
wt FXN	3.9 \pm 0.15
N146K	1.11 \pm 0.03
W155R	0.95 \pm 0.06
D122Y	3.12 \pm 0.06
G130V	1.875 \pm 0.14

3. Supplementary figure legends

Figure S1. Heterologous expression and purification of wild type human FXN. SDS-PAGE, 12% polyacrylamide gel, Coomassie blue staining. Lane 1, total extract of not induced sample (10 μ l); lane 2, total extract of IPTG-induced sample (10 μ l); lane 3, protein insoluble fraction (10 μ l); lane 4, protein soluble fraction (10 μ l); lane 5, FXN pool sample after anionic exchange chromatography (10 μ l); lane 6, FXN₉₀₋₂₁₀ pool sample after size exclusion chromatography (10 μ l).

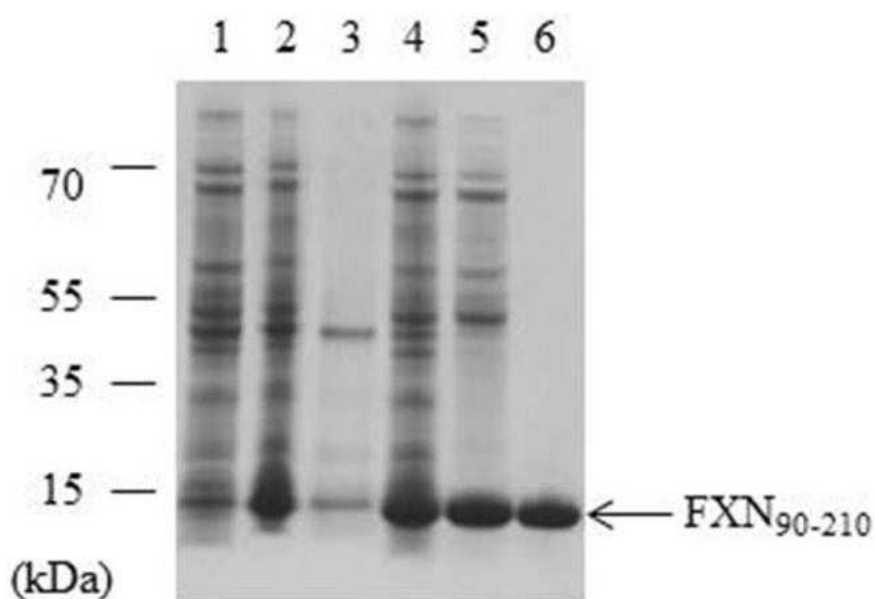


Figure S4. Superposition of $^1\text{H},^{15}\text{N}$ -SOFAST-HMQC spectra of human wild type FXN in absence (blue) and in presence iron. FXN concentration: 45 μM , 4 equivalents of Fe^{2+} (red in panel A) or of Fe^{3+} (green in panel B).

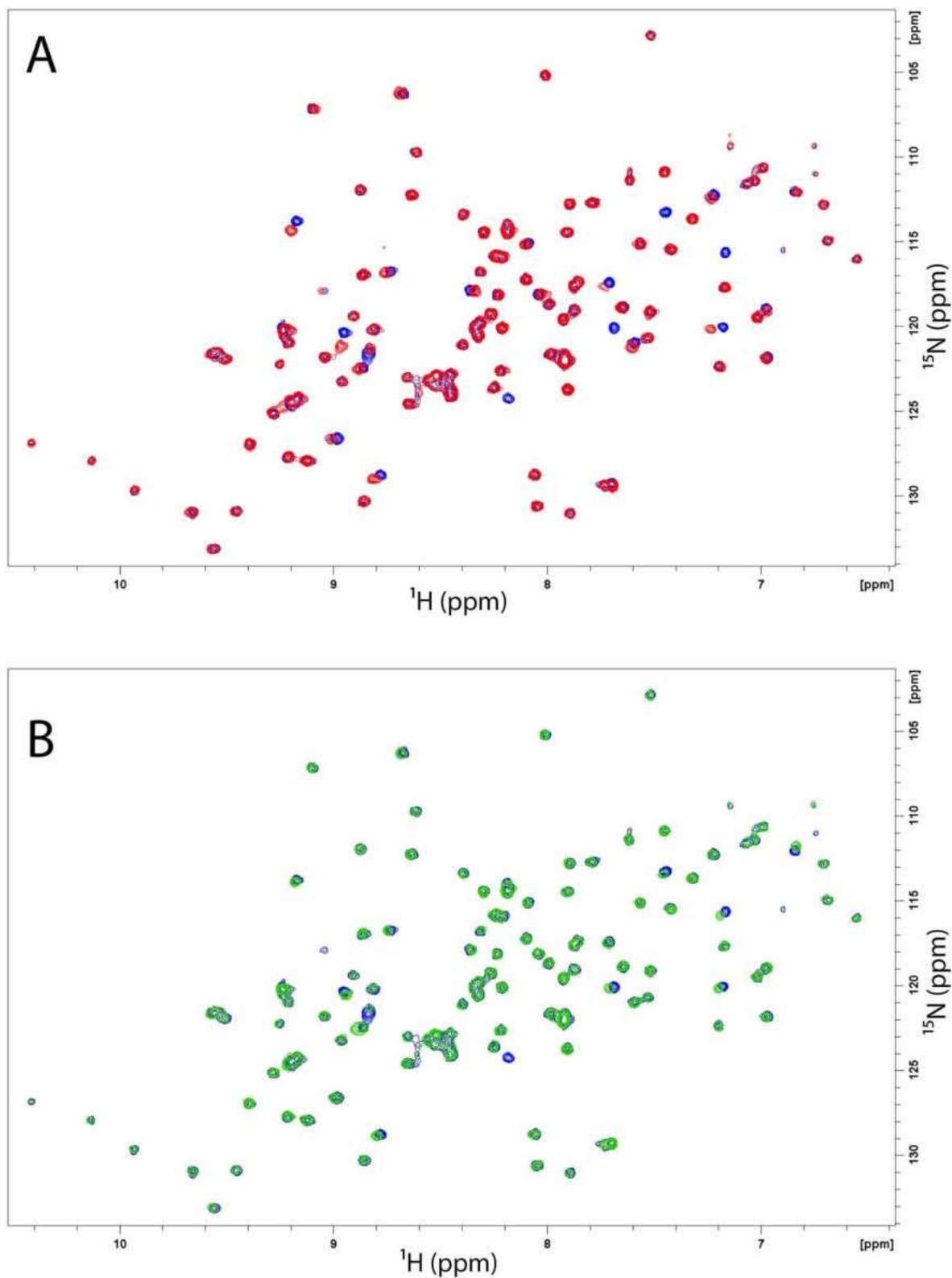


Figure S5. $^1\text{H},^{15}\text{N}$ -SOFAST-HMQC spectra of the four clinical mutants of human FXN studied in this work. The spectrum of each mutant (in red) is superimposed with the spectrum of the wild type protein (in blue). In all spectra the protein concentration was 45 μM FXN, in 25 mM Tris-HCl pH 7.0, 50 mM KCl.

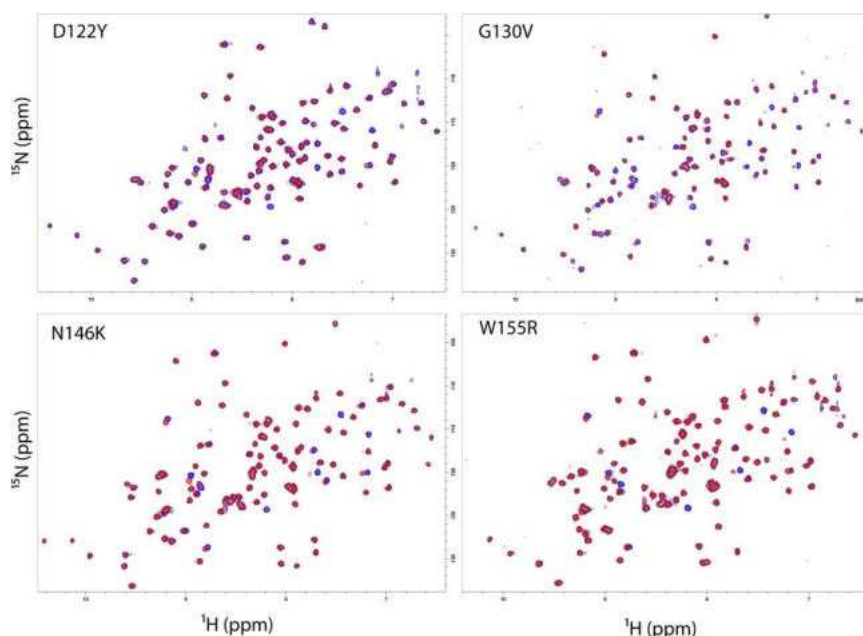


Figure S6. Structural effects of mutations on the structure of frataxin determined by chemical shift perturbation. Normalized chemical shift changes, between the wild type FXN and the mutants, larger than a one standard deviation of all the shifts are colored in red on the apo-FXN structure (PDBID: 1EKG). The mutated residues are represented in spheres. In black are represented prolines or residues corresponding to severe overlapped or unassigned peaks in wild type FXN while residues whose assignment could not be traced in the mutants are coloured in cyan.

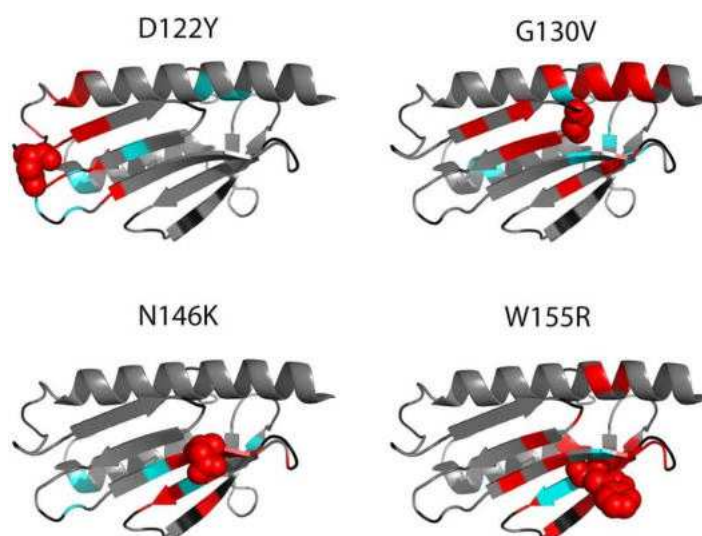


Figure S7. $^1\text{H},^{15}\text{N}$ -SOFAST-HMQC spectra of the four clinical mutants of human FXN studied in this work in absence or presence of four equivalents of Fe^{2+} . In all spectra the protein concentration was 45 μM FXN, in 25 mM Tris-HCl pH 7.0, 50 mM KCl.

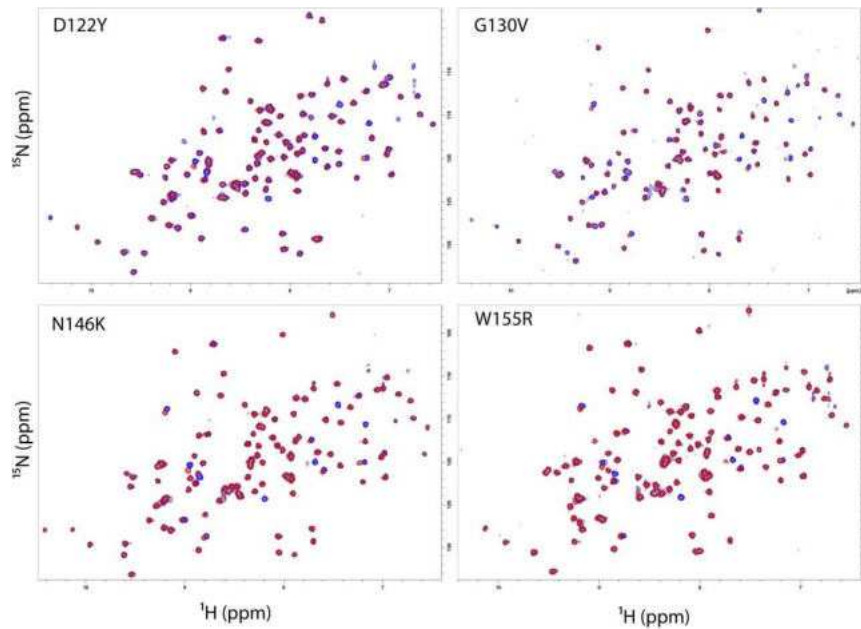


Figure S8. Heterologous expression and purification of human N-6his-tagged ISCU. Panel A, SDS-PAGE, 12% polyacrylamide gel, Coomassie blue staining. Lane 1, total extract of IPTG-induced sample (10 μl); lane 2, protein insoluble fraction (10 μl); lane 3, protein soluble fraction (10 μl); lane 5, ISCU pool sample after affinity chromatography (10 μl); lane 5, ISCU pool sample after size exclusion chromatography (10 μl). Panel B, Far-UV circular dichroism spectra of the relative purified protein. The spectrum shows a secondary structure content compatible with properly folded α/β species, as quantified by CDNN spectra deconvolution, whose data are reported in table 2 (Supplementary material).

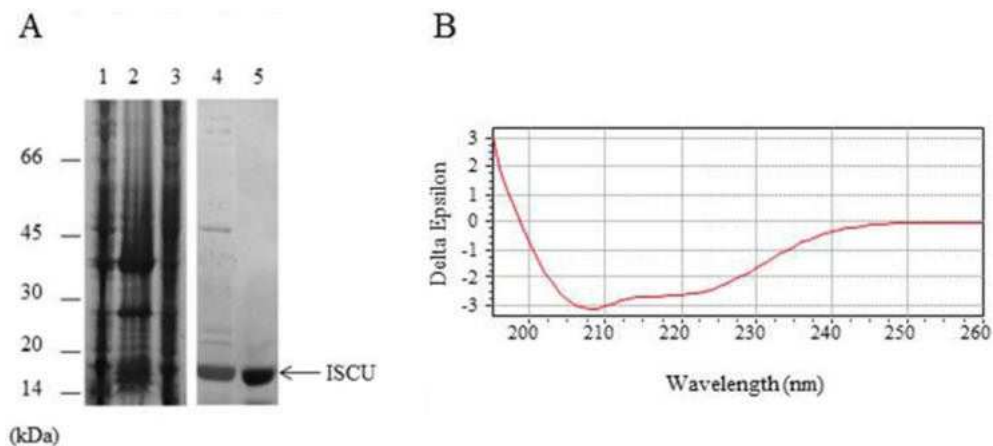


Figure S9. Effect of N-6his-tagged ISCU on the NMR spectra of FXN in absence of Fe²⁺. The superposition of the ¹H,¹⁵N-SOFAST-HMQC spectra of FXN (45μM), in absence (blue) and in presence (red) of N-6his-tagged ISCU (80μM) are shown in panel A. The spectra were acquired in 25 mM Tris-HCl pH 7.0, 50 mM KCl, without iron. The ratios of the peak intensities in the spectra without (I₀) and with (I) N-his-tag-ISCU are represented as a function of the residue number in panel B.

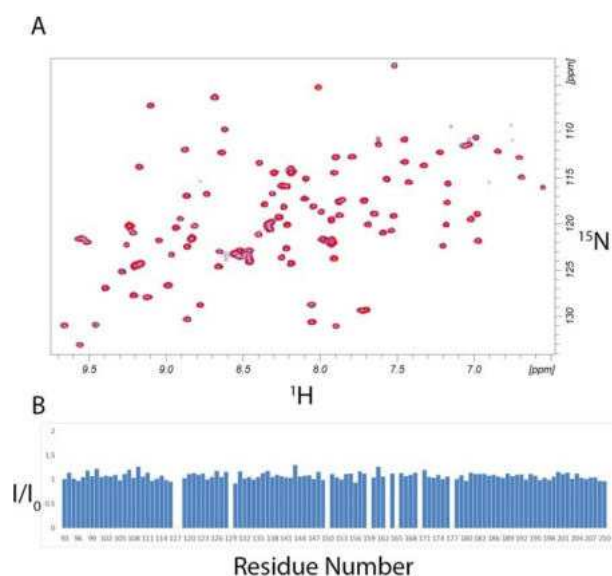


Figure S10. Effect of C-6his-tagged ISCU and untagged ISCU on the NMR spectra of FXN in presence of four equivalents of Fe²⁺. The superposition of the ¹H,¹⁵N-SOFAST-HMQC spectra of FXN, in absence (blue) and in presence (red) of untagged ISCU (panel A) or C-6his-tagged ISCU (panel). The spectra were all acquired in 25 mM Tris-HCl pH 7.0, 50 mM KCl, in presence of 180 μM Fe²⁺. The ratios of the peak intensities in the spectra without (I₀) and with (I) ISCU are represented as a function of the residue number at the bottom of each panel.

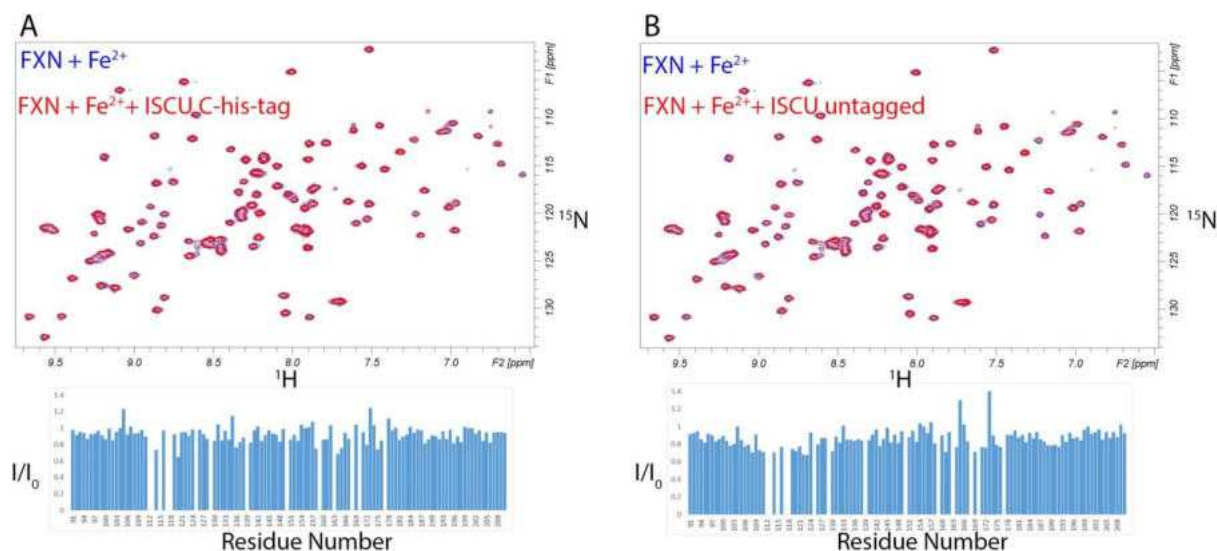
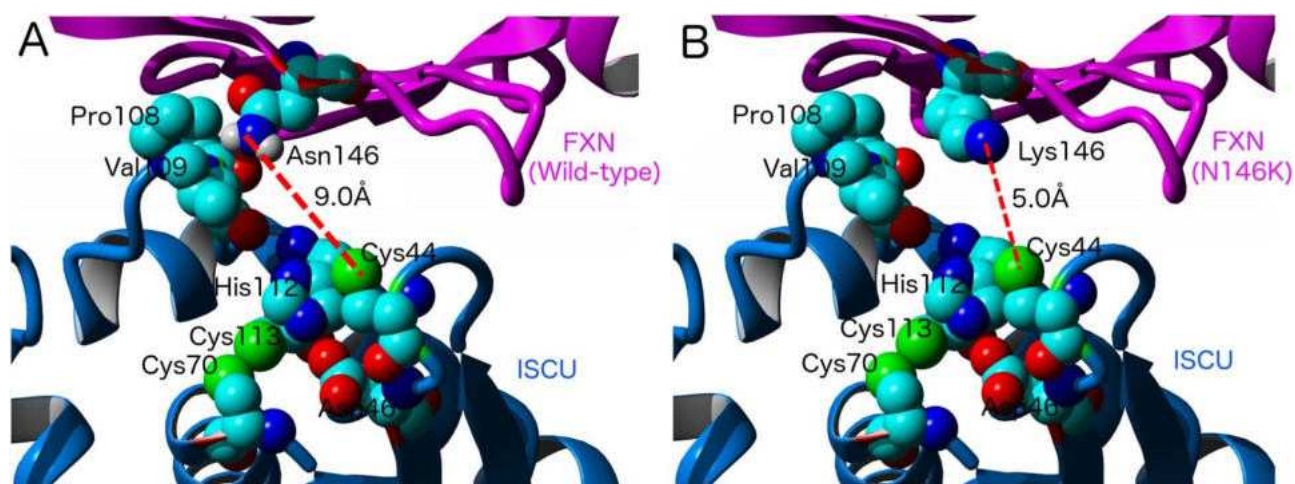


Figure S11. Mutation of FXN at residue Asn146 by Lys may alter the interaction with ISCU and the activity of the latter. Ribbon representation of FXN (magenta) and ISCU (blue) structures extracted from the model of the protein complex NFS1/ACP-ISD11/ISCU/FXN obtained by Cai and coworkers [69] showing (A) Asn146 from FXN and residues Pro108 and Val109 from ISCU. Additionally, residues from the active site of ISCU (Asp44, Cys44, 70 and 113 and His112) are also shown. In (B), Asn146 was replaced by Lys in order to infer possible effects of the mutation, assuming a similar interaction between both proteins. The distance between nitrogen from Asn or Lys side-chain and sulfur atom from Cys44 is shown by means of a dashed red line. Residues are numbered as in the PDB file available in [69].





Contents lists available at ScienceDirect

Archives of Biochemistry and Biophysics

journal homepage: www.elsevier.com/locate/yabbi

Relationship between activity and stability: Design and characterization of stable variants of human frataxin

Ignacio Hugo Castro^a, Mauro Bringas^b, Davide Doni^c, Martín Ezequiel Noguera^{a,d},
Luciana Capece^b, Martín Aran^e, Matías Blaustein^{a,f}, Paola Costantini^c, Javier Santos^{a,f,g,*}

^a Instituto de Biotecnología y Biología Traslacional (iB³). Departamento de Fisiología y Biología Molecular y Celular, Facultad de Ciencias Exactas y Naturales, Universidad de Buenos Aires. Intendente Güiraldes 2160, Ciudad Universitaria, C1428EGA, Buenos Aires, Argentina

^b Departamento de Química Inorgánica, Analítica y Química Física, Facultad de Ciencias Exactas y Naturales, Universidad de Buenos Aires. Instituto de Química Física de los Materiales, Medio Ambiente y Energía (INQUIMAE CONICET), C1428EGA, Buenos Aires, Argentina

^c Department of Biology, University of Padova, Viale G. Colombo 3, 35131, Padova, Italy

^d Instituto de Química y Físicoquímica Biológicas, Dr. Alejandro Paladini, Universidad de Buenos Aires, CONICET, Junín 956, C1113AAD, Buenos Aires, Argentina

^e Fundación Instituto Leloir, IIBBA-CONICET, Av. Patricias Argentinas 435, C1405BWE, Buenos Aires, Argentina

^f Consejo Nacional de Investigaciones Científicas y Técnicas, Rivadavia 1917, C1033AAJ, Buenos Aires, Argentina

^g Departamento de Química Biológica, Facultad de Ciencias Exactas y Naturales, Universidad de Buenos Aires. Intendente Güiraldes 2160, Ciudad Universitaria, C1428EGA, Buenos Aires, Argentina

ARTICLE INFO

Keywords:

Conformational stability
Protein-protein interaction
Iron-sulfur cluster assembly
Frataxin

ABSTRACT

The relationships between conformational dynamics, stability and protein function are not obvious. Frataxin (FXN) is an essential protein that forms part of a supercomplex dedicated to the iron-sulfur (Fe-S) cluster assembly within the mitochondrial matrix. In humans, the loss of FXN expression or a decrease in its functionality results in Friedreich's Ataxia, a cardio-neurodegenerative disease. Recently, the way in which FXN interacts with the rest of the subunits of the supercomplex was uncovered. This opens a window to explore relationships between structural dynamics and function. In this study, we prepared a set of FXN variants spanning a broad range of conformational stabilities. Variants S160I, S160M and A204R were more stable than the wild-type and showed similar biological activity. Additionally, we prepared SILCAR, a variant that combines S160I, L203C and A204R mutations. SILCAR was 2.4 kcal mol⁻¹ more stable and equally active. Some of the variants were significantly more resistant to proteolysis than the wild-type FXN. SILCAR showed the highest resistance, suggesting a more rigid structure. It was corroborated by means of molecular dynamics simulations. Relaxation dispersion NMR experiments comparing SILCAR and wild-type variants suggested similar internal motions in the microsecond to millisecond timescale. Instead, variant S157I showed higher denaturation resistance but a significant lower function, similarly to that observed for the FRDA variant N146K. We concluded that the contribution of particular side chains to the conformational stability of FXN might be highly subordinated to their impact on both the protein function and the stability of the functional supercomplex.

1. Introduction

The relationships between conformational stability, internal motions and protein function are not trivial and are the essence of the protein nature. The alteration of the conformational stability of proteins is a key factor for the development of pathogenicity in several human

diseases.

Numerous proteins exert their function by establishing specific protein-protein interactions. Although in some cases they interact transiently, in other cases they form stable protein complexes. The latter is the case of frataxin (FXN), an essential mitochondrial protein of 120 residues, which is nuclearly encoded. FXN is one of several proteins

Abbreviations: ACP, acyl carrier protein; CD, circular dichroism; CTR, C-terminal region; DLS, dynamic light scattering; Fe-S, iron-sulfur; FRDA, Friedreich's Ataxia; FXN, frataxin; HPLC, high-performance liquid chromatography; ISCU, iron-sulfur cluster assembly enzyme; ISD11, NFS1 interacting protein; NFS1, mitochondrial cysteine desulfurase enzyme; NMR, nuclear magnetic resonance; PAGE, polyacrylamide gel electrophoresis; PDB, Protein Data Bank; SDS, sodium dodecyl sulfate; SEC, size exclusion chromatography; WT, wild-type FXN

* Corresponding author. Instituto de Biotecnología y Biología Traslacional (iB³). Departamento de Fisiología y Biología Molecular y Celular, Facultad de Ciencias Exactas y Naturales, Universidad de Buenos Aires. Intendente Güiraldes 2160, Ciudad Universitaria, C1428EGA, Buenos Aires, Argentina.

E-mail address: javiersantosw@gmail.com (J. Santos).

<https://doi.org/10.1016/j.abbi.2020.108491>

Received 5 May 2020; Received in revised form 26 June 2020; Accepted 8 July 2020

Available online 21 July 2020

0003-9861/ © 2020 Elsevier Inc. All rights reserved.

that forms a supercomplex dedicated to the iron-sulfur (Fe-S) cluster assembly within the mitochondrial matrix. A myriad of enzymatic processes depends on its activity. In this supercomplex, FXN works as an activator that simultaneously interacts at least with two different proteins: ISCU, the scaffold protein, and the cysteine desulfurase NFS1, a PLP dependent enzyme that transfers -SH groups from the substrate (cysteine) to ISCU [1]. It is worthy of note that FXN interacts at the same time with both NFS1 subunits of the supercomplex (PDB ID: 6NZU).

Remarkably, in humans, the loss of FXN expression or a decrease in its functionality, and the subsequent deficiency in the iron-sulfur cluster (Fe-S) assembly in the mitochondria, result in Friedreich's Ataxia (FRDA), a cardio-neurodegenerative disease [2–10].

Although 95% of FRDA patients exhibit in each allele GAA triplet-repeat expansion in the first intron of the FXN gene, which determines a low expression of FXN, the remaining 5% of patients have a missense mutation in one of the alleles (in compound heterozygosis with the GAA triplet-repeat expansion in the other allele), modifying the conformational stability and/or the protein function; currently, there is only one report of patients showing homozygous missense mutation, R165C, [11].

Among many other compound variants, G130V [12], G137V [13], L198R [14], and the truncated form FXN81-193 (Δ CTR) [15,16] showed a significant decrease of the conformational stability of the protein. In principle, this feature is expected to yield a concomitant low protein concentration in the cell because of protein degradation. In the case of mutant G137V, no impairment of the structure or activity of the protein was found *in vitro* [13]; however, low FXN concentration was observed in the patient.

On the other hand, a significant reduction of conformational stability may additionally result in a decrease in protein function as a consequence of the loss of cooperativity with an increase of local unfolding events, the alteration of the internal motions as in the case of L198R or FXN81-193 (Δ CTR) [14].

Some FXN mutations perturb the supercomplex assembly, yielding a decrease in function, without necessarily causing a reduction of the conformational stability of FXN. This is the case of mutation N146K that significantly stabilizes the native conformation of FXN [17]; however, the activity of this variant decreases because N146 is very close to the ISCU-FXN interaction region, adjacent to W155, another key residue that is fundamental for this interaction [18,19]. Thus, the interaction surfaces of ISCU and FXN have coevolved and the contribution to the stability of the residues involved in coevolution might be highly subordinated to their impact on both protein function and the stability of the functional supercomplex.

Additionally, in principle, FXN interacts with iron by means of its "acidic ridge", a region of the protein that is very rich in Glu and Asp residues [12,20–22]. This metal ion binding process is thought to be relevant for the activation of the supercomplex, and the influence of these acidic residues on conformational stability was previously studied by the group of Gomes [23]. The mutation of the acidic residues to alanine resulted in a substantial stabilization of the native conformation. It is worthy of mention that several acidic residues are also involved in the interaction between FXN and NFS1 [1,19].

The behavior of the alanine variants of the acidic ridge added to that of the N146K mutant suggest a substantial tradeoff between conformational stability and function. On the other hand, the L203C variant [24,25], in which a core leucine residue is replaced by a cysteine, is more stable than the wild-type FXN and exhibited similar cysteine desulfurase activation. Then, a more complex relationship between stability and function needs to be invoked to explain these observations.

In this context, we decided to look for other FXN variants more stable than the wild-type protein and, at least, equally active *in vitro* and *in vivo*. Taking this into account, we explored the FXN structure by means of bioinformatic tools in order to locate residues that might be replaced by another one, increasing thermodynamic stability. We found

a series of feasible mutants. They were prepared and studied *in vitro*. Conformational features and stability and the capability of activating the supercomplex were analyzed side by side.

2. Materials and Methods

2.1. Bioinformatics

Stability and mutational effect calculations were performed using FOLDX [26]. For these calculations, PDB ID: 1EKG [27] was analyzed. Briefly, first all positions were evaluated by means of FOLDX to find positions that might be mutated producing an increase in the conformational stability of the protein. The PositionScan was applied using repair tool. It mutates each amino acid to the other 19.

2.2. Mutagenesis, protein expression and purification

Mutagenesis was carried out using the Q5® Site-Directed Mutagenesis Kit (New England Biolabs, U.S.A.). Wild-type FXN (residues 90–210) and mutants were expressed and purified as previously described for the wild-type variant [14]. Purity was > 98% as evaluated in SDS-PAGE. Identity was verified by DNA sequencing using Macrogen facility and by mass spectrometry analysis. The latter was performed in the National Laboratory of Research and Services in Peptides and Proteins using an LCQ DUO ESI ion trap (Thermo Finnigan) or QExactive Orbitrap (Thermo Scientific) spectrometers.

For ^{15}N -labeled protein, production cultures were grown in M9 minimal medium supplemented with ^{15}N - NH_4Cl obtained from Cambridge Isotope Laboratories (Andover, MA) and purified as the unlabeled samples. Extinction coefficients were calculated from amino acid sequences using the ProtParam tool on the ExPASy Server [28].

The DNA sequence corresponding to ISCU2 was optimized for *E. coli* expression by Explora Biotech (Rome Italy) and cloned in a pE22b vector, with a C-terminal His6 tag. Protein was induced by the addition of 1 mM IPTG (3 h, 37 °C and 250 rpm). The protein was purified using a Ni^{2+} -NTA-agarose column equilibrated in a buffer 20 mM Tris-HCl, 300 mM NaCl, pH 7.5. The elution was performed with a buffer 20 mM Tris-HCl, 300 mM NaCl, 500 mM imidazole, pH 7.5.

The DNA sequences corresponding to the human NFS1, ISD11 and ACP proteins were optimized for *E. coli* expression by Bio Basic (Markham ON, Canada). The cysteine desulfurase variant NFS1 Δ 55 (mature form, with an N-terminal His6 tag) and the ISD11 sequences were cloned in a pETduet plasmid and ACP was cloned in a pACYCDuet-1 vector. To prepare the protein complex (NFS1/ACP-ISD11)₂, the three proteins NFS1, ISD11 and ACP proteins were induced by the addition of 1 mM IPTG and co-expressed (overnight, 20 °C and 250 rpm). Purification was carried out using a Ni^{2+} -NTA-agarose column equilibrated in a buffer 20 mM Tris-HCl, 300 mM NaCl, 20 mM imidazole, pH 8.0. The elution was performed with a buffer 20 mM Tris-HCl, 300 mM NaCl, 500 mM imidazole, pH 8.0.

2.3. Circular dichroism spectroscopy

Circular dichroism (CD) measurements were carried out in a Jasco J-815 spectropolarimeter. Near-UV CD spectra were collected using a 1.0 path length cell, thermostated at 20 °C. Protein concentration was 25 μM and the buffer was 20 mM Tris-HCl, 100 mM NaCl, pH 7.0. Data were acquired at a scan speed of 20 nm min^{-1} , with a 1-nm bandwidth and a 0.1-nm data-pitch. Five scans for each sample were averaged, and the blank spectrum was subtracted to the average.

2.4. Light scattering and the hydrodynamic behavior of the FXN mutants

The hydrodynamic radius (R_h) of the FXN mutants was investigated using Dynamic Light Scattering (DLS, Zetaziser Nano-S, Malvern). Protein concentration was in the range of 70–140 μM (1–2 mg mL^{-1}).

The buffer was 20 mM Tris-HCl, 100 mM NaCl, pH 7.0. The experiments were carried out at 25 °C. On average, 10 runs were performed. Size distributions weighted by particle number were obtained.

Additionally, SEC-HPLC was performed using a Superose-6 column (GE Healthcare). Protein concentration was 25–75 μM, a volume of 50 μL was typically injected, and running buffer was 20 mM Tris-HCl, 100 mM NaCl, 1 mM EDTA, at pH 7.0. The experiment was carried out at room temperature (~25 °C) at a 0.5 mL min⁻¹ flow rate. A JASCO HPLC instrument was used. It was equipped with an automatic injector, a quaternary pump and a UV-VIS UV-2075 (elution was monitored at 280 nm).

2.5. Thermal shift assay

Temperature-induced denaturation of FXN variants was monitored by the change in the Sypro Orange dye fluorescence using protein at a 5.0 μM concentration in 50 mM sodium phosphate buffer, pH 7.0. Samples without protein were also included as controls. The dye was used at 2 × (as suggested by Thermo Fisher Scientific). The temperature slope was 1 °C min⁻¹ (from 20 to 90 °C). Excitation and emission ranges were 470–500 and 540–700 nm, respectively. The fluorescence signal was quenched in the aqueous environment but became unquenched when the probe bound to the apolar residues upon unfolding. Experiments by triplicate were carried out in a Step One Real-Time-PCR instrument (Applied Biosystems, CA, U.S.A.).

2.6. Equilibrium unfolding experiments

Isothermal unfolding experiments were performed incubating each FXN variant (3.7 μM) with different concentrations of denaturant (urea) in a buffer solution of 20 mM Tris-HCl, 100 mM NaCl, 1 mM EDTA, at pH 7.0 for 5 h at room temperature. A fresh urea solution (approximately 9.2 M) was prepared for each experiment, and the exact urea concentration was determined using refractive index measurements, using a Palm Abbe digital refractometer (Misco). Tryptophan fluorescence spectra measurements were taken at 20 °C. Excitation was carried out at 295 nm and spectra were acquired between 305 and 500 nm.

To calculate thermodynamic parameters, a linear dependence of the standard free energy of unfolding ($\Delta G_{\text{NU}}^{\circ}$) on denaturant concentration was assumed:

$$\Delta G_{\text{NU}}^{\circ} = \Delta G_{\text{NU,H}_2\text{O}}^{\circ} - m_{\text{NU}}[\text{urea}] \quad (1)$$

where $\Delta G_{\text{NU,H}_2\text{O}}^{\circ}$ is the free energy of unfolding in the absence of denaturant and m_{NU} is the dependence of free energy on denaturant. Defining C_m as the denaturant concentration in which $\Delta G_{\text{NU}}^{\circ} = 0$, it is deduced that:

$$\Delta G_{\text{NU}}^{\circ} = m_{\text{NU}}(C_m - [\text{urea}]) \quad (2)$$

A two-state unfolding mechanism was assumed, and the following equation was fitted to data:

$$S = \frac{(S_{0,\text{N}} + m_{\text{N}}[\text{urea}]) + (S_{0,\text{U}} + m_{\text{U}}[\text{urea}])e^{\left(\frac{m_{\text{NU}}[\text{urea}] - C_m}{RT}\right)}}{1 + e^{\left(\frac{m_{\text{NU}}[\text{urea}] - C_m}{RT}\right)}} \quad (3)$$

where $S_{0,\text{N}}$ and $S_{0,\text{U}}$ are the intrinsic tryptophan fluorescence signals for the native and unfolded states, respectively. Parameters m_{N} and m_{U} are the slopes of the pre- and post-transitions, respectively, assuming the linear dependences of $S_{0,\text{N}}$ and $S_{0,\text{U}}$ signals with urea concentration.

The correlation obtained in this work between the observed T_m values (unfolding monitored by Sypro-orange fluorescence) and free energy differences (urea unfolding experiments monitored by Trp fluorescence) was $y = (0.25 \pm 0.01)x - (16.27 \pm 0.54)$, with an $R^2 = 0.99$.

2.7. Controlled proteolysis

Resistance to proteolysis of the FXN variants was analyzed by SDS-PAGE and RP-HPLC profiles (C18). The variants at 1 mg mL⁻¹ protein concentration were incubated during 5 h reactions at 40 °C in buffer 20 mM Tris-HCl, 100 mM NaCl, 1 mM EDTA, pH 7.0 in the presence or in the absence of chymotrypsin (1:100 protease: protein ratio). The reactions were stopped by the addition of 2 × sample buffer for SDS-PAGE analysis and 1 mM PMSF (final concentration), or 1 mM PMSF (final concentration) and 0.05% (v/v) TFA for RP-HPLC. Protein controls without protease were simultaneously incubated, for the same period of time, and under exactly the same conditions of buffer and temperature. PMSF was added after the incubation. For HPLC, a JASCO system, equipped with an autoinjector, an oven (thermostated at 25 °C) and a UV detector, was used. A gradient from 0 to 100% acetonitrile was performed (0.05% TFA (v/v) was added to the solvents). The column used was an analytical C18 (Higgins Analytical, Inc. U.S.A.) and flow was 1.0 mL min⁻¹. Peptides were monitored at 220 nm. Wild-type FXN was included as a reference.

2.8. NFS1 cysteine desulfurase activity

Enzymatic desulfurization of cysteine to alanine and sulfide by the NFS1/ACP-ISD11/ISCU/FXN supercomplex was determined by the methylene blue method. Concentrations of proteins, substrate and the reducing agent DTT were set according to a previous paper by Tsai and Barondeau [29]. Reactions contained 1.0 μM NFS1, 1.0 μM ACP-ISD11, 3.0 μM ISCU and 3.0 μM FXN, and samples were supplemented with 10 μM PLP, 2 mM DTT, and 1.0 μM FeSO₄ (final concentrations). The reaction buffer was 50 mM Tris-HCl and 200 mM NaCl, pH 8.0, and reactions were started by the addition of 1 mM cysteine. Samples were incubated at room temperature for 30 min H₂S production was stopped by the addition of 50 μL of 20 mM N,N-dimethyl p-phenylenediamine in 7.2 M HCl and 50 μL of 30 mM FeCl₃ (prepared in 1.2 M HCl). Under these conditions, the production of methylene blue took 20 min. After that, samples were centrifuged for 5 min at 12000g, and the supernatant was separated. Absorbance at 670 nm was measured.

2.9. NMR samples, data acquisition and processing

Samples for NMR experiments contained 0.45 mM ¹⁵N-labeled protein in 20 mM Tris-HCl, 100 mM NaCl, 1.0 mM EDTA, at pH 7.0, supplemented with 5% D₂O. NMR experiments were performed at 22 °C in a Bruker 600 MHz Avance III spectrometer equipped with a TXI probe. The NMR data were processed with NMRPipe [30] and analyzed using NMRViewJ [31].

2.10. Backbone amide resonance assignment

The chemical shift assignments of nitrogen, and amide and alpha protons of loop-1 variants were performed by 3D¹⁵N-NOESY-HSQC and ¹⁵N-TOCSY-HSQC experiments (100 and 30 ms of mixing times, respectively), based on the available chemical shifts of the full-length C-terminal domain of FXN (BMRB 4342) [32]. The ¹H-¹⁵N-NOESY-HSQC spectrum of the wild-type FXN was recorded to assist in the assignment.

2.11. Relaxation dispersion experiments

Carr-Purcell Meiboom-Gill relaxation dispersion experiments were performed using published methods [33,34]. In these experiments, variable trains of refocusing pulses were applied during a constant relaxation period to suppress spectral broadening due to conformational exchange [33]. A constant-time relaxation-compensated pulse program was used for all variants, setting the constant time period (T_{CPMG}) to 100 ms in combination with the following CPMG frequencies (ν_{CPMG}): 40, 80, 120, 160, 200, 240, 280, 320, 360, 400, 480, 520, 600, 680,

760, 840, 920, 1000, 1080 and 1200 Hz. Two-dimensional data sets were acquired in an interleaved manner, with an interscan delay of 3 s and 256 increments in the nitrogen dimension. The observed transverse relaxation rate (R_2^{Obs}) for each frequency point was obtained from the signal intensity measured at the end of the T_{CPMG} period according to:

$$R_2^{Obs}(\nu_{CPMG}) = \frac{-1}{T_{CPMG}} \ln \left(\frac{I(\nu_{CPMG})}{I_0} \right) \quad (4)$$

where $I(\nu_{CPMG})$ and I_0 are the intensities of a given cross-peak measured with or without the CPMG period, respectively, for a specific spin-lock frequency (ν_{CPMG}).

The contribution of the exchange to the signal relaxation rate (R_{ex}) is estimated by:

$$R_2^{Obs}(\nu_{CPMG} \rightarrow 0) = R_{ex} + R_2^{Obs}(\nu_{CPMG} \rightarrow \infty) \quad (5)$$

where $R_2^{Obs}(\nu_{CPMG} \rightarrow \infty)$ is the intrinsic relaxation rate in the absence of exchange, at infinite ν_{CPMG} , estimated from the average of the R_2^{Obs} at the 3 highest ν_{CPMG} , whereas $R_2^{Obs}(\nu_{CPMG} \rightarrow 0)$ was approximated as R_2^{Obs} at the lowest ν_{CPMG} . The experiment was carried out at two different magnetic field strengths (14.1 and 16.5 T) and dispersion profiles were then analyzed as in a previous work [35]. Dispersion profiles were then analyzed using the Sherkhan server [36] to fit a completely general two-site exchange model to the dispersion data acquired at both magnetic fields, using the following equations:

$$R_2^{Obs} \left(\frac{1}{\tau_{CP}} \right) = \frac{1}{2} \left(R_{2A}^o + R_{2B}^o + k_{ex} - \frac{1}{\tau_{CP}} \cosh^{-1} [D_{\pm} \cosh(\eta_{\pm}) - D_{\pm} \cos(\eta_{\pm})] \right) \quad (6)$$

in which, k_{ex} is the observed constant for the conformational exchange, τ_{CP} is the delay between 180° pulses in the CPMG pulse train, R_{2A}^o and R_{2B}^o are the intrinsic (exchange-free and independent of the ν_{CPMG}) transverse relaxation rate constants for states A and B, respectively (it is assumed that $R_{2A}^o = R_{2B}^o$) and,

$$D_{\pm} = \frac{1}{2} \left[\pm 1 + \frac{\psi + 2\Delta\omega^2}{(\psi^2 + \zeta^2)^{1/2}} \right] \quad (7)$$

$$\eta_{\pm} = \frac{\tau_{CP}}{\sqrt{2}} \left[\pm \psi + (\psi^2 + \zeta^2)^{1/2} \right]^{1/2} \quad (8)$$

$$\psi = (R_{2A}^o - R_{2B}^o - p_A k_{ex} + p_B k_{ex})^2 - \Delta\omega^2 + 4 p_A p_B k_{ex}^2 \quad (9)$$

$$\zeta = 2\Delta\omega (R_{2A}^o - R_{2B}^o - p_A k_{ex} + p_B k_{ex}) \quad (10)$$

where $\Delta\omega$ is the chemical shift difference between states A and B, p_A and p_B are the populations of the states A and B. Finally, a F-test was carried out to confirm that the identified residues behave as a cluster.

The R_2^{Obs} profile corresponding to each residue was individually fitted using the NESSY program [37]. The relaxation profile was better described by an exchanging model compared with the no-exchange model, according to the corrected Akaike Information Criterion. This preliminary analysis was performed separately for the two protein variants and the two static magnetic fields. Most of the significant exchanging residues in the SILCAR variant are the same than the ones previously identified for the wild-type variant in our previous studies [35]. On the other hand, we were unable to assign the L103 residue in SILCAR and some relaxation profiles were too noisy precluding a confident estimation of the exchanging parameter, so these later profiles were excluded from the global fit. As a result, eight residues were included in a global fit using a general two-state equation for chemical exchange.

2.12. Molecular Dynamics Simulations

The coordinates corresponding to human FXN (PDB ID: 1EKG) and the SILCAR model obtained by *in silico* mutation of the wild-type

structure using FOLDX were solvated with the TIP3P water model molecules [38]. Protonation states of amino acid residues were set to correspond to those at pH 7.0. As in previous works, in the case of His residues, δ or ϵ protonation was established to favor hydrogen bond formation [39]. A standard minimization protocol was applied to the resulting structures to specifically remove steric clashes. The systems were heated up from 100 to the desired temperatures (300 or 340 K) using the Berendsen thermostat and constant volume conditions. 800 ps isobaric molecular dynamics were run to achieve an appropriate density. A 2-fs time step was used, and the SHAKE algorithm was applied [40]. Unrestrained 400 ns production MD simulations were performed with Amber 18 [41], using the ff14SB force field [42]. Analysis of production runs were performed using CPPTRAJ software from AmberTools. The fraction of time in which H-bond interaction is formed was calculated by integrating the first peak (from 3 to approximately 4.5 Å) of the probability density function.

3. Results

3.1. Finding point mutants more stable than the wild-type FXN

To evaluate the contribution of each amino acid residue to conformational stability, the FXN structure (PDB ID: 1EKG) was examined by means of the FOLDX bioinformatic tool (Fig. 1). A list of approximately 220 potential variants was found, in which the predicted stability was at least 0.5 kcal mol⁻¹ higher than that of the wild-type FXN. Next, these mutants were analyzed by considering the structure of the supercomplex [NFS1/ACP-ISD11/ISCU/FXN]₂ (PDB ID: 6NZU). Our purpose was to avoid mutations of positions involved in protein-protein interactions. Potential mutations of residues involved in FRDA sites or in the immediate vicinity of these residues were also discarded. However, the exception was K147M, near N146, a position involved in FRDA (N146K variant). K147M was not discarded given the possibility of blocking the ubiquitination site K147 in order to alter degradation *in vivo* [43,44]. Additionally, we discarded mutations of those residues located in the iron binding region (helix α 1, loop-1 and strand β 1), given the eventual disruption of metal-FXN and cysteine desulfurase NFS1-FXN interactions.

This protocol constrained the set of variants to a reduced group of approximately twenty plausible positions. In this context, we decided to prepare and study a preliminary set of seven mutants: K147M, S157I, S160I, S160M, A193L, T196I and A204R. We included mutant A204M in order to investigate the effect of a long side chain at this position, compared to the electrostatic effect of the long and positively charged side chain as the one corresponding to the arginine residue (Table 1), and we also studied the L203C variant previously identified by our laboratory as a stabilizing mutation ($\Delta\Delta G_{NU}^o = 1.0$ kcal mol⁻¹). Remarkably, the prediction of the effect of the cysteine sidechain is not captured by FOLDX at all; instead, it is predicted as a highly destabilizing mutation (Fig. 1, expected $\Delta\Delta G_{NU}^o = -3.0$ kcal mol⁻¹).

The conformational stability of the variants was also inferred from the FXN protein structure using the Dynamut tool [46], which included dynamic information for the predictions (Table 1). Whereas FOLDX predicted K147M significantly more stable than the wild-type, Dynamut predicted this mutation may be only slightly stabilizing; the same occurred for mutation T196I. On the other hand, A204M, which was predicted as a stabilizing mutation by FOLDX, was predicted as destabilizing by Dynamut. In addition, Dynamut failed to predict the stabilizing effect of L203C.

The FRDA variants D122Y, G130V, W155R and L198R that were previously shown to be less stable than wild-type FXN ($\Delta\Delta G_{NU}^o = -2.1, -2.9, -1.4$ and -4.2 kcal mol⁻¹, respectively, [12,24]) were included as a reference in our analysis. Additionally, the FRDA mutant N146K, which exhibits a higher resistance to thermal denaturation than wild-type FXN (observed $\Delta T_m \sim 5$ °C), was also integrated to the set of proteins analyzed [17].

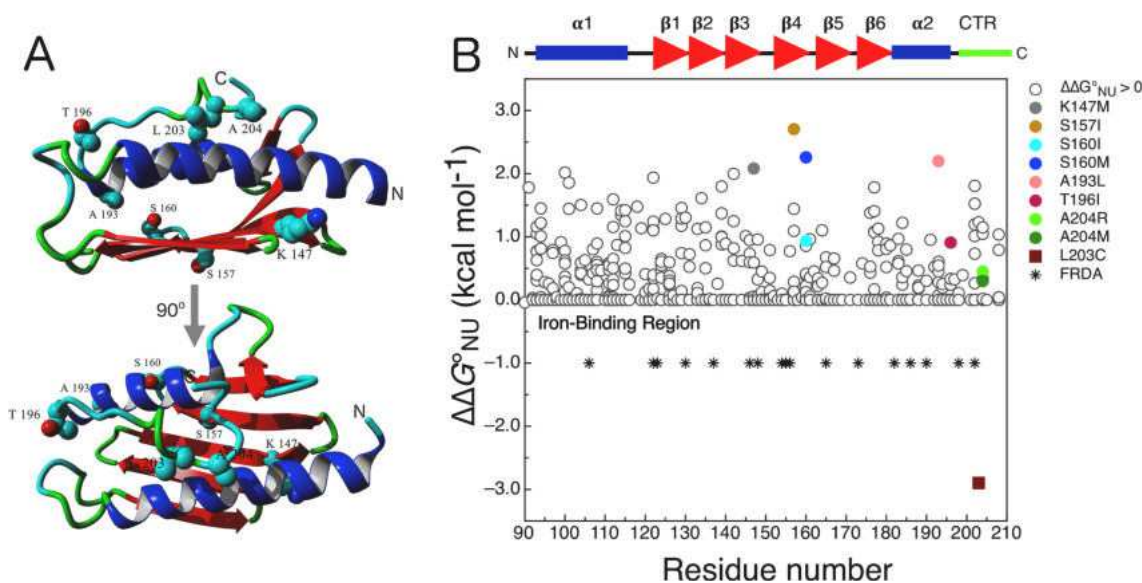


Fig. 1. Bioinformatic Inspection of FXN by FOLDX. (A) Ribbon representation of FXN structure showing the residues mutated in this work. Protein representations were prepared using YASARA [45]. (B) The structure (residues 90 to 108) was analyzed using FOLDX [26] and mutations that exhibited $\Delta\Delta G_{\text{NU}}^0 > 0$ were plotted (empty circles). Mutations prepared in this work are highlighted with color circles. The $\Delta\Delta G_{\text{NU}}^0$ prediction for L203C mutant is shown by a full-brown-square. $\Delta\Delta G_{\text{NU}}^0 = \Delta G_{\text{NU}}^0 \text{ mutant FXN} - \Delta G_{\text{NU}}^0 \text{ wild-type FXN}$ (positive values correspond to stabilizing mutations, e.g., L203C is predicted as destabilizing mutation). FRDA mutants currently known are indicated by asterisks at positions 106, 122, 123, 130, 137, 146, 148, 154, 155, 156, 165, 173, 182, 186, 190, 198 and 202. Note that the asterisks are not associated to $\Delta\Delta G_{\text{NU}}^0$ values; they are only included to indicate the residue involved. Secondary structure elements are depicted at the top of panel B; CTR is the C-terminal region. (For interpretation of the references to color in this figure legend, the reader is referred to the Web version of this article.)

The set of point mutant variants was prepared as described in Materials and Methods, purified (> 98%, SDS-PAGE and HPLC, data not shown) and studied. All variants were soluble. The analysis of dynamic light scattering experiments along with size exclusion chromatography (SEC-HPLC) showed that all of the variants are folded and behave as compact monomers in solution (Fig. 2A, and Table 1). The observed molecular mass values fall in the range 15000–13600 Da, as inferred by means of the calibration curve (Fig. 2A, inset).

We analyzed the tertiary structure of the variants by circular dichroism (CD) spectroscopy in the near-UV region. All the variants

showed near-UV CD spectra compatible with a fully conserved structure (Fig. 2); similar band shapes and intensities were observed. This result indicated comparable asymmetric environments for the aromatic residues, among the FXN variants.

3.2. Conformational stability of point mutants

Next, the resistance to temperature-induced unfolding followed by Sypro-orange fluorescence was explored (Fig. 3). Five of the seven mutants showed the observed T_m higher than the wild-type variant

Table 1
Parameters for FXN variants.

Variant	Properties and Predictions					
	Theoretical Molecular Mass ^a (Da)	Experimental Molecular Mass (Da)	R_H^b (nm)	FOLDX Stability ^{c,d} (kcal mol ⁻¹)	Dynamut Stability ^e (kcal mol ⁻¹)	Observed T_m^f (°C)
WT	13605.2	13604.9	2.0 ± 0.3	–	–	64.9 ± 0.6
K147M	13608.2	13607.7	1.9 ± 0.1	2.1	0.2	61.1 ± 0.4
S157I	13631.2	13630.4	2.5 ± 0.1	2.7	1.7	65.8 ± 0.2
S160I	13631.2	13630.0	2.4 ± 0.2	0.9	1.1	69.3 ± 0.2
S160M	13649.3	13647.3	2.3 ± 0.2	2.3	1.5	68.8 ± 0.2
A193L	13647.2	13646.0	2.1 ± 0.1	2.2	2.0	65.7 ± 0.3
T196I	13617.2	13617.2	2.4 ± 0.1	0.9	0.1	65.4 ± 0.2
L203C	13595.1	13600.0 ^h	2.0 ± 0.2	–2.9	–1.0	67.6 ± 0.2
A204M	13665.3	13664.0	2.0 ± 0.2	0.3	0.2	63.3 ± 0.1
A204R	13690.3	13689.2	1.8 ± 0.3	0.5	–0.3	66.8 ± 0.2
SILCAR ^g	13706.3	13705.5	2.5 ± 0.1	–	–	73.8 ± 0.1

^a Theoretical parameter inferred from the protein sequences calculated using EXPASY tool [28].

^b It was evaluated by DLS. Protein concentration was in the range 1–2 mg mL⁻¹. Size distributions were weighted by particle number.

^c $\Delta\Delta G_{\text{NU}}^0$ calculated using PDB ID: 1EKG [27].

^d Calculated using FOLDX repair tool [26]. Negative and positive values indicate destabilization and stabilization, respectively. Prior to stability calculation repair algorithm was applied. The analysis of the different FOLDX terms that contribute to the stability of each variant is shown in Fig. S1.

^e Negative and positive Dynamut [46] values indicate destabilization and stabilization, respectively (a correlation between FOLDX and Dynamut results is shown in Fig. S1).

^f Observed T_m was derived from temperature-induced unfolding experiments followed by Sypro-orange fluorescence.

^g The triple mutant variant S160I/L203C/A204R.

^h Mass measured by MALDI TOF. The rest of the variants were analyzed by ESI-MS as mentioned in Materials and Methods.

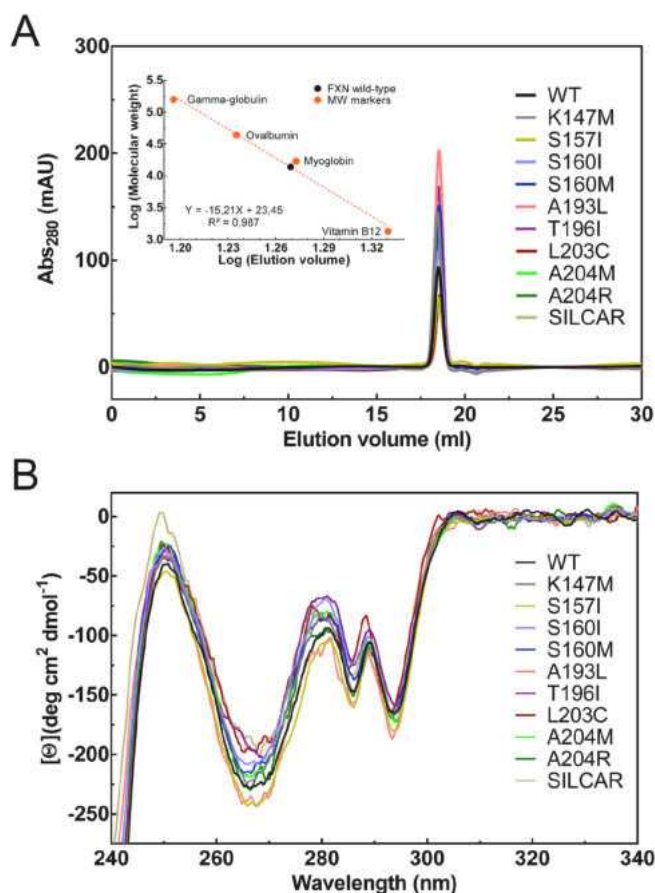


Fig. 2. Characterization of the FXN Variants. (A) Characterization of the hydrodynamic behavior of the FXN variants by SEC-HPLC. Protein concentration was 25–75 μM . Buffer was 20 mM Tris-HCl, 100 mM NaCl, pH 7.0. The inset shows the correlation between molecular weight and elution volume obtained from a chromatogram corresponding to the molecular weight markers gammaglobulin (158 kDa), ovalbumin (44 kDa), myoglobin (17 kDa), and vitamin B12 (1350 Da). (B) Characterization of the tertiary structure of the FXN variants by near-UV CD spectroscopy. Protein concentration was 25 μM and the buffer was 20 mM Tris-HCl, 100 mM NaCl, pH 7.0. Spectra were collected at 20 $^{\circ}\text{C}$.

(observed $\Delta T_m > 2$ $^{\circ}\text{C}$), whereas K147M and A204M mutants displayed considerably lower observed T_m values (observed $\Delta T_m < 2$ $^{\circ}\text{C}$), suggesting that conformational stability of the latter variants might be lower than that of the wild-type FXN. Therefore, (i) a long side chain at position 204 is not enough to yield FXN stabilization; (ii) K147M, which was predicted as a stabilizing mutation, on the contrary, is slightly destabilizing.

FRDA variants prepared as controls D122Y, G130V, W155R and L198R exhibited considerably lower observed T_m value than the wild-type protein, compatible with a destabilization of FXN conformation, whereas N146K showed a marked increase in the observed T_m , compatible with the stabilization of the native state of FXN.

Remarkably, three variants (S160I, S160M and A204R) exhibited substantially higher observed T_m values than the rest of the variants (Table 2), suggesting that these mutations might have stabilizing effects. In particular, S160I and S160M exhibited observed T_m values even higher than the stable variant L203C.

To evaluate more exhaustively the effect of the mutations on conformational stability, we carried out isothermal urea-induced unfolding experiments followed by tryptophan fluorescence for S160I, S160M, A204R. Wild-type and L203C variants were studied side by side with the mutants.

Human FXN has three tryptophan residues (Fig. 4A), one of them

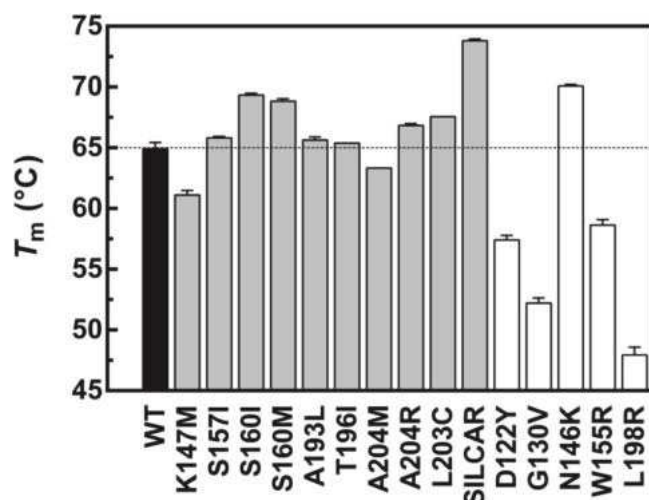


Fig. 3. Temperature-Induced Unfolding Followed by Sypro-Orange Fluorescence. Protein was at 5.0 μM . Buffer was 50 mM sodium phosphate, pH 7.0. The temperature slope was 1 $^{\circ}\text{C min}^{-1}$ (from 20 to 90 $^{\circ}\text{C}$). Excitation and emission ranges were 470–500 and 540–700 nm, respectively. Grey bars correspond to the designed variants, whereas white bars correspond to FRDA FXN variants. (For interpretation of the references to color in this figure legend, the reader is referred to the Web version of this article.)

Table 2
Thermodynamic parameters for equilibrium unfolding of FXN variants.

Variant	Urea-Induced Unfolding ^a		
	C_m (M)	$\Delta G^{\circ}_{\text{NU, H}_2\text{O}}$ (kcal mol ⁻¹)	$\Delta\Delta G^{\circ}_{\text{NU}}$ (kcal mol ⁻¹)
WT	4.88	9.02 \pm 0.16	–
S160I	5.37	9.94 \pm 0.08	0.92
S160M	5.34	9.88 \pm 0.25	0.86
L203C	5.48	10.14 \pm 0.08	1.12
A204R	5.23	9.67 \pm 0.07	0.65
SILCAR	6.20	11.46 \pm 0.06	2.44 (2.69) ^b

^a Parameters were obtained by least-squares fitting using a globally adjusted value of $m_{\text{NU}} = 1.85 \pm 0.04$ kcal mol⁻¹ M⁻¹ [24].

^b The value between parenthesis was calculated as: $\Delta\Delta G^{\circ}_{\text{NU SILCAR}} = \Delta\Delta G^{\circ}_{\text{NU S160I}} + \Delta\Delta G^{\circ}_{\text{NU L203C}} + \Delta\Delta G^{\circ}_{\text{NU A204R}}$.

(W155) located on the surface of the beta sheet and exposed to the solvent, and the other two (W168 and W173) in the core of the protein, both at a Van der Waals distance (~ 4 \AA). Tryptophan residues are excellent probes to monitor the FXN unfolding process (Fig. 4B). Fluorescence spectra corresponding to the native state of these mutants were completely superimposable to that of the wild-type variant, exhibiting a wavelength maximum (λ_{MAX}) of ~ 335 nm, suggesting as the near-UV CD results that the environment of tryptophan residues is preserved. On the other hand, the urea-induced unfolding resulted in all cases in a λ_{MAX} shift to 350 nm due to the solvent effect over the tryptophan-excited state. This is indicative of a full unfolding process at high urea concentrations (Fig. 4B).

Unfolding profiles showed that all the variants behaved as highly cooperative folding units and the analysis of two-state unfolding model fittings indicated that the conformational stability of S160I, S160M and A204R variants notably increases (Fig. 4 and Table 2). The stable variants exhibited higher C_m values (Table 2).

To obtain a highly stable variant, we chose to prepare a multiple mutant of FXN. It is worthy of mention that S157I and A193L were avoided because of a reduced function (see below) and lower observed T_m value, respectively. Therefore, we prepared a triple mutant variant that included S160I, L203C and A204R changes (SILCAR variant). In principle, if the effect of the mutations were completely additive, this variant should be ~ 3 kcal mol⁻¹ more stable than the wild-type ($\Delta G^{\circ}_{\text{NU}}$

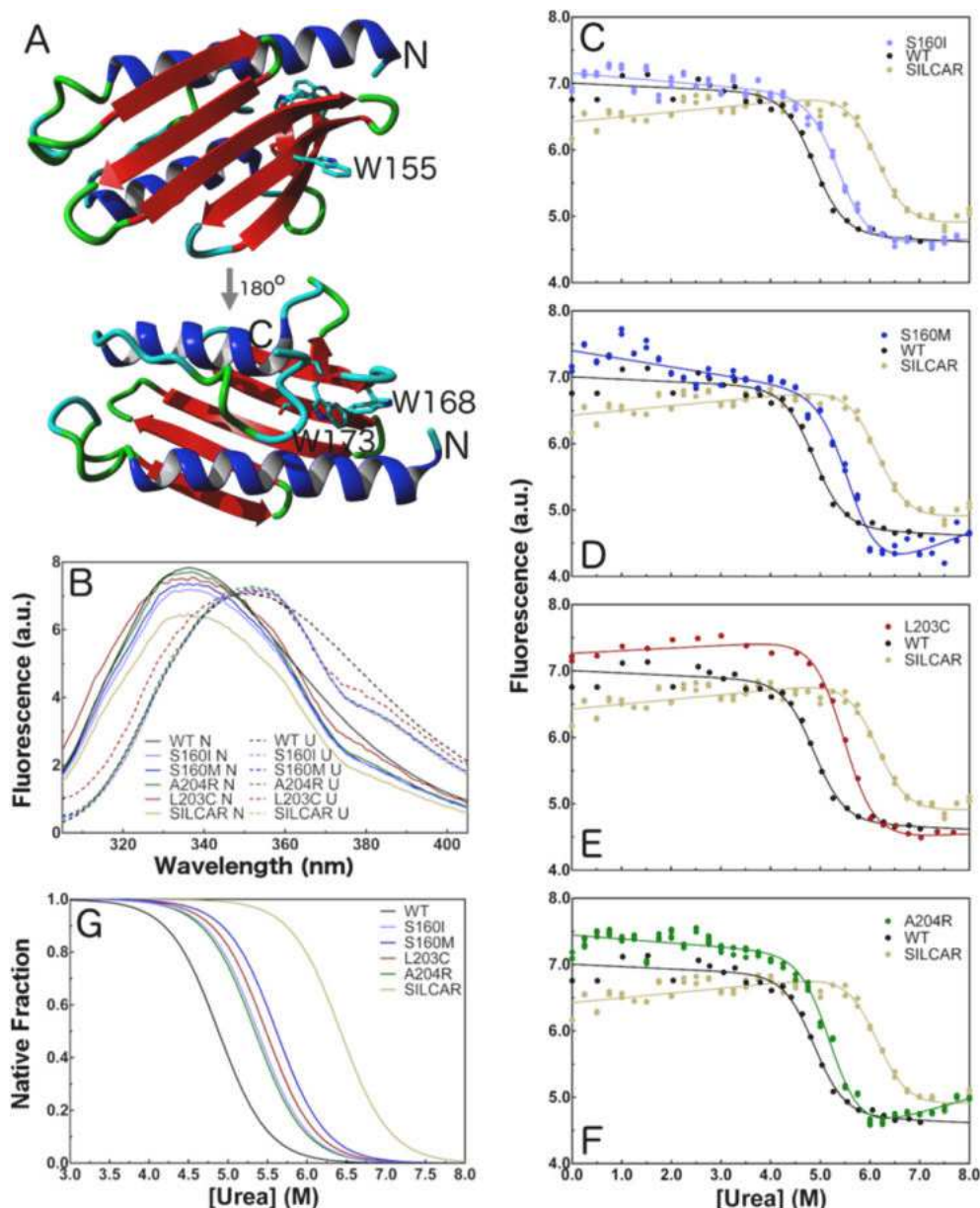


Fig. 4. Isothermal Urea-Induced Unfolding Followed by Tryptophan Fluorescence. (A) Tryptophan residues mapped on the human FXN structure (PDB ID 1EKG). (B) Tryptophan spectra corresponding to FXN variants incubated in buffer 20 mM Tris-HCl, 100 mM NaCl, 1 mM EDTA, pH 7.0, in the presence of 8 M urea (U, dashed) or in the absence of denaturant (N, solid line). Excitation was performed at 295 nm. Spectra were collected at 20 °C. Protein concentration was 3.7 μ M to avoid an inner filter effect. Panels (C), (D), (E) and (F) correspond to S160I, S160M, L203C and A204R, respectively. In panels C–F, the fluorescence intensity at 330 nm was plotted. Wild-type and the triple mutant SILCAR are included in each panel as references. (G) The native fraction calculated from the fitting of a two-state model to the experimental data are shown in panels C–F.

might reach the 12 kcal mol⁻¹). As expected, the SILCAR variant was structured (Fig. 2). We evaluated the conformational stability of this variant ($\Delta G_{\text{NU}}^{\circ} = 11.5$ kcal mol⁻¹, Table 2 and Fig. 4); taking into account the experimental error of $\Delta G_{\text{NU}}^{\circ}$ determinations (~ 0.25 kcal mol⁻¹), the analysis suggested that the partial effects of the mutations may be approximately additive.

It is worthy of note that the fittings of the two-state model to the data corresponding to the mutants and wild-type FXN were performed with a common m_{NU} parameter (the dependence of unfolding free energy with the chaotropic agent concentration $\frac{\partial \Delta G_{\text{NU}}^{\circ}}{\partial [\text{Urea}]}$) by a global fit of all the data, resulting in a $m_{\text{NU}} = 1.85 \pm 0.04$ kcal mol⁻¹ M⁻¹. The fact that a common m_{NU} could be applied, suggested that the difference in the solvent-accessible surface area ($\Delta \text{ASA}_{\text{NU}}$) between the native and unfolded states may be similar for the variants.

Remarkably, a good correlation between $\Delta G_{\text{NU}}^{\circ}$ (at 20 °C) and the observed T_{m} values was obtained (Fig. 5), reinforcing the idea that the variants share a common $\Delta S_{\text{NU}}^{\circ}$ at 20 °C [47], and suggesting that the variation in $\Delta G_{\text{NU}}^{\circ}$ at this temperature is essentially mediated by enthalpic differences among the variants. As previously showed by Schellman [48], this correlation was very useful for screening purposes,

in our experiments. Moreover, in the case of the SILCAR variant, the observed T_{m} value was significantly increased compared to that of the wild-type FXN ($\Delta T_{\text{m}} \sim 10$ °C, Table 1) and the correlation was also very good.

3.3. Resistance to proteolysis

Resistance to proteolysis comprises a combination of at least two different features of proteins, on the one hand, global stability and, on the other hand, local unfolding events and motions specific for native state dynamics; in both cases proteolytic sites have to be exposed to the protease active site.

At 20–25 °C, wild-type FXN is pretty resistant to proteolysis. When the reaction for wild-type was carried out at room temperature, after long incubation times with chymotrypsin, we observed only a singly cut; it occurred at position Tyr 205, in the C-terminal region. On the other hand, for some FRDA variants like L198R and G130V [12], or for the C-terminal truncated FXN 90–195, a distinctive sensitivity to proteolysis was observed, even with very short incubation times (2 min at 20 °C) and low protease concentration (1:200, protease: FXN ratio) [14].

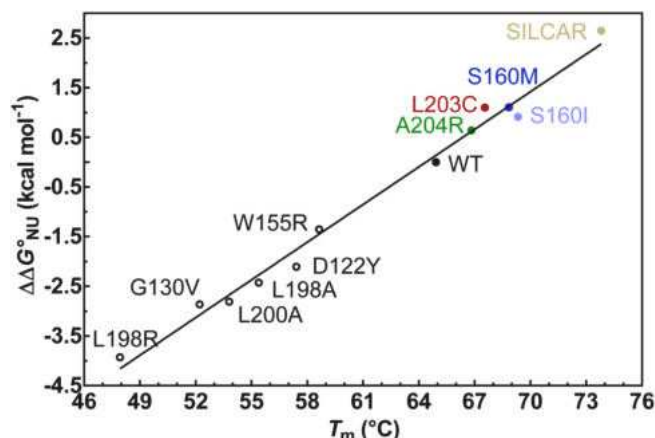


Fig. 5. Correlation between the Observed T_m and Conformational Stability. For the correlation we included data corresponding to the variants prepared for this work and the FRDA variants L198R, D122Y, W155R. Also, we included two CTR variants previously studied in our laboratory L198A and L200A. Free energy differences for D122Y, G130V and W155R were taken from Ref. [12]. The black straight line corresponds to the linear correlation ($R^2 = 0.99$). $\Delta\Delta G_{\text{NU}}^{\circ}$ values were calculated as $\Delta\Delta G_{\text{NU}}^{\circ} = \Delta G_{\text{NU}}^{\circ} \text{mutant FXN} - \Delta G_{\text{NU}}^{\circ} \text{wild-type FXN}$

Remarkably, at higher temperatures (40 °C), the wild-type variant is considerably more sensitive to chymotrypsin action. In fact, after a 5-h incubation (protease: FXN ratio 1:100), FXN was almost completely degraded, only < 10% of the total protein remained intact (elution peak between 34.3 and 34.6 min, Fig. 6A and Table S1).

In this condition, the stable variants S160I, L203C and A204R showed higher resistance to proteolysis than the wild-type FXN, as judged by the analysis of the RP-HPLC profiles, and the protein persisted intact after protease treatment (elution peak between 34.3 and 34.6 min, Fig. 6). Qualitatively, resistance to proteolysis was wild type \sim S160M < L203C < S160I < A204R (Fig. 6A–E). In particular, the fraction of protein that remained intact in the case of L203C and S160I was approximately 1.7 and 2.7 times (respectively) higher than that what was observed in the case of the wild-type FXN, whereas in the case of mutant A204R, the fraction of intact protein was more than 4.7 times the observed fraction for the wild-type, as judged by the area below the corresponding peaks. Therefore, A204R exhibited considerably higher resistance, compared to the other point mutant. Proteolysis was also evaluated for the SILCAR variant in the same conditions (with 100:1; FXN:chymotrypsin, 40 °C, 5 h). SILCAR was significantly more resistant than the wild-type variant (6.3 times, Table S1) and the point mutants, and even more resistant than A204R (Fig. 6F). The peak corresponding to the intact protein is signaled with a red asterisk at the top of each chromatographic profile. The values corresponding to the integration of the areas are in Table S1.

3.4. Activation of Cysteine Desulfurase NFS1 enzyme and frataxin function of the point mutants

Does the increase in stability affect the biological function of FXN? To investigate this issue, we evaluated the capability of the FXN mutants to activate the cysteine desulfurase enzyme. With the exception of variant S157I, all the variants showed similar activation to the exhibited by wild-type FXN (Fig. 7).

Variant S157I, however, exhibited only 50% of the specific activation of wild-type FXN. It is worthy of note that this variant exhibited only a slightly higher activation than the FRDA mutants N146K and W155R, suggesting a substantial effect of the S157I mutation on function, and possibly, a specific involvement of this residue in protein-protein interactions, most likely with ISCU, because S157 is located in the β -sheet oriented to the solvent and at only 5 Å of the FXN key-

residue W155. In fact, the structure of the supercomplex (PDB ID: 6NZU) shows that S157 forms a hydrogen bond with the backbone carbonyl oxygen of residue P133 of the ISCU subunit (Fig. S2).

Mutant K147M showed an activation similar to that observed for the wild-type FXN, suggesting the possibility of avoiding ubiquitination (which occurs in residue K147) and ubiquitin-mediated degradation *in vivo* [43,44], conserving the thermodynamic stability of wild-type protein by compensation of the negative effect of K147M (the observed T_m is approximately 4 °C lower than the observed for the wild-type) by making other mutations.

Whether or not SILCAR was useful to activate cysteine desulfurase NFS1 supercomplex was a major question because it was not clear enough if extreme enhancement stability might result in an increased rigidity or an alteration of other properties that could alter FXN activity. As shown in Fig. 7, this stable variant was able to activate the super-complex in the same fashion that wild-type FXN did.

The inspection of a plot of cysteine desulfurase activity vs. the observed T_m (Fig. 8) clearly shows that there is no correlation between stability and function. In fact, it is unlikely that the observed requirement for the activation depends on the native fraction of the FXN given that, even for the most unstable variant assayed in this work (L198R $\Delta G_{\text{NU}}^{\circ} = 5 \text{ kcal M}^{-1}$ [14]), the unfolded fraction is < 0.02% at room temperature. Furthermore, cysteine desulfurase activation seems to reach a maximal activity to what was observed for the wild-type, independently of the increase in the stability of the variant.

Nevertheless, from a practical point of view, FXN variants can be clustered in four different groups: (i) active and stable variants (relative activity \sim 1.0 and observed $T_m \geq 65$ °C); (ii) active but unstable (relative activity \sim 1.0 and observed $T_m < 65$ °C); (iii) inactive but stable (relative activity < 1.0 and observed $T_m \geq 65$ °C); and (iv) inactive and unstable (relative activity < 1.0 and observed $T_m < 65$ °C).

The K147M variant exhibits a reduced stability, although this mutant does preserve the protein function (group ii). The FRDA G137V variant recently studied by Faggianelli and coworkers [13] is a much more pronounced case of conformational instability in a context of similar activity compared with the wild-type FXN. Variants S157I (prepared in this work) and N146K (FRDA) can be clustered in group iii. On the other hand, the FRDA variants D122Y, G130V, W155R and L198R may be clustered in group iv; they are highly unstable and, simultaneously, they are significantly less active than the wild-type FXN.

3.5. The conformational dynamics of the SILCAR variant

Given that SILCAR variant exhibited remarkable resistance to proteolysis, we wondered whether these three mutations caused an alteration of the internal motions of FXN. To evaluate this issue, first we carried out all-atom molecular dynamics simulations for this mutant and for the wild-type variant (Fig. 9).

The analysis of the simulations carried out at 27 °C showed similar RMSF profiles for both variants (Fig. 9A), suggesting, in principle, comparable internal motions in the nanosecond timescale. A slightly lower internal mobility was observed for wild type, in particular, for stretches 115–121 (that comprises loop 1), 135–140, 158–162 (which includes S160I mutation in SILCAR), and 190–200. When simulations were run at a higher temperature (67 °C), some stretches of the wild-type variant exhibited higher mobility than SILCAR; nevertheless, other stretches proved to be more dynamic in the case of SILCAR. RMSD analysis showed no significant differences in global mean fluctuations between the wild-type and SILCAR nor in the C-terminal average motions (data not shown).

Interestingly, the interactions that R204 can establish seem to depend on the temperature. When simulations were carried out at 27 °C, the side chain of R204 established strong ionic interactions with E101 and also interacted with other acidic residues (D104 and E108) in SILCAR (Fig. 9B). On the other hand, when simulations were run at 67 °C the strongest interaction was formed between R204 and D104,

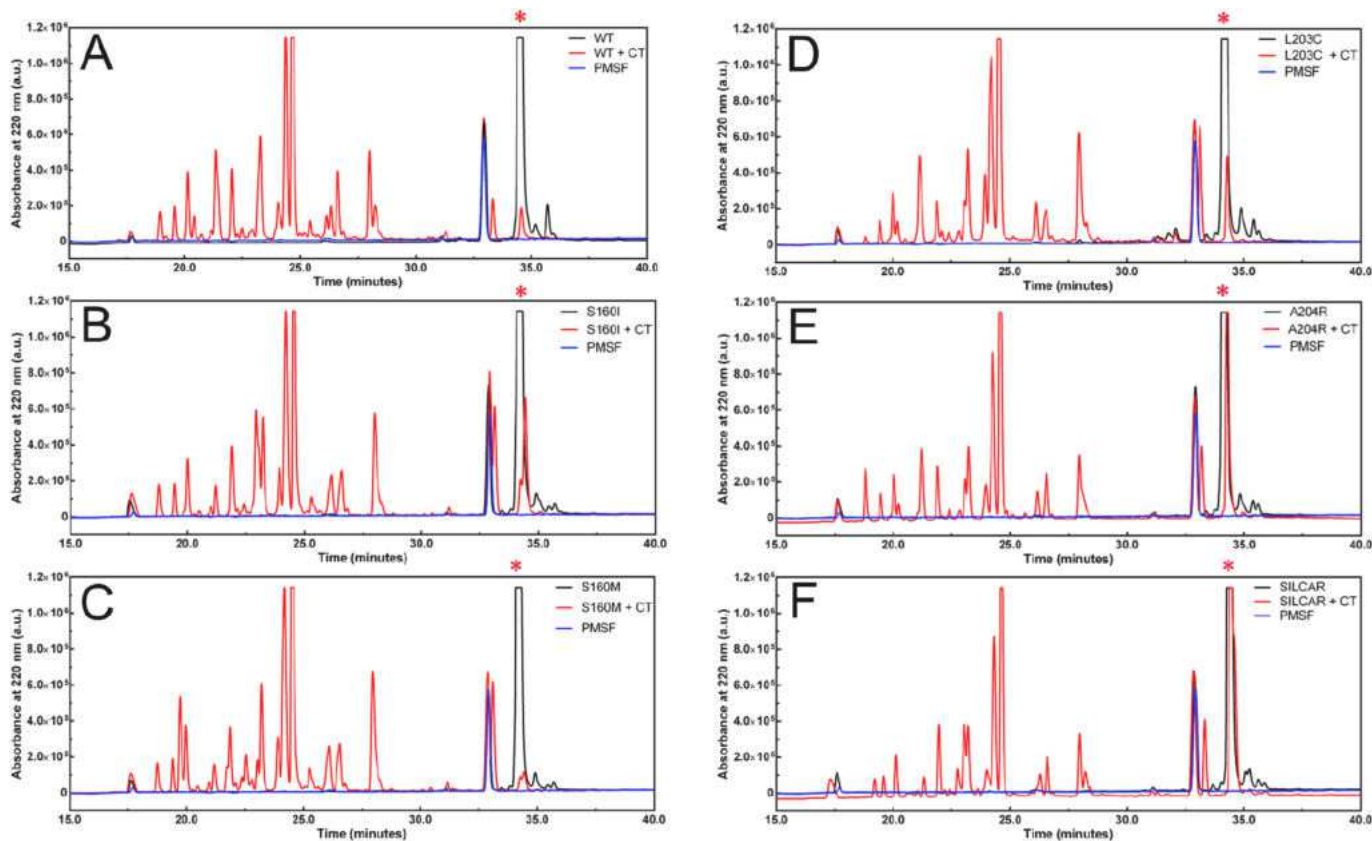


Fig. 6. Resistance to Proteolysis of the FXN Variants. RP-HPLC profiles corresponding to wild-type (A), S160I (B), S160M (C), L203C (D), A204R (E) and SILCAR variant (F). In each panel PMSF (blue) and the protein without protease (black) were included. Proteins (1 mg mL^{-1}) were incubated during 5 h at 40°C in buffer 20 mM Tris-HCl, 100 mM NaCl, 1 mM EDTA, pH 7.0 with 1:100 protease: protein (chymotrypsin). In all cases, the reactions were stopped by the addition of 1 mM PMSF (final concentration) and 0.05–0.1% (v/v) TFA. After that, a gradient from 0 to 100% acetonitrile (0.05% (v/v) TFA) was performed. The column used was analytical C18 (Higgins Analytical, Inc. U.S.A.) and peptides were monitored by absorbance at 220 nm. (For interpretation of the references to color in this figure legend, the reader is referred to the Web version of this article.)

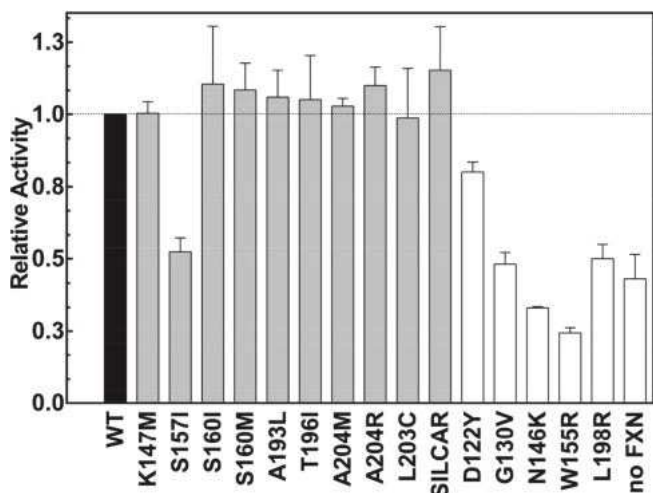


Fig. 7. Activation of Cysteine Desulfurase NFS1 by the FXN Variants. Enzymatic desulfurization of cysteine to alanine and sulfide by the (NFS1/ACP- ISD11/ISCU/FXN)₂ supercomplex was determined by the methylene blue method. Samples were incubated at room temperature for 30 min H_2S production was stopped and the production of methylene blue was measured by absorbance at 670 nm. Grey bars correspond to the designed variants, whereas white bars correspond to the FRDA FXN variants and a control without FXN (no FXN). (For interpretation of the references to color in this figure legend, the reader is referred to the Web version of this article.)

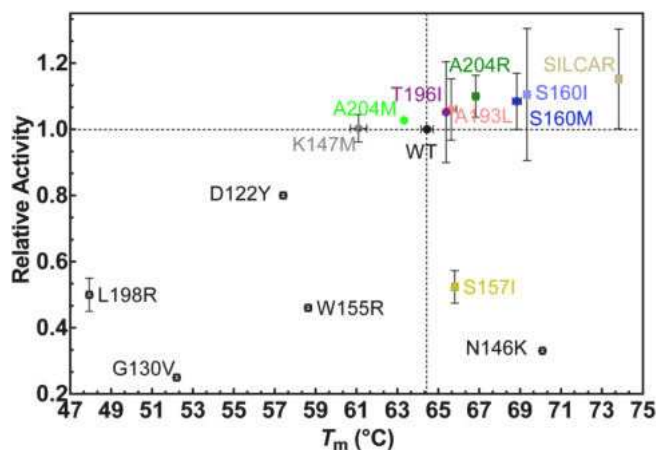


Fig. 8. Activation of Cysteine Desulfurase NFS1 by the FXN Variants vs. Resistance to Thermal Denaturation. Data shown in Fig. 5 and 8 were plotted.

whereas E101 and E108 only sporadically formed ionic pairs with the arginine, as judged by the distance analysis (Fig. 9B). Additionally, Y205 established a stronger hydrogen bond interaction with E101 in the case of the SILCAR variant compared to the wild-type FXN, and this was also evident when simulations were run at a higher temperature (Fig. 9C).

We calculated the fraction of time in which the H-bond between Y205 and E101 was formed. For the wild-type protein, 60% was

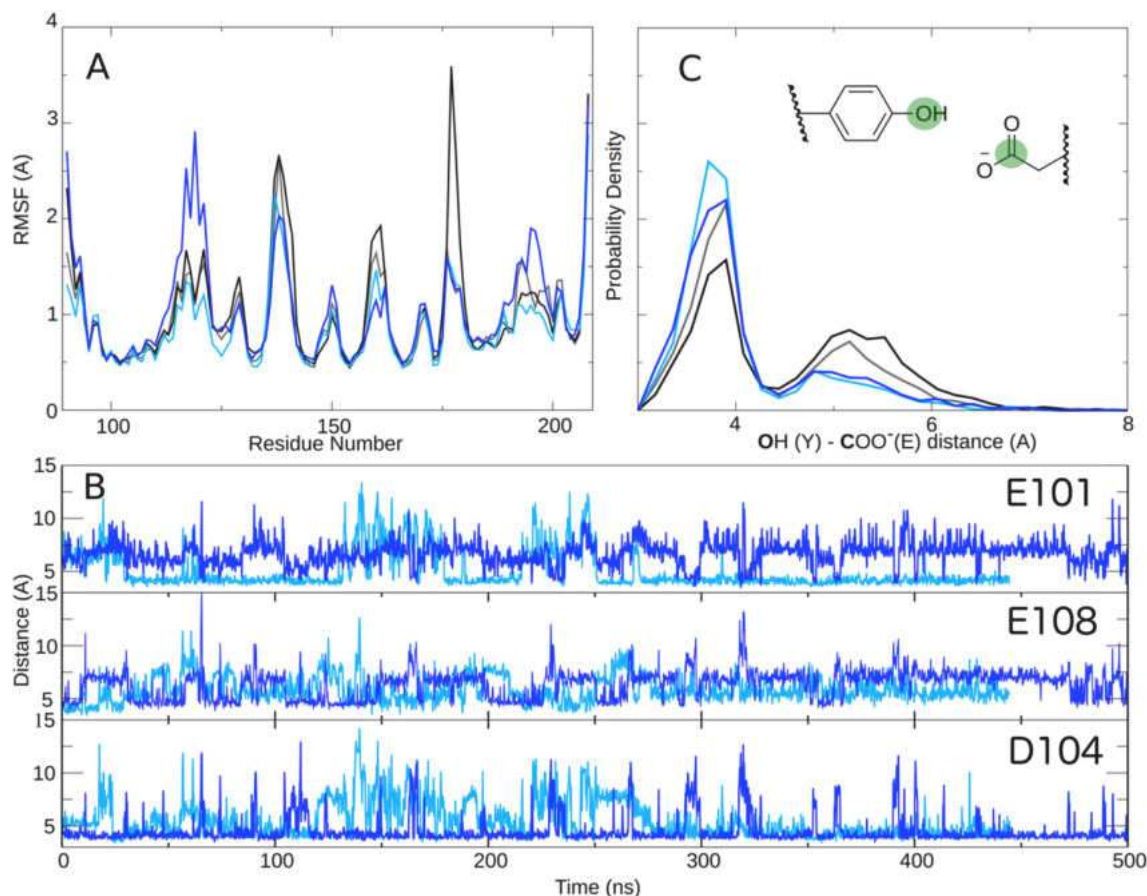


Fig. 9. Internal Motions of Human FXN Explored by Molecular Dynamics Simulations. (A) RMSF values corresponding to the wild-type (grey and black at 27 °C and 67 °C, respectively) and SILCAR (cyan and blue at 27 °C and 67 °C, respectively) variants. (B) Interaction distance between R204 and E101, D104 or E108 along the simulation time of SILCAR. (C) Histogram showing the distribution of the observed distances between residues Y205 and E101 along the simulation time of the wild-type (grey and black at 27 and 67 °C, respectively) and SILCAR (cyan and blue at 27 and 67 °C, respectively) variants. (For interpretation of the references to color in this figure legend, the reader is referred to the Web version of this article.)

estimated when simulated at 27 °C and 50% when the temperature was increased to 67 °C. In the SILCAR variant simulations, this interaction was present 80% and 75% of the time at 27 and 67 °C, respectively. This behavior may be related to the high resistance of SILCAR to chymotrypsin; that is, Y205 would be more rigid and structured in the case of SILCAR and consequently, less accessible to protease action.

Internal motions spread in a broad range of timescales. We wondered whether SILCAR exhibited alterations in its dynamics, in the range of the microsecond to milliseconds that might be relevant in protein function. Carr-Purcell-Meiboom-Gill (CPMG) relaxation dispersion NMR experiments are useful to explore motions in this timescale; thus we carried out this experiment for the ^{15}N -labeled SILCAR and wild-type FXN variants, for comparison (Fig. 10).

Prior to that, in the case of the SILCAR variant, the assignments were corroborated by means of NOESY-HSQC and TOCSY-HSQC spectra, because an important set of $\text{H-}^{15}\text{N}$ - groups exhibited significant chemical shift differences (Fig. 10A) compared to that of the wild-type FXN. Higher differences were observed for residues close in space to the mutation sites (S160I, L203C and A204R, Figs. S3 and S4).

If some residues were involved in a conformational exchange that occurs in this timescale, this exchange should positively contribute to the observed (effective) transversal relaxation (R_2^{obs}). Additionally, an increase in k_{ex} (the observed kinetic constant for the exchange process), or an increment in the population of the excited state (higher in energy than the ground state), or an increase in the difference between the chemical shifts of the excited state and the ground state may result in an increase in the R_2^{obs} [33,49,50].

The results indicate that the relaxation profiles corresponding to the variants are similar. Thus, in principle, both the SILCAR and the wild-type variants exhibit similar internal motions. However, some residues exhibiting high R_2^{obs} values in the wild-type variant have shown even higher values in SILCAR, suggesting that the exchange might be higher in the mutant (Fig. 10B and C). To study what the source of these differences was, we carried out two-state (ground and excited native states) global fittings (Fig. 10D and E) using the Sherekhan server [36], considering data sets acquired at two different magnetic field strengths (14.1 and 16.5 T). The analysis of the global fittings suggests that there are no significant differences in the conformational exchange rate (k_{ex} are 225 ± 31 and $216 \pm 16 \text{ s}^{-1}$ for wild-type and SILCAR, respectively) nor are there any changes in the populations of ground and excited states (p_{B} are 0.016 ± 0.002 and 0.019 ± 0.002 , for wild-type and SILCAR variants, respectively). Therefore, the origin of the increase in the effective R_2^{obs} values for these residues might come from a slight change in differences in the chemical shifts between the ground and excited states ($\Delta\omega$, Fig. 10D). Thus, these peculiarities observed for the R_2^{obs} values in SILCAR are more likely evidence of the subtle effects of the three mutations on the fine structure of the ground and/or excited states rather than alterations in the dynamics of the protein.

4. Discussion

4.1. FXN variants with high conformational stability

In this study we explored the structure of FXN in order to find

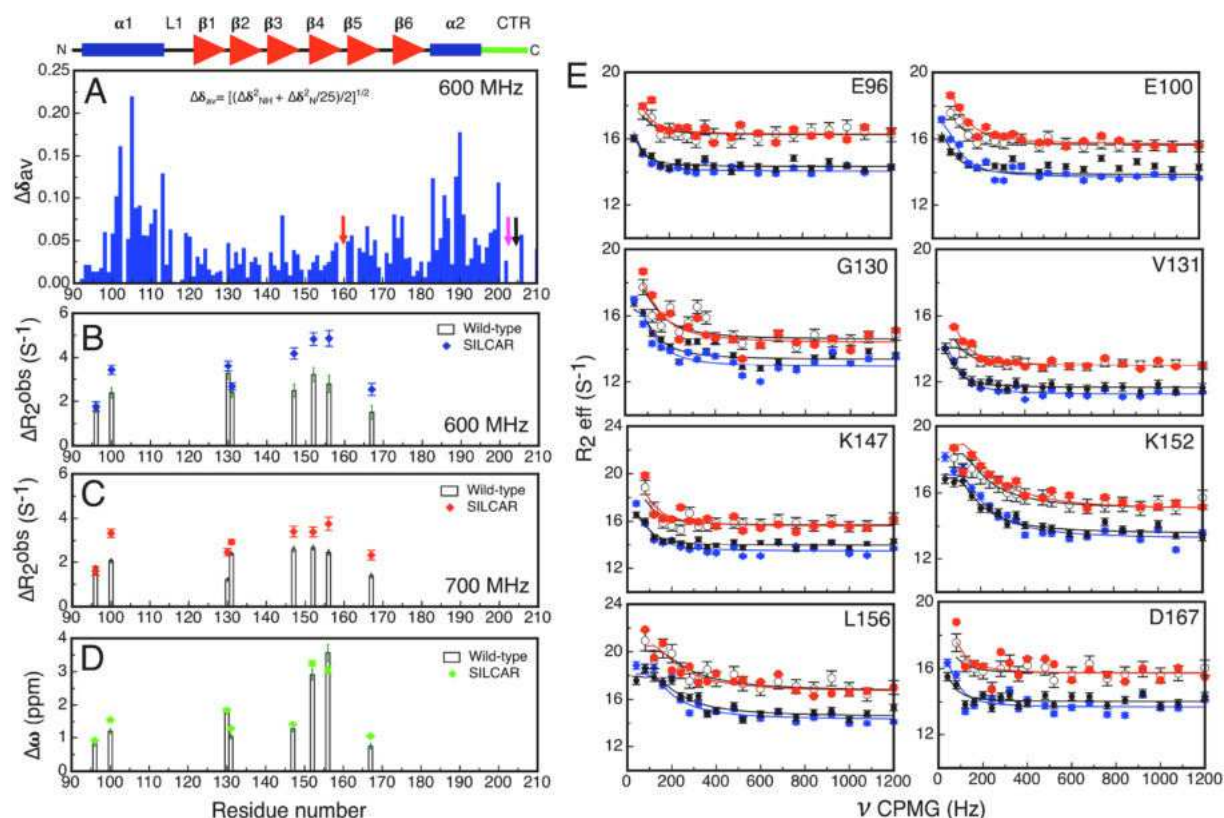


Fig. 10. NMR analysis of the SILCAR variant. (A) Chemical Shift Perturbation (CSP). ^1H - ^{15}N HSQC spectra corresponding to wild-type and SILCAR variants were analyzed to identify the effect of point mutations on the amide chemical shift using the parameter $\Delta\delta = [(\Delta\delta_{\text{H}}^2 + \Delta\delta_{\text{N}}^2/25)/2]^{0.5}$. The small arrows indicate the mutated residues in SILCAR, 160, 203 and 204. (B) The contribution of a conformational exchange to transverse relaxation, ΔR_2^{obs} , was estimated from the difference in R_2^{obs} at the lowest and highest CPMG frequency values and plotted along the FXN sequence (diamonds in blue and black bars correspond to the SILCAR and wild-type variants, respectively). The experiment was carried out at 14.1 T. (C) Similar to panel B, but the experiment was performed at 16.5 T. For clarity, only the subset of residues used for global fittings (E96, E100, G130, V131, K147, K152, L156 and D167) is shown. (D) The differences in chemical shifts between the ground and excited states from fittings to the Carver-Richards equation (see the Materials and Methods section) for the same subset of residues as in panel B. (E) The global fittings using data acquired at 14.1 (black-bold and blue circles, wild-type and SILCAR, respectively) and 16.5 T (black-empty and red-bold circles, wild-type and SILCAR, respectively). The residue corresponding to the cross-peak analyzed is indicated in each panel. Lines indicate the best-fit curves obtained using shared values for the exchange rate and state populations, according to previous work [35]. The residues analyzed are plotted on the FXN structure in Fig. S5, in Supplementary Material). (For interpretation of the references to color in this figure legend, the reader is referred to the Web version of this article.)

mutants with higher stability than the wild-type protein and similar biological activity. We identified several candidates by means of the FOLDX computational tool. Seven mutants were prepared and studied. Three of them (S160I, S160M and A204R) were significantly more stable than the wild-type variant and equally active as cysteine desulfurase NFS1 activators. Thus, these variants and L203C, previously studied in our laboratory, provided a good tool to explore structural dynamics-activity relationships spanning a broad range of conformational stabilities.

Taking into account the structure of FXN (PDB ID 1EKG), the structure of the supercomplex for the iron-sulfur cluster assembly (PDB ID 6NZU) and the computational models corresponding to the point mutant FXN variants, the following inferences can be made regarding the effect of the mutations on stability and function:

K147M: Residue K147 establishes an ionic interaction with E96 (2.5 Å). It might be inferred that this mutation can reduce the stability of the protein, cancelling this salt bridge. On the other hand, methionine might establish apolar interactions with L103 side chain (3.1 Å). The experimental results indicate that a destabilizing effect of the mutation prevailed.

S157I: This variant exhibits a slightly higher observed T_m value than the wild-type variant. I157 might establish stabilizing apolar contacts with V144 (distance is 3.7 Å). On the other hand, it is not odd that the S157I variant is a very poor activator of the cysteine

desulfurase NFS1 supercomplex because S157 appears to form a hydrogen bond with P133 from ISCU (Fig. S2) and the mutation cancels this interaction.

S160I: As predicted by FOLDX, it is more stable than the wild-type FXN. The analysis of the FXN structure suggests that the isoleucine at position 160 might establish apolar interaction with P159 (3.5 Å), stabilizing the β -turn structure between the β -strands 4 and 5.

S160M: It is more stable than the wild-type variant. A methionine residue in that place may interact with P159 and also with E189 (3.6 and 3.5 Å, respectively).

A193L: It is more stable than the wild-type; it is likely that leucine increases the number of apolar contacts with residues at the core of FXN: L140, L136 and Y143 (3.4, 3.6 and 3.3 Å, respectively).

T196I: The analysis of the structure suggests that isoleucine located in the first part of CTR region might interact with Tyr 108 from loop 1, making an apolar bridge. However, the fact that the observed T_m values corresponding to wild-type and T196I are very similar suggests that, if this interaction takes place, it is only transient or, on the other hand, the effect is negatively compensated in some way.

L203C: As previously described [24,25], a cysteine residue at position 203 can favorably interact with apolar side chains of the FXN core, whereas it can also interact with core polar residues such as H183 and S105 (distances = 3.4 and 3.3 Å, respectively) given its dual physicochemical behavior, which is not properly predicted by FOLDX or Dynamut software.

A204M: It exhibits a slight destabilizing effect compared to the wild-type variant, as judged by the observed T_m . It is possible that the larger apolar side-chain cannot be properly accommodated at this site.

A204R: it exhibits a marked gain in stability; the analysis of the structure indicates that R204 can establish a strong ionic interaction with E101.

In this work, we also carried out controlled proteolysis of the mutant proteins. Variants S160I, L203C and A204R showed more resistance than the wild-type FXN. In particular, A204R variant showed the highest resistance among the simple mutants. This arginine residue might create a new salt bridge between the CTR and helix $\alpha 1$. In this regard, relationships between conformational stability and C-terminal region (CTR) integrity of the FXN protein family were previously identified [15,51]. Furthermore, it was shown that CTR mutations essentially affect the stability of the native state but neither the stability of the folding transition state nor that of the intermediary state of the folding reaction [24] are altered.

Moreover, point mutation L198R at the CTR locally alters FXN internal motions. This behavior was also studied in detail in our laboratory by means of the engineered cysteine point mutants (located in the core: V134C, located in the CTR: L198C, L200C and L203C) and thiol-disulfide exchange dynamics. These experiments effectively showed that there is a correlation between local stability of the CTR and global stability of FXN [25]. On the other hand, complete truncation of the CTR ($\Delta 195$) perturbed internal motions in a global fashion, suggesting a conformational exchange between the native and unfolded states in the absence of a denaturant and at room temperature [14]. This is in agreement with the very low conformational stability of the CTR truncated variant [15].

To increase the stability of FXN, we have prepared the triple mutant SILCAR (S160I/L203C/A204R). Remarkably, SILCAR has two-point mutations located in the CTR. As expected, this variant was highly stable. Moreover, SILCAR was as active as the wild-type FXN and, notably, it was more resistant to proteolysis than each one of the simple mutants, suggesting a more compact structure.

Relaxation dispersion NMR experiments have shown that this mutant has internal motions similar to that of the wild-type variant at least in the micro-millisecond timescale. In this context, the fact that SILCAR was more resistant to chymotrypsin protease suggests the protection at specific proteolytic sites, a hypothesis that will be further investigated.

The capability of human FXN to exert its function *in vivo* seems to depend on a multiplicity of factors, among them: expression levels, ubiquitination and degradation [44,52], translocation and processing of the precursor (1–210) and intermediate (41–210) forms to yield the mature form (81–210) within the mitochondrial matrix, conformational stability, the establishment of proper protein-protein interactions (cysteine desulfurase NFS1 supercomplex), iron interaction and perhaps the inhibition of protein aggregation, which was described for some pathogenic variants *in vitro* [12,53]. All these features make the essence of FXN inside the cell.

Whether a highly stable variant as SILCAR is able to act as the wild-type FXN should be explored in more detail. Here we explored only a small part of the picture. More experiments should be done to evaluate if SILCAR is able to activate the [Fe-S] cluster assembly and if other possible moonlight functions of FXN inside the cells are carried out in a proper way by this variant. In this context, the combination of SILCAR mutations with K147M or K147R—which are less stable than the wild-type FXN but would not be substrates of the ubiquitin-mediated protein degradation pathway—may be good options to prepare a highly stable *in vivo* FXN variant for protein replacement therapies.

Funding sources

This study was supported by the *Agencia Nacional de Promoción*

Científica y Tecnológica (ANPCyT) through grant No. PICT 2016–2280, the *Consejo Nacional de Investigaciones Científicas y Técnicas* (CONICET), and the Friedreich's Ataxia Research Alliance (FARA).

UniProt accession IDs

Q9HD34: human LYR motif-containing protein 4 (ISD11); O14561: human mitochondrial acyl carrier protein (ACP); Q9Y697: human cysteine desulfurase (NFS1); Q9H1K1: human Iron-sulfur cluster assembly enzyme (ISCU); Q16595: human frataxin (FXN).

Acknowledgments

We thank Dr. María Laura Cerutti (CRIP, UNSAM) for her support concerning the R_h determination of proteins by DLS. JS thanks CONICET and Universidad de Buenos Aires for financial support. We thank Dr. Andres Binolfi and Dr. Rodolfo Rasia for support with NMR acquisitions and Plataforma Argentina de Biología Estructural y Metabólica (PLABEM) for access to NMR spectrometers.

Appendix A. Supplementary data

Supplementary data to this article can be found online at <https://doi.org/10.1016/j.abb.2020.108491>.

References

- [1] N.G. Fox, X. Yu, X. Feng, H.J. Bailey, A. Martelli, J.F. Nabhan, C. Strain-Damerell, C. Bulawa, W.W. Yue, S. Han, Structure of the human frataxin-bound iron-sulfur cluster assembly complex provides insight into its activation mechanism, *Nat. Commun.* 10 (1) (2019) 2210.
- [2] V. Campuzano, L. Montermini, M.D. Molto, L. Pianese, M. Cossee, F. Cavalcanti, E. Monros, F. Rodius, F. Duclos, A. Monticelli, F. Zara, J. Canizares, H. Koutnikova, S.I. Bidichandani, C. Gellera, A. Brice, P. Trouillas, G. De Michele, A. Filla, R. De Frutos, F. Palau, P.I. Patel, S. Di Donato, J.L. Mandel, S. Cocozza, M. Koenig, M. Pandolfo, Friedreich's ataxia: autosomal recessive disease caused by an intronic GAA triplet repeat expansion, *Science* 271 (5254) (1996) 1423–1427.
- [3] P.J. Lamont, M.B. Davis, N.W. Wood, Identification and sizing of the GAA trinucleotide repeat expansion of Friedreich's ataxia in 56 patients. Clinical and genetic correlates, *Brain* 120 (Pt 4) (1997) 673–680.
- [4] K. Ohshima, L. Montermini, R.D. Wells, M. Pandolfo, Inhibitory effects of expanded GAA.TTC triplet repeats from intron 1 of the Friedreich ataxia gene on transcription and replication *in vivo*, *J. Biol. Chem.* 273 (23) (1998) 14588–14595.
- [5] D. Marmolino, F. Acquaviva, Friedreich's Ataxia: from the (GAA) n repeat mediated silencing to new promising molecules for therapy, *Cerebellum* 8 (3) (2009) 245–259.
- [6] T. Punga, M. Buhler, Long intronic GAA repeats causing Friedreich ataxia impede transcription elongation, *EMBO Mol. Med.* 2 (4) (2010) 120–129.
- [7] M.M. Lufino, A.M. Silva, A.H. Nemeth, J. Alegre-Abarrategui, A.J. Russell, R. Wade-Martins, A GAA repeat expansion reporter model of Friedreich's ataxia recapitulates the genomic context and allows rapid screening of therapeutic compounds, *Hum. Mol. Genet.* 22 (25) (2013) 5173–5187.
- [8] Y. Li, Y. Lu, U. Polak, K. Lin, J. Shen, J. Farmer, L. Seyer, A.D. Bhalla, N. Rozwadowska, D.R. Lynch, J.S. Butler, M. Napierala, Expanded GAA repeats impede transcription elongation through the FXN gene and induce transcriptional silencing that is restricted to the FXN locus, *Hum. Mol. Genet.* 24 (24) (2015) 6932–6943.
- [9] A.M. Silva, J.M. Brown, V.J. Buckle, R. Wade-Martins, M.M. Lufino, Expanded GAA repeats impair FXN gene expression and reposition the FXN locus to the nuclear lamina in single cells, *Hum. Mol. Genet.* 24 (12) (2015) 3457–3471.
- [10] C.A. Galea, A. Hug, P.J. Lockhart, G. Tai, L.A. Corben, E.M. Yiu, L.C. Gurrin, D.R. Lynch, S. Gelbard, A. Durr, F. Pousset, M. Parkinson, R. Labrum, P. Giunti, S.L. Perlman, M.B. Delatycki, M.V. Evans-Galea, Compound heterozygous FXN mutations and clinical outcome in Friedreich ataxia, *Ann. Neurol.* 79 (3) (2016) 485–495.
- [11] A. Candayan, G. Yunisova, A. Cakar, H. Durmus, A.N. Basak, Y. Parman, E. Battaloglu, The first biallelic missense mutation in the FXN gene in a consanguineous Turkish family with Charcot-Marie-Tooth-like phenotype, *Neurogenetics* 21 (1) (2020) 73–78, <https://doi.org/10.1007/s10048-019-00594-1> Epub 2019 Oct 31.
- [12] A.R. Correia, C. Pastore, S. Adinolfi, A. Pastore, C.M. Gomes, Dynamics, stability and iron-binding activity of frataxin clinical mutants, *FEBS J.* 275 (14) (2008) 3680–3690.
- [13] N. Faggiannelli, R. Puglisi, L. Veneziano, S. Romano, M. Frontali, T. Vannocci, S. Fortuni, R. Testi, A. Pastore, Analyzing the effects of a G137V mutation in the FXN gene, *Front. Mol. Neurosci.* 8 (2015) 66.
- [14] S.E. Faraj, E.A. Roman, M. Aran, M. Gallo, J. Santos, The alteration of the C-

- terminal region of human frataxin distorts its structural dynamics and function, *FEBS J.* 281 (15) (2014) 3397–3419.
- [15] E.A. Roman, S.E. Faraj, M. Gallo, A.G. Salvay, D.U. Ferreira, J. Santos, Protein stability and dynamics modulation: the case of human frataxin, *PLoS One* 7 (9) (2012) e45743.
- [16] F. Sacca, A. Marsili, G. Puorro, A. Antenora, C. Pane, A. Tessa, P. Scoppettuolo, C. Nesti, V. Brescia Morra, G. De Michele, F.M. Santorelli, A. Filla, Clinical use of frataxin measurement in a patient with a novel deletion in the FXN gene, *J. Neurol.* 260 (4) (2013) 1116–1121.
- [17] M. Bellanda, L. Maso, D. Doni, M. Bortolus, E. De Rosa, F. Lunardi, A. Alfonsi, M.E. Noguera, M.G. Herrera, J. Santos, D. Carbonera, P. Costantini, Exploring iron-binding to human frataxin and to selected Friedreich ataxia mutants by means of NMR and EPR spectroscopies, *Biochim. Biophys. Acta Protein Proteomics* 1867 (11) (2019) 140254.
- [18] J. Bridwell-Rabb, A.M. Winn, D.P. Barondeau, Structure-function analysis of Friedreich's ataxia mutants reveals determinants of frataxin binding and activation of the Fe-S assembly complex, *Biochemistry* 50 (33) (2011) 7265–7274.
- [19] S. Schmucker, A. Martelli, F. Colin, A. Page, M. Wattenhofer-Donze, L. Reutenauer, H. Puccio, Mammalian frataxin: an essential function for cellular viability through an interaction with a preformed ISCU/NFS1/ISD11 iron-sulfur assembly complex, *PLoS One* 6 (1) (2011) e16199.
- [20] J. Huang, E. Dizin, J.A. Cowan, Mapping iron binding sites on human frataxin: implications for cluster assembly on the ISU Fe-S cluster scaffold protein, *J. Biol. Inorg. Chem.* 13 (5) (2008) 825–836.
- [21] D.S. Vazquez, W.A. Agudelo, A. Yone, N. Vizioli, M. Aran, F.L. Gonzalez Flecha, M.C. Gonzalez Lebrero, J. Santos, A helix-coil transition induced by the metal ion interaction with a grafted iron-binding site of the CyaY protein family, *Dalton Trans.* 44 (5) (2015) 2370–2379.
- [22] S. Adinolfi, M. Trifuoggi, A.S. Politou, S. Martin, A. Pastore, A structural approach to understanding the iron-binding properties of phylogenetically different frataxins, *Hum. Mol. Genet.* 11 (16) (2002) 1865–1877.
- [23] A.R. Correia, T. Wang, E.A. Craig, C.M. Gomes, Iron-binding activity in yeast frataxin entails a trade off with stability in the alpha1/beta1 acidic ridge region, *Biochem. J.* 426 (2) (2010) 197–203.
- [24] S.E. Faraj, R.M. Gonzalez-Lebrero, E.A. Roman, J. Santos, Human frataxin folds via an intermediate state. Role of the C-terminal region, *Sci. Rep.* 6 (2016) 20782.
- [25] S.E. Faraj, M.E. Noguera, J.M. Delfino, J. Santos, Global implications of local unfolding phenomena, probed by cysteine reactivity in human frataxin, *Sci. Rep.* 9 (1) (2019) 1731.
- [26] J. Schymkowitz, J. Borg, F. Stricher, R. Nys, F. Rousseau, L. Serrano, The FoldX web server: an online force field, *Nucleic Acids Res.* 33 (Web Server issue) (2005) W382–W388.
- [27] S. Dhe-Paganon, R. Shigetani, Y.I. Chi, M. Ristow, S.E. Shoelson, Crystal structure of human frataxin, *J. Biol. Chem.* 275 (40) (2000) 30753–30756.
- [28] M.R. Wilkins, E. Gasteiger, A. Bairoch, J.C. Sanchez, K.L. Williams, R.D. Appel, D.F. Hochstrasser, Protein identification and analysis tools in the ExPASy server, *Methods Mol. Biol.* 112 (1999) 531–552.
- [29] C.L. Tsai, D.P. Barondeau, Human frataxin is an allosteric switch that activates the Fe-S cluster biosynthetic complex, *Biochemistry* 49 (43) (2010) 9132–9139.
- [30] F. Delaglio, S. Grzesiek, G.W. Vuister, G. Zhu, J. Pfeifer, A. Bax, NMRPipe: a multidimensional spectral processing system based on UNIX pipes, *J. Biomol. NMR* 6 (3) (1995) 277–293.
- [31] B.A. Johnson, Using NMRView to visualize and analyze the NMR spectra of macromolecules, *Methods Mol. Biol.* 278 (2004) 313–352.
- [32] G. Musco, T. de Tommasi, G. Stier, B. Kolmerer, M. Bottomley, S. Adinolfi, F.W. Muskett, T.J. Gibson, T.A. Frenkiel, A. Pastore, Assignment of the 1H, 15N, and 13C resonances of the C-terminal domain of frataxin, the protein responsible for Friedreich ataxia, *J. Biomol. NMR* 15 (1) (1999) 87–88.
- [33] A.G. Palmer 3rd, C.D. Kroenke, J.P. Loria, Nuclear magnetic resonance methods for quantifying microsecond-to-millisecond motions in biological macromolecules, *Methods Enzymol.* 339 (2001) 204–238.
- [34] P.J. Farber, A. Mittermaier, Relaxation dispersion NMR spectroscopy for the study of protein allostery, *Biophysical Reviews* 7 (2) (2015) 191–200.
- [35] M.E. Noguera, M. Aran, C. Smal, D.S. Vazquez, M.G. Herrera, E.A. Roman, N. Alaimo, M. Gallo, J. Santos, Insights on the conformational dynamics of human frataxin through modifications of loop-1, *Arch. Biochem. Biophys.* 636 (2017) 123–137.
- [36] A. Mazur, B. Hammesfahr, C. Griesinger, D. Lee, M. Kollmar, ShereKhan-calculating exchange parameters in relaxation dispersion data from CPMG experiments, *Bioinformatics* 29 (14) (2013) 1819–1820.
- [37] M. Bieri, P.R. Gooley, Automated NMR relaxation dispersion data analysis using NESSY, *BMC Bioinf.* 12 (2011) 421.
- [38] W.L. Jorgensen, J. Chandrasekhar, J.D. Madura, Comparison of simple potential functions for simulating liquid water, *J. Chem. Phys.* 79 (1983) 926–935.
- [39] L. Capece, M.A. Marti, A. Crespo, F. Doctorovich, D.A. Estrin, Heme protein oxygen affinity regulation exerted by proximal effects, *J. Am. Chem. Soc.* 128 (38) (2006) 12455–12461.
- [40] J.-P. Ryckaert, G. Ciccotti, H.J.C. Berendsen, Numerical integration of the cartesian equations of motion of a system with constraints: molecular dynamics of n-alkanes, *J. Comput. Phys.* 23 (3) (1977) 327–341.
- [41] D.A. Case, I.Y. Ben-Shalom, S.R. Brozell, D.S. Cerutti, T.E. Cheatham, V.W.D. Cruzeiro, T.A. Darden, R.E. Duke, D. Ghoreishi, M.K. Gilson, H. Gohlke, A.W. Goetz, D. Greene, R. Harris, N. Homeyer, S. Izadi, A. Kovalenko, T. Kurtzman, T.S. Lee, S. LeGrand, P. Li, C. Lin, J. Liu, T. Luchko, R. Luo, D.J. Mermelstein, K.M. Merz, Y. Miao, G. Monard, C. Nguyen, H. Nguyen, I. Omelyan, A. Onufriev, F. Pan, R. Qi, D.R. Roe, A. Roitberg, C. Sagui, S. Schott-Verdugo, J. Shen, C.L. Simmerling, J. Smith, R. Salomon-Ferrer, J. Swails, R.C. Walker, J. Wang, H. Wei, R.M. Wolf, X. Wu, L. Xiao, D.M. York, P.A. Kollman, AMBER 2018, University of California, San Francisco, 2018.
- [42] J.A. Maier, C. Martinez, K. Kasavajhala, L. Wickstrom, K.E. Hauser, C. Simmerling, ff14SB: improving the accuracy of protein side chain and backbone parameters from ff99SB, *J. Chem. Theor. Comput.* 11 (8) (2015) 3696–3713.
- [43] M. Benini, S. Fortuni, I. Condo, G. Alfedì, F. Malisan, N. Toschi, D. Serio, D.S. Massaro, G. Arcuri, R. Testi, A. Rufini, E3 ligase RNF126 directly ubiquitinates frataxin, promoting its degradation: identification of a potential therapeutic target for friedreich ataxia, *Cell Rep.* 18 (8) (2017) 2007–2017.
- [44] A. Rufini, S. Fortuni, G. Arcuri, I. Condo, D. Serio, O. Incani, F. Malisan, N. Ventura, R. Testi, Preventing the ubiquitin-proteasome-dependent degradation of frataxin, the protein defective in Friedreich's ataxia, *Hum. Mol. Genet.* 20 (7) (2011) 1253–1261.
- [45] E. Krieger, G. Vriend, YASARA View - molecular graphics for all devices - from smartphones to workstations, *Bioinformatics* 30 (20) (2014) 2981–2982.
- [46] C.H. Rodrigues, D.E. Pires, D.B. Ascher, DynaMut: predicting the impact of mutations on protein conformation, flexibility and stability, *Nucleic Acids Res.* 46 (W1) (2018) W350–W355.
- [47] W.J. Becktel, J.A. Schellman, Protein stability curves, *Biopolymers* 26 (11) (1987) 1859–1877.
- [48] J.A. Schellman, The thermodynamic stability of proteins, *Annu. Rev. Biophys. Biophys. Chem.* 16 (1987) 115–137.
- [49] A. Mittermaier, L.E. Kay, New tools provide new insights in NMR studies of protein dynamics, *Science* 312 (5771) (2006) 224–228.
- [50] A.K. Mittermaier, L.E. Kay, Observing biological dynamics at atomic resolution using NMR, *Trends Biochem. Sci.* 34 (12) (2009) 601–611.
- [51] S. Adinolfi, M. Nair, A. Politou, E. Bayer, S. Martin, P. Temussi, A. Pastore, The factors governing the thermal stability of frataxin orthologues: how to increase a protein's stability, *Biochemistry* 43 (21) (2004) 6511–6518.
- [52] A. Rufini, F. Cavallo, I. Condo, S. Fortuni, G. De Martino, O. Incani, A. Di Venere, M. Benini, D.S. Massaro, G. Arcuri, D. Serio, F. Malisan, R. Testi, Highly specific ubiquitin-competing molecules effectively promote frataxin accumulation and partially rescue the aconitase defect in Friedreich ataxia cells, *Neurobiol. Dis.* 75 (2015) 91–99.
- [53] A.R. Correia, S. Naik, M.T. Fisher, C.M. Gomes, Probing the kinetic stabilities of Friedreich's ataxia clinical variants using a solid phase GroEL chaperonin capture platform, *Biomolecules* 4 (4) (2014) 956–979.

SUPPLEMENTARY MATERIAL

Relationship Between Activity and Stability: Design and Characterization of Stable Variants of Human Frataxin

Ignacio Hugo Castro,¹ Mauro Bringas,² Davide Doni,³ Martin Ezequiel Noguera,^{1,4}
Luciana Capece,² Martín Aran,⁵ Matías Blaustein,^{1,6} Paola Costantini,³ and Javier
Santos^{1,6,7,*}

¹Instituto de Biociencias, Biotecnología y Biología Traslacional (iB³). Departamento de Fisiología y Biología Molecular y Celular, Facultad de Ciencias Exactas y Naturales, Universidad de Buenos Aires. Intendente Güiraldes 2160, Ciudad Universitaria, C1428EGA, Buenos Aires, Argentina.

²Departamento de Química Inorgánica, Analítica y Química Física, Facultad de Ciencias Exactas y Naturales, Universidad de Buenos Aires. Instituto de Química Física de los Materiales, Medio Ambiente y Energía (INQUIMAE CONICET), C1428EGA, Buenos Aires, Argentina.

³Department of Biology, University of Padova, Viale G. Colombo 3, 35131 Padova, Italy.

⁴Instituto de Química y Fisicoquímica Biológicas, Dr. Alejandro Paladini, Universidad de Buenos Aires, CONICET, Junín 956, C1113AAD, Buenos Aires, Argentina.

⁵Fundación Instituto Leloir, IIBBA-CONICET, and Plataforma Argentina de Biología Estructural y Metabólica PLABEM, Av. Patricias Argentinas 435, C1405BWE, Buenos Aires, Argentina.

⁶Consejo Nacional de Investigaciones Científicas y Técnicas. Rivadavia 1917. C1033AAJ. Buenos Aires, Argentina.

⁷Departamento de Química Biológica, Facultad de Ciencias Exactas y Naturales, Universidad de Buenos Aires. Intendente Güiraldes 2160, Ciudad Universitaria, C1428EGA, Buenos Aires, Argentina.

***Corresponding Author:** Javier Santos at javiersantosw@gmail.com

Running Title: Stable variants of Human Frataxin

Keywords: conformational stability, protein-protein interaction, iron-sulfur cluster assembly, frataxin.

Abbreviations: ACP, acyl carrier protein; CD, circular dichroism; CTR, C-terminal region; DLS, dynamic light scattering; Fe-S, iron-sulfur; FRDA, Friedreich's Ataxia; FXN, frataxin; HPLC, high-performance liquid chromatography; ISCU, iron-sulfur cluster assembly enzyme; ISD11, NFS1 interacting protein; NFS1, mitochondrial cysteine desulfurase enzyme; NMR, nuclear magnetic resonance; PAGE, polyacrylamide gel electrophoresis; PDB, Protein Data Bank; SDS, sodium dodecyl sulfate; SEC, size exclusion chromatography.

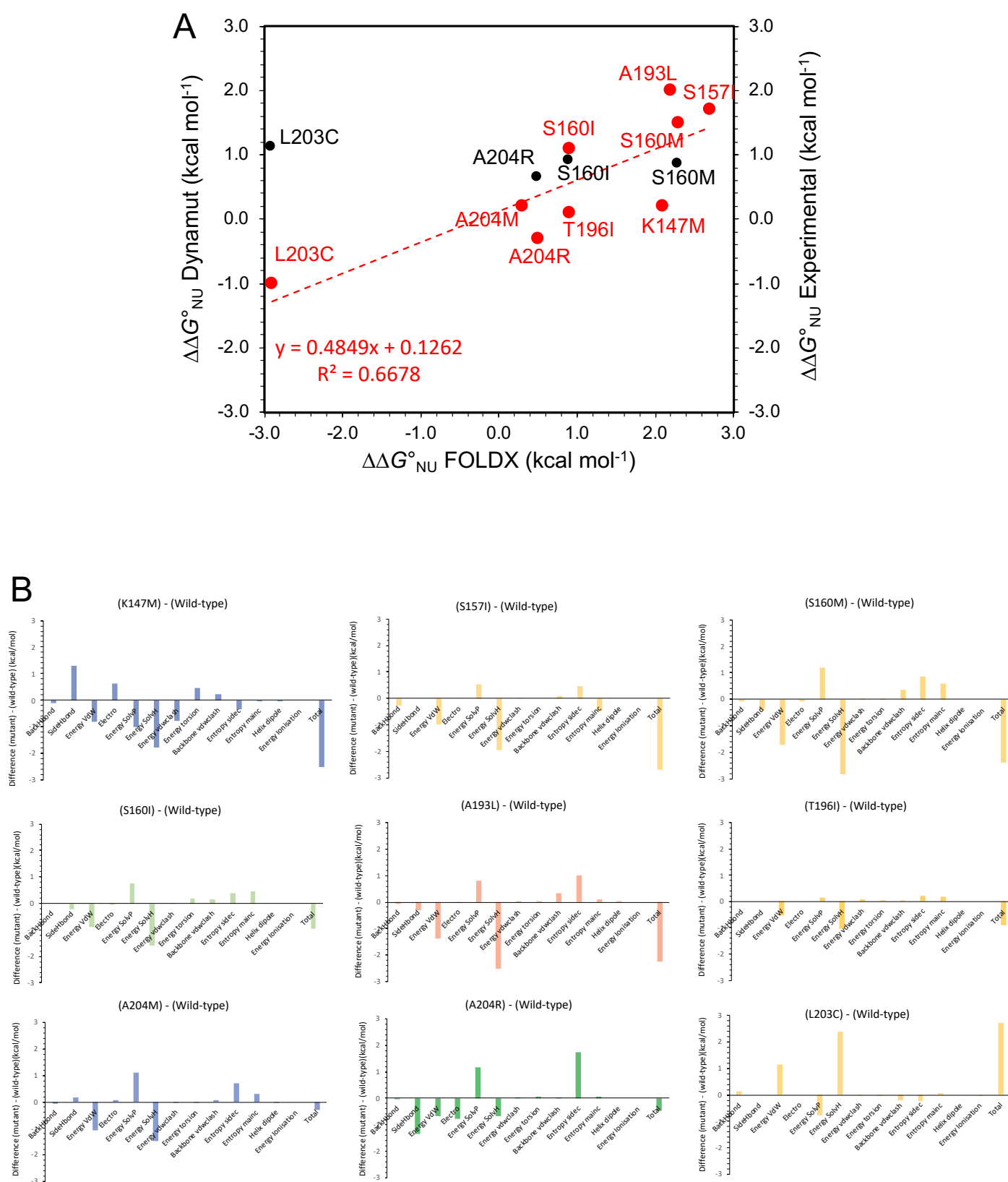


Figure S1. Predictions of the Mutational Effect on the Conformational Stability of FXN. (A) The predictions made by using FOLDX and Dynamut software are compared (Table 1). The results obtained for the point mutant variants prepared in this work

(K147M, S157I, S160I, S160M, A193L, T196I, L203C, A204M, A204R) are shown. Conformational stability values (from urea-induced unfolding, **Table 2**) for variants S160I, S1060M, L203, and A204R are plotted (black circles). It is worthy of mention that FOLDX is an empirical “physical” force field, whereas Dynamut evaluates the effect of mutations by means of a “statistical” force field which integrates the dynamics (as normal modes analysis). Thus, the way in which the conformational stability is calculated is different and both analyses might be complementary. Remarkably, both programs failed to predict the stabilizing effect of L203C mutation. For the reference we included the values corresponding to the experimental stability measured for the single point mutants using black circle. Positive and negative values of $\Delta\Delta G^{\circ}_{\text{NU}}$ indicate stabilization and destabilization, respectively **(B)** A detail of the energetics considered by FOLDX (Schymkowitz et al. 2005) for the set of point mutants is shown. For each mutant, each one of the FOLDX terms the free energy difference between mutant and wild-type (mutant-wild-type) was plotted. Negative values mean stabilization upon mutation whereas positive values mean destabilization compared to the wild-type protein.

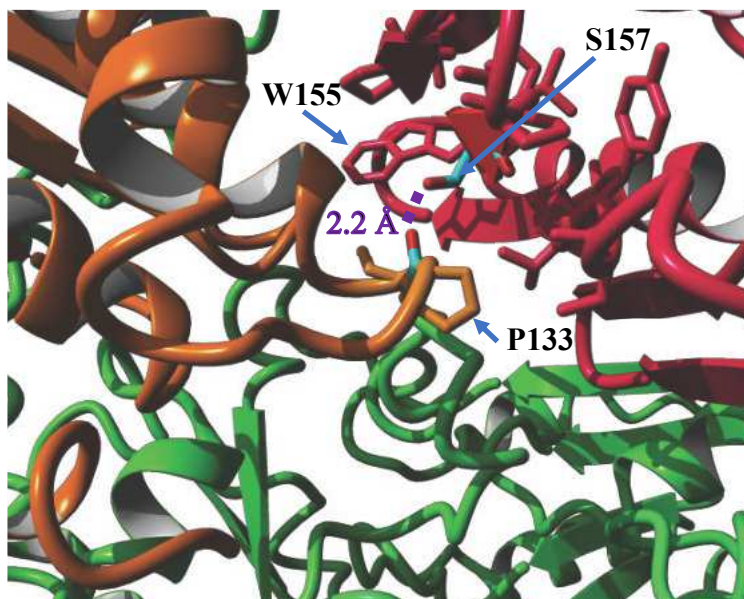


Figure S2. Involvement of S157 in the Interaction between FXN and ISCU. The interaction between hydroxyl oxygen of S157 (side chain) from FXN and the oxygen carbonyl of P133 (backbone) from ISCU is highlighted by a dashed line (violet, the distance= 2.2 Å). For the reference, the key residue W155 was included. FXN, ISCU and NFS1 are in red, orange and green, respectively. Figure was made using YASARA software and PDB ID: 6NZU.

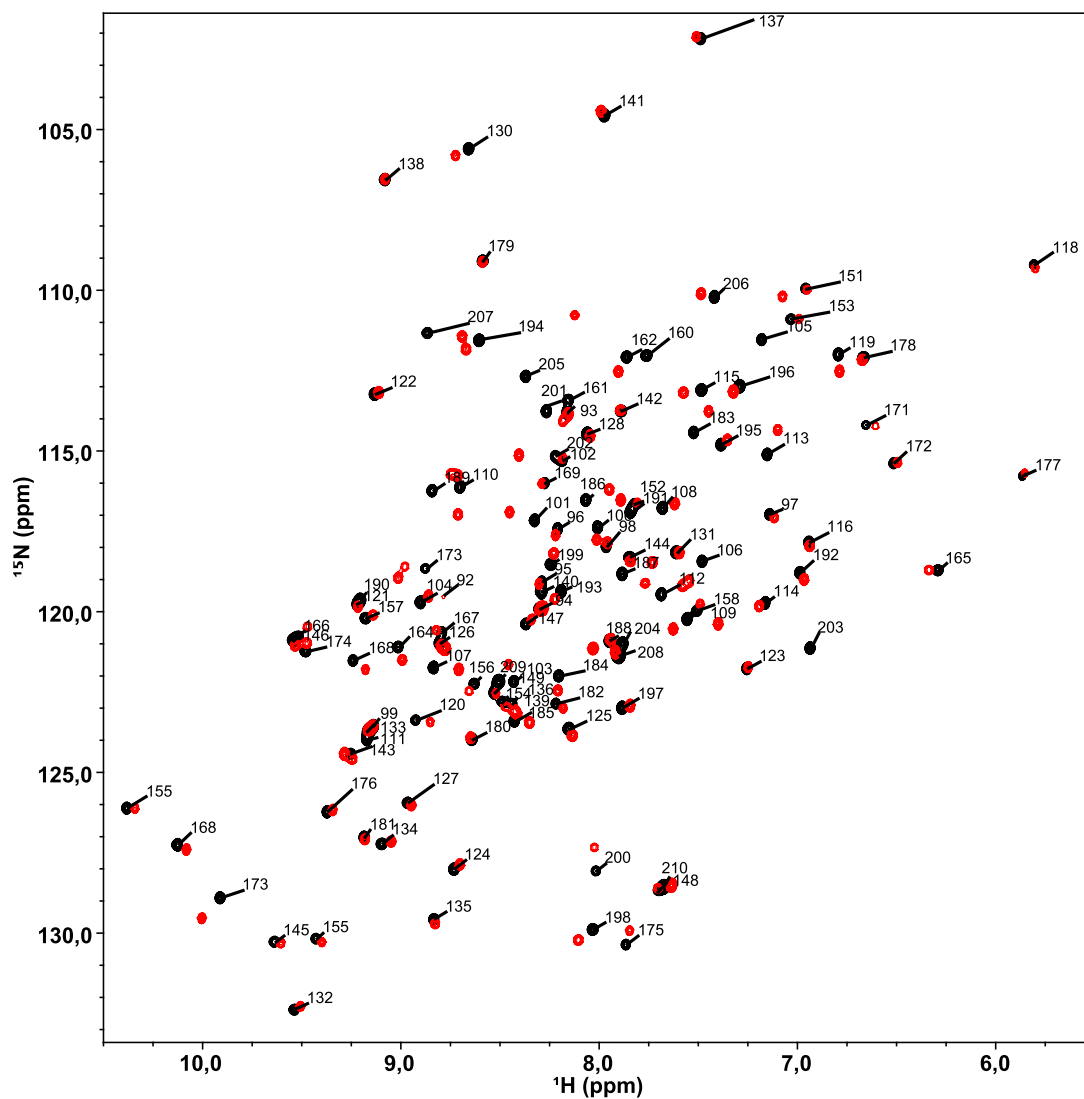


Figure S3. NMR Characterization of SILCAR Variant. ^1H - ^{15}N HSQC spectra corresponding to the wild-type FXN and SILCAR variant are shown in black and red, respectively. Peaks of the wild-type FXN are labeled. Residue numbering follows the same of the PDB ID 1EKG.

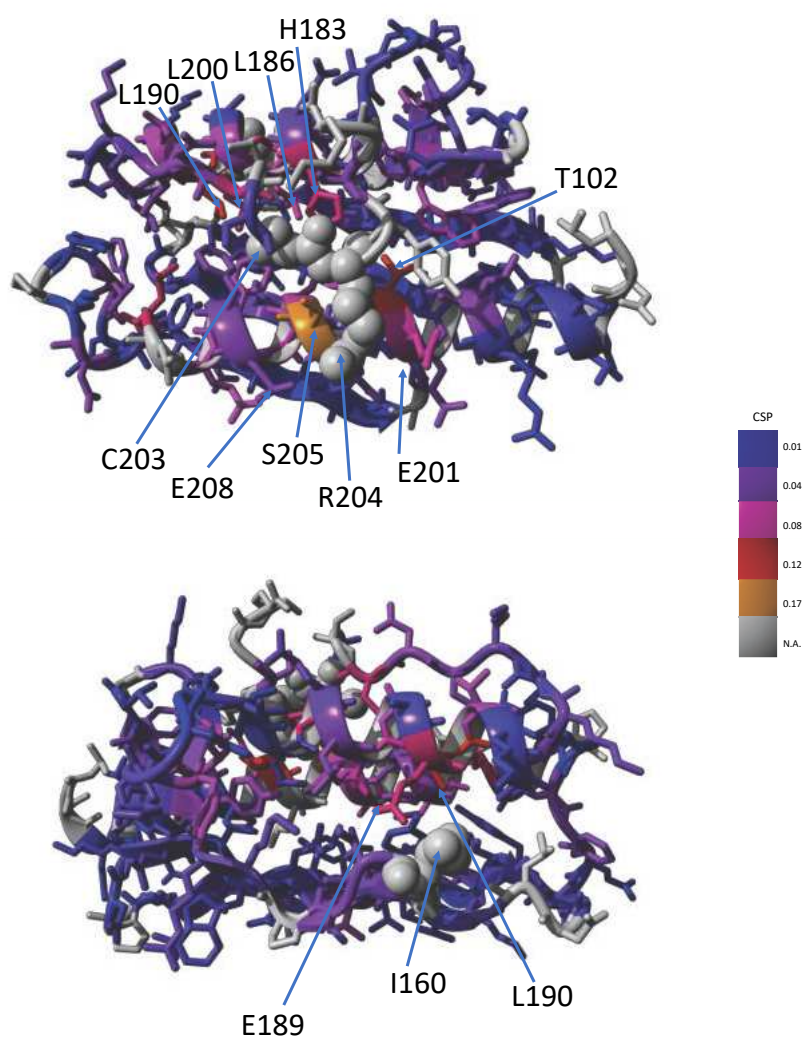


Figure S4. Chemical Shift Perturbation Mapped on the FXN Structure. Residues were colored according to their CSP values (Figure 10A). The corresponding CSP scale (from blue to orange: low to high CSP values, respectively) is shown on the right side. Prolines and residues that were not assigned in SILCAR are shown in grey. Residues that were mutated in SILCAR variant are in Van der Waals representation (I160, C203 and R204, in SILCAR). The labels of residues exhibiting high CSP values near the mutation sites are indicated. Two different views of the FXN structure are plotted, and the representations were made using YASARA software.

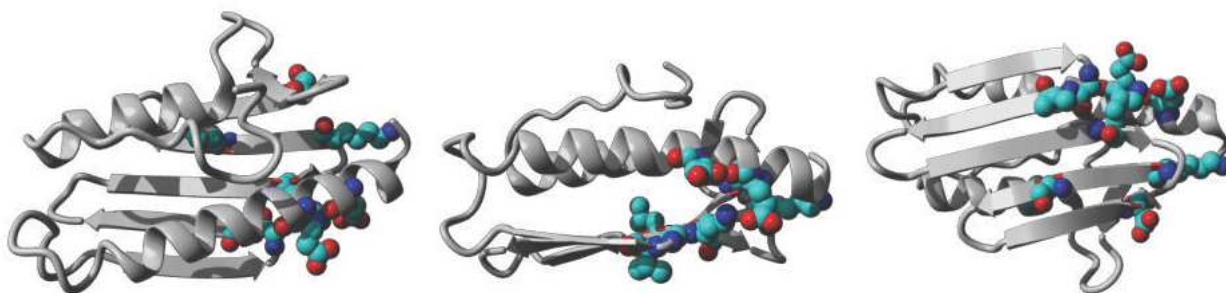


Figure S5. Residues Exhibiting high R_2^{obs} Values Mapped on the FXN structure. FXN is shown in three different orientations, and the group of residues included in the global fitting (E96, E100, G130, V131, K147, K152, L156 and D167) is shown in a van der Waals representation. Alternative fitting for relaxation data assuming different schemes to group residues with shared parameters were analyzed. None of these alternative schemes provided a better description of data than the global fit described in the manuscript. The representations were made using YASARA software.

Table S1. Quantitative analysis of the proteolytic profile of FXN variants. The RP-HPLC profiles shown in Figure 6 were analyzed.

Variant	Remaining intact protein (%) ¹	Relative protease resistance ²
Wild-type FXN	12	1
S160I	32	2.7
S160M	10	0.9
L203C	20	1.7
L204R	55	4.7
SILCAR	73	6.3

¹Peak area ratios of intact FXN in protease-treated to untreated samples (%). Because UV signal in the untreated sample was saturated, we can only estimate a lower bound for this value.

²Ratio of remaining intact protein in FXN variant to the wild-type.

References

Schymkowitz J, Borg J, Stricher F, Nys R, Rousseau F, Serrano L (2005) The FoldX web server: an online force field. *Nucleic Acids Res* 33 (Web Server issue):W382-388



Article

Effects of Fe²⁺/Fe³⁺ Binding to Human Frataxin and Its D122Y Variant, as Revealed by Site-Directed Spin Labeling (SDSL) EPR Complemented by Fluorescence and Circular Dichroism Spectroscopies

Davide Doni ¹, Leonardo Passerini ², Gérard Audran ³, Sylvain R. A. Marque ³, Marvin Schulz ³, Javier Santos ^{4,5} , Paola Costantini ¹, Marco Bortolus ^{2,*} and Donatella Carbonera ²

¹ Department of Biology, University of Padova, Viale G. Colombo 3, 35131 Padova, Italy; davide.doni.2@phd.unipd.it (D.D.); paola.costantini@unipd.it (P.C.)

² Department of Chemical Sciences, University of Padova, Via F. Marzolo 1, 35131 Padova, Italy; leonardo.passerini@studenti.unipd.it (L.P.); donatella.carbonera@unipd.it (D.C.)

³ Institut de Chimie Radicale, Aix Marseille Université, CNRS, ICR, UMR 7273, Case 551, Ave Escadrille Normandie Niemen, CEDEX 20, 13397 Marseille, France; g.audran@univ-amu.fr (G.A.); Sylvain.marque@univ-amu.fr (S.R.A.M.); marvin.schulz@univ-amu.fr (M.S.)

⁴ Departamento de Química Biológica, Instituto de Biociencias, Biotecnología y Biomedicina (iB3-UBA), Facultad de Ciencia Exactas y Naturales, Universidad de Buenos Aires, Intendente Güiraldes 2160—Ciudad Universitaria, 1428EGA CONICET, Godoy Cruz 2290, Buenos Aires C1425FQB, Argentina; javiersantosw@gmail.com

⁵ Instituto de Química y Fisicoquímica Biológicas Dr. Alejandro Paladini, Universidad de Buenos Aires, CONICET, Junín 956, Buenos Aires 1113AAD, Argentina

* Correspondence: marco.bortolus@unipd.it

Received: 14 November 2020; Accepted: 15 December 2020; Published: 17 December 2020



Abstract: Frataxin is a highly conserved protein whose deficiency results in the neurodegenerative disease Friederich's ataxia. Frataxin's actual physiological function has been debated for a long time without reaching a general agreement; however, it is commonly accepted that the protein is involved in the biosynthetic iron-sulphur cluster (ISC) machinery, and several authors have pointed out that it also participates in iron homeostasis. In this work, we use site-directed spin labeling coupled to electron paramagnetic resonance (SDSL EPR) to add new information on the effects of ferric and ferrous iron binding on the properties of human frataxin *in vitro*. Using SDSL EPR and relating the results to fluorescence experiments commonly performed to study iron binding to FXN, we produced evidence that ferric iron causes reversible aggregation without preferred interfaces in a concentration-dependent fashion, starting at relatively low concentrations (micromolar range), whereas ferrous iron binds without inducing aggregation. Moreover, our experiments show that the ferrous binding does not lead to changes of protein conformation. The data reported in this study reveal that the currently reported binding stoichiometries should be taken with caution. The use of a spin label resistant to reduction, as well as the comparison of the binding effect of Fe²⁺ in wild type and in the pathological D122Y variant of frataxin, allowed us to characterize the Fe²⁺ binding properties of different protein sites and highlight the effect of the D122Y substitution on the surrounding residues. We suggest that both Fe²⁺ and Fe³⁺ might play a relevant role in the context of the proposed FXN physiological functions.

Keywords: frataxin; iron; EPR; fluorescence; CD; Fe-S cluster assembly machinery

1. Introduction

Frataxin (FXN) is a small acidic protein that is highly conserved in most organisms, from bacterial to mammalian. A low FXN expression, primarily caused by an abnormal GAA triplet repeat expansion in the first intron of the frataxin gene, is associated with the neurodegenerative disease Friedreich's ataxia (FRDA; OMIM 229300) [1]; in addition, several FXN point mutations including nonsense, missense, insertions and deletions have been associated with compound heterozygous FRDA patients [1–4]. The main biochemical feature of FRDA is a large depletion of proteins relying on iron-sulphur clusters (ISC) for function (such as those of the mitochondrial respiratory chain complexes I, II and III or aconitase) with an accompanying increase in mitochondrial iron and oxidative stress [5–8].

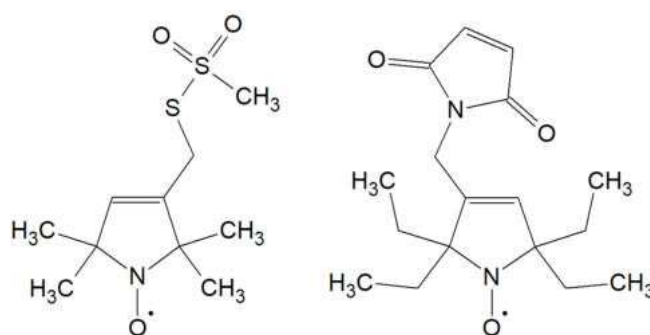
Human FXN is nuclear encoded, expressed in the cytoplasm as a precursor of 210 amino acids, and then imported into the mitochondria, where it undergoes two-step maturation by the mitochondrial processing peptidase (MMP) [9–11]. MMP first cleaves a portion of the N-terminus, the mitochondrial import signal, originating an intermediate form (FXN 42–210), and with a further cleavage MMP produces the mature FXN 81–210, which is the most abundant form found both in normal individuals and in FRDA patients [9]. Sequence alignment studies have distinguished the N-terminal frataxin region, which is intrinsically unfolded and poorly conserved among the different species, from the C-terminus highly conserved block of about 100–120 amino acids, which is considered the most important part for protein function [12]. The 3D structure of human FXN has been determined by both X-ray crystallography [13] and NMR [14], and the agreement between the results suggests the high stability and rigidity of the structure. The structure of the conserved C-terminus (81–210) consists of a mixed alpha-beta fold with two helices packing against a contiguous anti-parallel beta sheet, assembled in the sequence alpha-(beta)₇-alpha, which, despite its simplicity, is very rare. The N-terminal tail of human FXN (residues 81–92) was shown to be intrinsically unfolded [14]. Despite harboring a potential iron binding site [15], it is often truncated (obtaining FXN 90–210) for *in vitro* studies.

The proposed role of FXN as an allosteric regulator of the biosynthetic iron-sulphur cluster (ISC) machinery has recently found further confirmations [16–19]. The ISC biosynthetic pathway takes place in the mitochondria and is a multi-step process involving several proteins [19–21]: the early cluster assembly requires a yet-unidentified iron source and is performed by a pentameric quaternary protein complex. The complex is formed by FXN, the cysteine desulfurase NFS1 (extracting the sulphide from free cysteine), ISD11 (an accessory protein), ACP (an acyl-carrier protein), and ISCU (the scaffold protein on which the clusters are assembled). The structure of this complex has been recently solved via cryo-electron microscopy, showing FXN to be at the interface between NFS1 and ISCU [16]. Additionally, given its well-known ability to bind ferrous and ferric ions, FXN has been proposed as the iron donor ISC machinery complex [22–24]. Finally, FXN has been proposed as a key regulator of iron homeostasis [25] and ferroptosis [26,27], a recently identified iron-dependent form of cell death [28].

The latter functions point to the critical importance of the interaction between iron ions and FXN. While the binding of ferrous/ferric iron is ascertained through a wide range of chemical and biological techniques, some incongruities among the collected data remain. Using fluorescence analysis and calorimetry titrations with both ferric and ferrous iron, it was found that human frataxin 81–210 binds 6–7 ferrous/ferric ions [22]. Differently, through a combination of fluorescence, NMR, and mass spectrometry, a binding stoichiometry of only three equivalents was reported for Fe^{2+/3+} and Co²⁺ ions [15]. An NMR study concluded that FXN binds only one Fe²⁺ equivalent and has no binding interaction with Fe³⁺ [24]. In a previous paper, using EPR and NMR spectroscopies, we showed that FXN is able to bind both iron forms [29]. Another contested feature of FXN is the tendency to aggregate in presence of ferrous or ferric ions. Mature human FXN 81–210, and also yeast and bacterial orthologs (Yfh1 and CyaY), do not aggregate *in vitro* when overexpressed and purified. However, only human FXN has been reported to retain the monomeric form when added with ferrous ions, while the orthologs show a clear tendency to aggregation [30,31]. While human FXN aggregation in the presence of ferric ions has been alternatively dismissed [32] or confirmed [33], Yfh1 and CyaY are

prone to aggregation [34]. Since aggregation may affect the iron binding properties, it is important to determine its threshold in terms of protein concentration and compare it to the FXN concentrations commonly employed for the experimental determination of iron affinity.

In this work, we focus on the effects of ferrous/ferric iron binding on possible conformational changes of the mature human FXN 90–210 and its D122Y variant, the only pathological variant identified so far in the iron binding region. The effects of iron were explored also as a function of pH and protein concentration. We make use, for the first time, of the site-directed spin labeling (SDSL) technique coupled with electron paramagnetic resonance (EPR). This is a powerful tool for detecting changes in structure, dynamics, and oligomerization in proteins and was used here to get information on the protein structural changes following iron binding. We adopted two different spin labels, MTSSL and the reduction-resistant M-TETPO (see Scheme 1), to work with Fe^{3+} and Fe^{2+} , respectively. The EPR investigation has been supplemented by tryptophan fluorescence quenching and circular dichroism measurements to allow also comparison with previously adopted methods.



Scheme 1. The MTSSL and the M-TETPO nitroxide spin labels.

2. Results

2.1. Structural Remarks and Choice of Labeling Sites

The physiological role of human FXN is still uncertain, as mentioned in the introduction, but its ability to bind iron in its ferrous and ferric oxidation states, along with other ions, seems to be a key part of its function. The iron binding region of WT human FXN and that of its pathological variants has been studied previously [29,35]: FXN uses Asp and Glu residues to bind iron via chelation by carboxylate groups. All of the long alpha-helix, located towards the N-terminal portion of the mature protein, as well as the following loop region, are rich in negatively charged residues and constitute the main iron-binding region (the positions of these residues are shown in orange in Figure 1). D122Y is the only pathological variant currently known that carries a mutation in the iron-binding region (shown in yellow in Figure 1); this mutation has been shown to affect the conformation of the loop region and to influence iron binding [29].

The spectroscopic study of human FXN reported so far have taken advantage of the three native Trp residues (W155, W168, W173) for fluorescence experiments; the Trp are shown in green in ball-and-stick representation in Figure 1. The W155 residue is in the beta-sheet region, exposed to the solution: this Trp is involved in the interface of the FXN/ISCU/NFS1 complex [16], and the W155R variant is one of the known pathological mutations [2]. The other two Trp are spatially close together, W168 and W173 are separated by about 0.6 nm, while W155 is more distant (1.4/1.7 nm to W168/172 respectively); W168 is partially exposed to the solution, while W173 is buried. The fluorescence probably comes from one or two of them since they are very close to each other and homo-FRET can easily occur.

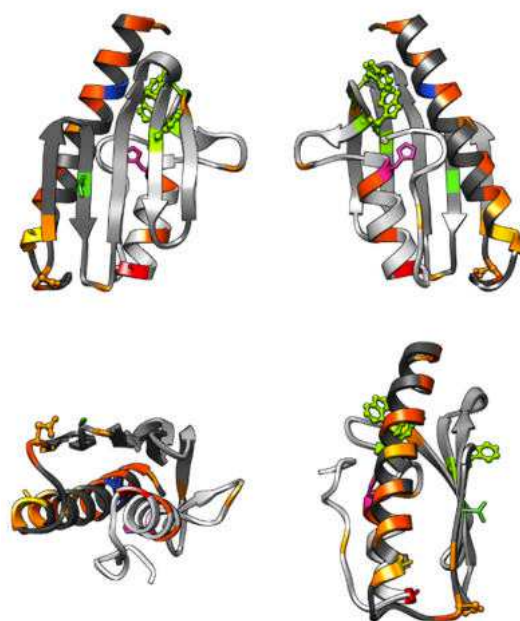


Figure 1. Structure of human FXN (PDB.ID 1EKG) from different angles, the N-terminus is in dark grey, the C-terminus is white. The Glu and Asp residues are colored dark and light orange, respectively. The three native Trp residues are colored bright green and shown in ball and stick representation. The spin labeling sites—A99 (blue), A114 (yellow), T133 (green), H183 (pink), A193 (red)—are shown in stick representation. The D122 residue in light orange, the site of the pathological D122Y mutation, is shown in ball and stick representation.

FXN has no native cysteine residues, and thus for SDSL EPR studies, cysteine mutants must be designed and expressed to place the spin label in the desired position. Five protein sites (namely A99, A114, T133, H183, A193, see Figure 1) were chosen with the aim of mapping possible changes in the protein structure and dynamics upon ferrous/ferric iron addition, probing the response of different protein regions. The A99 site is a buried site located at the beginning of the long alpha-helix, close to the iron binding region; A114, which is close to iron-binding sites and located to the end of the long alpha-helix, has been expressed both in the WT and in the D122Y variant; T133 belongs to the beta-sheet region involved in the interaction with the complex with ISCU/NFS1 [16]; H183 is located at the beginning of the second alpha helix, not involved either in the iron binding or the complex with ISCU/NFS1; A193 is located at the end of the second alpha helix, spatially close to the iron binding region. These sites have been singly mutated to Cys for the subsequent coupling reaction with nitroxide spin probes. Please note that the A99 position has a very limited solvent accessibility; therefore, it showed limited labeling efficiency (about 10%) and was thus viable only for the analysis with Fe^{2+} that was performed at higher concentration.

Since FXN is a small protein (MW = 14 kDa), its reorientation in aqueous solutions, at room temperature, is very rapid. This motion would mask any local contribution to the EPR spectral lineshape proper of the spin label; therefore, it is necessary to slow down the protein tumbling (quantified by the rotational correlation time, τ_c) performing the EPR experiments in viscous solution. Ficoll PM70, a synthetic glucose polymer, at a 28% *w/w* concentration, was suggested as one of the better thickening agents [36]. We calculated the FXN rotational correlation time τ_c , on the basis of the protein structure, at the viscosity of a buffer solution ($\eta_{\text{Water}} = 8.94 \times 10^{-4} \text{ Pa} \times \text{s}$) and at the viscosity of a 28% *w/w* Ficoll solution ($\eta_{\text{Ficoll}} = 1.92 \times 10^{-2} \text{ Pa} \times \text{s}$) using the program by M. Zerbetto et al. [37]: in buffer, $\tau_{c\text{Water}}$ was 5.6 ns, which is on a timescale comparable with that of the motions of the spin label side chain; in Ficoll, $\tau_{c\text{Ficoll}}$ was 122 ns, slow enough to observe an EPR spectral shape influenced exclusively by the spin probe and backbone mobility, rather than the protein tumbling.

2.2. EPR Spectra of FXN Interacting with Fe^{3+}

The EPR spectra of FXN mutants in a 28% *w/w* Ficoll solution, were recorded at increasing protein: Fe^{3+} molar ratios at different FXN concentrations to explore both the effects of iron binding and the influence of protein concentration on the binding equilibrium. The spectra of all mutants at 10 μ M concentration, labeled with MTSSL, are reported in Figure 2. As previously noted, mutant A99C showed very limited labeling efficiency (about 10%), which made it impossible to record EPR spectra at 10 μ M concentration.

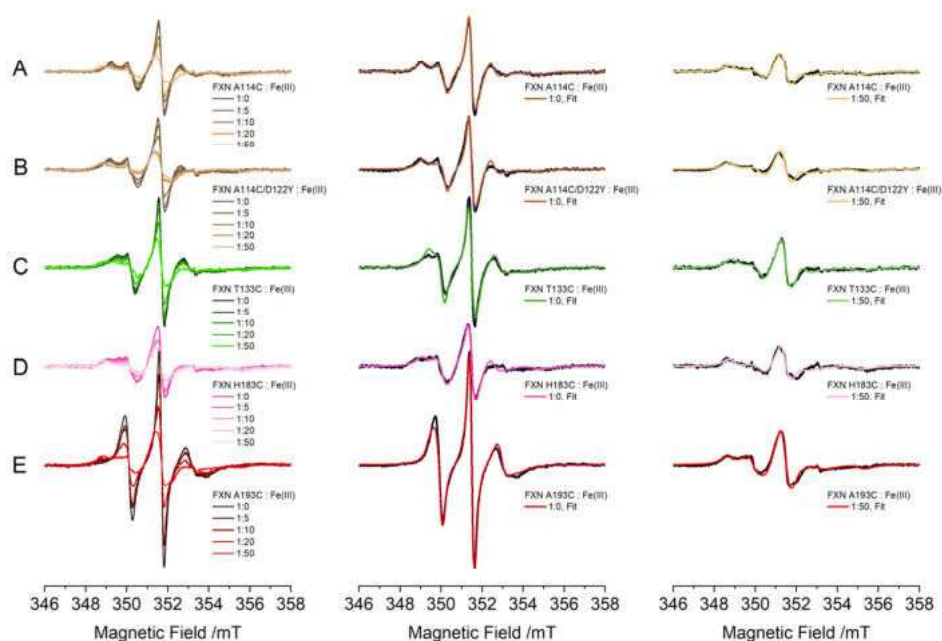


Figure 2. EPR spectra of FXN mutants at increasing protein: Fe^{3+} molar ratios from 1:0 to 1:50; protein concentration 10 μ M, MTSSL label. The colors are the same of the positions highlighted in Figure 1: (A) A114C—brown; (B) A114C/D122Y—brown; (C) T133C—green; (D) H183C—pink; (E) A193C—red. Central and Right panels: EPR spectra (black) and simulations (color) of FXN mutants at protein: Fe^{3+} molar ratios 1:0 (central) and 1:50 (right).

In the absence of iron, each mutant shows a characteristic spin label mobility proper of the site, which confirms that the protein molecular tumbling has been slowed enough by the Ficoll solution; this allows spectral differences to be distinguished due to the specific local motion of the spin probe. Among these mutants, A193C showed the least restrained mobility, suggesting that WT FXN secondary structure is not very rigid at the edge of its second alpha helix. On the contrary, A114C, which is in a similar position at the end of FXN long alpha helix, has a more restrained mobility indicating a stable helical terminal. The other two labeled sites show a mobility that is intermediate between those two. In the A114C-D122Y mutant, MTSSL shows minimal differences in the spectra compared to the WT form, whereas the M-TETPO label shows some difference, the WT protein being more rigid than the pathological mutant in this region (*vide infra*).

Upon addition of increasing amounts of Fe^{3+} , all the labeled positions show a progressively restrained mobility both for the WT and the D122Y variant. In fact, the spectral broadening proceeds until an almost complete spin label immobilization is observed, at all labeled sites, as shown by the spectra at a FXN: Fe^{3+} 1:50 ratio in Figure 2. The onset of the immobilization, at a protein concentration of 10 μ M, can be observed after the addition of about five equivalents of ferric iron. The rotational correlation time determined from the simulations of the spectra increases more than 2-fold going from a 1:0 to a 1:50 ratio, and, concurrently, the order parameter increases for all positions as shown

in Table 1: this indicates that the motion of the labeled sites becomes slower and more constricted, consistent with the formation of a new interfacial contact hindering the probe mobility.

Table 1. The rotational correlation times of the different FXN labeled positions in 28% *w/w* Ficoll solution. The *g* tensor principal components are: $g_{xx} = 2.0088$, $g_{yy} = 2.0070$, $g_{zz} = 2.0030$. The hyperfine tensor principal components are: $A_{xx} = 0.79$ mT; $A_{yy} = 0.54$ mT; $A_{zz} = 3.68$ mT. The spectrum of A193C at a FXN:Fe³⁺ 1:50 ratio is characterized by two components.

Position	FXN:Fe ³⁺ 1:0			FXN:Fe ³⁺ 1:50		
	β_D	S	τ_c	β_D	S	τ_c
A114C	17°	0.44	0.7 ns	0°	0.53	5.3 ns
A114C/D122Y	17°	0.44	0.7 ns	0°	0.53	5.3 ns
T133C	20°	0.36	0.9 ns	0°	0.53	3.8 ns
H183C	42°	0.44	3.9 ns	0°	0.53	8.4 ns
A193C	45°	0.44	1.8 ns	0°	0.53	3.6 ns
				0°	0	2.2 ns

The immobilization of the protein depends not only on the protein:iron ratio, but also on the absolute protein concentrations. The dependence of the immobilization on protein concentration and pH has been explored using the A193C mutant that has the highest sensitivity to immobilization since it is the one that changes its mobility most dramatically; the zoom of the left shoulders of the EPR spectra are shown in Figure 3A. We must note that ferric iron at neutral pH is not present in solution as a free isolated ion, and the main species are colloidal oxo-hydroxo suspensions. The formation of these complexes upon addition of Fe³⁺ stock solution has a very strong acidifying effect on the sample solution, and even small additions of Fe³⁺ lead to a drop in pH. Therefore, we checked the effective pH as a function of Fe³⁺ concentration as shown in Figure 3B, right axis: under our buffering conditions, nominal Fe³⁺ concentrations of 1 mM and above steadily drop the pH below 6.5. Since FXN isoelectric point is IP = 4.9 [38], Fe³⁺ concentrations of 1.5 mM and above will cause protein aggregation by acidic denaturation rather than by a specific iron effect. Please note that EPR, fluorescence and CD experiments detailed in the text are all performed at pH \geq 6.8.

The gradual spectral changes may be analyzed and reconstructed as combination of the two “pure” contributions (an example of the analysis is reported in the Supporting Information, Figure S1): (1) the initial, more mobile, nitroxide lineshape and (2) the final immobilized one, which does not change upon further Fe³⁺ addition. Importantly, the spectral analysis suggests that there are no further intermediate conformational states at significant concentration. The obtained percentage of immobilized protein (Figure 3B, left axis) has been plotted as a function of ferric iron nominal concentration concurrently with the effective pH of the solution (Figure 3B, right axis). Please note that irrespective of the final pH value, the immobilized shape is always the same, suggesting that high amounts of ferric iron lead to a denatured and/or strongly aggregated protein.

The immobilization starts at progressively lower FXN:Fe³⁺ ratios as the protein concentration gets higher, as shown by the plot in Figure 3C. At the lowest concentration that we explored, 5 μ M, the immobilization starts at 25 μ M Fe³⁺, but the spectra are only partially immobilized (< 20%) even at a 1:20 FXN:Fe³⁺ molar ratio.

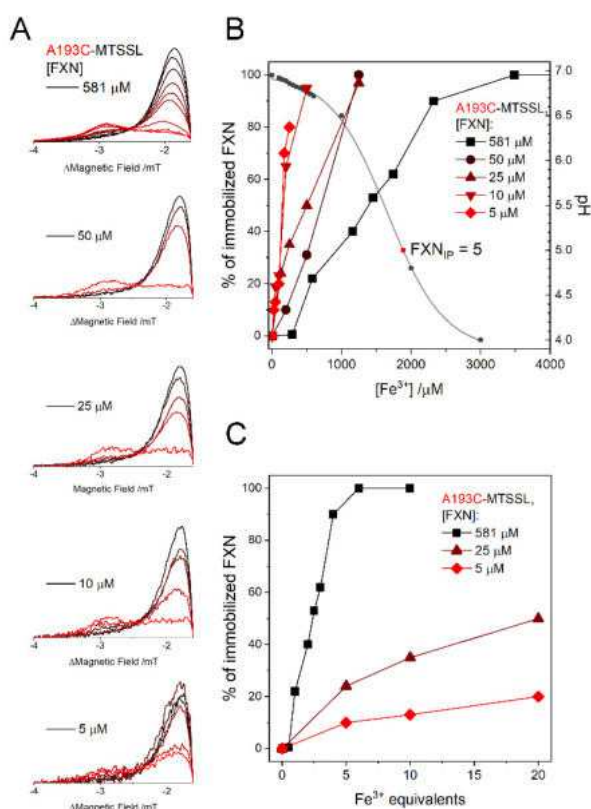


Figure 3. (A) From top to bottom, the left shoulder of the EPR spectrum of the A193C mutant labeled with MTSSL at progressively lower protein concentrations, the lighter the color the higher the FXN: Fe³⁺ ratio. (B) The percentage of immobilized protein (left axis, big dots) or the pH (right axis, small dots) vs. the nominal ferric iron concentration for different protein concentrations. (C) The percentage of immobilized protein vs. the FXN: Fe³⁺ molar ratio for three protein concentrations.

Detection of the EPR spectra in buffered aqueous solution without the addition of Ficoll was also performed in labeled FXN. The EPR spectra were detected both in the absence of iron and in the presence of Fe³⁺. In the absence of iron, the spectra show three sharp peaks in agreement with the averaging effect on the spectra exerted by the protein tumbling due to the small size of the protein. Upon addition of Fe³⁺, the spectral broadening occurs as it was observed for the samples in Ficoll; the effect, however, is much less noticeable since the intensity is dominated by the sharper mobile component (see Figure S2 in the Supporting Information). Centrifugation of the sample, followed by EPR analysis of the supernatant, showed that the protein fraction that is immobilized precipitates along the colloidal iron, leaving behind the fraction that showed no motional broadening (see Figure S2). These results confirm the suggestion that Fe³⁺ addition promotes protein oligomerization [33], slowing down the molecular tumbling due to the bigger size of the Fe³⁺-FXN formed complexes. Analogous results were obtained in centrifugation experiments performed in Ficoll solutions (not shown); however, they are less clear cut, since a density gradient is formed.

The reversibility of the immobilization effect has been checked by adding EDTA in a three-fold excess relative to Fe³⁺ to remove the bound iron ions. After a one-hour incubation, the amount of immobilized component decreases (see the Supporting Information, Figure S3), suggesting that the aggregation is at least partially reversible.

2.3. EPR Spectra of FXN Interacting with Fe²⁺

EPR spectra have been collected on the different FXN mutants after addition of increasing amounts of Fe²⁺ to the samples, to investigate possible conformational changes induced by the binding of the divalent ion, which could be relevant for protein function. To prevent iron oxidation, the proteins have

been prepared in strictly anaerobic conditions from the labeling stage and samples capillaries were prepared in an anaerobic glove box and sealed with wax at both ends.

We observed a very rapid signal loss in FXN labeled with MTSSL following the addition of Fe^{2+} . The reason for this lies in the quick reduction of the MTSSL nitroxide function to the EPR-silent nitroxylamine with concurrent oxidation of Fe^{2+} to Fe^{3+} : this unwanted reaction not only results in signal loss, but also makes it impossible to separate the spectral changes induced by Fe^{2+} from those induced by Fe^{3+} . For this reason, we changed the spin label to M-TETPO, a non-commercial spin label designed to be resistant to the cellular reducing environment [39]. Indeed, we verified that M-TETPO is also resistant to the reduction by Fe^{2+} in solution, making it the ideal probe in EPR studies of Fe^{2+} binding. We also confirmed that the M-TETPO-labeled protein shows the same behavior with Fe^{3+} as the MTSSL-labeled one (data reported in the Supporting Information, Figure S4).

The EPR spectra of FXN mutants labeled with M-TETPO in the presence of ferrous iron are reported in Figure 4 (samples in Ficoll, protein concentration 50 μM), the spectra recorded at 10 μM protein concentration were identical to the ones reported here save for the worse S/N ratio. When iron is not present, the spectra show a reduced mobility compared to FXN labeled with MTSSL, indicating that the side chain of M-TETPO has less degrees of freedom than the one of MTSSL. As mentioned above, unlike MTSSL, M-TETPO differentiates the A114C-D122Y mutant from the WT counterpart, the spectra of the former revealing a faster mobility which indicates a change in the local structure of the D122Y FXN around residue 114. The difference between the labels is determined by the different conformers and mobility of their sidechain.

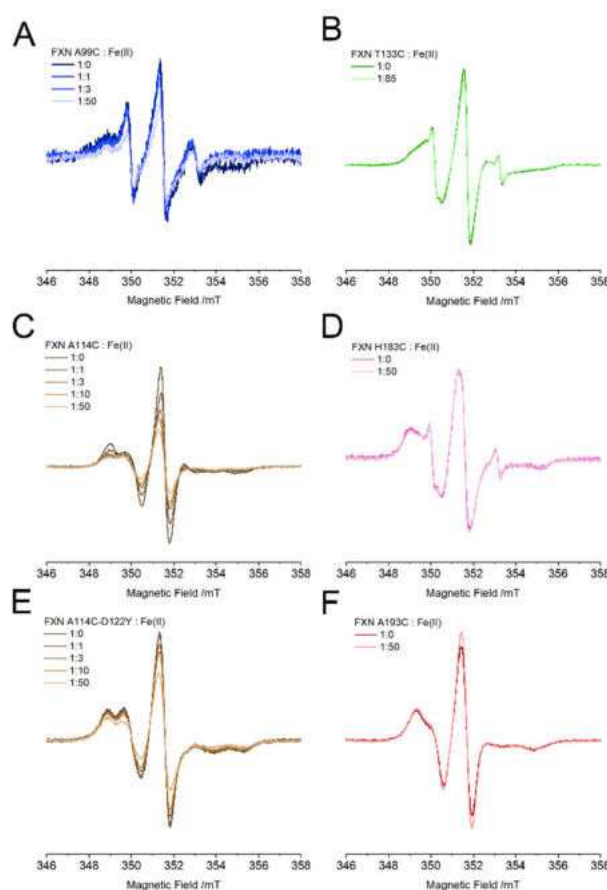


Figure 4. EPR spectra of different FXN mutants at increasing protein: Fe^{2+} molar ratios from 1:0 to 1:50; protein concentration 50 μM , M-TETPO label. (A) A99C—blue; (B) T133C—green; (C) A114C—brown; (D) H183C—pink; (E) A114C-D122Y brown; (F) A193C—red.

Once ferrous iron is added to the solution, we observe that the spectra of the sites that are located far from the iron binding region are unchanged even at a 1:50 FXN: Fe²⁺ ratio (T133, H183, A193, Figure 4B,D,F), while those close to the iron binding sites show an EPR intensity that gets progressively lower at higher iron content (A99, A114, A114-D122Y, Figure 4A,C,E).

The signal loss is less marked for the D122Y pathological variant than for the WT: at a 1:50 FXN: Fe²⁺ ratio, the signal loss for A114C-D122Y (and for A99C) is 40%, while that for A114C raises to 65%. For the A114 position the signal loss is accompanied by a change in shape, whereas no change is observed for the A99 position: this difference arises from the intrinsic mobility of the probe sidechain in the two positions and has been discussed more in-depth in the Supporting Information (Figures S5 and S6). The signal loss is independent of the presence of Ficoll (data not shown), and we verified that it is caused by a redox reaction of the M-TETPO nitroxide with Fe²⁺ as observed for MTSSL. To test this hypothesis, we removed protein-bound Fe²⁺ by treatment with 1,10-phenanthroline (PHEN) which forms a strongly colored red complex with Fe²⁺. Treating the sample with a three-fold molar excess of PHEN relative to iron leads to quantitative removal of Fe²⁺ from FXN, as evaluated spectrophotometrically by UV-Vis under anaerobic conditions from the absorption band at $\lambda_{\max} = 508$ nm (see Supporting Information, Figure S7) [40]. When stripping Fe²⁺ with PHEN from FXN, the solution turns red but the EPR signal is not restored, confirming that an irreversible reduction of the nitroxide has taken place.

We can then hypothesize that the signal loss is directly correlated with the presence of a nearby Fe²⁺ binding site. Indeed, signal loss does not originate from Fe²⁺ free in solution, as confirmed by the lack of effect in the three mutants labeled at positions far away from the iron-binding region. When a ferrous iron is close to the nitroxide of the spin label, the redox reduction can be favored by the vicinity between the redox partners, and nearby amino-acid residues might also favor the electron transfer kinetics. The exact mechanism will be tested in a future work; nevertheless, the redox reaction is a clear sign of proximity and this makes M-TETPO an interesting probe able to detect nearby Fe²⁺ binding sites.

2.4. Fluorescence Spectra of FXN Interacting with Fe³⁺

The quenching effect of Fe³⁺ addition to the fluorescence emission of the three Trp residues of wild type and D122Y FXN proteins was explored. Relative to what was previously reported [29], here we worked at a seven-fold lower protein concentration ([FXN] = 1.4 μ M) and with a greater focus on the sub-stoichiometric region since, as shown by the EPR experiments reported above, aggregation starts to occur when adding more than few equivalents. The fluorescence signals and their quenching are shown in Figure 5; quenching is reported as $(F - F_0)/F_0$, where F is the fluorescence intensity at the maximum of emission at a given amount of quencher and F₀ the intensity in the absence of quenchers. The normalized signal shapes of the WT and the D122Y FXN are identical, as expected (reported in the Supporting Information, Figure S8). In addition, the normalized emission profiles in the absence of iron and at 9.5 equivalents of iron do not show any difference neither in the position of the maxima nor in the shape of the band, indicating that the three Trp residues are equally quenched by the presence of Fe³⁺. The quenching of Trp fluorescence by Fe^{2+/3+} is likely due to an energy transfer mechanism, which is a distance dependent process [41]. Due to the short distance between Trp residues and to the homo-FRET, the observed quenching of the fluorescence could be due only to Fe^{2+/3+} ions close to any of the Trp residues.

The signal decreases sharply in the sub-stoichiometric region, levels off somewhat around 1.5 equivalents of Fe³⁺ and then falls off more sharply again at six equivalents and beyond. Visual inspection of the cuvette revealed no visible precipitate in the sub-stoichiometric region, but substantial precipitate already at six equivalents. It is, therefore, impossible to reliably assess a binding constant for Fe³⁺ with human FXN using fluorescence due to the presence of Fe³⁺-induced FXN aggregates (in agreement with the EPR results reported above). The WT and the D122Y variant show almost no difference in the quenching profile.

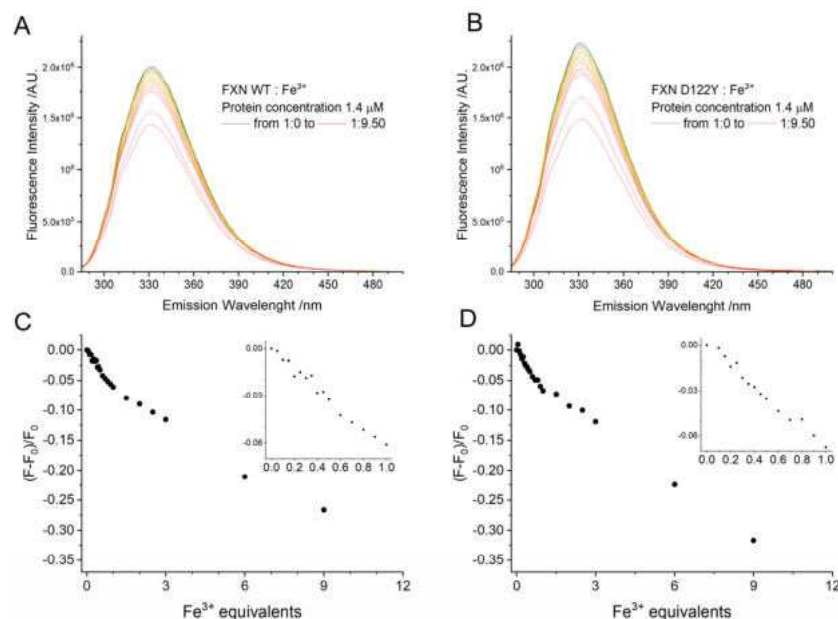


Figure 5. Tryptophan fluorescence spectra of WT FXN and D122Y variant at increasing amounts of Fe^{3+} . Protein concentration $1.4 \mu\text{M}$, 288 K , $\lambda_{\text{exc}} = 280 \text{ nm}$, $\lambda_{\text{max}} = 332 \text{ nm}$. (A,B) Fluorescence of FXN WT and D122Y, respectively; (C,D) fluorescence quenching by Fe^{3+} calculated at λ_{max} for FXN WT and D122Y, respectively; in the inset, a zoom of the sub-stoichiometric region.

2.5. Fluorescence Spectra of FXN Interacting with Fe^{2+}

The quenching effect of Fe^{2+} addition to the fluorescence emission of WT and D122Y FXN was explored using strictly anaerobic solutions at low concentration ($[\text{FXN}] = 1.4 \mu\text{M}$) and focusing on the sub-stoichiometric region. To ensure that the Fe^{2+} is not oxidized during the experiment, both the iron stock solution and the experimental cuvette were filled under nitrogen atmosphere and closed with silicon septa. The experimental compartment was flushed with nitrogen at all times. Fe^{2+} was injected into the cuvette through the septum using a Hamilton syringe flushed with nitrogen before any addition. The absorption of a stock solution of Fe^{2+} was checked and found it does not contribute significantly in the experimental conditions ($\lambda_{\text{exc}} = 280 \text{ nm}$).

The fluorescence signals and their quenching, expressed as $(F - F_0)/F_0$, are reported in Figure 6. As discussed above, the quenching from Fe^{2+} has the same mechanism as the one from Fe^{3+} , i.e., through an energy transfer mechanism from a bound iron ion to the nearest of the three Trp residues. From the normalized spectra (reported in the Supporting Information, Figure S8), Fe^{2+} does not alter the shape of the emission profiles even at 20 equivalents, indicating that all three Trp residues are equally quenched as for the case of Fe^{3+} .

The signal decreases sharply in the sub-stoichiometric region, levels off somewhat around 2.2 equivalents of Fe^{2+} , and then does not further decrease reaching a plateau. The absence of further quenching indicates that either Fe^{2+} populates only one binding site, or that the other binding sites are too far from the Trp to further quench them as further discussed below. This is true only in rigorously anaerobic conditions: in a control experiment in the presence of oxygen, quick conversion of Fe^{2+} to Fe^{3+} leads to a progressively increasing quenching (data not shown).

The WT shows a markedly more intense quenching than the D122Y variant, the $(F - F_0)/F_0$ being -0.08 vs. -0.06 at the 20 equivalents. The absolute quenching for Fe^{2+} in the sub-stoichiometric region is comparable for ferrous and ferric iron (about -0.08 for both oxidation states). Proceeding with the titration, at 10 equivalents the $(F - F_0)/F_0$ for WT is -0.08 for Fe^{2+} much lower than the quenching observed for Fe^{3+} , -0.27 . The titration curves have been analyzed according to a literature method [42], the details of the analysis are reported in the Supporting Information (see Figure S9); we obtained $K_D = 4.2 \times 10^{-7}$ for the WT and $K_D = 7.8 \times 10^{-7}$ for the D122Y variant, and for both cases a stoichiometry

of one strongly bound Fe^{2+} . These values must be considered only indicative, due to the low concentration used for the experiments which introduces a 10% error in the estimate.

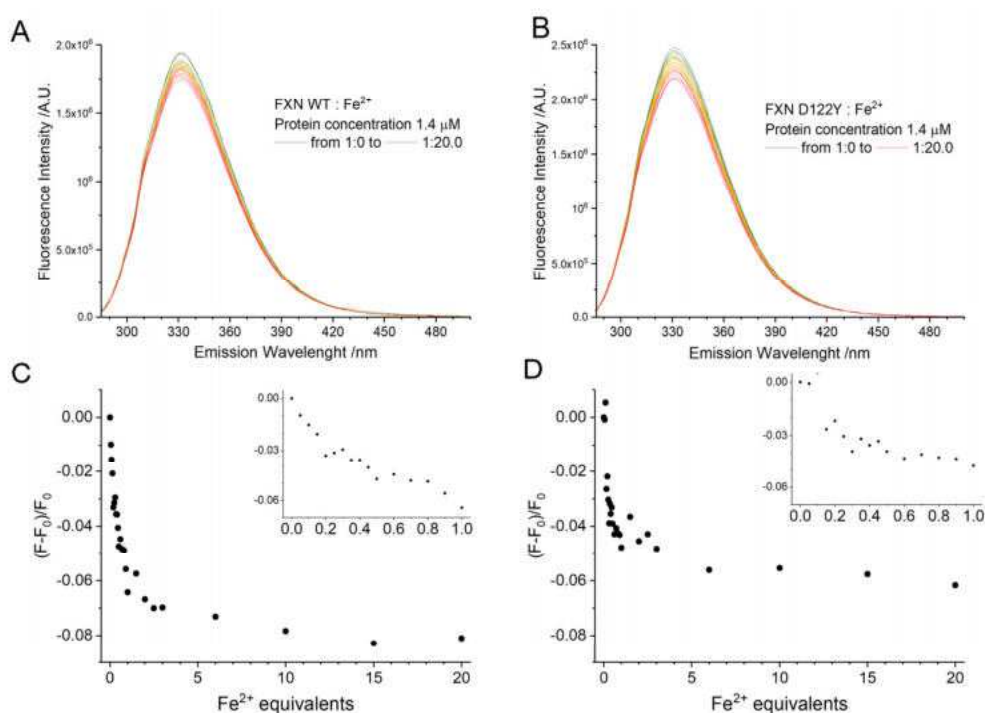


Figure 6. Tryptophan fluorescence spectra of WT FXN and D122Y variant at increasing amounts of Fe^{2+} . Protein concentration 1.4 μM , 288 K, $\lambda_{\text{exc}} = 280$ nm, $\lambda_{\text{max}} = 332$ nm. (A,B) Fluorescence of FXN WT and D122Y, respectively; (C,D) fluorescence quenching by Fe^{2+} calculated at λ_{max} for FXN WT and D122Y, respectively; in the inset, a zoom of the sub-stoichiometric region.

2.6. CD Spectra of FXN Interacting with Fe^{3+} and Fe^{2+}

The effects of iron binding on the secondary structure of human wild type and D122Y FXN proteins were evaluated by circular dichroism spectroscopy, as reported in Figure 7. In the absence of iron, the CD spectra for both WT and D122Y FXN are identical and show the typical shape of a mixed alpha-beta secondary structure [43].

Increasing addition of Fe^{3+} leads to a progressive loss of ellipticity across the whole spectral range for both proteins, Figure 7A,B. There are no marked changes in spectral shape and no well-defined isodichroic point can be observed; in addition, at high Fe^{3+} amounts, the low wavelength region shows signs of increased scattering. It was previously shown that a peptide derived from the main helix of FXN can bind one Fe^{3+} ion through its acidic residues and gains alpha-helical structure upon binding [44]. All these observations suggest that the loss of ellipticity cannot be interpreted as a loss of structure, but only as a sign of protein aggregation/precipitation as already proven by EPR spectroscopy.

On the contrary, additions of up to ten equivalents of Fe^{2+} do not change the CD spectra of WT and D122Y FXN, Figure 7C,D. Therefore, Fe^{2+} binding to FXN does not induce either significant secondary structure changes or protein aggregation.

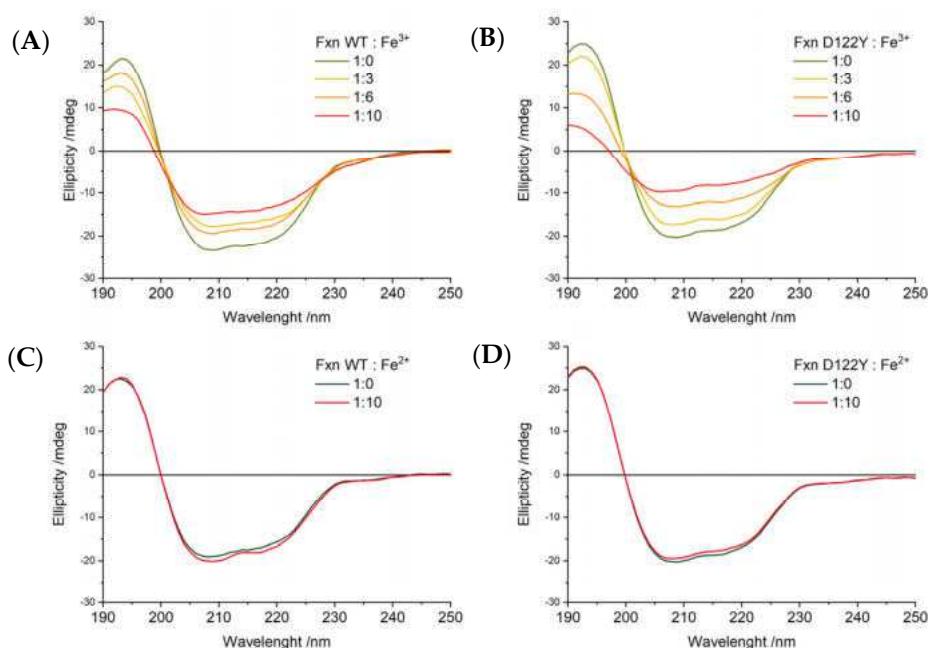


Figure 7. CD spectra of FXN of WT FXN and D122Y variant with either Fe³⁺ or Fe²⁺. Protein concentration 50 μ M. (A) WT FXN with increasing amounts of Fe³⁺; (B) D122Y FXN with increasing amounts of Fe³⁺; (C) WT FXN with Fe²⁺; (D) D122Y FXN with Fe²⁺.

3. Discussion

FXN has been proposed to have several physiological roles: allosteric regulator of ISC biogenesis [21,45], the iron source for building ISC clusters [24], regulator of iron homeostasis [25] and ferroptosis [26]. All the above roles involve iron ions; therefore, it is of key importance to understand the effects of ferrous and ferric iron on the structure and function of FXN. In this work, the response of human FXN, both WT and D122Y variant (the only pathological variant with a mutation in the iron-binding region), was investigated in the presence of ferrous and ferric ions using the SDSL EPR technique, which has never been used on FXN before, and the results were combined with those obtained by fluorescence and circular dichroism.

Ferrous iron binds human FXN without causing any large secondary structure changes as shown by CD, even at a 10-fold excess. On the other hand, EPR clearly indicates that Fe²⁺ binding does not alter local backbone dynamics of regions that are not involved in iron binding, as revealed by the lack of mobility changes of the spin probes at all the sites investigated. Moreover, no FXN oligomerization occurs in the presence of Fe²⁺, which is in agreement with previous results [30]. The M-TETPO probe that we adopted, was liable to reduction by Fe²⁺ bound in close proximity (at sites A99 and A114), thus proving that Fe²⁺ binds on both ends of the long α helix, in accordance with previous reports [15,29,35]. The majority of the EPR probe reduction takes place in the first three iron equivalents. The EPR results also put the results of fluorescence quenching into context. Fluorescence analysis leads to the conclusion that at least one strongly bound iron ion can be located in the long helix containing many Asp and Glu residues, close to W168/W173 (note that W155 is located in a region where putative Fe²⁺ binding sites are absent). This would be the site that reduces the spin label at position 99 (which is close to these two Trp). Conversely, the fluorescence measurements are not sensitive to binding of the Fe²⁺ ions in regions which are far from the Trp. Indeed, the Fe²⁺ binding site at the end of the helix suggested by the EPR spectra of A114C may escape fluorescence detection being out of range of the energy transfer Trp quenching mechanism. In conclusion, the number and the position of Fe²⁺ binding sites cannot be easily determined based on fluorescence quenching only, due to the presence of multiple Trp emitters spatially close to each other, and our results explain the apparent conflict in the number of iron binding sites reported in the literature.

In contrast to ferrous iron, ferric iron binding promotes FXN aggregation when few equivalents are added as shown EPR and CD experiments while the initial binding events at sub-stoichiometric ratios do not induce it. The WT protein exhibited a loss of ellipticity upon Fe^{3+} addition, and centrifugation of EPR samples showed the precipitation of the immobilized portion of the sample. We observed immobilization at sites placed not only in the long acidic α helix, which is the major putative iron binding region, but also in the second beta strand and the shorter helix. Thus, the interactions among monomers involve all the secondary structure elements and a large surface area is interested in the aggregation induced by iron binding: as such, it is likely that FXN does not form dimers, rather oligomers, and these are arranged in a globular fashion, without a preferential interface. Immobilization is the result of the constraint of the local motion of the labels, arising from new contacts between different protein monomers upon aggregation. Fe^{3+} -mediated oligomerization was previously suggested using SAXS, light scattering, and electron microscopy, at least at high FXN concentration (150–700 μM), with EM images suggesting that at least a portion of the aggregates are present as ring tetramers [33]. This was in contrast to previous reports, according to which human frataxin showed no tendency towards oligomerization, while the correspondent yeast and *E. coli* orthologs aggregate in the presence of both Fe^{2+} and Fe^{3+} [34]. Since Fe^{3+} promotes the formation of FXN aggregates, also at relatively low protein concentration, it is impossible to evaluate the dissociation constant of Fe^{3+} using fluorescence or calorimetry since the quenching or heat, respectively, have dominant contributions from aggregation and precipitation phenomena. Based on our results, the data previously reported for the dissociation constants and binding stoichiometry of human FXN with Fe^{3+} need to be critically reconsidered [22].

Our results may have some implication in the context of the physiological behavior of FXN. The lack of perturbation of the structure of FXN by Fe^{2+} suggests that ferrous iron might easily bind/unbind FXN without any change in structure and dynamics. Therefore, FXN might partake in the ISC machinery while exchanging Fe^{2+} from the solution to the complex. With respect to the aggregation induced by Fe^{3+} , we showed that it is strongly dependent on FXN concentration, thus large oligomers are not expected to be present at the low physiological concentrations of FXN in normal physiological states (FXN mitochondrial concentration is estimated to be between 0.1–1.0 μM in *S. cerevisiae*, by combining literature data [46,47]). However, in FRDA patients, a significant iron imbalance was observed [48–50], and pathological conditions are likely to trigger oligomerization. It seems unlikely, then, that the interaction of FXN with Fe^{3+} has no physiological function and reflects only a non-specific electrostatic effect. Indeed, a recent report linked FXN deficiency to cell death by ferroptosis [26]. Therefore, in conditions of an excess of ferric iron, a contribution of FXN to iron scavenging could be important, substantiating the function of FXN as a ‘ferritin-like’ scavenger helping iron homeostasis by keeping iron in a nontoxic, soluble and more bio-available form [51]. In this context, it is important to note that, as demonstrated by the effects of EDTA, the aggregation is reversible: therefore, once the imbalances in cell physiology that are responsible for the increase in ferric iron are overcome, FXN can potentially return monomeric.

Finally, the use of SDSL EPR allowed us to highlight differences in iron binding between the WT and the D122Y variant. A lower iron affinity of the D122Y FXN has been related before to a higher intrinsic mobility of the iron-binding region of the protein [52]. Indeed, an increased mobility of D122Y FXN in comparison with WT FXN is proved by the M-TETPO spin probe at the A114 position. The D122Y variant shows lower EPR signal loss in the presence of Fe^{2+} relative to the WT, and reduced fluorescence quenching, confirming a lower Fe^{2+} affinity. In addition, since the M-TETPO probe is sensitive to bound Fe^{2+} in the vicinity, the lower signal loss observed in the D122Y variant implies that the aspartate side chain in position 122 is directly involved in ferrous iron binding. In contrast, in the sub-stoichiometric region, the effects of Fe^{3+} on the fluorescence quenching show no difference between the WT and the D122Y variant. The differences in fluorescence quenching by Fe^{3+} between the WT and D122Y that were previously observed [29,52] are referred especially to the region dominated by precipitation, and as such depend strongly on the protein concentration as already described. Overall,

the different binding affinity with ferrous, but not ferric, iron likely arises from a combination of variations in the structural dynamics of the region and loss of the aspartate partaking in iron binding. Since it was previously observed that D122Y variant retains some capability to enhance the desulfurase activity *in vitro* [29], it is likely that the pathological nature of D122Y lies in a combination of lowered ability of the variant to participate in Fe^{2+} trafficking and less than optimal conformation hampering the interaction with the other proteins in the ISC cluster biogenesis complex.

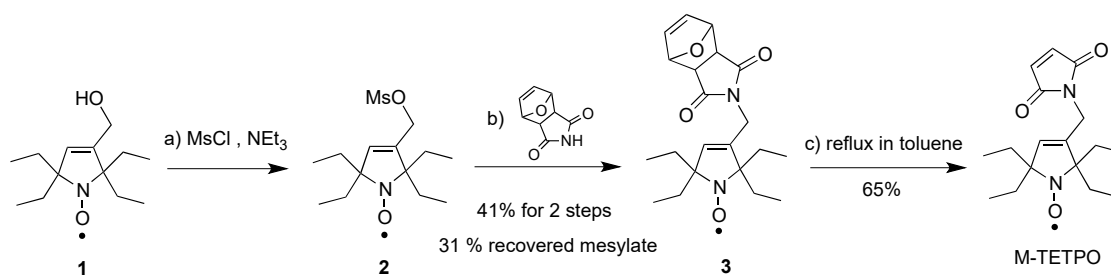
4. Materials and Methods

4.1. Materials

The spin label MTSSL, (1-Oxyl-2,2,5,5-tetramethyl- Δ^3 -pyrroline-3-methyl) Methanethiosulfonate, was purchased from Toronto Research Chemicals. M-TETPO was synthesized as described below. Unless otherwise specified, the buffer composition for spectroscopic experiments was: 25 mM HEPES (pH 7.0) 50 mM KCl. Ferrous iron solutions were prepared in anaerobic atmosphere in degassed deionized water slightly acidified starting from $(\text{NH}_4)_2\text{Fe}(\text{SO}_4)_2 \cdot 6\text{H}_2\text{O}$ (Mohr's Salt, >99% Fe^{2+} content). Ferric iron solutions were prepared from $\text{FeCl}_3 \cdot 6\text{H}_2\text{O}$ in HCl at pH = 0.8. Ficoll® PM 70 stock solution was prepared dissolving the polymer in degassed buffer at a 35% *w/w*% concentration, under anaerobic atmosphere. 1,10-Phenanthroline monohydrate was dissolved in dilute buffer. Unless otherwise specified, chemicals were purchased from Merck and used without further purification.

4.2. Synthesis of M-TETPO

The synthesis of M-TETPO is reported in Scheme 2; further details are reported in the Supporting Information (pages S12–13). It was prepared in three steps from alcohol **1**, which was synthesized according to a published procedure [53]. Thus, reaction of alcohol **1** with mesyl chloride (MsCl) and triethylamine (NEt_3), followed by the substitution of the crude resulting mesylate **2** with protected maleimide, afford compound **3** in 41% yield and the unreacted mesylate **2** in 31% yield. Finally, retro-Diels-Alder was performed with compound **3** by refluxing in toluene to afford pure M-TETPO in 65% yield. Analytical data were identical to those reported for TETPO [39].



Scheme 2. Synthetic way to prepare TETPO from alcohol **1**. (a) MsCl, Et_3N , DCM 0 °C to RT, 2 h; (b) protected maleimide, K_2CO_3 , DMF; (c) reflux, toluene.

4.3. Heterologous Expression and Purification of Human Wild Type and D122Y FXN Proteins

A plasmid containing the coding sequence of human wild type mature FXN, i.e., pET-9b/FXN (90–210), was previously obtained in our laboratory [54]. FXN mutants were obtained through site-directed mutagenesis with the QuickChange® II Site-Directed Mutagenesis Kit (from Agilent Technologies), using as template the pET-9b/FXN (90–210) plasmid and the couples of primers listed in the Supporting Information (see the Table S1 at page S2). Each sequence was checked by DNA sequencing (at GATC Biotech, Germany). *Escherichia coli* BL21 (DE3) cells were chemically transformed with the plasmids of interest and positive clones were selected by antibiotic resistance. The expression of the wild type and mutant proteins was induced by adding 1 mM isopropyl- β -thiogalactopyranoside (IPTG) in LB medium and incubating the bacteria cultures at 30 °C overnight at constant stirring. Cells were then harvested by centrifugation at 5000 \times g and 4 °C for 20 min, resuspended in lysis

buffer 25 mM HEPES (pH = 7.0) supplemented with protease inhibitors (1 $\mu\text{g}/\text{mL}$ pepstatin A, 1 $\mu\text{g}/\text{mL}$ leupeptin, 1 $\mu\text{g}/\text{mL}$ antipain, 100 μM PMSF) and lysed by French press. The supernatant fractions were isolated from cell debris by centrifugation at $17,000\times g$ and $4\text{ }^\circ\text{C}$ for 15 min and incubated with EDTA 10 mM for 1 h at $4\text{ }^\circ\text{C}$, in gentle agitation. Proteins were purified combining anionic exchange and size exclusion chromatographies. The first chromatographic step was performed using a cationic DEAE (Diethylaminoethyl) Sepharose column using 25 mM HEPES (pH = 7.0) as buffer of equilibration and 25 mM HEPES (pH = 7.0), 1 M KCl as elution gradient buffer. The fractions corresponding to frataxin, as assessed by SDS PAGE, were collected, pooled together, concentrated by centrifugal filters (Amicon Ultra Centrifugal Filter, 3000 NMWL, from Merck Millipore, Burlington, MA, USA) and purified by size-exclusion chromatography (SEC). For FXN mutants containing cysteines, an incubation with 1 mM of dithiothreitol (DTT) for 1 h at $4\text{ }^\circ\text{C}$ has been performed after cationic exchange. The second purification step was performed on a Superdex 200 GL 10 300 column (from GE Healthcare), equilibrated in a buffer containing 25 mM HEPES (pH = 7.0) and 50 mM KCl. To estimate the molecular weight of the protein samples, the column was equilibrated in the same buffer and calibrated with the standards thyroglobulin (669 kDa), ferritin (440 kDa), β -amylase (200 kDa), bovine serum albumin (67 kDa), carbonic anhydrase (29 kDa) and cytochrome *c* (12 kDa). The eluted fractions containing frataxin proteins were finally pooled together and the molar concentration of the protein samples was determined spectroscopically using $\epsilon_{280\text{nm}} = 26930\text{ M}^{-1}\text{cm}^{-1}$ for all mutants and $\epsilon_{280\text{nm}} = 28420\text{ M}^{-1}\text{cm}^{-1}$ for those containing D122Y point mutation (molar extinction coefficients evaluated by ExPASy ProtParam tool). Protein purity and integrity were finally assessed by 15% SDS-PAGE and Coomassie blue staining, prior to any spectroscopic experiment reported in this work.

4.4. Spin Labeling

Protein samples were labeled with MTSSL or M-TETPO for EPR experiments. Samples labeled with MTSSL were obtained by adding to the purified protein (at a concentration of about 150 μM) a sevenfold molar excess of spin label (dissolved in DMSO) and incubating the protein at $4\text{ }^\circ\text{C}$ overnight in the dark and gentle stirring. Excess of non-ligated spin label was removed from the protein by PD10 desalting column (GE Healthcare) using 25 mM HEPES (pH = 7.0) and 50 mM KCl as final buffer. For the experiments with Fe^{2+} , in order to avoid possible oxidation of iron, anaerobic conditions have been adopted in the labeling with MTSSL and all steps were performed under a glove box. For the labeling with M-TETPO, purified proteins (at a concentration of 50 μM) were previously incubated with DTT in a molar ratio of 1:100 at $4\text{ }^\circ\text{C}$ for 30 min in slow agitation. The excess of DTT was removed from the samples by PD10 desalting column (GE Healthcare) using 25 mM HEPES (pH = 7.0) and 50 mM KCl as elution buffer. Proteins were labeled with a tenfold molar excess of M-TETPO (dissolved in acetonitrile) and incubated at $4\text{ }^\circ\text{C}$ for 2 h in the dark and slow agitation. Labeled protein samples were concentrated by centrifugal filters (Amicon Ultra Centrifugal Filter, 3000 NMWL, from Merck Millipore, Burlington, MA, USA) and the excess of spin label was then removed by gel filtration using a Superdex 200 GL 10 300 column (from GE Healthcare) and 25 mM HEPES (pH = 7.0), 50 mM KCl as elution buffer. MTSSL/M-TETPO-labeled proteins were finally concentrated by centrifugal filters to a volume suitable for EPR spectroscopic analysis, and their concentration determined by UV-Vis spectroscopy as previously described.

4.5. Electron Paramagnetic Resonance (EPR) Spectroscopy

EPR spectra were recorded on an ELEXSYS E580 spectrometer equipped with a SHQ cavity, both from Bruker, Germany. The experiments were performed at room temperature, typically using the following parameters: microwave frequency 9.87 GHz, microwave power 10 mW (attenuation 12 dB), sweep width 150 mT, center field 352 mT, conversion time 164 ms, time constant 82 ms, modulation amplitude 1.6 mT, 1024 points, 3–25 averages (depending on protein concentration). Samples were prepared thoroughly mixing 32 μL of Ficoll PM70 stock solution (or buffer when needed), 7 μL of protein stock solution, and 1 μL of Fe^{2+} or Fe^{3+} solution; the resulting solution was

put in glass capillary (internal diameter 0.8 mm) and measured under nitrogen gas flow. The final protein concentration was typically 50 or 10 μM for Fe^{2+} or Fe^{3+} respectively, save for when differently stated. The different FXN: Fe^{2+} or Fe^{3+} molar ratios were prepared from an appropriate dilution of a concentrated stock solution.

4.6. Simulation of EPR Spectra

The simulation of the EPR spectra allows getting quantitative information on the mobility of the spin label and eventually pointing out the presence of multiple components. To perform the simulations, one must know or estimate the nitroxide g-tensor (\mathbf{g}) and hyperfine tensor (\mathbf{A}) and then adopt a model of the spin label motion based on the stochastic Liouville equation, Microscopic Order Macroscopic Disorder (MOMD) being the one used most often [55]. MOMD was developed considering that the spin label molecular motion is limited by the protein structure (microscopic order) and that the macromolecules adopt all the possible orientations with respect to the external magnetic field (macroscopic disorder). The MOMD model makes it possible to describe the spin label mobility in terms of the diffusion tensor \mathbf{D} , its orientation relative to the nitroxide frame expressed by the Euler angles Ω_{D} (but usually reduced to a single angle β_{D} for symmetry), and the order parameter S . The mobility is often discussed in terms of the rotational correlation time τ_c , which is derived from the diffusion tensor: for a nitroxide characterized by an axial diffusion $\tau_c = 1/6(D_{\parallel}D_{\perp})^{1/2}$. We used the MultiComponentEPR827.vi program by Christian Altenbach to perform the simulations. The program is written in LabVIEW (National Instruments) and can be freely downloaded from the following website: <http://www.biochemistry.ucla.edu/Faculty/Hubbell/>.

4.7. Fluorescence

Fluorescence experiments were performed on a FLS 1000 UV/Vis/NIR photoluminescence spectrometer by Edinburgh Instruments with a 450 W Xenon Arc lamp for excitation at 285 nm and a PMT-980 detector. The Peltier controlled holder allowed measuring at 288 K under stirring. The sample compartment was under constant nitrogen flow to avoid condensation on the windows and keeping an anaerobic atmosphere. Experiments were conducted using a fluorescence cuvette (117104F-10-40 from Hellma, Mülheim, Germany) with 10 \times 4 mm optical path length and gas tight screw cap with a silicon septum for addition of the ferrous/ferric iron solutions via a gas tight microsyringe (from Hamilton Company, Reno, NV, USA) under anaerobic atmosphere. Proteins were used at 1.4 μM concentration.

4.8. Circular Dichroism

CD measurements were performed with a Jasco J-1500 spectropolarimeter. Experiments were performed at 298 K using a Jasco PTC-423 Peltier cell holder connected to a Jasco PTC-423S Peltier controller. Far-UV CD spectra were collected using a cylindrical cell (121-0.20-40 from Hellma) with 0.2 mm optical path length using 50 μL of protein solution. Data were acquired at a scan speed of 20 nm/min and at least three scans were averaged. Proteins were used at a concentration of 50 μM , in a 0.5 mM Tris-HCl pH 7.0, 1 mM KCl buffer. For experiments with ferrous iron, the cuvette was filled and sealed under anaerobic atmosphere in a glove box; the compartment of the CD spectropolarimeter is anaerobic since it is constantly under nitrogen flow.

5. Conclusions

The results obtained through the combination of SDSL EPR, fluorescence and CD spectroscopies prove that human FXN interacts with Fe^{2+} and Fe^{3+} with a markedly different outcome. Fe^{3+} causes aggregation in a concentration-dependent fashion, starting when adding few equivalents, making difficult to evaluate the exact binding stoichiometry. Fe^{2+} , the physiological form of iron in cells, simply binds without affecting FXN conformation or inducing aggregation.

We suggest that both ions might be relevant in the context of the proposed FXN physiological functions. FXN role as a regulator of iron homeostasis and ferroptosis might be exerted by sequestering the excess of ferric iron through concentration dependent reversible aggregation. The absence of structural and dynamic effects of Fe²⁺ binding suggests that FXN is able to partake in ferrous iron trafficking even while bound to the ISC cluster assembly machinery, possibly intercepting the iron from the labile iron pool in solution and passing it to ISCU during cluster formation. The different binding affinity with ferrous, but not ferric, iron in D122Y pathological shows that the aspartate side chain in position 122 is directly involved in ferrous iron binding and that the mobility of the protein in the vicinity of the mutated site is increased compared to the WT. Both the effects may be related to the pathological nature of D122Y.

The next step will involve exploring the effects of Fe²⁺/Fe³⁺ on FXN structure and dynamics in the presence of the other partners of the ISC cluster assembly machinery, ISCU, NFS1 and the accessory proteins. We will use the currently available spin labeled sites plus new others strategically chosen in light of the available structure of the complex.

Supplementary Materials: Supplementary materials can be found online at <http://www.mdpi.com/1422-0067/21/24/9619/s1>.

Author Contributions: P.C., M.B., D.C. conceived and designed the experiments; D.D., L.P., M.B. performed the experiments; M.B. and D.C. analyzed the data; G.A., S.R.A.M., M.S., J.S., P.C. contributed reagents/materials; D.D., M.B., D.C. wrote the paper. All authors have read and agreed to the published version of the manuscript.

Funding: M.B. acknowledges the support of the MIUR through the “Dipartimenti di Eccellenza” grant NExuS.

Acknowledgments: Fluorescence measurements were performed with an Edinburgh FLS 1000 UV/Vis/NIR photoluminescence spectrometer, funded by the MIUR—“Dipartimenti di Eccellenza” grant NExuS.

Conflicts of Interest: The authors declare no conflict of interest.

References

1. Campuzano, V.; Montermini, L.; Molto, M.D.; Pianese, L.; Cossee, M.; Cavalcanti, F.; Monros, E.; Rodius, F.; Duclos, F.; Monticelli, A.; et al. Friedreich's Ataxia: Autosomal Recessive Disease Caused by an Intronic GAA Triplet Repeat Expansion. *Science* **1996**, *271*, 1423–1427. [[CrossRef](#)] [[PubMed](#)]
2. Galea, C.A.; Huq, A.; Lockhart, P.J.; Tai, G.; Corben, L.A.; Yiu, E.M.; Gurrin, L.C.; Lynch, D.R.; Gelbard, S.; Durr, A.; et al. Compound Heterozygous FXN Mutations and Clinical Outcome in Friedreich Ataxia. *Ann. Neurol.* **2016**, *79*, 485–495. [[CrossRef](#)] [[PubMed](#)]
3. De Castro, M.; García-Planells, J.; Monrós, E.; Cañizares, J.; Vázquez-Manrique, R.; Vilchez, J.J.; Urtasun, M.; Lucas, M.; Navarro, G.; Izquierdo, G.; et al. Genotype and Phenotype Analysis of Friedreich's Ataxia Compound Heterozygous Patients. *Hum. Genet.* **2000**, *106*, 86–92. [[CrossRef](#)] [[PubMed](#)]
4. Gellera, C.; Castellotti, B.; Mariotti, C.; Mineri, R.; Seveso, V.; DiDonato, S.; Taroni, F. Frataxin Gene Point Mutations in Italian Friedreich Ataxia Patients. *Neurogenetics* **2007**, *8*, 289–299. [[CrossRef](#)]
5. Chiabrando, D.; Bertino, F.; Tolosano, E. Hereditary Ataxia: A Focus on Heme Metabolism and Fe-S Cluster Biogenesis. *Int. J. Mol. Sci.* **2020**, *21*, 3760. [[CrossRef](#)]
6. Rötig, A.; de Lonlay, P.; Chretien, D.; Foury, F.; Koenig, M.; Sidi, D.; Munnich, A.; Rustin, P. Aconitase and Mitochondrial Iron-Sulphur Protein Deficiency in Friedreich Ataxia. *Nat. Genet.* **1997**, *17*, 215–217. [[CrossRef](#)]
7. Puccio, H.; Simon, D.; Cossée, M.; Criqui-Filipe, P.; Tiziano, F.; Melki, J.; Hindelang, C.; Matyas, R.; Rustin, P.; Koenig, M. Mouse Models for Friedreich Ataxia Exhibit Cardiomyopathy, Sensory Nerve Defect and Fe-S Enzyme Deficiency Followed by Intramitochondrial Iron Deposits. *Nat. Genet.* **2001**, *27*, 181–186. [[CrossRef](#)]
8. Schulz, J.B.; Dehmer, T.; Schols, L.; Mende, H.; Hardt, C.; Vorgerd, M.; Burk, K.; Matson, W.; Dichgans, J.; Beal, M.F.; et al. Oxidative Stress in Patients with Friedreich Ataxia. *Neurology* **2000**, *55*, 1719–1721. [[CrossRef](#)]
9. Koutnikova, H.; Campuzano, V.; Koenig, M. Maturation of Wild-Type and Mutated Frataxin by the Mitochondrial Processing Peptidase. *Hum. Mol. Genet.* **1998**, *7*, 1485–1489. [[CrossRef](#)]
10. Condò, I.; Ventura, N.; Malisan, F.; Rufini, A.; Tomassini, B.; Testi, R. In Vivo Maturation of Human Frataxin. *Hum. Mol. Genet.* **2007**, *16*, 1534–1540. [[CrossRef](#)]
11. Schmucker, S.; Argentini, M.; Carelle-Calmels, N.; Martelli, A.; Puccio, H. The in Vivo Mitochondrial Two-Step Maturation of Human Frataxin. *Hum. Mol. Genet.* **2008**, *17*, 3521–3531. [[CrossRef](#)] [[PubMed](#)]

12. Huynen, M.A.; Snel, B.; Bork, P.; Gibson, T.J. The Phylogenetic Distribution of Frataxin Indicates a Role in Iron-Sulfur Cluster Protein Assembly. *Hum. Mol. Genet.* **2001**, *10*, 2463–2468. [[CrossRef](#)] [[PubMed](#)]
13. Sirano, D.P.; Shigeta, R.; Chi, Y.I.; Ristow, M.; Shoelson, S.E. Crystal Structure of Human Frataxin. *J. Biol. Chem.* **2000**, *275*, 30753–30756. [[CrossRef](#)]
14. Musco, G.; Stier, G.; Kolmerer, B.; Adinolfi, S.; Martin, S.; Frenkiel, T.; Gibson, T.; Pastore, A. Towards a Structural Understanding of Friedreich's Ataxia: Solution Structure of Frataxin. *Structure* **2000**, *8*, 695–707. [[CrossRef](#)]
15. Gentry, L.E.; Thacker, M.A.; Doughty, R.; Timkovich, R.; Busenlehner, L.S. His86 from the N-Terminus of Frataxin Coordinates Iron and Is Required for Fe-S Cluster Synthesis. *Biochemistry* **2013**, *52*, 6085–6096. [[CrossRef](#)]
16. Fox, N.G.; Yu, X.; Feng, X.; Bailey, H.J.; Martelli, A.; Nabhan, J.F.; Strain-Damerell, C.; Bulawa, C.; Yue, W.W.; Han, S. Structure of the Human Frataxin-Bound Iron-Sulfur Cluster Assembly Complex Provides Insight into Its Activation Mechanism. *Nat. Commun.* **2019**, *10*, 1–8. [[CrossRef](#)]
17. Patraa, S.; Barondeau, D.P. Mechanism of Activation of the Human Cysteine Desulfurase Complex by Frataxin. *Proc. Natl. Acad. Sci. USA* **2019**, *116*, 19421–19430. [[CrossRef](#)]
18. Gervason, S.; Larkem, D.; Mansour, A.B.; Botzanowski, T.; Müller, C.S.; Pecqueur, L.; Le Pavec, G.; Delaunay-Moisan, A.; Brun, O.; Agramunt, J.; et al. Physiologically Relevant Reconstitution of Iron-Sulfur Cluster Biosynthesis Uncovers Persulfide-Processing Functions of Ferredoxin-2 and Frataxin. *Nat. Commun.* **2019**, *10*, 1–12. [[CrossRef](#)]
19. Srour, B.; Gervason, S.; Monfort, B.; D'Autréaux, B. Mechanism of Iron-Sulfur Cluster Assembly: In the Intimacy of Iron and Sulfur Encounter. *Inorganics* **2020**, *8*, 55. [[CrossRef](#)]
20. Braymer, J.J.; Lill, R. Iron-Sulfur Cluster Biogenesis and Trafficking in Mitochondria. *J. Biol. Chem.* **2017**, *292*, 12754–12763. [[CrossRef](#)]
21. Maio, N.; Jain, A.; Rouault, T.A. Mammalian Iron-Sulfur Cluster Biogenesis: Recent Insights into the Roles of Frataxin, Acyl Carrier Protein and ATPase-Mediated Transfer to Recipient Proteins. *Curr. Opin. Chem. Biol.* **2020**, *55*, 34–44. [[CrossRef](#)] [[PubMed](#)]
22. Yoon, T.; Cowan, J.A. Iron-Sulfur Cluster Biosynthesis. Characterization of Frataxin as an Iron Donor for Assembly of [2Fe-2S] Clusters in ISU-Type Proteins. *J. Am. Chem. Soc.* **2003**, *125*, 6078–6084. [[CrossRef](#)] [[PubMed](#)]
23. Mühlhoff, U.; Richhardt, N.; Ristow, M.; Kispal, G.; Lill, R. The Yeast Frataxin Homolog Yfh1p Plays a Specific Role in the Maturation of Cellular Fe/S Proteins. *Hum. Mol. Genet.* **2002**, *11*, 2025–2036. [[CrossRef](#)] [[PubMed](#)]
24. Cai, K.; Frederick, R.O.; Tonelli, M.; Markley, J.L. Interactions of Iron-Bound Frataxin with ISCU and Ferredoxin on the Cysteine Desulfurase Complex Leading to Fe-S Cluster Assembly. *J. Inorg. Biochem.* **2018**, *183*, 107–116. [[CrossRef](#)] [[PubMed](#)]
25. Alsina, D.; Purroy, R.; Ros, J.; Tamarit, J. Iron in Friedreich Ataxia: A Central Role in the Pathophysiology or an Epiphenomenon? *Pharmaceuticals* **2018**, *11*, 89. [[CrossRef](#)]
26. Du, J.; Zhou, Y.; Li, Y.; Xia, J.; Chen, Y.; Chen, S.; Wang, X.; Sun, W.; Wang, T.; Ren, X.; et al. Identification of Frataxin as a Regulator of Ferroptosis. *Redox Biol.* **2020**, *32*. [[CrossRef](#)]
27. Grazia Cotticelli, M.; Xia, S.; Lin, D.; Lee, T.; Terrab, L.; Wipf, P.; Hurn, D.M.; Wilson, R.B. Ferroptosis as a Novel Therapeutic Target for Friedreich's Ataxia. *J. Pharm. Exp. Ther.* **2019**, *369*, 47–54. [[CrossRef](#)]
28. Stockwell, B.R.; Jiang, X. The Chemistry and Biology of Ferroptosis. *Cell Chem. Biol.* **2020**, *27*, 365–375. [[CrossRef](#)]
29. Bellanda, M.; Maso, L.; Doni, D.; Bortolus, M.; De Rosa, E.; Lunardi, F.; Alfonsi, A.; Noguera, M.E.; Herrera, M.G.; Santos, J.; et al. Exploring Iron-Binding to Human Frataxin and to Selected Friedreich Ataxia Mutants by Means of NMR and EPR Spectroscopies. *Biochim. Biophys. Acta Proteins Proteom.* **2019**, *1867*, 140254. [[CrossRef](#)]
30. Cavadini, P.; O'Neill, H.A.; Benada, O.; Isaya, G. Assembly and Iron-Binding Properties of Human Frataxin, the Protein Deficient in Friedreich Ataxia. *Hum. Mol. Genet.* **2002**, *11*, 217–227. [[CrossRef](#)]
31. Bou-Abdallah, F.; Adinolfi, S.; Pastore, A.; Laue, T.M.; Dennis Chasteen, N. Iron Binding and Oxidation Kinetics in Frataxin CyaY of Escherichia Coli. *J. Mol. Biol.* **2004**, *341*, 605–615. [[CrossRef](#)] [[PubMed](#)]

32. Yoon, T.; Dizin, E.; Cowan, J.A. N-Terminal Iron-Mediated Self-Cleavage of Human Frataxin: Regulation of Iron Binding and Complex Formation with Target Proteins. *J. Biol. Inorg. Chem.* **2007**, *12*, 535–542. [[CrossRef](#)] [[PubMed](#)]
33. Ahlgren, E.C.; Fekry, M.; Wiemann, M.; Söderberg, C.A.; Bernfur, K.; Gakh, O.; Rasmussen, M.; Højrup, P.; Emanuelsson, C.; Isaya, G.; et al. Iron-Induced Oligomerization of Human FXN81-210 and Bacterial CyaY Frataxin and the Effect of Iron Chelators. *PLoS ONE* **2017**, *12*, e0188937. [[CrossRef](#)] [[PubMed](#)]
34. Adinolfi, S.; Trifuoggi, M.; Politou, A.S.; Martin, S.; Pastore, A. A Structural Approach to Understanding the Iron-Binding Properties of Phylogenetically Different Frataxins. *Hum. Mol. Genet.* **2002**, *11*, 1865–1877. [[CrossRef](#)]
35. Huang, J.; Dizin, E.; Cowan, J.A. Mapping Iron Binding Sites on Human Frataxin: Implications for Cluster Assembly on the ISU Fe-S Cluster Scaffold Protein. *J. Biol. Inorg. Chem.* **2008**, *13*, 825–836. [[CrossRef](#)]
36. López, C.J.; Fleissner, M.R.; Guo, Z.; Kusnetzow, A.K.; Hubbell, W.L. Osmolyte Perturbation Reveals Conformational Equilibria in Spin-Labeled Proteins. *Protein Sci.* **2009**, *18*, 1637–1652. [[CrossRef](#)]
37. Barone, V.; Zerbetto, M.; Polimeno, A. Hydrodynamic Modeling of Diffusion Tensor Properties of Flexible Molecules. *J. Comput. Chem.* **2009**, *30*, 2–13. [[CrossRef](#)]
38. Pastore, A.; Puccio, H. Frataxin: A Protein in Search for a Function. *J. Neurochem.* **2013**, *126* (Suppl. S1), 43–52. [[CrossRef](#)]
39. Karthikeyan, G.; Bonucci, A.; Casano, G.; Gerbaud, G.; Abel, S.; Thomé, V.; Kodjabachian, L.; Magalon, A.; Guigliarelli, B.; Belle, V.; et al. A Bioresistant Nitroxide Spin Label for In-Cell EPR Spectroscopy: In Vitro and In Oocytes Protein Structural Dynamics Studies. *Angew. Chem. Int. Ed.* **2018**, *57*, 1366–1370. [[CrossRef](#)]
40. Braterman, P.S.; Song, J.I.; Peacock, R.D. Electronic Absorption Spectra of the Iron(II) Complexes of 2, 2'-Bipyridine, 2, 2'-Bipyrimidine, 1, 10-Phenanthroline, and 2, 2':6',2''-Terpyridine and Their Reduction Products. *Inorg. Chem.* **1992**, *31*, 555–559. [[CrossRef](#)]
41. Ilari, A.; Latella, M.C.; Ceci, P.; Ribacchi, F.; Su, M.; Giangiacomo, L.; Stefanini, S.; Chasteen, N.D.; Chiancone, E. The Unusual Intersubunit Ferroxidase Center of *Listeria innocua* Dps Is Required for Hydrogen Peroxide Detoxification but Not for Iron Uptake. A Study with Site-Specific Mutants. *Biochemistry* **2005**, *44*, 5579–5587. [[CrossRef](#)] [[PubMed](#)]
42. Sawyer, W.H.; Winzor, D.J. Theoretical Aspects of the Quantitative Characterization of Ligand Binding. *Curr. Protoc. Protein Sci.* **1999**, *16*, 1–40. [[CrossRef](#)]
43. Faraj, S.E.; González-Lebrero, R.M.; Roman, E.A.; Santos, J. Human Frataxin Folds Via an Intermediate State. Role of the C-Terminal Region. *Sci. Rep.* **2016**, *6*, 1–16. [[CrossRef](#)] [[PubMed](#)]
44. Vazquez, D.S.; Agudelo, W.A.; Yone, A.; Vizioli, N.; Arán, M.; González Flecha, F.L.; González Lebrero, M.C.; Santos, J. A Helix-Coil Transition Induced by the Metal Ion Interaction with a Grafted Iron-Binding Site of the CyaY Protein Family. *Dalt. Trans.* **2015**, *44*, 2370–2379. [[CrossRef](#)] [[PubMed](#)]
45. Bridwell-Rabb, J.; Fox, N.G.; Tsai, C.L.; Winn, A.M.; Barondeau, D.P. Human Frataxin Activates Fe-S Cluster Biosynthesis by Facilitating Sulfur Transfer Chemistry. *Biochemistry* **2014**, *53*, 4904–4913. [[CrossRef](#)] [[PubMed](#)]
46. Garber Morales, J.; Holmes-Hampton, G.P.; Miao, R.; Guo, Y.; Münck, E.; Lindahl, P.A. Biophysical Characterization of Iron in Mitochondria Isolated from Respiring and Fermenting Yeast. *Biochemistry* **2010**, *49*, 5436–5444. [[CrossRef](#)] [[PubMed](#)]
47. Seguin, A.; Sutak, R.; Bulteau, A.L.; Garcia-Serres, R.; Oddou, J.L.; Lefevre, S.; Santos, R.; Dancis, A.; Camadro, J.M.; Latour, J.M.; et al. Evidence That Yeast Frataxin Is Not an Iron Storage Protein in Vivo. *Biochim. Biophys. Acta Mol. Basis Dis.* **2010**, *1802*, 531–538. [[CrossRef](#)]
48. Harding, I.H.; Raniga, P.; Delatycki, M.B.; Stagnitti, M.R.; Corben, L.A.; Storey, E.; Georgiou-Karistianis, N.; Egan, G.F. Tissue Atrophy and Elevated Iron Concentration in the Extrapyramidal Motor System in Friedreich Ataxia: The IMAGE-FRDA Study. *J. Neurol. Neurosurg. Psychiatry* **2016**, *87*, 1260–1263. [[CrossRef](#)]
49. Lamarche, J.B.; Côté, M.; Lemieux, B. The Cardiomyopathy of Friedreich's Ataxia Morphological Observations in 3 Cases. *Can. J. Neurol. Sci. J. Can. Des Sci. Neurol.* **1980**, *7*, 389–396. [[CrossRef](#)]
50. Bradley, J.L.; Blake, J.C.; Chamberlain, S.; Thomas, P.K.; Cooper, J.M.; Schapira, A.H.V. Clinical, Biochemical and Molecular Genetic Correlations in Friedreich's Ataxia. *Hum. Mol. Genet.* **2000**, *9*, 275–282. [[CrossRef](#)]
51. Zanella, I.; Derosas, M.; Corrado, M.; Cocco, E.; Cavadini, P.; Biasiotto, G.; Poli, M.; Verardi, R.; Arosio, P. The Effects of Frataxin Silencing in HeLa Cells Are Rescued by the Expression of Human Mitochondrial Ferritin. *Biochim. Biophys. Acta Mol. Basis Dis.* **2008**, *1782*, 90–98. [[CrossRef](#)] [[PubMed](#)]

52. Correia, A.R.; Pastore, C.; Adinolfi, S.; Pastore, A.; Gomes, C.M. Dynamics, Stability and Iron-Binding Activity of Frataxin Clinical Mutants. *FEBS J.* **2008**, *275*, 3680–3690. [[CrossRef](#)] [[PubMed](#)]
53. Wang, Y.; Paletta, J.T.; Berg, K.; Reinhart, E.; Rajca, S.; Rajca, A. Synthesis of Unnatural Amino Acids Functionalized with Sterically Shielded Pyrroline Nitroxides. *Org. Lett.* **2014**, *16*, 5298–5300. [[CrossRef](#)] [[PubMed](#)]
54. Roman, E.A.; Faraj, S.E.; Gallo, M.; Salvay, A.G.; Ferreiro, D.U.; Santos, J. Protein Stability and Dynamics Modulation: The Case of Human Frataxin. *PLoS ONE* **2012**, *7*, e45743. [[CrossRef](#)] [[PubMed](#)]
55. Budil, D.E.; Sanghyuk, L.; Saxena, S.; Freed, J.H. Nonlinear-Least-Squares Analysis of Slow-Motion EPR Spectra in One and Two Dimensions Using a Modified Levenberg-Marquardt Algorithm. *J. Magn. Reson. Ser. A* **1996**, *120*, 155–189. [[CrossRef](#)]

Publisher's Note: MDPI stays neutral with regard to jurisdictional claims in published maps and institutional affiliations.



© 2020 by the authors. Licensee MDPI, Basel, Switzerland. This article is an open access article distributed under the terms and conditions of the Creative Commons Attribution (CC BY) license (<http://creativecommons.org/licenses/by/4.0/>).

Supplementary Information

for

Effects of Fe²⁺/Fe³⁺ binding to human frataxin and its D122Y variant, as revealed by Site Directed Spin labelling (SDSL) EPR complemented by Fluorescence and Circular Dichroism spectroscopies

Davide Doni¹, Leonardo Passerini², Gérard Audran³, Sylvain R. A. Marque³, Marvin Schulz³, Javier Santos^{4,5}, Paola Costantini¹, Marco Bortolus^{2*} and Donatella Carbonera²

¹Department of Biology, University of Padova, Viale G. Colombo 3, 35131 Padova, Italy

²Department of Chemical Sciences, University of Padova, Via F. Marzolo 1, 35131 Padova, Italy

³Aix Marseille Université, CNRS, ICR, UMR 7273, case 551, Ave Escadrille Normandie Niemen, 13397 Marseille Cedex 20, France

⁴Instituto de Biociencias, Biotecnología y Biomedicina (iB3-UBA). Departamento de Química Biológica, Facultad de Ciencia Exactas y Naturales, Universidad de Buenos Aires. Intendente Güiraldes 2160 - Ciudad Universitaria, 1428EGA CONICET, Godoy Cruz 2290, C1425FQB. C.A.B.A. Argentina

⁵Instituto de Química y Fisicoquímica Biológicas, Dr. Alejandro Paladini, Universidad de Buenos Aires, CONICET, Junín 956, 1113AAD C.A.B.A., Argentina

*to whom correspondence should be addressed: marco.bortolus@unipd.it

Table of contents:

List of primer	S2
Analysis of immobilized FXN	S3
Centrifugation experiment	S4
Reversibility of Fe ³⁺ aggregation via chelation by EDTA	S5
M-TETPO labelled FXN with Fe ³⁺	S6
Sidechain conformer analysis of A99C and A114C labelled with M-TETPO	S7-8
Removal of bound Fe ²⁺ via chelation by PHEN	S9
Normalized fluorescence spectra	S10
Fe ²⁺ fluorescence quenching analysis	S11
Synthesis of M-TETPO	S12-13

Table S1 List of primer

<u>FXN mutant</u>	<u>Primer name</u>	<u>Primer sequence</u>
FXN_D122Y	FXN_D122Y_for	5' - GCCATACACGTTTGAGTACTATGATGTCTCCTTTGG - 3'
	FXN_D122Y_rev	5' - CCAAAGGAGACATCATAGTACTCAAACGTGTATGGC - 3'
FXN_A99C	FXN_A99C_for	5' - GAGACCACCTATGAAAGACTATGCGAGGAAACGCTGGACTC - 3'
	FXN_A99C_rev	5' - GAGTCCAGCGTTTCCTCGCATAGTCTTTCATAGGTGGTCTC - 3'
FXN_A114C	FXN_A114C_for	5' - CAGAGTTTTTTGAAGACCTTTGCGACAAGCCATACACGTTTGAG - 3'
	FXN_A114C_rev	5' - CTCAAACGTGTATGGCTTGTCGCAAAGGTCTTCAAAAACTCTG - 3'
FXN_T133C	FXN_T133C_for	5' - TCCTTTGGGAGTGGTGTCTTATGTGTCAAACCTGGGTGG - 3'
	FXN_T133C_rev	5' - CCACCCAGTTTGACACATAAGACACCACTCCCAAAGGA - 3'
FXN_H183C	FXN_H183C_for	5' - CGGCGTGTCCCTCTGTGAGCTGCTGGCC - 3'
	FXN_H183C_rev	5' - GGCCAGCAGCTCACAGAGGGACACGCCG - 3'
FXN_A193C	FXN_A193C_for	5' - GGCCGCAGAGCTCACTAAATGCTTAAAAACCAAACCTGGAC - 3'
	FXN_A193C_rev	5' - GTCCAGTTTGGTTTTTAAGCATTTAGTGAGCTCTGCGGCC - 3'

Analysis of immobilized FXN

The gradual spectral changes upon Fe^{3+} addition have been analyzed as combination of the two “pure” contributions shown in Figure S1 left:

- 1) the mobile nitroxide lineshape obtained from the A193C in the absence of Fe^{3+} , red spectrum;
- 2) the immobilized lineshape obtained from the A193C at 100 μM with a FXN: Fe^{3+} 1:50 ratio, pink spectrum.

A weighted sum of the two components (previously normalized to the same number of spins by dividing each spectrum by its double integral) has been performed to reproduce the spectra at various FXN concentrations and FXN: Fe^{3+} molar ratios. A full example is reported in the right panel of Figure S1.

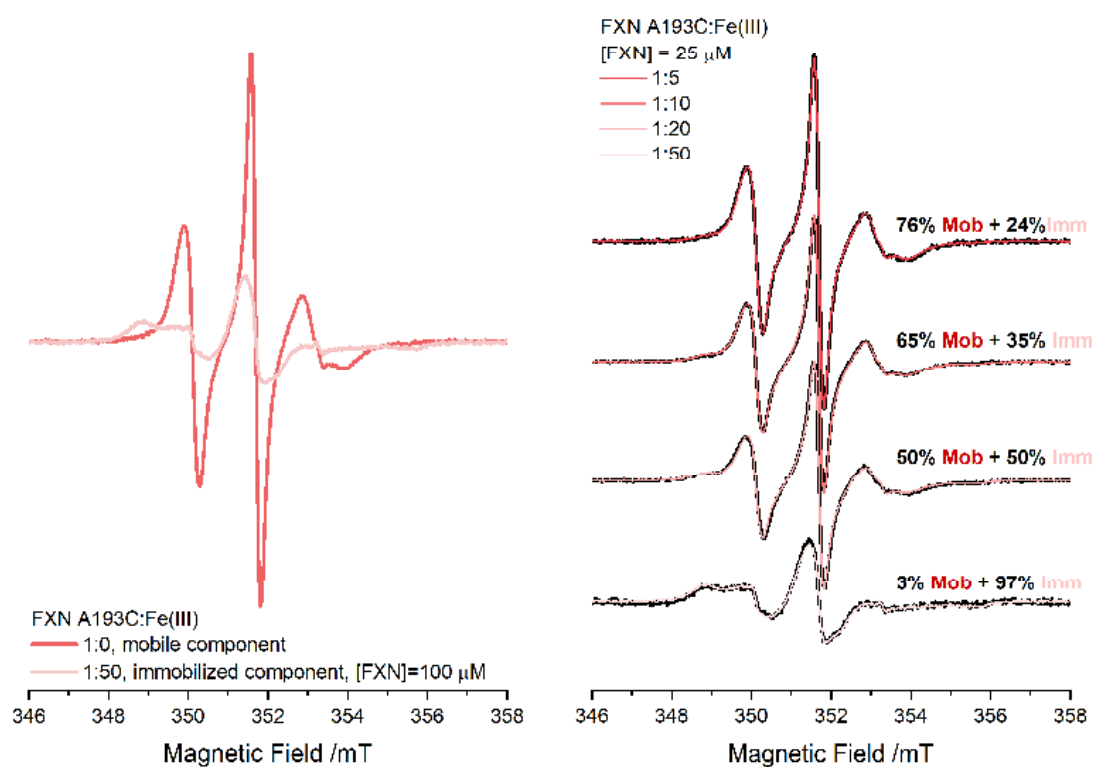


Figure S1 Left, the experimental spectra of A193C in the absence, mobile component (red) and in the presence of $\text{Fe}(\text{III})$ at a FXN: Fe^{3+} 1:50 ratio, immobilized component (pink); [FXN] = 100 μM . Right, experimental spectra (black) and simulations (color) obtained as a weighted sum of the components on the left.

Centrifugation experiment

A193C mutant labelled with MTSSL in buffered solution (no Ficoll) was incubated at a FXN:Fe³⁺ 1:20 ratio, [FXN] = 10 μ M. The lineshape, shown in Figure S2, shows a partial averaging of the different components relative to the sample in Ficoll, as expected from the fast tumbling of FXN. Nevertheless, the immobilized component is visible as indicated by the arrows (black spectrum). Upon centrifugation of the sample, the EPR spectrum of the supernatant shows only the mobile component, indicating that the immobilized component has been precipitated.

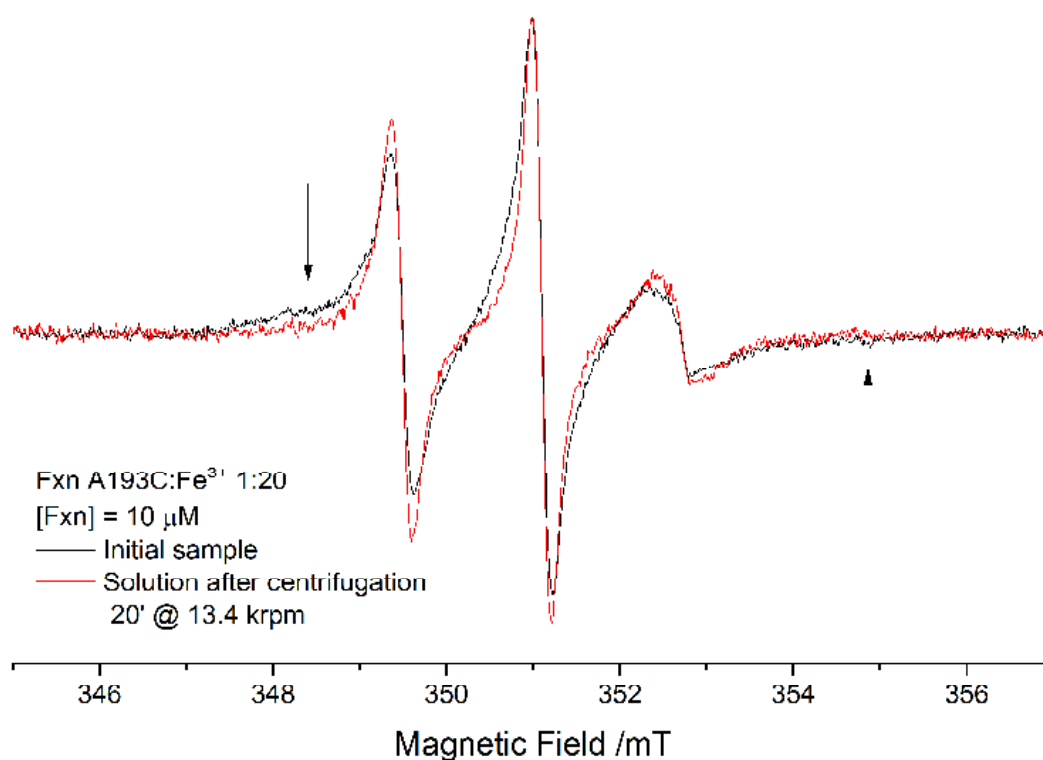


Figure S2 The experimental spectra of A193C in buffer solution at a FXN:Fe³⁺ 1:20 ratio, [FXN] = 10 μ M. The figure shows the spectrum before (black) and after (red) centrifugation. The arrows indicate the features of the immobilized component.

Reversibility of Fe³⁺ aggregation via chelation by EDTA

The reversibility of FXN aggregation was checked by incubating the sample with A193C at a 1:20 FXN:Fe³⁺ molar ratio, taking the EPR spectrum before (red) and after (pink) incubation of the sample with a three-fold molar excess of EDTA relative to iron, as can be seen from Figure S3 left. The lineshape partially reverts to the one in the absence of Fe³⁺, showing that aggregation is at least partially reversible. As a control that EDTA does not perturb the protein, we report the spectra of the protein with/without EDTA in the absence of Fe³⁺, Figure S3 right.

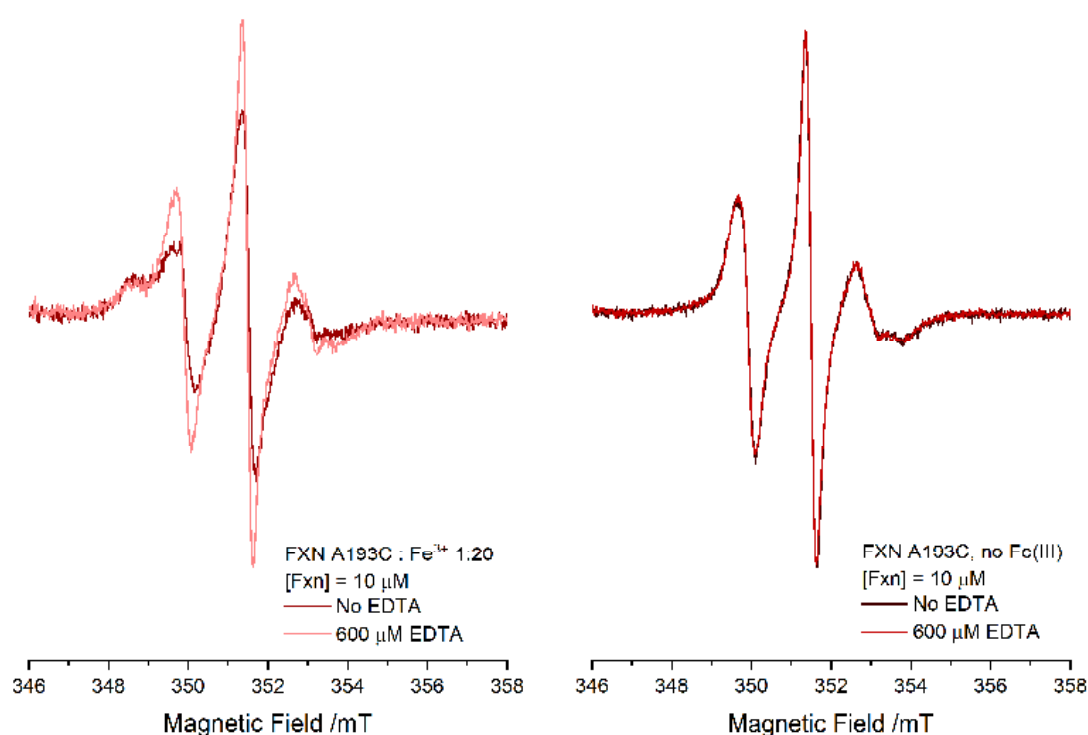


Figure S3 Left, the experimental spectra of A193C in the absence (red) and in the presence (pink) of EDTA. FXN:Fe³⁺ 1:50 ratio, [FXN] = 10 μM. Right, experimental of A193C with no Fe³⁺ present in the absence (red) and in the presence (pink) of EDTA.

M-TETPO-labelled FXN with Fe³⁺

To check that the protein labelled with M-TETPO behaves like the one labelled with MTSSL, we analyzed three mutants A114C, A114C/D122Y, and A193C in the presence of Fe³⁺. As can be seen from the spectra reported in FigureS4, all mutants show a progressive immobilization upon increasing Fe³⁺ additions, like their MTSSL-labelled counterparts.

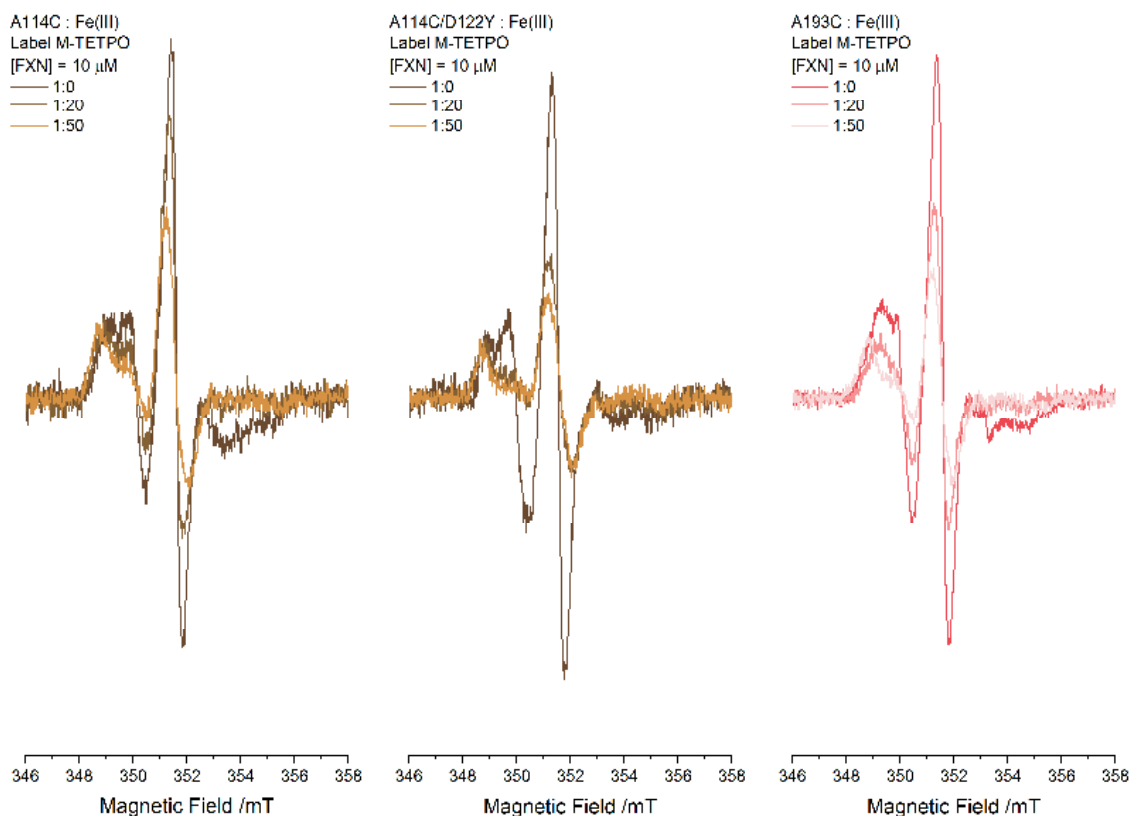


Figure S4 Experimental spectra of A114C (left), A114C/D122Y (middle), and A193C (right) at increasing FXN:Fe³⁺ ratios, [FXN] = 10 μM.

Sidechain conformer analysis of A99C and A114C labelled with M-TETPO

The A99C, A114C, and A114C/D122Y mutants labelled with M-TETPO show a progressive signal loss at increasing amounts of Fe^{2+} , unlike the other labelled positions which show no effects of Fe^{2+} . In the spectra of A114C and A114C/D122Y mutants, the signal loss is accompanied by a change in shape, whereas no change is observed for A99C position. This difference arises from the different conformers of the nitroxide sidechain that are present in the two positions, as shown in the figures below. The conformers have been obtained using the program MMM [Jeschke, G. (2018), MMM: A toolbox for integrative structure modeling. *Protein Science*, 27: 76-85. doi:[10.1002/pro.3269](https://doi.org/10.1002/pro.3269)]. As can be seen from FigureS5 top right, A114C has a multitude of possible conformers. The other views show the top three conformers (azure, light blue, and dark blue) that alone account for 76% of the energy accessible conformers. Only the azure and light blue conformers are close to a Fe^{2+} binding site and can thus be reduced, whereas the dark blue one is not. Thus, the reduction in intensity in A114C is accompanied by a change in shape, since the bulky sidechain of M-TETPO does not quickly explore its possible conformations. On the contrary, as can be seen from FigureS6, A99C has only a single conformer that is energetically accessible, all other possible conformations of the sidechain are not present due to steric clashes with the protein backbone. Therefore, when a nearby Fe^{2+} atom reduces the M-TETPO nitroxide only a reduction of intensity can be observed.

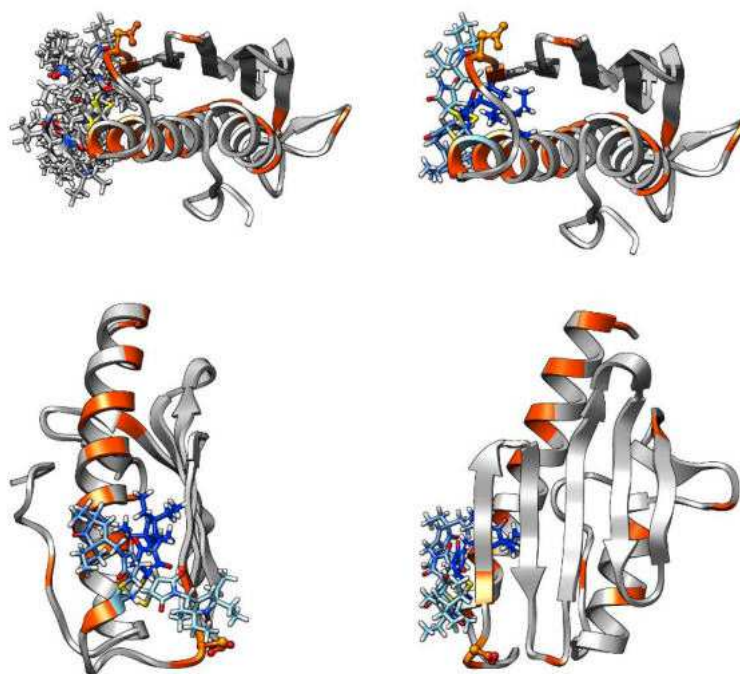


Figure S5 Conformers of the M-TETPO nitroxide attached to the A114 position. Top, view of FXN (PDB ID: 1EKG), with all possible conformers (left) or just the top three (right). Bottom, FXN with the top three conformers shown from different angles.

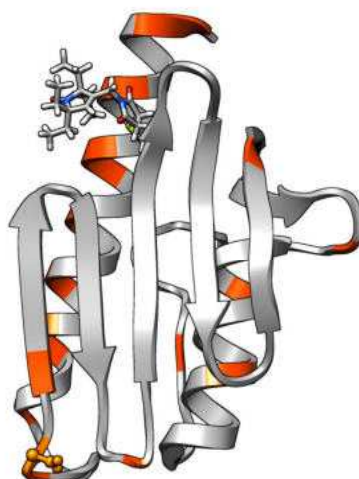


Figure S6 The single sterically allowed conformer of the M-TETPO nitroxide attached to the A99 position of FXN (PDB ID: 1EKG).

Removal of bound Fe²⁺ via chelation by PHEN

We verified the presence of an irreversible redox reaction of the M-TETPO nitroxide with Fe²⁺, as observed for MTSSL, via chelation of the protein-bound Fe²⁺ by treatment with 1,10-phenanthroline (PHEN). FigureS7 left, shows that, upon PHEN addition to a sample of the A114C/D122Y mutant - 1:50 FXN:Fe²⁺ molar ratio, the spectral intensity does not recover, even though Fe²⁺ has been chelated as verified by the solution turning red. FigureS7 right, shows the quantitative formation of the band, $\epsilon = 11200 \text{ (cm}\cdot\text{M)}^{-1}$ [*Inorg. Chem.* 1992, 31, 4, 555–559 <https://doi.org/10.1021/ic00030a006>].

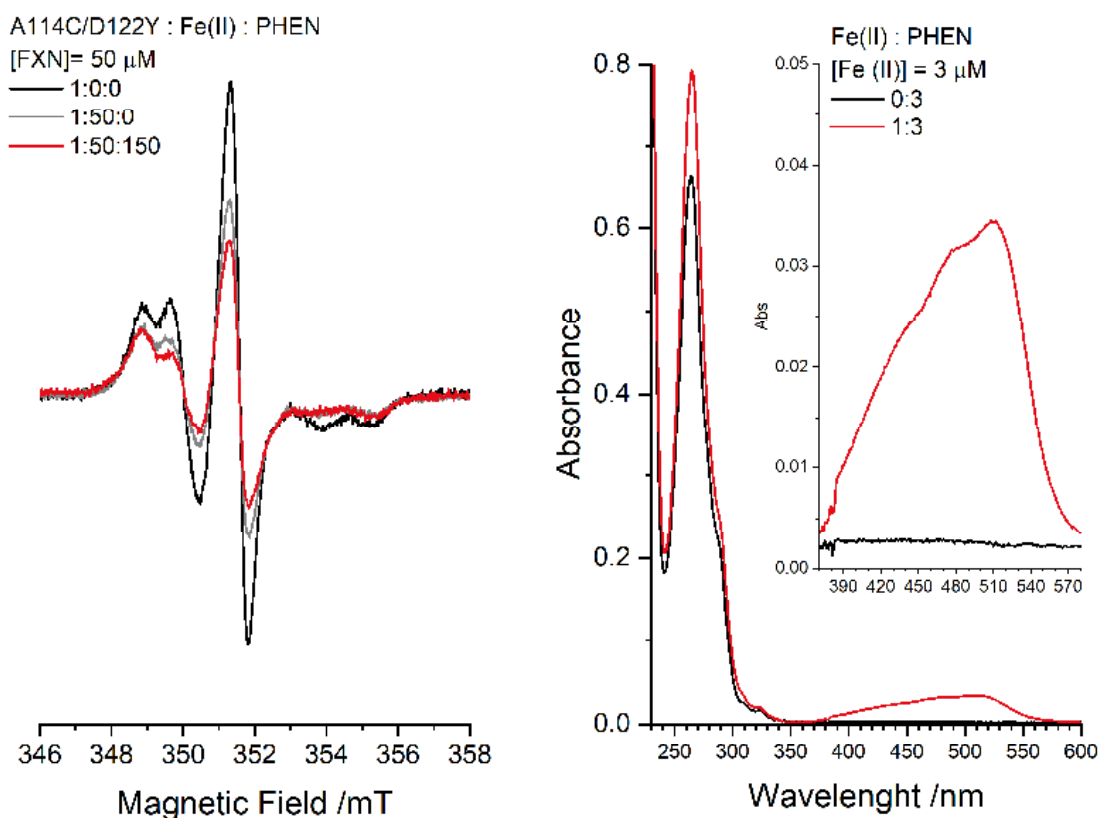


Figure S7 Left, the experimental spectra of A114C/D122Y alone (black), at a FXN: Fe²⁺ 1:50 ratio (grey), and at a FXN: Fe²⁺:PHEN 1:50:150 ratio (red); [FXN] = 50 μM . Right, UV-Vis spectra of the solution without (black) and with (red) Fe²⁺.

Normalized fluorescence spectra

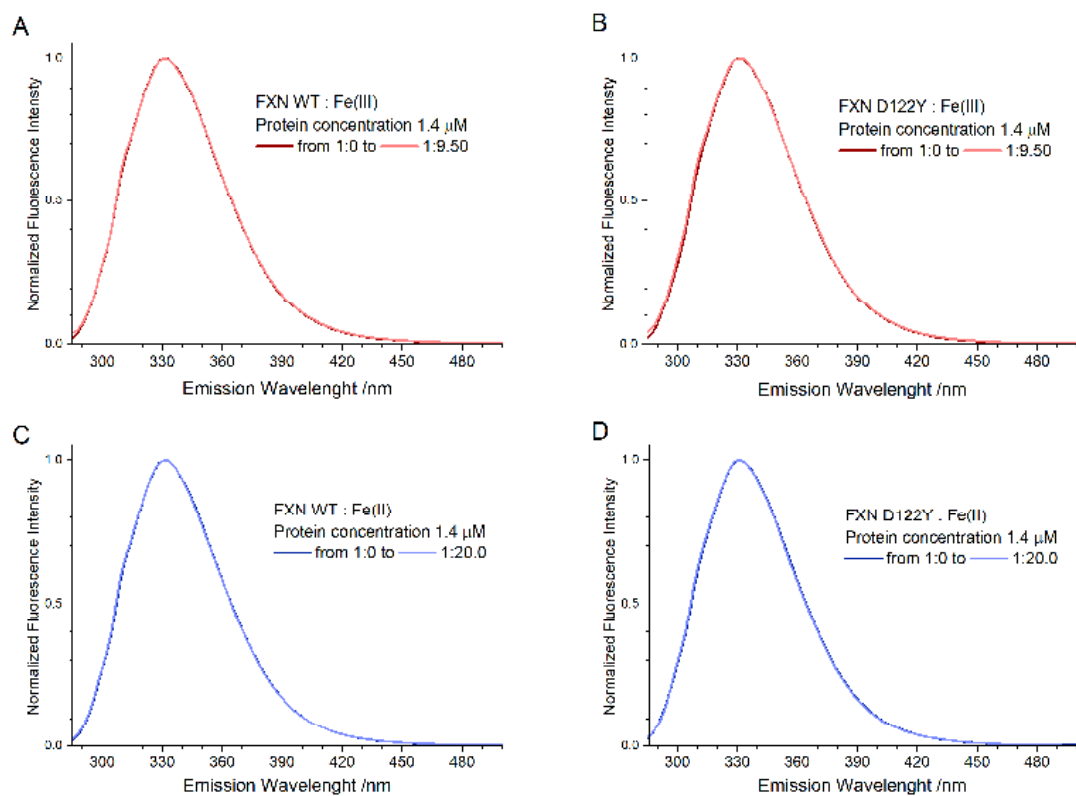


Figure S8 Normalized fluorescence spectra of WT (left, A, C) and D122Y FXN (right B, D): top with Fe(III); bottom with Fe(II).

Fe²⁺ fluorescence quenching analysis

The fluorescence quenching curves of WT and D122Y FXN with Fe²⁺ were analyzed according to the method reported in the literature (Sawyer, W. H.; Winzor, D. J. Theoretical Aspects of the Quantitative Characterization of Ligand Binding. *Curr. Protoc. Protein Sci.* **1999**, 16 (1), 1–40. <https://doi.org/10.1002/0471140864.psa05as16>). The analysis is reported in Figure S9. Briefly, from the fractional saturation ($fa = \frac{(F-Ff)}{(Fb-Ff)}$, where F is the fluorescence at a given Fe²⁺ concentration, Ff the one without Fe²⁺ and Fb the one at saturating Fe²⁺ concentrations) the number of binding sites on the acceptor (p) is determined at the crossing of the two blue lines as shown in the top part of Figure S9; the result is $p=1$ for both proteins.

Once the stoichiometry has been determined, the binding function (r) can be evaluated from a titration in which the acceptor concentration is close to the dissociation constant for the binding equilibrium. The value of the dissociation constant Kd is obtained from a linear regression of the titration according to the equation *A.5A.10* in the reference: $\frac{1}{r} = p^{-1} + Kd \frac{1}{pCs}$. The value of r is established at each value of Cs , the concentration of free ligand: $Cs = \overline{Cs} - r\overline{Ca}$, where \overline{Cs} and \overline{Ca} are the total concentration of Fe²⁺ and acceptor (i.e. the protein), respectively.

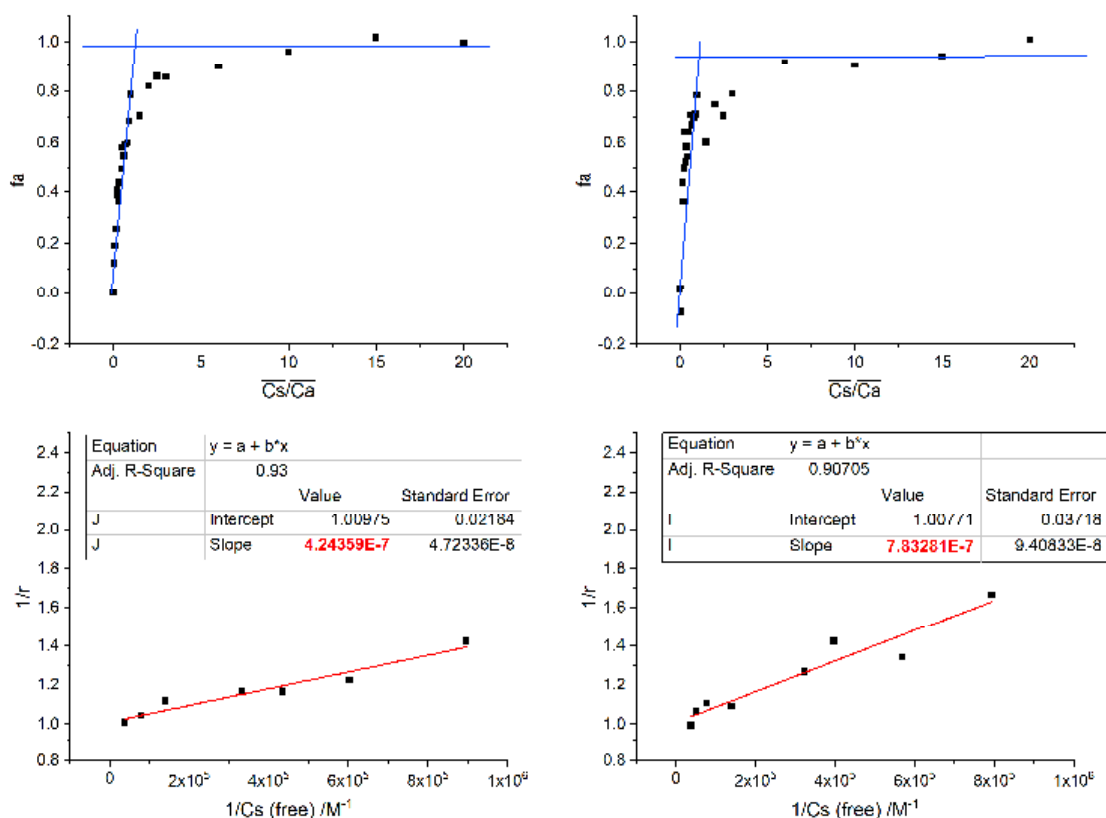
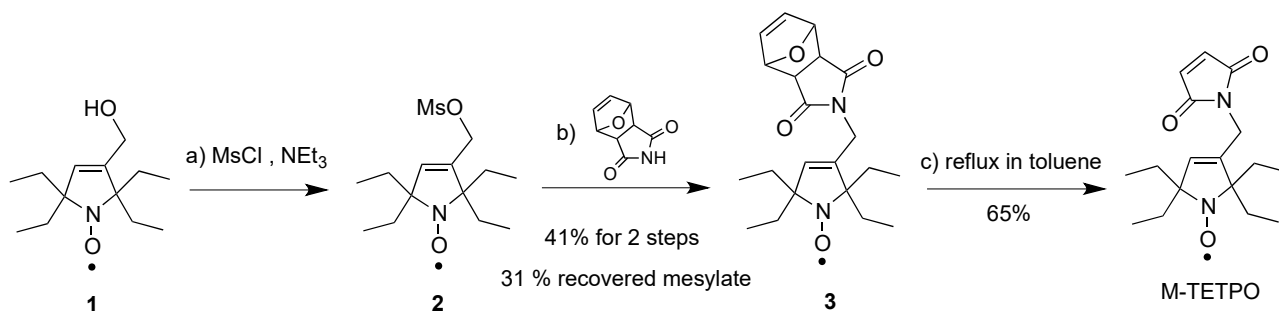


Figure S9 Analysis of the fluorescence quenching experiments with Fe²⁺, for FXN WT (left) and its D122Y variant (right).

Synthesis of M-TETPO

Chemicals were purchased from Sigma-Aldrich or TCI and were used as received. All experiments were performed under anhydrous conditions and an inert atmosphere of argon and, except where stated, using dried apparatus and employing standard techniques for handling air-sensitive materials. High-resolution mass spectra (HRMS) were performed on a SYNAPT G2 HDMS (Waters) spectrometer equipped with atmospheric pressure ionization source (API) pneumatically assisted. Samples were ionized by positive electrospray mode as follows: electrospray tension (ISV): 2800 V; opening tension (OR): 20 V; nebulization gas pressure (nitrogen): 800 L/h. Analytical thin layer chromatographies (TLC) were carried out on Macherey Nagel DC-Fertigfolien alugram Xtra SIL G plates. Flash column chromatographies were carried out on Merck Kieselgel 60 (230–400 mesh). For EPR measurements to test the products, samples with 0.5 mM concentration of nitroxide were prepared in non-degassed solvents. Experiments were performed on an EMX Bruker machine.

Procedure to prepare M-TETPO from alcohol **1**:



Methanesulfonyl chloride (50 μ L, 0.65 mmol) was added to a solution of alcohol **1** (134 mg, 0.59 mmol) and NEt₃ (90 μ L, 0.65 mmol) in CH₂Cl₂ (10 mL) at 0°C and the solution was stirred at ambient temperature. After 2h, the reaction was quenched with 1M HCl solution (5 mL) and extracted with CH₂Cl₂ (3 x 10 mL). The combined organic layers were washed with brine (10 mL), dried over MgSO₄, filtered and the solvent was removed in vacuum. The residue oil was dissolved in DMF (10 mL), K₂CO₃ (245 mg, 1.77 mmol) and protected maleimide (195 mg, 1.18 mmol) were added. After stirring at 60 °C for 16 h, the reaction was diluted with H₂O (10 mL) and extracted with EtOAc (3 x 10 mL). The combined organic layers were washed with brine (2 x 10 mL), dried over MgSO₄, filtered and the solvent was removed in vacuum. The residue was purified by column chromatography (SiO₂, petroleum ether-EtOAc 2:1) to yield unreacted mesylate **2** (55 mg, 0.18 mmol, 31 %, R_f = 0.54) and the compound **3** (90 mg, 0.24 mmol, 41%, R_f = 0.26) as a yellow solid; mp = 118°C. EPR: *g*-value = 2.004; a_N = 14.46 G. IR (ATR): 2967 (w), 2937 (w), 2881 (w), 1703 (s), 1670 (s), 1383 (m), 1088 (m), 880 (m) cm⁻¹. HRMS (ESI-TOF): *m/z* calcd for C₂₁H₂₉N₂O₄Na [M + Na⁺]: 396.2020; found 396.2018.

A solution of compound **3** (74 mg, 0.20 mmol) in toluene (10 mL) was heated to reflux for 3 h. After removal of the solvent in vacuum, the residue was purified by column chromatography (SiO₂, petroleum ether-EtOAc 2:1, R_f = 0.50) to yield M-TETPO (41 mg, 0.13 mmol, 65%) as an orange oil. EPR: *g*-value = 2.005; a_N =

14.36 G. IR (ATR): 2967 (w), 2937 (w), 2880 (w), 1707 (s), 1405 (m), 1152 (m), 828 (m), 693 (m) cm^{-1} .
HRMS (ESI-TOF): m/z calcd for $\text{C}_{17}\text{H}_{25}\text{N}_2\text{O}_3\text{Na}$ [$\text{M} + \text{Na}^+$]: 328.1757; found 328.1757.

RESEARCH ARTICLE

The displacement of frataxin from the mitochondrial cristae correlates with abnormal respiratory supercomplexes formation and bioenergetic defects in cells of Friedreich ataxia patients

Davide Doni¹ | Giovanni Rigoni¹ | Elisa Palumbo² | Elisa Baschiera^{3,4} |
 Roberta Peruzzo¹ | Edith De Rosa¹ | Federico Caicci¹ | Leonardo Passerini¹ |
 Daniela Bettio^{3,4} | Antonella Russo²  | Ildiko Szabò¹ | Maria Eugenia Soriano¹ |
 Leonardo Salviati^{3,4,5} | Paola Costantini¹ 

¹Department of Biology, University of Padova, Padova, Italy

²Department of Molecular Medicine, University of Padova, Padova, Italy

³Clinical Genetics Unit, Department of Women's and Children's Health, University of Padova, Padova, Italy

⁴Istituto di Ricerca Pediatrica (IRP) Città della Speranza, Padova, Italy

⁵Myology Center, University of Padova, Padova, Italy

Correspondence

Paola Costantini, Department of Biology, University of Padova, Viale G. Colombo 3, Padova 35131, Italy.
Email: paola.costantini@unipd.it

Funding information

Department of Biology, University of Padova: COST_FINA_P14_02 to P.C. and BIRD179997/17 to M.E.S.; Department of Molecular Medicine, University of Padova: PRID/SID 2019 to A.R. and PRID/SID 2017 to E.P.; MIUR: PRIN 20155795S5W to I.S.; Fondazione Città della Speranza, Padova to L.S.

Abstract

Friedreich ataxia (FRDA) is a neurodegenerative disease resulting from a severe decrease of frataxin (FXN). Most patients carry a GAA repeat expansion in both alleles of the *FXN* gene, whereas a small fraction of them are compound heterozygous for the expansion and a point mutation in the other allele. FXN is involved in the mitochondrial biogenesis of the FeS-clusters. Distinctive feature of FRDA patient cells is an impaired cellular respiration, likely due to a deficit of key redox cofactors working as electrons shuttles through the respiratory chain. However, a definite relationship between FXN levels, FeS-clusters assembly dysregulation and bioenergetics failure has not been established. In this work, we performed a comparative analysis of the mitochondrial phenotype of cell lines from FRDA patients, either homozygous for the expansion or compound heterozygotes for the G130V mutation. We found that, in healthy cells, FXN and two key proteins of the FeS-cluster assembly machinery are enriched in mitochondrial cristae, the dynamic subcompartment housing the respiratory chain. On the contrary, FXN widely redistributes to the matrix in FRDA cells with defects in respiratory supercomplexes assembly and altered respiratory function. We propose that this could be relevant for the early mitochondrial defects afflicting FRDA cells and that perturbation of mitochondrial morphodynamics could in turn be critical in terms of disease mechanisms.

KEYWORDS

FeS-cluster assembly, mitochondria, mitochondrial morphology, respiration

Abbreviations: BNGE, blue native gel electrophoresis; ETC, mitochondrial electron transport chain; FCCP, carbonilcyanide p-trifluoromethoxyphenylhydrazine; FXN, frataxin; FRDA, Friedreich ataxia; ISCU, iron-sulfur cluster assembly enzyme; LCL, lymphoblastoid cell line; MICOS, mitochondria contact site and cristae organization system; NFS1, cysteine desulfurase, Nitrogen Fixation 1 Homolog (*S. cerevisiae*); OCR, oxygen consumption rate; OXPHOS, oxidative phosphorylation; OPA1, optic atrophy protein 1; SCs, supercomplexes; TEM, transmission electron microscopy.

1 | INTRODUCTION

Friedreich ataxia (FRDA; OMIM 229 300) is the most common inherited ataxia, affecting 1 in 50 000 in the Caucasian population.^{1,2} FRDA is a neurodegenerative disorder associated to multiple symptoms including slowly progressive gait and limb ataxia, areflexia, dysarthria, and loss of proprioceptive sensation, while cognitive functions are preserved. Symptoms typically manifest in childhood and gradually worsen over time, with patients usually becoming wheelchair-dependent 15–20 years after the onset of the disease. Non-neurological features comprise diabetes mellitus and hypertrophic cardiomyopathy, which affects at least 60% of patients and at final stages may cause severe, life threatening arrhythmias that lead to premature death.^{3,4} To date, no specific therapeutic measures are known to modify the progression of the disease and patient medical care is essentially aimed at mitigating the symptoms. FRDA is usually caused by an abnormally expanded GAA triplet repeat in the first intron of the *FXN* gene, on chromosome 9q21. The expansion leads to transcriptional silencing of *FXN* through heterochromatinization of the expanded region, and to a reduced expression of frataxin, a ubiquitous and highly conserved mitochondrial protein.^{1,5,6} The severity of the disease increases with the length of the expansion, which ranges from 6 to 36 in healthy individuals and 70–1700 (most commonly 600–900) in FRDA patients.¹ The majority of the patients harbor two expanded *FXN* alleles, and it is usually the size of the shorter expansion that correlates with the clinical phenotype. Approximately, 5% of the patients are compound heterozygous for the GAA expansion and a point mutation in the *FXN* gene, including nonsense, missense, insertions, and deletions.^{7–10} All patients have about 5%–30% estimated residual frataxin levels.⁵ Constitutive deletion of the *FXN* gene in mice causes embryonic lethality,¹¹ indicating that the complete loss of frataxin is not compatible with life.

Impaired mitochondrial oxidative phosphorylation, bioenergetics failure, deficit of FeS-protein, iron overload, and increased sensitivity to oxidative stress commonly occur in cells of patients with FRDA.^{12–22} The precise function of frataxin remains unclear, but several roles have been proposed, ranging from heme and FeS-clusters biogenesis^{23,24} to iron-chaperone and binding/storage activities.^{25,26} All these functions are in agreement with the mitochondrial phenotype of FRDA cells; however, due to the tight link between these crucial cellular pathways, it is difficult to clearly identify the primary event(s) leading to the metabolic impairment and to disease onset and progression. It is worth noting that mitochondrial energy production relies heavily on FeS-clusters (respiratory complexes I, II, and III) and heme (respiratory complex IV) as prosthetic groups; but the biogenesis of FeS-clusters itself takes place in mitochondria, which contain the specific assembly machinery.²⁷ Human frataxin was shown

to interact in vitro with multiple core components of this machinery, however, its exact molecular function at this level remains unclear.^{28–32} Although a cytosolic FeS-cluster biogenesis system exists in eukaryotes, the assembly machinery described above is also essential to all extra-mitochondrial FeS-proteins.³³ This puts mitochondria physiology more in general at the core of the metabolic pathways involving FeS-proteins.³⁴

Most mitochondrial functions are closely linked to their morphology: mitochondria are highly dynamic organelles which continually fuse, divide and remodel their cristae to cope with the variable energy demands and to participate to other processes such as calcium homeostasis, apoptosis, and autophagy (see 35 for a comprehensive review on this topic). In the complex architecture of a mitochondrion, cristae have a remarkable structural variability³⁶ and are considered a functional subcompartment per se since they host the assembled respiratory complexes. The physiological relevance of the cristae is supported by the direct correlation between their density and the respiratory capacity of mitochondria.³⁷ Moreover, cristae shape and their dynamic remodeling are fundamental for the assembly of the respiratory complexes in supercomplexes, quaternary structures which in healthy cells increase the electron flow channeling and the overall mitochondrial respiratory efficiency.^{38–40}

Energy-intensive cells, such as neurons and skeletal/cardiac myocytes, are particularly vulnerable to mitochondrial dysfunctions as indicated by the fact that several neurodegenerative diseases are caused by mutations in genes directly involved in mitochondrial dynamics.^{35,41} In disorders associated with defects in the FeS-cluster assembly process, such as FRDA, perturbations of mitochondrial ultrastructure and dynamics could be also critical for the pathogenesis of the disease. Based on these premises, in this work, we explored the relationship between frataxin, mitochondrial ultrastructure, and bioenergetics in four cell lines from FRDA patients, three homozygous for the GAA triplet expansion, the other compound heterozygous for the GAA expansion and the G130V point mutation, which is one of the most frequently found in clinically affected heterozygous patients.

2 | MATERIALS AND METHODS

2.1 | Cell lines and culture conditions

Lymphoblastoid cell lines (LCLs) were obtained from the Coriell Institute for Medical Research (NJ, USA) and cultured in RPMI1640 (GIBCO Life Technologies), supplemented with 15% FBS, 2 mM L-glutamine, 100 U/mL penicillin, and 100 µg/mL streptomycin, under 5% CO₂ at 37°C. FRDA LCLs were from four unrelated clinically affected patients: GM04079 (homozygous for the GAA expansion in the *FXN*

gene, with alleles carrying 541 and 420 repeats at sampling), GM16227 (homozygous for the GAA expansion, with alleles carrying 630 and 830 repeats at sampling), GM15850 (homozygous for the GAA expansion, with alleles carrying 650 and 1030 repeats at sampling), and GM21542 (with one *FXN* allele carrying 900-950 GAA repeats, as determined in this work by long-range PCR, Figure S1 (see below in the next paragraph) and the second carrying a G130V point mutation and a normal number of repeats); control LCLs were from two clinically unaffected subjects (with both *FXN* alleles in the normal range of GAA repeats): GM07533 and GM15851 (brother of patient GM15850). GM04079, GM16227, and GM15850 are indicated throughout the text as FRDA 1, FRDA 2, and FRDA 3, respectively. Cytogenetic analysis was performed on the lymphoblastoid cell lines used for the experiments, according to standard laboratory procedures. A normal karyotype was observed in all the 20 Q-banded metaphases analyzed for each case (Figure S2).

2.2 | Genotyping and RT-PCR

About 4×10^6 cells from each line, were harvested, sedimented, washed twice with PBS, and resuspended in lysis buffer (10 mM Tris-HCl pH 8.0, 1 mM EDTA pH 8.0, 0.1% SDS, and 400 $\mu\text{g}/\text{mL}$ Proteinase K). Samples were incubated at 50°C overnight. Genomic DNA was purified with phenol: chloroform: isoamyl alcohol (25:24:1) according to standard procedures. For *FXN* expression analysis, total RNA was isolated from 3×10^6 cells using the RNeasy mini kit (Qiagen). DNA and RNA samples were quantified using ND-1000 spectrophotometer (Nanodrop, Wilmington, DE, USA). The genotype of all cell lines employed in this work was verified by long-range PCR. In the case of GM21542, derived from the compound heterozygote carrying the G130V mutation and one expanded allele of unknown length, we found that the GAA expansion consists of 900-950 repeats (Figure S1). A 50 ng of each DNA sample were amplified with the QIAGEN LongRange PCR Kit (Qiagen) according to manufacturer's instructions using a primer set specific for the amplification of the expanded GAA-repeat (forward: 5'-GGAGGGATCCGTCTGGGCAAAGG-3'; reverse: 5'-CAATCCAGGACAGTCAGGGCTT-3'; amplicon length: 1350 + 3n GAA).¹ A sample of 2 μg of RNA was retrotranscribed (EuroScript M-MLW Reverse Transcriptase RNase H-, Euroclone) and 2 ng of cDNA were used as template in the quantitative real-time PCR (qRT-PCR) using the following primer pairs (*FXN*: forward: 5'-CCTTGCAGACAAGCCATACA-3', reverse: 5'-GGTCCACTGGATGGAGAAGA-3'; *GAPDH*: forward: 5'-CCTCAACGACCACTTTGTCA-3', reverse: 5'-TTCCTCTTGTGCTCTTGCTG-3'). qRT-PCR was performed using an Applied Biosystems 7500 Fast Real-Time

PCR System according to the following amplification protocol: 95°C for 10 minutes, 95°C for 15 seconds, and 60°C for 60 seconds (40 cycles). qRT-PCR reactions were always performed in triplicate amplifying the cDNA deriving from two independent reverse transcription reactions. Amplification efficiency of *FXN* and *GAPDH* genes was verified using the standard curve method. *FXN* expression was normalized to that measured in the non-mutated cell line (GM07533 or GM15851), using the comparative delta CT method ($2^{-\Delta\Delta\text{CT}}$) implemented in the 7500 Real Time System software.

2.3 | SDS-PAGE and protein immunoblotting

About 5×10^6 cells from each line were harvested, sedimented, washed once with cold PBS and lysed for 30 minutes on ice in 1 mL of RIPA lysis buffer (50 mM Tris-HCl pH 7.5, 150 mM NaCl, 1% NP-40, 100 μM phenylmethylsulfonyl fluoride, 1 $\mu\text{g}/\text{mL}$ aprotinin, 1 $\mu\text{g}/\text{mL}$ leupeptin, and 1 $\mu\text{g}/\text{mL}$ pepstatin). Lysates were sedimented at full speed in a microcentrifuge for 15 minutes at 4°C, the supernatants transferred to clean tubes and the protein concentration determined by the Bradford assay. Equal protein amounts, as determined by Bradford assay (Bradford Reagent, Sigma-Aldrich), were solubilized in Laemmli gel sample buffer containing 5% 2-mercaptoethanol and separated electrophoretically by SDS-PAGE on 4%-15% gels (BioRad), except for the analyses of OPA1 in which the gels were 8%. Proteins were then transferred on nitrocellulose membranes (0.45 μM , BioRad), which were eventually probed with different primary antibodies (listed in Table S1) and with horseradish peroxidase-conjugated goat anti-mouse or anti-rabbit IgG. Labeled proteins were then visualized with an ECL western blotting detection kit (Thermo Scientific Pierce Protein Research). Reaction product levels were quantified by scanning densitometry using ImageJ software and normalized to those of β -actin or the mitochondrial protein TOM20.

2.4 | Blue native gel electrophoresis (BNGE)

For BN extraction, 40×10^6 cells from each line were collected, sedimented and washed once with cold PBS. Cell pellets were homogeneously resuspended in 200 μL of PBS and 200 μL of a freshly prepared solution of 8 mg/mL digitonin were added. After incubation for 10 minutes in ice, 1 mL of cold PBS was added to each sample to be then centrifuged at 9600 $\times g$, 10 minutes, 4°C. Pretreated cells were washed once with cold PBS and sedimented again at 9600 $\times g$, 10 minutes, 4°C in order to remove the excess of residual digitonin. After centrifugation, the pellets containing the mitochondrial fraction were solubilized in 100 μL of Loading Native Buffer

1X containing Protease Inhibitor Cocktails (PIC, 1:100) and 10 μ L of a freshly prepared solution of digitonin 10%. After 5 minutes of incubation in ice, samples were centrifuged at maximal speed in a microcentrifuge, 25 minutes, 4°C, and the supernatant containing mitochondrial complexes was collected. In the final step, 5 μ L of 5% Coomassie Blue G-250 (Invitrogen) were added to each sample. The electrophoresis in native conditions was performed by loading 20 μ L of each sample in a precast native Bis-Tris gel 3%-12% (Invitrogen). A first electrophoretic run was done at 150V in presence of Anode buffer and Dark cathode buffer (Invitrogen), 45 minutes, 4°C. The Dark buffer was then replaced with Light buffer (Invitrogen) and a second run was done at 250V, 90 minutes, 4°C. Then, a part of the gel was stained with Coomassie Brilliant Blue R-250, not shown in the Results), and the other part containing the replicates was blotted onto a PVDF membrane at 33V, overnight, 4°C. After transfer, the membrane was fixed with acetic acid 8% for 15 minutes, washed with water and let it dry. The membrane was then re-activated for 1 minute in pure methanol and incubated with the indicated antibodies (reported in Table S1). Protein bands were visualized as described above.

2.5 | Biochemical analysis of respiratory complexes

The activities of the mitochondrial electron transport chain (ETC) complexes were measured according to the protocol described by Spinazzi et al.⁴² Briefly, 50×10^6 cells from each line were harvested, sedimented, washed twice with PBS and prepared to obtain the mitochondrial-enriched fraction. Each sample protein content was then quantified according to the Bradford method and the activity of complex I (NADH: ubiquinone oxidoreductase), complex II (succinate dehydrogenase), complex III (decylubiquinol cytochrome *c* oxidoreductase), complex IV (cytochrome *c* oxidase), and citrate synthase (CS) was measured by means of a single-wavelength multicuvette spectrophotometer (Varian Cary UV-Vis 100) at 37°C. Activities of the mitochondrial OXPHOS complexes were normalized to CS activity.

2.6 | Oxygen consumption studies

Cells from each line were collected, sedimented, and re-suspended in DMEM without serum and sodium bicarbonate, supplemented with 10 mM sodium pyruvate and 2 mM glutamine. About 2.5×10^5 cells/well were seeded into a Seahorse plate after precoating with Cell Tak reagent (Corning), following the protocol described by the manufacturer. The plate was then centrifuged for 2 minutes at 600 xg

to ensure cells adhesion to the bottom of the wells. The oxygen consumption rate (OCR) was measured with an extracellular flux analyzer (Seahorse) at fixed time points and after the addition of the following compounds: oligomycin (2 μ g/mL), FCCP (400 nM), and antimycin A (1 μ M). At the end of each experiment, every plate well was directly observed using an optic microscope (not shown), to exclude wells with a massive detachment of cells from the analysis. To assess mitochondrial functionality, bioenergetic parameters were calculated as follows: ATP-linked respiration is the difference between OCR before and after the addition of oligomycin; proton leak is the difference between OCR measured after the treatment with oligomycin and after the treatment with antimycin; maximal respiration was obtained by subtracting the OCR value measured after the addition of antimycin from the OCR value observed upon the addition of FCCP; spare respiratory capacity is the difference between the respiration obtained after the addition of FCCP and basal respiration; non-mitochondrial respiration is OCR value of cells incubated with antimycin.

2.7 | Immunogold staining and electron microscopy

Cells were fixed in a 24 wells plate with 4% paraformaldehyde (freshly prepared) in PBS (pH 7.4) for 30 minutes at room temperature. After fixation, cells were washed five times with PBS (5 minutes each), blocked and permeabilized with 5% normal goat serum and 0.1% saponin in PBS for 30 minutes, and then incubated 2 hours at room temperature with the primary antibody of interest in PBS, 5% normal goat serum and 0.05% saponin. After five washes with PBS (5 minutes each), cells were incubated 1 hour at room temperature with the secondary antibody Nanogold Fab GAR Ultra Small (Aurion). After 5 washes, cells were fixed with 2% glutaraldehyde in PBS for 30 minutes. After 5 washes with water (5 minutes each) cells were incubated with Gold Enhancer (Nanoprobes), washed with water and prepared as for classical electron microscopy sample. Briefly, samples were postfixated with 1% osmium tetroxide/1% ferrocyanide in 0.1 M sodium cacodylate buffer for 1 hour at 4°C; after three water washes, samples were dehydrated in a graded ethanol series and embedded in an epoxy resin (Sigma-Aldrich). Ultrathin sections (60-70 nm) were obtained with an Ultratome V (LKB) ultramicrotome, counterstained with uranyl acetate and lead citrate, and finally, examined under a Tecnai G² (FEI) transmission electron microscope operating at 100 kV at the electron microscopy facility of the Department of Biology, University of Padova. Images were captured with a Veleta (Olympus Soft Imaging System) digital camera. Antibody used for immunogold analyses were anti-frataxin, anti-NFS1, and anti-ISCU. Controls for specificity of immunolabeling were made by omitting the primary antibodies.

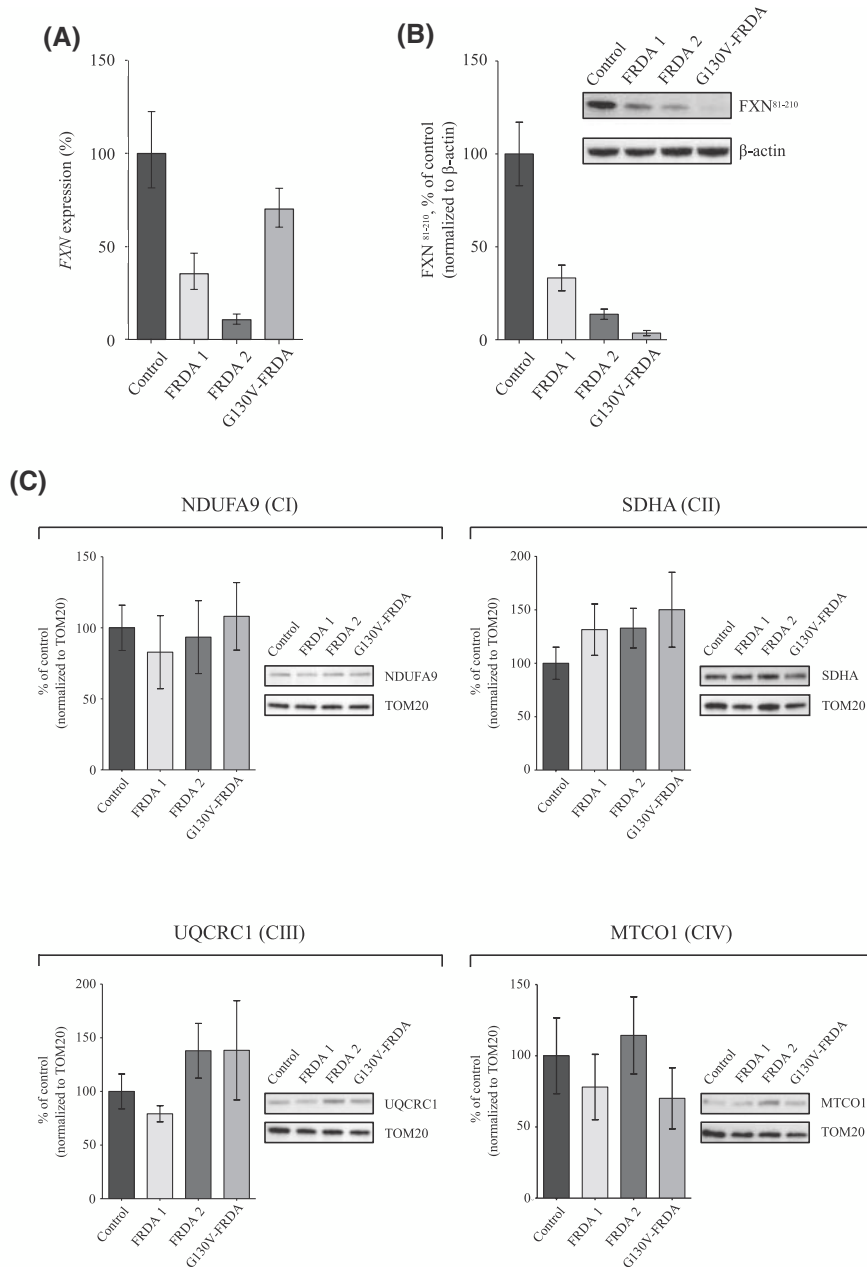


FIGURE 1 Comparative analysis of frataxin and mitochondrial respiratory complexes I-IV subunits in healthy control, homozygous FRDA, and heterozygous G130V-FRDA LCLs. A, *FXN* expression measured by qRT-PCR in unaffected control, FRDA (1 and 2) and G130V-FRDA LCLs. *FXN* expression levels are normalized to those detected in the non-mutated control cell line, expressed as 100%. Error bars represent gene expression range calculated according to the standard deviation of the $\Delta\Delta CT$ value. B, Western blotting analysis of FXN protein (mature form) in whole cell extracts from unaffected control, FRDA (1 and 2) and G130V-FRDA LCLs. Equal amounts of protein (i.e., 60 μ g) were loaded in each lane. β -actin was used as loading control. Protein levels were quantified after normalization with β -actin and expressed as a percentage of control level. Reported data result from the mean of four independent experiments \pm SEM. C, Western blotting analysis of respiratory complexes subunits, that is, NDUFA9 (complex I), SDHA (complex II), UQCRC1 (complex III), and MTCO1 (complex IV), in whole cells extracts from FRDA (1 and 2), G130V-FRDA and unaffected control LCLs. Equal amounts of protein (i.e., 25 μ g) were loaded in each lane. TOM20 was used as loading control. Protein levels were quantified after normalization with TOM20 and expressed as a percentage of control level. Reported data result from the mean of three independent experiments \pm SEM. Statistical significance was determined using One-way ANOVA with Dunnett's post hoc test

2.8 | Morphometric analysis of mitochondria

The mitochondrial ultrastructure was analyzed using ImageJ software. For each mitochondrion, two morphological

parameters were assessed in 2D: (i) mitochondria length, evaluated as the longest distance between any two points of the selected mitochondrion (Feret's maximum diameter); (ii) cristae width, evaluated as the widest point of the selected crista. For each cell line, TEM micrographs

ranging from 30 to 150 (mitochondrial length) and from 165 to 600 (cristae width) were analyzed, as specified in the Figure legends. For both morphological descriptors, frequency distribution and fitting analysis were performed using Origin. Briefly, the relative frequencies, expressed as percentage of mitochondria, were fitted by a nonlinear regression as singular or sum of Gaussian functions, according to the data distribution.

2.9 | Statistical analysis

All numerical data, analyzed by GraphPad Prism, are expressed as mean \pm SEM. Statistical analysis and significance were performed and assessed as specified in the Figure legends, with $P \leq .05$ accepted as statistically significant.

3 | RESULTS

3.1 | Comparative analysis of frataxin and respiratory complexes I-IV subunits in FRDA patients' cells

We evaluated *FXN* transcription by qRT-PCR in four lymphoblastoid cell lines (LCLs). Three of them were derived from FRDA patients, two homozygous for the GAA expansion (GM04079/FRDA 1 and GM16227/FRDA 2) and the other carrying the G130V point mutation and an expanded allele (GM21542/G130V-FRDA). The other LCL was derived from a clinically unaffected control, that is, GM07533 (with two unexpanded alleles). We detected the lowest levels of *FXN* mRNA in the homozygous FRDA cell lines (Figure 1A). In the G130V-FRDA, *FXN* expression was comparable to the expression levels usually detected in a heterozygous carrier (not shown, E.P. and A.R., personal communication). Frataxin protein levels were then analyzed by western blotting in whole-cell extracts. Frataxin is synthesized in the cytosol as a full-length precursor (i.e., FXN^{1-210}), and then, imported into the mitochondria, where it undergoes to a two-step proteolytic processing resulting in the mature, shorter form (i.e., FXN^{81-210}).⁴³⁻⁴⁵ Figure 1B shows that the amount of mature frataxin is reduced in the three FRDA patient cells when compared to the control. The lowest protein levels were found in LCLs from the G130V-FRDA heterozygous patient. Clark and colleagues showed that G130V mutation impairs the frataxin processing from FXN^{42-210} to FXN^{81-210} in FRDA patients' fibroblasts.⁴⁶ Figure S3 indicates that $FXN^{42-210}/FXN^{81-210}$ ratio is increased also in the G130V-FRDA LCLs used in our experiments, in agreement with Clark et al, and, on the contrary, that the amount of the

intermediate FXN^{42-210} has the same trend of the mature FXN^{81-210} , as they are both strongly reduced.

We next examined by western blotting analysis the relative abundance of several respiratory chain subunits in healthy control, homozygous (FRDA 1 and FRDA 2) and heterozygous G130V-FRDA LCLs. Figure 1C shows that the levels of complex I (NDUFA9), complex II (SDHA), complex III (UQCRC1), and complex IV (MTCO1) subunits are comparable in LCLs from healthy and FRDA patient cells. The same membranes were stripped and incubated with an antibody against TOM20 as a mitochondrial protein loading control. As a further control, a quantification normalized to β -actin is reported in Figure S4.

3.2 | Biochemical and functional analysis of mitochondrial respiratory complexes in FRDA patients' cells

The activities of the individual respiratory complexes in the LCLs (ie, control, FRDA 1, FRDA 2, and G130V-FRDA) were then measured by spectrophotometric assays (Figure 2A). Results were variable: the FRDA 1 and FRDA 2 displayed essentially a partial reduction of complex III, while other complexes were only mildly decreased (complex I), or unaffected (complex II). The cells from patient with the G130V mutation had a partial reduction of complexes I and IV, while complex II was only mildly affected, and complex III was normal. Complex IV does not contain FeS-clusters and the observed reduction in its activity could be explained by the involvement of frataxin in the biosynthesis of heme,^{23,47} an essential cofactor of this complex.

Since in healthy cells individual stability and function of the mitochondrial respiratory complexes are improved by their organization in supercomplexes (SCs),^{38,39} we next determined the pattern of SCs assembly in the different cell lines. SCs of different composition and stoichiometry have been described. The most functionally relevant are SCs [I + III], [I + III+IV], and [III-IV], which can be visualized by blue-native gel electrophoresis.^{38,39,48-50} Figure 2B shows that the relative abundance of higher molecular-weight CI-containing supercomplexes (among which the respirasome) is decreased in FRDA 1, FRDA 2, and G130V-FRDA LCLs compared to healthy control cells.

We next measured the oxygen consumption rate of LCLs by means of a Seahorse flux analyzer. We found that, compared to healthy control, FRDA 1, FRDA 2, and G130V-FRDA LCLs have decreased maximal respiration and spare respiratory capacity, with no difference both in basal and in ATP-linked respiration (Figure 2C). This result could indicate an impaired capability of FRDA cells to increase mitochondrial oxygen consumption rate in conditions of increased energy demand.

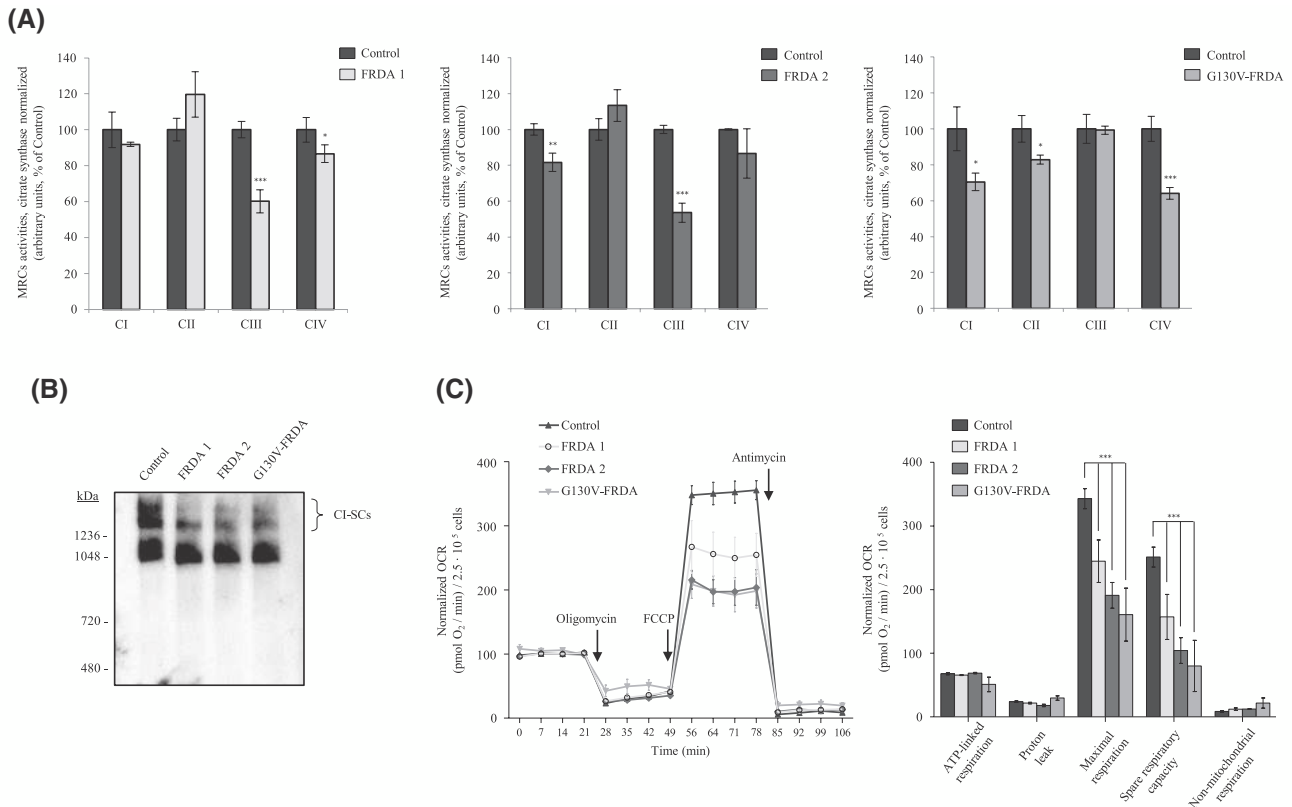


FIGURE 2 Mitochondrial respiratory activity is impaired in FRDA LCLs. A, Complex I-IV individual activities (nmol/min mg of protein) in control, FRDA (1 and 2) and G130V-FRDA LCLs. All activity values were normalized to citrate synthase and expressed as percentage of control activity. Reported data result from the mean of four independent experiments \pm SEM. Statistical significance was determined using unpaired *t*-test (* $P \leq .05$, ** $P \leq .01$, *** $P \leq .001$, compared to control). B, Western blotting after BN-PAGE of CI-containing SCs from digitonin-treated control, FRDA (1 and 2) and G130V-FRDA LCLs. The blot was immunodecorated with an antibody against NDUFA9. C, Oxygen consumption rates (OCR) of cells were measured in real time under basal conditions and after injection of oligomycin, FCCP and antimycin as indicated in the figure. Values were normalized with respect to basal respiration which was considered as 100%. OCR values at basal condition were 275.9 ± 26.9 , 281.5 ± 33.5 , 247.8 ± 14.5 , and 250.3 ± 50.9 (pmol O₂/min)/2.5 × 10⁵ cells in control, FRDA 1, FRDA 2, and G130V-FRDA LCLs, respectively. Bioenergetic parameters were calculated as described in Materials and Methods. Reported data result from the mean of three independent experiments \pm SEM. Statistical significance was determined using Two-way ANOVA with Bonferroni's post hoc test (*** $P \leq .001$, compared to control)

3.3 | Frataxin co-localizes with the FeS-cluster assembly machinery in the mitochondrial cristae in healthy cells and redistributes to the matrix in FRDA patients' cells

Because frataxin has been claimed to play a role in the biogenesis of FeS-clusters, and it was previously shown that in *Saccharomyces cerevisiae* two other proteins involved in this pathway (i.e., NFS1, the sulfur donor to the assembly machinery, and the accessory protein ISD11) are closely attached to the mitochondrial inner membrane and enriched in the cristae,⁵¹ we investigated if the FeS-cluster assembly machinery is localized in the cristae also in the human LCLs used in our work. We addressed this issue by immunogold-labeling in control and FRDA LCLs the proteins NFS1 and ISCU (i.e., the scaffold upon which the FeS-cluster is synthesized),²⁷ as described in detail in Material and Methods. Both proteins are expressed

in control, FRDA 1, FRDA 2, and G130V-FRDA cells without any significant difference, as assessed by the western blotting analyses reported in Figure S5. Figure 3 shows that in the four LCLs, NFS1 and ISCU are mostly localized in the cristae. Negative controls experiments, performed in parallel in absence of primary antibody, did not show electron-dense deposits in the cristae (Figure S6), supporting the presence of the immunolabeled proteins mainly in this subcompartment, as in *S. cerevisiae*. We next explored the sublocalization of frataxin in mitochondria of healthy control and FRDA LCLs by the same immunogold-labeling approach. It is clearly visible in Figure 4 that in healthy LCLs frataxin is in fact enriched in the cristae. As for NFS1 and ISCU proteins, negative control experiments in which primary antibody was omitted support the specificity of the approach. Some gold particles are also present at the inner boundary and outer membranes and likely label the full-length precursor of frataxin (i.e., FXN¹⁻²¹⁰). Frataxin levels are strongly reduced in the three FRDA patient LCLs used in

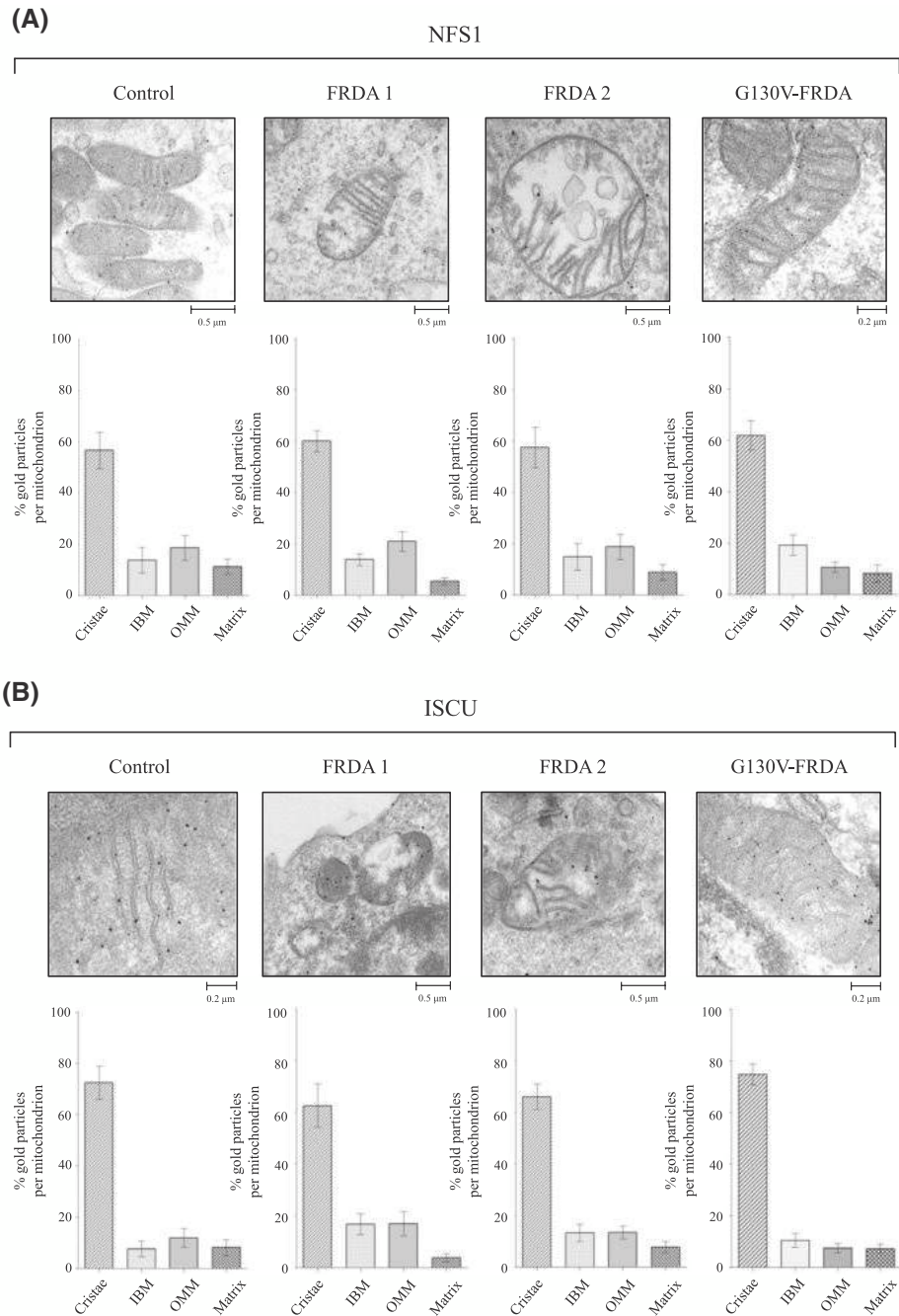


FIGURE 3 The NFS1 desulfurase and ISCU scaffold proteins of the mitochondrial FeS-cluster assembly machinery are closely associated to the cristae membranes of healthy control, FRDA and G130V-FRDA LCLs. A, refers to NFS1, B, refers to ISCU. In both panels: top, representative images of the immunogold-labeling coupled to electron microscopy; bottom, quantitative analyses of the gold particles distribution in different mitochondrial subcompartments, expressed as percentage of particles per mitochondrion. Reported data result from the mean of three independent experiments \pm SEM. Mitochondria from 20 to 45 cells were analyzed. IBM, inner boundary membrane; OMM, outer mitochondrial membrane. Scale bars are indicated in the figure

these experiments (Figure 1), nevertheless we were able to detect immunogold particles both in homozygous FRDA 1 and FRDA 2 and in the heterozygous G130V-FRDA LCLs, albeit at a smaller extent. Interestingly, a close inspection of mitochondria of FRDA LCLs revealed that their residual frataxin is partially redistributed to the matrix even in the presence of intact cristae (Figure 4).

3.4 | Biochemical and functional analyses of mitochondria from GM15850 FRDA cells

The experimental plan of this work included the analysis of a third homozygous patient's LCL, that is, GM15850 (here indicated as FRDA 3). These cells are indeed largely used in FRDA research and are considered a validated model, along

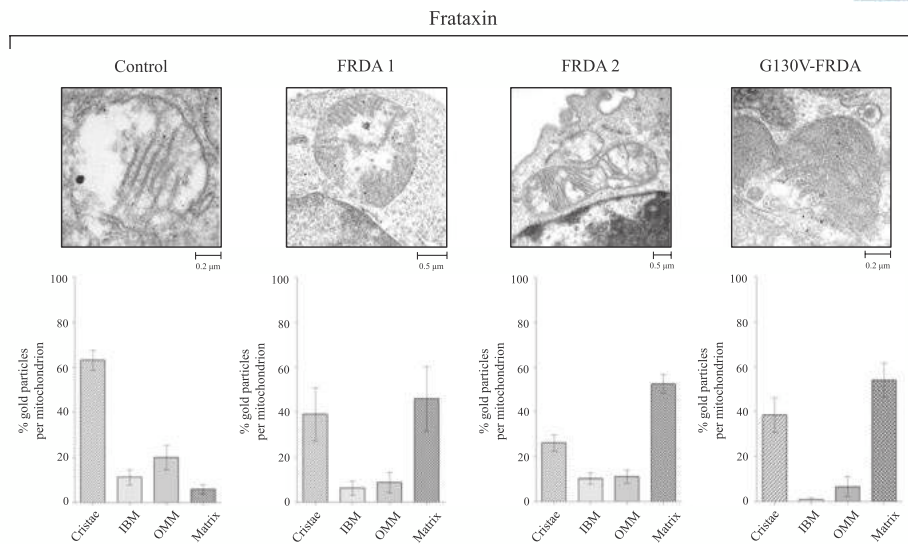


FIGURE 4 Frataxin is enriched in the mitochondrial cristae of healthy control and moves to the matrix in FRDA LCLs. Top, representative images of the immunogold-labeling coupled to electron microscopy of control, FRDA (1 and 2) and G130V-FRDA LCLs; bottom, quantitative analyses of the gold particles distribution in different mitochondrial subcompartments, expressed as percentage of particles per mitochondrion. Reported data result from the mean of three independent experiments \pm SEM. Mitochondria from 20 to 45 cells were analyzed. IBM, inner boundary membrane; OMM, outer mitochondrial membrane. Scale bars are indicated in the figure

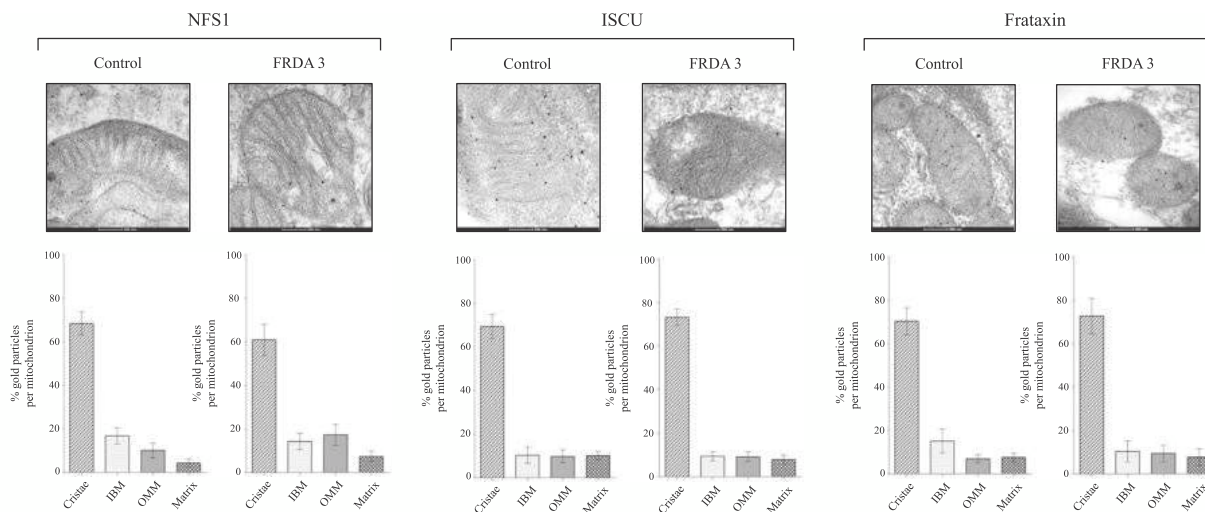


FIGURE 5 NFS1, ISCU, and frataxin proteins are associated to the cristae membranes in mitochondria of homozygous GM15850 LCLs. Top, representative images of the immunogold-labeling coupled to electron microscopy; bottom, quantitative analyses of the gold particles distribution in different mitochondrial subcompartments, expressed as percentage of particles per mitochondrion. Reported data result from the mean of three independent experiments \pm SEM. Mitochondria from 20 to 45 cells were analyzed. IBM, inner boundary membrane; OMM, outer mitochondrial membrane. Scale bars are indicated in the figure. Healthy control LCLs, GM15851; FRDA 3 LCLs, GM15850

with the GM15851 LCL derived from a healthy brother of the patient GM15850.⁵²⁻⁵⁷ We found that these FRDA cells have reduced levels of frataxin (Figure S7, panel A). Moreover, as in the other FRDA LCLs analyzed in this work, in FRDA 3 cells the levels of respiratory complexes subunits (Figure S7, panel B) as well as of NFS1 and ISCU proteins (Figure S7, panel G) are similar to those of control cells, as assessed by western blotting. Surprisingly, unlike the other FRDA LCLs, in the GM15850 cells the residual frataxin is enriched in the

mitochondrial cristae along with the NFS1 and ISCU proteins not only in the healthy control, but also in the FRDA 3 LCLs (Figure 5). The biochemical and functional analyses of mitochondrial respiratory complexes of these cells, performed as described above, indicate that in FRDA 3 LCLs the enzymatic activities of single complexes (Figure S7, panel C), their assembly in respirasome (Figure S7, panel D) and the overall oxygen consumption rate (Figure S7, panel E), are unaffected when compared to the healthy control.

3.5 | Mitochondrial cristae morphology in FRDA patients' cells

Cristae morphology as well as their dynamic remodeling are crucial to keep the respiratory complexes properly assembled and functional^{37,40} and in the same way they could be relevant to keep in site the FeS-cluster biogenesis machinery and frataxin. Therefore, we analyzed by transmission electron microscopy the mitochondrial ultrastructure of healthy controls and FRDA LCLs. In all LCLs used in this work, mitochondria are mostly localized near the plasma membrane and inside the nuclear invagination that is typically present in lymphoblasts (Figure S8). On the contrary, while mitochondria of healthy and FRDA 3 cells have an overall architecture with groups of parallel cristae extending through the entire body of the organelle, those of FRDA 1, FRDA 2, and G130V-FRDA cells are reduced in length and contain cristae significantly shorter and wider than healthy control (Figure 6 and S7, panel F). Frataxin is a free-soluble protein devoid of any transmembrane domains^{58,59} and this morphological change could be relevant for its partial loss from the cristae membranes. Because cristae shape could have per se an impact in the mitochondrial phenotype of the FRDA LCLs, to exclude an upstream defect in the mitochondrial-shaping proteins background we next analyzed in these cells the

expression levels of two proteins involved in the formation and maintenance of the cristae, that is, mitofilin and OPA1. Mitofilin is a key component of the protein complex MICOS (mitochondria contact site and cristae organization system); OPA1 has a fundamental role in cristae architecture and exists in eight tissue-specific isoforms, which are proteolytically processed to form several long and short forms (see 37 for a comprehensive review). The western blotting analysis reported in Figure S9 and in the panel H of Figure S7 indicates that healthy controls and FRDA LCLs have comparable levels of mitofilin and share a similar pattern of the detected long/short forms of OPA1, except for the smallest, which is slightly increased in FRDA 1, FRDA 2, and G130V-FRDA LCLs, as expected in cells with respiratory defects.⁶⁰

4 | DISCUSSION

In the present study, we report a comparative analysis of the mitochondrial phenotype of lymphoblastoid cell lines derived either from “classic” Friedreich ataxia patients (homozygous for the GAA triplet expansion in the *FXN* gene) or from a compound heterozygous patient harboring the expansion on one *FXN* allele and a G130V point mutation on the other. The GAA expansion, that is present in at least one allele in

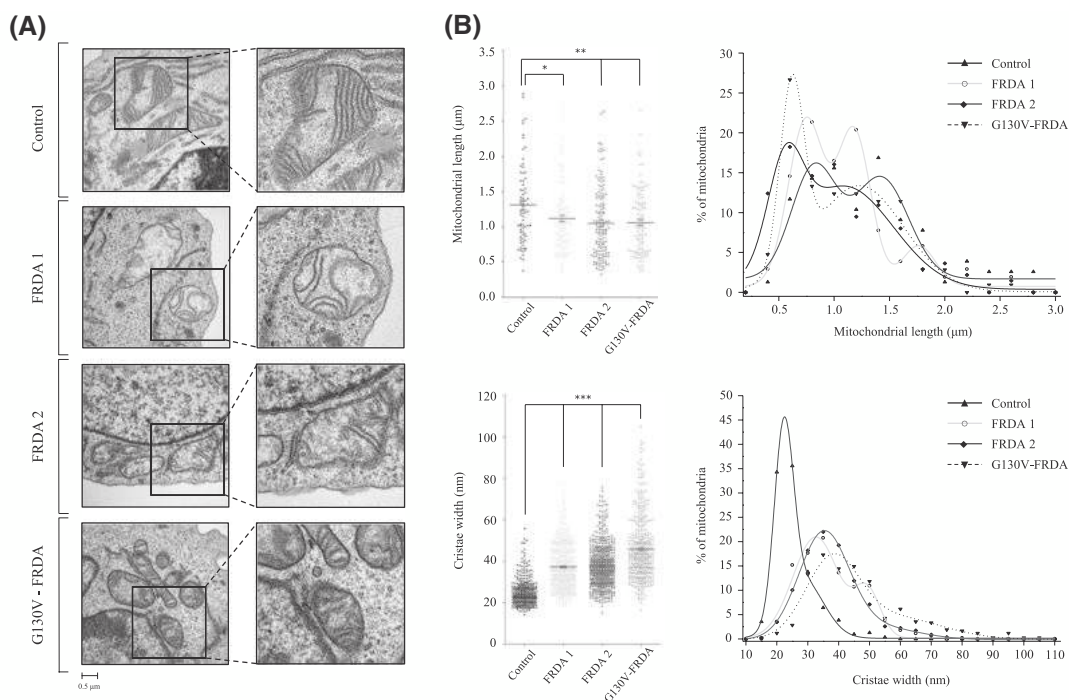


FIGURE 6 Cristae morphology is altered in mitochondria of FRDA LCLs. A, Representative electron micrographs of control, FRDA (1 and 2) and G130V-FRDA LCLs. Cells were fixed and TEM images of randomly selected fields were acquired. Scale bars: 0.5 μm. Boxed areas represent a 4X magnification. B, Morphometric analysis. To estimate mitochondrial length, 80 to 150 mitochondria were analyzed in each experiment; to estimate cristae width, 300 to 600 cristae were analyzed in each experiment. Data represent mean \pm SEM of three independent experiments. Statistical significance was determined using One-way ANOVA with Dunnett's post hoc test ($*P \leq .05$, $**P \leq .01$, and $***P \leq .001$, compared to control). For each morphological parameter, the frequency distribution plot of the experimental data is reported on the right. Symbols represent the relative frequencies expressed as percentage of mitochondria and lines represent the Gaussian fit curves for each individual data set.

virtually all patients, causes a transcriptional repression of the gene, resulting in the production of reduced amounts of otherwise normal frataxin,^{1,61} an iron-binding protein able to functionally interact with the FeS-cluster assembly machinery.²⁷⁻³² The G130V mutation, frequently found in heterozygous patients with a severe frataxin deficiency,⁶¹ has been reported to alter the protein conformation, leading to a higher tendency toward aggregation *in vitro*,⁶²⁻⁶⁵ and to impair the processing from the intermediate FXN⁴²⁻²¹⁰ toward the mature FXN⁸¹⁻²¹⁰.⁴⁶ Accordingly, we found the lowest levels of residual frataxin (Figure 1) and an increased FXN⁴²⁻²¹⁰/FXN⁸¹⁻²¹⁰ ratio (Figure S3) in the G130V-FRDA lymphoblastoid cells, confirming the previous observations. On the contrary, in these cells intermediate and mature FXN proteins are both strongly reduced compared to healthy control. Therefore, the alterations of the mitochondrial phenotype that we observe in G130V-FRDA LCLs are likely due to a decrease of overall frataxin levels, as in homozygous FRDA cells.

Deficiencies in oxidative phosphorylation and alteration of respiratory complexes have been observed in FRDA patients' cells^{12,66} and in the cerebellum of a frataxin-deficient FRDA mouse model (KIKO mouse),²⁰ and confirmed in three of the four FRDA LCLs analyzed in our work (i.e., FRDA 1, FRDA 2, and G130V-FRDA), although with a certain variability which could be due to different adaptation mechanisms of the immortalized cell lines. We found that the assembly of higher molecular weight respiratory supercomplexes and the spare respiratory capacity are also decreased in these FRDA LCLs (Figure 2), indicating that they are unable to boost the respiratory function in response to an increase in energy demands.

The role of frataxin in the mitochondrial phenotype of FRDA cells could be related to an impaired assembly of the FeS-clusters, key prosthetic groups moving the electrons through mitochondrial respiratory complexes I, II, and III.²⁴ Although its specific contribution to this pathway has not been yet definitively clarified, an emerging role is that it could act as an allosteric activator of cysteine binding to the NFS1 desulfurase and ensuing sulfur transfer to the ISCU scaffold protein.^{31,32,67,68} This relies on its transient interaction with multiple core components of the assembly machinery, which has been confirmed by several independent experiments *in vitro* using purified recombinant proteins.^{27-29,65,69} A relevant novel finding of the present work is that in healthy cells mitochondrial cristae, which house the respiratory complexes, are enriched of frataxin as well as of NFS1 and ISCU, as assessed by immunogold-labeling coupled to electron microscopy (Figures 3 and 4). The localization of some proteins of the FeS-cluster assembly complex in the mitochondrial cristae was previously found in the yeast *S. cerevisiae*,⁵¹ and therefore, our data suggest that it could be an evolutionary conserved feature essential to drive an efficient biogenesis of these key redox cofactors. An indication that frataxin localizes

at or near the inner mitochondrial membrane was previously obtained by Campuzano and colleagues in transfected HeLa cells overexpressing a recombinant full-length FXN¹⁻²¹⁰.⁵ To the best of our knowledge, our data provide the first direct evidence that in healthy cells endogenous frataxin is mostly associated with the mitochondrial cristae. This subcompartmentalization would put the FeS-cluster biogenesis complex in close proximity to frataxin, enabling key structural and functional interactions, and with the respiratory chain complexes, which rely on these cofactors for their redox activity. Interestingly, we found that a significant proportion of residual frataxin moves toward the matrix in FRDA 1, FRDA 2, and G130V-FRDA LCLs, while NFS1 and ISCU proteins are mostly associated to the mitochondrial cristae as in control cells (Figures 3 and 4). This could, in turn, prevent or decrease its binding to the FeS-cluster assembly machinery. The frataxin expressed by heterozygous G130V-FRDA cells is expected to be a mixture of wild-type and mutant proteins, which are both recognized by the antibody used in the immunogold-labeling experiments, so we cannot rule out the possibility that the point mutation itself could have an impact in the localization of residual frataxin in the cristae. In any case, this would lead to a poor structural stability and contribute to a further decrease of residual frataxin at this level. In a previous work, we showed that a recombinant G130V-frataxin protein retains the capability to interact with the scaffold protein ISCU, to enhance the NFS1 desulfurase activity and to bind iron *in vitro*.⁶⁵ Therefore, the pathological phenotype of G130V-FRDA cells is likely related to the instability of the mutant protein rather than to a loss of function. Taken together, these data support a major role of frataxin enrichment in the mitochondrial cristae of healthy cells as a key factor to allow an efficient biogenesis of FeS-clusters and in turn a proper assembly of functional respiratory complexes. It is worth noting that in mitochondria of healthy mammalian cells almost all complex I, the major entry point of the respiratory chain substrates, is usually found to be associated with supercomplexes, and this increases its stability.^{38,39,70-72} We also found a defect in respirasome formation in FRDA 1, FRDA 2, and G130V-FRDA cells (Figure 2): to our best knowledge, this is the first experimental evidence that respiratory chain supercomplexes are destabilized in cells with a severe deficiency of frataxin and altered respiratory function. Despite FRDA 3 cell line (i.e., GM15850) was largely used in several studies focused on the molecular mechanisms of frataxin deficiency,⁵²⁻⁵⁷ in our set of data it represents an outlier with respect to the mitochondrial respiratory phenotype. It should be noted that conflicting findings concerning this aspect have been reported in the literature for the GM15850 cell line, since some authors found alterations in the activity of respiratory complexes, whereas others showed an unaffected respiration.^{73,74} We found that, under our experimental conditions, the mitochondrial phenotype of GM15850 cells

is superimposable to that of control LCLs, with no detectable alterations in function and assembly of respiratory complexes in supercomplexes, oxygen consumption rate and ultrastructure (Figure S7, panels D, E, and F). Interestingly, in these cells residual frataxin is concentrated in the mitochondrial cristae, along with the proteins of FeS-cluster assembly machinery, as in the healthy control LCLs (Figure 5). This would further support the functional link between frataxin enrichment in this subcompartment and respiratory features. Nevertheless, the relationship between frataxin depletion in the mitochondrial cristae and reduced ability to assemble functional respiratory supercomplexes, as well as the molecular mechanisms that allow the GM15850 FRDA cells to keep their residual frataxin in the cristae, require additional experiments to be completely clarified.

To date, we do not know exactly which metabolic consequences primarily occur after frataxin depletion and would be most relevant for early FRDA therapy strategies. Our finding that beside housing respiratory (super)complexes cristae are also enriched in proteins of the FeS-cluster assembly machinery, including frataxin, is relevant because it opens up a new working perspective aimed at addressing if and how the perturbation of mitochondrial morphology and dynamics are involved in the events leading to bioenergetic defects in cells from FRDA patients. The redistribution of frataxin in mitochondrial subcompartments upon changes of the cell physiological state defines a novel framework to address the pathogenesis of Friedreich ataxia and to explore if manipulation of mitochondria shaping-proteins could correct the bioenergetic defects afflicting patient cells, as in other mitochondrial diseases.^{75,76}

ACKNOWLEDGEMENTS

This work was supported by grants COST_FINA_P14_02 to P.C. from Department of Biology, University of Padova; PRID/SID 2019 to A.R. from Department of Molecular Medicine, University of Padova; PRID/SID 2017 to E.P. from Department of Molecular Medicine, University of Padova; PRIN 20155795S5W to I.S. from MIUR; BIRD179997/17 to M.E.S. from Department of Biology, University of Padova; a grant from Fondazione Città della Speranza, Padova, to L.S. We are grateful to Dr Luca Scorrano for interesting and stimulating discussions.

CONFLICT OF INTEREST

The authors declare no conflicts of interest.

AUTHOR CONTRIBUTIONS

D. Doni performed and interpreted all the experiments and analyzed data; G. Rigoni, E. Palumbo, E. Baschiera, R. Peruzzo, E. De Rosa, L. Passerini, and F. Caicci performed experiments and analyzed data; D. Bettio performed the cytogenetic analysis; A. Russo, I. Szabò, M.E. Soriano, and

L. Salviati supervised the experiments and provided scientific expertise and critical suggestions throughout the study; P. Costantini designed the research, supervised all the experiments, and wrote the manuscript. All authors have read, reviewed, and approved the final manuscript.

ORCID

Antonella Russo  <https://orcid.org/0000-0001-6691-257X>

Paola Costantini  <https://orcid.org/0000-0001-7941-5177>

REFERENCES

- Campuzano V, Montermini L, Moltó MD, et al. Friedreich's ataxia: autosomal recessive disease caused by an intronic GAA triplet repeat expansion. *Science*. 1996;271:1423-1427.
- Koeppen AH. Friedreich's ataxia: pathology, pathogenesis, and molecular genetics. *J Neurol Sci*. 2011;303:1-12.
- Pandolfo M. Friedreich's ataxia: the clinical picture. *J Neurol*. 2009;256:3-8.
- Dürr A, Cossée M, Agid Y, et al. Clinical and genetic abnormalities in patients with Friedreich's ataxia. *N Engl J Med*. 1996;335:1169-1175.
- Campuzano V, Montermini L, Lutz Y, et al. Frataxin is reduced in Friedreich ataxia patients and is associated with mitochondrial membrane. *Hum Mol Genet*. 1997;6:1771-1780.
- Nachbauer W, Wanschitz J, Steinkellner H, et al. Correlation of frataxin content in blood and skeletal muscle endorses frataxin as a biomarker in Friedreich ataxia. *Mov Disord*. 2011;26:1935-1938.
- Cossée M, Dürr A, Schmitt M, et al. Friedreich's ataxia: point mutations and clinical presentation of compound heterozygotes. *Ann Neurol*. 1999;45:200-206.
- De Castro M, García-Planells J, Monrós E, et al. Genotype and phenotype analysis of Friedreich's ataxia compound heterozygous patients. *Hum Genet*. 2000;106:86-92.
- Gellera C, Castellotti B, Mariotti C, et al. Frataxin gene point mutations in Italian Friedreich ataxia patients. *Neurogenetics*. 2007;8:289-299.
- Galea CA, Huq A, Lockhart PJ, et al. Compound heterozygous FXN mutations and clinical outcome in Friedreich ataxia. *Ann Neurol*. 2016;79:485-495.
- Cossée M, Puccio H, Gansmuller A, et al. Inactivation of the Friedreich ataxia mouse gene leads to early embryonic lethality without iron accumulation. *Hum Mol Genet*. 2000;9:1219-1226.
- Rötig A, de Lonlay P, Chretien D, et al. Aconitase and mitochondrial iron-sulphur protein deficiency in Friedreich ataxia. *Nat Genet*. 1997;17:215-217.
- Puccio H, Simon D, Cossée M, et al. Mouse models for Friedreich ataxia exhibit cardiomyopathy, sensory nerve defect and Fe-S enzyme deficiency followed by intramitochondrial iron deposits. *Nat Genet*. 2001;27:181-186.
- Schulz JB, Dehmer T, Schols L, et al. Oxidative stress in patients with Friedreich ataxia. *Neurology*. 2000;55:1719-1721.
- Schmucker S, Puccio H. Understanding the molecular mechanisms of Friedreich's ataxia to develop therapeutic approaches. *Hum Mol Genet*. 2010;19:R103-R110.
- Lynch DR, Lech G, Farmer JM, et al. Near infrared muscle spectroscopy in patients with Friedreich's ataxia. *Muscle Nerve*. 2002;25:664-673.

17. Lodi R, Cooper JM, Bradley JL, et al. Deficit of *in vivo* mitochondrial ATP production in patients with Friedreich ataxia. *Proc Natl Acad Sci USA*. 1999;96:11492-11495.
18. Ristow M, Pfister M, Yee A, et al. Frataxin activates mitochondrial energy conversion and oxidative phosphorylation. *Proc Natl Acad Sci USA*. 2000;97:12239-12243.
19. Gonzalez-Cabo P, Vazquez-Manrique RP, Garcia-Gimeno MA, Sanz P, Palau F. Frataxin interacts functionally with mitochondrial electron transport chain proteins. *Hum Mol Genet*. 2005;14:2091-2098.
20. Lin H, Magrane J, Rattelle A, et al. Early cerebellar deficits in mitochondrial biogenesis and respiratory chain complexes in the KIKO mouse model of Friedreich ataxia. *Dis Model Mech*. 2017;10:1343-1352.
21. Chiang S, Kalinowski DS, Jansson PJ, Richardson DR, Huang ML. Mitochondrial dysfunction in the neuro-degenerative and cardio-degenerative disease, Friedreich's ataxia. *Neurochem Int*. 2018;117:35-48.
22. Clark E, Johnson J, Dong YN, et al. Role of frataxin protein deficiency and metabolic dysfunction in Friedreich ataxia, an autosomal recessive mitochondrial disease. *Neuronal Signalling*. 2018;2:NS201800600.
23. Yoon T, Cowan JA. Frataxin-mediated iron delivery to ferrochetalase in the final step of heme biosynthesis. *J Biol Chem*. 2004;279:25943-25946.
24. Huynen MA, Snel B, Bork P, Gibson TJ. The phylogenetic distribution of frataxin indicates a role in iron-sulfur cluster protein assembly. *Hum Mol Genet*. 2001;10:2463-2468.
25. Yoon T, Cowan JA. Iron-sulfur cluster biosynthesis. Characterization of frataxin as an iron donor for assembly of [2Fe-2S] clusters in ISU-type proteins. *J Am Chem Soc*. 2003;125:6078-6084.
26. Cavadini P, O'Neill HA, Benada O, Isaya G. Assembly and iron-binding properties of human frataxin, the protein deficient in Friedreich ataxia. *Hum Mol Genet*. 2002;11:217-227.
27. Boniecki MT, Freibert SA, Mühlenhoff U, Lill R, Cygler M. Structure and functional dynamics of the mitochondrial Fe/S cluster synthesis complex. *Nat Commun*. 2017;8:1287.
28. Gerber J, Mühlenhoff U, Lill R. An interaction between frataxin and Isu1/Nfs1 that is crucial for Fe/S cluster synthesis on Isu1. *EMBO Rep*. 2003;4:906-911.
29. Schmucker S, Martelli A, Colin F, et al. Mammalian frataxin: an essential function for cellular viability through an interaction with a preformed ISCU/NFS1/ISD11 iron-sulfur assembly complex. *PLoS One*. 2011;6:e16199.
30. Shan Y, Napoli E, Cortopassi G. Mitochondrial frataxin interacts with ISD11 of the NFS1/ISCU complex and multiple mitochondrial chaperones. *Hum Mol Genet*. 2007;16:929-941.
31. Parent A, Elduque X, Cornu D, et al. Mammalian frataxin directly enhances sulfur transfer of NFS1 persulfide to both ISCU and free thiols. *Nat Commun*. 2015;6:5686.
32. Bridwell-Rabb J, Fox NG, Tsai CL, Winn AM, Barondeau DP. Human frataxin activates Fe-S cluster biosynthesis by facilitating sulfur transfer chemistry. *Biochemistry*. 2014;53:4904-4913.
33. Martelli A, Wattenhofer-Donzè M, Schmucker S, Bouvet S, Reutenauer L, Puccio H. Frataxin is essential for extramitochondrial Fe-S cluster proteins in mammalian tissues. *Hum Mol Genet*. 2007;16:2651-2658.
34. Lill R, Mühlenhoff U. Maturation of iron-sulfur proteins in eukaryotes: Mechanisms, connected processes, and diseases. *Annu Rev Biochem*. 2008;77:669-700.
35. Pernas L, Scorrano L. Mito-Morphosis: mitochondrial fusion, fission, and cristae remodeling as key mediators of cellular function. *Annu Rev Physiol*. 2016;78:505-531.
36. Zick M, Rabl R, Reichert AS. Cristae formation-linking ultrastructure and function of mitochondria. *Biochim Biophys Acta*. 2009;1793:5-19.
37. Cogliati S, Enriquez JA, Scorrano L. Mitochondrial cristae: where beauty meets functionality. *Trends Biochem Sci*. 2016;41:261-273.
38. Schägger H, Pfeiffer K. Supercomplexes in the respiratory chains of yeast and mammalian mitochondria. *EMBO J*. 2000;19:1777-1783.
39. Schägger H, Pfeiffer K. The ratio of oxidative phosphorylation complexes I-V in bovine heart mitochondria and the composition of respiratory chain supercomplexes. *J Biol Chem*. 2001;276:37861-37867.
40. Cogliati S, Frezza C, Soriano ME, et al. Mitochondrial cristae shape determines respiratory chain supercomplexes assembly and respiratory efficiency. *Cell*. 2013;155:160-171.
41. Chan DC. Mitochondrial dynamics and its involvement in disease. *Annu Rev Pathol*. 2020;15:235-259.
42. Spinazzi M, Casarin A, Pertegato V, Salviati L, Angelini A. Assessment of mitochondrial respiratory chain enzymatic activities on tissues and cultured cells. *Nat Protoc*. 2012;7:1235-1246.
43. Koutnikova H, Campuzano V, Koenig M. Maturation of wild-type and mutated frataxin by the mitochondrial processing peptidase. *Hum Mol Genet*. 1998;7:1485-1489.
44. Condò I, Ventura N, Malisan F, Rufini A, Tomassini B, Testi R. *In vivo* maturation of human frataxin. *Hum Mol Genet*. 2007;16:1534-1540.
45. Schmucker S, Argentini M, Carelle-Camels N, Martelli A, Puccio H. The *in vivo* mitochondrial two-step maturation of human frataxin. *Hum Mol Genet*. 2008;17:3521-3531.
46. Clark E, Butler JS, Isaacs CI, Napierala M, Lynch DR. Selected missense mutations impair frataxin processing in Friedreich ataxia. *Ann Clin Transl Neurol*. 2017;4:575-584.
47. Schoenfeld RA, Napoli E, Wong A, et al. Frataxin deficiency alters heme pathway transcripts and decreases mitochondrial heme metabolites in mammalian cells. *Hum Mol Genet*. 2005;14:3787-3799.
48. Enriquez JA. Supramolecular organization of respiratory complexes. *Annu Rev Physiol*. 2016;78:533-561.
49. Acín-Pérez R, Fernández-Silva P, Peleato ML, Pérez-Martos A, Enriquez JA. Respiratory active mitochondrial supercomplexes. *Mol Cell*. 2008;32:529-539.
50. Dudkina NV, Kudrayashev M, Stahlberg H, Boekema EJ. Interaction of complexes I, III and IV within the bovine respirasome by single particle cryoelectron tomography. *Proc Natl Acad Sci USA*. 2011;108:15196-15200.
51. Vogel F, Bornhövd C, Neupert W, Reichert AS. Dynamic subcompartmentalization of the mitochondrial inner membrane. *J Cell Biol*. 2006;175:237-247.
52. Herman D, Jenssen K, Burnett R, Soragni E, Perlman SL, Gottesfeld JM. Histone deacetylase inhibitors reverse gene silencing in Friedreich's ataxia. *Nat Chem Biol*. 2006;2:551-558.
53. Groh M, Lufino MMP, Wade-Martins R, Gromack N. R-loops associated with triplet repeat expansions promote gene silencing in Friedreich Ataxia and Fragile X syndrome. *PLoS Genet*. 2014;10:e1004318.
54. Ly Y, Polak U, Bhalla AD, et al. Excision of expanded GAA repeats alleviates the molecular phenotype of Friedreich's ataxia. *Mol Ther*. 2015;23:10551065.

55. Erwin GS, Grieshop MP, Ali A, et al. Synthetic transcription elongation factors license transcription across repressive chromatin. *Science*. 2017;358:1617-1622.
56. Jasoliya M, Sacca F, Sahdeo S, et al. Dimethyl fumarate dosing in humans increases frataxin expression: a potential therapy for Friedreich's Ataxia. *PLoS One*. 2019;14:e0217776.
57. Stevanoni M, Palumbo E, Russo A. The replication of *Frataxin* gene is assured by activation of dormant origins in the presence of a GAA-repeat expansion. *PLOS Genet*. 2016;12:e1006201.
58. Musco G, Stier G, Kolmerer B, et al. Towards a structural understanding of Friedreich's ataxia: the solution structure of frataxin. *Structure*. 2000;8:695-707.
59. Dhe-Paganon S, Shigeta R, Chi YI, Ristow M, Shoelson SE. Crystal structure of human frataxin. *J Biol Chem*. 2000;275:30753-30756.
60. Duvezin-Caubet S, Jagasia R, Wagener J, et al. Proteolytic processing of OPA1 links mitochondrial dysfunction to alterations in mitochondrial morphology. *J Biol Chem*. 2006;281:37972-37979.
61. Lazaropoulos M, Dong Y, Clark E, et al. Frataxin levels in peripheral tissue in Friedreich ataxia. *Ann Clin Transl Neurol*. 2015;2:831-842.
62. Correia AR, Adinolfi S, Pastore A, Gomes CM. Conformational stability of human frataxin and effect of Friedreich's ataxia related mutations on protein folding. *Biochem J*. 2006;398:605-611.
63. Correia AR, Pastore C, Adinolfi S, Pastore A, Gomes CM. Dynamics, stability and iron-binding activity of frataxin clinical mutants. *FEBS J*. 2008;275:3680-3690.
64. Faggianelli N, Puglisi R, Veneziano L, et al. Analyzing the effects of a G130V mutation in the *FXN* gene. *Front Mol Neurosci*. 2015;8:66.
65. Bellanda M, Maso L, Doni D, et al. Exploring iron-binding to human frataxin and to selected Friedreich ataxia mutants by means of NMR and EPR spectroscopies. *Biochim Biophys Acta Proteins Proteom*. 2019;1867:140254.
66. Salehi MH, Kamalidehghan B, Houshmand M, et al. Gene expression profiling of mitochondrial oxidative phosphorylation (OXPHOS) complex I in Friedreich ataxia (FRDA) patients. *PLoS One*. 2014;9:e94069.
67. Tsai CL, Barondeau DP. Human frataxin is an allosteric switch that activates the Fe-S cluster biosynthetic complex. *Biochemistry*. 2010;49:9132-9139.
68. Colin F, Martelli A, Clemancey M, et al. Mammalian frataxin controls sulfur production and iron entry during de novo Fe4S4 cluster assembly. *J Am Chem Soc*. 2013;135:733-740.
69. Fox NG, Yu X, Feng X, et al. Structure of the human frataxin-bound iron-sulfur cluster assembly complex provides insight into its activation mechanism. *Nat Commun*. 2019;10:2210.
70. Acín-Pérez R, Bayona-Bafaluy MP, Fernández-Silva P, et al. Respiratory complex III is required to maintain complex I in mammalian mitochondria. *Mol Cell*. 2004;13:805-815.
71. Schägger H, de Coo R, Bauer MF, Hofmann S, Godinot C, Brandt U. Significance of respirasomes for the assembly/stability of human respiratory chain complex I. *J Biol Chem*. 2004;279:36349-36353.
72. Acín-Pérez R, Enriquez JA. The function of the respiratory supercomplexes: the plasticity model. *Biochim Biophys Acta*. 2014;1837:444-450.
73. Zhao H, Li H, Hao S, et al. Peptide SS-31 upregulates frataxin expression and improves the quality of mitochondria: implications in the treatment of Friedreich ataxia. *Sci Rep*. 2017;7:9840.
74. Télot L, Rousseau E, Lesuisse E, et al. Quantitative proteomics in Friedreich's ataxia B-lymphocytes: a valuable approach to decipher the biochemical events responsible for pathogenesis. *BBA Mol Basis Dis*. 2018;1864:997-1009.
75. Varanita T, Soriano ME, Romanello V, et al. The Opa1-dependent mitochondrial cristae remodeling pathway controls atrophic, apoptotic, and ischemic tissue damage. *Cell Metab*. 2015;21:834-844.
76. Civileto G, Varanita T, Cerutti R, et al. Opa1 overexpression ameliorates the phenotype of two mitochondrial disease mouse models. *Cell Metab*. 2015;21:845-854.

SUPPORTING INFORMATION

Additional Supporting Information may be found online in the Supporting Information section.

How to cite this article: Doni D, Rigoni G, Palumbo E, et al. The displacement of frataxin from the mitochondrial cristae correlates with abnormal respiratory supercomplexes Formation and bioenergetic defects in cells of friedreich ataxia patients. *The FASEB Journal*. 2021;35:e21362. <https://doi.org/10.1096/fj.202000524RR>

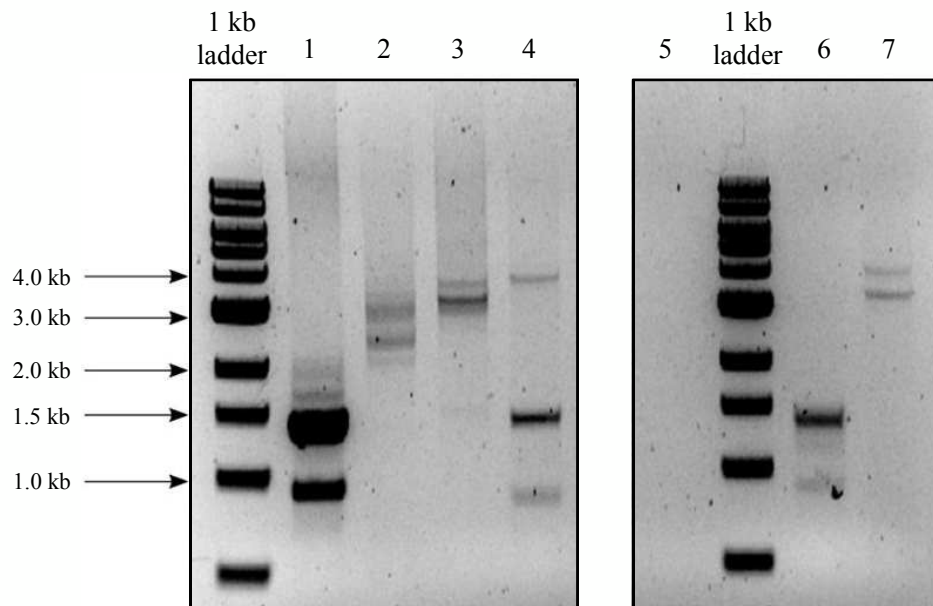


Figure S1: the length of *FXN* alleles for the six LCLs was assessed by long-range PCR. Lane 1: GM07533 (healthy control); lane 2: GM04079 (homozygous FRDA 1); lane 3: GM16227 (homozygous FRDA 2) lane 4: GM21542 (heterozygous G130V-FRDA); lane 5: no template control; lane 6: GM15851 (second healthy control); lane 7: GM15850 (homozygous FRDA 3). Molecular weight of the 1kb ladder bands of interest are indicated by an arrow. Amplicon length is calculated as follow: amplicon length (bp) = 1350 + 3n GAA (n = number of GAA repeats).

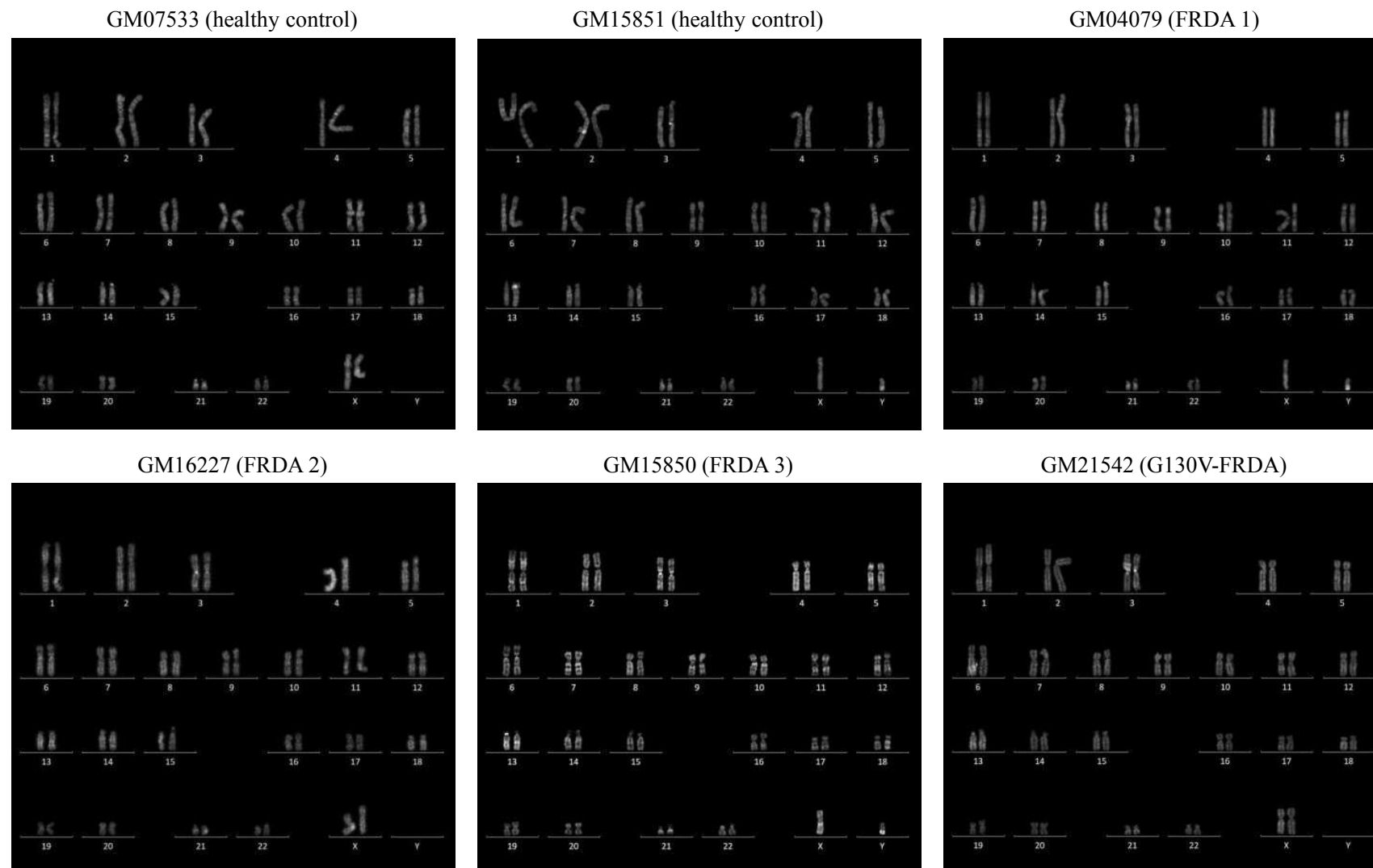


Figure S2: normal karyotypes obtained from healthy controls, FRDA (1, 2 and 3) and G130V-FRDA LCLs

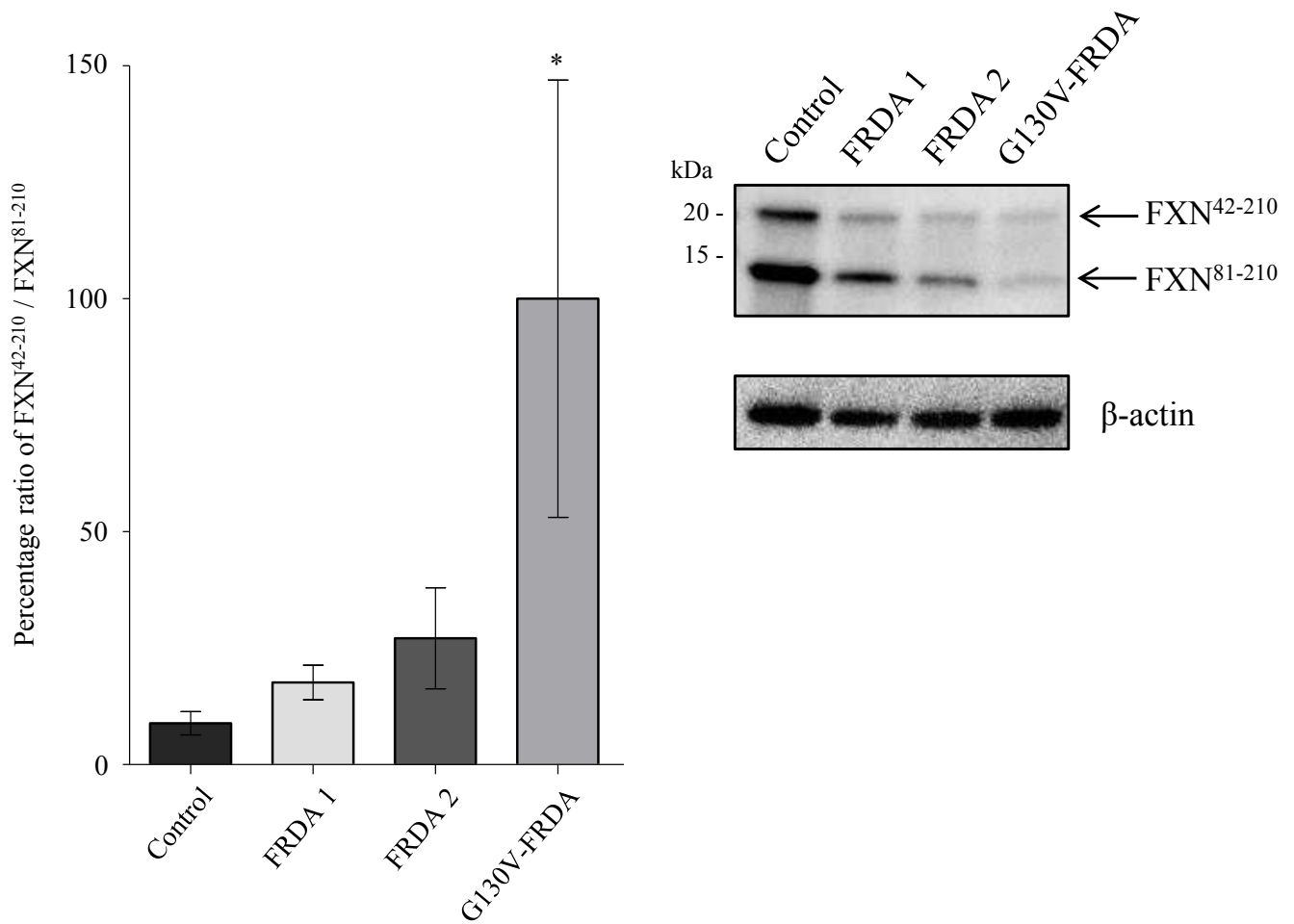


Figure S3: impaired frataxin processing from FXN⁴²⁻²¹⁰ to FXN⁸¹⁻²¹⁰ in lymphoblasts from G130V-FRDA patient. Equal amounts of protein (*i.e.* 60 μ g) were loaded in each lane. β -actin was used as loading control. FXN⁴²⁻²¹⁰ and FXN⁸¹⁻²¹⁰ were detected by western blot. FXN levels were quantified and expressed as ratio of FXN⁴²⁻²¹⁰ to FXN⁸¹⁻²¹⁰. Reported data result from the mean of four independent experiments \pm SEM. Statistical significance was determined using One-way ANOVA with Dunnett's post-hoc test (* $p \leq 0.05$, compared to control).

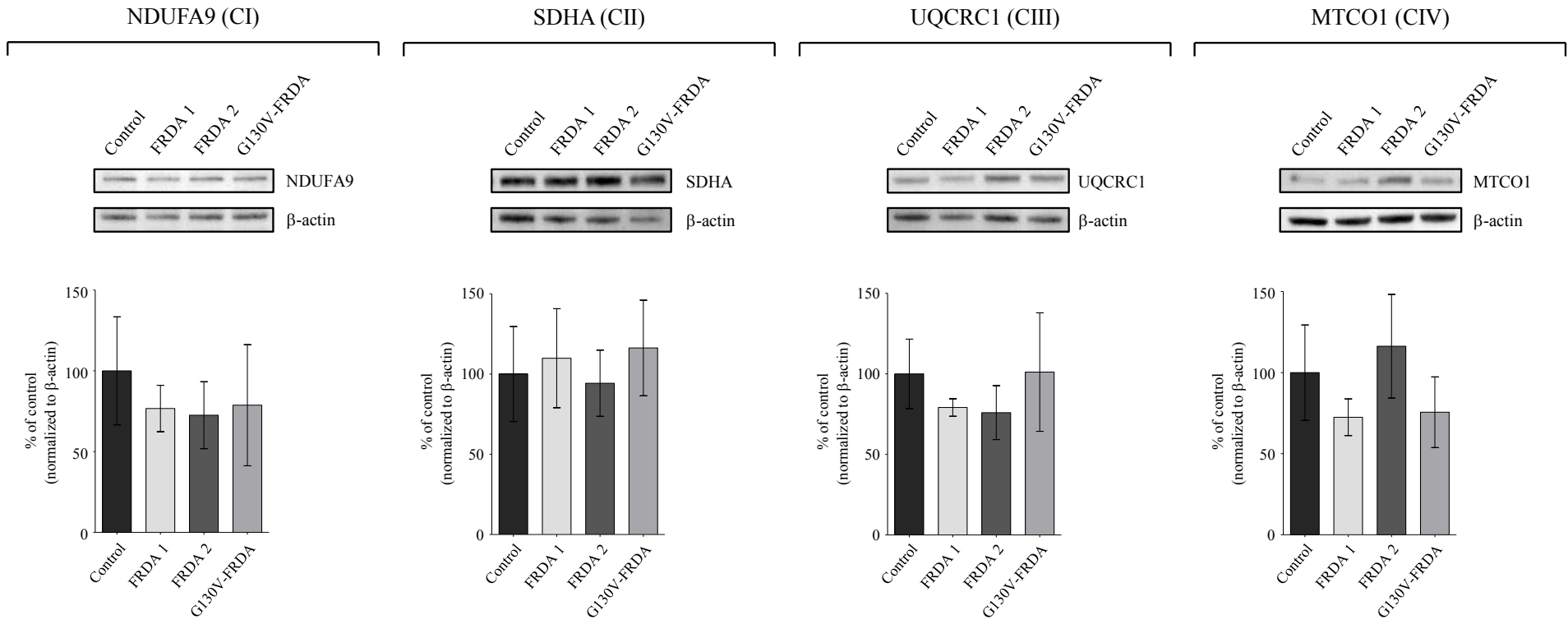


Figure S4: western blotting analysis of respiratory complexes subunits, *i.e.* NDUFA9 (complex I), SDHA (complex II), UQCRC1 (complex III) and MTCO1 (complex IV) in whole cell extracts from FRDA (1 and 2), G130V-FRDA and unaffected control LCLs. Equal amounts of protein (*i.e.* 25 μ g) were loaded in each lane. β -actin was used as loading control. Protein levels were quantified after normalization with β -actin and expressed as percentage of control level. Reported data result from the mean of three independent experiments \pm SEM. One-way ANOVA with Dunnett's post hoc test was used for statistical analysis.

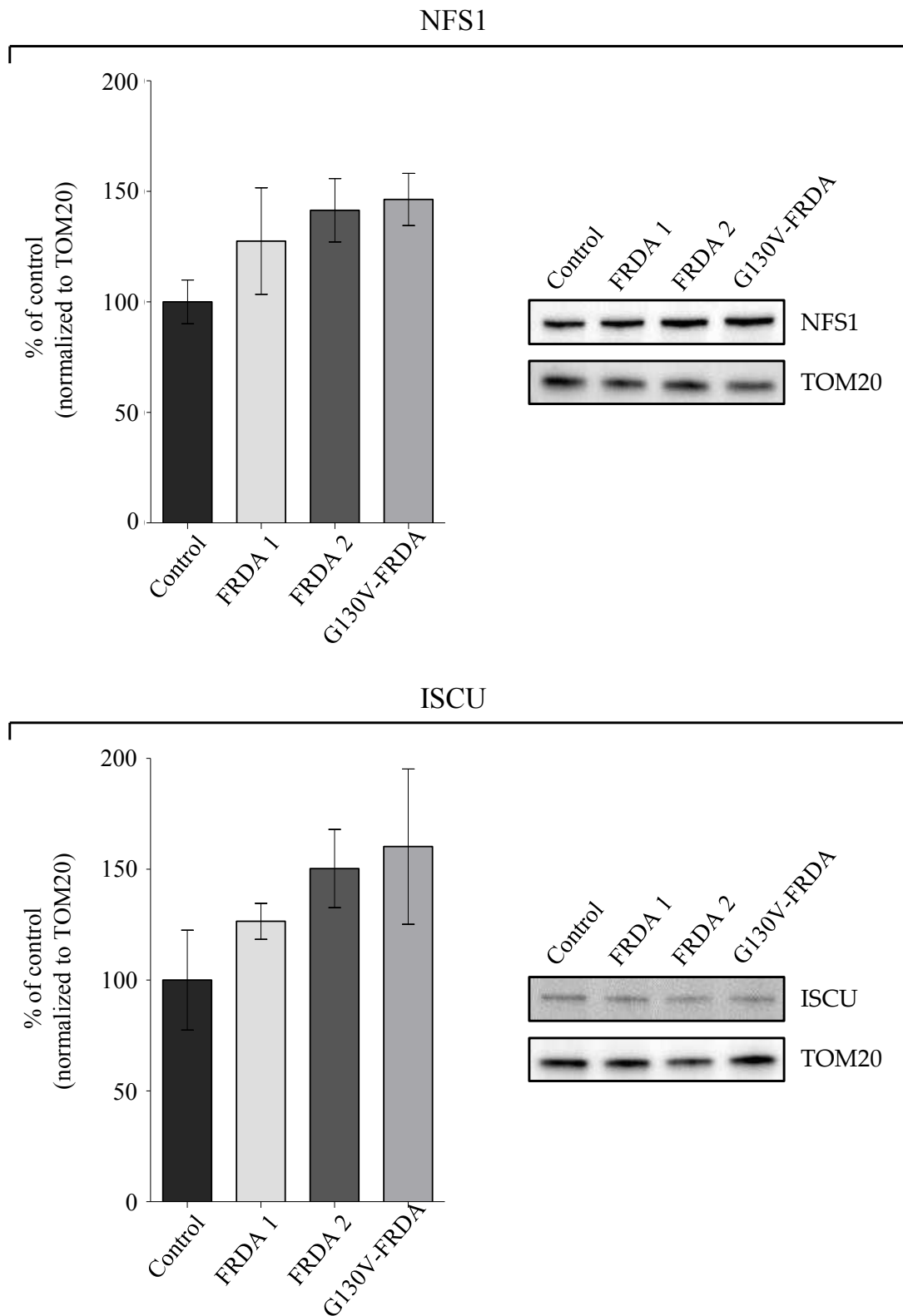


Figure S5: western blotting analyses of NFS1 and ISCU proteins in whole cell extracts from FRDA (1 and 2), G130V-FRDA and unaffected control LCLs. Equal amounts of protein (*i.e.* 25 μ g) were loaded in each lane. TOM20 was used as loading control. Protein levels were quantified after normalization with TOM20 and expressed as percentage of control level. Reported data result from the mean of six independent experiments \pm SEM. One-way ANOVA with Dunnett's post hoc test was used for statistical analysis.

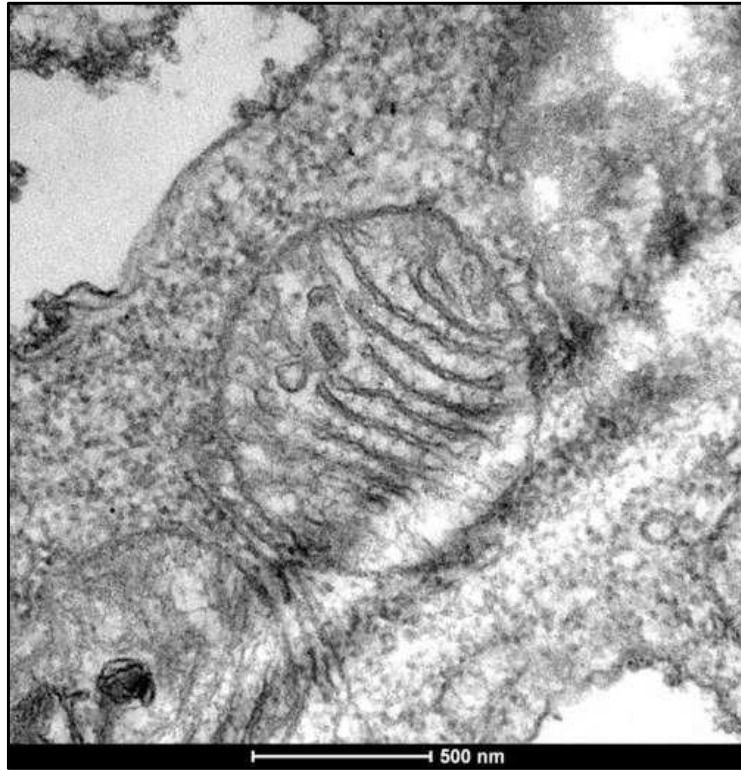


Figure S6: control cells were fixed and prepared for immunogold staining exactly as described in Materials and Methods except for the rabbit primary antibody (against human NFS1, ISCU or FXN proteins), which was omitted.

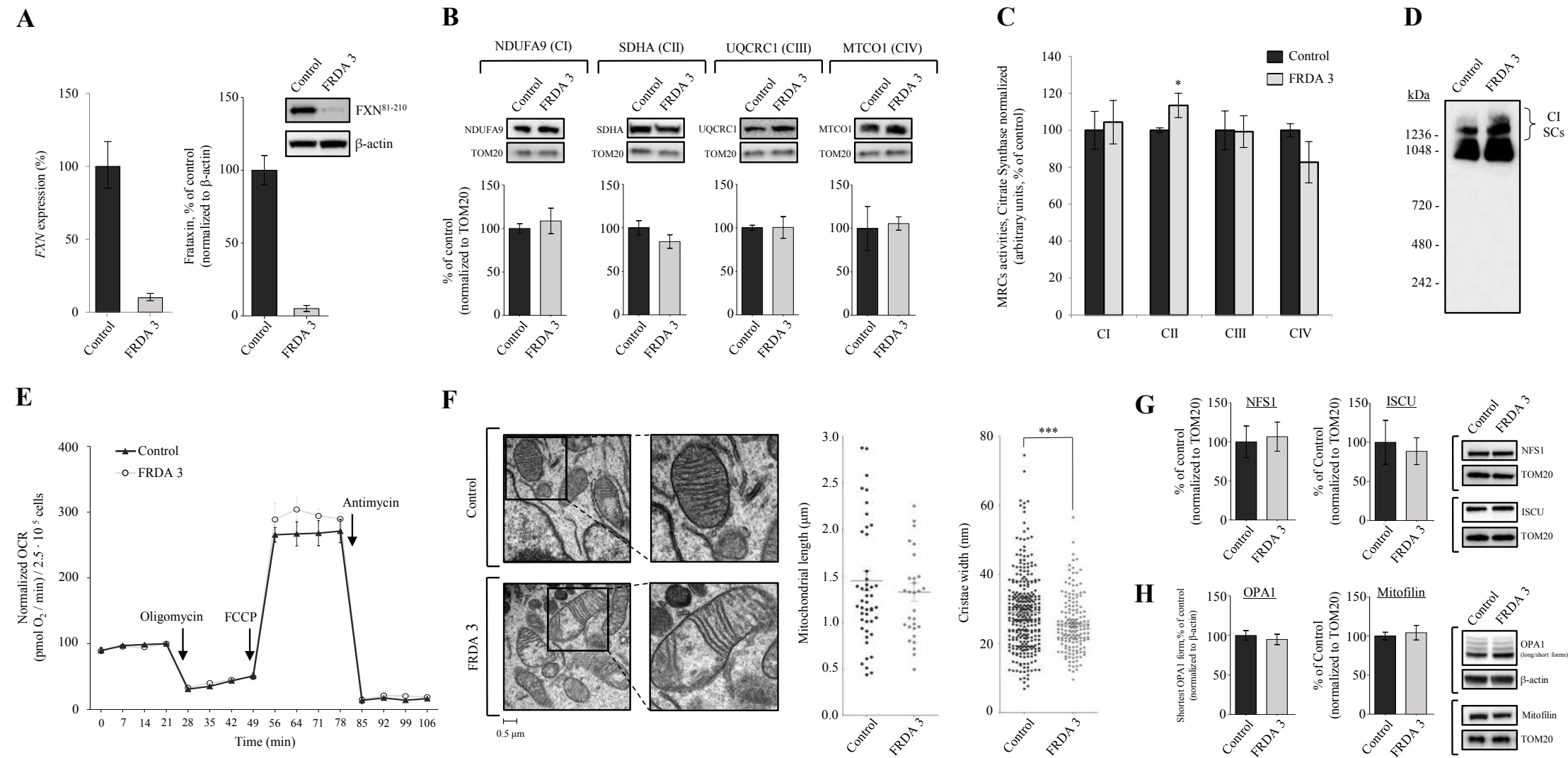
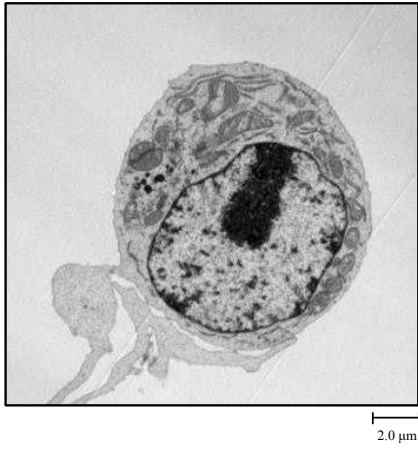
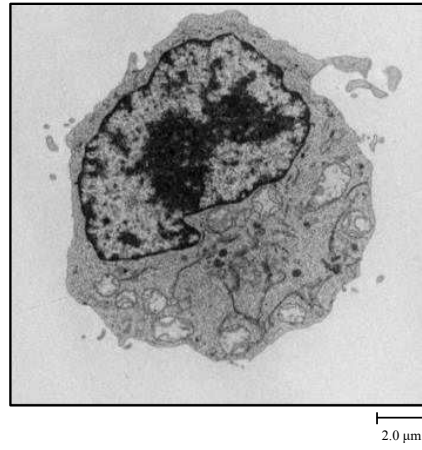


Figure S7: biochemical, functional and structural characterization of mitochondria from GM15851 (healthy control) and GM15850 (FRDA 3) LCLs. Experimental conditions were exactly as those described in the legends of figures 1 (for panels A and B), 2 (for panels C, D and E), 6 (for panel F), S5 (for panel G) and S9 (for panel H). Panel E, OCR values at basal condition were 338.9 ± 33.37 and 295.3 ± 30.65 (pmol O₂/min)/2.5 · 10⁵ cells in control and FRDA 3 LCLs, respectively. Statistical significance was determined using unpaired t-test.

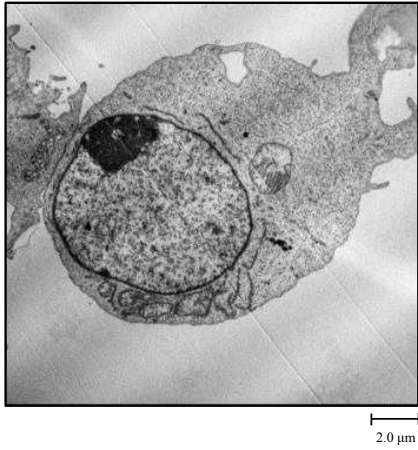
Healthy control (GM07533)



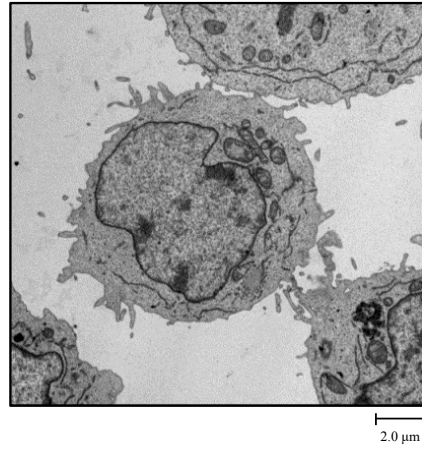
FRDA 1



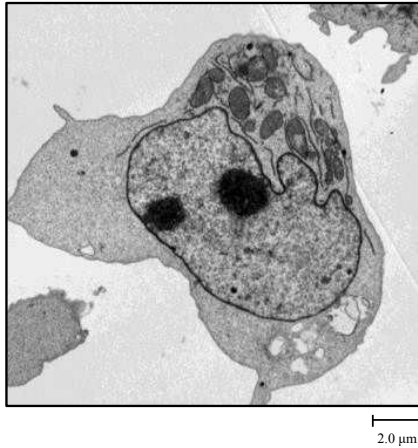
FRDA 2



G130V-FRDA



Healthy control (GM15851)



FRDA 3

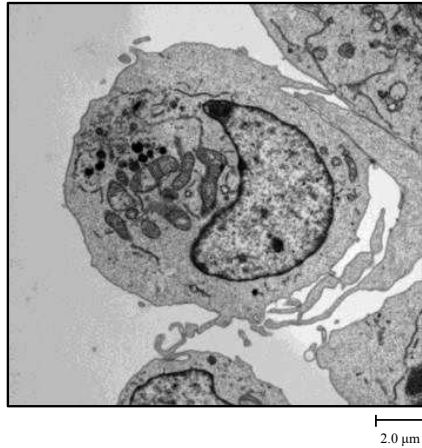


Figure S8: representative electron micrographs of healthy controls, FRDA (1, 2 and 3) and G130V-FRDA LCLs used in this work.

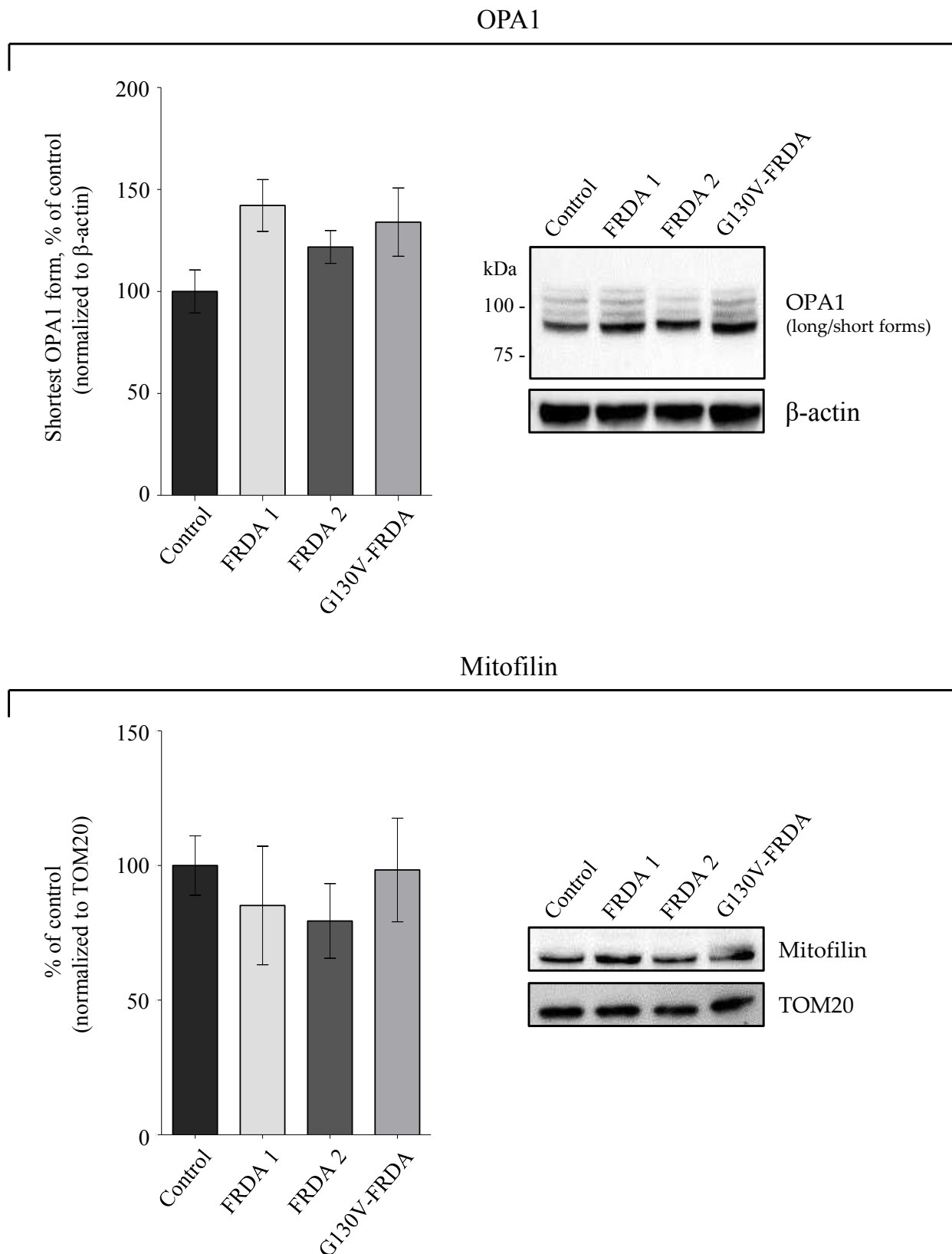


Figure S9: western blotting analyses of OPA1 and mitofilin in whole cell extracts from FRDA (1 and 2), G130V-FRDA and unaffected control LCLs. Equal amounts of protein (*i.e.* 325 μ g) were loaded in each lane. β -actin and TOM20 were used as loading controls. Protein levels were quantified after normalization with β -actin or TOM20 and expressed as percentage of control level. Reported data result from the mean of three (mitofilin) or six (OPA1) independent experiments \pm SEM. One-way ANOVA with Dunnett's post hoc test was used for statistical analysis.

Supplementary table 1. List of antibodies used in this work for western blotting and immunogold-labeling analyses

Antibody	Supplier	Condition of use
Anti – β -actin	Merck; MAB1501	1 : 20 000 in TTBS1X 5% milk – 3h, RT
Anti – TOM20	Santa Cruz; SC-11415	1 : 1000 in TTBS1X 5% milk – 3h, RT
Anti – NDUFA9	Abcam; ab14713	1 : 1000 in TTBS1X 5% milk – O/N, 4°C
Anti – SDHA	Abcam; ab14715	1 : 8000 in TTBS1X – O/N, 4°C
Anti – UQCRC1	Santa Cruz; SC-65238	1 : 1000 in TTBS1X 5% milk – O/N, 4°C
Anti – MTCO1	Abcam; ab14705	1 : 1000 in TTBS1X 5% milk – O/N, 4°C
Anti – OPA1	BD Biosciences; 612607	1 : 1000 in TTBS1X 5% milk – O/N, 4°C
Anti – mitofilin	proteintech; 10179-1-AP	1 : 1000 in TTBS1X 5% milk – O/N, 4°C
Anti – frataxin	proteintech; 14147-1-AP	1 : 500 in TTBS1X 5% milk – O/N, 4°C
Anti – NFS1	LSBio; LS-C482672	1 : 1000 in TTBS1X – O/N, 4°C
Anti – ISCU	LSBio; LS-C157839	1 : 500 in TTBS1X – O/N, 4°C
Anti – mouse peroxidase	Sigma Aldrich; A4416	1 : 10 000 in TTBS1X – 1h, RT
Anti – rabbit peroxidase	Sigma Aldrich; A0545	1 : 20 000 in TTBS1X – 1h, RT



Article

A Combined Spectroscopic and In Silico Approach to Evaluate the Interaction of Human Frataxin with Mitochondrial Superoxide Dismutase

Davide Doni ¹, Marta Meggiolaro ^{1,2}, Javier Santos ^{3,4} , Gérard Audran ⁵, Sylvain R. A. Marque ⁵, Paola Costantini ¹, Marco Bortolus ^{2,*} and Donatella Carbonera ²

¹ Department of Biology, University of Padova, Viale G. Colombo 3, 35131 Padova, Italy; davide.doni.2@phd.unipd.it (D.D.); marta.meggiolaro@studenti.unipd.it (M.M.); paola.costantini@unipd.it (P.C.)

² Department of Chemical Sciences, University of Padova, Via F. Marzolo 1, 35131 Padova, Italy; donatella.carbonera@unipd.it

³ Instituto de Biociencias, Biotecnología y Biología Traslacional (iB3), Departamento de Fisiología y Biología Molecular y Celular, Facultad de Ciencias Exactas y Naturales, Universidad de Buenos Aires, Intendente Güiraldes 2160, Ciudad Universitaria, Buenos Aires C1428EGA, Argentina; javiersantosw@gmail.com

⁴ Departamento de Química Biológica, Facultad de Ciencias Exactas y Naturales, Universidad de Buenos Aires, Intendente Güiraldes 2160, Ciudad Universitaria, Buenos Aires C1428EGA, Argentina

⁵ Aix Marseille Université, CNRS, ICR, UMR 7273, case 551, Ave Escadrille Normandie Niemen, CEDEX 20, 13397 Marseille, France; g.audran@univ-amu.fr (G.A.); sylvain.marque@univ-amu.fr (S.R.A.M.)

* Correspondence: marco.bortolus@unipd.it



Citation: Doni, D.; Meggiolaro, M.; Santos, J.; Audran, G.; Marque, S.R.A.; Costantini, P.; Bortolus, M.; Carbonera, D. A Combined Spectroscopic and In Silico Approach to Evaluate the Interaction of Human Frataxin with Mitochondrial Superoxide Dismutase. *Biomedicines* **2021**, *9*, 1763. <https://doi.org/10.3390/biomedicines9121763>

Academic Editor: Jan Ježek

Received: 23 October 2021

Accepted: 22 November 2021

Published: 25 November 2021

Publisher's Note: MDPI stays neutral with regard to jurisdictional claims in published maps and institutional affiliations.



Copyright: © 2021 by the authors. Licensee MDPI, Basel, Switzerland. This article is an open access article distributed under the terms and conditions of the Creative Commons Attribution (CC BY) license (<https://creativecommons.org/licenses/by/4.0/>).

Abstract: Frataxin (FXN) is a highly conserved mitochondrial protein whose deficiency causes Friedreich's ataxia, a neurodegenerative disease. The precise physiological function of FXN is still unclear; however, there is experimental evidence that the protein is involved in biosynthetic iron–sulfur cluster machinery, redox imbalance, and iron homeostasis. FXN is synthesized in the cytosol and imported into the mitochondria, where it is proteolytically cleaved to the mature form. Its involvement in the redox imbalance suggests that FXN could interact with mitochondrial superoxide dismutase (SOD2), a key enzyme in antioxidant cellular defense. In this work, we use site-directed spin labelling coupled to electron paramagnetic resonance spectroscopy (SDSL-EPR) and fluorescence quenching experiments to investigate the interaction between human FXN and SOD2 in vitro. Spectroscopic data are combined with rigid body protein–protein docking to assess the potential structure of the FXN-SOD2 complex, which leaves the metal binding region of FXN accessible to the solvent. We provide evidence that human FXN interacts with human SOD2 in vitro and that the complex is in fast exchange. This interaction could be relevant during the assembly of iron-sulfur (FeS) clusters and/or their incorporation in proteins when FeS clusters are potentially susceptible to attacks by reactive oxygen species.

Keywords: frataxin; Friedreich's ataxia; SDSL-EPR; fluorescence; protein-protein docking; molecular dynamics

1. Introduction

Frataxin (FXN) is a small, soluble protein that is highly conserved in most organisms, from bacteria to mammalian. The neurodegenerative disease Friedreich's ataxia (FRDA; OMIM 229300) [1] results from low FXN expression, primarily caused by an abnormal GAA triplet repeat expansion in the first intron of the frataxin gene. In addition to low expression levels of FXN, several point mutations of FXN, including nonsense, missense, insertions, and deletions, have been associated with compound heterozygous FRDA patients [1–4]. The principal effect of FRDA is a large depletion of proteins containing iron–sulfur clusters (ISC) as cofactors, such as respiratory chain complexes (complex I-III) or other enzymes,

such as aconitase. Protein depletion is also associated with a disruption of iron homeostasis with a marked increase in mitochondrial iron overload and increased levels of oxidative stress [5–8].

Nuclear-encoded human frataxin is synthesized in the cytoplasm as a precursor polypeptide of 210 amino acids; subsequently, it is imported inside mitochondrion where it undergoes a two-step maturation by the mitochondrial processing peptidase (MMP) [9–11]: MMP first cleaves a portion of the N-terminus, the mitochondrial import signal, producing the intermediate form (FXN 42–210), and in the second step, MMP produces the mature form (FXN 81–210), which is the most abundant form found both in normal individuals and FRDA patients [9]. The FXN C-terminus consists of a highly conserved block of about 100–120 amino acids, which is considered the most important part for protein function [12]. Residues 81–92 of the N-terminal portion are intrinsically unfolded [13] and are often partially truncated for in vitro studies [14] to obtain FXN 90–210. The structure of the folded portion of mature human FXN is relatively rare and consists of the sequence alpha-beta-alpha, where the two alpha helices are located side-by-side on the same side of the contiguous antiparallel beta sheet. FXN folding is remarkably stable, and the secondary structure has limited dynamics, as demonstrated by the high level of similarity between NMR [13] and X-ray crystallography [15] structures. The function of FXN is uncertain, and among the several proposed roles, FXN appears to act as a kinetic activator of the biosynthetic iron–sulphur cluster (ISC) machinery [16–20] and/or as a regulator of iron homeostasis [21] and ferroptosis [22,23], a recently identified iron-dependent form of cell death [24]. Furthermore, it has been suggested to be a protector against the oxidative damage commonly present in the pathological states of the mitochondrial respiratory chain [25–28].

Interestingly, in the context of the latter function, yeast FXN has been shown to interact with superoxide dismutases (SODs) [29]. SODs, a ubiquitous class of antioxidant enzymes, play a crucial role in the response to oxidative stress, catalyzing the dismutation of superoxide radicals into molecular oxygen and hydrogen peroxide. SODs are considered the first line of defense against reactive oxygen species (ROS), whose unbalanced concentration within the cell can dramatically contribute to the pathophysiological mechanisms of several diseases [30]. Up to now, three different SOD isoforms have been identified in mammals: two of them, SOD1 (or Cu/Zn-SOD) and SOD2 (or Mn-SOD), are cellularly localized, while the third isoform, SOD3 (or EC-SOD), is located in extracellular spaces [31]. SOD1 is mainly localized in the cytoplasm, although it is partially localized in the mitochondrial intermembrane space [30]. SOD2 is located exclusively in the mitochondria and exerts a pivotal role in the defense against superoxide radicals produced by electron transport chain complexes, the major source of ROS in cells. SOD2 is a homotetrameric enzyme containing one Mn³⁺ ion (in the resting state) per monomer as a cofactor.

In this work, building on previous in vitro work by Han et al. on the interactions between yeast FXN and bovine SOD1 and between yeast FXN and human SOD2 [29], we focus on the study of human FXN in its mature form (FXN 90–210) and human SOD2. Since human and yeast FXN show a good degree of homology, the interaction is likely to be conserved, and we use human proteins to confirm the interaction and gain a deeper molecular insight into the interface of the complex with a combined in vitro and in silico approach. We make use of the site-directed spin labelling technique (SDSL) coupled to electron paramagnetic resonance spectroscopy (EPR). This is a powerful tool for detecting changes in structure, dynamics, and oligomerization in proteins that was previously used to detect the effects of iron binding to FXN [32]. The EPR investigation is completed by endogenous tryptophan fluorescence experiments and Molecular Dynamics (MD) simulations. Finally, based on the experimental data, we perform a guided protein–protein docking between FXN and SOD2 to identify the interface region and suggest a possible structure for the FXN/SOD2 complex.

2. Materials and Methods

Materials Unless otherwise specified, chemicals were purchased from Merck and used without further purification. Ferric iron solutions were prepared from $\text{FeCl}_3 \cdot 6\text{H}_2\text{O}$ in HCl at pH 0.8. Human mitochondrial SOD (SOD2) was purchased as a His-tag recombinant protein from Technical Novusbio; the SOD2 buffer was Tris HCl buffer (20 mM, pH 8) containing 20% glycerol. The M-TETPO label was synthesized as previously described [32].

Heterologous expression and purification of human wild-type FXN and mutants A plasmid containing the coding sequence of human wild-type mature FXN, pET-9b/FXN(90–210), was previously obtained in our laboratory [33]. FXN mutants were obtained as previously described [32]. The two additional frataxin mutants used in this work, H177C and S202C, were obtained using the pET-9b/FXN(90–210) plasmid as a template and the couples of primers listed in the SI. Each sequence was checked by DNA sequencing (at Macrogen). *Escherichia coli* BL21 (DE3) cells were chemically transformed with the plasmids of interest, and positive clones were selected by antibiotic resistance. Expression of the wild-type and mutant proteins was induced by adding 1 mM isopropyl- β -thiogalactopyranoside (IPTG) in LB medium and incubating the bacteria cultures at 30 °C overnight under constant stirring. Cells were then harvested by centrifugation at $5000 \times g$ and 4 °C for 20 min, resuspended in lysis buffer (25 mM HEPES, pH 7.0) supplemented with protease inhibitors (1 $\mu\text{g}/\text{mL}$ pepstatin A, 1 $\mu\text{g}/\text{mL}$ leupeptin, 1 $\mu\text{g}/\text{mL}$ antipain, 100 μM PMSF) and lysed by French press. The supernatant fractions were isolated from cell debris by centrifugation at $17,000 \times g$ and 4 °C for 15 min and incubated with 10 mM EDTA for 1 h at 4 °C under gentle agitation. Proteins were purified by combining anionic exchange and size exclusion chromatographies. The first chromatographic step was performed using a cationic DEAE (Diethylaminoethyl) Sepharose column using 25 mM HEPES (pH = 7.0) as the buffer of equilibration and 25 mM HEPES (pH = 7.0), 1 M KCl as the elution gradient buffer. The fractions corresponding to frataxin, as assessed by SDS PAGE, were collected, pooled together, concentrated by centrifugal filters (Amicon Ultra Centrifugal Filter, 3000 NMWL, from Merck Millipore, Burlington, MA, USA), and purified by size-exclusion chromatography (SEC). For FXN mutants containing cysteines, incubation with 1 mM of dithiothreitol (DTT) was performed for 1 h at 4 °C after cationic exchange. The second purification step was performed on a Superdex 200 GL 10–300 column (from GE Healthcare, Chicago, IL, USA) equilibrated in a buffer containing 25 mM HEPES (pH = 7.0) and 50 mM KCl. To estimate the molecular weights of the protein samples, the column was equilibrated in the same buffer and calibrated with the standards thyroglobulin (669 kDa), ferritin (440 kDa), β -amylase (200 kDa), bovine serum albumin (67 kDa), carbonic anhydrase (29 kDa), and cytochrome c (12 kDa). The eluted fractions containing frataxin proteins were finally pooled together, and the molar concentrations of the protein samples were determined spectroscopically using $\epsilon_{280\text{nm}} = 26,930 \text{ M}^{-1}\text{cm}^{-1}$ for all mutants (molar extinction coefficients were evaluated with the ExPASy ProtParam tool). Protein purity and integrity were finally assessed by SDS-PAGE and Coomassie blue staining (see Supplementary Materials, Figure S1).

Spin Labelling Protein samples were labelled with M-TETPO for the EPR experiments. Purified proteins (at a concentration of 50 μM) were incubated with DTT in a molar ratio of 1:100 at 4 °C for 30 min under slow agitation. Excess DTT was removed from the samples with a PD10 desalting column (GE Healthcare) using 25 mM HEPES (pH = 7.0) and 50 mM KCl as the elution buffer. Proteins were labelled with a tenfold molar excess of M-TETPO (dissolved in acetonitrile) and incubated at 4 °C for 2 h in the dark under slow agitation. Labelled protein samples were concentrated by centrifugal filters (Amicon Ultra Centrifugal Filter, 3000 NMWL, from Merck Millipore), and excess spin label was then removed by gel filtration using a Superdex 200 GL 10 300 column (from GE Healthcare) and 25 mM HEPES (pH = 7.0) and 50 mM KCl as the elution buffer. M-TETPO-labelled proteins were finally concentrated by centrifugal filters to a volume suitable for EPR spectroscopic analysis, and their concentrations were determined by UV-Vis spectroscopy, as previously described.

SDS-PAGE electrophoresis and Western Blot analysis Protein purity and integrity were assessed by SDS-PAGE and Coomassie blue staining prior to any spectroscopic experiment reported in this work. Samples of each step of FXN expression and purification and a small aliquot of recombinant SOD2 were solubilized in a Laemmli gel sample buffer containing 5% 2-mercaptoethanol and heated for 10 min at 95 °C on a heating block. Samples were then loaded into precast 4–20% polyacrylamide gel (GenScript® ExpressPlus™ PAGE, Piscataway, NJ, USA). The run was done at 100 volts using Tris-MOPS-SDS Running Buffer Powder GenScript® as the running buffer. At the end of the run, the gel was incubated with Coomassie Brilliant Blue colorant and subsequently destained using a solution of acetic acid 7.5%–methanol 10%. Correct separation and the molecular weights of the proteins were estimated using a marker of molecular weight loaded on the same gel.

For SOD2, an immunoblot assay was performed to assess the identity of the protein (see the Supplementary Materials, Figure S2). After the electrophoretic run, the gel was transferred to a nitrocellulose membrane (Life Science) through a semi-dry Trans-Blot® Turbo™ Transfer System (BioRad, Hercules, CA, USA). The membrane was then blocked with 10% milk in Tris-buffered Saline (TBS) for 1 h at room temperature and subsequently incubated at 4 °C overnight with the primary antibody (alpha-SOD2-HPA001814, Merck KGaA, Darmstadt, Germany) diluted 1:1000 in Tris-buffered Saline with 0.05% Tween20 (TBS-T). After incubation with the anti-rabbit IgG HRP-conjugate antibody (A0545, Merck KGaA, Darmstadt, Germany) diluted 1:20,000 at room temperature for 1 h, the protein was visualized using Immobilon® Forte Western HRP Substrate (Millipore) with an Imager CHEMI Premium Detector (VWR).

Fluorescence experiments were performed on a FLS 1000 UV/Vis/NIR photoluminescence spectrometer (Edinburgh Instruments) with a 450 W Xenon Arc lamp for excitation at 285 nm and a PMT-980 detector. The Peltier controlled holder allowed measurement at 288 K under stirring. The sample compartment was under constant nitrogen flow to avoid condensation on the windows and to maintain an anaerobic atmosphere. Experiments were conducted using a fluorescence cuvette (117104F-10-40 from Hellma, Müllheim, Germany) with a 10 × 4 mm optical path length and a gas tight screw cap with a silicon septum. The buffer was a mix of the SOD buffer (910 µL of 20 mM TRIS-HCl, pH = 8) and FXN buffer (90 µL of 25 mM HEPES, pH = 7.0, 50 mM KCl) to mimic the composition of the buffer in EPR experiments. The final concentrations of the proteins were as follows: FXN, 1.4 µM; SOD2, 1.9 µM.

Electron Paramagnetic Resonance (EPR) spectroscopy EPR spectra were recorded on an ELEXSYS E580 spectrometer equipped with a SHQ cavity, both from Bruker BioSpin GmbH (Rheinstetten, Germany). The experiments were performed at room temperature, typically using the following parameters: microwave frequency 9.86 GHz, microwave power 19 mW (attenuation 9 dB), sweep width 150 mT, center field 351.4 mT, conversion time 164 ms, time constant 82 ms, and modulation amplitude 1.6 mT (1024 points, 25 averages per spectrum). Samples were prepared by thoroughly mixing 18 µL of SOD buffer or SOD2 protein stock solution (both in 20% *v/v* glycerol) with 2 µL of FXN stock solution to give a final FXN concentration of 10 µM; the resulting solution was put in a glass capillary (internal diameter 0.8 mm) and measured under nitrogen gas flow. The experiments with Fe³⁺ were performed on the same solution as above with the addition of 1 µL of Fe³⁺ stock solution. As previously verified [32], this volume of acidic iron solution does not change the pH of the solution.

Simulation of EPR spectra the simulation of the EPR spectra allowed quantitative information on the mobility of the spin label to be obtained. To perform the simulations, one must know or estimate the nitroxide *g*-tensor (**g**) and hyperfine tensor (**A**) and then adopt a model of spin-label motion based on the stochastic Liouville equation [34]. In this work we describe the spin-label mobility in terms of an isotropic diffusion tensor **D**. While this model is simplified, it fully allowed us to rationalize our results for all mutants in terms of the rotational correlation time τ_c , which is derived from the diffusion tensor: $\tau_c = 1/6D_{iso}$. We used the MultiComponentEPR827.vi program designed by Christian

Altenbach to perform the simulations. The program is written in LabVIEW (National Instruments) and can be freely downloaded [35].

Protein–Protein docking The molecular docking simulations were performed using four docking software packages that are freely available as webservers on the web. All of them allow the input of one or more residues to be considered for the interface: ClusPro [36], ZDOCK [37], GRAMM-X [38], and PatchDock [39,40]. The generation of the docking poses, the potential energy function that evaluates the energy of each docking pose, and the additional steps performed to rank the final docking poses all depend on the individual program (for details, we refer the reader to the relative references). ZDOCK, GRAMM-X, and ClusPro are based on a FFT approach to probe a fine grid for the generation of the docking poses. PatchDock adopts a different approach to accelerate the generation of the possible docking poses by matching the surfaces of two proteins based on their geometric complementarity. All programs perform additional steps to score the docking poses, each characterized by a different function. Therefore, to compare the results, the top solutions of each program were pooled together and re-ranked using a common scoring function. Among the different possibilities, we chose to adopt CONSRank, a freely available webserver that allows the solutions from all programs to be easily scored at the same time without only minimal formatting on the output files [41–43]. The re-ranking was based on the frequency of inter-residue contacts appearing in the solutions. Visualization, analysis, and plotting of the docking models were performed using UCSF Chimera software, developed by the Resource for Biocomputing, Visualization, and Informatics at the University of California, San Francisco with support from NIH P41-GM103311 [44].

Molecular Dynamics simulations Molecular Dynamics (MD) simulations and the analysis of production runs were carried out using the YASARA Structure [45] on the following hardware: Processor Intel CORE i7 10,700 10th generation; SOCKET 1200 2.9 GHZ (Max 4.8 GHZ) 16 M cores/threads 8/16, 2; Memory Kingston HX426C16FB3/8G HyperX 2666 Mhz; Disc SSD Kingston A400 240GB SATA 7 mm; Linux Ubuntu 20.04 LTS 64 bit. The coordinates corresponding to wild-type FXN (PDB ID: 1EKG) were solvated, and standard minimization protocols were applied to remove steric clashes. The simulation cell was prepared by maintaining a 20 Å water-filled space around the protein with a density of 0.997 g/mL. The system (cubic cell, periodic boundaries, and 8.0 Å cut-off for long-range coulomb electrostatics forces) was neutralized with 0.9% NaCl, and the temperature was maintained at 298 K with a pH of 7.4. After the initial steepest descent minimization, unrestrained replicas of 100 ns MD simulations using an ff14SB Amber force field [46] were carried out with 2.50 fs time steps. Snapshots were saved every 0.1 ns. The root-mean-square deviation (RMSD), root mean square fluctuation (RMSF), and secondary structure content were calculated.

3. Results

3.1. Choice of Labelling Sites and Molecular Dynamics of FXN

Mature FXN has a natively unfolded N-terminal region, followed by a region rich in Asp and Glu residues constituted by a long alpha helix and a loop, which constitute the main iron binding region that was characterized previously [47,48]. The beta-sheet region has been shown to be part of the interface in the ISC maturation complex, with W155 playing a key role [16]. We previously produced a library of FXN site-directed mutants across the protein where a native amino acid was mutated to cysteine and labeled with a spin probe to study the effect of Fe^{2+/3+} binding [32]. In this work, we used these mutants to investigate the possible interaction between FXN and SOD2 and produced two additional mutants to also map the loop region between the beta sheet and the short alpha helix (H177C) and the C-terminal portion of the protein (S202C). All positions where the spin labels were introduced are shown in sphere representation in Figure 1.

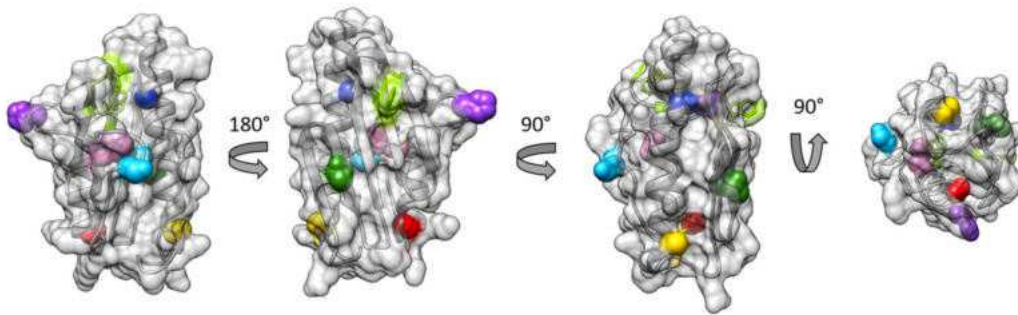


Figure 1. Structure of human FXN (pdb.id 1EKG) from different angles. The three native Trp residues are colored bright green and shown in stick representation. The spin labelling sites, A114 (yellow), T133 (green), H177 (purple), H183 (pink), A193 (red), and S202 (light blue), are shown in sphere representation. The third view from the left is the same as the one that appears below in the proposed models of the FXN/SODs complexes.

The local mobility of the residues, together with the tumbling of the protein, is reflected in the lineshapes of the EPR spectra of the spin probes. The internal motion of the wild type frataxin was studied by all-atom molecular dynamics (MD) simulations (nanosecond timescale) to investigate the mobility of the labeled positions (Figures 2 and S6). The results are reported in Figure 2, showing the root-mean-square fluctuations (RMSF) along the protein chain; the mutated sites are shown in color using the same color code as used in Figure 1. The MD simulations clearly show that the H177 and S202 positions are more mobile than the rest of the labeled positions. Furthermore, H177 is part of a flexible stretch of the protein.

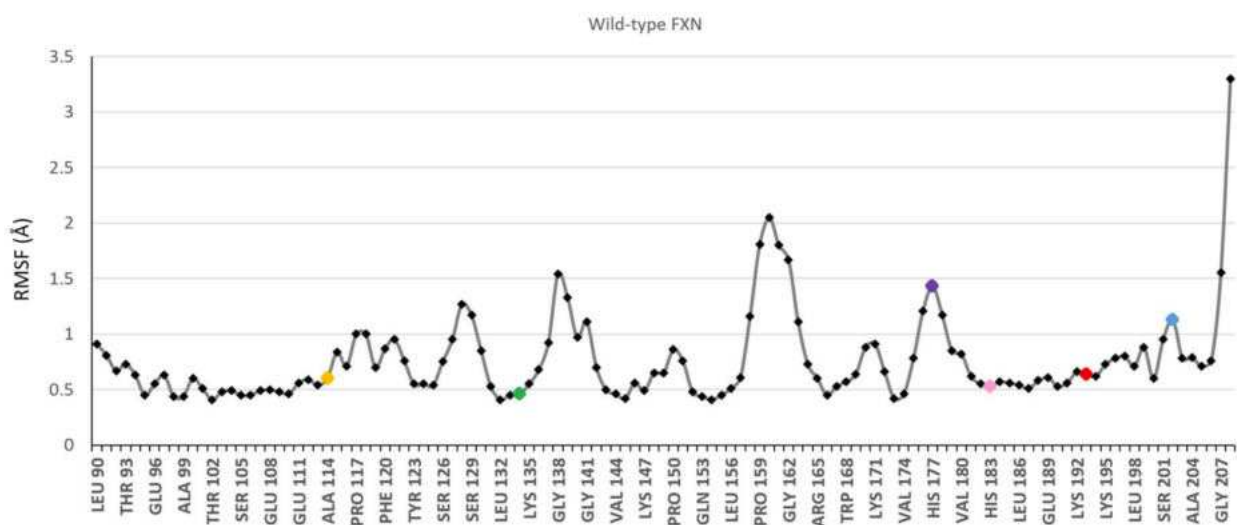


Figure 2. Root-mean-square fluctuations along the protein chain determined from the MD simulations on WT FXN (90-210). The spin labelling sites are shown as colored dots: A114 (yellow); T133 (green); H177 (purple); H183 (pink); A193 (red); S202 (light blue).

3.2. EPR Spectra of FXN Interacting with SOD2

We performed EPR experiments on FXN spin-labeled in different regions to try and pinpoint the interface formed by FXN and SOD2. The formation of an interface in the position where the nitroxide probe is located would result in a marked slowdown of side-chain motion, leading to a broader EPR spectrum. However, FXN is a small protein (MW = 13.64 kDa), and its tumbling motion in aqueous solutions at room temperature is rapid. The protein tumbling motion would mask any local contribution to the EPR spectral lineshape proper of the spin label; therefore, it was necessary to slow it down by carrying out the EPR experiments in viscous solution. We performed the experiments

in 20% *v/v* glycerol, which slowed down the FXN tumbling enough to observe an EPR spectral shape influenced not only by the protein tumbling but also by the mobility of the spin probe sidechain and the backbone mobility.

The EPR spectra of 10 μM FXN mutants in the absence or presence of 40 μM SOD2, giving a final FXN:(SOD2)₄ molar ratio of 1:1, are reported in Figure 3. In the absence of SOD2, each mutant shows a characteristic spin label mobility, which confirms that the addition of glycerol slows the molecular tumbling of the protein enough that the spectrum reports both local mobility and general mobility. The mobility of the two new sites studied in this work (H177 and S202), as judged by the EPR spectra, faithfully reflects the high mobility of the native residues, as shown by the MD simulations presented in Figure 2. H177 is positioned in the loop between the beta sheet and the short helix and has the highest mobility among the studied residues, which is aided by the low level of crowding by nearby sidechains. Accordingly, it shows an EPR spectrum typical of very fast motion. S202 is in a relatively rigid part of the C-terminal region (residues 196–210), but it has greater mobility relative to neighboring residues, and its EPR spectrum indicates faster mobility than that of all other positions other than H177.

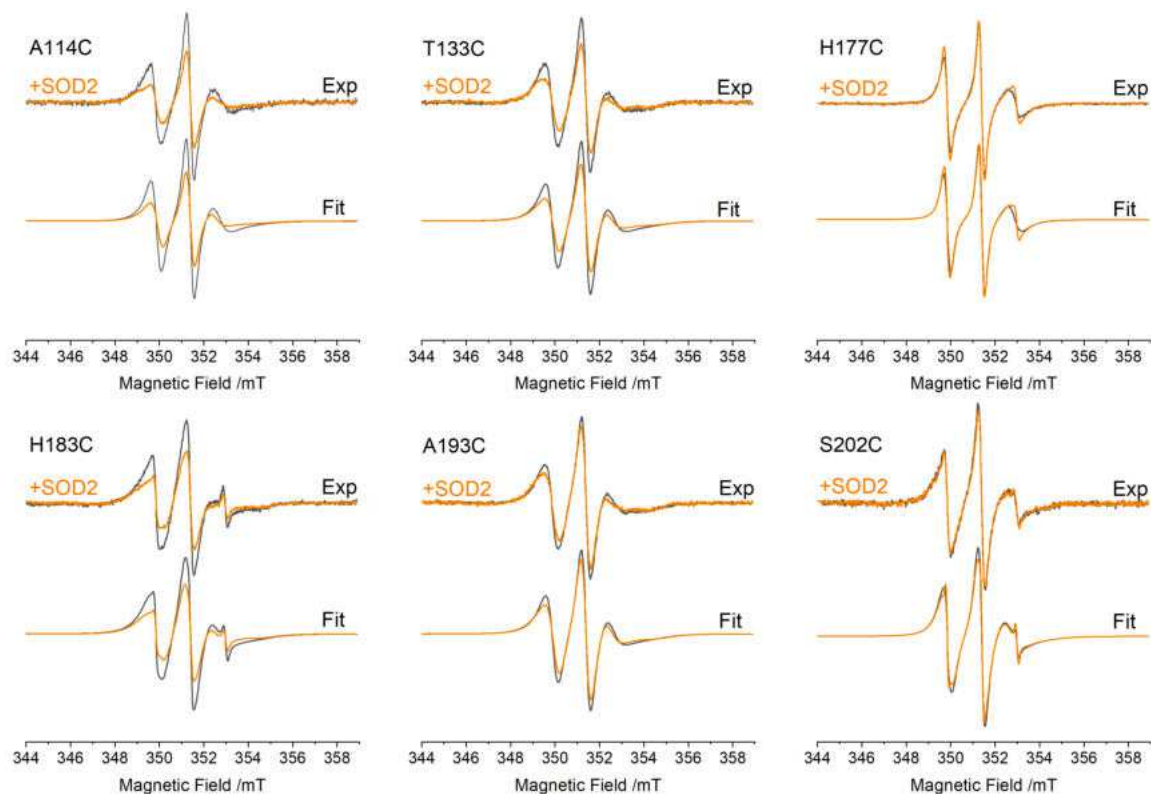


Figure 3. EPR spectra of FXN mutants (10 μM) in the absence (dark grey) and presence (orange) of SOD2 (40 μM) at a FXN:(SOD2)₄ molar ratio of 1:1. For each mutant: top, experimental spectra; bottom, fitting. All spectra have been normalized to the same number of spins to compare the spectral shape in terms of the spin-probe mobility.

Following the addition of an equimolar quantity of tetrameric SOD2, all positions were affected similarly, except for positions H177 and S202, for which the effect was almost null. Similar but slightly less pronounced effects were obtained with a FXN:(SOD2)₄ ratio of 1:0.5, closer to that used in the fluorescence experiments reported below (see the Supplementary Materials, Figure S3). The spectral changes clearly indicate an interaction between FXN and SOD2.

To better quantify the effects of SOD2 on FXN, we fitted the EPR spectra by obtaining the rotational correlation time, τ_C (the fittings are reported in Figure 3 as grey and orange lines). The slow motion of the EPR probe was assumed to be isotropic. This simple model

captures the spectral variations induced by SODs quite well and makes it easy to discuss the spectral variations in terms of the changes in the rotational correlation times ($\Delta\tau_C$), reported in Table 1 as the difference between τ_C in the presence of SOD (τ_C^{+SOD}) and the one in its absence (τ_C^{-SOD}).

Table 1. Isotropic rotational correlation times for FXN mutants alone (τ_C^{-SOD}) in the presence of 1:1 tetrameric SOD (τ_C^{+SOD}) and their variation ($\Delta\tau_C$) obtained from the fitting of the EPR spectra. All values are presented in nanoseconds. The error estimate was derived from the error in the fitting following standard error propagation methods. The g tensor principal components are $g_{xx} = 2.0088$, $g_{yy} = 2.0070$, and $g_{zz} = 2.0030$. The hyperfine tensor principal components are $A_{xx} = 0.79$ mT, $A_{yy} = 0.54$ mT, and $A_{zz} = 3.68$ mT.

Mutant	τ_C^{-SOD}/ns	τ_C^{+SOD}/ns	$\Delta\tau_C (\tau_C^{+SOD} - \tau_C^{-SOD})/\text{ns}$
A114C	2.52 ± 0.06	2.96 ± 0.06	0.44 ± 0.09
T133C	2.70 ± 0.06	3.10 ± 0.07	0.40 ± 0.095
H177C	1.13 ± 0.03	1.24 ± 0.03	0.11 ± 0.04
H183C	2.77 ± 0.06	3.33 ± 0.06	0.56 ± 0.10
A193C	2.77 ± 0.06	3.18 ± 0.06	0.41 ± 0.10
S202C	2.30 ± 0.05	2.47 ± 0.05	0.16 ± 0.08

A homogeneous reduction in dynamic $\Delta\tau_C$ was observed for four sites (A114, T133, H183, A193) spread over a large region of the protein. The observed change likely reflects the slowdown in protein tumbling following the formation of the complex with bulky SOD2. In particular, H183, being an internal residue with limited sidechain and backbone dynamics, has the lowest mobility (highest τ_C) of all sites and almost purely reflects the protein tumbling. Given that the changes in protein tumbling are the dominant effect on spin-label mobility, we cannot exclude the idea that one or more of the exposed sites (A114, T133, A193) are located at the interface between the two proteins. On the other hand, $\Delta\tau_C$ indicates that the mobility of H177, and S202 remains almost unchanged upon the addition of SOD2. Their mobility is always dominated by the fast backbone and sidechain motions (lowest τ_C), making them insensitive to protein tumbling changes. This excludes the idea that these latter residues partake in the protein–protein interface: if they were at the interface, their sidechain motion would be strongly reduced, bringing down their τ_C to that characteristic of protein tumbling (that of the internal site H183).

Another important aspect that emerged from the simulation of the EPR spectra was that only one motional component was present in all spectra, even after the addition of SOD2, suggesting that the interaction between the proteins is in the fast-exchange regime.

Previously, we showed that the addition of excess iron slows FXN motion by inducing its aggregation at all positions [32]. Here, we tested the effects of Fe^{3+} addition in the presence of SOD2 by performing EPR experiments at a ratio of FXN:(SOD2)₄: Fe^{3+} 1:0.5:20. The spectra, reported in the Supplementary Materials in Figures S4 and S5, clearly show that the presence of SOD2 has no effect on FXN aggregation at this molar ratio.

3.3. Fluorescence Spectra of FXN Interacting with SOD2

The interaction between FXN and SOD2 was tested using the fluorescence emission of the tryptophan residues and comparing the fluorescence of the individual proteins with the fluorescence of the mixed solution. The results are reported in Figure 4. We must note that the spectra show the Raman scattering peak of the buffer at 310 nm (corresponding to a Raman shift $\bar{\nu} = 3456 \text{ cm}^{-1}$).

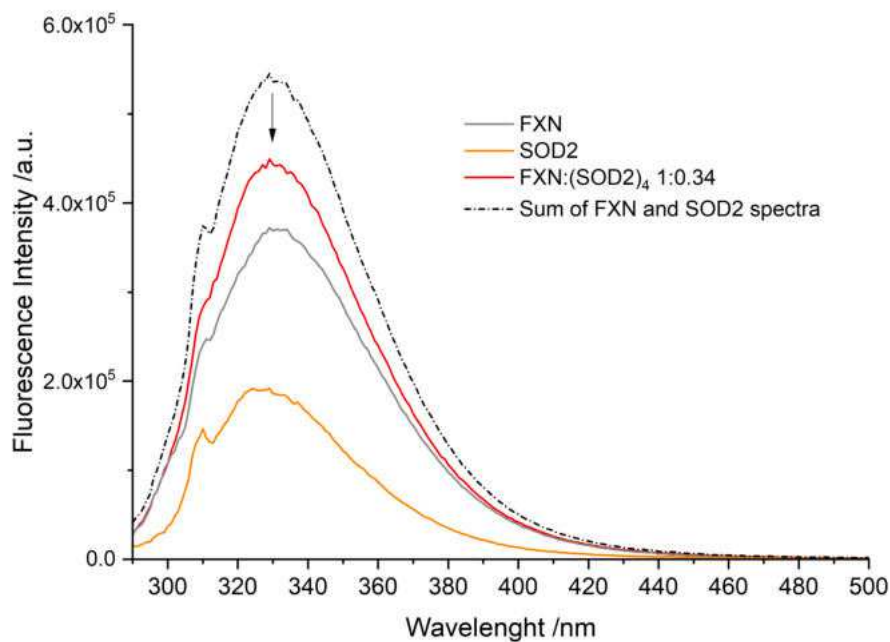


Figure 4. Tryptophan fluorescence spectra of WT FXN (1.4 μM) and SOD2 (1.9 μM). Temperature 288 K, $\lambda_{\text{exc}} = 280$ nm. FXN alone, grey; SOD2 alone, orange; SOD2 and FXN (molar ratio FXN:(SOD2)₄ 1:0.34), red; sum of the individual fluorescence spectra of SOD2 and FXN, red. The peak at 310 nm is the Raman peak of the buffer.

Human FXN has three native Trp residues (W155, W168, W173); the Trp residues are shown in green in stick representation in Figure 1. While the W155 residue is in the beta sheet region and exposed to the solution, W168 is partially exposed and W173 is completely buried. It should be noted that all three Trp residues are spatially close together and, therefore, interact with each other via energy transfer, affecting the overall fluorescence in a complex way. W155, being the only fully exposed Trp residue, is likely the most sensitive to the presence of quenchers in solution. We must note here that, in our previous study, we verified that fluorescence experiments based on Trp quenching may be not fully reliable when the quencher binds far away from the Trp region [32]. For Frataxin, the fluorescence spectrum, therefore, results in a peak at 332 nm (grey line in Figure 4).

Human SOD2 has six Trp residues per protein chain (W78, W123, W125, W161, W181, and W186), most of them buried in the protein interior and in proximity to each other, either in the same chain or in neighboring chains in the tetramer, with only W181 and W186 exposed to the solution. SOD2 fluorescence is largely self-quenched, and the limited solvent exposition leads to it being blue-shifted relative to FXN with a peak at 328 nm (orange line in Figure 4).

The fluorescence spectrum of the mixed FXN:(SOD2)₄ solution at a molar ratio of 1:0.34 (red line in Figure 4) shows marked quenching relative to the sum of the experimental spectra of the individual proteins (17% less fluorescence, black dashed line in Figure 4). The quenching, highlighted by the arrow in the figure, suggests that the two proteins come into contact and that the exposed Trp residues are close to the interaction surface, leading to fluorescence quenching. We propose that the quenching stems from the energy transfer from the exposed W155 (or possibly also W168) in FXN to the tryptophan network in SOD2 through the solvent-exposed W181/W186.

3.4. Protein–Protein Docking of FXN and SOD2

To complement the experimental data and gain further insight into the interaction, we decided to model the structure of the FXN:(SOD2)₄ 1:1 complex using protein–protein molecular docking. We performed both blind docking simulations and simulations using site-specific information from SDSL-EPR and fluorescence as restraints. The struc-

tures used for the docking calculations were as follows: FXN (pdb.id 1EKG [15]); SOD2 (pdb.id 5VF9 [49]).

The top fifteen models obtained from the blind docking simulations were analyzed collectively to identify which residues of FXN and SODs were most often found at the interface of the protein complex. The full details of the docking simulations are reported in the materials section. Briefly, the docking protocol involved three steps: (1) docking simulations using four programs freely available as webservers (ZDOCK [37], ClusPro [36], GRAMM-X [38], PatchDock [39,40]); (2) re-ranking of the solutions using a common scoring function with CONSRank; and (3) analysis of the interface regions in the top 15 re-ranked docking poses using PDBePISA. The normalized frequency with which each residue appeared at the interface in the top 15 models was represented as a histogram and then mapped on the protein surface; the results for the blind docking are shown in Figure 5. In this set of simulations, FXN interacted with a single monomer of SOD2, contacting only a second monomer close to the interface. The SOD2 region involved in the interaction is the hollow region on top of the N and C-terminal tails of the protein on the other side of the active site facing the inner tetrameric cavity. The interaction region for FXN is concentrated mostly around the top part of the protein comprising the N- and C-termini, leaving the beta-sheet region exposed to the solution. These models show a good surface complementarity with several hydrogen bonds and salt bridges being possible; however, they contrast with the experimental evidence. First, a site that is almost always found at the interface is H177 (present in more than 90% of the models), which is in marked contrast to the EPR experimental results, which show limited effects of the complex formation on H177 mobility. Furthermore, the exposed Trp residues for SOD2 are also relatively far away from the interface, as is W155 from FXN, while the other FXN Trp residues are close to the interaction region. Overall, because the Trp residues of the two proteins are far from each other and do not change their solvent exposition, the obtained docking poses make it hard to justify the observed fluorescence quenching.

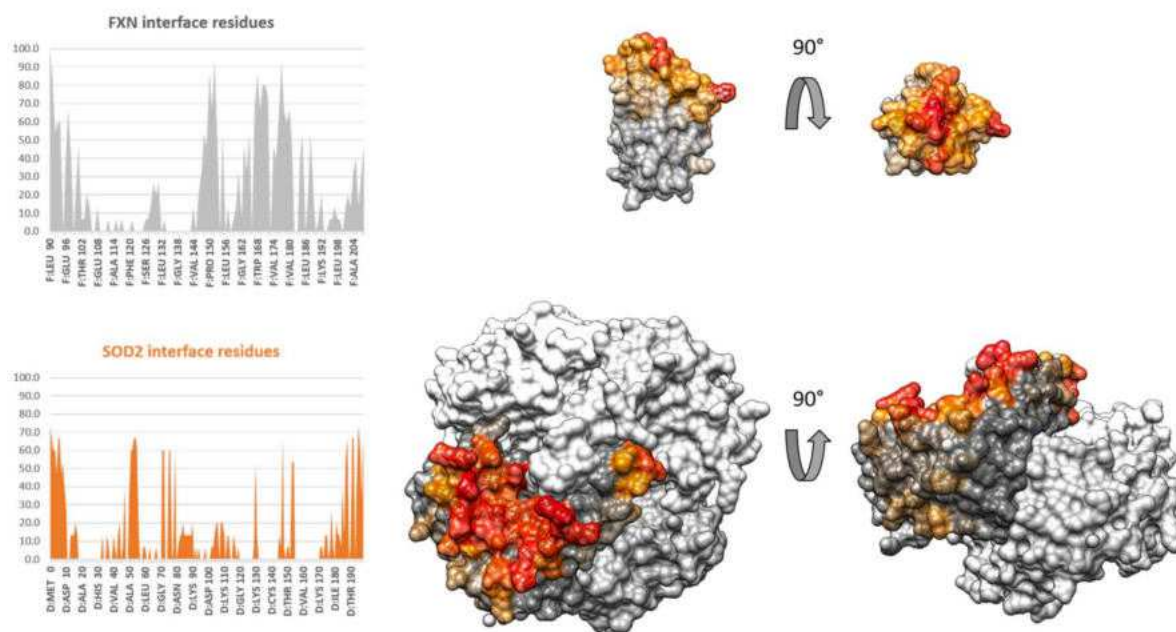


Figure 5. Blind docking simulations FXN/(SOD2)₄. Left—histogram of the normalized frequency of appearance of each amino acid at the interface: grey, FXN; orange, SOD2. Right—surface mapping of the frequency of appearance at the interface: the frequency with which an individual residue is involved in the interaction lowers going from red to orange; grey residues are never involved in an interaction. SOD2 has only one monomer mapped. FXN is represented with the beta-sheet shown to the reader in the left image.

Given that the blind-docking analysis did not agree with the observations from the spectroscopic data, the docking simulations were also performed using the data as restraints. We chose not to exclude any residue from the interface, even if H177 and S202 could be excluded based on the EPR results. Instead, we opted to locate only W181 and/or W186 from SOD2 close to the binding interface, if possible, as Trp fluorescence was strongly affected. No Trp residue from FXN was chosen, since, while W155 is the only Trp residue that is fully solvent-exposed, W168 is also sufficiently close to the surface and could potentially act as a potential conduit for quenching. In this set of calculations, we specified the Trp residues belonging to a single SOD2 chain as restraints. This is reasonable since the exposed Trp residues of SOD2 are located far from the tetramer interfaces and FXN and, being smaller than a SOD2 monomer, would be unable to reach the other SOD2 monomers when interacting with the Trp region. The best docking model of the restrained simulations is reported in Figure 6 from two different angles. The structure of this complex involves a different region from the blind docking simulations, as expected. The active site of SOD2 is still accessible, as is the iron-binding region of FXN. Although the complementarity of the surface is reduced relative to the blind-docking simulations, and the specific interactions are limited to two hydrogen bonds, this structure satisfies both the fluorescence and the EPR data. FXN now contacts SOD2 using the beta-sheet region, bringing W155 close to the exposed Trp of SOD2; the closest interatom distance between W155 and W186 is only 0.8 nm. Additionally, both H177 and S202 are now far from the region of interaction, which justifies the smaller changes in mobility for these two residues from the EPR data. The full accessibility of the iron-binding region is also in line with experiments conducted in the presence of Fe^{3+} .

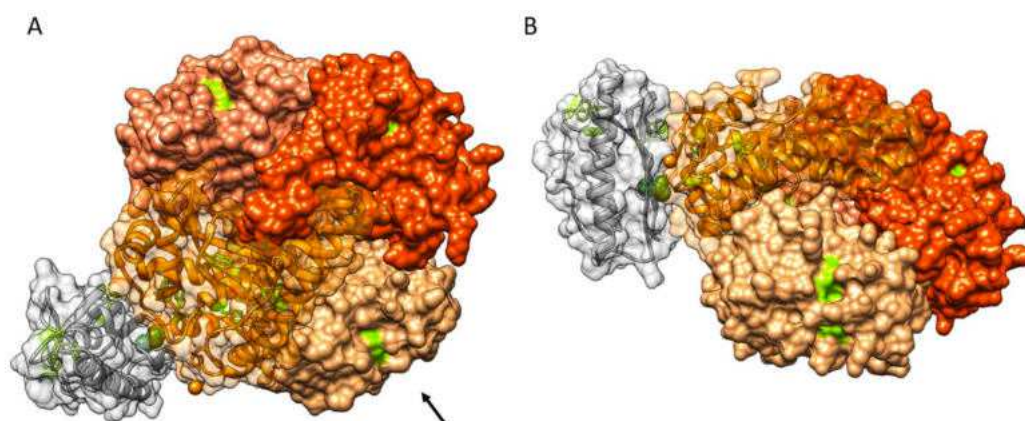


Figure 6. Docking model of the FXN:(SOD2)₄ 1:1 complex. FXN is shown in grey; SOD2 is shown in shades of orange, one shade per protein chain. Tryptophan residues are shown in light green with stick representation; T133 is shown in dark green with sphere representation. The protein chains involved in the interaction are represented by a partially transparent surface. (A) SOD2 viewed in the same orientation as in Figure 4; (B) the complex as viewed from the direction of the arrow to better highlight the orientation of FXN.

4. Discussion

This study stemmed from previous work by Han et al. [29], which reported on the interaction between yeast FXN and SODs (bovine and human, in that work). To give full meaning to the results, however, the question of whether the same interaction could be detected between human FXN and human SODs needed to be addressed. In this work, we investigated the interaction between the mature form of FXN and mitochondrial SOD2, since Han and coworkers estimated that at physiological concentrations a complex between FXN and SOD1 could not be formed within the mitochondria [29]. Furthermore, since SOD1 is primarily a cytosolic protein, it would probably interact with the immature form of FXN. EPR experiments suggested that human SOD2 interacts with mature FXN. All positions showed a slowdown in dynamics upon the addition of SOD2, which was

likely the result of the large increase in the hydrodynamic radius. We did not observe two different spectral populations, suggesting that the proteins undergo fast exchange in solution, and therefore the kinetics of association/dissociation are fast, in the order of tens of nanoseconds. The results of the fluorescence experiments confirm an interaction with SOD2: the fluorescence when both proteins are present was reduced by 17% relative to the sum of the individual contributions. Interestingly, Han et al. observed a ~13% fluorescence enhancement by mixing yeast FXN with human SOD2, as opposed to the quenching we observed. While yeast FXN only has two Trp residues, the diametrically different result suggests that the details of the interaction between human proteins are significantly different from those of the mixed-species system. Together, our experimental results suggest a definite interaction between human FXN and SOD2 in vitro. A quantitative estimation of the K_D would require additional experiments and is beyond the scope of the present work.

Several experimental works point to a possible direct or indirect role of FXN in SOD2 activity, giving a potential physiological relevance for the in vitro interaction that we observed. Both SOD2 and FXN [28] are able to regulate the detoxifying enzymatic mechanisms and inhibit ROS production, and they might act synergistically, since the two proteins are located in the same mitochondrial compartment. Recently, it has been demonstrated that FXN is enriched in the mitochondrial cristae, and its involvement in stabilizing the organization of respiratory chain has been hypothesized based on functional and biochemical analyses [50]. Interestingly, recent cryo-EM studies showed that SOD2 is associated with respiratory supercomplexes in both mycobacteria [51] and *Caenorhabditis elegans* [52], an association that can provide local protection against ROS damage. FXN and SOD2 are both involved in the biochemical hallmarks of FRDA pathophysiology, i.e., increased susceptibility to oxidative stress, iron overload, and a deficit in ISC biogenesis. FXN deficiency correlates with a lower cell antioxidant capacity, especially for SOD2 [53,54]. In the yeast model of FRDA, SOD2 is overexpressed but shows lower activity that can be recovered with manganese supplementation [55]. Furthermore, iron overload plays a role in the inactivation of SOD2, since it can compete with manganese for binding to SOD2, inactivating the enzyme [56,57]. In this context, we propose two hypotheses on the physiological relevance of the FXN/SOD2 interaction, but we cannot exclude the possibility that the link between FXN and SOD2 discussed above is more a consequence of their common involvement in mitochondrial function than the result of a direct interaction. One possibility is that the interaction between the two proteins acts as a modulator of antioxidant mechanism in the vicinity of respiratory complexes, given their localization and their involvement in oxidative stress. A second possibility is that under pathological conditions of excess iron, FXN transiently interacts with SOD2, lowering the local iron concentration, since one FXN can bind several Fe^{2+}/Fe^{3+} ions, thus preventing manganese substitution with the consequent inactivation of SOD2. The structure of the proposed complex (Figure 6), in which the iron binding region of FXN is exposed to the solution and does not block the active site of SOD2, could be in line with both hypotheses.

In conclusion, the results obtained through the combination of SDSL-EPR, fluorescence, and molecular docking prove that mature human FXN interacts with human SOD2 in vitro, confirming the previously observed interaction between yeast FXN and human SOD2. An aspect that should be investigated is whether the currently known pathological variants of FXN affect the interaction. Several involve mutations in the beta-sheet region of FXN (for example, N146K, W155R, R165C), which we found to be important for the interaction with SOD2 as well as with the FeS assembly protein complex. Taking into account the increasing amount of evidence that both proteins are present in the region around respiratory chain complexes and that iron interacts with both, the FXN/SOD2 interaction could be relevant for the protection of FeS clusters during assembly and/or incorporation when FeS clusters are potentially exposed to attacks by reactive oxygen species. All things considered, we suggest that the observed interaction merits further

investigation to better frame it within the context of the uncertain physiological role of FXN and the molecular mechanisms of FRDA.

Supplementary Materials: The following are available online at <https://www.mdpi.com/article/10.3390/biomedicines9121763/s1>, Figure S1: DS-PAGE followed by Coomassie Brilliant Blue staining for the expression and purification steps of recombinant human FXN90-210, Figure S2: Left - SDS-PAGE followed by Coomassie Brilliant Blue staining. Right - Western Blot analysis, Figure S3: EPR spectra of FXN mutants in the absence (dark red) and in the presence of (SOD2)₄ at a 1:0.5 (red) and 1:1 (orange) molar ratio, Figure S4: EPR spectra of FXN mutants in the absence (black) and in the presence (red) of Fe³⁺, Figure S5: EPR spectra of FXN mutants with Fe³⁺ in the absence (black) and in the presence (orange) of SOD2, Figure S6: Molecular Dynamics simulation, Table S1: The primer sequences for FXN mutants S202C and H177C.

Author Contributions: Conceptualization, M.B.; software, M.B. and J.S.; investigation, M.M., D.D. and M.B.; writing—original draft preparation, M.B. and D.D.; writing—review and editing, all authors; supervision, D.C. and P.C.; funding acquisition, M.B., D.C. and P.C. All authors have read and agreed to the published version of the manuscript.

Funding: This work was supported by the following grants: P-DiSC#02BIRD2020-UNIPD, awarded to M.B. by the Department of Chemistry, University of Padova; PRID 2020, awarded to P.C. by the Department of Biology, University of Padova; and the Iniziativa di Cooperazione Universitaria-2019, University of Padova, awarded to P.C.

Institutional Review Board Statement: Not applicable.

Informed Consent Statement: Not applicable.

Data Availability Statement: The data presented in this study are available on request from the corresponding author.

Acknowledgments: Fluorescence measurements were performed with an Edinburgh FLS 1000 UV/Vis/NIR photoluminescence spectrometer, funded by the MIUR—“Dipartimenti di Eccellenza” through a NExUS grant.

Conflicts of Interest: The authors declare no conflict of interest.

References

1. Campuzano, V.; Montermini, L.; Molto, M.D.; Pianese, L.; Cossee, M.; Cavalcanti, F.; Monros, E.; Rodius, F.; Duclos, F.; Monticelli, A.; et al. Friedreich's Ataxia: Autosomal Recessive Disease Caused by an Intronic GAA Triplet Repeat Expansion. *Science* **1996**, *271*, 1423–1427. [[CrossRef](#)] [[PubMed](#)]
2. Galea, C.A.; Huq, A.; Lockhart, P.J.; Tai, G.; Corben, L.A.; Yiu, E.M.; Gurrin, L.C.; Lynch, D.R.; Gelbard, S.; Durr, A.; et al. Compound heterozygous FXN mutations and clinical outcome in friedreich ataxia. *Ann. Neurol.* **2016**, *79*, 485–495. [[CrossRef](#)] [[PubMed](#)]
3. De Castro, M.; García-Planells, J.; Monrós, E.; Cañizares, J.; Vázquez-Manrique, R.; Vílchez, J.J.; Urtasun, M.; Lucas, M.; Navarro, G.; Izquierdo, G.; et al. Genotype and phenotype analysis of Friedreich's ataxia compound heterozygous patients. *Hum. Genet.* **2000**, *106*, 86–92. [[CrossRef](#)] [[PubMed](#)]
4. Gellera, C.; Castellotti, B.; Mariotti, C.; Mineri, R.; Seveso, V.; DiDonato, S.; Taroni, F. Frataxin gene point mutations in Italian Friedreich ataxia patients. *Neurogenetics* **2007**, *8*, 289–299. [[CrossRef](#)]
5. Chiabrando, D.; Bertino, F.; Tolosano, E. Hereditary ataxia: A focus on heme metabolism and fe-s cluster biogenesis. *Int. J. Mol. Sci.* **2020**, *21*, 3760. [[CrossRef](#)]
6. Rötig, A.; de Lonlay, P.; Chretien, D.; Foury, F.; Koenig, M.; Sidi, D.; Munnich, A.; Rustin, P. Aconitase and mitochondrial iron-sulphur protein deficiency in Friedreich ataxia. *Nat. Genet.* **1997**, *17*, 215–217. [[CrossRef](#)]
7. Puccio, H.; Simon, D.; Cossée, M.; Criqui-Filipe, P.; Tiziano, F.; Melki, J.; Hindelang, C.; Matyas, R.; Rustin, P.; Koenig, M. Mouse models for Friedreich ataxia exhibit cardiomyopathy, sensory nerve defect and Fe-S enzyme deficiency followed by intramitochondrial iron deposits. *Nat. Genet.* **2001**, *27*, 181–186. [[CrossRef](#)]
8. Schulz, J.B.; Dehmer, T.; Schols, L.; Mende, H.; Hardt, C.; Vorgerd, M.; Burk, K.; Matson, W.; Dichgans, J.; Beal, M.F. Oxidative stress in patients with Friedreich ataxia. *Neurology* **2000**, *55*, 1719–1721. [[CrossRef](#)]
9. Koutnikova, H.; Campuzano, V.; Koenig, M. Maturation of wild-type and mutated frataxin by the mitochondrial processing peptidase. *Hum. Mol. Genet.* **1998**, *7*, 1485–1489. [[CrossRef](#)]
10. Condò, I.; Ventura, N.; Malisan, F.; Rufini, A.; Tomassini, B.; Testi, R. In vivo maturation of human frataxin. *Hum. Mol. Genet.* **2007**, *16*, 1534–1540. [[CrossRef](#)]

11. Schmucker, S.; Argentini, M.; Carelle-Calmels, N.; Martelli, A.; Puccio, H. The in vivo mitochondrial two-step maturation of human frataxin. *Hum. Mol. Genet.* **2008**, *17*, 3521–3531. [[CrossRef](#)]
12. Huynen, M.A.; Snel, B.; Bork, P.; Gibson, T.J. The phylogenetic distribution of frataxin indicates a role in iron-sulfur cluster protein assembly. *Hum. Mol. Genet.* **2001**, *10*, 2463–2468. [[CrossRef](#)]
13. Musco, G.; Stier, G.; Kolmerer, B.; Adinolfi, S.; Martin, S.; Frenkiel, T.; Gibson, T.; Pastore, A. Towards a structural understanding of Friedreich's ataxia: Solution structure of frataxin. *Structure* **2000**, *8*, 695–707. [[CrossRef](#)]
14. Gentry, L.E.; Thacker, M.A.; Doughty, R.; Timkovich, R.; Busenlehner, L.S. His86 from the N-terminus of frataxin coordinates iron and is required for Fe-S cluster synthesis. *Biochemistry* **2013**, *52*, 6085–6096. [[CrossRef](#)]
15. Sirano, D.P.; Shigeta, R.; Chi, Y.I.; Ristow, M.; Shoelson, S.E. Crystal structure of human frataxin. *J. Biol. Chem.* **2000**, *275*, 30753–30756. [[CrossRef](#)]
16. Fox, N.G.; Yu, X.; Feng, X.; Bailey, H.J.; Martelli, A.; Nabhan, J.F.; Strain-Damerell, C.; Bulawa, C.; Yue, W.W.; Han, S. Structure of the human frataxin-bound iron-sulfur cluster assembly complex provides insight into its activation mechanism. *Nat. Commun.* **2019**, *10*, 1–8. [[CrossRef](#)]
17. Patraa, S.; Barondeau, D.P. Mechanism of activation of the human cysteine desulfurase complex by frataxin. *Proc. Natl. Acad. Sci. USA* **2019**, *116*, 19421–19430. [[CrossRef](#)]
18. Gervason, S.; Larkem, D.; Mansour, A.B.; Botzanowski, T.; Müller, C.S.; Pecqueur, L.; Le Pavec, G.; Delaunay-Moisan, A.; Brun, O.; Agramunt, J.; et al. Physiologically relevant reconstitution of iron-sulfur cluster biosynthesis uncovers persulfide-processing functions of ferredoxin-2 and frataxin. *Nat. Commun.* **2019**, *10*, 1–12. [[CrossRef](#)]
19. Srour, B.; Gervason, S.; Monfort, B.; D'Autréaux, B. Mechanism of Iron–Sulfur Cluster Assembly: In the Intimacy of Iron and Sulfur Encounter. *Inorganics* **2020**, *8*, 55. [[CrossRef](#)]
20. Campbell, C.J.; Pall, A.E.; Naik, A.R.; Thompson, L.N.; Stemmler, T.L. Molecular Details of the Frataxin–Scaffold Interaction during Mitochondrial Fe–S Cluster Assembly. *Int. J. Mol. Sci.* **2021**, *22*, 6006. [[CrossRef](#)]
21. Alsina, D.; Purroy, R.; Ros, J.; Tamarit, J. Iron in friedreich ataxia: A central role in the pathophysiology or an epiphenomenon? *Pharmaceuticals* **2018**, *11*, 89. [[CrossRef](#)] [[PubMed](#)]
22. Du, J.; Zhou, Y.; Li, Y.; Xia, J.; Chen, Y.; Chen, S.; Wang, X.; Sun, W.; Wang, T.; Ren, X.; et al. Identification of Frataxin as a regulator of ferroptosis. *Redox Biol.* **2020**, *32*. [[CrossRef](#)] [[PubMed](#)]
23. Grazia Cotticelli, M.; Xia, S.; Lin, D.; Lee, T.; Terrab, L.; Wipf, P.; Huryn, D.M.; Wilson, R.B. Ferroptosis as a novel therapeutic target for Friedreich's ataxia. *J. Pharmacol. Exp. Ther.* **2019**, *369*, 47–54. [[CrossRef](#)] [[PubMed](#)]
24. Stockwell, B.R.; Jiang, X. The Chemistry and Biology of Ferroptosis. *Cell Chem. Biol.* **2020**, *27*, 365–375. [[CrossRef](#)] [[PubMed](#)]
25. Vázquez-Manrique, R.P.; González-Cabo, P.; Ros, S.; Aziz, H.; Baylis, H.A.; Palau, F. Reduction of *Caenorhabditis elegans* frataxin increases sensitivity to oxidative stress, reduces lifespan, and causes lethality in a mitochondrial complex II mutant. *FASEB J.* **2006**, *20*, 172–174. [[CrossRef](#)]
26. Runko, A.P.; Griswold, A.J.; Min, K.-T. Overexpression of frataxin in the mitochondria increases resistance to oxidative stress and extends lifespan in *Drosophila*. *FEBS Lett.* **2008**, *582*, 715–719. [[CrossRef](#)]
27. Busi, M.V.; Maliandi, M.V.; Valdez, H.; Clemente, M.; Zabaleta, E.J.; Araya, A.; Gomez-Casati, D.F. Deficiency of Arabidopsis thaliana frataxin alters activity of mitochondrial Fe-S proteins and induces oxidative stress. *Plant J.* **2006**, *48*, 873–882. [[CrossRef](#)]
28. Uceda, A.B.; Donoso, J.; Frau, J.; Vilanova, B.; Adrover, M. Frataxins Emerge as New Players of the Intracellular Antioxidant Machinery. *Antioxidants* **2021**, *10*, 315. [[CrossRef](#)]
29. Han, T.H.L.; Camadro, J.-M.M.; Barbault, F.; Santos, R.; El Hage Chahine, J.-M.M.; Ha-Duong, N.-T.T. In Vitro interaction between yeast frataxin and superoxide dismutases: Influence of mitochondrial metals. *Biochim. Biophys. Acta-Gen. Subj.* **2019**, *1863*, 883–892. [[CrossRef](#)]
30. Fukai, T.; Ushio-Fukai, M. Superoxide Dismutases: Role in Redox Signaling, Vascular Function, and Diseases. *Antioxid. Redox Signal* **2011**, *15*, 1583–1606. [[CrossRef](#)]
31. Zelko, I.N.; Mariani, T.J.; Folz, R.J. Superoxide dismutase multigene family: A comparison of the CuZn-SOD (SOD1), Mn-SOD (SOD2), and EC-SOD (SOD3) gene structures, evolution, and expression. *Free Radic. Biol. Med.* **2002**, *33*, 337–349. [[CrossRef](#)]
32. Doni, D.; Passerini, L.; Audran, G.; Marque, S.R.A.; Schulz, M.; Santos, J.; Costantini, P.; Bortolus, M.; Carbonera, D. Effects of Fe²⁺/Fe³⁺ Binding to Human Frataxin and Its D122Y Variant, as Revealed by Site-Directed Spin Labeling (SDSL) EPR Complemented by Fluorescence and Circular Dichroism Spectroscopies. *Int. J. Mol. Sci.* **2020**, *21*, 9619. [[CrossRef](#)]
33. Roman, E.A.; Faraj, S.E.; Gallo, M.; Salvay, A.G.; Ferreiro, D.U.; Santos, J. Protein Stability and Dynamics Modulation: The Case of Human Frataxin. *PLoS ONE* **2012**, *7*, e45743. [[CrossRef](#)]
34. Budil, D.E.; Sanghyuk, L.; Saxena, S.; Freed, J.H. Nonlinear-least-squares analysis of slow-motion EPR spectra in one and two dimensions using a modified levenberg-marquardt algorithm. *J. Magn. Reson.-Ser. A* **1996**, *120*, 155–189. [[CrossRef](#)]
35. MultiComponent. Available online: <http://www.biochemistry.ucla.edu/Faculty/Hubbell/> (accessed on 23 November 2021).
36. Kozakov, D.; Hall, D.R.; Xia, B.; Porter, K.A.; Padhorney, D.; Yueh, C.; Beglov, D.; Vajda, S. The ClusPro web server for protein-protein docking. *Nat. Protoc.* **2017**, *12*, 255–278. [[CrossRef](#)]
37. Pierce, B.G.; Wiehe, K.; Hwang, H.; Kim, B.H.; Vreven, T.; Weng, Z. ZDOCK server: Interactive docking prediction of protein-protein complexes and symmetric multimers. *Bioinformatics* **2014**, *30*, 1771–1773. [[CrossRef](#)]
38. Tovchigrechko, A.; Vakser, I.A. GRAMM-X public web server for protein-protein docking. *Nucleic Acids Res.* **2006**, *34*, W310–W314. [[CrossRef](#)]

39. Schneidman-Duhovny, D.; Inbar, Y.; Nussinov, R.; Wolfson, H.J. PatchDock and SymmDock: Servers for rigid and symmetric docking. *Nucleic Acids Res.* **2005**, *33*, 363–367. [[CrossRef](#)]
40. Andrusier, N.; Nussinov, R.; Wolfson, H.J. FireDock: Fast interaction refinement in molecular docking. *Proteins Struct. Funct. Genet.* **2007**, *69*, 139–159. [[CrossRef](#)]
41. Chermak, E.; Petta, A.; Serra, L.; Vangone, A.; Scarano, V.; Cavallo, L.; Oliva, R. CONSRANK: A server for the analysis, comparison and ranking of docking models based on inter-residue contacts. *Bioinformatics* **2015**, *31*, 1481–1483. [[CrossRef](#)]
42. Oliva, R.; Vangone, A.; Cavallo, L. Ranking multiple docking solutions based on the conservation of inter-residue contacts. *Proteins Struct. Funct. Bioinforma.* **2013**, *81*, 1571–1584. [[CrossRef](#)] [[PubMed](#)]
43. Vangone, A.; Cavallo, L.; Oliva, R. Using a consensus approach based on the conservation of inter-residue contacts to rank CAPRI models. *Proteins Struct. Funct. Bioinforma.* **2013**, *81*, 2210–2220. [[CrossRef](#)] [[PubMed](#)]
44. Pettersen, E.F.; Goddard, T.D.; Huang, C.C.; Couch, G.S.; Greenblatt, D.M.; Meng, E.C.; Ferrin, T.E. UCSF Chimera - A visualization system for exploratory research and analysis. *J. Comput. Chem.* **2004**, *25*, 1605–1612. [[CrossRef](#)] [[PubMed](#)]
45. Land, H.; Humble, M.S. YASARA: A Tool to Obtain Structural Guidance in Biocatalytic Investigations. In *Protein Engineering. Methods in Molecular Biology*; Bornscheuer, U., Höhne, M., Eds.; Humana Press: New York, NY, USA, 2018; Volume 1685, pp. 43–67. ISBN 978-1-4939-7366-8.
46. Maier, J.A.; Martinez, C.; Kasavajhala, K.; Wickstrom, L.; Hauser, K.E.; Simmerling, C. ff14SB: Improving the Accuracy of Protein Side Chain and Backbone Parameters from ff99SB. *J. Chem. Theory Comput.* **2015**, *11*, 3696–3713. [[CrossRef](#)]
47. Bellanda, M.; Maso, L.; Doni, D.; Bortolus, M.; De Rosa, E.; Lunardi, F.; Alfonsi, A.; Noguera, M.E.; Herrera, M.G.; Santos, J.; et al. Exploring iron-binding to human frataxin and to selected Friedreich ataxia mutants by means of NMR and EPR spectroscopies. *Biochim. Biophys. Acta-Proteins Proteom.* **2019**, *1867*, 140254. [[CrossRef](#)]
48. Huang, J.; Dizin, E.; Cowan, J.A. Mapping iron binding sites on human frataxin: Implications for cluster assembly on the ISU Fe-S cluster scaffold protein. *J. Biol. Inorg. Chem.* **2008**, *13*, 825–836. [[CrossRef](#)]
49. Azadmanesh, J.; Trickel, S.R.; Borgstahl, G.E.O. Substrate-analog binding and electrostatic surfaces of human manganese superoxide dismutase. *J. Struct. Biol.* **2017**, *199*, 68–75. [[CrossRef](#)]
50. Doni, D.; Rigoni, G.; Palumbo, E.; Baschiera, E.; Peruzzo, R.; De Rosa, E.; Caicci, F.; Passerini, L.; Bettio, D.; Russo, A.; et al. The displacement of frataxin from the mitochondrial cristae correlates with abnormal respiratory supercomplexes formation and bioenergetic defects in cells of Friedreich ataxia patients. *FASEB J.* **2021**, *35*, e21362. [[CrossRef](#)]
51. Gong, H.; Li, J.; Xu, A.; Tang, Y.; Ji, W.; Gao, R.; Wang, S.; Yu, L.; Tian, C.; Li, J.; et al. An electron transfer path connects subunits of a mycobacterial respiratory supercomplex. *Science* **2018**, *362*, eaat8923. [[CrossRef](#)]
52. Suthammarak, W.; Somerlot, B.H.; Opheim, E.; Sedensky, M.; Morgan, P.G. Novel interactions between mitochondrial superoxide dismutases and the electron transport chain. *Aging Cell* **2013**, *12*, 1132–1140. [[CrossRef](#)]
53. Jiralerspong, S.; Ge, B.; Hudson, T.J.; Pandolfo, M. Manganese superoxide dismutase induction by iron is impaired in Friedreich ataxia cells. *FEBS Lett.* **2001**, *509*, 101–105. [[CrossRef](#)]
54. Chantrel-Groussard, K. Disabled early recruitment of antioxidant defenses in Friedreich's ataxia. *Hum. Mol. Genet.* **2001**, *10*, 2061–2067. [[CrossRef](#)]
55. Irazusta, V.; Cabisco, E.; Reverter-Branchat, G.; Ros, J.; Tamarit, J. Manganese Is the Link between Frataxin and Iron-Sulfur Deficiency in the Yeast Model of Friedreich Ataxia. *J. Biol. Chem.* **2006**, *281*, 12227–12232. [[CrossRef](#)]
56. Yang, M.; Cobine, P.A.; Molik, S.; Naranuntarat, A.; Lill, R.; Winge, D.R.; Culotta, V.C. The effects of mitochondrial iron homeostasis on cofactor specificity of superoxide dismutase 2. *EMBO J.* **2006**, *25*, 1775–1783. [[CrossRef](#)]
57. Irazusta, V.; Obis, E.; Moreno-Cermeño, A.; Cabisco, E.; Ros, J.; Tamarit, J. Yeast frataxin mutants display decreased superoxide dismutase activity crucial to promote protein oxidative damage. *Free Radic. Biol. Med.* **2010**, *48*, 411–420. [[CrossRef](#)]

Supporting Information

for

A combined spectroscopic and *in silico* approach to evaluate the interaction of human frataxin with mitochondrial superoxide dismutase

Davide Doni¹, Marta Meggiolaro^{1,2}, Javier Santos^{3,4}, Gérard Audran⁵, Sylvain R. A. Marque⁵, Paola Costantini¹, Marco Bortolus^{2*}, and Donatella Carbonera²

¹Department of Biology, University of Padova, Viale G. Colombo 3, 35131 Padova, Italy

²Department of Chemical Sciences, University of Padova, Via F. Marzolo 1, 35131 Padova, Italy

³Instituto de Biociencias, Biotecnología y Biomedicina (iB3-UBA). Departamento de Química Biológica, Facultad de Ciencia Exactas y Naturales, Universidad de Buenos Aires. Intendente Güiraldes 2160 - Ciudad Universitaria, 1428EGA CONICET, Godoy Cruz 2290, C1425FQB. C.A.B.A. Argentina

⁴Instituto de Química y Fisicoquímica Biológicas, Dr. Alejandro Paladini, Universidad de Buenos Aires, CONICET, Junín 956, 1113AAD C.A.B.A., Argentina

⁵Aix Marseille Université, CNRS, ICR, UMR 7273, case 551, Ave Escadrille Normandie Niemen, 13397 Marseille Cedex 20, France

*to whom correspondence should be addressed: marco.bortolus@unipd.it

1) *Mutagenesis primers for FXN H177C and S202C*

In Table S1 below, we report the primer sequences for FXN mutants S202C and H177C used in this study for SDSL.

Table S1: The primer sequences for FXN mutants S202C and H177C.

<u>FXN mutant</u>	<u>Primer name</u>	<u>Primer sequence</u>
FXN_H177C	FXN_H177C_for	5' - GGTGTACTCCT <u>GCG</u> ACGGCGTGT - 3'
	FXN_H177C_rev	5' - CAGTTTTTCCCAGTCCAGTC - 3'
FXN_S202C	FXN_S202C_for	5' - GGACTTGTCTT <u>GCT</u> TGGCCTATT - 3'
	FXN_S202C_rev	5' - AGTTTGGTTTTTAAGGCTTTAGTG - 3'

2) FXN expression and purification

In the Figure S1 below, we report a SDS-PAGE gel showing the different steps of expression and purification of recombinant human FXN₉₀₋₂₁₀. FXN mutants for SDSL have been expressed and purified with the same procedure.

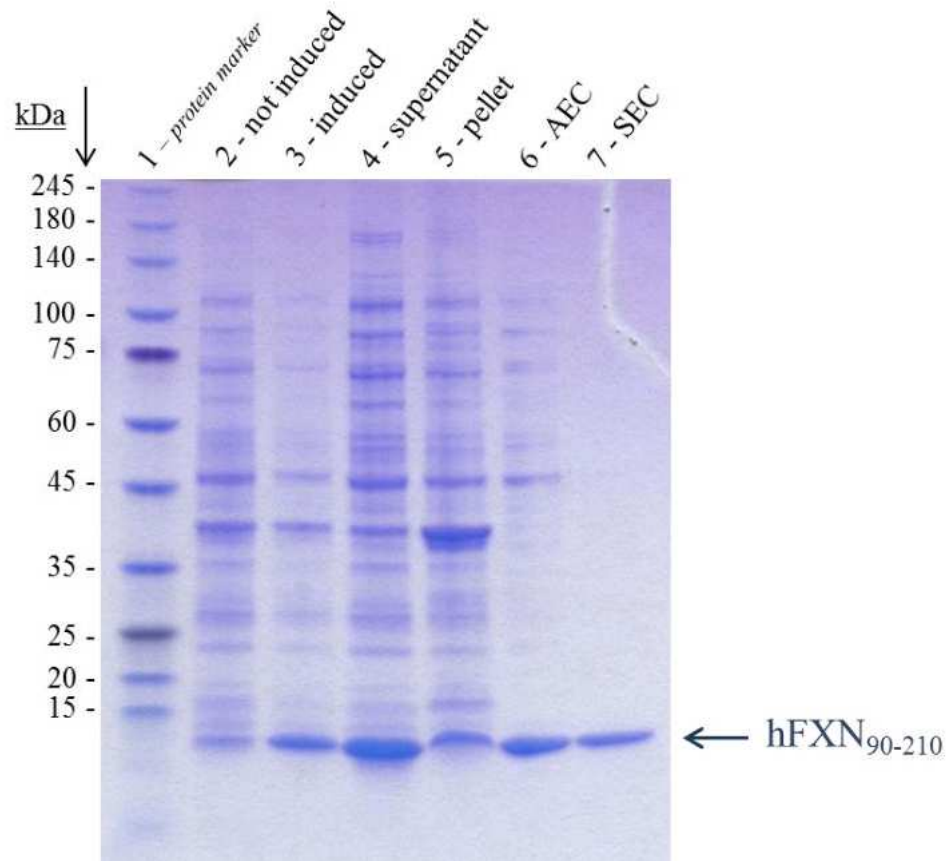


Figure S1. SDS-PAGE followed by Coomassie Brilliant Blue staining for the expression and purification steps of recombinant human FXN₉₀₋₂₁₀. Lane (1): molecular weight protein ladder. Lanes (2) and (3) correspond to the bacterial culture before and after the induction with IPTG, respectively. Lane (4) and (5) represent the soluble and insoluble fraction of the total cellular lysate. Lane (6) corresponds to the protein pool after the first purification step performed by anionic exchange chromatography (AEC). Lane (7) corresponds to the protein pool after the second purification step performed by size exclusion chromatography (SEC).

3) SOD2 purity and identity control

In Figure S2 below, we report the SDS-PAGE gel and relative Western Blot analysis of recombinant human SOD2 performed to verify the purity and identity of SOD2 used in EPR and fluorescence spectroscopy experiments. The SDS-PAGE gel shows that recombinant SOD2 is present in high purity, and the Western Blot confirmed the identity of the protein.

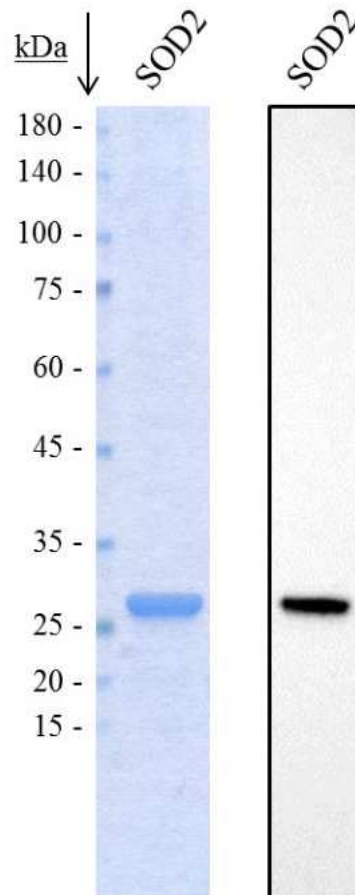


Figure S2. Left - SDS-PAGE followed by Coomassie Brilliant Blue staining. Right - Western Blot analysis.

4) FXN:SOD2 experiments at different ratios

The effects of two different ratio of FXN:SOD2 on the mobility of the spin labels of FXN mutants are reported in Figure S3. FXN and SOD2 have been mixed at a 1:0 (dark red), 1:0.5 (red), and 1:1 (orange) ratio. The spectra show a progressive slowdown at all spin label positions, but the spectral shape does not significantly change, a sign that most of the proteins are already involved in the complex.

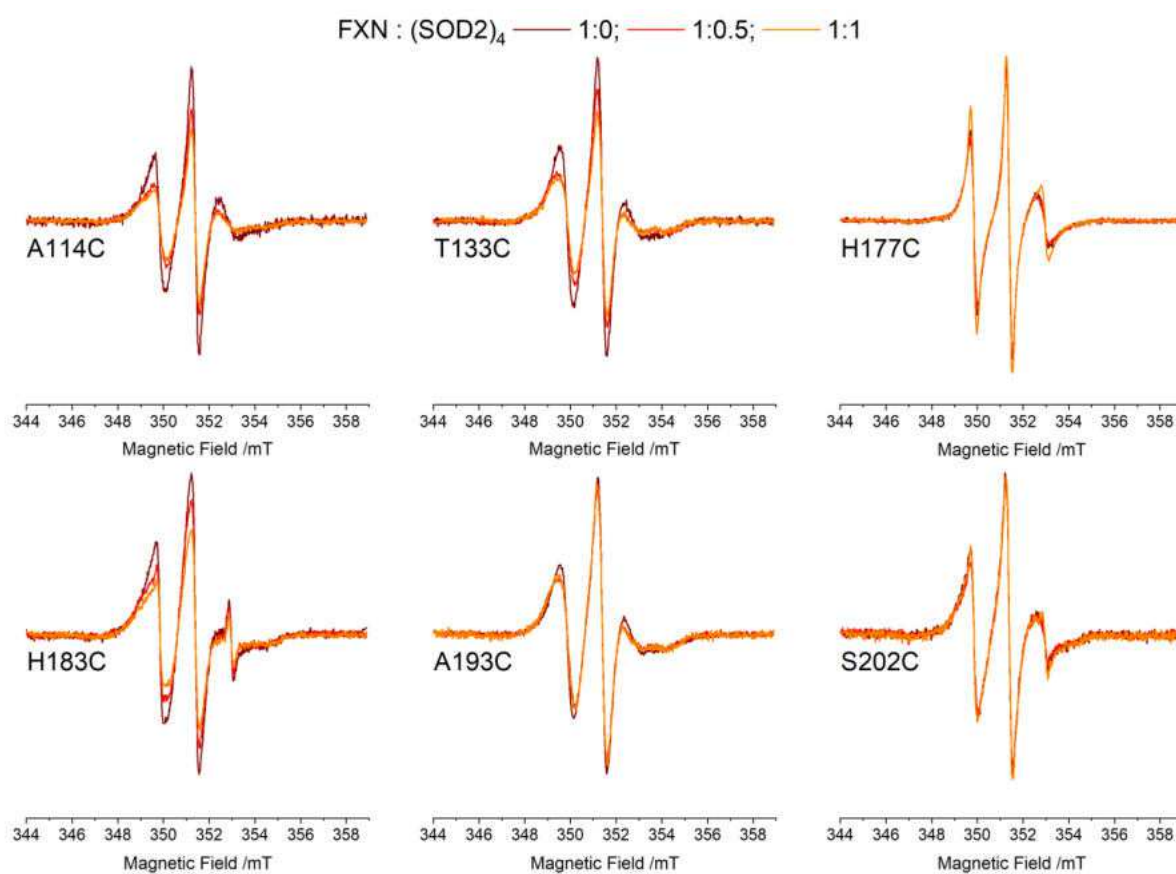


Figure S3. EPR spectra of FXN mutants in the absence (dark red) and in the presence of (SOD2)₄ at a 1:0.5 (red) and 1:1 (orange) molar ratio. All spectra have been normalized to the same number of spins to compare the spectral shape in terms of spin probe mobility.

5) FXN/SOD2 experiments with Fe^{3+}

The effects of Fe^{3+} on FXN in the presence/absence of SOD2 have been evaluated using EPR spectroscopy. Previously, we showed that the addition of excess iron slows down FXN motion by inducing its aggregation at all positions [noi].

Here, we show in Figure S4 that the effects are still present also for the new mutated positions (H177 and S202) with the formation of new slow components on the side wings of the spectra (red spectra).

The effects of Fe^{3+} in the presence of SOD2 are reported in Figure S5. FXN and SOD2 have been mixed, and then Fe^{3+} has been added. The spectra do not change significantly when SOD2 is present (orange spectra).

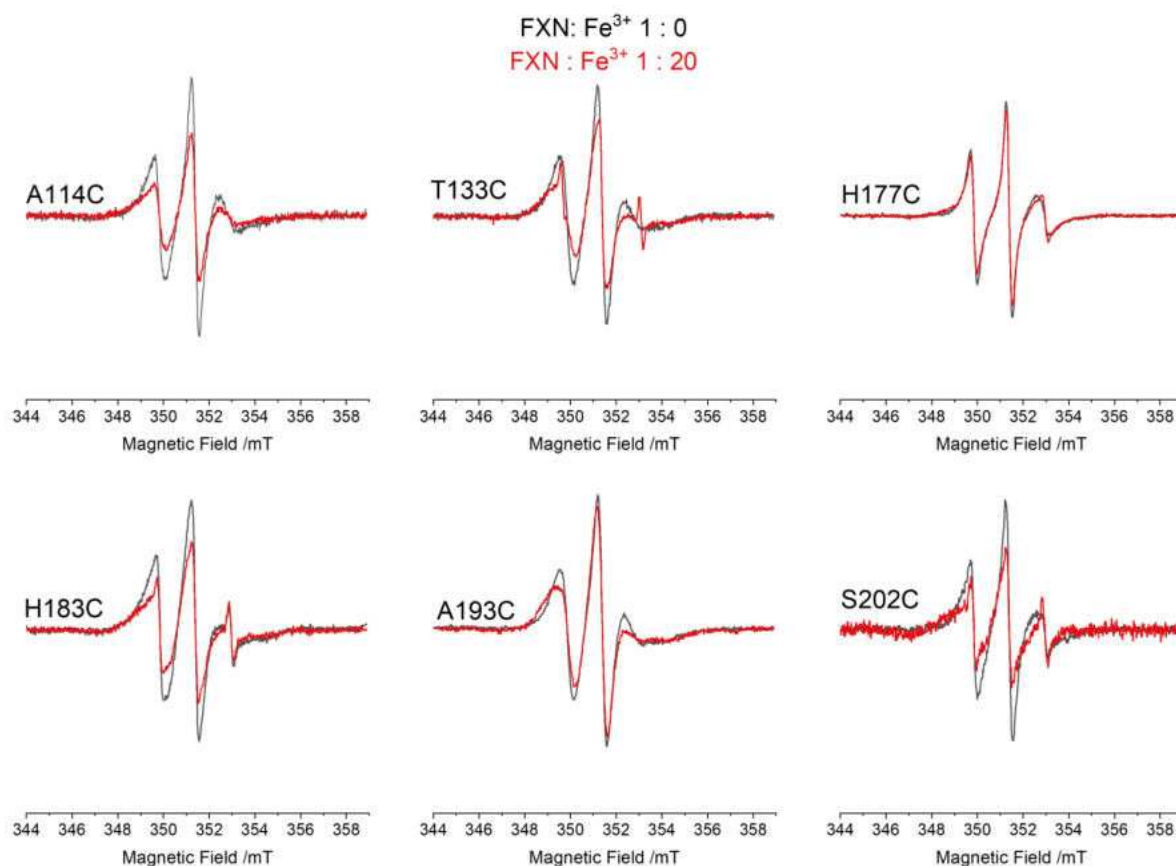


Figure S4. EPR spectra of FXN mutants in the absence (black) and in the presence (red) of Fe^{3+} . $[FXN] = 10 \mu M$; $[Fe^{3+}] = 0/200 \mu M$. All spectra have been normalized to the same number of spins to compare the spectral shape in terms of spin probe mobility.

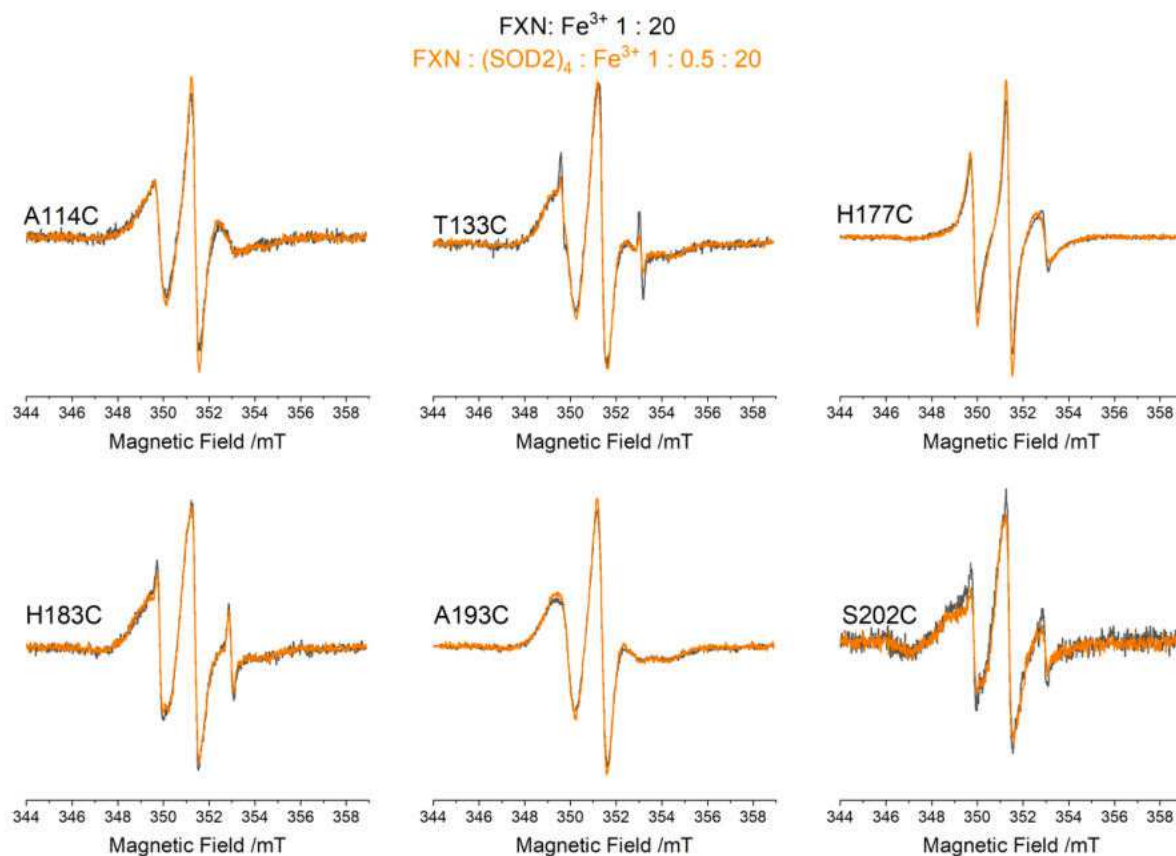


Figure S5. EPR spectra of FXN mutants with Fe³⁺ in the absence (black) and in the presence (orange) of SOD2. [FXN] = 10 μ M; [SOD2] = 0/20 μ M; [Fe³⁺] = 200 μ M. Black, FXN:(SOD2)₄:Fe³⁺ 1:0:20; orange, FXN:(SOD2)₄:Fe³⁺ 1:0.5:20. All spectra have been normalized to the same number of spins to compare the spectral shape in terms of spin probe mobility.

6) Molecular Dynamics simulation

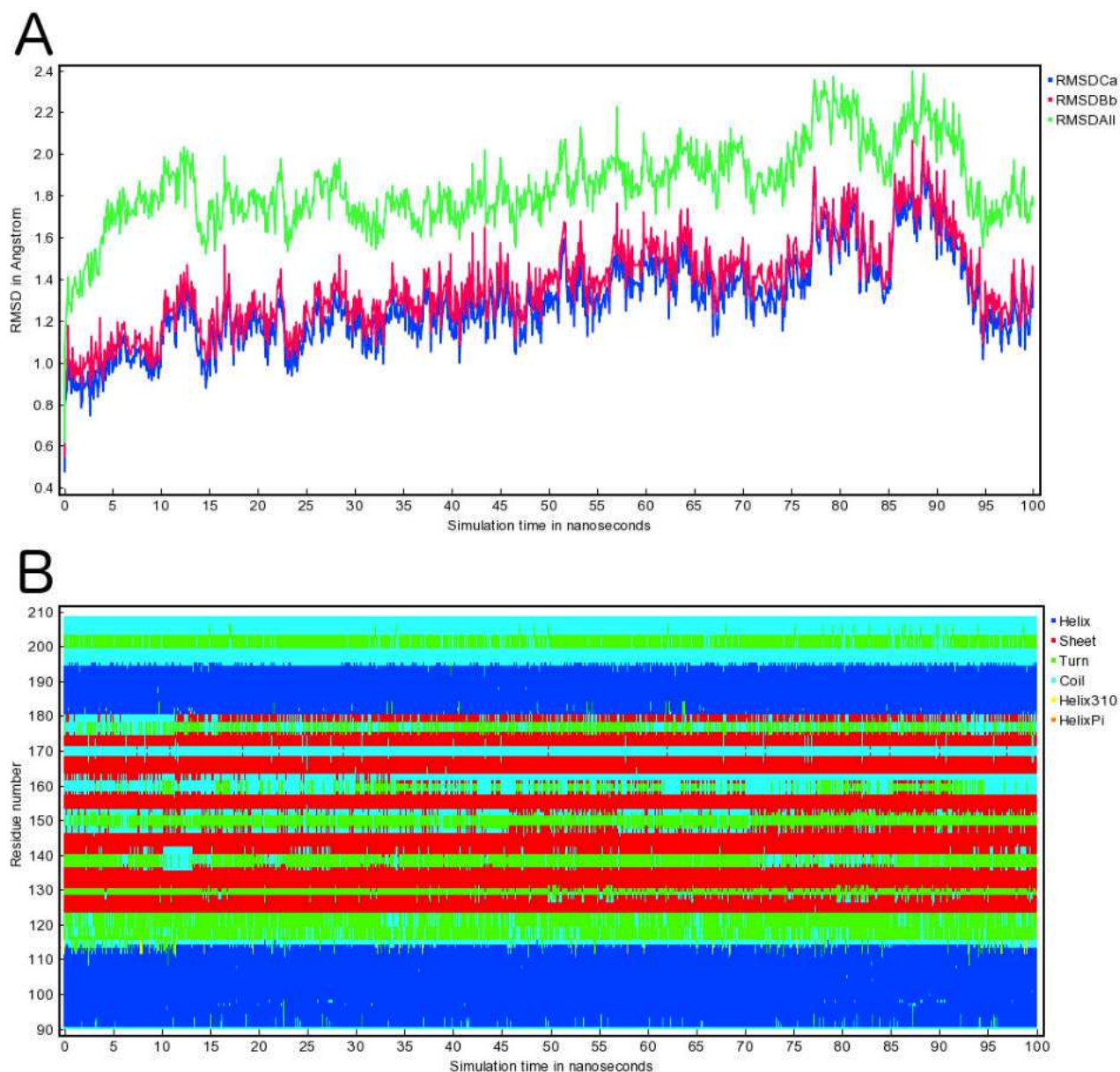


Figure S6. Molecular Dynamics simulation. (A) The root-mean-square deviation (RMSD). The plot shows Calpha (RMSDCa), backbone (RMSDBb) and all-heavy atom (RMSDAII)]. (B) The secondary structure content (B) along the simulation time. The analysis of production runs was carried out using YASARA Structure [1].

[1] H. Land, M.S. Humble, YASARA: A Tool to Obtain Structural Guidance in Biocatalytic Investigations, *Methods Mol Biol* 1685 (2018) 43-67.

Ringraziamenti

A conclusione di questo percorso, desidero ringraziare *in primis* il mio supervisor, la Prof.ssa Paola Costantini, che in questi tre anni di Dottorato mi ha dato la possibilità di lavorare al suo fianco, facendomi avvicinare al mondo della ricerca con passione e dedizione, spronandomi a dare il meglio di me, a crescere “scientificamente”, dedicandomi tempo e ascolto, sostenendomi e aiutandomi in ogni momento attraverso il confronto e il rispetto reciproco. Per questi motivi sono, e gliene sarò, sempre grato.

Desidero ringraziare la Prof.ssa Donatella Carbonera, mia co-supervisor, per avermi incoraggiato ad intraprendere questo percorso, sostenendomi e aiutandomi ogni qualvolta ne avessi bisogno. Non finirò mai di dirLe grazie per aver sempre creduto in me, sin dall’inizio.

Ringrazio il Dott. Marco Bortolus, senza il quale parte del presente lavoro di tesi non sarebbe stato possibile.

Porgo inoltre un sentito ringraziamento al Prof. Leonardo Salviati e al Prof. Luigi Bubacco, per essere stati presenti durante il mio percorso di Dottorato con i loro suggerimenti e le loro critiche costruttive.

Un ringraziamento speciale va al Prof. Javier Santos dell’Università di Buenos Aires e a tutto il suo team, per avermi dato l’opportunità di svolgere parte della mia attività di ricerca presso il loro laboratorio, accogliendomi e facendomi sentire parte del loro gruppo. Porterò sempre nel cuore questa esperienza e la ricorderò come una tra le più gratificanti della mia vita.

Un sincero ringraziamento lo rivolgo a tutte le persone che, in piccolo o in grande, mi hanno aiutato per la realizzazione del presente lavoro di tesi.

Infine, ma di certo non per importanza, desidero ringraziare la mia famiglia e in particolare i miei genitori, che mi hanno sempre sostenuto e hanno sempre rispettato le mie decisioni, credendo in me, incoraggiandomi ad essere sempre me stesso e a perseguire le mie idee e le mie ambizioni, e senza i quali non sarei arrivato a questo importante traguardo.